THE HYDROTHERMAL ALTERATION OF KIMBERLITE

by

Ian Mark James Hodgson

LIBRARY
MIN. RES. ENG. DEPT.
IMPERIAL COLLEGE
LONDON SW7 2BP

Thesis submitted for the degree of
Doctor of Philosophy
and the
Diploma of Imperial College

Department of Mineral Resources Engineering
Imperial College of Science and Technology
LONDON SW7 2BP

December 1981

I:M.J. HODGSON

THE HYDROTHERMAL ALTERATION OF KIMBERLITE

ABSTRACT

A review of kimberlite processing and kimberlite geology has been carried out with particular emphasis on alteration processes and diamond liberation. It was seen that although kimberlitic minerals alter readily, little use is made of this in conventional processing plants, despite the tendency of large diamonds to break during ordinary comminution.

The nature and extent of alteration of a kimberlite sample from the Wesselton Mine has been studied using X-ray diffraction, infra-red spectroscopy, atomic absorption spectroscopy, scanning electron microscopy and thermal techniques. Residual head mineral assays for olivine and serpentine have been estimated (to ± 5% relative) using a new X-ray diffraction method. Clay phase proportions were estimated semi-quantitatively from a new computerised elemental mass balance procedure.

By reacting carefully prepared samples in acidic, aluminium-rich chloride media (0.3-1.5M H^+, 0.1-0.4M Al^{3+}) at elevated temperatures (70-350°C) over 1-24 h, the kimberlite was altered to form phyllosilicates. The main product phases were chlorites, vermiculites, smectites, kaolinites and serpentine together with amorphous hydroxy-oxides. Data was collected in the form of semi-quantitative

predominance phase diagrams showing the interrelation of the phases under the different conditions employed. Adequate correlation was obtained with similar diagrams derived on theoretical grounds.

From a study of the time dependence of the reactions a general mechanism of alteration has been proposed. This mechanism is complicated by the effects of localised ion concentrations due to reactions taking place in cavities and at solid/solution interfaces. Overall, alteration proceeded according to a diffusion-controlled shrinking core model and appropriate rate equations have been proposed.

New bench scale semi-continuous alteration equipment has been constructed, and is capable of degrading 92% of a 25 g -6.18+3.18 mm charge to -600 μm within 8 h at 100°C under conditions of simultaneous attrition. This treatment was more effective than long term reactions at room temperature. The advantages and limitations of the process have been considered and it is concluded that further work should be undertaken.

ACKNOWLEDGEMENTS

I would like to thank the following people who have helped me during the course of this project :

Firstly, my supervisor, Dr A.W.L. Dudeney, for his constructive criticism in the interpretation of experimental data and the preparation of the final text.

Secondly, Mr R. Shaw, Mr D. Shillam and Mr R. Curtis for their advice and assistance with respect to methods of mineralogical analysis.

Thirdly, Miss A. Rutledge for her careful typing of the final script.

Finally, the academic and technical staff of the Department of Mineral Technology for their assistance and active encouragement throughout the three years.

Special thanks go to Mr J.A. Hodgson for many of the photographs included in the thesis.

To Rio Tinto Zinc I am indebted for the financial support which formed the Bursary awarded to me in 1978. My appreciation is recorded. I should also like to thank De Beers Diamond Consolidated Mines Ltd, especially Mr T.J. Napier-Munn, for providing temporary research facilities in South Africa and for arranging visits to Premier and Finsch Mines.

CONTENTS

		Page
ABSTRACT		i
ACKNOWLEDGEMENTS		iii
TABLE OF CONTENTS		iv
LIST OF PLATES		viii
LIST OF FIGURES		ix
LIST OF TABLES		xix
CHAPTER 1	LITERATURE SURVEY	
1.1	Introduction	1
1.2	Kimberlite Geology and Processing	4
1.2.1	Origin and location of diamondiferous ores	4
1.2.2	Kimberlite processing	6
1.2.3	Petrology of kimberlite	12
1.3	Degradation of Kimberlite Minerals	16
1.3.1	Natural alteration of olivine	20
1.3.2	Laboratory alteration of olivine	23
1.3.3	Natural alteration of serpentine	26
1.3.4	Laboratory alteration of serpentine	27
1.3.5	Alteration of pyroxene-amphibole group minerals	28
1.3.6	Other alterations	30
1.4	Synthesis of Clay Minerals	31
1.4.1	Synthesis of 1:1 layer (7 Å) minerals	34
1.4.2	Synthesis of 2:1 layer (10-16 Å) minerals	44
1.5	Discussion	50
CHAPTER 2	ANALYTICAL METHODS	
2.1	Introduction	52
2.2	Sampling and Preliminary Analysis of the Kimberlite	52
2.2.1	Sampling and sample preparation	52
2.2.2	Mineral analysis	55
2.2.3	Analytical requirements	64
2.3	X-ray Diffraction	67
2.3.1	Principles	67
2.3.2	Qualitative methods	69
2.3.3	Quantitative methods	73
2.3.4	Error sources and their correction	76
2.3.5	Olivine and serpentine quantitative analysis : assumptions on which the method is based	77

	2.3.6	Extraction of olivine and serpentine standards	78
	2.3.7	Formulation of sample mixture for analysis	85
	2.3.8	Size calibration	88
	2.3.9	Concentration calibration	96
	2.3.10	Error correction and final form	99
2.4		Other Analytical Methods	103
	2.4.1	Thermal analysis	103
	2.4.2	Infra-red spectroscopy	106
	2.4.3	Chemical analysis	107
2.5		Quantitative Estimation of Clay Minerals	111
	2.5.1	Applications of mass balances to quantitative analysis	111
	2.5.2	Outline of the revised method of clay analysis	115
	2.5.3	Development of the trial program and inter-elemental concentration relationships	116
	2.5.4	Development of the final program : extensions to the original EM form	125
	2.5.5	Estimation of the uncertainties in clay mineral proportions obtained	129
2.6		Discussion	139
CHAPTER 3		ALTERATION OF KIMBERLITE : PHASE DIAGRAMS	
3.1		Introduction	143
3.2		Reactions with 1-9M Sulphuric Acid at 70°C	144
	3.2.1	Apparatus and procedures	144
	3.2.2	Results and discussion	145
3.3		Reactions with 0.0001-1.5M Mineral Acids at 70 and 100°C	156
	3.3.1	Apparatus and procedures	156
	3.3.2	Results of reactions in the presence/ absence of the Al^{3+} ion	158
	3.3.3	Results of reactions in the presence of ions additional to the Al^{3+}, H^{+} species	168
	3.3.4	Results and discussion : Mass balances	173
	3.3.5	Results : Phase diagrams in the Al^{3+}-H^{+} system I. Initial hydrochloric acid concentration 0.3l and 1.5M at 100°C	178
	3.3.6	Scanning electron photomicrographs	189
3.4		Reactions with 0.3lM Hydrochloric Acid at 100-350°C	201
	3.4.1	Apparatus and procedures	201
	3.4.2	Results : Phase diagrams in the Al^{3+}-H^{+} system II. Initial acid concentration 0.3lM at 100-350°C	203
3.5		Discussion : Comparison of Experimental Results with Theoretical Reaction Equilibria and Phase Diagrams	210
	3.5.1	Phase diagrams in the Al^{3+}-H^{+} system III. Reaction equilibria at 100°C	211
	3.5.2	Reaction equilibria at 150-350°C	222
	3.5.3	Phase diagrams in the Al^{3+}-H^{+} system IV. Mineral-solution equilibria at 100°C	224

		3.5.4 Free-energy-temperature relationships for mineral-solution equilibria at 100-300°C	237
CHAPTER 4		ALTERATION OF KIMBERLITE : KINETICS AND MECHANISMS OF REACTIONS IN CHLORIDE MEDIA	
	4.1	Introduction	244
	4.2	Systems Containing 0.45M Al^{3+} and 0.31M H^{+}; 0.22M Al^{3+} and 1.5M H^{+} at 100°C	244
		4.2.1 Procedures	244
		4.2.2 Results : DOA, residual olivine and serpentine proportions and residual solution concentrations	245
		4.2.3 Results : Mass balances	252
		4.2.4 Results and interpretation : Infra-red analyses	256
	4.3	Systems Containing 0.22/0.45M Al^{3+} and 0.31M H^{+} at 215, 260, 300°C	261
		4.3.1 Procedures	261
		4.3.2 Results : DOA and residual solution concentrations	262
		4.3.3 Results : Mass balances	271
		4.3.4 Results and interpretation : Infra-red analyses	273
	4.4	Estimation of Clay Phases Formed at 100-300°C	286
		4.4.1 Results and discussion : Qualitative X-ray diffraction analyses	286
		4.4.2 Computed proportions of phases produced at 100°C	298
		4.4.3 Computed proportions of phases produced at 215, 260 and 300°C	304
	4.5	Discussion : Reaction Mechanisms	317
		4.5.1 Reactions at 100°C	318
		4.5.2 Reactions at 150 and 215°C	320
		4.5.3 Reactions at 260 and 300°C	326
		4.5.4 Overall mineral equilibria : Confirmatory mass balances	332
	4.6	Alteration Reaction Kinetics	335
		4.6.1 Alteration stages and products	335
		4.6.2 Overall rate equations	339
		4.6.3 The rate determining step	352
CHAPTER 5		PRELIMINARY PROCESS DESIGN	
	5.1	Introduction	357
	5.2	Effect of Variation of Al^{3+} and H^{+} Ion Concentrations on Degradation	357
	5.3	Semi-Continuous Alteration of Kimberlite at 100°C	364
		5.3.1 Apparatus and Procedures	364
		5.3.2 Results and discussion : -1180+850 µm feed	371
		5.3.3 Results and discussion : -6.18+3.18 mm feed	376
	5.4	Discussion : Process Design	386
		5.4.1 The semi-continuous alteration process : Optimised conditions	386
		5.4.2 Process considerations	388

APPENDIX 1	CHEMICAL COMPOSITIONS AND MODE OF FORMATION FOR KIMBERLITE MINERALS AND THEIR ALTERATION PRODUCTS	397
APPENDIX 2	FORMULAE USED IN THE EVALUATION OF SAMPLING AND GRAIN COUNTING ERRORS	402
APPENDIX 3	PROGRAM CSDF : ANALYSIS OF COULTER COUNTER DATA	404
APPENDIX 4	DERIVATION OF FINAL EQUATIONS FOR XRD QUANTITATIVE ANALYSIS	409
APPENDIX 5	PROGRAM CECPM : QUANTITATIVE CLAY PHASE ANALYSIS	413
APPENDIX 6	OVERALL MASS BALANCES : DETAIL OF THE PROCEDURES EMPLOYED	427
REFERENCES		433

LIST OF PLATES

		Page
1.1	View of the open pit at Finsch (1979)	3
1.2	Samples of Blue and Yellow Ground as found in the Finsch Open Pit	18
1.3	Sharp contact between the Blue and Yellow Ground at Finsch	18
1.4 and 1.5	Alteration in Premier Type II kimberlite	19
1.6	Model of a 1:1 (7 Å) layer silicate	32
1.7	Model of a 2:1 (9 Å) layer silicate	32
1.8	Model of a 2:1 (14-16 Å) layer silicate	33
2.1-2.8	Photomicrographs of Wesselton kimberlite in thin section	59-62
2.9	Elutriation apparatus employed in olivine/mica and serpentine/mica separations	82
2.10	Detail of the elutriation tubes	83
2.11	Coulter Counter as used in sizing ground samples for quantitative XRD	89
2.12	Stanton "Massflow" Thermobalance	105
3.1-3.19	Scanning electron photomicrographs	191-200
3.20	Autoclave apparatus used for testwork at 100-350°C	202
3.21	Detail of autoclave bomb	202
5.1	Semi-continuous alteration equipment	368
5.2	Stirrer, reaction cartridge and unaltered/altered kimberlite	369

LIST OF FIGURES

		Page
1.2.1	Progressive stages of the formation of a kimberlite pipe	5
1.2.2	Worldwide distribution of kimberlites	7
1.2.3	Generalised flowsheet for diamond recovery	9
1.3.I	Position of the phase boundary between forsterite and serpentine for various investigations in the system $MgO-SiO_2-H_2O$	25
1.4.1	Solubility in relation to pH	35
1.4.2	Sol stability : relation between log (gel time) and pH	35
1.4.3	Schematic representation of relationships among phases in the system $Al_2O_3-H_2O$	38
1.4.4	Phase diagram for minerals in the $Al_2O_3-SiO_2-H_2O$ system	38
1.4.5	Coordination states of aluminium relative to silicon in aluminosilicate synthesis	40
1.4.6	Phase diagram of minerals synthesized at 20°C showing their relationship to initial SiO_2/Al_2O_3 composition and equilibrium pH	42
1.4.7	Relationship between the concentrations of the special Al^{3+}, $Si(OH)_4$, H^+ and the nature of the minerals formed at 20°C, 100 kPa.	42
1.4.8	Effect of system studied and temperature on nature of products synthesized	46
1.4.9	Phase diagram for 7 Å and 14 Å minerals generated in the range 420-600°C in a $MgO-SiO_2-Al_2O_3$ system	49
1.4.10	Formation of mica-montmorillonite from gels	48
1.4.11	Smectite mineral formation as related to initial magnesium content and pH of solution (conditions 30 ppm SiO_2, 3 ppm Al_2O_3, 20°C, 3 months' reaction time)	49

2.2.1	Sampling scheme for kimberlite	54
2.3.1	Principles of X-ray diffraction analysis	68
2.3.2	X-ray diffractograms for a) Wesselton kimberlite b) serpentine c) olivine d) calcite e) phlogopite-mica f) aluminium hydroxyoxides (amorphous)	70-72
2.3.3	Flowsheet for extraction of olivine and serpentine XRD standards	80
2.3.4	Size distributions for ground olivine : Coulter Counter data as indicated by ● with associated regressed lines based on the Gaudin Schumann and Rosin Rammler functions	91
2.3.5	Variation in magnitude of absolute size constant and size modulus with increasing degree of comminution of mineral standards	92
2.3.6	Size calibration for olivine standard : relation between relative peak intensity and absolute size constant (olivine concentration 15%)	94
2.3.7	Size calibration for serpentine standard : relation between relative peak intensity and absolute size constant, serpentine concentration (after correction) 37.2%	95
2.3.8	Concentration calibration for olivine standard	97
2.3.9	Concentration calibration for serpentine standard	98
2.3.10	Error calibration for olivine standard	100
2.3.11	Error calibration for serpentine standard	101
2.5.1	Graphical representation of clay phase proportions using an elemental mass balance approach	114
2.5.2	Relation between the position of the basal (001) layer peak and the number of aluminium ions per unit cell (28 oxygen equivalents) for chlorites	119
2.5.3	Relation between silicon assay and number of silicon ions per unit cell (28 oxygen equivalents) for chlorites	120
2.5.4	Boundary limits for silicon and aluminium assays for chlorite minerals adopted in program	121
2.5.5	Boundary limits for magnesium and iron assays for chlorite minerals adopted in program	122
2.5.6	Distribution of silicon and aluminium assays for montmorillonites	124

2.5.7	Relationship between computed phase concentrations and associated coefficient of variation as attributable to chemical assay error (e_{cv})	132
2.5.8	Frequency distribution chart for computed chlorite concentrations	134
2.5.9	Frequency distribution charge for computed vermiculite concentrations	135
2.5.10	Frequency distribution chart for computed kandite concentrations	136
2.5.11	Frequency distribution chart for computed aluminium hydroxyoxides (gibbsite-boehmite) concentrations	137
2.6.1	Scheme of analytical procedures employed in the testwork	140
3.2.1	Relation between DOA and initial concentration of sulphuric acid for a feed agitated at 70°C, 24 h the feed sizes being -1180+850 µm (A), -6.18 +3.18 mm (B). The effect of various chloride concentrations, for a system involving a 10 g -1180+850 µm feed in a 9M sulphuric acid solution is shown above (c).	146
3.2.2	Relationship between the proportion of total magnesium, iron and calcium reporting to the residual solution and the initial sulphuric acid concentration for 10 g -1180+850 µm feed agitated at 70°C for 24 h.	147
3.2.3	X-ray diffractograms for samples reacted with 4.5M sulphuric acid 70°C, 24 h a) +75 µm fraction b) -75 µm fraction	148
3.2.4	Relationship between DOA and the proportion of magnesium, iron and calcium reporting to the residual solution, and the time of reaction for 10 g -1180+850 µm kimberlite agitated with 40 ml 9M sulphuric acid at 70°C	150
3.2.5	Relationship between the proportion of total magnesium, iron and calcium reporting to the residual solution and the initial sulphuric acid concentration for a 10 g -6.18+3.18 mm feed agitated at 70°C for 24 h	153
3.3.1	Relation between the DOA and the initial hydrochloric/sulphuric acid concentration for a 10 g -1180+850 µm feed agitated/stirred at 70/100°C for 7 h	159

3.3.2	Relation between the proportion of total magnesium and calcium reporting to the residual solution and the initial hydrochloric/ sulphuric acid concentration for a 10 g -1180+ 850 µm feed agitated at 70°C for 7 h	160
3.3.3	Relation between the proportion of total magnesium and calcium reporting to solution and the initial hydrochloric/sulphuric acid concentration for a 10 g -1180+850 µm feed stirred at 100°C for 7 h	161
3.3.4	Relation between the proportion of total magnesium, iron and calcium reporting to solution and the initial nitric acid concentration for a 10 g -1180+850 µm feed stirred at 100°C for 7 h	162
3.3.5	X-ray diffractograms of -1180+850 µm kimberlite reacted with 0.31M sulphuric acid, 100°C, 7 h a) +75 µm fraction b) -75 µm fraction X-ray diffractograms of -1180+850 µm kimberlite reacted with 0.31M hydrochloric acid, 100°C, 7 h c) +75 µm fraction d) -75 µm fraction	164-165
3.3.6	Infra-red recordings for a) kimberlite head b) -75 µm fraction from fraction with 0.31M sulphuric acid at 100°C for 7 h, c) as b; hydrochloric acid used instead	167
3.3.7	a) X-ray diffractogram for the residual -75 µm fraction from reacting 10 g -1180+850 µm kimberlite with 40 ml 0.44M aluminium chloride 0.31M hydrochloric acid at 100°C for 7 h	169
	b) Infra-red trace for the product noted in Figure 3.3.7a	170
	c) Differential thermal analysis of the same product	
3.3.8	Relation between DOA, proportion of total aluminium and magnesium reporting to solution and the initial concentration of aluminium chloride/nitrate for 10 g -1180+850 µm kimberlite reacted with a solution containing 0.31M hydrochloric/nitric acid at 100°C, for 7 h with various aluminium ion concentrations	172
3.3.9	Phase predominance diagram showing the influence of initial aluminium concentration and the pH on the nature of the -75 µm product formed at 100°C 7 h, initial acid concentration being 0.31M	181
3.3.10	Phase predominance diagram showin the influence of initial aluminium concentration and the pH on the nature of the -75 µm product formed at 100°C, 7 h, initial acid concentration being 1.5M	182

3.3.11	X-ray diffractograms of selected -75 µm products as featured in Figure 3.3.9 a) 7.0-7.4 Å aluminium kandites b) mixed layer vermiculite-chlorite with residual mica X-ray diffractograms of selected -75 µm products as featured in Figure 3.3.10 a) 9-11 Å alumino-silicate phases d) mixed layer saponite-vermiculite-chlorite	184 185
3.3.12	Relation between the DOA, proportion of total magnesium, aluminium, iron and calcium reporting to solution and the initial aluminium ion concentration for 10 g -1180+850 µm kimberlite reacted with 1.5M hydrochloric acid at 100°C, 7 h	188
3.4.1	Phase predominance diagram showing the influence of initial aluminium concentration on the nature of the -75 µm product formed after 8 h total reaction time, initial acid concentration being 0.31M	204
3.4.2	X-ray diffractograms for selected -75 µm products as featured in Figure 3.4.1 a) 9-11 Å aluminosilicate b) kaolinite-dickite c) vermiculite-chlorite d) montmorillonite	206 207
3.4.3	Infra-red traces for selected -75 µm products featured in Figure 3.4.1 a) 9-11 Å aluminosilicate b) kaolinite-dickite c) vermiculite-chlorite d) montmorillonite	209
3.5.1	Relation between hydrogen ion requirement/ regeneration and the extent of aluminium substitution in the tetrahedral lattice for phyllosilicates	215
3.5.2	Theoretical relationship between the aluminium and hydrogen ion requirement and the nature of the product formed from the alteration of kimberlite	218
3.5.3	Theoretical mineral-solution phase diagram for kimberlite alteration products at 100°C	234
3.5.4	Free energy of formation-temperature relationships for alteration products of kimberlite	241
4.2.1	Relation between DOA, proportion of calcium entering solution and reaction time for systems A and B	246
4.2.2	Relation between proportion of magnesium and iron entering solution and reaction time for systems A and B	247
4.2.3	Relation between proportion of total aluminium reporting to a solid +75/-75 µm fraction and reaction time for systems A and B	249

4.2.4	Relationship between residual concentrations of olivine and serpentine in the final +75 µm fraction and time of reaction, for system A, the mineral assays being expressed as a percentage of their head values	250
4.2.5	Relationship between residual concentrations of olivine and serpentine in the final +75 µm fraction and time of reaction, for system B, the mineral assays being expressed as a percentage of their head values	251
4.2.6	Elemental mass distributions for the +75 µm, -75 -75 µm and solution phases generated at various reaction times for system A	254
4.2.7	Elemental mass distributions for the +75 µm, -75 µm and solution phases generated at various reaction times for system B	255
4.2.8	Infra-red spectrograms for -75 µm products obtained from system A reacted at 100°C for a) 5h; b) 6 h; c) 7 h; d) 14 h; e) 20 h; f) 24 h	257
4.2.9	Infra-red spectrograms for -75 µm products obtained from system B reacted at 100°C for a) 2 h; b) 4 h; c) 7 h; d) 14 h; e) 20 h; f) 24 h	258
4.2.10	Relation between relative IR peak intensity and reaction time for -75 µm products generated in systems A and B	260
4.3.1	Relation between DOA and reaction time for system C at various temperatures	263
4.3.2	Relation between DOA and reaction time for system D at various temperatures	264
4.3.3	Relation between proportion and concentration of magnesium entering solution and reaction time for system C at various temperatures	266
4.3.4	Relation between proportion and concentration of magnesium entering solution and reaction time for system D at various temperatures	267
4.3.5	Relation between proportion and concentration of iron entering solution and reaction time for system C at various temperatures	268
4.3.6	Relation between proportion and concentration of iron entering solution and reaction time for system D at various temperatures	269
4.3.7	Relation between proportion of calcium entering solution and reaction time for systems C and D at various temperatures	270

4.3.8	Infra-red spectrograms for -75 μm products obtained from system E reacted at 215°C for a) 1 h; b) 2 h; c) 4 h; d) 6 h; e) 8 h	275
4.3.9	Infra-red spectrograms for -75 μm products obtained from system C reacted at 215°C for a) 1 h; b) 2 h; c) 4 h; d) 5 h; e) 6 h; f) 8 h	276
4.3.10	Infra-red spectrograms for -75 μm products obtained from system D reacted at 215°C after a) 1 h; b) 2 h; c) 4 h; d) 6 h; e) 8 h	277
4.3.11	Infra-red spectrograms for -75 μm products obtained from system C reacted at 260°C for a) 1 h; b) 2 h; c) 3 h; d) 4 h; e) 5 h; f) 6 h; g) 8 h	279
4.3.12	Infra-red spectrograms for -75 μm products obtained from system D reacted at 260°C for a) 1 h; b) 2 h; c) 3 h; d) 4 h; e) 5 h; f) 6 h; g) 8 h	280
4.3.13	Relation between relative IR peak intensities reaction time for -75 μm products generated in systems C and D at 260°C	281
4.3.14	Infra-red spectrograms for -75 μm products obtained from system C reacted at 300°C for a) 1 h; b) 2 h; c) 3 h; d) 4 h; e) 5 h; f) 6 h; g) 8 h	283
4.3.15	Infra-red spectrograms for -75 μm products obtained from system D reacted at 300°C for a) 1 h; b) 2 h; c) 3 h; d) 4 h; e) 5 h; f) 6 h; g) 8 h	284
4.3.16	Relation between relative IR peak intensities and reaction time for -75 μm products generated in systems C and D at 300°C	285
4.4.1	X-ray diffractograms for -75 μm products obtained from system C reacted at 215°C for a) 1 h; b) 2 h; c) 5 h; d) 6 h	289
4.4.2	X-ray diffractograms for -75 μm products obtained from system D reacted at 215°C for a) 1 h; b) 3 h; c) 4 h; d) 6 h; e) 8 h	290
4.4.3a	X-ray diffractogram of 9-11 Å aluminosilicate obtained using system E at 215°C after 5 h	291
4.4.3b	X-ray diffractogram of 9-11 Å aluminosilicate obtained from reaction of olivine standard with 0.31M hydrochloric acid at 100°C for 24 h	292
4.4.4	X-ray diffractograms for -75 μm products from system C reacted at 260°C for a) 1 h; b) 2 h; c) 3 h; d) 4 h; e) 5 h; f) 6 h; g) 8 h	294

4.4.5	X-ray diffractograms for -75 µm products obtained from system D reacted at 260°C for a) 1 h; b) 2 h; c) 3 h; d) 4 h; e) 5 h; f) 6 h; g) 8 h	295
4.4.6	X-ray diffractograms for -75 µm products obtained from system C reacted at 300°C for a) 1 h; b) 2 h; c) 4 h; d) 6 h; e) 8 h	296
4.4.7	X-ray diffractograms for -75 µm products obtained from system D reacted at 300°C for a) 1 h; b) 2 h; c) 4 h; d) 5 h; e) 8 h	297
4.4.8	Computed proportions of phases in the -75 µm product generated at various reaction times for system A at 100°C	302
4.4.9	Computed proportions of phases in the -75 µm product generated at various reaction times for system B at 100°C	303
4.4.10	Computed proportions of phases in the -75 µm product generated at various reaction times for system C at 215°C	305
4.4.11	Computed proportions of phases in the -75 µm product generated at various reaction times for system D at 215°C	306
4.4.12	Computed proportions of phases in the -75 µm product generated at various reaction times for system C at 260°C	308
4.4.13	Computed proportions of phases in the -75 µm product generated at various reaction times for system D at 260°C	309
4.4.14	Computed proportions of phases in the -75 µm product generated at various reaction times for system C at 300°C	311
4.4.15	Computer proportions of phases in the -75 µm product generated at various reaction times for system D at 300°C	312
4.4.16	Trends in the octahedral and tetrahedral structure of the 9-11 Å silicates formed in aluminium-rich conditions at 215-300°C	317
4.5.1	Scheme for calculating moles of ions residual in solution	333
4.6.1	Schematic representation of alteration reaction mechanism which relates to microscale inter-reactions	336
4.6.2	The nature of the degradation induced in kimberlite in accordance with the proposed reaction mechanism	336

4.6.3	Initial rate kinetics : Residual number of moles of olivine and serpentine after 0.25 h	341
4.6.4	Relation between the reciprocal for the residual moles of olivine in the +75 µm fraction, ξ_{ol}^{-1} and the reaction time for systems A and B	343
4.6.5	Relation between the reciprocal of the residual moles of serpentine in the +75 µm fraction, ξ_{sp}^{-1}, and the reaction time for systems A and B	344
4.6.6	Relation between ξ_{ol}^{-1} and reaction time at various temperatures for system A	346
4.6.7	Arrhenius plot for system A : olivine reaction	346
4.6.8	Relation between residual concentrations of magnesium, iron and calcium in solution and the square root of the reaction time for system A	354
4.6.9	Relation between residual concentrations of magnesium, iron and calcium in solution and the square root of the reaction time for system B	355
5.2.1	Diagram showing the effect of the initial aluminium and hydrogen ion concentrations on the DOA (%) for a 10 g -1180+850 µm feed reacted at 100°C for 7 h	359
5.2.2	Diagram showing the effect of the initial aluminium and hydrogen ion concentration on the proportion of total magnesium, iron and calcium entering solution (%)	360
5.2.3	Diagram showing the effect of the initial aluminium and hydrogen ion concentrations on the proportion of aluminium reporting to a solid product (%)	362
5.2.4	Diagram showing the effect of the initial aluminium and hydrogen ion concentrations on the residual proportion of olivine and serpentine in the system (% of head value)	363
5.3.1	Semi-continuous alteration apparatus	365
5.3.2	Diagram representing circulation of reaction solution	366
5.3.3	pH/time relation for semi-continuous alteration of a 25 g -1180+850 µm feed. 1.0 g $AlCl_3.6H_2O$ charge added at 0 h	372
5.3.4	pH/time relation for a semi-continuous alteration of a 25 g -1180+850 µm feed. 5.0 g $AlCl_3.6H_2O$ charge added at 0 h	374

5.3.5a	pH/time relation for semi-continuous alteration of a 25 g -6.18+3.18 mm feed. 5.0 g $AlCl_3.6H_2O$ charge added at 0 h	377
5.3.5b	Cross section of a reacted particle (x4.5)	377
5.3.6	pH/time relation for semi-continuous alteration of a 25 g -6.18+3.18 mm feed. 0-6.3 g $AlCl_3.6H_2O$ added	380
5.3.7	X-ray diffractograms for -600 µm products	383
5.3.8	pH/time relation for semi-continuous alteration of kimberlite -6.18+3.18 mm feed	385
5.4.1	General flowsheet for diamond recovery by hydrothermal alteration of kimberlite	392
5.4.2	Conceptual flowsheet for diamond recovery by hydrothermal alteration of kimberlite	393

LIST OT TABLES

		Page
1.1.1	Properties of diamond	2
1.4.1	Stability data for aluminium-silicate hydrates	36
2.2.1	Qualitative analysis of relative density fractions	56
2.2.2	Mineral assays evaluated from particle point counting	58
2.2.3	Mineral assays evaluated from thin section analysis	63
2.2.4	Analytical methods used in mineral analysis	65
2.3.1	Effect of glycolation and heating on various clay minerals	75
2.3.2	Properties of the olivine and serpentine standards	85
2.3.3	Composition of the sample for quantitative X-ray diffraction analysis	86
2.3.4	Size calibration for olivine	96
2.4.1	Quantitative and semi-quantitative chemical analysis for kimberlite, olivine and serpentine	109
2.4.2	Chemical assay data for the kimberlite, olivine and serpentine standards	110
2.5.1	Mineral systems in Program CECPM	128
2.5.2	Chemical assay error determination : effect of variation of assay on computed phase proportions	131
3.2.1	Additives tested in conjunction with 4.5M sulphuric acid, 70°C, 24 h	149
3.2.2	Percentage elemental distribtuions for the reaction with 4.5M sulphuric acid	154
3.3.1	Additives tested in conjunction with 0.41M aluminium chloride, 0.31M hydrochloric acid, 100°C, 7 h	173
3.3.2	Partial elemental mass balances of typical alteration reactions in acidic media	175
3.5.1	Gibbs free energies of formation for cationic oxides and hydroxides as present in silicates ($kJ\ mol^{-1}$)	227

3.5.2	Gibbs free energies of formation for minerals at 100°C and aqueous species in solution at 100-300°C (kJ mol^{-1})	229
3.5.3	Calculated standard Gibbs free energies of formation for minerals from solution at various temperatures (150-300°C)	238-239
4.3.1	The physicochemical conditions tested as represented by systems A, B, C, D, E	262
4.3.2	Percentage elemental distribution at various reaction times for system C at 215°C and 300°C	272
4.4.1	Compositional data for 9-15 Å aluminosilicates I : systems A and B	301
4.4.2	Compositional data for 9-15 Å aluminosilicates II : system C	315
4.4.3	Compositional data for 9-15 Å aluminosilicates III : systems C and D	316
4.6.1	Values of the Arrhenius equation constants for systems A and B	345
5.3.1	Elemental mass balance data for semi-continuous alteration of kimberlite : -6.18+3.18 mm; three reaction cycles	381
5.4.1	Procedures adopted for long term and short term degradation processes	388
5.4.2	Comparison of tested alteration procedures	389

CHAPTER 1

LITERATURE SURVEY

1.1 Introduction

Diamonds have been a focus of attention for some three thousand years since their properties of reflective brilliance and permanence were first recognised. The charisma and rarity of these previous stones has made them the cause of legend and strife throughout the ages. More effort is currently directed into investigating the nature of diamond than any other mineral.[1]

Some of the properties of diamond are given in Table 1.1.1.[2] The mineral is the hardest substance known. Furthermore, it has the highest thermal conductivity at room temperature and the highest bulk modulus. It also exhibits a remarkably high resistance to corrosion, but will burn in air like coal.

The recovery of diamond from the enormously greater mass of host rock (Plate 1.1) represents a remarkable achievement. From the time records were first kept, some 5×10^9 tonnes of rock, gravel and sand have been excavated and processed to yield only 320 tonnes of diamonds.[3] The most productive diamond mines are in Southern Africa : Premier, Finsch, Koffiefontein, Wesselton in South Africa; Orapa and Jwaneng in Botswana, and CDM on the Namaqualand coast in South West Africa (Namibia). Many stones are lost during processing however, and improved techniques are urgently required.

As a prerequisite of new work in the field of improved diamond recovery, a literature survey has been carried out and this forms the

TABLE 1.1.1. PROPERTIES OF DIAMOND[2]

Property	Value	Notes
Chemical composition	Composed largely of carbon	Impurities : N, 0.2%; Al, 150ppm; B, 3-270ppm; Others < 100ppm
Classification	Types Ia, Ib, II	Ia : most natural stones with N segregated into sheets; Ib : synthetic stones; N dispersed; II : rare; N free
Crystal structure	Cubic cell	
Density	3.515	meaned value at 25°C
Graphitization temperature	600°C	in presence of O_2; (1500°C in inert atmosphere)
Hardness (Moh's scale)	10	hardest known material (5700-10400 kg m^{-6} Knoop scale)
Compressibility	1.7×10^{-9} m^2 kg^{-1}	
Bulk modulus	5.4 - 5.8 GPa	
Tensile strength	13 - 40 MPa	
Shear strength	87 MPa	
Compressive strength	86.8 MPa, 165.3 MPa	at initiation of flow, maximum tolerance
Thermal conductivity	90 - 260 W K^{-1} m^{-1}	at 20°C
Specific heat	6.1884 J mol^{-1}	
Refractive index	2.4237, 2.4099	using Hg green (546.1 nm), Hg_α red (656.3 nm)
Dielectric constant	5.55 - 5.61	at 293 K and 0.3 kHz

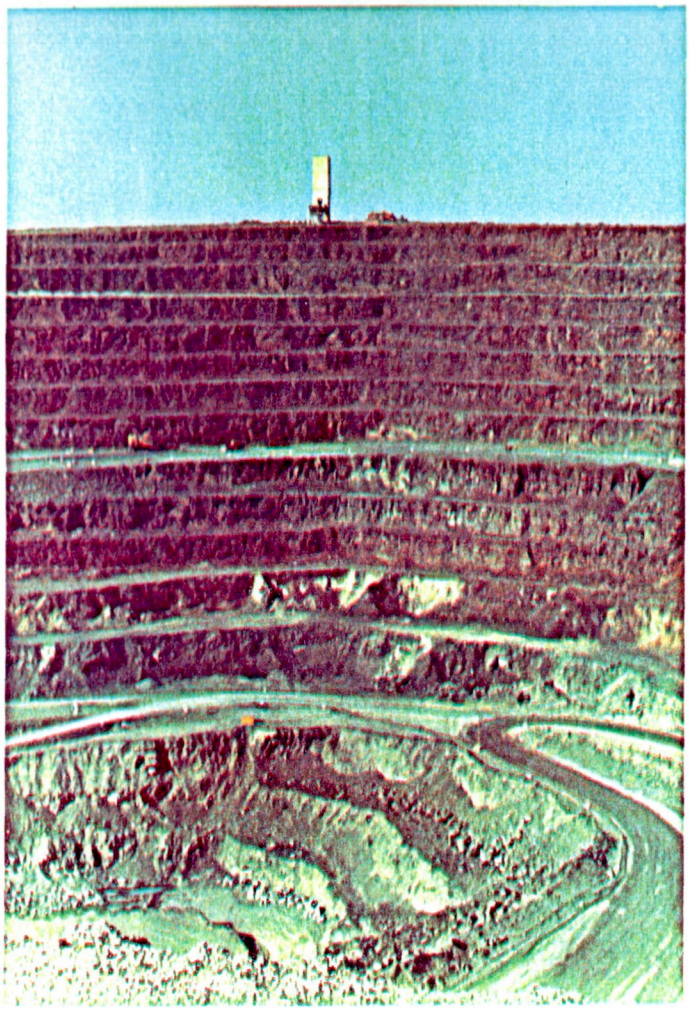


Plate 1.1 View of the open pit at Finsch (1979). A front end loader and shovel can be seen on the eighth bench.

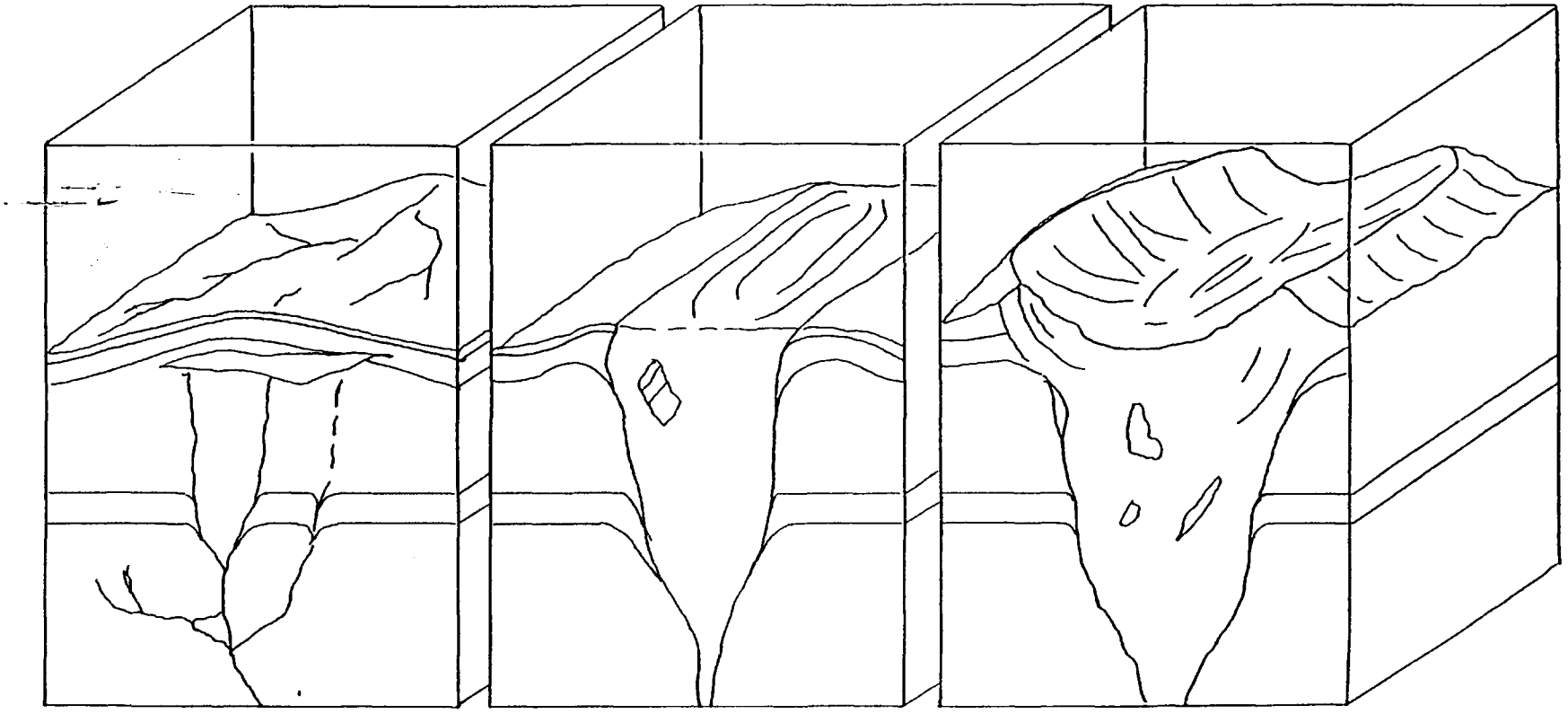
main part of the present chapter. The survey deals briefly with kimberlite geology and processing and in more detail with studies reported on the degradation of kimberlite minerals. The related subject of clay mineral synthesis is also considered in some detail.

1.2 Kimberlite Geology and Processing

1.2.1 Origin and location of diamondiferous ores

There are two principal modes of occurrence of diamonds : in host rock associations, namely kimberlites, and as marine terrace and alluvial deposits, which are derived from kimberlite alteration and erosion.[1,3] Kimberlites are ultrabasic igneous rocks (silica content of less than 40%) having a porphrytic texture[4,5] (see later). They occur in volcanic pipes, which can be of substantial proportions : the outcrop at Premier Mine, as noted by Bruton,[1] measured 883m x 426m at surface and is estimated to extend into the mantle to a depth of 150 - 200 km.

Figure 1.2.1 shows schematically the progressive stages of emplacement of a kimberlite pipe, which have been deduced by Woolsey et al,[6] McCallum[7] and Harris and Middlemost.[8] Magma originating at more than 600 km below the cratonic area is considered to have moved upwards by a process of "solution stoping". Stage A in the figure illustrates the situation to a depth of 150 - 200 km. The temperature at this depth was low enough for crystallization to commence. Major metallic elements - magnesium, iron, aluminium, calcium, sodium and silica began to be concentrated in the form of ferromagnesian minerals, leaving behind residual liquid and gaseous components consisting principally of water and carbon dioxide.[8] The fluid character of the magma and the associated high pressure caused the opening up of dyke-like channels as shown. As the remaining magma progressed upwards,



A : Pressure of intruded magma causes crust fracture. Initial magma crystallization.

B : Exsolution of volatiles causes magma to behave as fluidized mass.

C : Expansion of conduit to form cratonic area.

Figure 1.2.1 Progressive stages of the formation of a kimberlite pipe[6-8]

further cooling and release of volatile material caused the whole system to behave as a rapidly rising gas-liquid fluidised mass, eroding the walls of the conduit to form a funnel-shaped pipe called a diatreme (stage B). Eruption of the magma at the surface produced the crater shown in stage C. This type of crater was very susceptible to erosion,[3] the bulk of contained minerals at the surface being rapidly degraded and transported away in the drainage system. The most resistant minerals, ilmenite, garnet, magnetite and diamond were removed and concentrated either in river beds (alluvial deposits) or in the sea (in some cases later to form marine terraces).

In general, kimberlites are confined to ancient shield areas and platforms, and vary in age from 130 my (Mannhiem Kimberlite, USA)[9,10] to 1750 my (Premier Kimberlite, South Africa).[10,11] The most numerous formations are found in the upland plateau of South Africa, the Tanzanian plateau and the Siberian Arnaback Shield. Other pipe locations include the North West Territories and Ontario (Canada); Montana, Wyoming and Colorado (USA);[10] the Kola Peninsula, Sea of Azov and Kharkov (USSR);[11] and Sierra Leone; Botswana; Brazil;[8] Western Australia;[12] Ghana, Zaire;[3] and Czechoslovakia.[13] The world wide distribution of Kimberlites is shown in Figure 1.2.2. Important alluvial deposits are found in India[1] and the Orange Free State, South Africa. Marine terraces occur on the coast of South West Africa.[14]

1.2.2 Kimberlite processing

Methods of diamond extraction have gradually developed over many years,[1,3] but it was not until the discovery of the diamondiferous kimberlite pipes at Koffiefontein in 1870, and at Kimberley in 1871 that extraction was carried out on a large scale.[1] Most of the processing operations have been carried out in Southern Africa, and



Figure 1.2.2 Distribution of kimberlites[33]

Kimberlite provinces 1 = South Africa 2 = South West Africa
3 = Tanzanian Plateau 4 = West Africa
5 = Western Australia 6 = Yakutia USSR
7 = Colorado Plateau USA
Other occurrences given by ●

these have been described by various authors.[14-19] The stages of diamond processing can be subdivided into two groups[20,21] concerned with liberation and concentration respectively. Most of the techniques employed (Figure 1.2.3) find application in the wider field of mineral processing[22] but a few have been developed to capitalise specifically on the particular characteristics of diamond namely

a) intense fluorescence when subjected to X-ray radiation (employed in Sortex XR21 sorters in extracting diamonds from concentrates[23])
b) high electrical conductivity (utilised in electrostatic separators at CDM[3,15])
c) hydrophobicity (employed on grease tables at Premier and elsewhere).

The main techniques of diamond extraction are shown in the generalised flow sheet in Figure 1.2.3.[20] As can be seen, the run-of-mine product is crushed to liberate contained diamonds in two or three stages of primary comminution (e.g. Finsch). 'Scrubbing' with water then follows to remove fine sized materials, the resulting suspensions being thickened (settled) and dumped. The washed ore is graded by screening and conveyed as different size fractions to primary and secondary concentration sections. Undersize material, particles < 600 μm (Kimberley Area) or < 2 mm (CDM) join the tailings stream and are dumped. The primary and secondary concentration sections consist primarily of dense media separation (Premier) or washing pans (Finsch). A variety of recovery processes are subsequently employed. For example, at Finsch, magnetic separators are used to remove ilmenite and magnetite contaminants. Grease tables, followed by X-ray sorters produce the final concentrate. Coarse tailings are

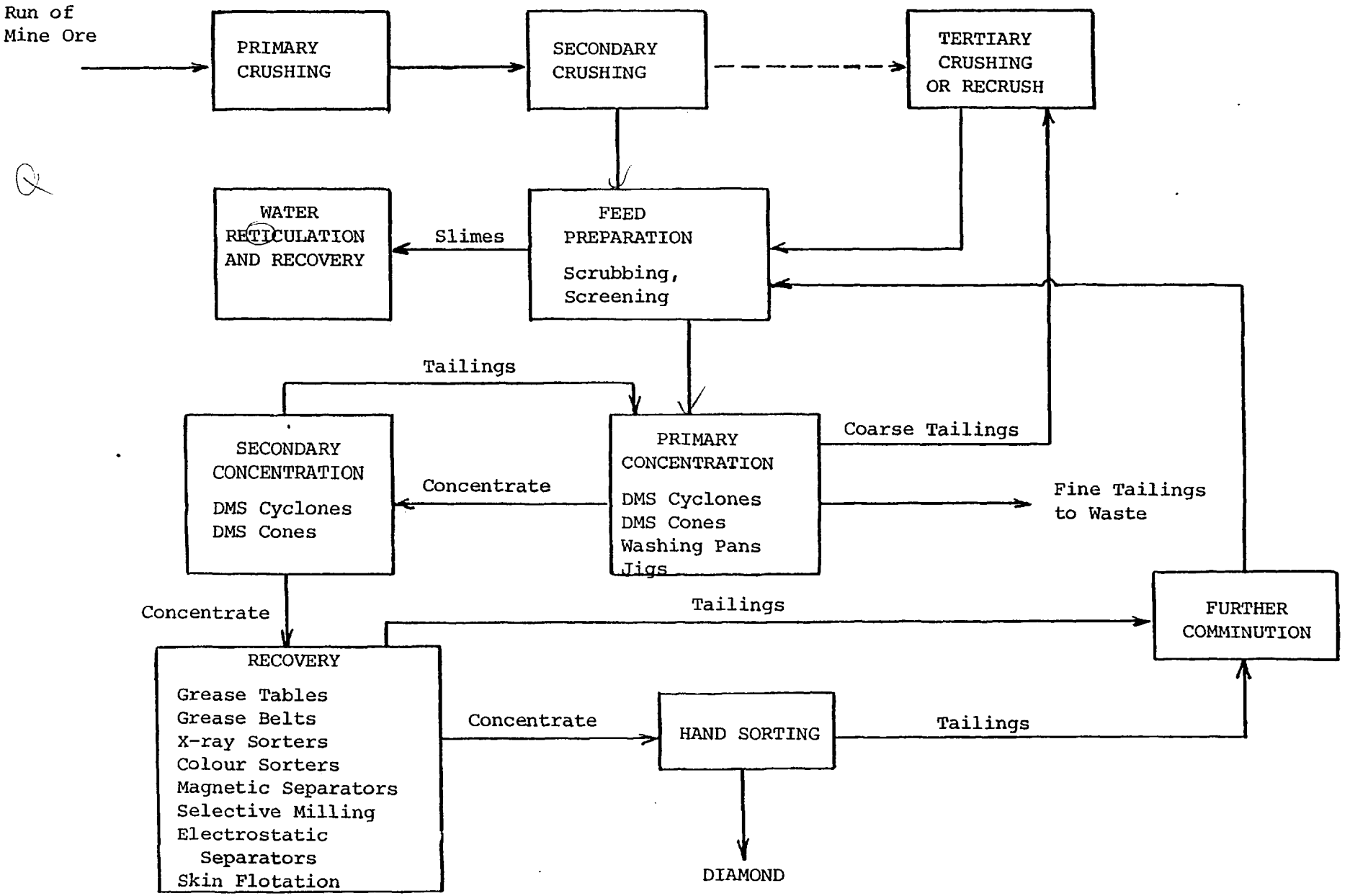


Figure 1.2.3[20] Generalized flowsheet for diamond recovery

generally routed to the previous concentration stage or recrushed to liberate the finer diamonds from middling fractions. Concentrates are hand-sorted at the Central Sorting Office, Kimberley, for classification and marketing.

Adamson[16] and Napier-Munn[20] have recorded the particular problems encountered in diamond extraction. According to these workers the major problems are as follows :

a) The headgrades of diamondiferous kimberlites are extremely low, and according to Cleasby et al[24] there is a great variation in headgrade within the pipe (from 0.01 - 0.6 ppm). A "tremendous" concentration[16,22] has to be effected in comparison to other types of ores.

b) Owing to the more than exponential increase in the value of diamonds with particle size,[20] the diamonds must be liberated at their natural grain sizes as far as possible, without breakage, during comminution.

c) Diamonds are valued as discrete entities with a large range of sizes being economically recoverable.[24] This leads to complex liberation and sizing practices as compared with many metallurgical operations. Unlike such operations, for which the mineral value remains essentially constant provided particles are larger than 'slime' size (i.e. > 10 μm), diamond operations have to take account of the fact that stones below 600 μm have no gem value while above 600 μm the value increases more than exponentially with size.[25] In particular, diamonds are valued at their recovered size, which will be less than the natural grain size unless the process techniques are highly efficient. It may be noted that industrial diamonds have value at sizes as low as 2 μm but these are mostly obtained from larger 'flawed' stones and industrial syntheses.

In diamond plant comminution, processes are controlled to achieve the optimum compromise between reduction of the ore to a size at which separation processes can be used on the liberated diamonds and minimization of the probability of crushing a precious stone.[20] The largest size after crushing employed at present is 40 mm[16,20,26] and the kimberlite is progressively broken to 4 mm which is suitable for preliminary concentration. Stones larger than 40 mm have been recovered, by good fortune, before they entered the crushing plant[4] (e.g. the Premier Rose (1978)). Measures taken to increase the recovery of large diamonds include careful visual searching of the feed as it enters the processing plant and X-ray sorting of the -75+25 mm feed from preliminary screening of the run-of-mine ore.[20] To ensure recovery of diamonds of intermediate size and liberation of smaller ones, it has become standard practice to recrush coarse tailings (e.g. Premier[20,21]). Adamson and Hodgson[21] note, however, that liberation problems still exist at finer sizes. Indeed, there is apparently no well-established method of assessing the diamondiferous material lost to the tailings through inefficient breakage during processing.

To improve the efficiency of liberation, two types of approach are currently under investigation :

Physical methods : These make use of the textural properties of the rock. Experimentation has taken place at the Diamond Research Laboratory (Johannesburg, South Africa) to evaluate the application of continuous planetary milling.[27] The planetary mill utilises the high resistance of diamond to abrasion,[1,2] the host rock being preferentially abraided. Electro-crushing techniques are being investigated by Andres.[28] Here, high voltage pulses are applied to the rock via

suitable electrodes in a dielectric medium, thus causing preferential fracturing along mineral grain boundaries.[23]

Physiochemical degradation of kimberlite : Some examples are found to readily alter. Wagner[4] describes a practice, used in the early days of kimberlite processing, called "Natural Pulverization" or "Flooring", in which the kimberlite at Bultfontein and Dutoitspan was spread out and allowed to weather naturally. Some 12 - 18 months were required to guarantee sufficient breakdown for processing without intensive comminution.[23] The method was labour intensive (Rhodes hired 1000 convicts for the purpose of kimberlite collection at one time[1]) and applicable to certain types of kimberlite only. Recent work has been carried out at the Warren Spring Laboratory (Stevenage, UK) by LeRoux et al[29] into the biochemical reactions that occur in kimberlite. This work was also aimed at mineral disruption. Tests showed that bacteria were present in unusually high concentrations in the kimberlites from Premier, Kimberley, Koffiefontein, Voorspoed and Letseng, and demonstrated their ability to degrade some of the matrix minerals. Hydrothermal alteration is a further alternative yet to be studied fully. A detailed summary of the petrology of kimberlite is a necessary prerequisite to a fuller discussion of these alteration processes.

1.2.3 Petrology of kimberlite

The petrology (the study of minerals and textures) of kimberlite has been considered by many authors, and represents an extraordinarily complex study. In a simple manner, kimberlite may be classified as a micaceous peridotite,[30] one type of ultrabasic rock of mantle origin, whose texture is related to the mode of occurrence. Dawson[31] gives the definition of kimberlite as "a hybrid rock that results from the incorporation of xenocrysts and xenoliths of mantle origin (i.e.

different from that of the kimberlite magma) into a liquid or fluid of very different chemical composition". The main groundmass or matrix minerals (as recorded by Clement[32]) are olivine, monticellite, clinopyroxene, or the pyroxene, amphibole, biotite-phlogopite, calcite and serpentine. Owing to alteration processes, some of these may have been converted to their intermediary or residual breakdown products.

It is generally agreed that kimberlites possess a porphyritic texture.[9,10,33,34] McCallum[7] states that kimberlite pipes are renowned for their variability of content. The most impressive compositional difference between pipes often involves the nature and concentration of included xenocrystic and xenolithic material. Dawson[35] lists the minerals which constitute the first of these categories of such material - entrained phenocrysts :

a) Olivine. Nixon et al[9] state that the olivine-forming phenocrysts in kimberlite are principally forsteritic or magnesium-rich. The olivine has been noted to alter at Gross Brukkaros, South West Africa, to the serpentine minerals chrysotile, antigorite (with associated magnetite), mica, smectite and calcite.[36]

b) Garnet. The magnesium-rich garnets in kimberlite vary in composition from pyrope-almandine[9], and differ from those produced by regional metamorphic forces or those found in eclogite.[13] Reid and Manor[13] and Nixon et al[9] observe that the phenocrysts tend, in general, to be rounded and enclosed by a hydrothermal alteration product termed kelyphite - a mixture of biotite, pyroxene, amphibole and plagioclase feldspar.

c) Pyroxenes. Stephens and Dawson[33] have recognised five chemically distinct orthopyroxenes (enstatite-bronzite group) and ten

different clinopyroxenes (diopside group) in kimberlite. Tremolite and actinolite are recorded as alteration products.

d) Ilmenite. Phenocrysts of this mineral are generally present in kimberlite. They are also magnesium-rich[37] and together with garnet and diopside act as exploration "indicator" minerals for kimberlite.[3]

e) Micas. In kimberlites these are principally phlogopite[9] and its alteration product vermiculite.[9,37,38] Smith et al[39] report that they can vary greatly in composition but are either magnesium- or iron-rich.

f) Less common phenocrysts. Spinel, graphite, carbonates, chromite and others have been reported.[37]

The second category of material, texturally dissimilar to that constituting the kimberlite matrix, is represented by the ultramafic nodules - oval bodies not exceeding 256 mm in diameter.[30] Seven types of nodules have been recognised,[40-50] all of mantle origin.[46]

a) Lherzolites. These nodules are the most common in kimberlite.[9] O'Hara et al[46] list clinopyroxene, orthopyroxene and olivine as the most important minerals. Additional minerals, principally chromium spinel,[41,45] rutile[42] and garnet[36,44] are present and serve further to categorise lherzolites (garnet lherzolite being the most common[46]). Accessory minerals include phlogopite,[44] chromite and graphite.[45] Lherzolite are products of the original mantle magma,[46] crystallizing at 1500°C.[41] McCallum et al[51] and others[9,43] note that such nodules in Northern Colorado, Southern Wyoming and elsewhere can undergo extensive alteration. Alteration products include serpentine, haematite, carbonates, talc, quartz,[51] amphibole, mica[43] and kelyphite. Ferguson et al[36] attribute

this metasomatic change to fenitization (discussed in a later section).

b) Harzburgites. These are similar in composition to lherzolites, the important minerals being orthopyroxene[30,33,38] and olivine[46]. Again chromium spinel[41,45] and garnet (almandine[41]) serve to classify these phases. Beyth et al[38] and Dawson[11] note chromite, magnetite and pyrite as accessory minerals. Harzburgites also crystallize at 1500°C forming from a lherzolite melt with a simultaneous increase in the CaO/Al_2O_3 ratio.[46]

c) Wehrlite. Wilshire and Shervais[40] have identified these olivine rich-pyroxene nodules in kimberlite. Varieties can be garnetiferous[46] or micaceous.[43]

d) Websterite. This nodule type also contains clinopyroxene, orthopyroxene[41] and olivine[46] though it is noted to differ from the above in crystallization temperature (520 - 620°C) and in chemical composition. (Websterite has a lower MgO and higher CaO, Al_2O_3 and SiO_2 proportions.)

e) Dunites. These consist almost entirely of olivine.[46]

f) Eclogites.[52] These consist essentially of sodium-aluminium rich clinopyroxene (diopside-jadeite) and garnet (pyrope-almandine-grossular[9,53-55]) and are of special interest in that diamonds are many thousands of times more abundant in them than in kimberlite as a whole. Diamondiferous eclogites (as at Mir, USSR[55]) are, however, comparatively scarce.[35] Eclogites crystallize at similar temperatures to lherzolites and harzburgites[50] and alter mainly to serpentine, anthophyllite, talc, chlorite, phlogopite and goethite[38].

g) Pyroxenites. According to Borley and Suddaby[56], such nodules are found in the Jagersfontein kimberlite. The general mineralogy is forsteritic olivine,[40] phlogopite,[43] diopside-enstatite and garnet

(pyrope-almandine). Rodgers et al[57] note the presence, additionally, of picotite or magnetite in other localities.

The third category of included material is xenolithic.[58] This section will concentrate on three principal classes as found in the field :

a) Blocks of rock types derived from formations which existed at the time of the kimberlite intrusions but which were either included in the fluidized magma or removed by erosion to attain a lower stratigraphic horizon. Typical examples are dolerites, shales and mudstones (as found in Lesotho kimberlites[35]).

b) Deep seated xenoliths. Rickwood and Mathias[55] note these to originate from high mantle levels. Stephens and Dawson[33] state that peridotites are the most common of this group. The peridotites found at Matsoku[48] and the Lashire volcano, Tanzania[49], typify the mineralogy of these rocks, namely olivine, pyroxene, garnet and chromite. Metasomatic alteration can produce phlogopite, ilmenite, rutile, pyrrhotite, pentlandite and chalcopyrite.

c) Igneous post-emplacement intrusions. An example is the dolerite-gabbro sill at Premier Mine, South Africa.

A comprehensive list of minerals found in kimberlite together with their nature of formation and composition is given in Appendix 1. Typical chemical analyses are also given.

1.3 Degradation of Kimberlite Minerals

Two main types of alteration process cause degradation of kimberlite minerals : weathering and hydrothermal alteration.

Weathering

The essential feature of weathering is that it affects rocks in situ.[30] In this process rock is broken down and decomposed to varying degrees by the action of external agencies such as wind, rain, temperature changes, plants and bacteria. Weathering affects kimberlite pipes to produce three zone types as follows :[9,29,59,60]

a) Yellow Ground. This is a surface feature where the kimberlite has been extensively hydrated and oxidized to form loosely consolidated deposits. Yellow ground generally extends to no more than 30 m in depth from the surface, but actual depths are quite variable depending upon the particular circumstances of weathering,[5] e.g. Kimberley 19.8 m; Jagersfontein 18.3 m; Voorspoed 27.4 m; Premier 10.6 m; Koffiefontein 21.3 m.

b) Blue Ground. In this case the kimberlite is deeper and has undergone alteration to a limited extent only.[37] (Plate 1.2 illustrates samples of both blue and yellow ground at Finsch.) Three varieties of blue ground have been observed, being defined according to their textures and their field relationships with the surrounding country rock. The contact between blue and yellow ground is sharp, as shown in Plate 1.3.

c) Hardebank. This is essentially unaltered kimberlite[37] adopting a diatreme or hypabyssal facies, i.e. a texture intermediate between that of very fine grained igneous rocks which cooled quickly near the earth's surface or that of very deeply emplaced magmatic intrusions.[30]

Hydrothermal Alteration

Examples include serpentinization and chloritization. Both involve thermal metamorphism by interaction with high temperature fluids originating from an external source or from the kimberlite magma itself. Alteration takes place in the latter stages of

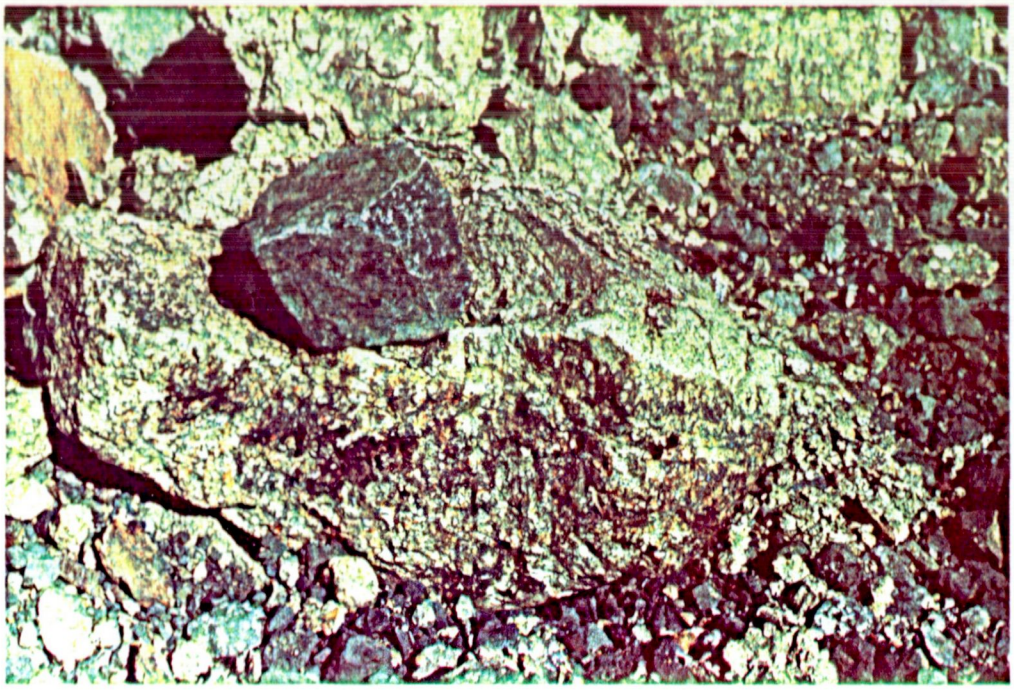


Plate 1.2 Samples of Blue and Yellow Ground as found in the Finsch open pit

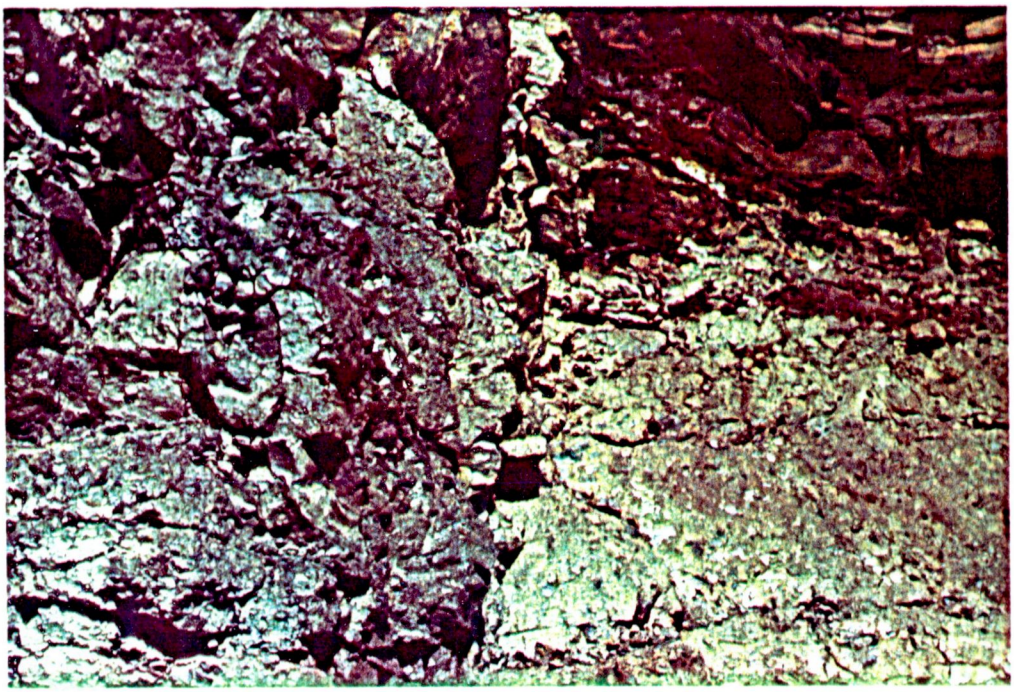


Plate 1.3 Sharp contact between the Blue and Yellow Ground at Finsch. The difference in the textures is apparent, in that some of the petrological features of the original kimberlite are visible (e.g. xenolithic, serpentitic) in the former, whereas the latter is completely degraded.

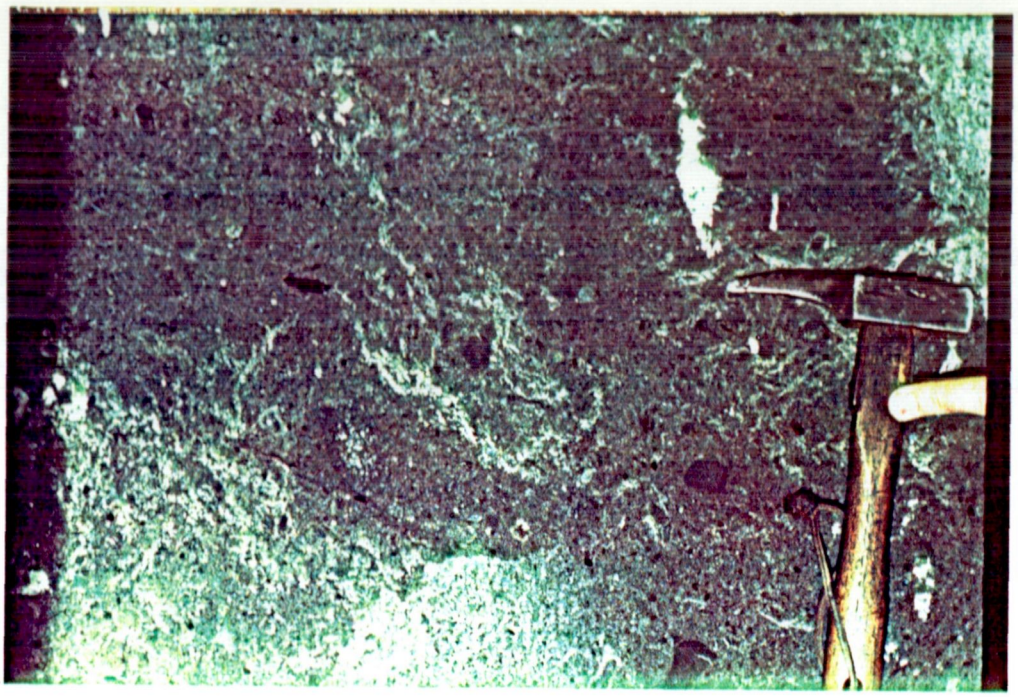


Plate 1.4

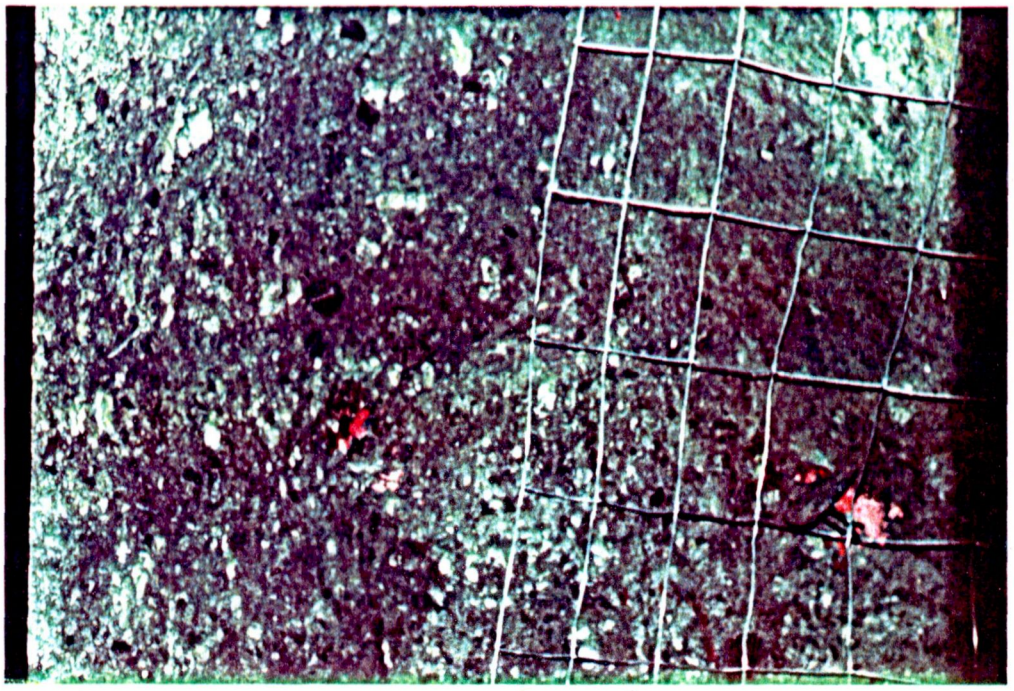


Plate 1.5

Plates 1.4 and 1.5 Alteration in Premier Type II kimberlite[61] (location : Heading T116). Both photographs were taken in the same development heading at Premier. Plate 1.4 illustrates a competent kimberlite composed chiefly of pyroxenes, illite-phlogopite, serpentine and chlorite. Some 10m from the heading end where this kimberlite was examined the material illustrated in Plate 1.5 was observed. This rock was friable (reflected by the mesh support for grouting) and was composed of talc, montmorillonite, serpentine and chlorite. The proximity of the two kimberlites, below the yellow ground region, suggests that localised hydrothermal alteration occurred during consolidation of the pipe.

cooling and consolidation[61] (Plates 1.4 - 1.5).

In detail, kimberlite decomposition reactions are complex. The behaviour of each mineral component is discussed in turn.

1.3.1 Natural alteration of olivine

The natural alteration of olivine has been widely reported.[62-80] In general, olivine alters first to a serpentine phase and thence to a variety of products.[62] Indeed, Deer et al state that serpentinization of olivine is one of the most commonly observed alteration processes.[63] The formation of products other than serpentine is governed by the physio-chemical nature of the environment; in particular by the proximity of different reactive phases (see later).

Coleman[64] proposed several equations to account for the chemistry of serpentinization :

$$\underset{\text{Mg-olivine}}{2Mg_2SiO_4} + 3H_2O \leftrightarrow \underset{\text{serpentine}}{Mg_3Si_2O_5(OH)_4} + Mg(OH)_2 \qquad (1.3.1)$$

$$2Mg_2SiO_4 + 2H_2O \leftrightarrow Mg_3Si_2O_5(OH)_4 + MgO \qquad (1.3.2)$$

$$3Mg_2SiO_4 + 4H_2O + SiO_2 \leftrightarrow 2Mg_3Si_2O_5(OH)_4 \qquad (1.3.3)$$

In their descriptions of serpentinized olivine textures, Wicks and Whittaker[65] and Butler[66] have noted the presence of brucite as an accessory product and/or the concurrent loss of magnesium. Most authors[62-67] agree that water plays an essential part in the process. The occurrence and mechanism of magnesium removal has, however, stimulated discussion regarding the addition or subtraction of other mineral species in the serpentinization equations. Particular controversy surrounds the roles that iron, oxygen and silica play in the process,[64] and this is linked with an ongoing debate concerning whether or not a volume increase

accompanies the reaction. Hostetler et al[67] favour a volume increase of 30 - 40%, which necessitates silica addition, as in equation 1.3.3. They consider extraction of silica unlikely on thermodynamic grounds. Thayer[68] however considers serpentinization to be a constant volume process, 30% by weight of magnesia and silica being removed from the altered harzburgites, dunites and peridotites studied, and this weight replaced by the elements of water included in the newly formed serpentine. A later publication,[72] after a discussion by Page,[73] concludes that "where evidence is definitive serpentinization appears to have involved no significant change in volume but expansion may occur in other situations", stating the reaction as :

$$5Mg_2\ SiO_4 + 4H_2O \leftrightarrow Mg_3\ Si_2O_5(OH)_4 + 4MgO + SiO_2(\text{removed}) \quad (1.3.4)$$

Coleman[64] rationalizes the situation by assuming both types of reaction may occur. For instance, constant volume reactions should be favoured where the rock is made subject to enclosing stress, whereas volume increases are to be expected in sheared and faulted areas, permitting the release of pressure.[67-71]

Barnes and O'Neill[71] favour the following sequence of reactions, (which on addition in suitable proportions yield equation (1.3.1)) :

$$Mg_2\ SiO_4 + 4H^+ \leftrightarrow 2Mg^{2+} + H_4\ SiO_4 \quad (1.3.5)$$

$$Mg^{2+} + 2OH^- \leftrightarrow Mg(OH)_2 \quad (1.3.6)$$

$$3Mg^{2+} + 2H_4\ SiO_4 + H_2O \leftrightarrow Mg_3\ Si_2O_5(OH)_4 + 6H^+ \quad (1.3.7)$$

The authors, however, emphasise that the fitting of ultramafic rocks and their subsequent alteration products to a simplified $MgO-SiO_2-H_2O$ system is "dangerous". They state that few systems can be effectively explained unless a system comprising the following species is employed :

CO_2-Cr_2O_3-FeO-CaO-NiO-Na_2O-Al_2O_3-H_2-O_2-Fe_2O_3-MgO-SiO_2-H_2O. For example, Coleman[64] gives the following unbalanced equations covering reactions for dunites and harzburgites containing iron :

$$(Mg,Fe)_2\ SiO_4 + H_2O + O_2 \leftrightarrow (Mg,Fe^{2+})\ (OH)_2 + (Mg,Fe^{2+})\ Si_2O_5\ (OH)_4 + (Mg,Fe^{3+},Fe^{2+})_3\ Si_2O_5\ (OH)_4 \pm Fe_3O_4 \pm FeNi \quad (1.3.8)$$

chrysotile; lizardite; magnetite; awaruite

This shows that oxygen pressure exerts a control on the phases produced. Carbon dioxide is quoted by Deer et al[72] as aiding the serpentinization reaction by removing magnesium as soluble carbonate.[67] The addition of aluminium into the system can yield platy aluminium serpentines.[65]

The type of alteration involved varies according to the temperature of the above reactions (equations 1.3.1-4) : weathering, or hydrothermal reactions taking place in the cooling magma. Barnes and O'Neill[71] first put forward evidence that serpentinization could take place at low temperatures, i.e. at about the mean annual temperature of the earth's surface. Campbell[73] supported this from observations of present-day serpentinization occurring in Western Australia. Page[74] gives a scheme by which the various secondary minerals, chrysotile, lizardite, magnetite and brucite crystallize with decreasing temperature. From field studies the most important temperature noted is that of the olivine/serpentine transformation. Wicks and Whittaker[65] state that olivine can be hydrated to yield serpentine±brucite±magnesia at 380°C. Coleman[64] states that lower temperatures also result in this hydration : 100-300°C, whereas Hostetler et al[67] mention 240-360°C in the same

context.

Other alteration products have been noted. Coleman[64] reports that in small ultramafic nodules being serpentinized or undergoing regional high grade metamorphism, it is not unusual for carbon dioxide or silica to be introduced to yield talc, chlorites or carbonates. For instance, iddingsite, a type of swelling chlorite, has been recorded in Les Causses du Larzac[75] and is thought to have been formed by weathering processes involving iron (II) oxidation, magnesium leaching and precipitative concentration of sodium and calcium. A different example is that of the chlorite at Lady Julia Percy Island near Portland, Australia. This chlorite[76] is believed to have been formed from hydrothermal reactions between gases, water and olivine under oxidizing conditions during the final cooling of the magma. Other similar occurrences are found at Kiluaea,[77] and New Mexico.[78] Elsewhere, olivine is recorded as altering to a large variety of products : iddingsite, bowlingite, nontronite,[79] saponite, vermiculite[80] and other smectites.[81] In the latter case Wilshire and Hobbs recognised the substitution of magnesium by iron which was later removed from the rock matrix in conjunction with silica and possibly aluminium.[82] Alternatively olivine can alter to yield a more consolidated product; for example, melilite, phlogopite and magnetite as at Saltpetre Kop, South Africa.[83]

1.3.2 Laboratory alteration of olivine

There have been relatively few laboratory investigations of serpentinization and other alteration reactions of olivine. However, this mineral and others have been synthesized and interconverted from pure chemicals under a variety of hydrothermal conditions. As the type of information obtained is complementary this discussion will be

concerned with both alteration and synthesis, but is restricted to the 0 - 600°C temperature range within which diamond is stable with respect to graphitization (Table 1.1.1).

The first successful synthesis of serpentine and olivine was made by Bowen and Tuttle.[84] By reacting mixtures of finely ground magnesia and silica with water in sealed bombs, at elevated temperatures and pressures, they demonstrated the stability limit of pure chrysotile to be 400°C, above which forsterite became stable; this temperature decreasing with the iron content of the minerals formed. Although Yoder[85], Kitahara and Kennedy[86] and Kitahara et al[87] obtained similar results for similar reaction times (10 hours - 38 days) Johannes[88] demonstrated that these boundary limits between serpentine and olivine related to the synthesis conditions only. The curve occurs generally at 60°C lower than 400°C if sufficient time for equilibration is allowed (Figure 1.3.1). The worker found that the effect of the proportion of iron was smaller than that previously noted, the difference being 20° rather than 80°C for a 10% fayalitic (iron-rich) olivine composition. The principal serpentine allotrope formed was chrysotile, as also noted by Coleman[64] and Moody.[89] Iron and/or aluminium were noted as being associated with the formation of metastable platy serpentines (e.g. lizardite) which later transformed to chrysotile. In the latter study, the effect of pressure was slight, in the range 20 - 2000 MPa. Hazen[90] has connected the relative ease of serpentinization of forsterite and fayalitic olivines with the influence of iron on their crystal structures. Iron appeared to enlarge the unit cell, thus facilitating faster reactions. Moody[89] summarized the serpentinization reactions by considering end member elements (cf equation 1.3.1).

$$\underset{\text{forsterite}}{5Mg_2SiO_4} + \underset{\text{fayalite}}{Fe_2SiO_4} + 9H_2O \leftrightarrow 3Mg_3Si_2O_5(OH)_4 + Mg(OH)_2 + 2Fe(OH)_2 \qquad (1.3.9)$$

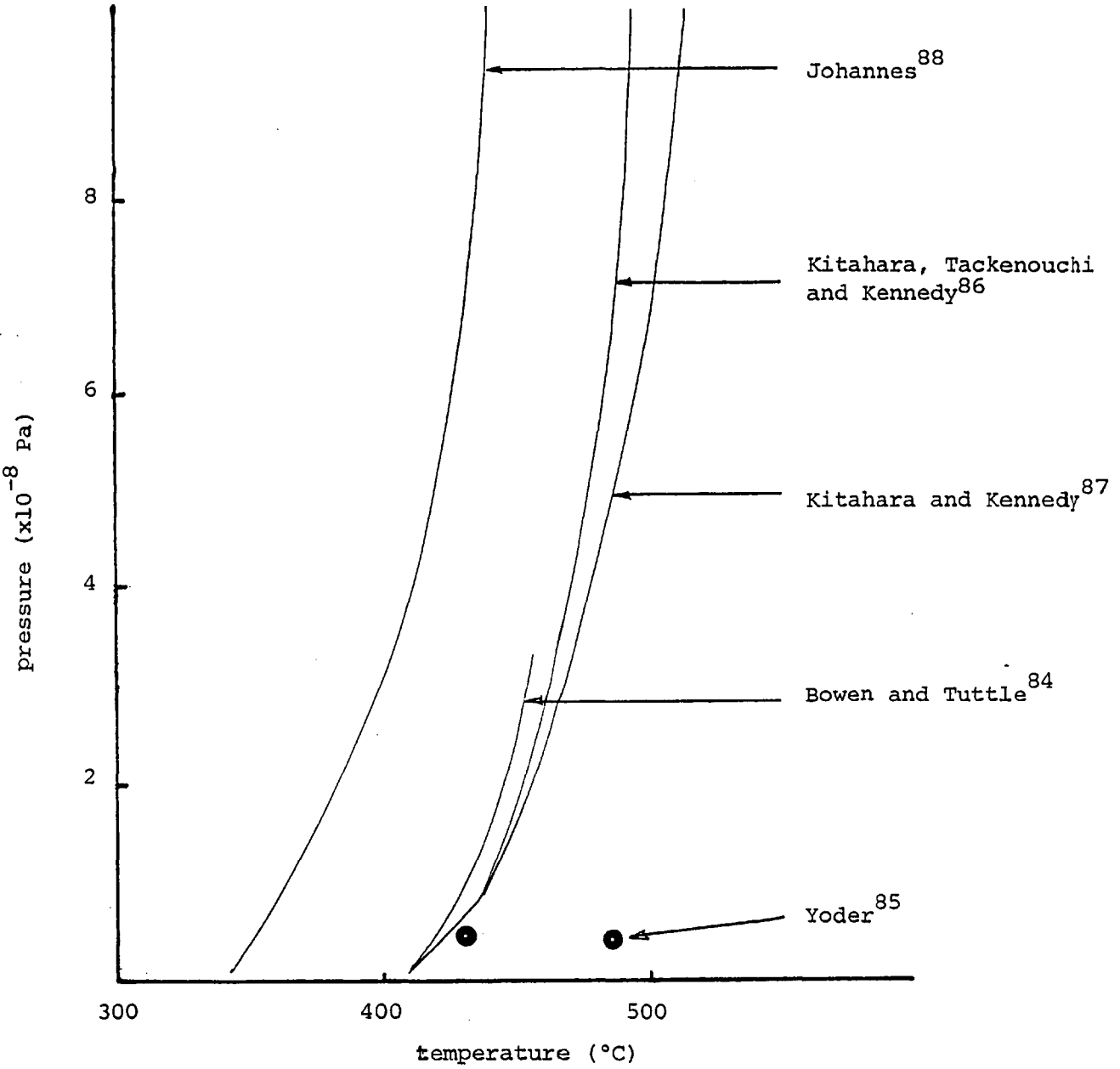


Figure 1.3.1[88] Position of the phase boundary between forsterite and serpentine for various investigations in the system $MgO-SiO_2-H_2O$

$$3Fe(OH)_2 \leftrightarrow Fe_3O_4 + 2H_2O + H_2 \qquad (1.3.10)$$

In a later work Korytkova et al[91] achieved serpentinization at lower temperatures by utilizing alkaline and acidic media. Alkaline media (∿ 0.75M sodium hydroxide) reacted with olivine to yield serpentines at 200°C. Acidic media proved more effective however, concentrations as low as 10^{-3} - 10^{-5}M being sufficient to achieve a similar objective at the same temperature.

1.3.3 Natural alteration of serpentine

A great variety of products have been reported to arise from serpentine degradation. For example Tantar Borash[92] states that in the Belozersk Area, USSR, the following minerals resulted from the alteration or interaction of chemical species with the serpentine-rich rocks of the area : talc; calcite; chlorite; actinolite; magnetite; biotite; iron oxides; quartz; breunnerite and other hydroxides. Butler[66,93] reports illite, kaolinite, montmorillonite, chlorite and talc to be weathering products derived from serpentines in the Lizard, Cornwall, and Nordmarka, Norway areas. Vermiculite is an alternative possibility.[61,94] Bricker et al[95] and Deer et al[72] also confirm talc as an alteration product of serpentine as follows :

$$Mg_3 Si_2O_5(OH)_4 + 1.16\ SiO_2 \leftrightarrow 0.79\ Mg_3 Si_4O_{10}(OH)_2 + 0.63\ MgO + 1.21\ H_2O \qquad (1.3.11)$$

The introduction of carbon dioxide gas can stimulate carbonate formation, which provides a means of removing magnesium, in the carbonatization of serpentinized olivine to yield talc[96] :

$$2Mg_3 Si_2O_5(OH)_4 + 3CO_2 \leftrightarrow Mg_3 Si_4O_{10}(OH)_2 + 3Mg\ CO_3 + 3H_2O \qquad (1.3.12)$$

Further evidence for carbonatization accompanying serpentinization is quoted by Naldrett[97] where talc - carbonate alteration is observed in ultramafic peridotites in Ontario :

$$16.75\ Mg_3Si_2O_5(OH)_4 + 1.93\ Fe_3O_4 + 28.78\ CO_2 \leftrightarrow 8.38\ (Mg_{.98}Fe_{.02})Si_4O_{10}(OH)_2 + 28.78\ (Mg_{.89}Fe_{.11})CO_3 + 0.71\ Fe_3O_4 + 25.12\ H_2O + 0.59\ O_2 \quad (1.3.13)$$

Milashev[96] has demonstrated a close association between the serpentine and talc stability fields in Russian kimberlites, the degree of replacement of serpentine by talc being dependent upon the amount of silica liberated. These stability fields are greatly dependent on the activities of carbon dioxide and water.

Two other alteration products of serpentine are vermiculite and montmorillonite. Bayliss[98] notes that the incongruent leaching of the brucite layer in serpentine, generates a magnesian vermiculite. Wildman et al[99] compared the thermodynamic stability of serpentine with the associated iron-rich montmorillonites found in California. Iron and aluminium resulting from surface weathering processes were found to replace magnesium in first-formed serpentine. The iron-aluminium serpentines then degrade to yield clays. This model appears to be plausible as iron and aluminium form a more stable hydroxide layer than magnesium. This type of reaction would appear to occur during kimberlite alteration to produce aluminium-rich clays.[100]

1.3.4 Laboratory alteration of serpentine

As discussed above, there is a maximum temperature (340°C - 400°C[84,88]) for which serpentine is stable with respect to olivine. Serpentine breakdown will proceed at lower temperatures. Compared

with other minerals, e.g. the micas, there are relatively few investigations reported.

Nagy and Bates[101] have demonstrated that serpentine minerals can be readily attacked by hydrochloric acid at 25°C, chrysotile being more susceptible than antigorite. Wildman et al[102] also achieved serpentine dissolution using carbon dioxide-charged solutions at room temperature, which suggested that this reaction played an important part in the breakdown of serpentinites in soil :

$$Mg_3\ Si_2O_5(OH)_4 + 6H^+ \leftrightarrow 3Mg^{2+} + 2Si(OH)_4 + H_2O \qquad (1.3.14)$$

Further evidence for dissolution stages in serpentine alteration was provided by Seyfried and Bischoff.[103] In their studies on seawater interaction on basalts at 70°C at 10 MPa and 150°C at 50 MPa they clearly showed that ion exchange of the species Mg^{2+};Ca^{2+};Si^{4+};Fe^{3+};K^+;Ba^{2+};Na^+ took place leading to an iron-rich smectite from a rock known to contain serpentine as an important constituent.

1.3.5 Alteration of pyroxene-amphibole group minerals

Pyroxene group minerals are commonly found in kimberlite assemblages and frequently found associated with olivine and serpentine.[30,61] Alteration studies have been concerned with similar mineral associations though in different igneous or metamorphic rocks. Butler[96] quotes two examples of pyroxene alteration : in serpentine rocks from the Lizard, Cornwall, and in a hypersthene monzonite (a pyroxene-rich igneous rock[30]) from the Nordmarka area near Oslo.[66] In both cases the identity of the alteration product is obscured because of the presence of other minerals but it was concluded that talc formed together with chlorite-vermiculite as intermediate mixed layered minerals. Wilshire[80] discussed the alteration of Australian and Californian orthopyroxenes

in conjunction with that of olivine, the final product being smectite-chlorite with goethite. The reaction was deemed to have occurred at a late stage of consolidation of the magma and involved leaching of magnesium and silica from the primary minerals. The probability of such leaching reactions taking place has been verified by the field work carried out by Ellis and Mahon[104] on the effects of thermal water activity in New Zealand. Barnes and O'Neill[71] in their alteration studies on dunites, harzburgites and peroditites consider dissolution of pyroxenes by ground water to take place at low termperatures (approx. 25°C) by :

$$Mg\ SiO_3 + 2H^+ + H_2O \leftrightarrow Mg^{2+} + Si(OH)_4 \qquad (1.3.15)$$

This results in the recrystallization from the residual solution of a serpentine talc/brucite assemblage. Deer et al[105] note that depending on the temperature and pressure, interaction with water of either meteoric (i.e. ground water) or hydrothermal origin can generate a variety of products according to the nature of other mineral and chemical species available for interaction. Typical initial products are amphiboles. For example, in the crystallization of gabbroic and noritic magmas cummingtonite-tremolite forms :

$$\underset{\text{enstatite}}{7(Mg,Fe)\ SiO_3} + H_2O + SiO_2 \leftrightarrow \underset{\text{cummingtonite-tremolite}}{(Mg,Fe)\ Si_8O_{22}(OH)_{22}} \qquad (1.3.16)$$

Alternatively retrograde metamorphism can occur in dalradian epidiorites yielding chlorites as additional products :

$$10\ Ca\ (Mg,Fe)\ Si_2O_6 + \underset{\text{anorthosite}}{Ca\ Al_2\ Si_2O_8} + 5H_2O \qquad (1.3.17)$$

$$\leftrightarrow Ca_2\ (Mg,Fe)_5\ Si_8O_{22}(OH)_2 + \underset{\text{chlorite}}{(Mg,Fe)_5\ Al_2\ Si_3O_{10}(OH)_8} + 9\ CaO + 11\ SiO_2$$

Chloritization can also be induced by interaction with chloride rich waters.[106] The introduction of aluminium noted in equation 1.3.17 has also been observed in the consolidation of the Premier kimberlite,[61] which probably explains the presence of hornblende. Carbon dioxide may also interact with pyroxenes.[107] In the carbonatite occurrences described the pyroxenes altered to phlogopite and calcite.

Various products can result from the amphibole minerals formed.[92] In the Belozersk area amphiboles are altered by carbon dioxide to talc and dolomite :

$$Ca_2\ Mg_5\ Si_8\ O_{22}(OH)_2 + CO_2 \leftrightarrow Mg_3\ Si_4\ O_{10}\ (OH)_2 + 2\ Ca\ Mg\ (CO_3)_2 + 4Si\ O_2 \qquad (1.3.18)$$

Aluminium interactions may also take place. Currie and Ferguson[108] have observed the result of fenitization on mafic rocks in the Callender Bay Complex, Ontario. Fenitization is described as the introduction of the species $K^+/Na^+/Al^{3+}/Ca^{2+}/Mg^{2+}/Fe^{2+}$ and the removal of "Si^{4+}" :[108]

$$Al^{3+} + Ca_2\ (Fe\ Mg)_4\ Al_2\ Si_7\ O_{22}\ (OH)_2 + Na^+ \leftrightarrow Ca_{1.5}\ Na\ (Fe\ Mg)_4\ Al_3\ Si_6\ O_{22}\ (OH)_2 + \tfrac{1}{2}\ Ca^{2+} + "Si^{4+}" \qquad (1.3.19)$$

Fenitization is an important process to be considered as it has been observed to be associated with degradation of minerals in kimberlites[106] where the presence of chloride ions was found to be of significance.

1.3.6 Other alterations

Of the kimberlite minerals other than those discussed above, the micas, namely phlogopite-biotite, have been the focus of many alteration studies. The formation of vermiculite-chlorite via hydrobiotite intermediary was shown in the field by Butler,[66,93] Barshad[109] and others.[110-112] Wilson[113] indicated the importance of interlayer

potassium removal in mica breakdown. Later Stoch and Sikara[114] verified Wilson's hypothesis that biotite could eventually yield a kaolinite product. These transformations were reproduced in the laboratory, using an ion-exchange approach by Barshad[115] and Newman and Brown[116] who also emphasized the importance of an oxidizing environment. Hoda and Hood[117] and Robert[118] related the ease of interlayer ion removal to mineral structure and Kittrick[119] identified the rate determining step of the reaction to diffusion of ions to the exchange site rather than the actual exchange itself. The introduction of polymerizing aluminium hydroxide groups was found to stabilise the alteration products formed[120] such that equilibria summarising mica breakdown could be presented[121] :

$$\text{mica-}K^+ + H_2O \leftrightarrow \text{mica-}H^+ + K^+ + OH^- \quad \text{(simple hydrolysis)}$$

$$\text{mica-}3H^+ + Al^{3+} \leftrightarrow \text{mica-}Al^{3+} + 3H^+ \quad \text{(aluminization)}$$

$$\text{mica-}Al^{3+} + H_2O \leftrightarrow \text{mica-Al } OH^{2+} + H^+ \quad (Al^{3+} \text{ hydroxylation})$$

Referring to other kimberlite minerals of calcite breakdown consists of simple solibulization[122] :

$$Ca\,CO_3 + 2H^+ \leftrightarrow Ca^{2+} + CO_2 + H_2O \qquad (1.3.20)$$

though it can be involved in more complex reactions of other minerals.[92]

Dimanche and Bartholone[123] have outlined the weathering of ilmenite, which yields principally rutile under sequential acidic and oxidizing environments.

1.4 Synthesis of Clay Minerals

The previous section described the reactions by which kimberlite minerals break down under geological and laboratory conditions. Clay minerals are often products of these reactions as mentioned previously.

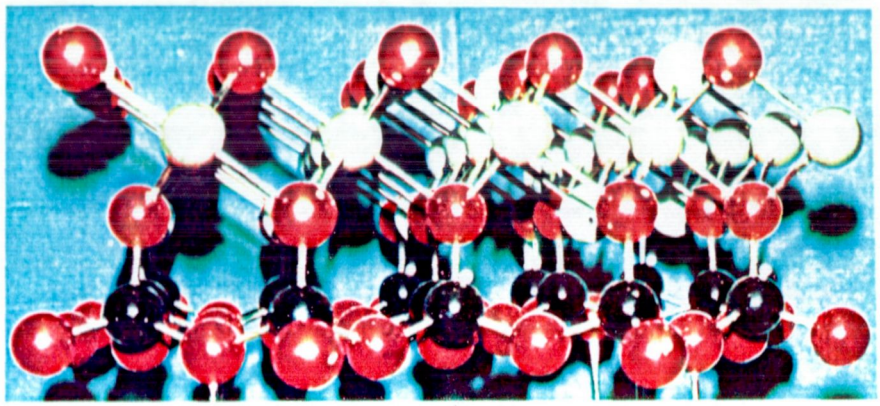


Plate 1.6 Model of a 1:1 (7Å) layer silicate. The basal tetrahedral layer consists of Si^{4+} (and Al^{3+}) ions (black) bonded to O^{2-} (red). The second layer consists of cations (Mg^{2+}, Fe^{2+}, Fe^{3+}, Al^{3+}) (silver) octahedrally coordinated with the O^{2-} and OH^{-} anions.
Examples : serpentine, kaolinite, septechlorites

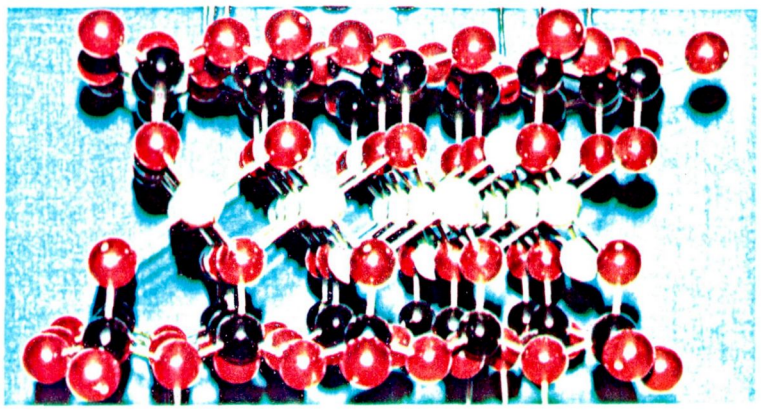


Plate 1.7 Model of a 2:1 (9Å) layer silicate. The structure incorporates that of a 1:1 layer silicate. An additional tetrahedral layer is present and is bonded to the octahedral layer as shown.
Examples : pyrophyllite, talc

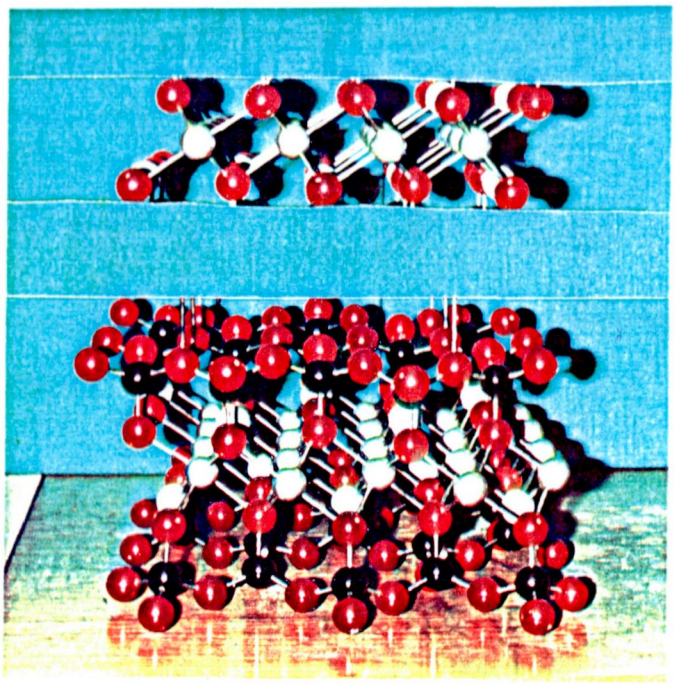


Plate 1.8 Model of a 2:1 (14-16Å) silicate. This structure is based on a 9Å one. The additional octahedral interlayer which separates the 9Å structures consists of cations (silver) bonded either to OH^- ions (chlorite) or water molecules by hydrogen bonding (vermiculite, smectite).

A large body of separate information about the formation of such clays exists and this will be reviewed now in two sections : the formation of simple 1:1 layer (7Å) kandite structures (Plate 1.6), e.g. kaolinite and related 9Å structures (Plate 1.7) and the formation of 2:1 layer (10-16Å) minerals, e.g. smectites (Plate 1.8).

1.4.1 Synthesis of 1:1 layer (7Å) minerals

Iler[124] states that there is "considerable evidence" for the existence of silicilic acid - $Si(OH)_4$ - in solution, the solubility of this hydroxide being enhanced by the presence of chloride ions and alkaline salts. From Figure 1.4.1[125] it is evident that saturated solutions of silica containing 2-3 mmol l^{-1} SiO_2 can be readily obtained in acidic and neutral media. Under these conditions polymerization of silicilic acid is assumed to occur to yield crystalline, cryptocrystalline or gel-like silicates, depending upon conditions. Wey[126] interprets the process as a base catalysed condensation reaction in which silicon temporarily achieves octahedral coordination :

$$2Si(OH)_4 + OH^- \leftrightarrow (HO)_5 Si^-\overset{H}{-}O\text{-}Si(OH)_3 \qquad (1.4.1)$$

$$(HO)_5 Si^-\overset{H}{-}O\text{-}Si(OH)_3 \leftrightarrow (HO)_3Si\text{-}O\text{-}Si(OH)_3 + OH^- + H_2O \qquad (1.4.2)$$

Continuation of the reaction results in the formation of large molecular weight species commonly as a sol or gel.[124] Iler notes several reagents which can affect the rate of condensation, namely pH (Figure 1.4.2) and the concentrations of the species F- and Al^{3+}. Details of Figure 1.4.2 will be considered later.

Various attempts have been made to synthesize hydrous aluminium silicates by silicilic acid gels. Results have been summarized by Roy and Osborn[127] and are given in Table 1.4.1. They indicate a range of platy aluminosilicates are obtainable. The workers carried out 2000 runs

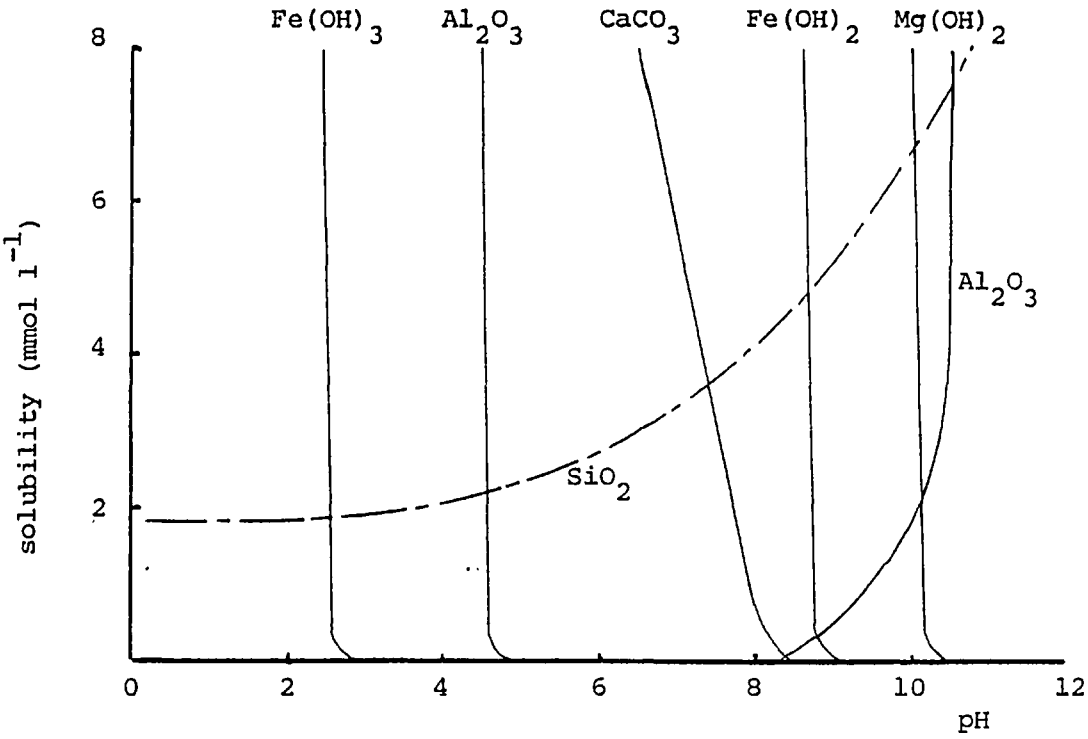


Figure 1.4.1[125] Solubility in relation to pH (∿ 25°C)

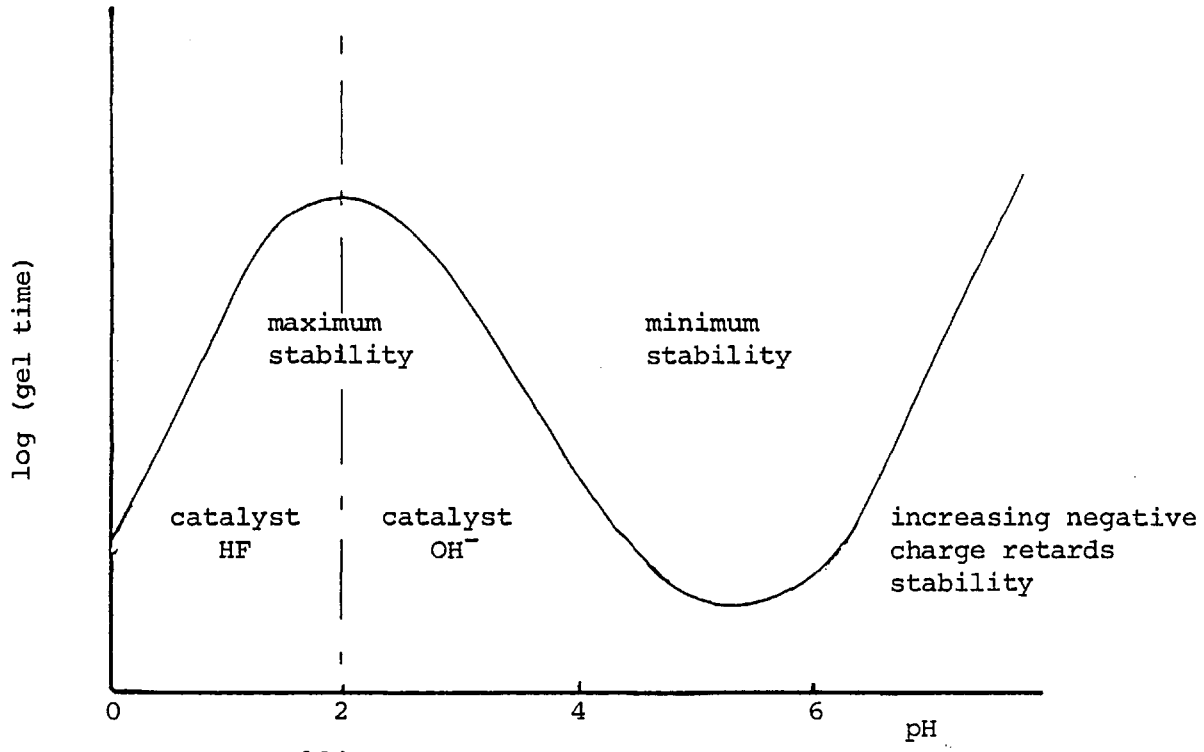


Figure 1.4.2[124] Sol stability : relation between log (gel time) and pH

TABLE 1.4.1 STABILITY DATA FOR ALUMINIUM-SILICATE HYDRATES[127]

Mineral	Minimum Temperature (°C)	Maximum Temperature (°C)	Minimum Pressure (MPa)	Maximum Pressure (MPa)	Time for Formation (days)
kaolinite	250	310/400	4.14	10.00/ 31.03	10
dickite	345	365	15.97	20.68	10
nacrite	335		31.03		6
beidellite	350	390	17.24	26.89	10
montmorillonite	Same ranges as kaolinite				
pyrophyllite	400	500	31.03	55.17	

using coprecipitated aluminate-silicate gels made subject to various temperatures and pressures. The phase relationships for the two types of system (Al_2O_3-H_2O and Al_2O_3-SiO_2-H_2O) are shown in Figures 1.4.3 and 1.4.4. The former illustrates the stagewise dehydration of hydrous aluminates which occurs with increasing temperature at different pressures, while the latter shows how these dehydration reactions are modified in the presence of silica. It is clear that the effect of pressure is of secondary importance in both cases, an observation substantiated in a later study.[128] Figure 1.4.4 represents the stability limits of the various minerals obtained and indicates the relative difficulty experienced in the synthesis of 2:1 layer minerals e.g. pyrophyllite. Roy and Osborn[127] attributed this to some of the aluminium having to go into tetrahedral coordination with silica, whereas in all other cases at lower temperatures, it was present in the octahedral state. In a later work Sand et al[129] showed that by adding sodium to the above ternary (Al_2O_3-SiO_2-H_2O) system a more varied phase diagram from which upper stability limits for sodium-montmorillonite, sodalite, analcite and paragonite could be obtained. Carr and Fyfe[130,131] investigated the ternary system Al_2O_3-SiO_2-H_2O in more detail, concluding that variables in the crystalline state of the reactants produced different phase diagrams. However a similar sequence of mineral transformations could be recognised :

		initial reactants
kaolinite→pyrophyllite	corundum	amorphous Al_2O_3 + quartz
	mullite	kaolinite + amorphous silica
	andulusite/ mullite	kaolinite + quartz

Rodrique et al[132] studied the influence of temperature on kaolinite formation at 175-250°C using alumino-silicilic gels at pH 0-4.8. It could be seen that kaolinite crystallized at 200°C (pH 4.8), the degree

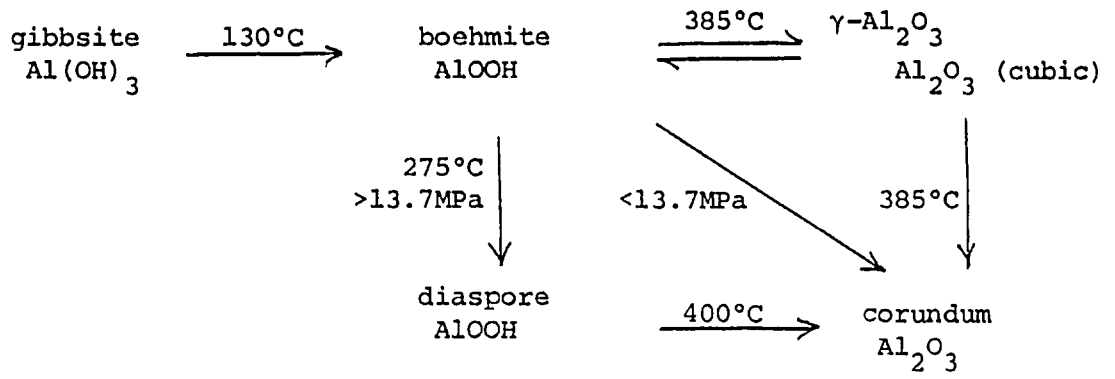


Figure 1.4.3[127] Schematic representation of relationships among phases in the system Al_2O_3-H_2O

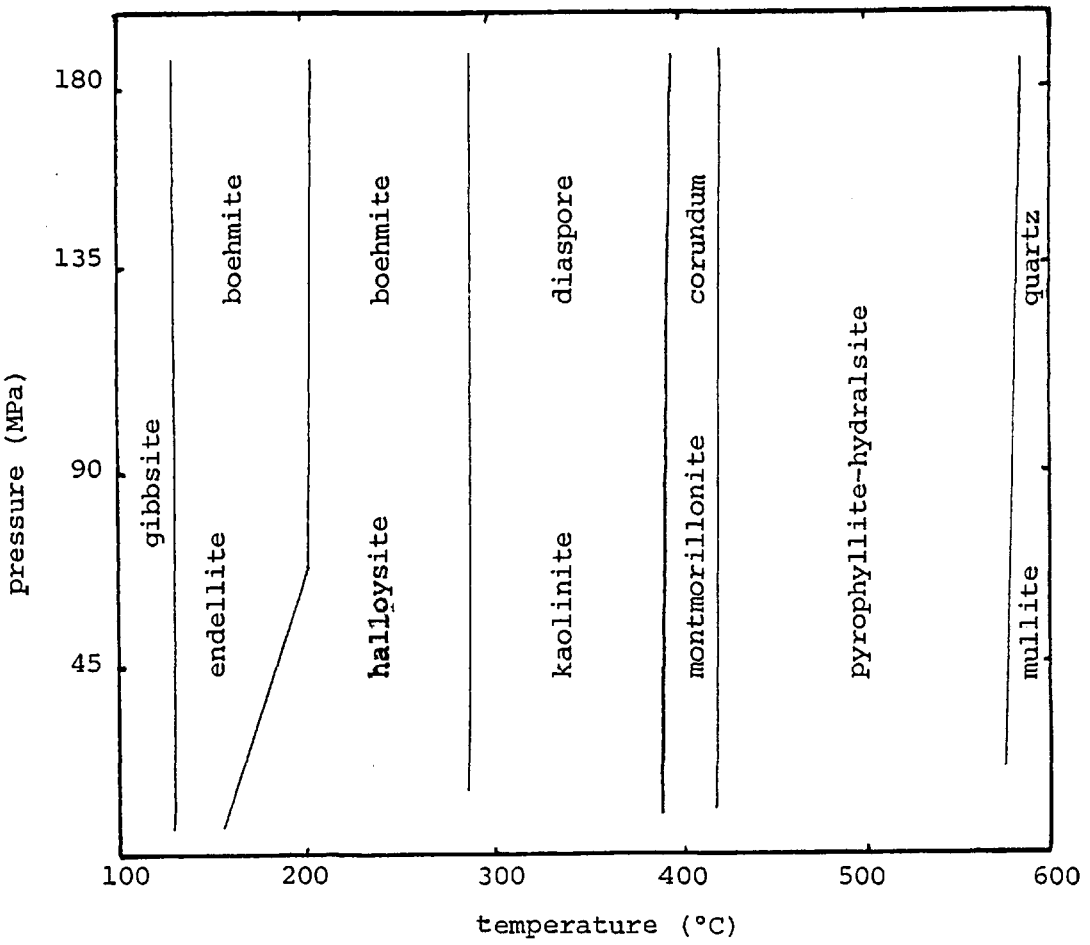


Figure 1.4.4[127] Phase diagram for minerals in the Al_2O_3-SiO_2-H_2O.system

of crystallinity increasing with temperature (up to 250°C) and increasing acidity above 220°C. Other associated products were boehmite and pseudoboehmite which formed where higher aluminium proportions were used. The workers noted that kaolinite formed directly from a depolymerized gel by a process of silica subtraction instead of via a boehmite intermediary.[133] This direct transformation requires a smaller activation energy than that of silicification "of a poorly crystalline alunic support" (i.e. boehmite) which is in accordance with the observations made in lower temperature systems.[134]

The hydrothermal relationships between kaolinite, pyrophyllite and other associated species at higher temperatures (350-450°C) was investigated by Eberl and Hower.[135] Using gels in sealed gold tubes reacted for 12 - 100 days they demonstrated that the silicon/aluminium ratio was an important criterion governing the crystal order and thermal stability of kaolinite products. For ratios greater than 2, kaolinite reacted with quartz to form pyrophyllite at 345°C :

$$Al_2\ Si_2O_5(OH)_4 + 2SiO_2 \leftrightarrow Al_2\ Si_4O_{10}(OH)_2 + H_2O \qquad (1.4.3)$$

For silicon/aluminium ratios less than 2 the transition occurs at 405°C :

$$2Al_2\ Si_2O_5(OH)_4 \leftrightarrow Al_2\ Si_4O_{10}(OH)_2 + 2AlOOH + 2H_2O \qquad (1.4.4)$$

Ordered kaolinite was favoured by high temperature and a low silicon aluminium ratio, being formed at temperatures of 150°C or above from a halloysite polymorph. Extending the study in a later work, Eberl[136] generated pyrophyllites and associated mixed layers using alumino-silicilic gels and quartz mixtures in the correct stoichiometric ratios at 350°-450°C over a period of 11 - 38 days.

The success of syntheses of aluminosilicates at elevated

temperature and pressure prompted investigations into the possibility of synthesis at lower temperatures (25-]50°C), so as to model present day weathering phenomena. Brindley and Dekimpe[137] synthesized kaolinite from agitated alumino-silicilic gels at 150°C, 500 kPa, and pH 1.5 or below. For pHs greater than 1.9 gibbsite was the sole crystalline phase. Dekimpe et al[138] furthered the study by demonstrating that the formation of kaolinite at low pHs was facilitated by stabilisation of the hexacoordinated state of the aluminium ion. At higher pHs a micaceous-kandite was reported, the proportion of tetrahedrally coordinated aluminium increasing in the gel structure to a maximum value of 30-40% of the total aluminosilicate layer.[133] Magnesium clays developed more readily owing to their non-interaction with the silicon polymerisation reactions. From base exchange capacity measurements[138] and infra-red data[133] equilibria governing the transformation between the two coordination states of aluminium have been deduced. A scheme is shown below.

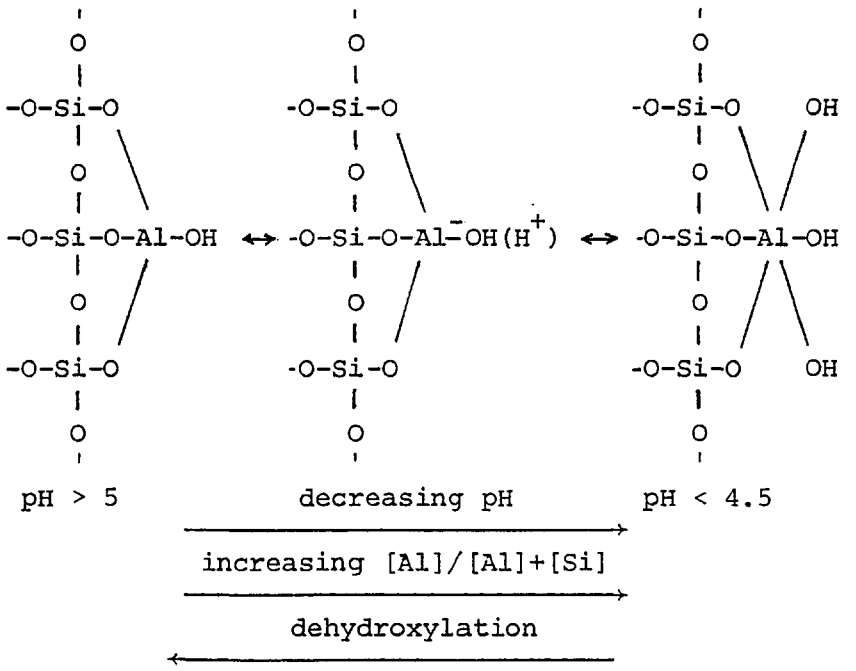


Figure 1.4.5 Coordination states of aluminium relative to silicon in aluminosilicate synthesis (124,133,138,139)

Following syntheses of kaolinite from gibbsite-ethyl silicate mixtures in acidic conditions (pH1-2) at 170°C for 10 days, Dekimpe et al[139] and Dekimpe[133] showed time and temperature to be the most important criteria, gibbsite ageing first to boehmite and thence to kaolinite at pH 1.5 - 2.0. A temperature increase was attributed to increase the crystallization rate, namely the rate of silica fixation with respect to the Al-OH layer. The model proposed for kaolinite formation, involving a solid state transformation via an amorphous phase incorporating Al^{VI}-O-Si polymerization as opposed to one of dissolution-reprecipitation, was further substantiated by Dekimpe and Fripiat.[134] This work involved acid hydrolysis of zeolites and their subsequent conversion to kaolinite. However, by noting the thermodynamic readiness of kaolinite to precipitate from solution[140-2] Kittrick achieved kaolinization of montmorillonites over a period of 3 - 4 years according to the precipitation reaction which assumes the prior breakdown of montmorillonite to monomeric silica

$$2Al^{3+} + 2Si(OH)_4 + H_2O \leftrightarrow 6H^+ + Al_2 Si_2 O_5 (OH)_4 \qquad (1.4.5)$$

Kittrick stresses the importance of a solution being super-saturated with respect to kaolinite for the reaction to proceed.

The criteria discussed above were successfully exploited by Linares and Huestas[144] to produce a variety of semi-crystalline products. Using sodium silicate solutions as the monomeric silica source, reactions at 20°C for 1 month with aluminium in the form of fulvic acid complexes gave the products illustrated in Figure 1.4.6. The diagram shows that, regardless of pH, provided the aluminium concentration is high enough, the hexacoordinated state of the ion (as stabilised by fulvic acid) can force kaolinite precipitation. At low aluminium concentrations the products grade through the various

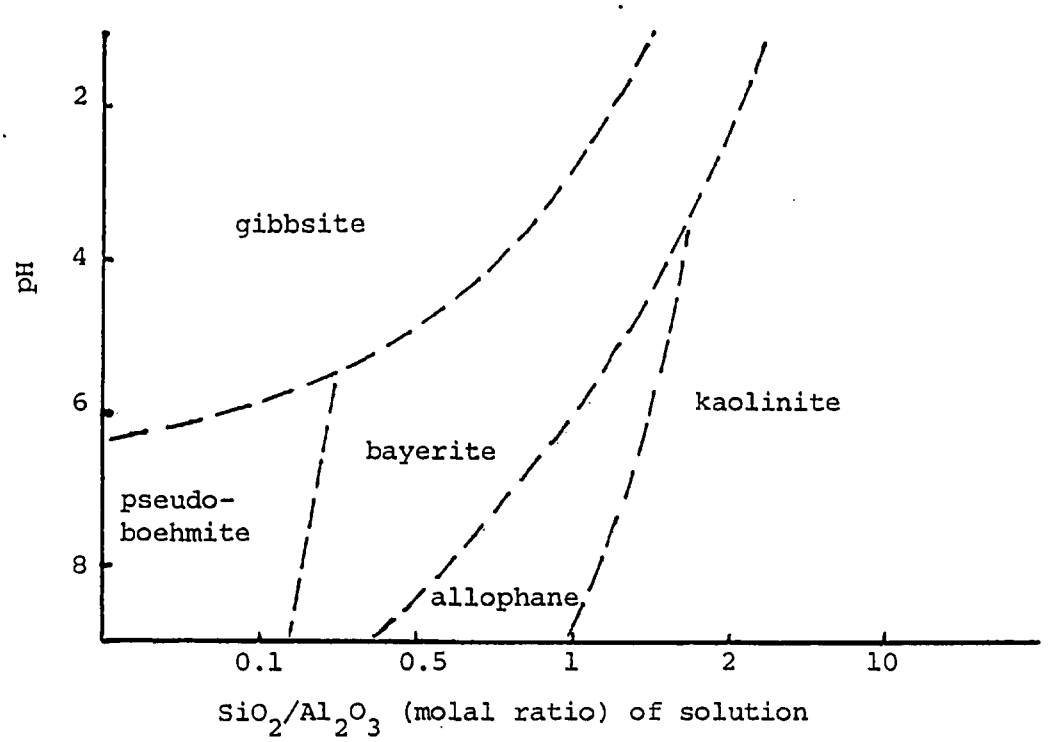


Figure 1.4.6[144] Phase diagram of minerals synthesized at 20°C showing their relationship to initial SiO_2/Al_2O_3 composition and equilibrium pH

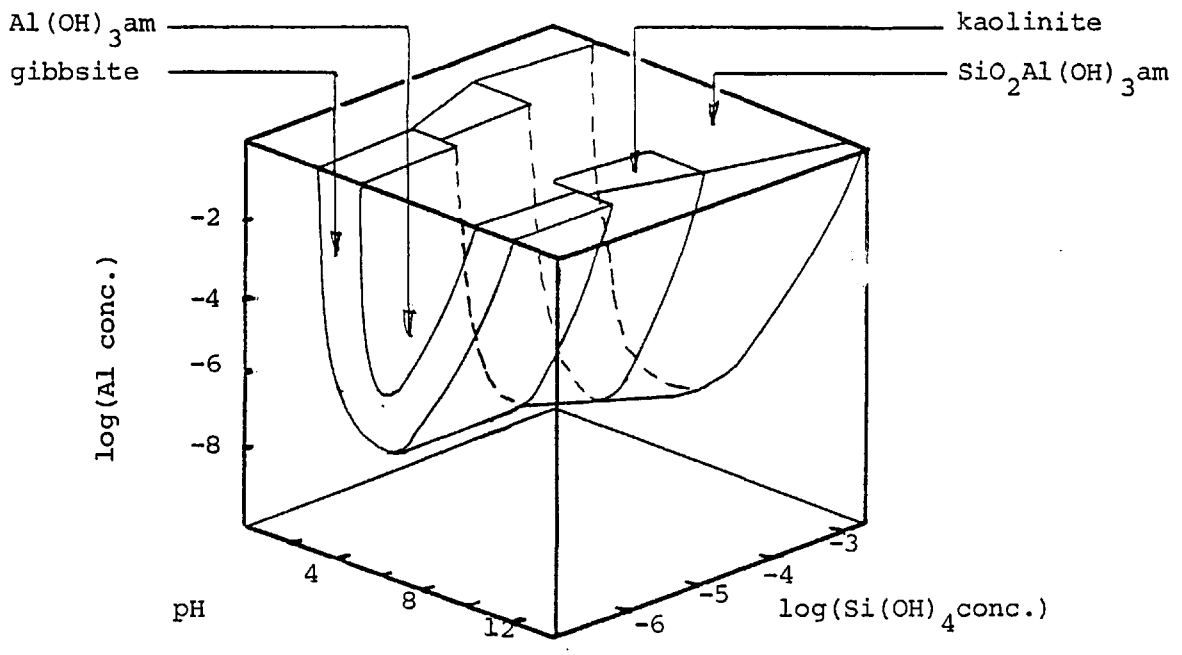


Figure 1.4.7[153] Relationship between the concentrations of the species Al^{3+}, $Si(OH)_4$, H^+ and the nature of the minerals formed at 20°C, 100kPa.

aluminium hydroxyoxides. Similar results were obtained by McHardy and Thompson[145] and Hem and Lind.[146] In the latter study quercutin was found to enhance Al-O-Si bonding in kaolinite formation in tests which took place over 6 months at 25°C.

Siffert and Wey[147] summarised the principal difficulty encountered in kaolinite crystallization as the tendency of aluminium ions to surround themselves with a tightly bound shell of water molecules and/or the formation of sparingly soluble aluminium polycations. Complexing using organic acids[148,149] is one method of overcoming this, an alternative is the prevention of highly concentrated zones of ions by slowly changing the pH of the reaction solution[148] employing anionic ion-exchange resins in the (OH) form. The anionic nature of the solution was noted by La Iglesia and Martin Vivaldi[148] to have an effect : the species NO_3^-, Cl^-, $CH_3\ COO^-$ yielded flocculent precipitates of kaolinite whereas SO_4^{2-}, COO^-, $(COO)_2^{2-}$ yielded basic salts to the detriment of kaolinite formation. Tests using alkaline solutions in contact with cationic resins in the (H^+) form,[150] and homogenous precipitation following feldspar hydrolysis have also rendered good results.[151]

$$K\,Al_3\,Si_3\,O_{10}\,(OH)_2 + 4H^+ + H_2O \leftrightarrow Al_2\,Si_2\,O_5\,(OH)_4 + K^+ + Al^{3+} + Si(OH)_4 \qquad (1.4.6)$$

La Iglesia and Van Oosterwyck Gastauche[152] summarised the crystallization conditions at low temperature for kaolinite-gibbsite formation. By making assumptions regarding the chemical nature of the gels that may be formed, a stability diagram based on thermodynamic calculations was put forward indicating the concentrations of the species Al^{3+}, $Si(OH)_4$, H^+ required for mineral crystallization as shown in Figure 1.4.7. Using the successful synthesis results based on the information given in Figure 1.4.7 the methods by which kaolinite

could be successfully synthesised were summarised as follows :

a) Direct precipitation from solution

b) Slow introduction/departure of ions on a crystallization base originating from either slow formation/dissolution of gels/crystalline phases or homogeneous precipitation as induced by slow pH changes or gradual mineral hydrolysis.

The rate of the reaction :

$$Al^{VI}\text{-Si gel (O,OH) } H_2O \rightarrow \text{halloysite} \rightarrow \text{metahalloysite} \rightarrow \text{kaolinite} \qquad (1.4.7)$$

was discussed in a second paper,[153] in conjunction with high temperature syntheses. In conclusion,

a) temperature affects both the rate and the type of crystallization low temperatures favouring 1:1(7Å) kandites, high temperatures 2:1(9Å) layered minerals;

b) the use of gels produces a higher rate of reaction than that of ground oxides;

c) various types of apparatus have been used resulting in a large range in the stability limits to be reported (there is a need for standardization of equipment);

d) although the species Al^{3+}, $Si(OH)_4$, H^+ must react in the correct ratio, the concentration required for crystallization is very low; and

e) acidic pHs favour kaolinite formation.

1.4.2 Synthesis of 2:1 layer (10-16Å) minerals

Contemporary with the studies made into 7Å kandite synthesis various investigations were made into the conditions for the formation

of 10-16Å minerals, which are based on the 9Å pyrophyllite-talc structure (Plate 1.7) and possess an interlayer consisting of cations bonded to either water molecules or hydroxide ions (Plate 1.8).[154] The present literature survey considers the conditions required to form a mineral type which includes the 10Å micas, 14Å chlorites and vermiculites, and 15-16Å smectites, which from field evidence are most likely to form the stable alteration end products of kimberlite degradation.[9,35] The problem of synthesis has been approached from two viewpoints : the conversion of a material that already has a phyllosilicate type of structure and the formation of phyllosilicates from constituent ions in solution gels or ground oxides at elevated or room temperatures.

Alteration of phyllosilicate minerals : Various authors have demonstrated that simple reactions can cause reversible transformations from one clay mineral type to another. Examples include leaching of potassium from illite to produce montmorillonite;[155] hydrolysis of swelling chlorites to produce smectites. The latter models interlayer clay formation as seen in nature.[156-8] The addition of alkali or magnesium cations reverses such chlorite-smectite transformations.[159] Other dehydroxylations of chlorites have been studied.[160,161]

Synthesis at elevated temperatures (100-500°C) : The initial studies in this field used a similar approach to those in section 1.4.1, differing from them in the inclusion of magnesium in the systems. Roy and Roy[162,163] carried out more than a thousand synthesis experiments using a variety of apparatus (inconel, stellite and stainless steel pressure vessels) containing metal oxides as the initial reagents and equilibrates at temperatures and pressures up to 900°C, 9-138 MPa respectively. Their results are shown in the phase diagram in Figure 1.4.8 which illustrates the stability limits for minerals in the system $MgO-Al_2O_3-SiO_2-H_2O$.

System	100	200	300	400 temperature °C
Al_2O_3-H_2O	gibbsite	boehmite	boehmite	diaspore | pyro. mont. qtz
MgO-H_2O	brucite			
Al_2O_3-SiO_2-H_2O	endellite	halloysite-kaolinite		Al mont. pyro. hydralsite
MgO-SiO_2-H_2O	serpentine + brucite			forst.
Al_2O_3-MgO-H_2O	brucite + gibbsite	brucite + diaspore		spinel
Al_2O_3-MgO SiO_2-H_2O	metastable kaolinite, montmorillonite, chlorite interlayers in absence of H_2O; Al serpentine and clinochlore			

Abbreviations : forst. forsterite; mont. montmorillonite
pyro. pyrophyllite; qtz.quartz

Figure 1.4.8 Effect of system studied and temperature on nature of products synthesized[154]

Difficulties were experienced in chlorite synthesis. These were further studied by Nelson and Roy[164] who, using similar procedures, managed to generate chlorites above 400°C. As indicated in the previous work,[154,163] 7Å magnesium-aluminium kandites were produced, which due to their chemical similarity to chlorites, were termed septechlorites.[164] The structural relationship between septechlorites and chlorites is shown in Plates 1.6 and 1.8. Nelson and Roy[164] synthesized a complete series of septechlorite minerals, differing according to their chemical composition. A minimum aluminium concentration in the reagent mixture was necessary to produce the chloritic products as the ion entered into both tetrahedral and octahedral coordination with silicon and magnesium respectively. In conjunction with iron, aluminium concentration has a great effect on the resultant chlorite structure formed.[165] Investigations into magnesium-aluminium clay synthesis were also made by Gillery.[166] Reacting gels of the composition $(6-x)MgO(4-x)SiO_2$ x Al_2O_3 in the range 400-620°C, 103-386 MPa, chlorites were generated having a composition $(Si_{4-x}Al_x)(Mg_{6-x}Al_x)O_{10}(OH)_8$ where x has a value larger than 0.5 provided the temperature exceeded 500°C. The worker put forward a phase diagram relating temperature and proportion of tetrahedrally coordinated aluminium to the various phases produced (Figure 1.4.9).

Synthesis of dioctahedral clay minerals (namely those containing trivalent rather than divalent ions in the octahedral layer) was achieved by Granquist and Pollock.[167] By reacting diatomaceous earth slurries with sodium and aluminium hydroxide solutions at 280-300°C for 72 hours, an interstratified mica-montmorillonite was produced. A mechanism was put forward from kinetic studies as follows :

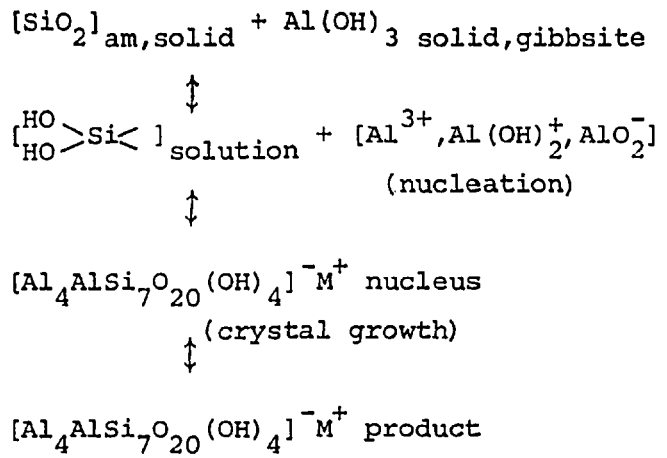


Figure 1.4.10 Formation of mica-montmorillonite from gels[167]

Ilyama and Roy[168] and Velde[169] have also synthesized saponites and smectites using gels mixed in their correct stoichiometric proportion. Velde demonstrated that the synthetic products had similar phase relationships to those found in nature.

Synthesis at low temperatures (25-100°C) : Initial investigations involved precipitation from solution. Henin[170] used very dilute solutions ($\sim$ 0.1ppm) of silica containing metal hydroxides at 60°C to yield montmorillonites and antigorites. Orientation between the reacting species was found to be important in facilitating absorption by the polymerizing silicate layer of the cations. Wey and Siffert[171] obtained similar results noting that the species Na^+, Cl^-, SO_4^{2-}, Ca^{2+} had no beneficial effect. Caillère and Henin[172] and Gastauche et al[82] state that such phyllosilicate formation passes through an amorphous phase during which the tetrahedral layer "conserves the organization of the clay structure". Their experiments substantiated the view that aluminium has a significant influence on silica precipitation and that in alkaline conditions, 2:1 layer structures formed (cf. section 1.4.1). The incorporation of magnesium within the clay product only occurred in the pH range 6.8-10.4.[159] In summarising

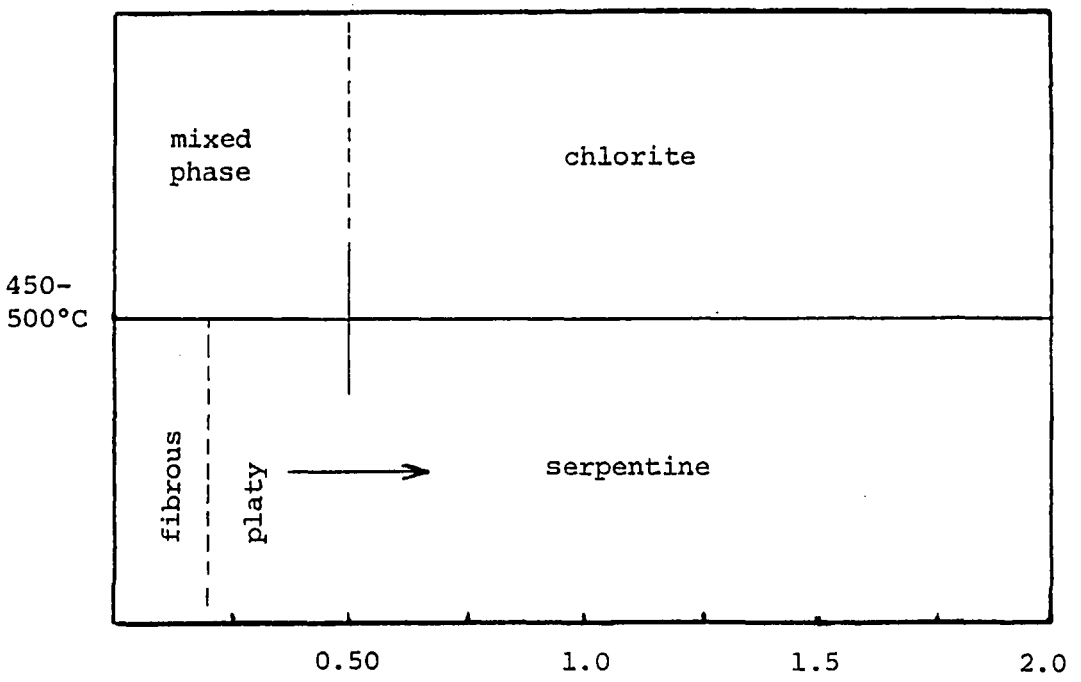


Figure 1.4.9[166] Phase diagram for 7Å and 14Å minerals generated in the range 420-600°C in a $MgO-SiO_2-Al_2O_3$ system

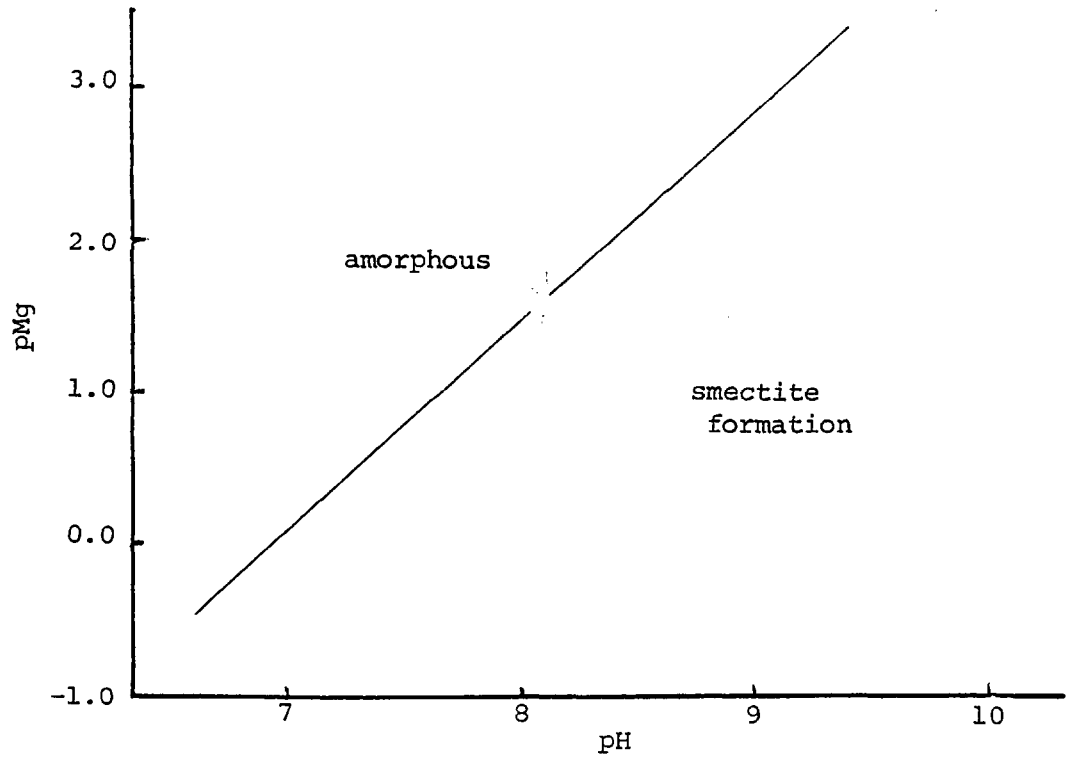


Figure 1.4.11 Smectite mineral formation as related to initial magnesium content and pH of solution. (Conditions 30ppm SiO_2, 3ppm Al_2O_3, 20°C, 3 months' reaction time)

the results of these and other workers,[173,174] Harder[175] listed important criteria to be considered in the chemisorption of metal hydroxide species by silica which results in clay precipitation :

a) Polymerized $Si(OH)_4$ preferentially adsorbs metal hydroxides

b) Ratio of aluminium to silicon in the initial solution

c) More silica is found on hydroxide precipitates at lower temperatures

d) Hydroxide precipitation is controlled by pH

e) Sorption takes place more readily on amorphous material than on crystallized forms.

Harder[175] also notes that magnesium can facilitate the formation of hexacoordinated aluminium resulting in the generation of brucite-gibbsite interlayers in the clay mineral structure. A critical balance exists between the aluminium, silica and magnesium concentrations which control the nature of the product.[176] The effect of magnesium is demonstrated by the minimum concentration requirement for smectite formation as shown in Figure 1.4.11. Harder[177] undertook a similar investigation concerning iron aluminosilicate synthesis. The worker demonstrated that reducing conditions resulted in nontronite formation, where the iron/silicon ratio was 1:10-1:3 or chamosite (a septechlorite) synthesis where the same ratio ranges from 1:1 to 1:2.

1.5 Discussion

It is now widely accepted that diamonds are broken in the comminution stages of processing. Several investigations are presently being pursued in which conventional methods of rock breakage are eliminated, e.g. electrocrushing. Another approach, which awaits research,

involves the natural degradation of kimberlite. Kimberlite is a complex rock texturally and mineralogically, some examples of which exhibit extensive alteration. Much work has been done on mineral breakdown as observed in nature, in the laboratory, as well as on the synthesis of clays from gels under idealised conditions. Little work has been performed on artificially inducing rock breakage through degradation and there is confusion and speculation regarding the mechanisms of alteration.

The objectives of this new study can be summarised as :

a) Improving the understanding of alteration reactions such that the two aspects of rock disruption and subsequent synthesis of a new suite of minerals are inter-related.

b) Proposing an optimum method of liberating diamond, without comminution, by employing such reactions.

CHAPTER 2

ANALYTICAL METHODS

2.1 Introduction

The mineralogical and chemical complexity of kimberlite necessitates special care in sampling, sample preparation and analysis if reproducible results are to be obtained in experimental work. In particular, particles in test samples should remain as essentially unliberated mineral-aggregates while being of small enough size for the (representative) samples to be handled conveniently in the laboratory. Furthermore, as definitive phase and elemental analysis of kimberlite cannot be expected from the direct application of available analytical techniques, a group of modified, mutually supportive, methods needs to be available.

This chapter deals principally with, firstly, the sampling and sample preparation scheme developed for kimberlite, and secondly, the established analytical procedures which have been selected namely X-ray diffraction, thermal analysis and infra-red spectroscopy. The advantages and limitations of each method are reviewed and these methods have been extended in consideration of the analytical requirements of the experimental work. A new method has been developed for estimating the proportions of clay phases which form the products of hydrothermal reaction.

2.2 Sampling and Preliminary Analysis of the Kimberlite

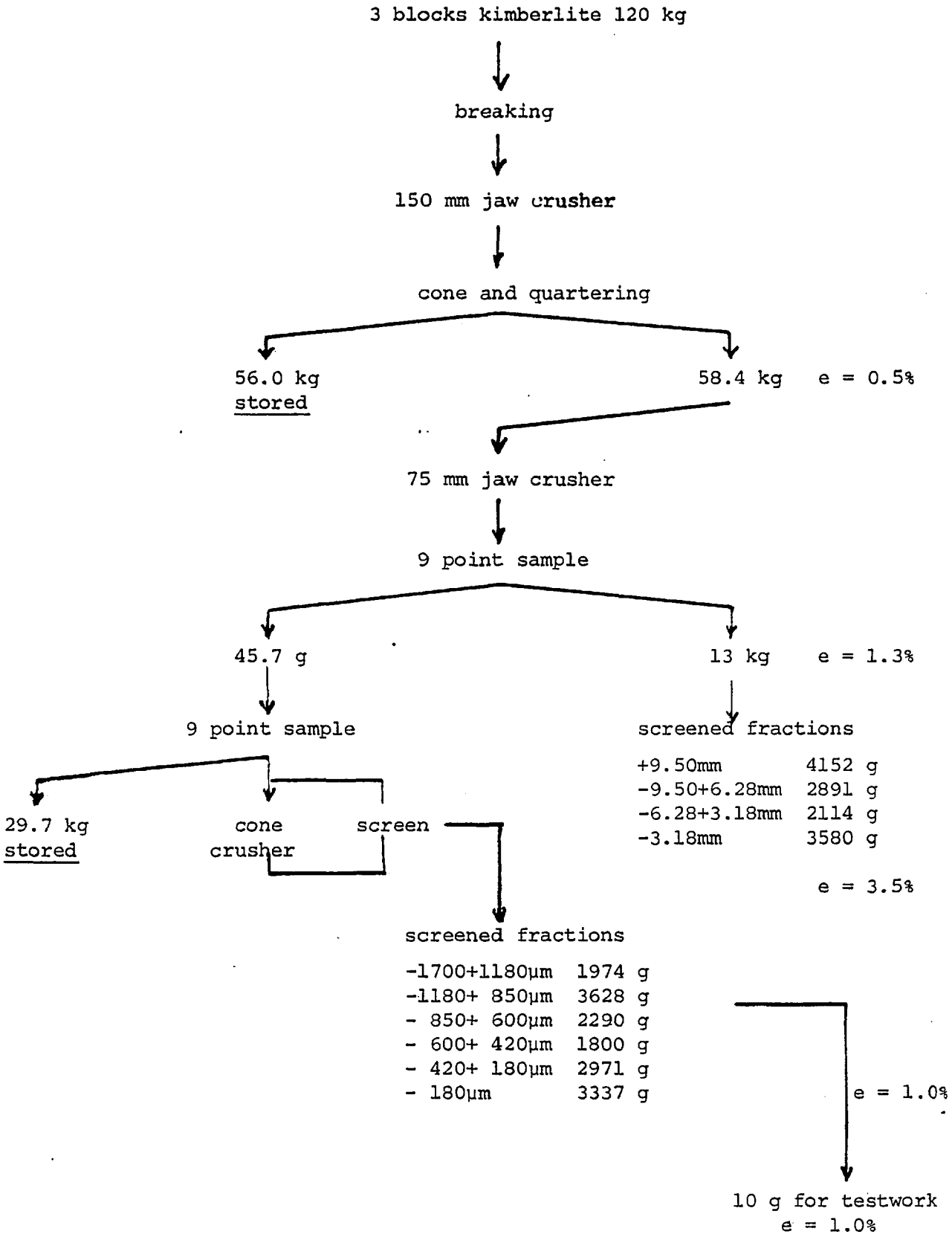
2.2.1 Sampling and sample preparation

The blocks of kimberlite used in the testwork had a total mass

of 120 kg and were three of a number, which had been excavated from the open pit at Wesselton in 1896 and sent to the Royal School of Mines for exhibition purposes. Preliminary examination of hand specimens showed that the kimberlite was essentially unaltered and therefore ideal for a degradation study.

The sampling scheme in Figure 2.2.1 was adopted to facilitate reproducible preparation of sufficiently large quantities of material for mineral identification, standards preparation and experimental work. The scheme was based on preliminary mineralogical investigations using X-ray diffraction and thin-section microscopy of arbitrarily selected hand samples (see later for details of these methods). The presence of olivine, serpentine, mica and calcite was revealed. Rough estimates of liberation size were made by measuring the grain size of particles in the thin sections, employing a specially etched disc to calibrate the graticule in the microscope. The approximate phase proportions were also deduced by a point counting technique which is described in Section 2.2.2. The data obtained enabled sampling errors to be calculated. Different methods have been put forward for sampling error estimation,[178,179] some involving non-gaussian distributions;[180] those due to Barbery[181] and Gy [182,183] being employed in this case. In these calculations, a phase of interest (characterising the sample) required to be selected. Calcite was chosen, as this mineral had an appropriate head assay (about 10%). In general, size fractions were taken having overall errors not exceeding 3.5% thus ensuring that the fractions were reasonably representative of the kimberlite as a whole.

The sampling scheme started with the breaking of the three large blocks of kimberlite by means of a sledge hammer. As soon as suitably sized fragments were obtained they were fed to a Blake 150 mm



Notes : (a) Cumulative error denoted by e, stated at each size
(b) Error calculation based on 10% calcite, liberation size 150µm
(c) Grinding stages operated to minimise fines production

Figure 2.2.1 Sampling scheme for kimberlite

jaw crusher. Care was taken to ensure that the rock was fractured, rather than ground, to reduce the proportion of fines; consequently the exit set of the crusher was adjusted to its maximum value (44.5 mm). After all the kimberlite had been crushed at this setting, it was divided into two portions of 56.0 and 58.4 kg by the coning and quartering technique. The 56.0 kg portion was stored whereas the other was further broken in a laboratory Blake 75 mm jaw crusher set at 10 mm. Here, the equipment was 'choke fed' to further reduce fines production. The broken kimberlite was again separated into two streams, 13 kg being sampled from the rest using the nine point technique and was used for further mineral investigation and standards extraction. The other stream (45.7 kg) was reserved exclusively for the preparation of feed for testwork. One third of the latter was sampled by the nine point method and the remainder stored. The sampled fraction was carefully and successively broken in a laboratory cone crusher and screened, in closed circuit, until all the kimberlite passed 1.7 mm. The material was closely screened into fractions between 1700 and 180 μm. The -1180+850 μm fraction was selected for testwork, as this size range best satisfied the criteria outlined in the introduction. This fraction was approximately at ten times liberation size (see later) while a sample of 10 g mass could be taken with a sampling error of 1%. This size also represented roughly the minimum economic size for diamonds.

2.2.2 Mineral analysis

Making use of the -3.18 mm fraction (Figure 2.2.1), 330 g was sampled using the nine point technique and screened to yield intermediate size fractions between 2400 and 45 μm. Each, when observed under the binocular microscope, showed that although some calcite was liberated at 620 μm, essentially complete liberation of all

the major phenocrystic and matrix minerals apparently occurred only at sizes below 150 μm. There was no evidence of extensive preferential liberation. Consequently the -150+106 μm portion was selected for detailed examination of the phases present.

Twenty gramme quantities of the -150+106 μm fraction were subjected to dense medium separation[184] at a relative density of 2.96 (using tetrabromoethane in conjunction with a small separating funnel and filter). The 'sinks' were further separated into +3.26 and -3.26 +2.96 density products using di-iodomethane. The 'floats' were subdivided into four less dense portions : -2.38; -2.60+2.38; -2.70 +2.60; -2.96+2.70 with the aid of various tetrabromoethane-trichloroethane mixtures. The six fractions were thoroughly washed with acetone or alcohol, dried, weighed and examined under the binocular microscope. Samples of each were also taken for analysis by X-ray diffraction. Results are shown in Table 2.2.1. As can be seen the principal phases were serpentine, olivine, calcite and mica. Smaller concentrations of other phases were noted : apatite, spinel, pyroxene and ilmenite.

TABLE 2.2.1 QUALITATIVE ANALYSES OF RELATIVE DENSITY FRACTIONS

Fraction	Abundance		
	high	medium	low
-2.38	calcite	serpentine	
-2.60+2.38	serpentine	calcite	mica
-2.70+2.60	mica	calcite	serpentine
-2.96+2.70	mica	calcite	serpentine
			olivine
			ilmenite
-3.26+2.96	olivine	pyroxene	calcite mica
		serpentine spinel	ilmenite
			apatite
+3.26	olivine	clinoenstatite	mica
		serpentine	ilmenite
			magnesioferrite
			magnesiochromite
			apatite

To obtain a semi-quantitative analysis, 50 g of the coarsest fraction (+9.50 mm) was taken in accordance with Gy's procedure.[183] The sample was progressively broken to -150 μm by the laboratory cone crusher. The resulting (12 g) -150+106 μm fraction was deslimed, riffled, separated by tetrabromoethane and both sinks and floats subjected to assay by the following method, which employed the binocular microscope.

In order to identify the phases so that they could be counted when observed under a binocular microscope, 10-20 grains of each mineral type were hand-picked from the fraction discarded during riffling. These grains were then subjected to tests outlined by Jones and Fleming[184] for systematic particle identification. These tests are based on diagnostic mineral properties : colour, habit, lustre, cleavage, relative density, refractive index, streak and chemical reactivity. For the purposes of particle counting, colour and habit were particularly useful properties. For example, mica was distinguished by its flaky, lamellar habit, whereas olivine grains were light green and opaque, with a subhedral habit. Serpentine grains were darker green with a poorer habit. The two fractions of sampled particles were separately shaken, mixed and presented on microscope slides as randomly distributed monolayers. The mounted particles were viewed through the binocular microscope, identified and counted where they crossed the lines of an arbitrarily selected section of the graticule. The field of view was progressively changed by moving the slide until most of the particles presented had been observed. The counts obtained yielded the following assays outlined in Table 2.2.2.

TABLE 2.2.2 MINERAL ASSAYS EVALUATED FROM PARTICLE POINT COUNTING

Mineral	Assay (%)	Error (±%)
serpentine	68	± 3
olivine	20	± 0.5
calcite	9	± 1
mica	2	± 0.8
spinels and others	0.6	± 0.2

The error given was that encountered in estimating the proportion of the phase of interest, as based on the binomial theorem (Appendix 2). The error stated does not include errors involved in identification and lack of liberation.

The kimberlite was further examined in thin section. The thin sections were prepared by a parallel sided slice being cut from a hand specimen, smoothed on one face and mounted on a glass slide using deaerated araldite. The desired thickness of 30 μm was then attained by progressively finer grinding on circular diamond paste laps. The minerals, in thin section were observed under polarised light conditions using a Vickers petrological microscope. Identification of the various minerals was based on a combination of the following properties : habit, colour, cleavage, refractive index, intergrowths, pleochroism, extinction and birefringence. Photomicrographs were taken of selected views using a specially adapted binocular petrological microscope equipped with a camera. These photo micrographs are shown in Plates 2.1-2.8 and illustrate the porphyritic texture. The majority of the light green-colourless subhedral olivine grains were seen to exhibit alteration in varying degrees ranging from that restricted to superficial effects

Plates 2.1 - 2.8 Photomicrographs of Wesselton kimberlite in thin section (all under crossed nicols).

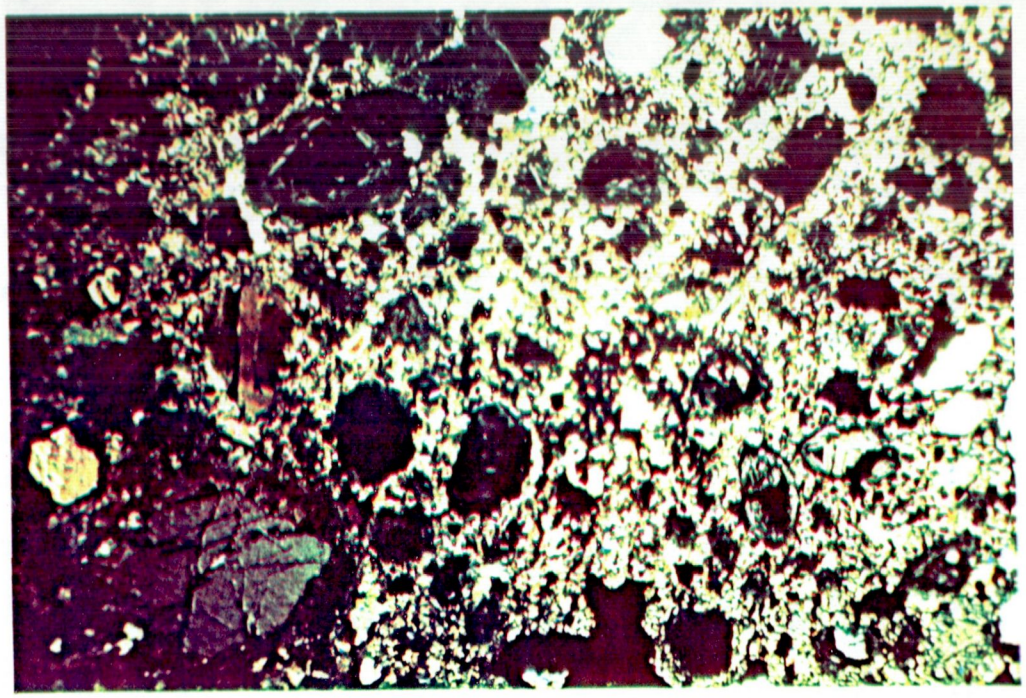


Plate 2.1 General view (x11). The plate shows the heterogeneous porphrytic texture of Wesselton kimberlite. The prominent phenocrysts consist of olivine (bottom left); phlogopite (centre left) and serpentine (top left). Calcite is discretely disseminated through serpentitic matrix.

Plates 2.2 - 2.4 Progressive alteration of olivine.

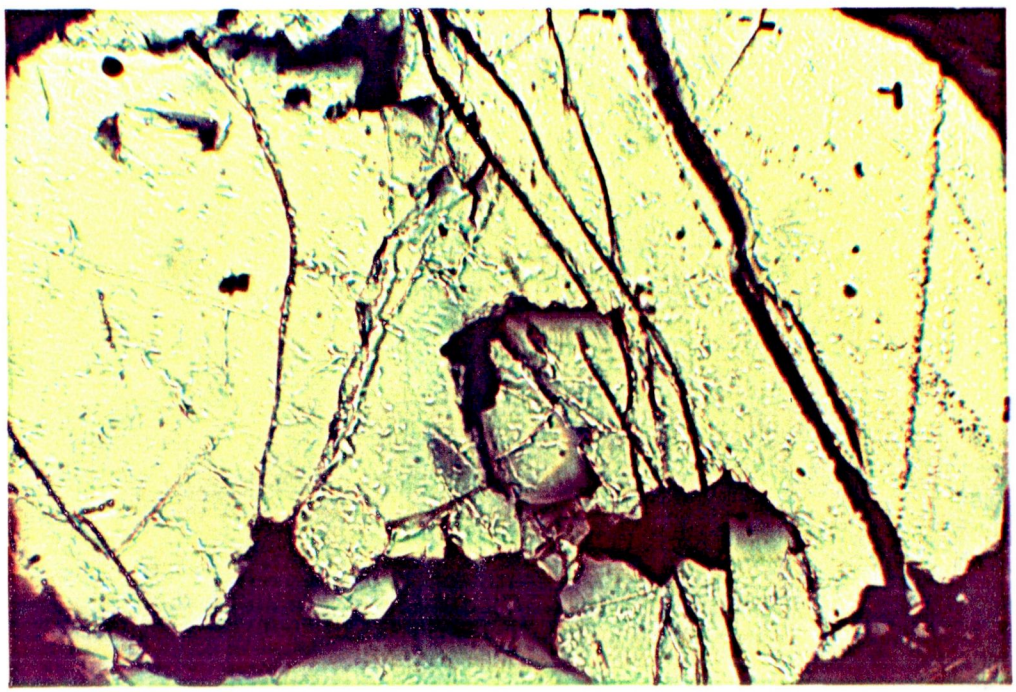


Plate 2.2 Unaltered olivine (x35).

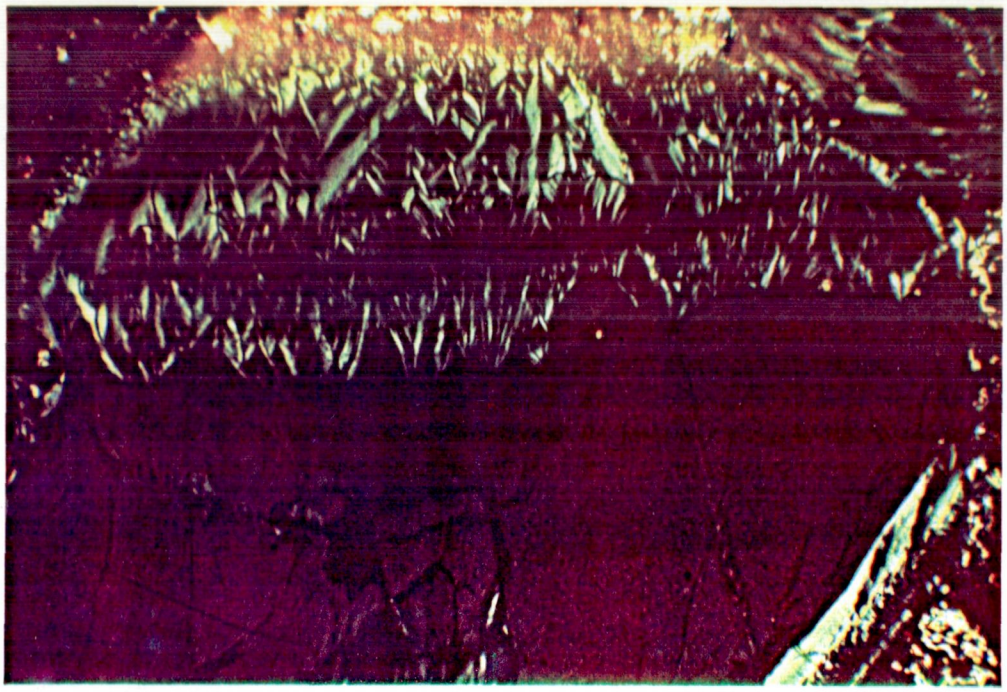


Plate 2.3 Serpentinization of olivine (x35). As shown, serpentine replaces the olivine forming characteristic fibrous crystallites. It appears that alteration of olivine occurred after consolidation of the kimberlite as indicated by the two stages of serpentine crystallisation, the reaction channels crossing the olivine and the cavity which has developed between the two minerals.



Plate 2.4 A serpentine pseudomorph after olivine (x70). Here, serpentine has completely replaced olivine. Large crystals have grown in the interior of the cavity so formed, with finer crystallites bordering the pseudomorph.



Plate 2.5 A reaction rim (cf. Plate 2.3) with serpentine replacing olivine (x70). The plate indicates the presence of reaction channels (arrowed) which seem to provide access for alteration solutions from the rock (left) to the olivine (right). Note the uneven contact between the olivine and serpentine.

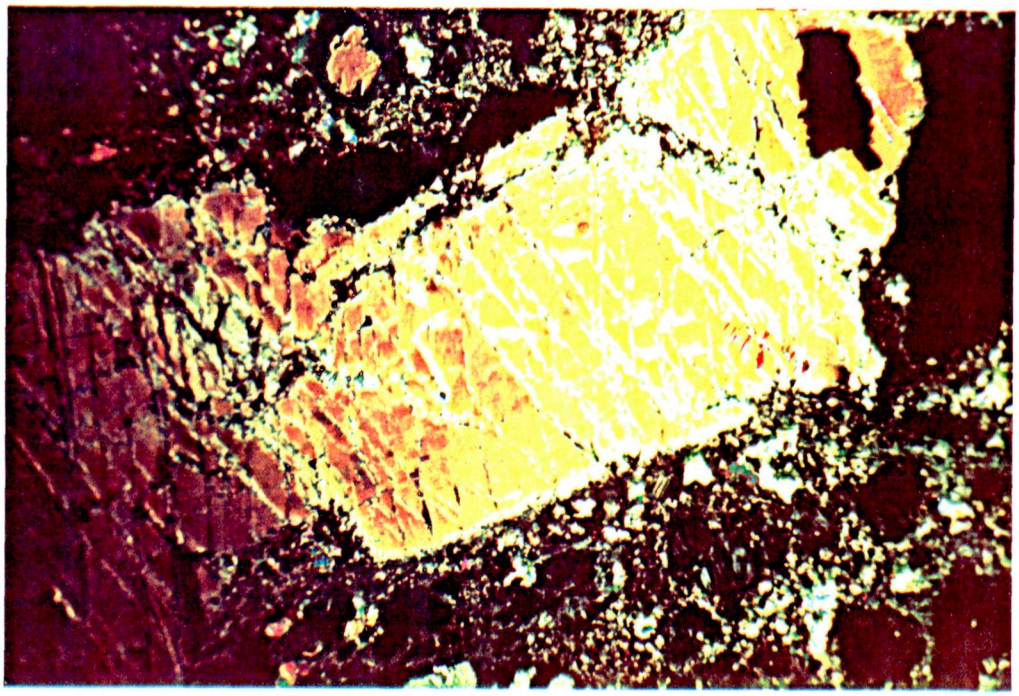


Plate 2.6 Unaltered phlogopite-biotite (x11). A narrow diffuse reaction rim (cf. Plate 2.7) is seen next to this otherwise unaltered phenocryst.

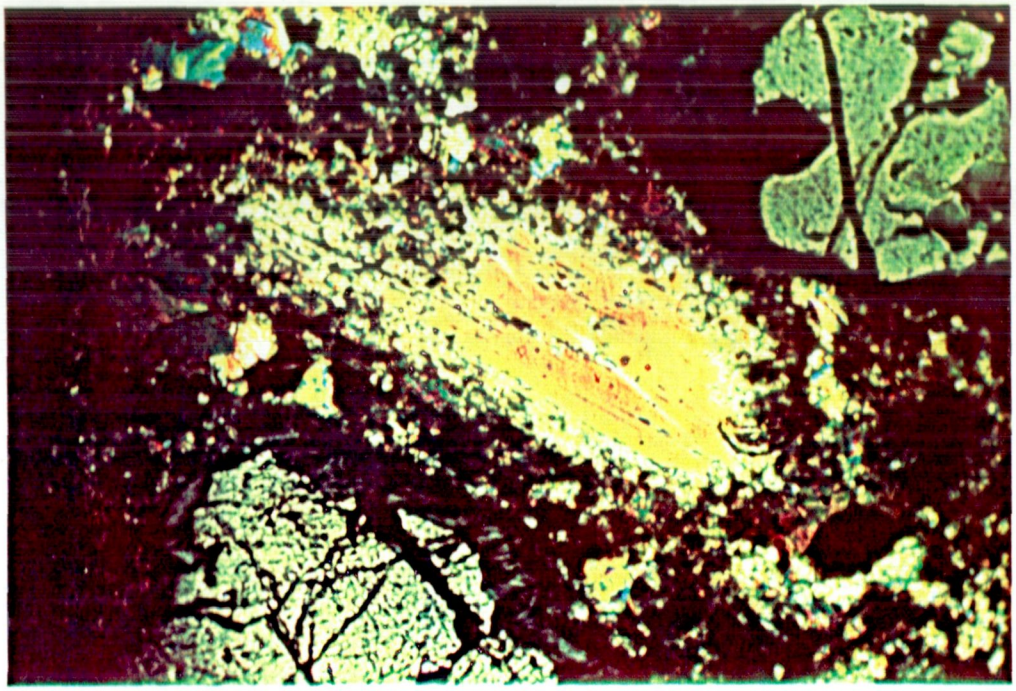


Plate 2.7 Altered phlogopite-biotite (x35). As shown the phenocryst has broken into lighter coloured buff microcrystallites and is surrounded by a band of recrystallised calcite (multicoloured). Serpentinized olivine is at the top right and bottom left.

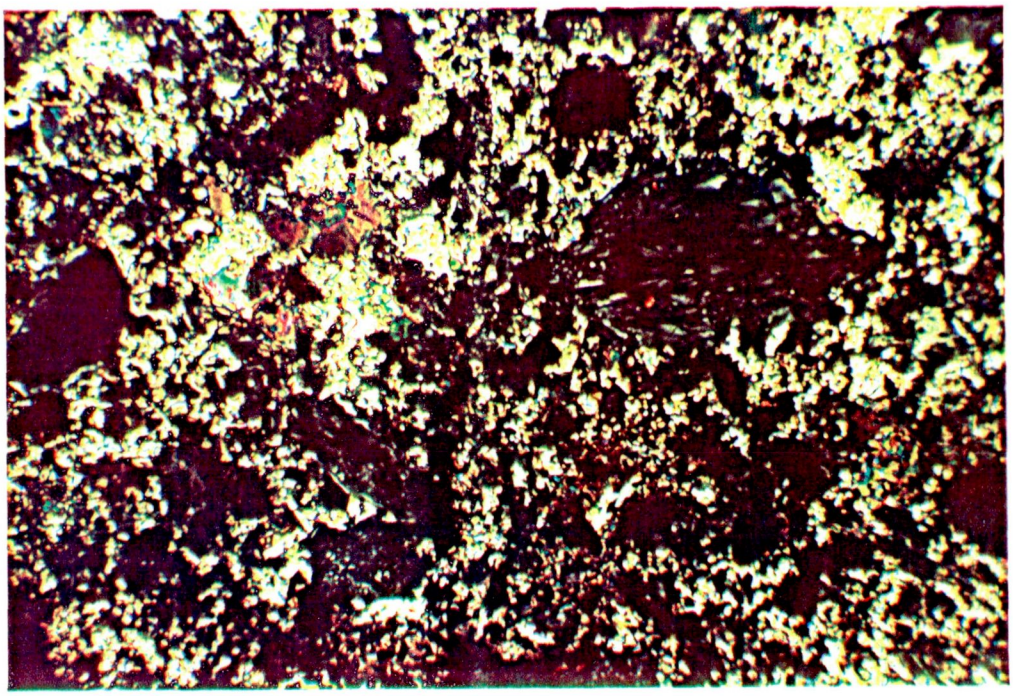


Plate 2.8 Kimberlite matrix (x70). The matrix consists of microcrystallites of serpentine (dark), calcite (blue, red, green), disseminated olivine (light) and alteration products. The plate is indicative of the small liberation size about < 70 μm of the mineral grains.

(Plate 2.2) to complete pseudomorphic replacement by serpentine (Plate 2.4). Serpentine was distinguishable by its darker green colour and fibrous habit, and formed a substantial proportion of the finely-grained matrix. Phlogopite-biotite exhibited some alteration, the vivid yellow brown unaltered lathes (Plate 2.6) contrasting sharply with the dull brown product (Plate 2.7) believed to be hydrobiotite-vermiculite. No other alteration products were apparent.

A quantitative analysis was then made, noting the textural distribution of each of the mineral constituents. The analytical procedure involved decentralising the stage of the petrological microscope and recording the mineral that intersected with the cross wires as the stage was rotated at regular intervals of 360°. By moving the position of the slide on the stage most of the area of the section could be covered. The results are shown in Table 2.2.3.

TABLE 2.2.3 MINERAL ASSAYS EVALUATED FROM THIN SECTION ANALYSIS

Mineral	Phenocryst		Matrix		Total	Error
	assay (%)	distribution (%)	assay (%)	distribution (%)	Assay (%)	(± %)
serpentine	61	71	51	29	57	± 3
olivine	22	60	32	40	26	± 3
calcite	8	52	16	48	11	± 2
mica	2	77	1	23	2	± 0.9
altered mica	1.7	100			1	± 0.7
spinels	1.3	100			1	± 0.5
others	3	100			2	± 1

Notes : (a) Phenocryst proportion of rock : 68%

The error was calculated in a similar manner to that already described before.

2.2.3 Analytical requirements

The work in the preceding sections confirmed that Wesselton kimberlite, although less complex in mineral associations than many more altered kimberlites[3,61,115,185-188] nevertheless represented a complex starting material for fundamental testwork. Table 2.2.4 shows some of the methods of elemental and phase analysis which might be attempted in such testwork. The table, which is an adaptation and extension of that of Zussman,[189] lists a series of methods varying widely in the nature of information provided, general complexity and precision attainable. It follows from the discussion below that no single method is suitable for comprehensively describing the mineralogical transformations that occur in kimberlite alteration. A combination of techniques had therefore to be used to build up an overall representation of these reactions and their sequences. Furthermore, the information obtainable had to be set against the availability and 'turnaround' time of equipment.

The first three methods listed in the table have already been discussed, their use being principally limited to the petrological analysis of the kimberlite. Although microscopic examination is in principle a complete tool for phase analysis, the method is too laborious for routine work and cannot deal effectively with finely divided solids. Of the chemical methods available, gravimetry and titrimetry can be laborious, subject to various forms of chemical interferences and require experienced operators. They are relatively precise being employed in umpire analyses of 'one-off' samples, rather than for routine work. Colorimetric methods can be faster though

TABLE 2.2.4 ANALYTICAL METHODS USED IN MINERAL ANALYSIS[61,189-195]

Method	Use	Advantages	Disadvantages
Hand specimen Examination (Visual inspection)	Qualitative overview of petrographic features : textures, mineral proportions	Readily performed. No special equipment required	Requires trained and experienced observer for good assessments to be made. Misinterpretations common
Mineral Separations	Preparation of concentrates suitable for testwork	Inexpensive. Can yield quantitative estimates of phases present. Insensitive to scale of operation	Requires previous knowledge of phases for selection of separating process. Slow. Separations between silicates difficult. Essentially complete liberation required
Microscopy	Detailing of observations made from hand specimen	Inexpensive. Good qualitative and quantitative tool (errors ~5%). Sole means of assessing rock textures	Requires experienced observer, especially in silicate identification. Slow. Restricted to analysis of +100 μm particles and is laborious in quantitative work
Classical Methods			
Gravimetry	Umpire analysis	Extremely precise	Very slow. Applicable to major constituents only
Titrimetry	Umpire and evaluation analysis	Extremely precise	Very slow. Applicable to major constituents only
Colourimetry	Rough estimation of solubilised complexed phases	Precise in well defined system. Fast	Imprecise due to interferences.
Instrumental Methods			
X-ray Fluorescence (XRF)	Qualitative and quantitative analysis of elements (at no. ≥ 9)	Wide sensitivity range (100%-ppm). Very good reproducibility (0.4%)	Expensive. Slow. Lack of simple concentration-intensity relationship
Emission Spectrography	Qualitative and quantitative study of trace element distribution (at no. ≥ 3)	Rapid method which can analyse up to 20 elements simultaneously. Relatively cheap (bar capital cost). Limited structural data can be deduced	Calibration complex. Experienced operator needed. Reproducibility 2-10%. Not applicable to non-metals. Sensitivity range (~1 ppm -1%). Interferences
Electron Probe Micro-analysis/Microscopy	Qualitative and quantitative elemental distribution. Microstructure investigations	Analysis of small regions (1 μm^2)	Expensive. Slow. Careful sample preparation required
Autoradiography	Qualitative and quantitative analysis of radioactive materials	Sensitive to extremely low concentrations	Limited to radioactive minerals only
Nuclear Magnetic Resonance (NMR)	Qualitative determinations of hydrated minerals		Limited in application, especially in the case of silicates. Quantitative measurement very rare
Atomic Absorption (AA)	Qualitative and quantitative elemental analysis (at no. ≥ 3)	Fast. Readily performed. Relatively inexpensive	Sensitivity range dependent on element. Element interferences. Reproducibility error 2-5%
X-ray Diffraction (XRD)	Qualitative and semi-quantitative mineral analysis	Only rapid instrumental method for general mineral phase analysis. Can be made quantitative under carefully controlled conditions	Sensitivity relatively low and varies with type and crystalline nature of phase. Numerous corrections required in accurate work. X-ray intensity affected by many factors. Quantitative silicate analysis difficult. Not suitable for direct quantitative assay of clay minerals
Thermal Analysis : DTA, TG, DTG	Qualitative mineral analysis	Rapid. DTA and TG very useful for clay mineral studies. TG useful for quantitative studies. Very sensitive	DTA peaks virtually irreproducible. Clay minerals are only silicate minerals that can be analysed as well as other simple compounds
Infra-Red Spectroscopy (IR)	Analysis of structural groups	Only known method for this purpose. Fast, readily performed	Very limited qual. and quant. use still to be fully extended in the mineral analysis field

have similar limitations as above.

In the case of instrumental methods (comprising the remainder of the table) the emission spectrograph/spectrometer, nuclear magnetic resonance spectrometer and the autoradiograph seem to have little application in kimberlite analysis. X-ray fluorescence analysis and electron probe microanalysis (including electron diffraction) can be employed to a limited extent but results are costly in terms of time and money for routine use. The former is limited to elemental assays and the latter to detailed elemental investigation of very small areas of a sample surface. Atomic absorption, however, finds application in the rapid elemental analysis of solutions, having a precision of about 5% (relative). It is not designed for phase identification - unlike X-ray diffraction.

XRD in principle, provides, like microscopy, a complete tool for phase analysis but is also inferior with respect to chemical assay. It can be readily applied to the investigation of fine sized material, unobservable under the microscope, and with careful development be extended to yield quantitative estimates. Thermal methods are widespreadly utilised for investigations of physical phenomena of compounds (e.g. sublimation, absorption, crystallisation). Various approaches are practised : differential thermal analysis (DTA) which, in clay mineral work gives good qualitative information. Thermo-gravimetry (TG) and differential thermogravimetry (DTG) can be adapted to provide estimations of clay phase proportions. Thermal methods require samples with a high degree of purity as the data generated is not as distinguishable as that produced using other methods. They are relatively inexpensive, rapid methods, some of which can be operated with ease.

Infra-red spectroscopy is one of the few analytical methods

the response of which does not depend on the crystalline state of the rock or mineral, yet is capable of generating data concerning the constituent structural groups. This enables mineral transformations to be examined in greater detail. Its use as a qualitative and quantitative tool for phase analysis is limited in comparison.

From the table it was concluded that XRD was suitable for mineral phase analysis and AAS for elemental assay. Thermal methods would provide useful complimentary information chiefly in regard of clay minerals. Structural group transformations producing such minerals would be best studied using IR.

2.3 X-Ray Diffraction

2.3.1 Principles

The basic features[189] of X-ray diffraction are illustrated in Figure 2.3.1 Monochromatic X-rays, generated at the source are incident upon the sample at an angle θ and are diffracted on striking the structural planes of the mineral(s) to emerge (also at an angle θ) on to the detector. As shown rays penetrating to different surface layers, travel different distances (related in a simple manner to the separation between the layers), and interfere upon emergence in accordance with the principle of superposition. Certain values of θ provide for constructive interference, resulting in large detector signals, and a pattern of such reinforced signals can be related to the fundamental structures of the mineral(s) in the sample, provided the degree of crystallinity is sufficiently high.

Powdered samples offer the simplest means of obtaining XRD data. They consist of randomly-orientated, finely-divided crystals. When X-rays strike the sample a number of the crystals are in the correct orientation to 'reflect' the beam, which outlines a cone of

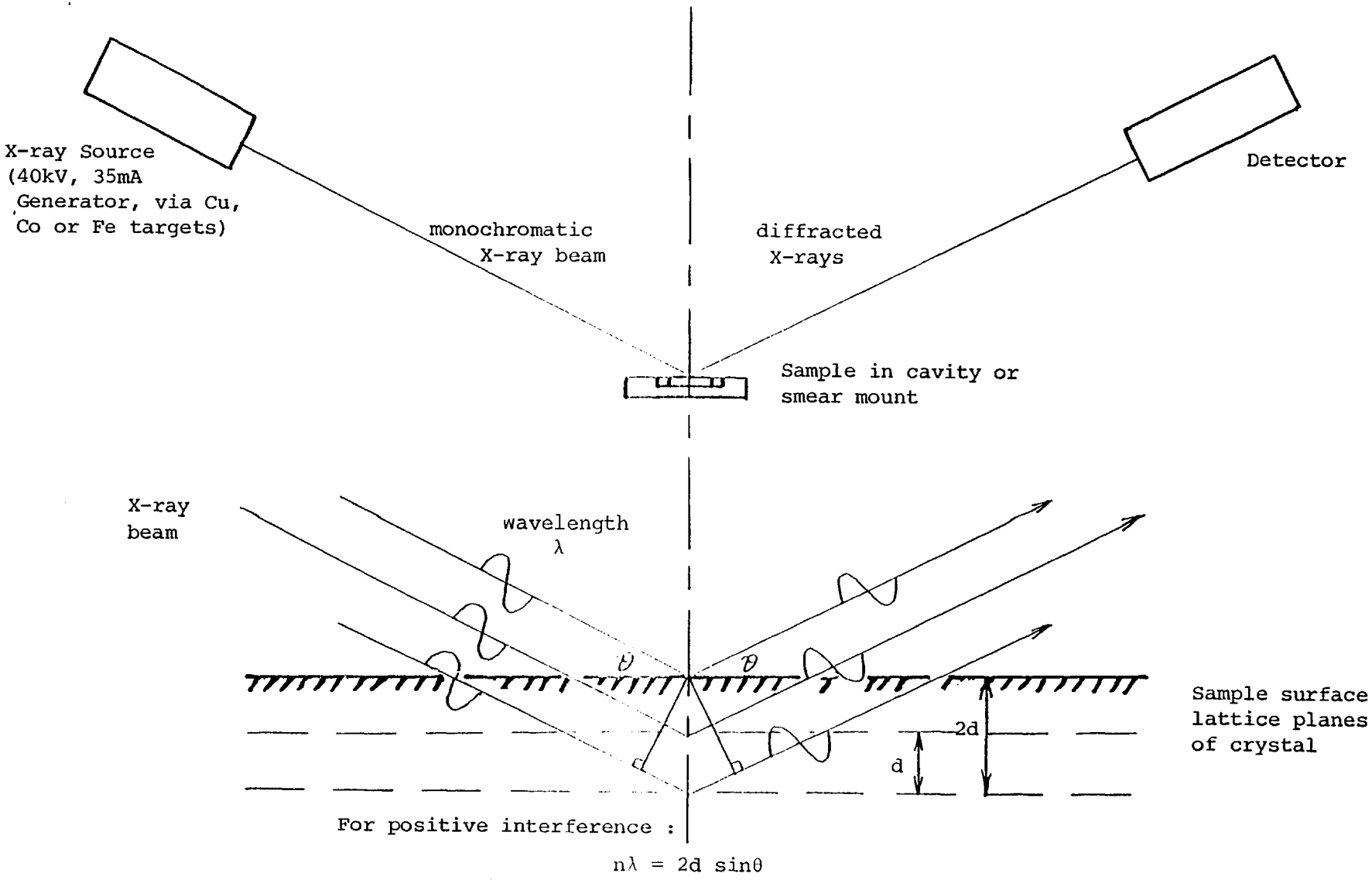


Figure 2.3.1 Principles of X-ray diffraction analysis

scattered radiation, part of which is detected.[196] Different planes of a crystal give reinforcements at different values of θ, and the diffraction spectrum or spectrogram can be obtained by plotting signal or peak intensity against angle of incidence. A group of peaks is characteristic of a particular mineral phase, and their intensities are roughly proportional to the phase concentration in the sample. Each peak corresponds to a structural plane and by convention is labelled by the intercept method due to Miller[30] e.g. the main cleavage plane of mica is termed 001.

2.3.2 Qualitative methods

The principal criterion which governs the ease of identification of a mineral by XRD is the degree of crystallinity.[189] Figure 2.3.2 illustrates X-ray diffractograms recorded for Wesselton kimberlites (a) and its constituent minerals ((b) - (e)). Olivine (c), calcite (d) and mica (e) have a high degree of crystallinity as shown by the symmetrical sharp, well-defined peaks of these primary minerals. Such is not the case for serpentine (b) where the peaks are broader and less intense, reflecting a more variable chemical composition. Part of the serpentine is of secondary origin being an alteration product of olivine. A more direct comparison between different states of crystallinity is seen between Figure 2.3.2c-e and Figure 2.3.2f which is an amorphous aluminium hydroxyoxide. In the latter no peaks are discernible. A combination of the spectra Figure 2.3.2b-e in suitable phase proportion leads to a close approximation of the kimberlite diffractogram shown.

The regularity of ordering of the crystal structure of minerals like olivine greatly facilitates their identification by XRD. In the case of clay minerals, however, the markedly smaller natural grain size (∿ 1 μm), the more variable chemical composition, and the poorer crystalline state renders XRD identification difficult. Ameliorative measures include "orientating" the sample (by careful sedimentation or preparing the sample as a smear mount[195]) or by chemical treatments to

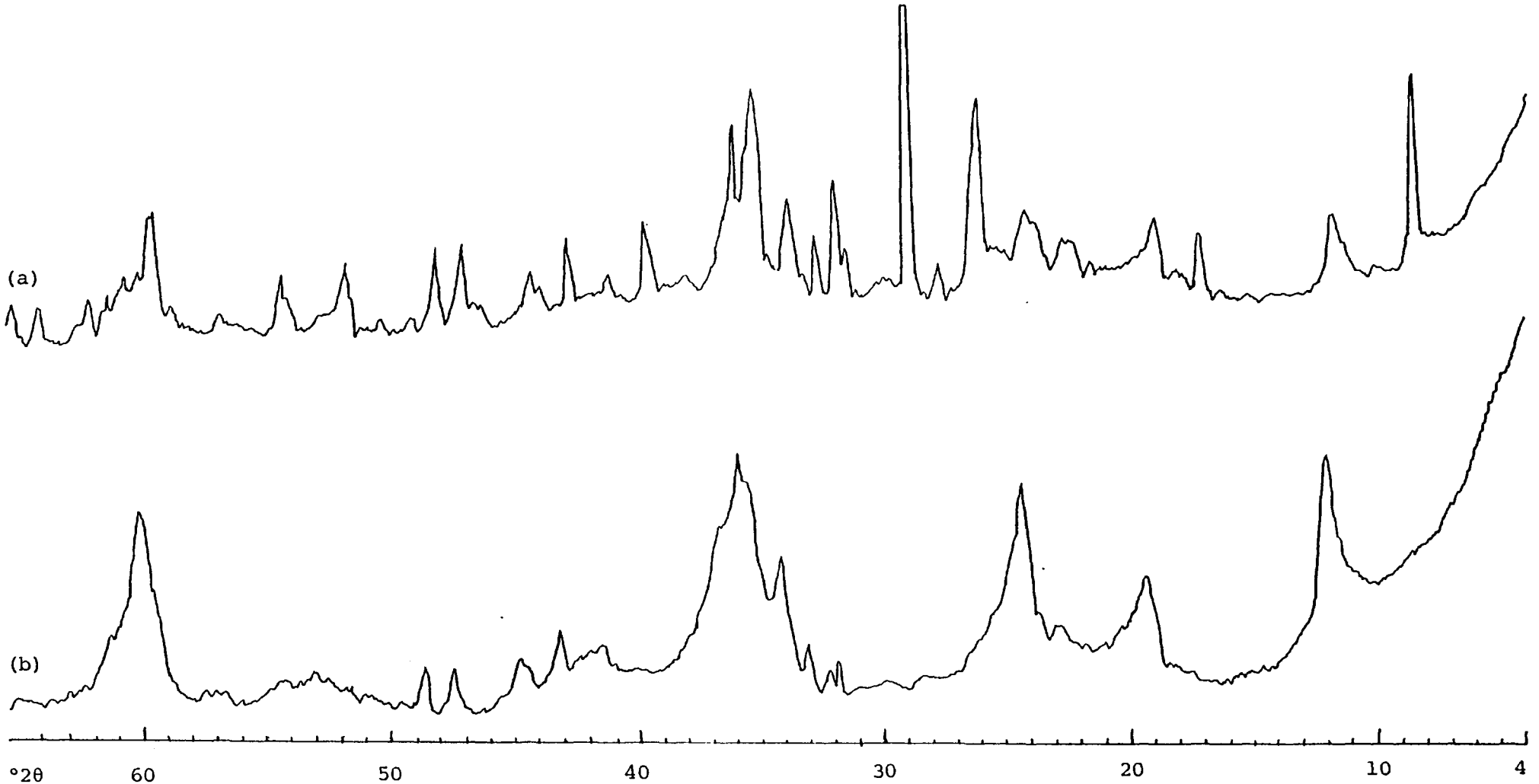


Figure 2.3.2 X-ray diffractogram for

(a) Wesselton kimberlite
(b) serpentine

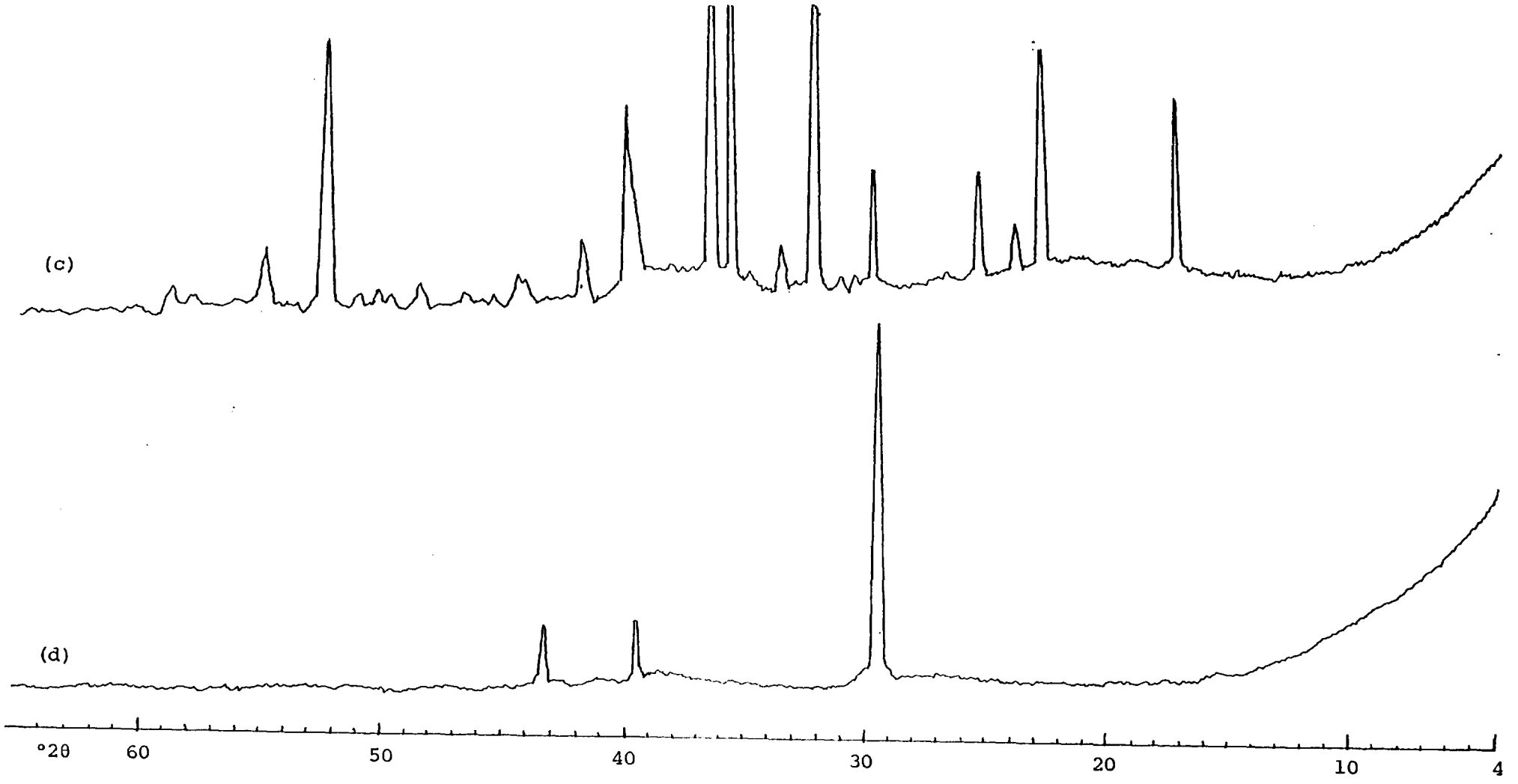


Figure 2.3.2 X-ray diffractograms for

(c) olivine
(d) calcite

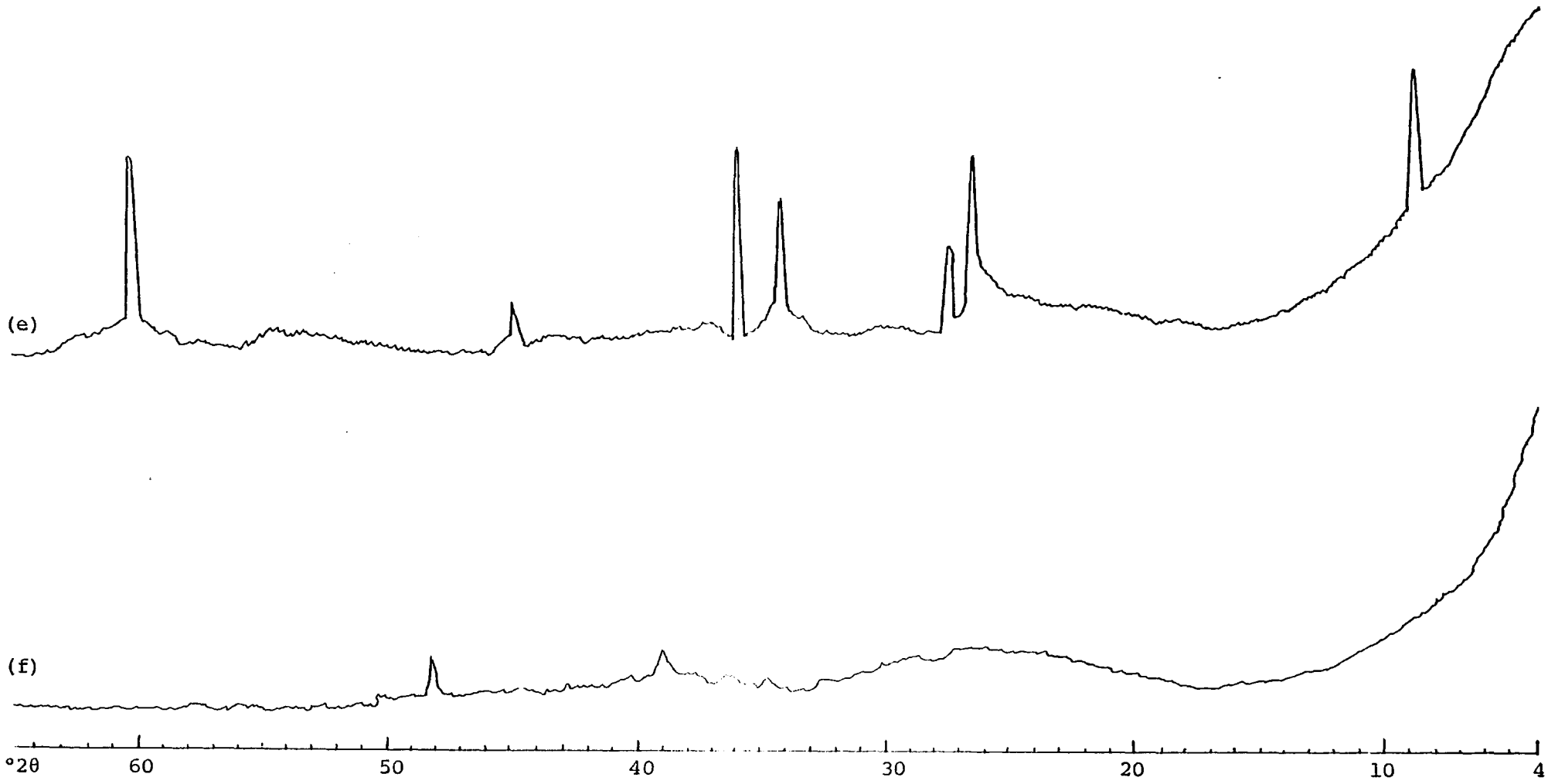


Figure 2.3.2 X-ray diffractograms for

(e) phlogopite-biotite
(f) aluminium hydroxyoxides (amorphous)

produce characteristic peak shifts in the diffractograms. Greene-Kelly[197] employed lithium as an exchange ion for montmorillonite recognition. Glycolation which expands the clay lattice was used by Gibbs[198] and Carroll[199] who summarised the effects of heating and glycolation of clays (Table 2.3.1). Table 2.3.1 lists the most important lattice or 'd' spacings of the principal clay mineral groupings. Montmorillonites are typified by glycolation, whereas the others exhibit differing reactions to heat treatment. Thorez[200] gives a comprehensive survey of chemical and physical pre-treatments for clay mineral identification (e.g. saturation with potassium salt solutions).

2.3.3 Quantitative methods

Various authors acknowledge that the peak intensity of diffracted X-rays can be a quantitative measure of the concentration of the associated mineral species in a mixture.[201-204] For quantitative determinations it is necessary to include two types of standard. One, a mineral standard, which is used to make up a set of known mixtures against which an unknown is compared and the second, an internal standard. The latter accounts for errors inherent in the apparatus (e.g. short-term instability) in that the recorded diffractogram of the standard is an indicator of the behaviour of the equipment at a particular time, more or less independent of varying concentrations of phases of interest. Cody and Thompson[205] have listed the requirements of an internal standard. Such a compound

a) exhibits suitable crystallinity and sharp peaks,.

b) is readily available,

c) does not cause superimposition of the peaks of interest, and

TABLE 2.3.1 EFFECT OF GLYCOLATION AND HEATING ON VARIOUS CLAY MINERALS

Mineral	Most intense basal spacings (Å)	Glycolation effect 1 hr 60°C	Heating effect (1 hr)
Fe-Chlorite	14	-	C 800°C+
Mg-Chlorite	14	-	I 650°C C 800°C+
Illite	10	-	I on water loss 700°C similar to mica
Mica	10, 5	-	I on heating to 700°C
Montmorillonite	15	expands to 17 Å	Becomes 9 Å at 300°C+
Vermiculite	14	-	300°C+ dehydrates : 14-13.8-11.6-9 Å
Mixed layered minerals		expands if mont. present	Varied according to composition
Kaolinite	7.15, 3.75	-	Amorphous at 575-625°C+
Dickite) Nacrite)	similar to kaolinite		
Halloysite	10-7.2	-	Dehydrates at 110°C

Abbreviations I Intensifies
C Collapses

d) is not otherwise present in the sample to be analysed.

Suitable internal standards are lithium fluoride, sodium fluoride, aluminium oxide, calcium fluoride and potassium chloride,[204] molybdenum sulphide, zinc hydroxide and aluminium.[205]

Examples of quantitative methods involving internal standards include those due to Mitchell,[202] Norrish and Taylor[203] and Cody and Thompson.[205] Mitchell expresses the amount of unknown component, x, in terms of an arbitrarily defined scale of intensities

$$x = (100a\ I_{mx}\ I_s)/(s\ I_x\ I_{sm}) \qquad (2.3.1)$$

where a is the weight of internal standard used; I_{mx} is the measured intensity of line of unknown; I_s the arbitrary scale intensity of line of the standard; s, the weight of sample used; I_x, the arbitrary scale intensity of unknown peak; I_{sm}, the measured intensity of line of standard.

Norrish and Taylor's method[203] also involved the setting of an arbitrary scale but their expression related peak intensity to intensive properties (e.g. mass absorption coefficient) which affect the path of the X-rays through the crystal. A similar expression was given by Cody and Thompson[205] who also included corrections for orientation effects :

$$(I_{JA}\ x_{Ju}/I_{sA}\ x_{JA}) = (K_u\ a_{Ju}\ a_{sA}\ I_{Ju})/(K_A\ a_{sA}\ a_{JA}\ I_{su}) \qquad (2.3.2)$$

where I denotes the intensity of the peak as inferred from the subscripts; A : mineral standard; J : component in unknown sample u; s : internal standard. a denotes an absorption coefficient and K is a constant

depending on the characteristics of component J in the unknown sample u and on the geometry of the X-ray diffractometer.

In the case of clay minerals, the quantitative determination by comparison of peak intensities cannot be performed owing to differences in the mass absorption of individual minerals, grain orientation, mount thickness, unevenness of spread, differences in crystal perfection, polytypism, and others.[195] Ordinary mineral standards cannot be used owing to the difficulty of finding grains of a similar crystalline state as the clays of interest.[199] Using standards extracted from the samples, Gibbs[198] put forward the following expression for the concentration of an unknown component, x :

$$x = kI_l/I_s \qquad (2.3.3)$$

where K is constant; I, the peak area intensity of l, the unknown mineral; s, the standard.

Gibbs was successful but he had to adopt a very complicated separation and purification procedure for standard extraction. In a general way it appears preferable to take standards directly from the samples to be analysed.

2.3.4 Error sources and their correction

A number of factors regulate the intensity of X-rays diffracted by an assembly of crystals. Some have already been discussed above, with reference to quantitative clay analysis. Orientation, which results in peak intensities out of proportion to the amount of clay present has been controlled in various ways :

a) grinding the sample with a thermoplastic organic cement to yield equidimensional particles[206,207]

b) smearing the sample on a glass slide[199,208] and

c) use of partially orientated powder press.[208]

Dilution of the sample using an X-ray amorphous material, e.g. gum arabic, can reduce absorption effects.[204]

Particle size is a particularly important factor affecting peak intensity.[197,198,203-205,207-210] Gordon and Harris,[209] for instance, showed that a maximum peak intensity occurred at 10-20 μm for quartz grains. Other minerals have apparently not been studied in this respect.

2.3.5 Olivine and serpentine quantitative analysis : assumptions on which the method is based

A reliable accurate measure of the extent of rock degradation is provided by the mass of the unreacted major constituents. Further to the considerations in Sections 2.3.3-3.4 quantitative methods for the analysis of olivine and serpentine in kimberlite were developed on the following assumptions.

a) The phase proportions of both liberated and unliberated grains are best determined by reference to standards extracted from the kimberlite samples themselves.

b) Intergranular effects (such as varying particle orientation and compaction) that occur in assemblies of grains can be regulated by the use of a standardized procedure involving the internal standard molybdenum sulphide together with other specific additives.

c) Peak intensity can be measured by peak area, in the form of the product of the height, h, and the width at h/2.

d) The measurement of the ratio of intensities of olivine (or serpentine) to that of molybdenum sulphide or other internal standard can eliminate errors arising from instrumental instability.

e) The (large) effect of variations in particle size distribution can be taken into account by direct calibration employing a size parameter.

The extraction of standards in accordance with (a) now follows.

2.3.6 Extraction of olivine and serpentine standards

Preliminary testwork to extract purified mineral standards was carried out using the -150+106 μm density fractions described in Section 2.2.2. Leaching techniques were studied, with the objective of selectively removing serpentine and calcite from the respective olivine- and serpentine-rich density products. Although calcite dissolved readily, serpentine was slow to react. Moreover, the micas proved to be resistant to all mineral acids used in the test programme (e.g. concentrated (18M) sulphuric acid seemed to have no effect over a period of 66 hrs). Prolonged acid attack, however, affected the olivine. It was concluded that acid treatment was of limited use : calcite could be readily removed but prolonged exposure could have deleterious effects on both serpentine and olivine. The tests also demonstrated that mica removal would be difficult by chemical means.

Attempts were made to remove mica selectively by flotation, utilising conditions recommended by Bearson et al[211] and others.[212] Despite the addition of selective promoters, the separation was unsatisfactory principally due to the presence of platy serpentines with similar surface properties. The solution to the problem was indicated by successful tests using a superpanner - a small-scale batch device which separates minerals on the basis of relative density and the shape of the particles.

Another useful property for separation was found to be magnetic susceptibility. Some serpentine grains appeared to be iron-

rich, and a darker variety could be seen to be preferentially attracted towards a hand magnet. The olivine was non-magnetic.

By utilising aspect ratio (shape), relative density and relative magnetism as criteria for separation, olivine and serpentine mineral standards were finally obtained according to the flowsheet in Figure 2.3.3. Details are given below.

The remainder of the -3 mm fraction (Figure 2.2.1) was riffled once. One half was stored and the rest stage-ground using a laboratory cone crusher. Undersize was screened out at 420 μm. All material passing 420 μm was then sized to obtain the -150+106 μm fraction which was used in the mineral standard extraction procedure.

The -150+106 fraction was deslimed by wet screening at 75 μm and tabled twice employing a Wifley laboratory shaking table. The diagram shows the collecting launder of the shaking table divided to accept three products. In the first separation the inclination and speed of vibration of the table was adjusted so that a majority of large mica flakes remained on table surface. Olivine and serpentine concentrates were routed as shown and the middlings consisting of fine serpentines, mica and calcite forwarded to the second table. Here the conditions of separation were altered so that a serpentine-rich product could be collected with a residual mica-rich tailing, which was deposited in the third section of the launder.

The olivine and serpentine product streams were upgraded using dense medium separations. Although the table was efficient in removing approximately 50-70% of the mica, coarser serpentine particles had reported with finer olivine ones. Dense medium separations were used to purify the concentrates, re-routing misplaced minerals. Tetra-bromoethane media, of relative density (2.96) intermediate between that of olivine and serpentine, were used first and the sinks and floats

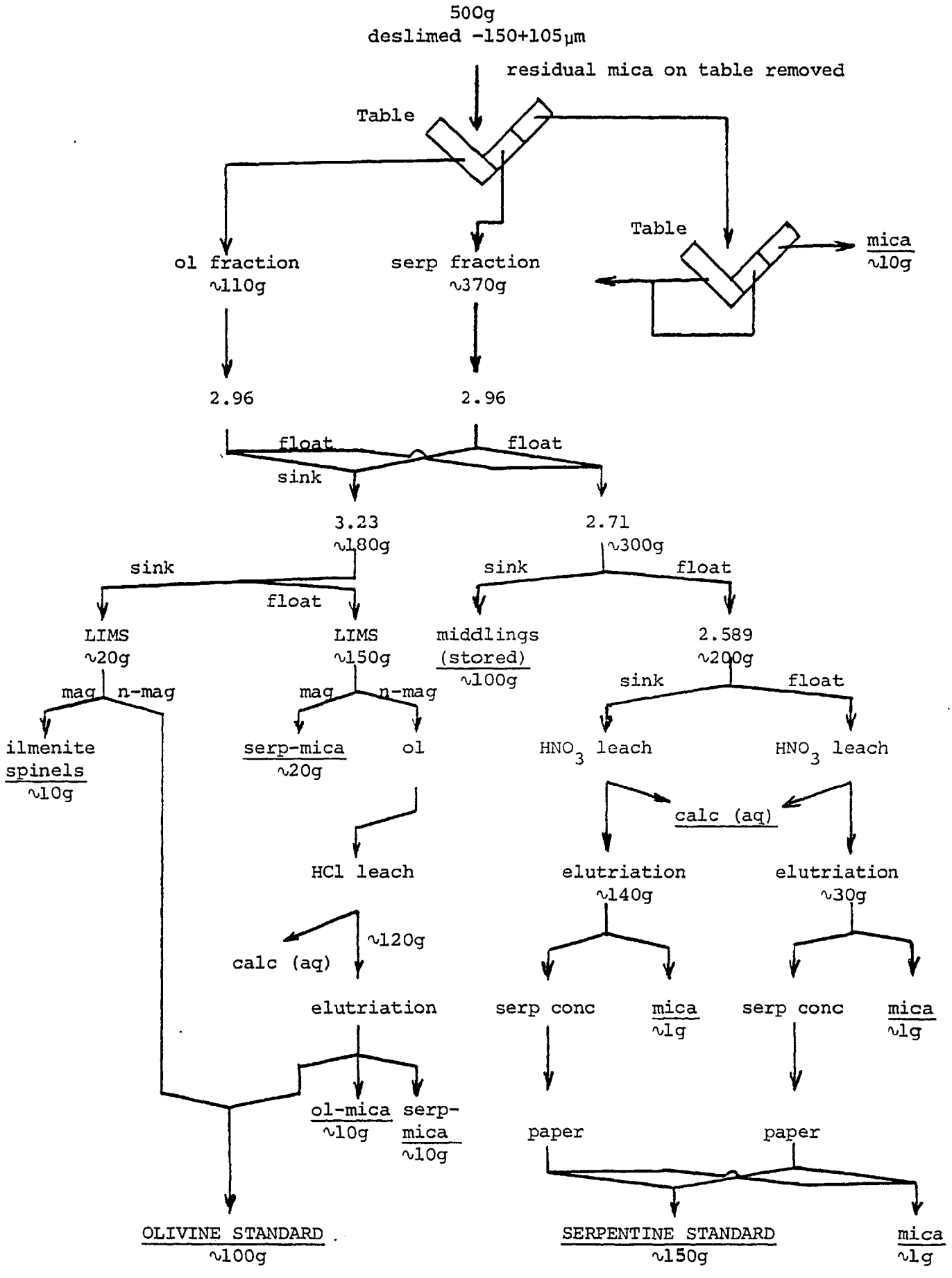


Figure 2.3.3 Flowsheet for extraction of olivine and serpentine XRD standards

Notes : (a) Abbreviations : ol = olivine; serp = serpentine; calc = calcite

treated with di-iodomethane (s.g. = 3.23) and tetrabromoethane-trichloroethane (s.g. = 2.71) respectively. The relative densities of the second set of separations were chosen as they were the respective lower and upper specific gravity limits for olivine and serpentine. At this stage care was taken to minimise crowding and agglomeration effects in the separating flasks. A "dilute" feed was subsequently used in each separation and the mixture was stirred at various intervals before being allowed to settle.

To purify the olivine concentrate obtained, dry low-intensity magnetic separation was applied to remove ilmenites and spinels from the +3.23 fraction and magnetic serpentines from the -3.23+2.96 product. The former gave a non-magnetic olivine concentrate which appeared pure under the binocular microscope. The latter magnetic separation gave an olivine rich product contaminated by mica and calcite. Dilute acid was added to this product to solubilize the calcite. As soon as effervescence ceased, the acid was quickly diluted with an excess of water to render attack on the olivine negligible. To extract the micaceous serpentine still present, an elutriation technique was employed. The elutriation apparatus was that as used by Beavan and Napier-Munn[213] and is illustrated in Plates 2.9 and 2.10. The apparatus consisted of a constant head tank which supplied a mixing chamber, employed for homogenizing the feed with water, prior to entry into the elutriation tubes. These tubes are shown in Plate 2.10 which were arranged in order of increasing diameter. As the feed entered a tube, finer particles of larger aspect (diameter/thickness) ratio were swept upward with the current flow. The velocity of the water current was controlled by the width of the glass elutriation vessel. Coarser rounded particles gravitated downwards for collection. Mica could be readily extracted from the olivine concentrate feed, a majority of the

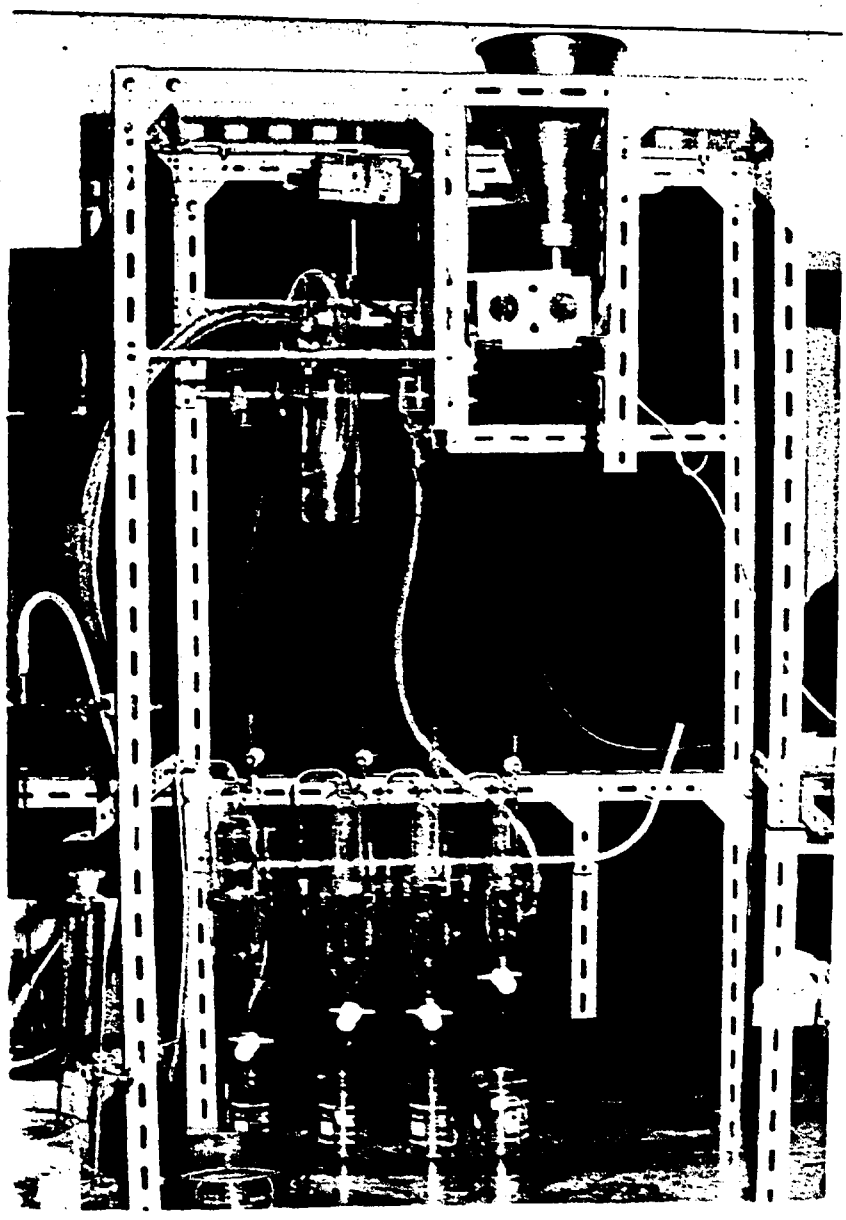


Plate 2.9 Elutriation apparatus[213] employed in olivine/mica and serpentine/mica separations.

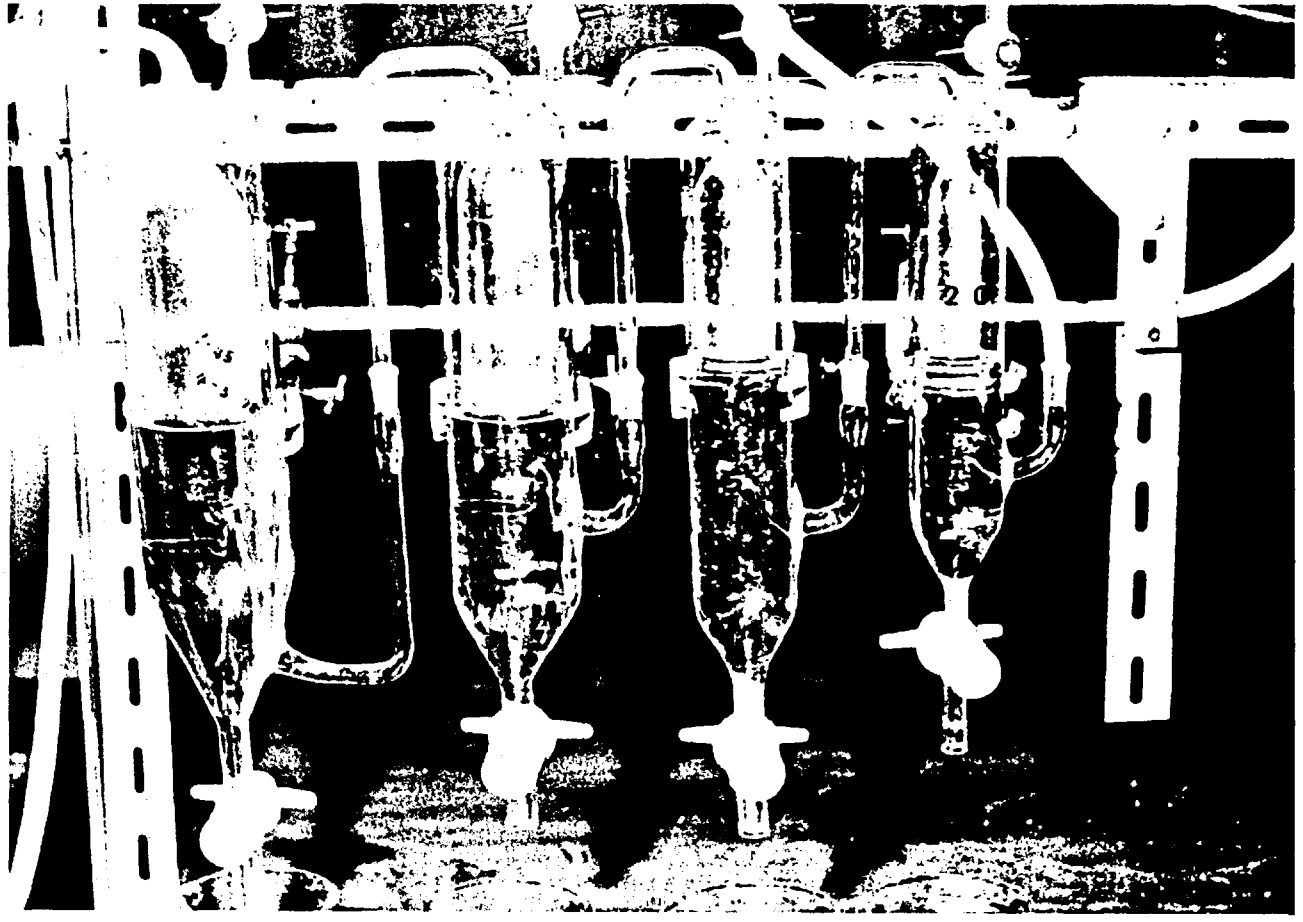


Plate 2.10 Detail of the elutriation tubes. The flow of the particulate stream is from right to left. Rounded denser grains on entering the tube gravitate through the aperture at the bottom of the internal tube. Lamellar, lighter particles are swept upwards by the water stream.

flakes reporting to the wider bore tubes. To increase gravitation and accentuate the sharpness of separation the smaller bore vessels were inclined.[214] A final olivine standard concentrate was obtained.

The serpentine stream of the flowsheet consisted of material floated at a s.g. of 2.71. The associated sinks were stored as olivine-serpentine-pyroxene-mica middlings. The floats were further separated in a medium of s.g. 2.60 so as to obviate any deleterious density effects in the elutriation stages to follow. Both products were leached with dilute nitric acid to remove calcite. Nitric acid was preferred to hydrochloric acid which has been recorded as readily attacking serpentine.[72] Elutriation followed, a similar procedure being adopted to that used before. Great care had to be exercised in the optimisation of agitation, feed rate and the degree of inclination of the elutriation vessels. The optimum angle was 40° from the vertical. The resultant serpentine concentrate was still contaminated by rounded mica particles and these could only be removed by use of their electrostatic properties. By gently tapping a portion of the dried serpentine concentrate on a piece of paper, a substantial amount of the mica was found to adhere preferentially to the paper, whereas serpentine could be removed from it. By repeating this procedure a separate serpentine mineral standard was produced.

The two standards were analysed by X-ray diffraction. The olivine product was essentially pure whereas the serpentine appeared to contain residual mica grains. Point counting however, showed the extracted standard to be 99.55 ± 0.7% serpentine with negligible mica. The X-ray diffraction result might be attributable to orientation effects.

Chemical and mineralogical properties for the extracted standards are listed in Table 2.3.2 below :

TABLE 2.3.2 PROPERTIES OF THE OLIVINE AND SERPENTINE STANDARDS

Property		Olivine	Serpentine
Colour		light green	dark green
Lustre		vitreous	dull, resinous
Cleavage		imperfect	platy on occasions
Density		3.2 - 3.4	2.4 - 2.7
Hardness (Moh's Scale)		6 - 7	2 - 3
Composition	Mg%	25.9	17.8
	Si%	18.5	18.2
	Fe%	7.6	7.3
	Ca%	1.7	3.1
	Al%	0.1	2.4

Chemical formulae for the mineral standards could not be calculated at this stage. Further data were required as outlined in Section 2.4.

2.3.7 Formulation of sample mixture for analysis

In accordance with the second assumption in Section 2.3.5 materials were added to the mineral standards or samples prior to analysis in order to control effects mentioned there. Two additives were selected at first : gum arabic to reduce absorption effects[205] and molybdenum sulphide as the internal standard.[204] At the outset, mixtures of each standard (purified olivine or serpentine) were combined with the two additives in various proportions so as to estimate the optimum conditions for the detection of the minerals. These conditions are summarised in Table 2.3.3.

TABLE 2.3.3 COMPOSITION OF THE SAMPLE MIXTURE FOR QUANTITATIVE X-RAY DIFFRACTION ANALYSIS

Component	Mass (g)	Notes
test sample	0.6000	
sodium fluoride	0.1000	diluent
molybdenum sulphide	0.0050	internal standard
gum arabic	0.2950	absorption correction
TOTAL	1.0000	

The powder mixture (in 1 g amounts) was made homogeneous by means of a vibratory mill, charged with glass balls. The lightness of the balls and the short, but efficient mixing time ($\sim$ 30 s) caused minimal comminution. (Observations using a binocular microscope confirmed that the mixture was homogeneous.) For each mixture, 0.8 g was weighed into a Phillips (automatic) powder diffraction mount, smoothed, and compacted carefully using a glass slide, to standardise the degree of compaction. The sample was analysed under the following conditions (which were afterwards employed throughout the quantitative analytical testwork) : a Phillips PW1310 X-ray generator and PW1050/25 goniometer using Cu K_{α} radiation; 2° slit; time constant 2 s; recording rate 1000 counts/s (Phillips PW1352 counter and scaler) and scanned at 2° 2θ/min.

From these initial trials the following were evident :

a) The olivine had a relatively high degree of crystallinity, so that sharp peaks were observed and a full scale deflection recorded

for concentration of the order of 60% olivine. On the other hand serpentine produced smaller, broader, peaks, the pure mineral only giving 40% full scale deflection.

b) The diffraction pattern of the molybdenum sulphide did not interfere with that of olivine or serpentine over the range of concentrations of internal standard employed (0.5-5%). Its platy morphology gave one principal, distinct, peak at 6.03 Å. In practice a very small concentration was required in the mixture (0.5% overall) to produce a peak of suitable size and any orientation effects were consequently small.

c) Gum arabic (a polysaccahride) had a substantial effect on the diffractograms : an increase in concentration enhanced the peak intensity of olivine relative to the internal standard.

Owing to (c), another inert additive, sodium fluoride, was added as a diluent. This was necessary because in the relationship between XRD response and varying concentration of the standard material (see later) it was desirable to keep constant the overall mass of the mixture. The proportion of gum arabic would then remain constant and was set at 29.50% for each sample (Table 2.3.3). This percentage seemed to represent the best compromise between the clarity of the serpentine peaks and the reduction of absorption effects. Sodium fluoride was suitable as a diluent as its presence did not interfere with the position or the relative intensity of the characteristic peaks of olivine, serpentine, and molybdenum sulphide.

As such small amounts of material were involved (particularly in the case of molybdenum sulphide) special care was taken over the taring and re-zeroing of the balance, before and after each weighing. The same Oertling two pan balance was employed throughout, so that errors were minimised. The precision of the weigh ings as deduced

from relative peak intensity measurements from a set of nine replicates was ± 1.3%.

2.3.8 Size calibration

Owing to the relatively small masses of products available from the experimental work (2-6 g) and the need for rapid and precise results, size distributions of ground material were determined by means of a Coulter Counter (model ZBII). The apparatus is illustrated in Plate 2.11. Briefly, a potential was set between two electrodes on either side of an aperture of known dimensions (200 μm diameter in this case). The ground sample was suspended in a special azide free electrolyte (Isoton II) in which the tube containing the orifice was immersed. A set volume (0.5 ml) of the suspension was drawn through the aperture and a series of pulses noted - increases in potential above the arbitrarily set threshold - which were taken to be a quantitative measure of the particle size. The set threshold voltage itself was calibrated in terms of particle size using specially prepared latex standards, the size distribution of which was fixed between closely defined limits. Systematic variation of the threshold and the recording of the counted pulses produced a size distribution for the sample in terms of cumulative per cent coarser or cumulative per cent finer. A computer program was written to interpret the Coulter Counter data (Appendix 3).

Samples of the olivine and serpentine standards were separately ground for times varying from 2 to 16 minutes using a vibratory agate mill. An ethanol medium was employed so as to preserve the degree of crystallinity of the standards. Each sample was then sized by the Coulter Counter. In the analysis of the computed data, it was convenient to employ a readily calculable parameter which represented the size distribution of a sample adequately by means of a single value.

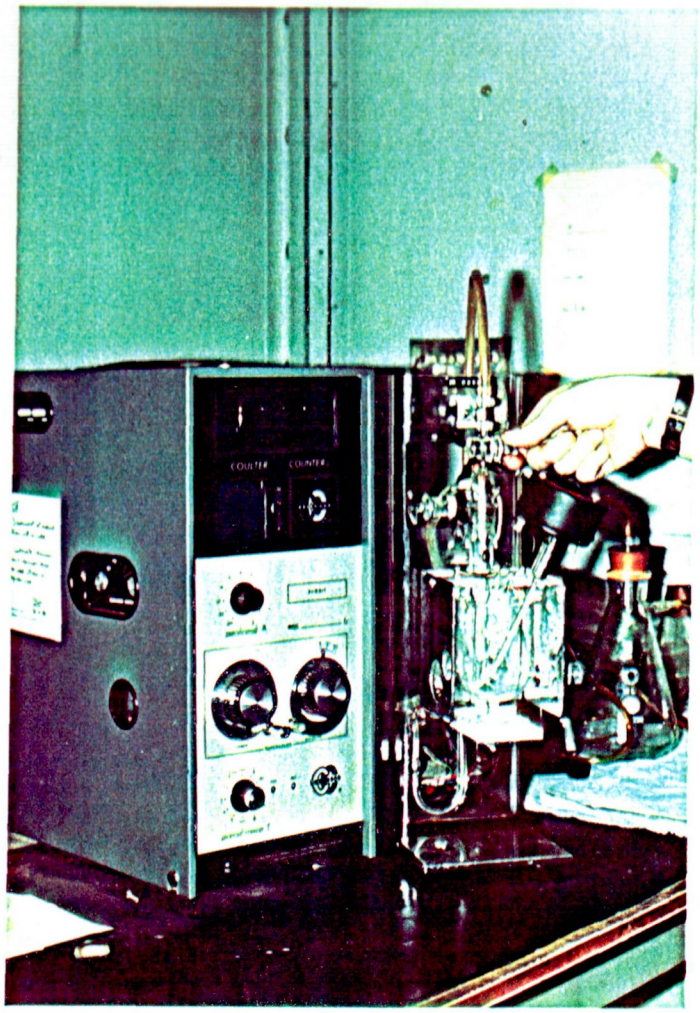


Plate 2.11 Coulter Counter as used in sizing ground samples for quantitative XRD. The aperture is sited at the base of the tube dipping into the electrolyte. The tap being manipulated draws a set volume of liquid upwards and a count is recorded.

Consequently Gaudin Schumann and Rosin Rammler functions[214,215] were fitted to the data with the aid of a linear regression subroutine. This subroutine was based on the method of least squares. The functions were expressed as follows :

$$\text{Gaudin Schumann} : W_F = 100(x/k)^m \qquad (2.3.4)$$

where W_F is the cumulative weight per cent finer than particle size x; k, the size modulus; m, the distribution modulus.

$$\text{Rosin Rammler} : W_R = (100 - W_F)$$
$$= 100 \exp - (x/x_o)^n \qquad (2.3.5)$$

where W_R is the cumulative weight per cent coarser than particle size x; x_o, the absolute size constant; n, the uniformity coefficient.

An example of the agreement between the data obtained and the two size distribution functions deduced by linear regression is shown in Figure 2.3.4. As can be seen, both functions fitted the data closely, the correlation coefficients being greater than 0.95 in both cases. No further distribution models were considered. The most useful parameters describing the size distributions were the size modulus (SM) from the Gaudin Schumann regression fit and the absolute size constant (ASC) from the Rosin Rammler function. The SM and ASC values for the ground standards were plotted against the time of grinding and are shown in Figure 2.3.5. From the figure a larger variation was observed for the Rosin Rammler distribution function and so the more sensitive ASC was selected for further work.

Samples of the extracted olivine and serpentine fractions were ground, sized and prepared for analysis in accordance with the

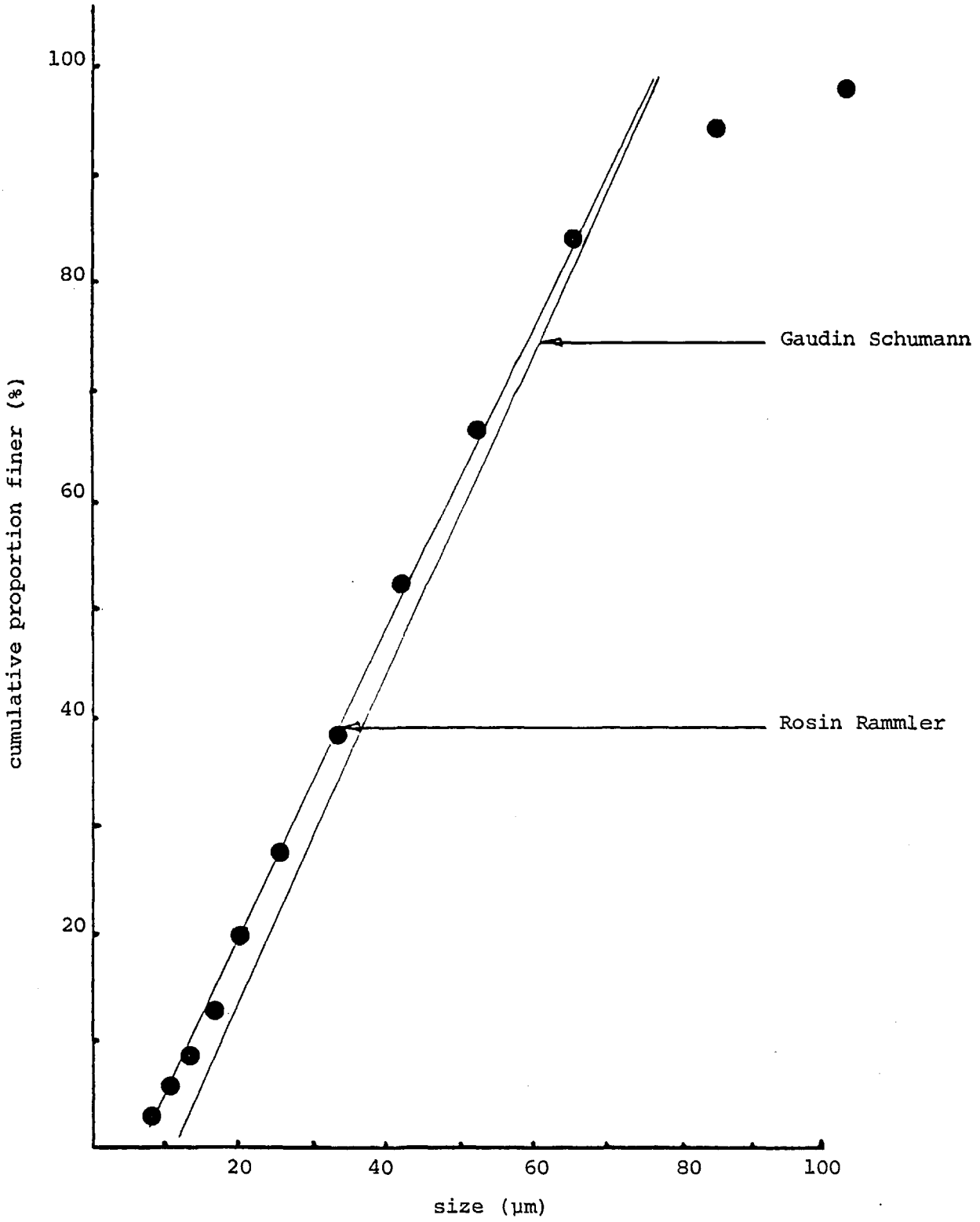


Figure 2.3.4 Size distributions for ground olivine : Coulter counter data as indicated by ● with associated regressed lines based on the Gaudin Schumann and Rosin Rammler Functions.

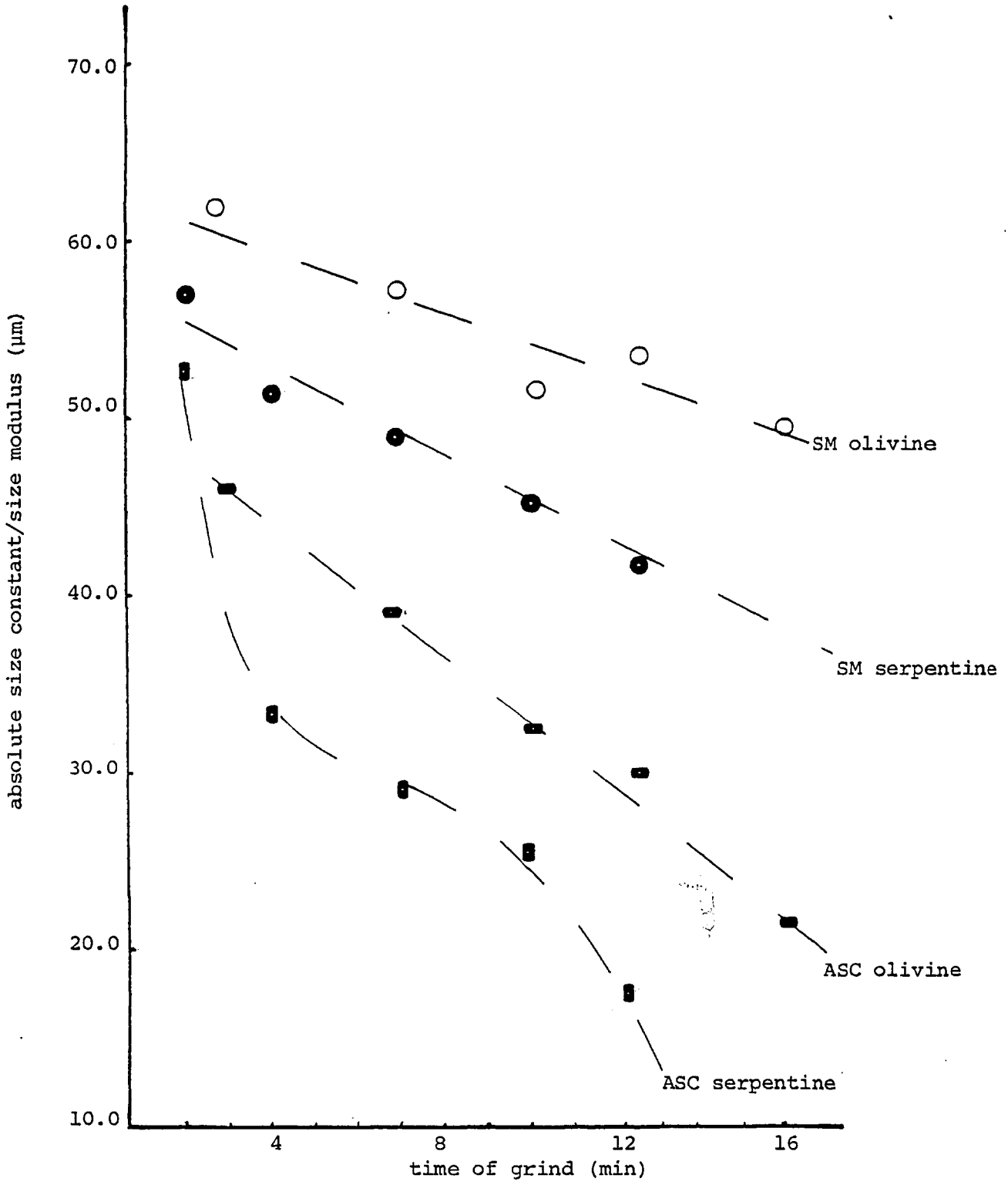


Figure 2.3.5 Variation in magnitude of absolute size constant and size modulus with increasing degree of comminution of mineral standards

mixture proportions listed in Section 2.3.7. In the case of olivine 0.0900 g of standard was used which was equivalent to an unknown sample concentration of (0.09/0.60).100 or 15%. (9% overall for the mixture as prepared.) This value was chosen to be roughly equivalent to the head concentration of olivine as observed in point counting (Section 2.2.2). For a similar reason 0.30 g of the serpentine standard was used in separately prepared mixtures. When subjected to XRD analysis peak intensities were measured by the peak area (assumption (c), Section 2.3.5) and the response expressed as the ratio of the peak intensity of the characteristic line of the mineral involved to that of the internal standard. Four such lines were tested for olivine at 5.10 Å, 2.76 Å, 2.46 Å, 1.75 Å. However, only the penultimate of these yielded a relationship between XRD response and ASC. The 2.46 Å line corresponded to the 100(hkl = 112) line for forsterite. This is illustrated in Figure 2.3.6. The S-shaped graph shown was analogous to one of the limbs of a similar plot obtained for quartz by Gordon and Harris[209] (inset). It would appear that the finer the grain size the greater the intensity of the diffracted X-rays. To assign an equation to the line for the purpose of its inclusion in the overall equation for olivine (as deduced later) a B-spline curve fit procedure was adopted. This is a method which splits a curve into several sections in proportion to the number of data points available. A correlation is then made for each of the sections in turn. The regressions were made by use of NAGFILE subroutine E02BAF made available by the Imperial College Computer Centre and the results are listed in Appendix 4. For ASC values ranging from 33 to 52, the B-spline fitted the data quite well. This was not the case for values 21-33 μm, and a linear regression provided a better fit. A summary of the equations and values used for the olivine standard size

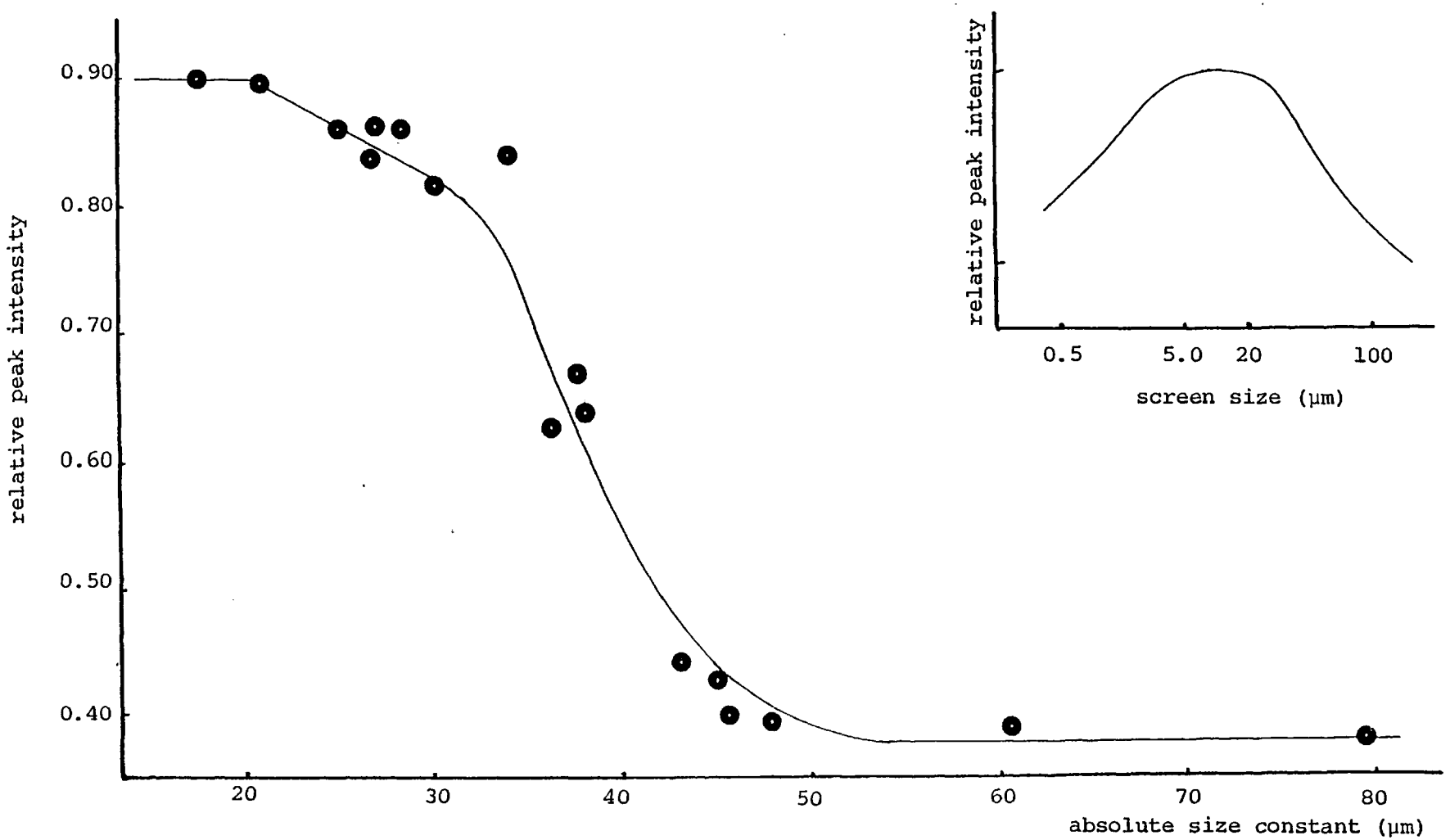


Figure 2.3.6 Size calibration for olivine standard : relation between relative peak intensity and absolute size constant (olivine concentration 15%). (Quartz calibration due to Gordon and Harris[209] is shown inset)

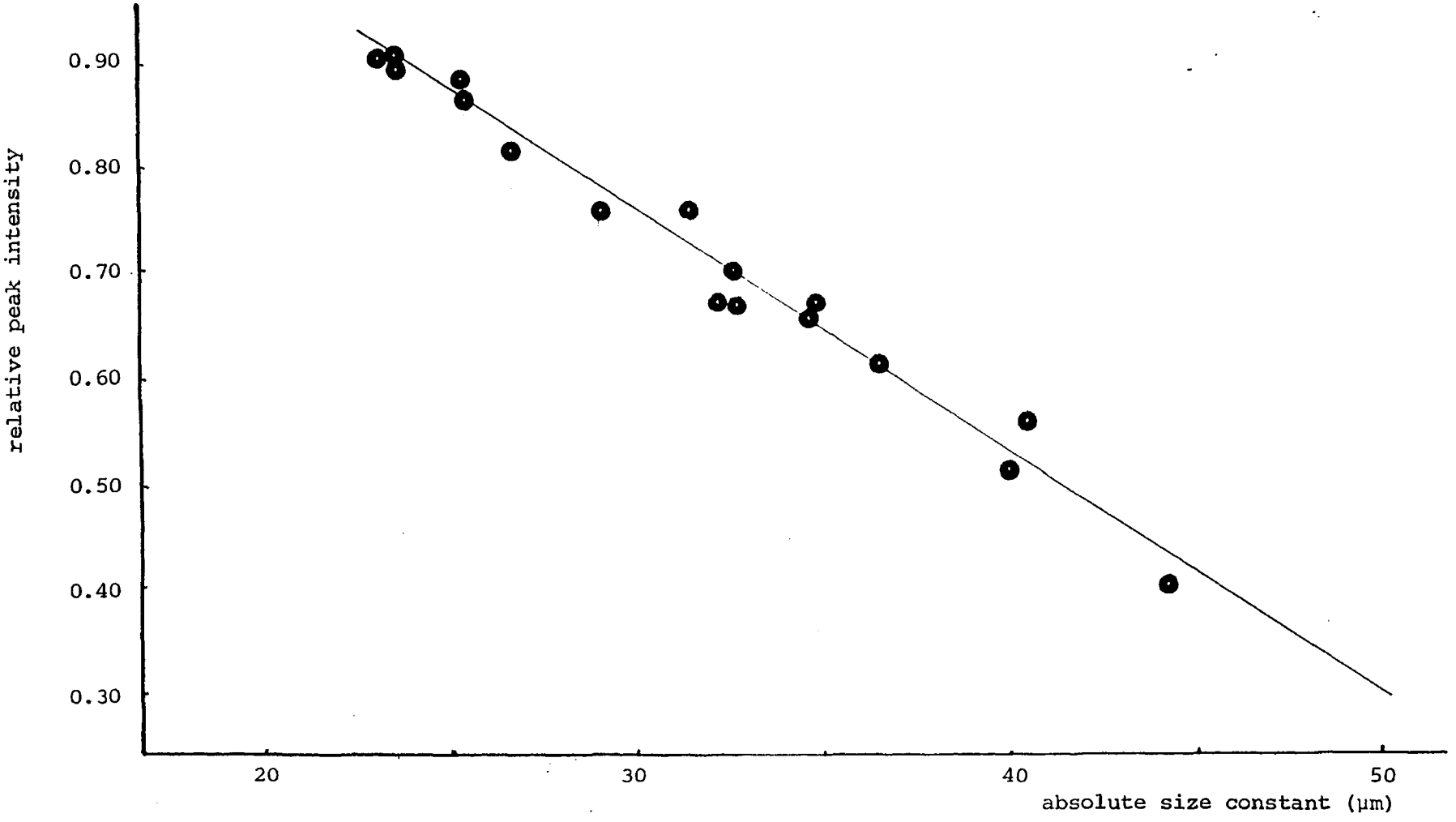


Figure 2.3.7 Size calibration for serpentine standard : relation between relative peak intensity and absolute size constant, serpentine concentration (after correction) 37.2%.

calibration curve is given below :

TABLE 2.3.4 SIZE CALIBRATION FOR OLIVINE

Absolute size constant range (μm) (ASC)	Value/equation for relative intensity : $X_{s,ol}$
<21	0.90
21 - 33	1.06 - 0.0078 (ASC)
33 - 52	B-spline
>52	0.37

The size calibration was simpler for the serpentine standard which is illustrated in Figure 2.3.7. This linear relationship is similar to that recorded for olivine, and it is possible that beyond the limits of the line, the graph tails off as in the previous case. The regression equation was found to be :

$$X_{s,sp} = 1.454 - 0.0231 \text{ (ASC)} \qquad (2.3.6)$$

where $X_{s,sp}$ is the value for the relative intensity of serpentine (sp) for varying size (s), concentration constant (at 37.2%).

2.3.9 Concentration calibration

A relationship was obtained between the concentration of the standard minerals and the XRD response. The mass ratio of each standard to the amount of sodium fluoride was varied to give plots of concentration against peak intensity. These were linear.

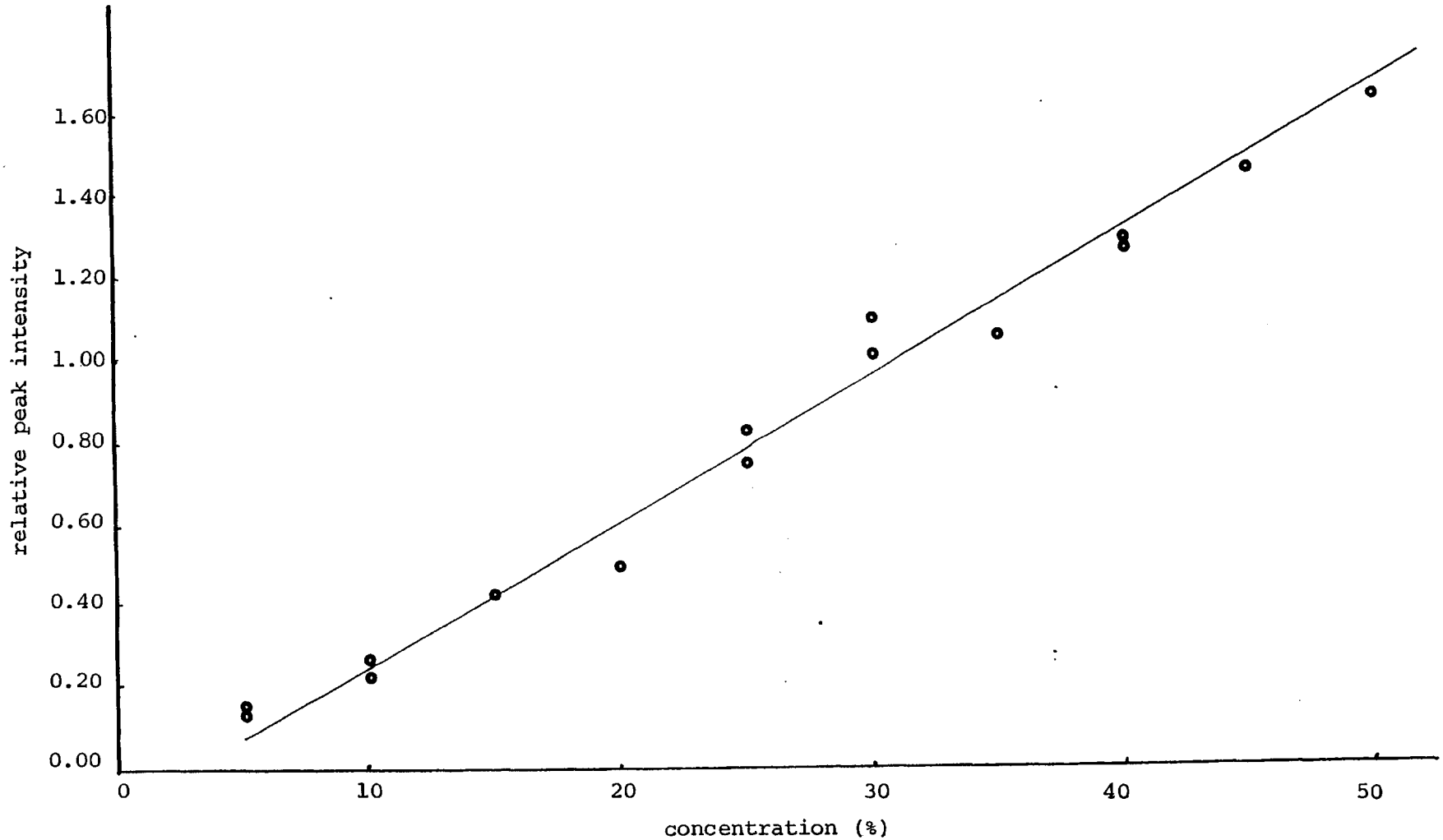


Figure 2.3.8 Concentration calibration for olivine standard

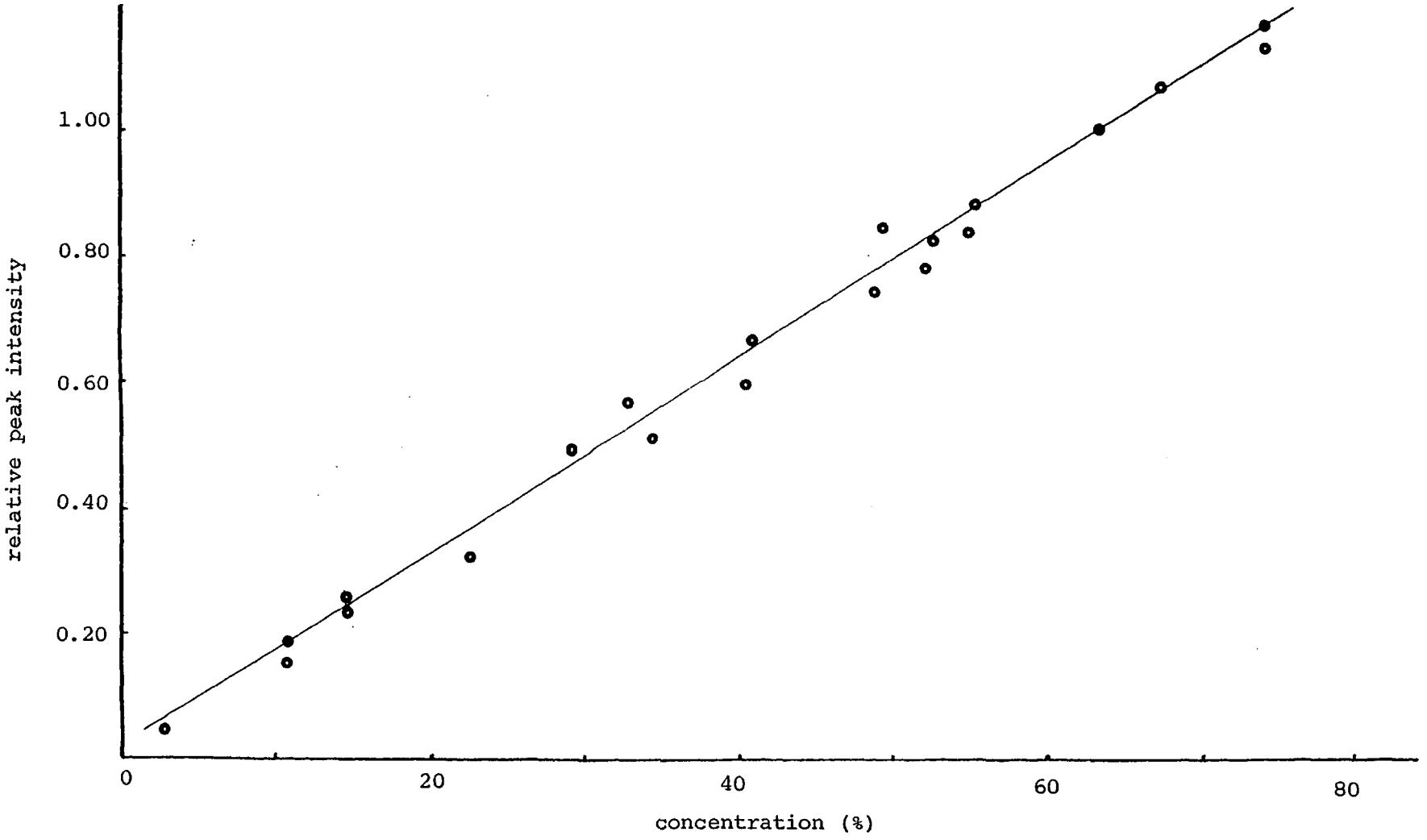


Figure 2.3.9 Concentration calibration for serpentine standard

On further examination of the XRD traces it was evident that the serpentine standard did contain some olivine. Apparently, some of the olivine had a smaller liberation size than that employed in the extractive procedure. To correct for this peak intensities were recorded for the olivine present in each of the mixtures used in the serpentine size and concentration calibrations. Making use of the size calibration in Figure 2.3.6 these relative peak intensities were adjusted so that they could be interpreted using the concentration calibration graph for olivine (Figure 2.3.8). (An example of this calculation is given in Appendix 4.) The concentrations of olivine in the serpentine mixtures were then read from the figure. It was noted that the newly evaluated olivine assays were directly proportional to the masses of the serpentine standard that had been used. Averaged results showed that the concentration of olivine in the serpentine standard was 25 ± 1.5%. The concentration calibration plot was redrawn for serpentine, as shown in 2.3.9. The correlation equations were :

$$X_{c,ol} = -0.095 + 0.035\ \%ol \quad (ASC = 42\ \mu m) \qquad (2.3.7)$$

$$X_{c,sp} = 0.010 + 0.016\ \%sp \quad (ASC = 39\ \mu m) \qquad (2.3.8)$$

where $X_{c,x}$ is the relative peak intensity for x of concentration c.

2.3.10 Error correction and final form

To test the method various combinations of the ground mineral standards were treated according to the procedure described (Section 2.3.7). The theoretical and experimental intensities are shown in Figures 2.3.10 and 2.3.11. In the case of olivine the gradient was virtually unity at low concentration levels indicating little error in the method. At higher concentration levels (i.e. at relative

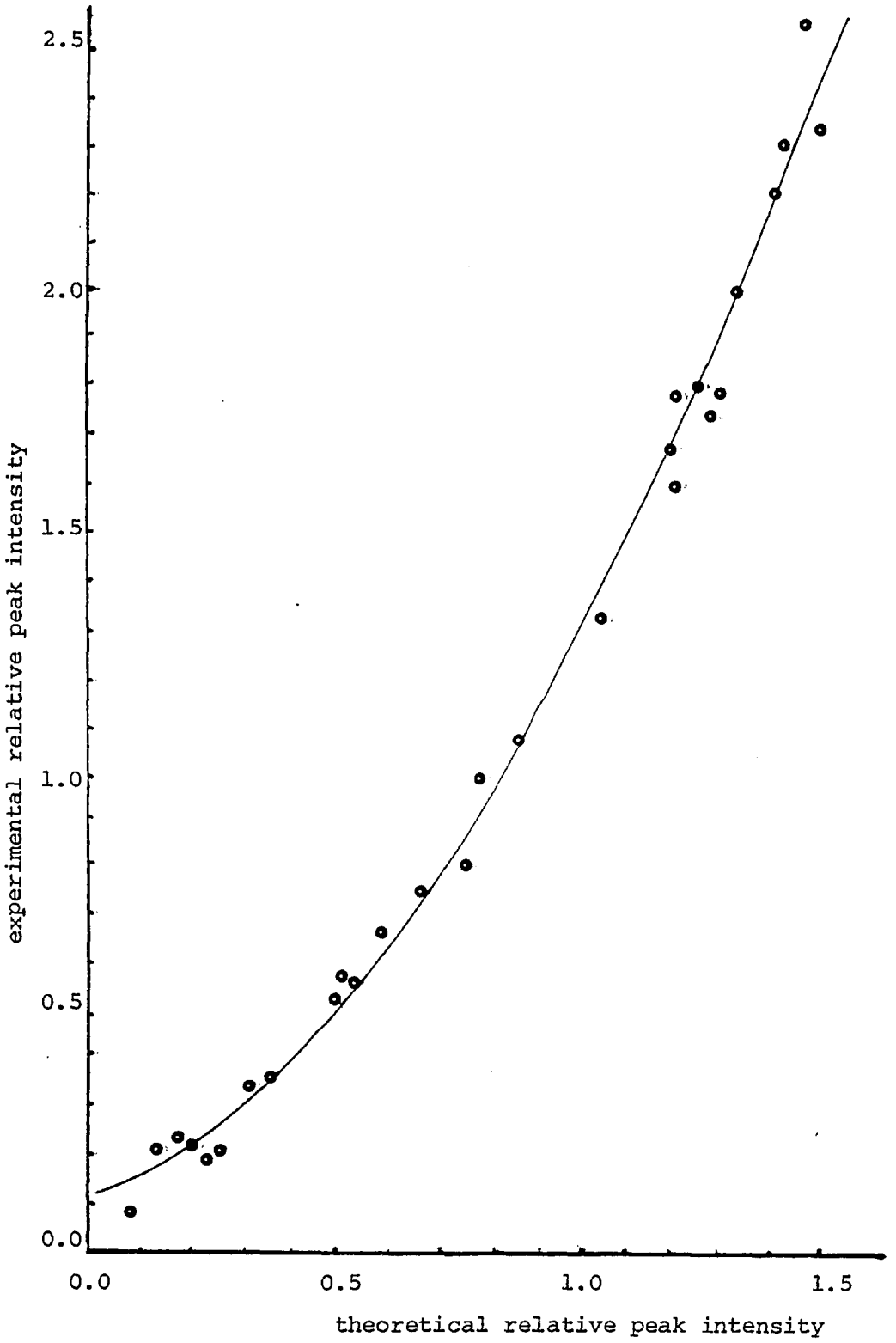


Figure 2.3.10 Error calibration for olivine standard

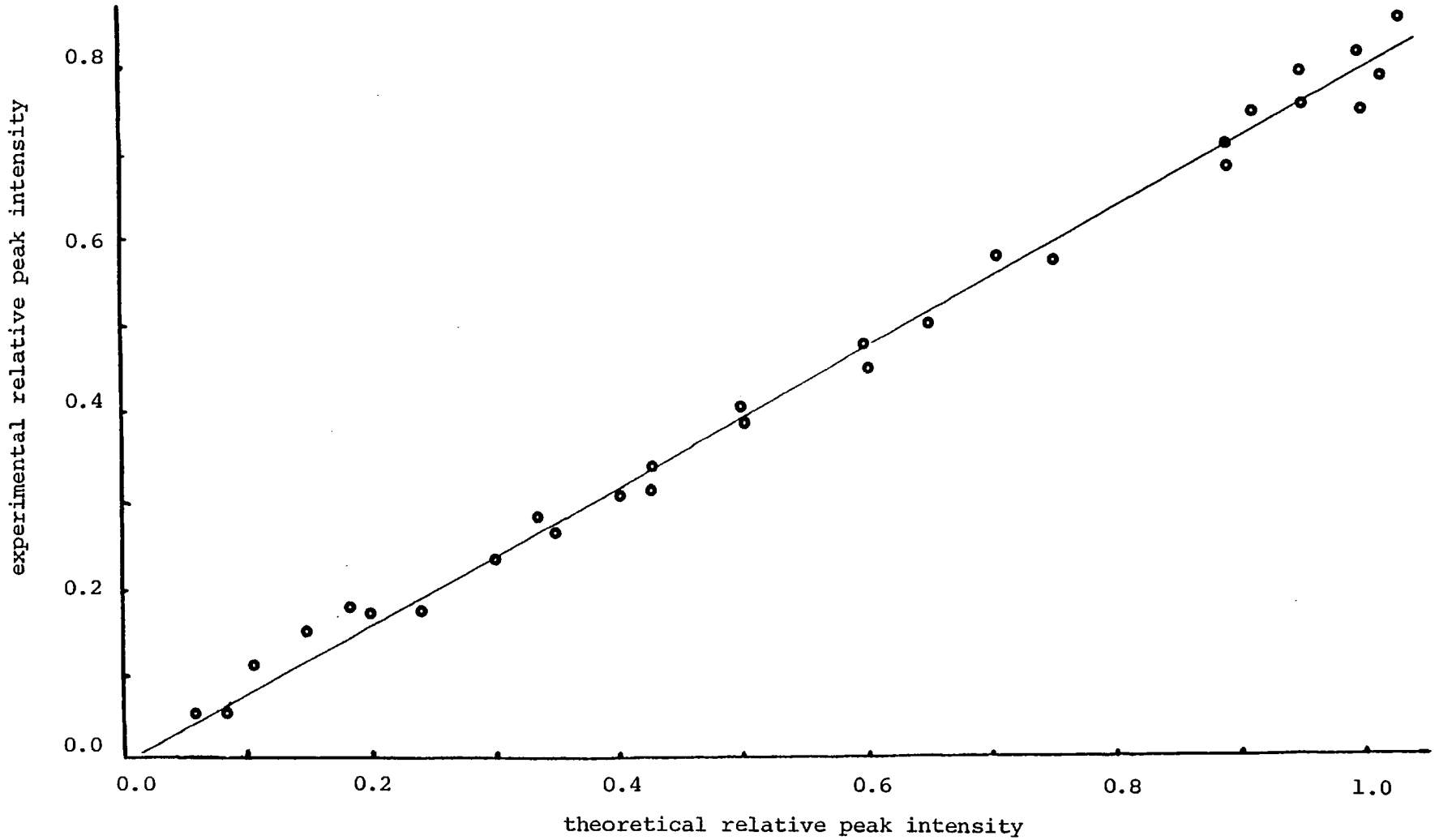


Figure 2.3.11 Error calibration for serpentine standard

intensities greater than 1.0) there was a progressive deviation. For serpentine a linear trend was noticeable, the gradient of which was less than unity. It was evident that though effects discussed above had not been entirely removed by the standardisation of the preparative procedure, they were under control. An error calibration was added as an integral part of the analytical technique which was deduced after further trials :

$$X_{th,ol} = 0.135 + 0.474\ X_{app,ol} + 0.731\ X^2_{app,ol} \quad (2.3.9)$$

$$X_{th,sp} = -0.022 + 0.815\ X_{app,sp} \quad (2.3.10)$$

where $X_{th,x}$ is the theoretical intensity of standard x; $X_{app,x}$ the experimentally found intensity.

To obtain the final forms of the analytical method the size and concentration calibrations were combined algebraically and equated with the error calibrations above. The two separate equations realised were then re-ordered to express the concentrations of olivine and serpentine in terms of XRD intensity and size (details are given in Appendix 4).

$$\%ol = (1.66 + 5.81\ X_{app,ol} + 8.96\ X^2_{app,ol})/X_{s,ol} + 2.73 \quad (2.3.11)$$

$$\%sp = (52.2\ X_{app,sp} - 1.41)/(2.45 - 0.039\ ASC) - 0.655 \quad (2.3.12)$$

One critical test of the method was the evaluation of the head values of olivine and serpentine. The head values of replicate samples were found to be 34.6 ± 1.3% olivine, 47.3 ± 1.8% serpentine. These values produced a better agreement with the elemental assays recorded for the head than the original concentrations of olivine and

serpentine as evaluated from binocular microscope point counting. Furthermore kimberlites from the Kimberley area have been found to have similar concentrations of olivine and serpentine as those inferred by the XRD method.[216] It is interesting to note that the olivine and serpentine assays attained from point counting of the thin sections, 25.8 and 57.6% respectively, were comparable with the XRD values and their algebraic sums were virtually equivalent. It would appear that this new XRD method of quantitatively estimating olivine and serpentine has the same order of precision and is more convenient and reliable than the only alternative method available, namely thin section microscopy.

2.4 Other Analytical Methods

As stated in Section 2.2.3 the most appropriate techniques (in addition to XRD) for studying alteration phenomena were thermal analysis, infra-red spectroscopy and atomic absorption spectroscopy. The applications of these in the kimberlite research are discussed below.

2.4.1 Thermal analysis

There are three principal types of thermal analysis relevant to mineralogical investigations : differential thermal analysis (DTA), thermogravimetric analysis (TGA) and differential thermogravimetric analysis (DTG),[217] of which the first two are considered the most important. DTA involves two samples, one an unknown, the other an inert reference, being heated simultaneously. A recording of the evolution and/or absorption of heat by the unknown is made by means of recording the temperature difference between the two samples as they are heated. In TGA the mass of the sample is continually measured as

it is heated. The proportionately large weight losses in various temperature ranges represent the data of primary interest. Both DTA and TGA are diagnostic of the dynamic thermal reactions that occur.[189,218]

Most minerals are detectable by DTA.[219] Several authors give tables and graphs of many compounds[204,219,220] which illustrate the usefulness of the method as a qualitative tool. The application of DTA to quantitative analysis, in particular to clays (Grim,[221] Carthew[222] and others[223,224]) has proved successful under closely controlled conditions. When suitable standards are not available, however, quantitative interpretations for complex mixtures are virtually impossible. In the present work attempts were made to produce an auxilliary quantitative method for serpentine analysis using DTA, but the results obtained were irreproducible. Some of the more important parameters which cause deleterious effects in this respect include particle size,[220] variation in chemical composition of the sample[223] and various instrumental factors, such as thermocouple positioning in the sample[224] and the heating rate.[225] Similar comments apply to TGA[226] all of which can be effectively controlled by the careful use of standardised conditions. It is sometimes possible to make quantitative use of overall weight losses for quite complicated mixtures (see later), although the qualitative application of the method is limited. In the testwork a Stanton "Massflow" thermobalance was employed and this is illustrated in Plate 2.12. An example of the data produced is given on the left hand side of the plate where progressive weight loss is charted side by side with temperature rise. The instrument was operated in accordance with the manufacturer's recommended procedures. It was found unnecessary to employ an inert atmosphere in the analyses conducted.

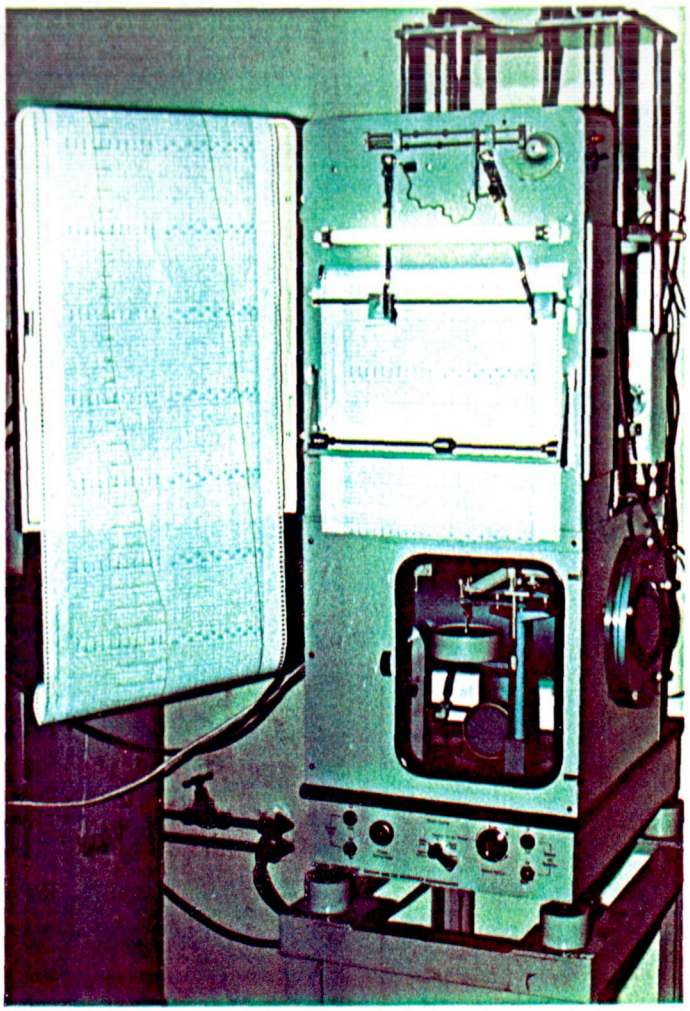


Plate 2.12 Stanton "Massflow" Thermobalance

The thermobalance analysed samples weighing 0.04-0.12g. Mass losses recorded were 5-30% of the original. Errors in mass losses were +4%. The balance has also the facility for simultaneous DTA.

2.4.2 Infra-red spectroscopy

Electromagnetic radiation of different energy levels has markedly different effects on atomic and molecular associations. The infra-red part of the spectrum principally affects the vibration modes of molecules; and spectra characteristic of particular structural groups can be drawn as a result of stretching, twisting or bending motions induced by the incident radiation.

Although the use of IR spectroscopy has been widely discussed with regard to qualitative and quantitative analysis of minerals,[189,194,227-31] its principal application lies in the description of structural groupings. In the present work, the application to groupings in clay minerals is of most interest. Stubican and Roy[232,233] described the effect of various ion exchange reactions on the infra-red spectrum of the clay minerals. These workers showed that aluminosilicate infra-red spectra are sensitive to the substitution of ions of different charge. Examples include the species Al^{3+} replacing Si^{4+} in tetrahedral, and Mg^{2+} for Al^{3+} or vice versa in octahedral coordination. Ion substitutions are recorded in the infra-red spectrum by a shift in the peak position to a higher or lower wavenumber and/or a variation of intensity. An example of the former is the displacement of the Si-O 1000-1100 cm^{-1} peak to 950-990 cm^{-1} with increasing aluminium substitution and of the latter the replacement of aluminium by divalent ions causes a decrease in the HO-Al peak intensity at 3650 cm^{-1}.

In the testwork a Perkin-Elmer 599B double beam infra-red spectrometer was employed and operated in accordance with the manufacturer's instructions. Samples were prepared according to the potassium bromide disc method.[189] This involved mixing 2 mg of the fine particulate sample with 200 mg of potassium bromide and pressing the homogeneous mixture into a disc 10 mm x 1 mm, care being taken to minimise water

absorption from the atmosphere. The prepared disc was then analysed in comparison with a blank potassium bromide disc.

2.4.3 Chemical analysis

X-ray diffraction had indicated the elements likely to be present in the kimberlite (from a knowledge of the chemical compositions of the minerals identified). A fuller qualitative and semi-quantitative analysis of the kimberlite was carried out by the analytical service department of Imperial College using X-ray fluorescence (XRF) analysis. Briefly, this method involved directing an X-ray beam through samples of the kimberlite, olivine or serpentine standards and monitoring the resultant absorption of X-rays which were assumed to give a qualitative measure of the elemental concentrations. The results, given in Table 2.4.1, indicate the general elemental complexity of the samples analysed, but also confirm the relative importance of magnesium, iron and silicon. The first two were subsequently analysed in the reaction solution as a means of assessing the extent of degradation (Section 2.6). Silicon was assayed in the solid residual fractions. Two other elements were selected for routine analysis : calcium and aluminium. Their importance is discussed in Section 2.6 and Chapters 3 and 4.

Atomic absorption spectroscopy (AAS) was employed to determine magnesium, iron, calcium and aluminium. This technique involves atomising aqueous species in a gas flame. These species absorb radiation of wavelength characteristic of the element involved, the radiation being supplied as a monochromatic beam directed through the flame. Absorbance is recorded and is taken to be directly proportional to the concentration of the absorbing species. The apparatus is calibrated by means of chemical standards of varying concentrations.

From a consideration of the inter-ion interferences possible,[234] magnesium and calcium were analysed using a nitrous oxide-acetylene

gas mixture. Otherwise, the conditions were those normally recommended. Magnesium, calcium, aluminium and iron analyses were made on solutions generated from reactions as well as on solid products. In the case of the former, the filtered reaction solution was made up to a known volume after sufficient Analar hydrochloric acid had been added to give an overall concentration of 5% HCl. The acid was added to prevent precipitation of ions. Calibration standards were made up in a similar manner and the analyses made within the ppm concentration ranges recommended.[234] To analyse a solid product, the sample was first ground to -75 μm in an ethanol medium using an agate mill, and dried. 0.04-0.10 g of solid was placed in a zirconium crucible, mixed and fused with 1.00 g of Analar sodium peroxide. The residue was dissolved in distilled water and made up to 500 ml containing 5% Analar hydrochloric acid. The solution also contained 10% absolute ethanol by volume (for reasons explained below). The solution was then analysed using an appropriate set of standards. In this case the standards contained similar concentrations of sodium peroxide and ethanol as in the analysed solution.

Silicon analysis by AAS proved to be more difficult. The main problem was due to the very low sensitivity recorded even when an extremely hot flame was used. A different approach was tested. This involved an ultra-violet spectrophotometric technique based on the formation of a molybdosilicilic acid complex.[235,236] Although the element was readily detectable the reproducibility of results on the kimberlite head samples was extremely poor. This was attributed to the presence of trace elements (Table 2.4.1) which adversely affected the absorption characteristics of the complex. The problem of rapid silicon analysis was solved by resorting to AAS and using solutions which were treated with ethanol, which produced a more fuel-rich flame than that which could be ordinarily achieved. The treatment was effective :

TABLE 2.4.1 QUALITATIVE AND SEMI-QUANTITATIVE CHEMICAL ANALYSIS FOR KIMBERLITE, OLIVINE AND SERPENTINE

Approximate Concentration Range	Kimberlite	Olivine*	Serpentine*
> 5%	Mg Si	Mg Si Fe	Mg Si Fe
5 - 0.5%	Al K P Ca Ti Fe Ba	Ni	K Ca Ti
0.5 - 0.05%	S Cl Cr Mn Ni	Ca Ti Cr Mn	P Cr Mn Ni Ba Zr
< 0.05%	Cu Zn Sr Nb Rb	Cl K Zn Sn Zn Nb	S Cl Zn Sr I Nb Rb Sr

* Al excluded from analysis

silicon could be detected at 2-3 ppm and the response increased by 100-200%. Similar beneficial effects were noted for the other elements. Data obtained for the kimberlite, olivine and serpentine standards are shown in Table 2.4.2.

Applying the data from the XRF and XRD analyses, chemical formulae for the olivine and serpentine standards could be calculated. These are shown in Table 2.4.2. In the case of olivine the charge balance required a divalent ion of atomic weight 47-65 to be present apart from the magnesium, calcium and iron already identified. Nickel, an ion commonly found in olivines,[63] was the most probable on the basis of XRF results (Table 2.4.1). In the case of serpentine, the true chemical composition could only be calculated after adjusting for the olivine present (as measured by XRD). The chemical compositions and formulae for the lead and standard minerals are given below in Table 2.4.2.

TABLE 2.4.2 CHEMICAL ASSAY DATA FOR THE KIMBERLITE, OLIVINE AND SERPENTINE STANDARDS

Composition	Kimberlite	Olivine	Serpentine
Mg%	16.1	25.9	15.0
Si%	16.3	18.5	19.4
Fe%	6.1	7.7	7.3
Ca%	6.3	1.7	3.8
Al%	1.0	0.1	3.2

Chemical formulae

olivine $Ca_{.07}Mg_{1.62}Fe_{.21}Ni_{.10}Al_{.01}SiO_4$

serpentine $Ca_{.28}Mg_{1.80}Fe_{.39}Al_{.34}Si_2O_5(OH)_4$

2.5 Quantitative Estimation of Clay Minerals

2.5.1 Applications of mass balances to quantitative analysis

In order to deduce mechanisms of the alteration reactions described in Section 4.5 estimates of the mineralogical composition of reaction products were, of course, essential. Clays were expected to cause particular difficulties in this regard. The previous discussions in Sections 2.2.3, 2.3.2 - 4, 2.4.1, have cited the advantages and limitations of the instrumental methods commonly applied to qualitative and semi-quantitative clay mineral analysis. The principal difficulties encountered arise from the diversity and variability of these minerals. One approach to acceptable assay is as follows.

a) Qualitative determination of phases present by an instrumental method. XRD is the most useful technique in this respect and DTA yields confirmatory information.

b) Quantitative determination of major elements by AAS or XRF analysis.

c) By combining (a) and (b) on the basis of mass balance and stoichiometry, calculation of phase proportions.

This type of approach is now discussed. The method used in the interpretation of the data in this investigation was developed from one put forward by Pearson.[237] In Pearson's work, the individual proportions of clays in a rock (said to contain 69% of combined phyllosilicates solely as kaolinite, illite and chlorite) were determined with the aid of equations of the form :

$$\%chl\%E_{chl} + \%kao\%E_{kao} + \%ill\%E_{ill} = 100\%E_{T} \qquad (2.5.1)$$

where %chl is the proportion of chlorite in the rock and $\%E_{chl}$ is the proportion of a specified element expressed as the oxide : SiO_2, Al_2O_3, K_2O, FM(MgO+FeO+Fe_2O_3), Na_2O, CaO or H_2O in chlorite. (Similarly for kaolinite and illite represented as kao and ill respectively.) The term E_T is the experimentally determined total concentration of the element in question in the mineral mixture.

It may be noted that clay minerals do not, in general, exhibit the constant composition typical of chemical compounds : the phases exist over reasonably clearly defined ranges of composition, reflected in their elemental assays. These ranges need to be taken into account for each element in the equation(s) and are most conveniently handled by means of published maximum and minimum assay figures (Appendix 5). To simplify the procedure for the solution of the equations, Pearson employed the relationship

$$\%chl + \%kao + \%ill = \%clay \qquad (2.5.2)$$

where %clay is the proportion of clays in the sample (69%).

Expressing %chl in terms of the other variables, this term can be eliminated from the general form (2.5.1); thus on rearrangement :

$$\%clay\ \%E_{chl} + \%kao\ (\%E_{kao} - \%E_{chl}) + \%ill\ (\%E_{ill} - \%E_{chl}) = 100\%E_T \qquad (2.5.3)$$

From a consideration of the range of values of elemental assays it was noted that kaolinite varies relatively little in composition and could be taken to have a constant composition. Hence by sequentially substituting maximum and minimum assays for chlorite ($\%E_{chl}$) and illite ($\%E_{ill}$) in equation (2.5.3), four equations could be obtained for each

elemental species, for example :

$$\%clay\ \%E_{\overline{chl}} + \%kao\ (\%E_{kao} - \%E_{\overline{chl}}) + \%ill\ (\%E_{\overline{ill}} - \%E_{\overline{chl}}) = 100\%E_T \qquad (2.5.4)$$

where a bar over the mineral name represents a maximum assay value. A similar equation was obtained for each elemental species employing the minimum tabulated values. When plotted, some of these lines clearly delineated an area ABCDE of interest (Figure 2.5.1) within which the correct mineralogical composition (%ill, %kao and %chl) ought to lie. Recalculated maximum and minimum assay limits were obtained for SiO_2, Al_2O_3 and FM by using derived proportionality relationships between these and the K_2O assay for illite, making the assumption that all the potassium resides in this mineral. The redrawn maximum (rmax) and minimum (rmin) limits are also shown in Figure 2.5.1 and delineate a smaller area (shaded in the diagram) which represents the final set of possible solutions.

Pearson produced a computer program which was used to calculate the phase proportions of kaolinite, chlorite and mica on the basis of chemical assays deduced for each mineral. The program was subsequently used to detect phase concentration differences between various mudstones.

Pearson's method, however, could not be adopted in the present work for the following reasons :

a) the program developed was written for the analysis of a particular mineral assemblage
b) it was not possible to apply the method to vermiculite and smectite analysis, and
c) the method could not take account of phases for

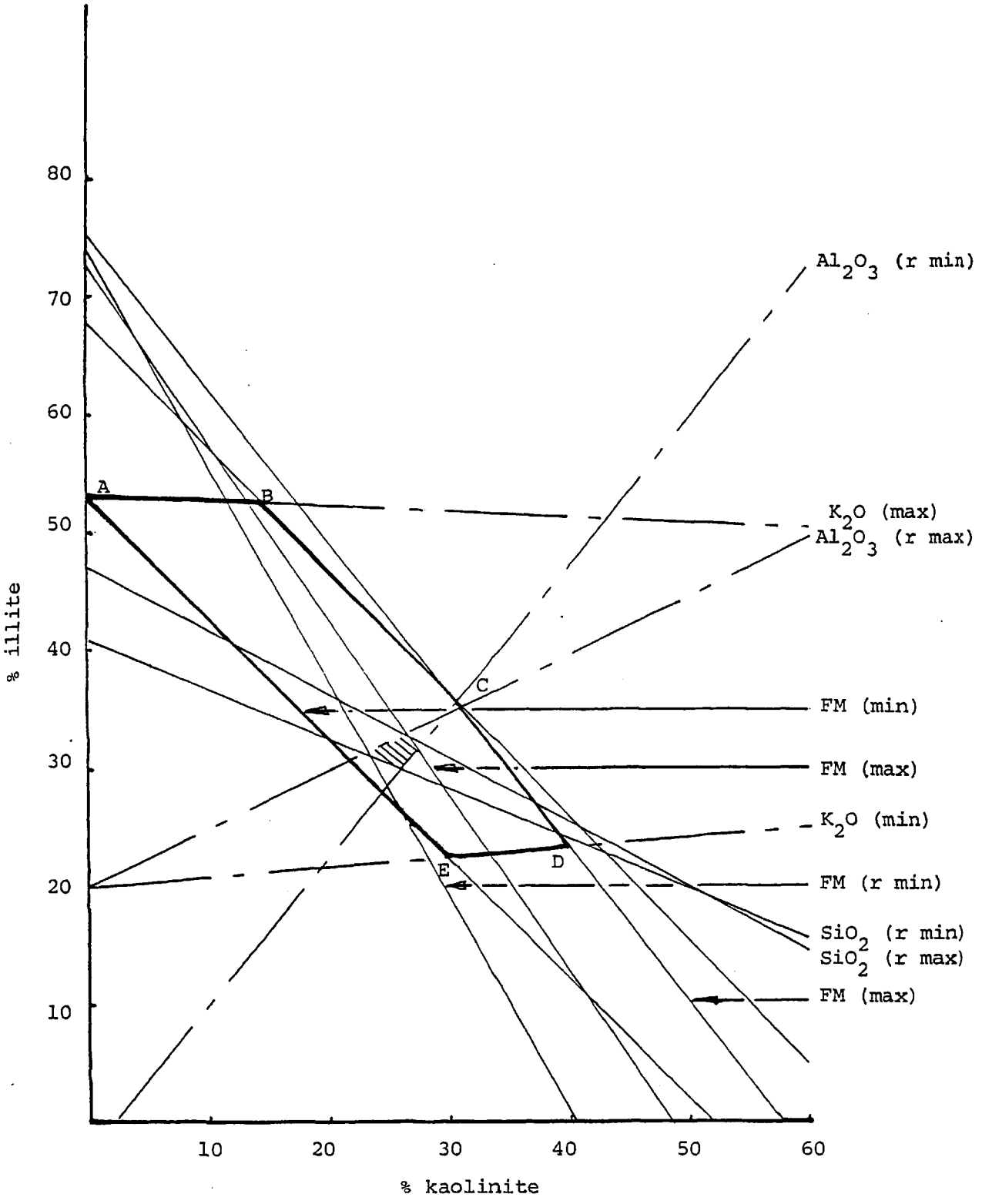


Figure 2.5.1 Graphical representation of calculation of clay phase proportions using an elemental mass balance approach.[237]

Notes : FM = ($MgO+FeO+Fe_2O_3$)

r max = line replotted using recalculated maximum elemental assay value

which published data were unavailable.

A new method was required, which could take account of these difficulties.

2.5.2 Outline of the revised method of clay analysis

In the present work, the products were assumed to consist largely of a mixture of four mineral types i.e. four from chlorite, vermiculite, smectite, kaolinite, serpentine, boehmite, gibbsite and other aluminosilicate varieties to be specified - these being the major phases variously present in the products, based on preliminary XRD analysis. This assumption was made on the grounds that it was only possible to make four different quantitative AAS assays routinely, i.e. for the elements Si, Al, Fe, Mg. These assays, however, could characterise the phyllosilicate minerals. Hence only four equations could be employed in the mass balance, in a manner analogous to Pearson's method, which involve four unknown mineral concentrations. A unique set of solutions may be then obtained. Adopting the form of equation 2.5.1, typical equations are :

$$\%chl\%Si_{chl}+\%verm\%Si_{verm}+\%kao\%Si_{kao}+\%sm\%Si_{sm} = 100\%Si_T$$

$$\%chl\%Al_{chl}+\%verm\%Al_{verm}+\%kao\%Al_{kao}+\%sm\%Al_{sm} = 100\%Al_T$$

$$\%chl\%Fe_{chl}+\%verm\%Fe_{verm}+\%kao\%Fe_{kao}+\%sm\%Fe_{sm} = 100\%Fe_T$$

$$\%chl\%Mg_{chl}+\%verm\%Mg_{verm}+\%kao\%Mg_{kao}+\%sm\%Mg_{sm} = 100\%Mg_T \qquad (2.5.5)$$

Acceptable solutions were found by inverting the 4 x 4 matrix form of these equations and eliminating those inconsistent with physical reality. For the purposes of calculation, the following further assumptions were made.

a) The mineral phases generated would have a chemical composition comparable with those found in natural mineral systems. Tabulated assay values should be employed to take account of water, major and minor elemental constitutents. Idealised structural formulae would prove inadequate (except in the case of metastable phases - see later).

b) Where little variation was observed for an elemental concentration in a mineral phase a meaned value could be quoted and treated as a constant in further calculations (e.g. the silicon assay in vermiculite may be taken as 16.3 ± 0.4%).

c) All real compositional solutions to the simultaneous equations were non-negative and their sum approximated to 100%. A value falling between the limits 95 - 105% was deemed acceptable. A further check could be afforded by undertaking a 'water' mass balance for the expected constituent minerals and the assayed fines fraction. TGA could be used to determine the water loss in the mixture.

d) By systematic use, in turn, of the highest and the lowest (and, where possible, selected intermediate) values of particular elemental concentrations such that all permutations were made, the means of the various tested individual solutions would yield good estimates of the actual clay mineral concentrations.

2.5.3 Development of the trial program and inter-elemental concentration relationships

At first a hypothetical system was tested employing a trial

program (not described in detail here, the final program is reproduced, however, in Appendix 5). Applying the above assumptions and solving four simultaneous equations (equations 2.5.5) for four unknowns : the concentrations of chlorite, vermiculite, kaolinite and smectite. These minerals were selected as they are usually the most important alteration products of kimberlites. The elemental concentrations of each mineral phase were represented as a 4 x 4 matrix in the matrix form of equation 2.5.5 (equation 2.5.6). This matrix is referred to hereafter as the elemental-mineral or EM matrix. On the basis of assumption (b) certain elements of the matrix took constant values (represented by K in equation 2.5.6). Otherwise high (H) or low (L) estimations of the silicon, aluminium, iron, magnesium assays were tested in turn according to assumption (d). As shown, equation 2.5.6 also contained the 4 x 1 matrices relation to mineral and total elemental concentrations.

$$\begin{pmatrix} H/L & K & K & H/L \\ H/L & H/L & K & H/L \\ H/L & H/L & O & H/L \\ H/L & H/L & O & H/L \end{pmatrix} . \begin{pmatrix} \%chl \\ \%verm \\ \%kao \\ \%sm \end{pmatrix} = \begin{pmatrix} \%Si_T \\ \%Al_T \\ \%Fe_T \\ \%Mg_T \end{pmatrix} \qquad (2.5.6)$$

EM matrix — mineral concentration matrix — elemental head matrix

Typically a set of assay data was read into the computer (CDC 4120) in the form of the right hand side of equation 2.5.6. The program was run through the 2^{11} permutations implied by the possible values in the EM matrix. The simultaneous equations were solved by using the NAGFILE subroutine F04ATF as provided by the Imperial College Computer Centre. Computed solutions were automatically tested

according to assumption (c) and those accepted (about 40 in number) meaned to produce the final set of phase proportions. In order to reduce the range and hence the uncertainty in the final estimated proportions, constraints imposed by the inter-elemental relationships described below were incorporated.

Chlorite : Deer et al[72] describe a relationship between the d spacing of the 001 (basal) layer and the proportion of tetrahedrally coordinated aluminium. Gillery[166] showed that a similar relationship existed for synthetic chlorites. These relationships are illustrated in Figure 2.5.2. As the sum of silicon and aluminium ions per unit cell in the tetrahedral layer equals a constant, (8 on the basis of 28 oxygen equivalents) a plot between the number of silicon ions per unit cell and silicon assay could be obtained, as shown in Figure 2.5.3. It is clear (present work) that from the d spacing of the diffractogram the silicon concentration of the chlorite could then be estimated for unknown samples. The silicon assay deduced, characterised the type of chlorite as can be seen in Figure 2.5.4. This diagram illustrates the silicon and aluminium assay limits for the various chlorite minerals, the data being obtained from Deer et al.[72] Hence, given a particular silicon assay, the range of possible aluminium assay values could be substantially reduced. The principle was extended also to the magnesium and iron concentrations. As shown in Figure 2.5.5, limits of uncertainty can be ascribed to the various assays of these two cations in chloritic minerals. Furthermore, a high correlation existed between the magnesium and iron assay.

The identification of a chlorite species was prone to error in the estimation of the d spacing because of the breadth of the peaks normally observed. Two d spacings were read - at the edges of the peak encountered in the 14.0-14.4 Å region, yielding two possible end-

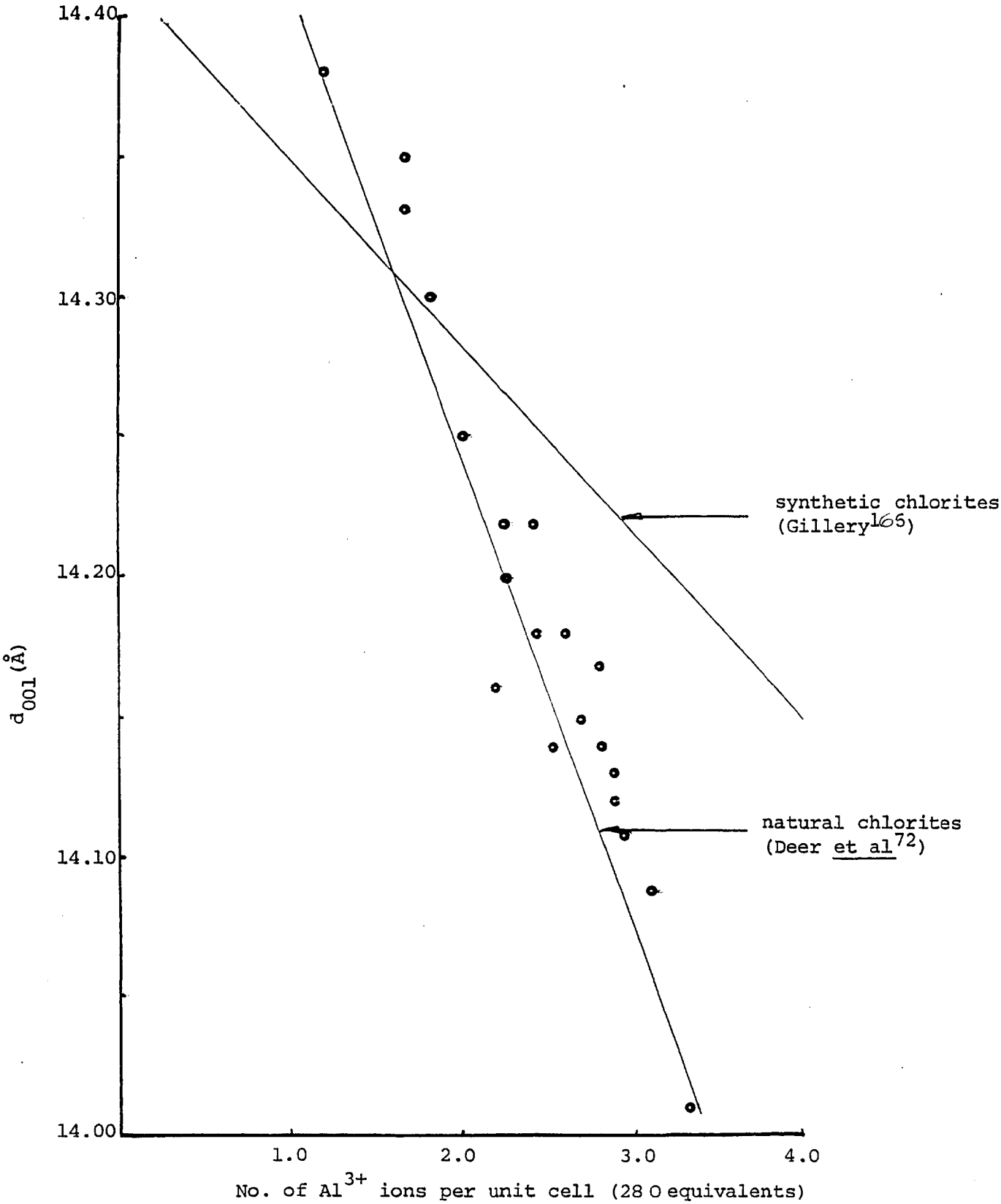


Figure 2.5.2 Relation between the position of the basal (001) layer peak and the number of aluminium ions per unit cell (28 oxygen equivalents) for chlorites.

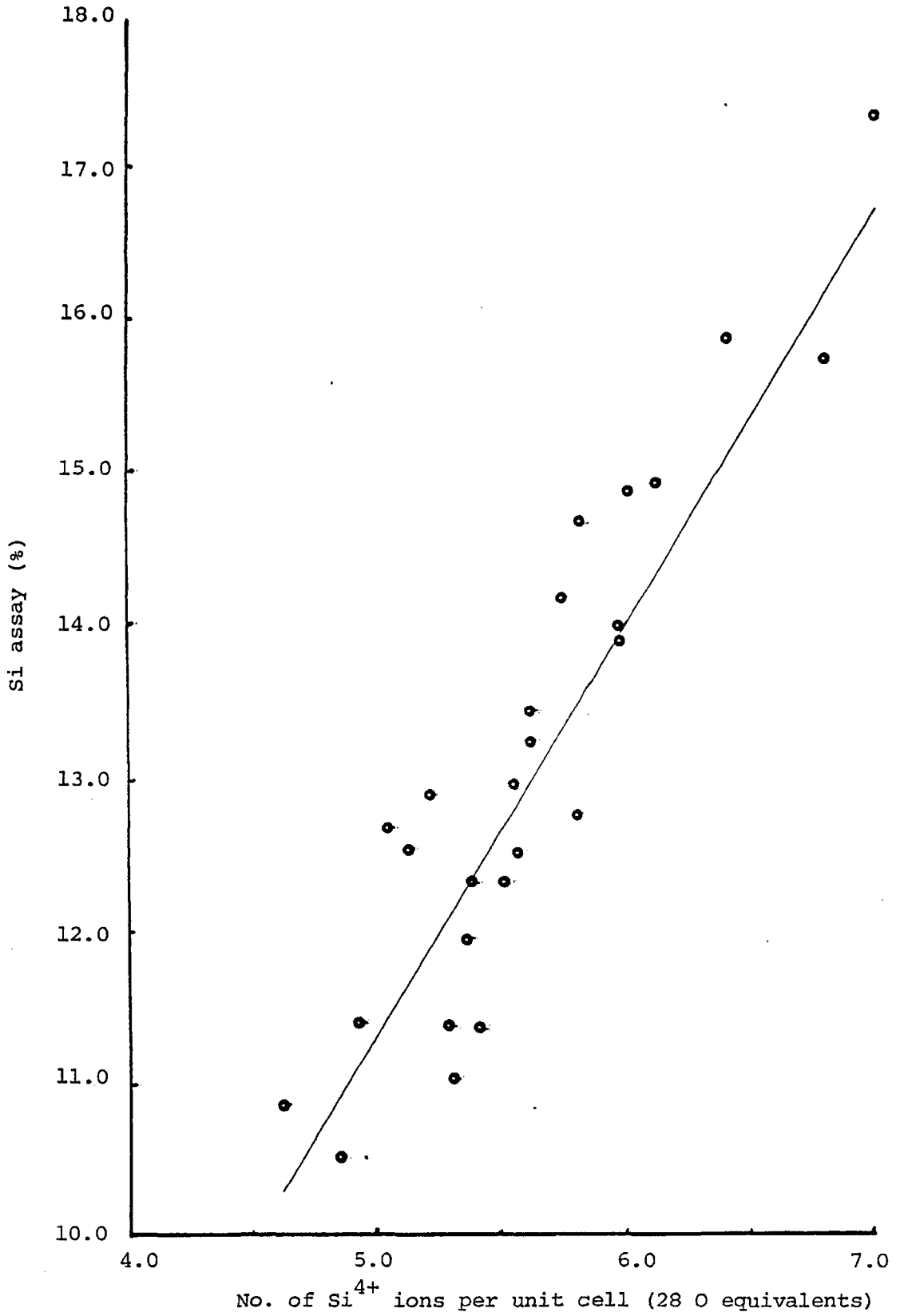


Figure 2.5.3 Relation between silicon assay and number of silicon ions per unit cell (28 oxygen equivalents) for chlorites.

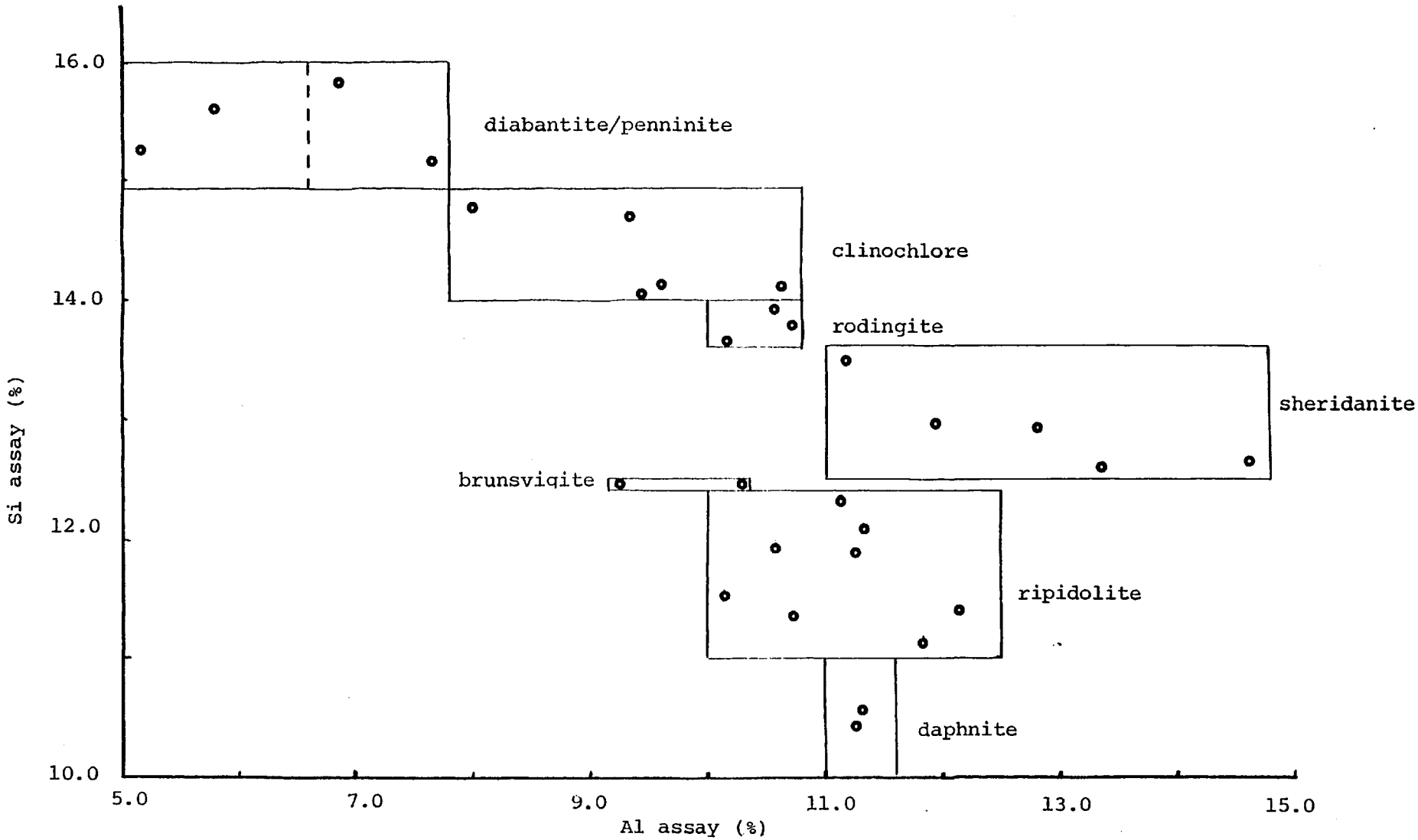


Figure 2.5.4 Boundary limits for silicon and aluminium assays for chlorite minerals adopted in program.

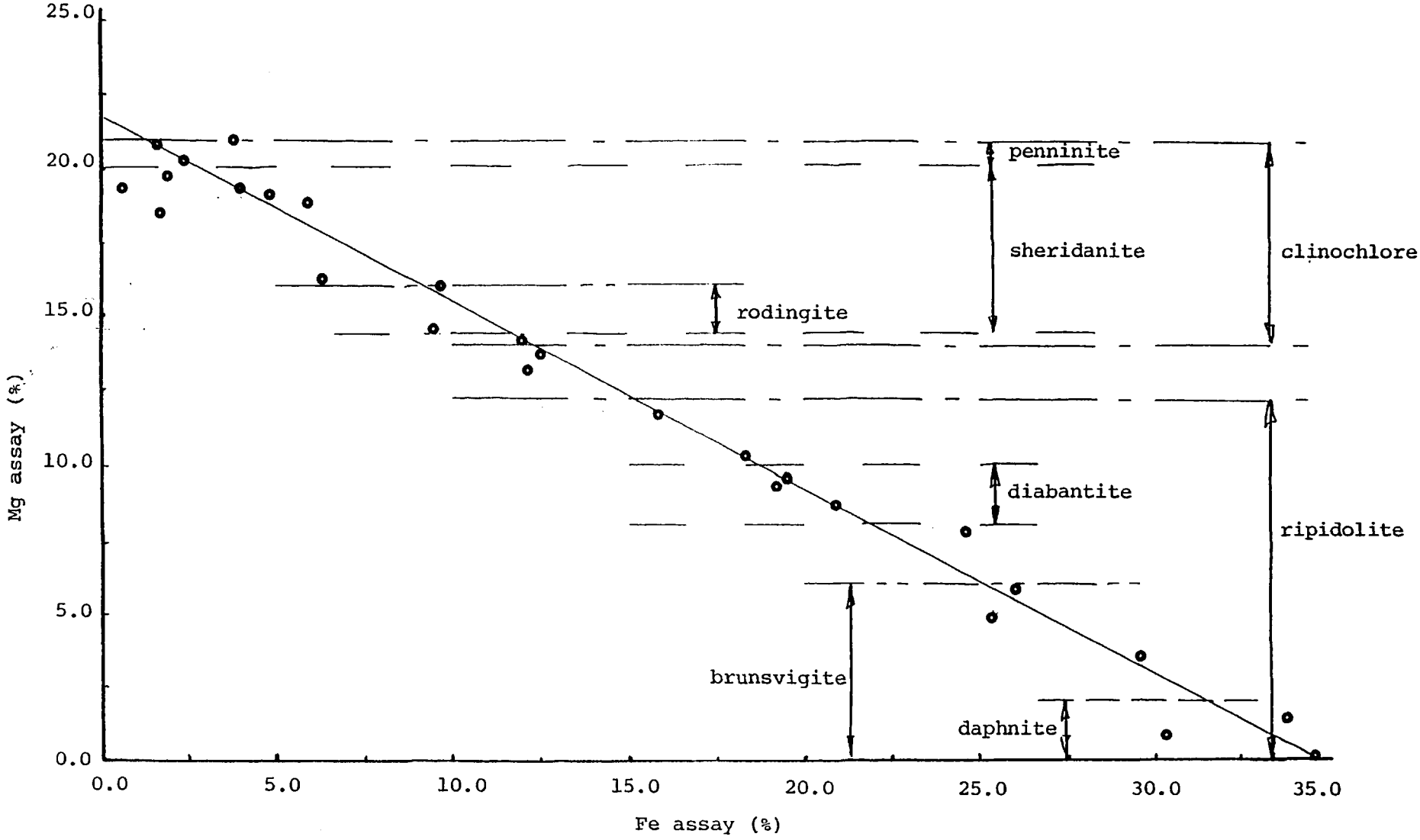


Figure 2.5.5 Boundary limits for magnesium and iron assays for chlorite minerals adopted in program.

member chlorites. The computation subsequently evaluated possible solutions for first one chlorite then the second end-member. (Later, the program included a procedure by which the d spacing was increased in equal steps from the minimum to the maximum set limit.) By applying these inter-relationships the uncertainty of the chlorite mineral assays could be substantially reduced.

Vermiculite : The silicon concentration in various samples of this mineral reported by Deer et al[72] exhibited little variation. The concentration was therefore treated as a meaned value of 16.3% (assumption (b)). No interrelationships were found between the ion species.

Smectite (dioctahedral) : The principal smectite produced in reactions as identified by XRD was of the montmorillonite type. No useful correlation between silicon and aluminium could be discerned, but a plot between the two elemental concentrations, as shown in Figure 2.5.6 demonstrated two areas of data points. In accordance with assumption (b) two meaned values for the silicon and aluminium assays were calculated and are indicated in the figure. The separation between the meaned silicon values is distinct. Although such a clear distinction could not be made for the aluminium the data was treated in a similar manner as it was apparent that the averaged points (indicated in Figure 2.5.6) represented two main types of montmorillonite mineral. Magnesium and iron exhibited apparently random variation in their values (all less than 5%).

The effect of such inter-elemental relationships was made clear by re-writing the EM matrix :

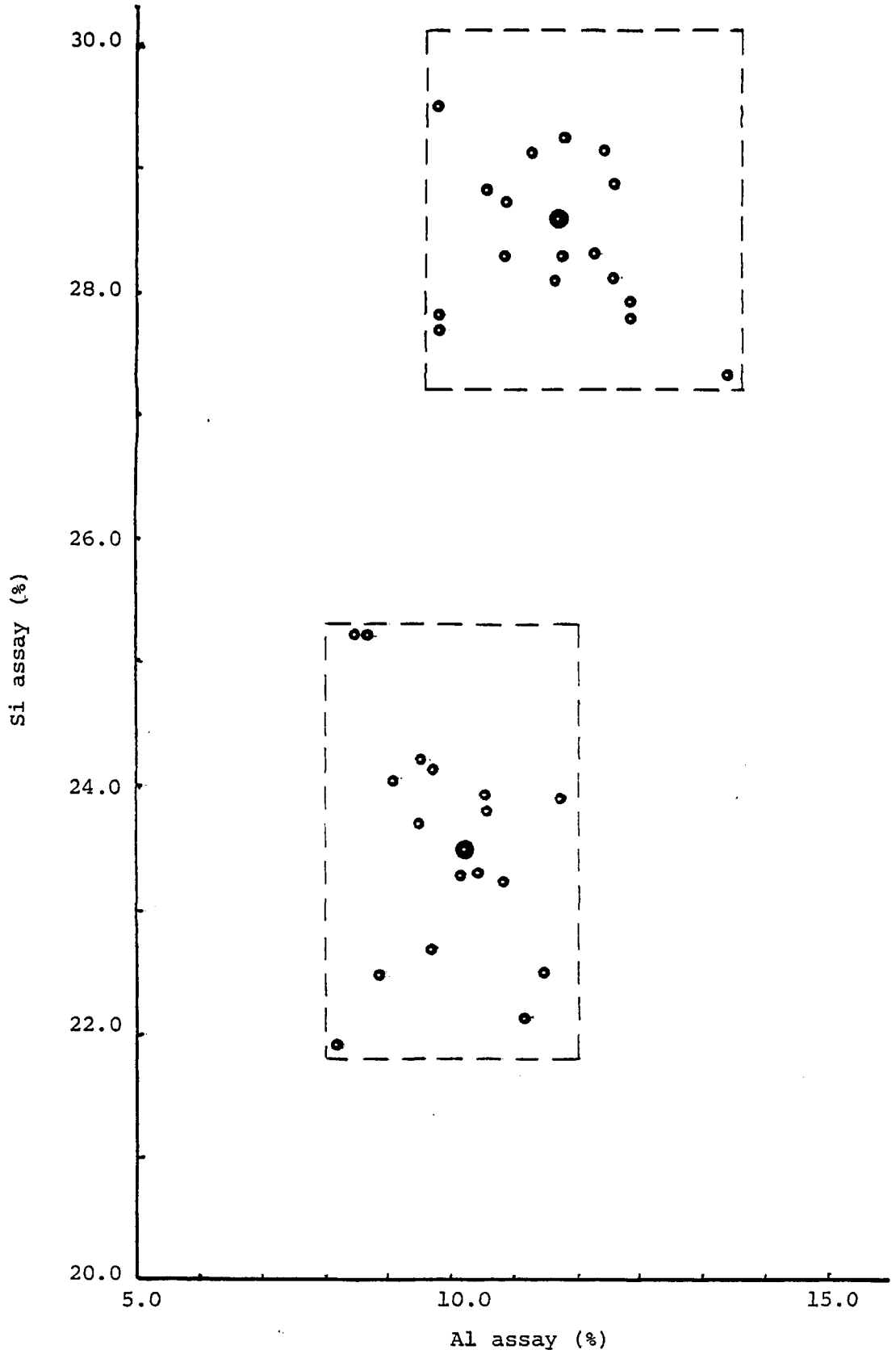


Figure 2.5.6 Distribution of silicon and aluminium assays for montmorillonites. Meaned values represented by ●

	chl	verm	kao	sm
Si	$f(d_{001})$	K	K	H/L
Al	H/L_f	H/L	K	H/L
Fe	H/L_f	H/L	O	H/L
Mg	H/L_f	H/L	O	H/L

where $f(d_{001})$ represents an elemental concentration being a function of the d_{001} spacing; H/L_f, the assay limits being influenced by d_{001} spacing; ⌐↳ limits interrelated or a function with each other.

The number of permutations possible were consequently reduced from 2^{11} (2048) to 2^9 (512) as was the standard deviation of the calculated phase proportions.

2.5.4 Development of the final program : extensions to the original EM form

Procedures described in the previous section did not always give suitable solutions to the simultaneous equations; in particular, when considering systems such as chlorite - vermiculite - kaolinite - smectite difficulties were sometimes encountered. To obtain quantitative phase analyses for these -75 μm products it was necessary to include consideration of an amorphous product i.e. one which could not be readily identified by XRD. Many examples of these products appeared to incorporate aluminium hydroxyoxides as indicated by the high assay of this cation. By replacing one of the crystalline mineral phases by another which characterised these amorphous hydroxides, solutions to the simultaneous equations could always be obtained. In effect, this phase acted as a 'sink' for excess ions not involved in clay formation. Particular examples described in more detail in Chapters 3 and 4, involved products obtained using high aluminium concentrations in the reagent mixture.

Here, a kandite (kaolinite/serpentine) - vermiculite - smectite - aluminium hydroxide system produced solutions to the EM matrix. Chlorite, although present, was now taken to be of minor significance. This system is illustrative of two important features added to the program.

a) The incorporation of an amorphous product the metal content of which is set to vary between known bounds, e.g., for aluminium hydroxyoxide, the aluminium assay varied from 34% (gibbsite : $Al(OH)_3$) to 44% (boehmite AlO(OH)). As the structural formula of the product was unknown, the metal content was incremented in regular steps between the limits set.

b) The introduction of the kandite (kand) group of minerals. These can be visualised as having two end-members - serpentine $Mg_3Si_2O_5(OH)_4$ and the aluminium equivalent, kaolinite $Al_2Si_2O_5(OH)_4$.

The program was such that high-low elemental variations were entered as before with the exception that as either one or the other end-member was considered to be present, at any one time, then either serpentine or kaolinite elemental assays were entered respectively into the EM matrix.

Summarising these features, an example of a modified EM matrix can be described as follows :

	kand	verm	sm	Al-OH
Si	$serp/_{kao}$	K	H/L	O
Al		H/L	H/L	H↔L
Fe		H/L	H/L	O
Mg		H/L	H/L	O

where serp/kao represents the Si,Al,Fe,Mg assays characteristic of serpentine or those of kaolinite entered into the matrix; H↛L indicates high, low or intermediate assay values entered.

The necessary introduction of amorphous systems to the EM matrix proved to be useful as it verified that the products were likely to contain mixed amorphous and crystalline minerals which is in accordance with the broad envelopes noted in several of the XRD patterns obtained (Chapter 3). In the case of other synthetic products the inclusion of one type of amorphous product (e.g. a hydroxyoxide) did not yield solutions, whereas by applying a different one the program computed a satisfactory answer. An example was in the kinetic experiments (Chapter 4) where the aluminium concentration was insufficient for all the liberated ions to be precipitated out as aluminosilicate clays. Careful analysis of the relevant XRD traces indicated peaks occurring in the 9-11 Å region. These apparently metastable clay products could be modelled on the basis of chemical composition and subsequently inserted into the program. The products and procedures for estimating their concentrations are described in Section 4.4.1.

The final form of the program (CECPM) used is shown in Appendix 5. The various mineral system which modelled the phase mixture in the -75 μm products subsequently analysed were indexed by two numbers as follows in Table 2.5.1.

TABLE 2.5.1 MINERAL SYSTEMS IN PROGRAM CECPM

Code		Minerals
1	0	chl-verm-kand-9-11 Å phase
1	1	chl-verm-kand-Al-OH
1	2	chl-verm-kand-9-11 Å phase-Al-OH*
2	0	kao-serp/mg carb-9-11 Å phase-Al-OH
3	0	sm-verm-kand-9-11 Å phase
3	1	sm-verm-kand-Al-OH
3	2	sm-verm-kand-9-11 Å phase-Al-OH*
4	0	chl-verm-kand-sm
4	2	chl-verm-kand-sm-Al-OH*

* In exceptional cases five phase analysis was possible owing to an excess of aluminium in the -75 μm product. In such instances, the concentration of the aluminium hydroxyoxide was estimated and the head aluminium assay reduced accordingly. This readjusted head aluminium assay was used to calculate the phase proportions of the remaining four mineral phases as before.

An example of the output for a set of data is also given in Appendix 5. A series of ten solutions to the simultaneous equations are given together with the meaned phase concentrations, water and elemental assay concentrations and structural formulae (in terms of Si,Al,Fe,Mg number per 22 — 28 oxygen equivalents). The latter were estimated by obtaining correlations between the Si,Al,Fe,Mg assays and the number of the element as appearing in the mineral phase of the form

$$X_y = a + b\%Si + c\%Al + d\%Fe + e\%Mg + f\%Si^2_y + g\%Al^2_y + h\%Fe^2_y + i\%Mg^2_y \qquad (2.5.7)$$

where X_y represents the number of element X (Si,Al,Fe or Mg) appearing in the structural formula for mineral y. For example, the number of silicon ions in the chlorite mineral structure was given by :

$$X_y = Si_{chl} = 1.53 + 0.112\%Si_{chl} + 0.0132\%Al_{chl} - 0.0151\%Fe_{chl} - 0.0148\%Mg_{chl} + 0.0023\%Si^2_{chl} - 0.0021\%Al^2_{chl} + 0.0002\%Fe^2_{chl} - 0.0007\%Mg^2_{chl}$$

The equations for these correlations are given in Appendix 5.

2.5.5 Estimation of the uncertainties in clay mineral proportions obtained

The assessment of precision and accuracy presents a more difficult problem than that encountered with the quantitative XRD analysis of olivine and serpentine presented in Section 2.3.10. The estimation of precision and accuracy of this new computer method is complicated firstly by the inclusion of other methods of analysis (XRD, AAS, TGA) and secondly the absence of a separate alternative established analytical tool which is capable of measuring the proportions of the clay phases involved. It was not possible to assess the uncertainty associated with each computed phase assay solution by testing mixtures of mineral standards as such standards were either unavailable (e.g. chlorite) or were insufficiently pure. Hence, in order to assign an estimate of the error to the computed phase proportions attempts were made to identify the separate sources of error and to discuss their effect on the general reliability of the method. Three main types of error were considered :

a) Phase-identification error

b) Assay error

c) Reference-data selection error

Phase-identification error. This relates to the reliability of the identification of the phases present in the -75 μm product as assessed mainly by XRD. Although the misinterpretation of the XRD data could lead to an inaccurate result, it appeared that the elemental assay and water mass balance prevented real solutions being recorded in such cases. For example, pyrophyllite was originally entered in the system coded 2 0 (Section 2.5.4) (kao-serp/mg carb-9-11 Å phase-Al-OH). Solutions were only obtained when the pyrophyllite was replaced by the 9-11 Å phase. (Furthermore, in most instances, such as the interpretation of kinetic data, there were strictly defined conditions such that the variation of phase concentrations was of greater importance than precise mineral identification.) In conclusion, no value could be attributed to the identification error.

Assay error. The accuracy of the revised method was controlled to a certain extent by the chemical assays recorded for the -75 μm products. Replicate analyses of the kimberlite head, olivine and serpentine showed that the overall error in the assay measurement varied slightly with the element involved and was of the order of 5% relative.[238] To relate the effect of this error to the revised computer method, an investigation was made into the sensitivity of selected program results to variations in the input data. A synthesised product from the testwork was selected, and using the error range associated with the AAS determinations possible high (h) and low (l) values were assigned to each of the measured elemental concentrations. Different permutations

TABLE 2.5.2 CHEMICAL ASSAY ERROR DETERMINATION : EFFECT OF VARIATION OF ASSAY ON COMPUTED PHASE PROPORTIONS

Elemental Assay Variation	Phase Proportion (%) chlorite	vermiculite	kandite	Al-OH
hlhh	17.0	53.3	20.3	9.4
lhll	15.6	49.6	17.6	17.2
lhhh	17.4	49.9	15.6	16.1
hhhl	14.7	53.1	19.7	12.5
hllh	15.5	55.4	19.6	9.5
lhhl	16.6	48.5	17.8	17.1
llll	13.9	53.7	16.4	15.0
hhhh	17.7	49.0	20.4	12.9
meaned values of above	16.1	51.6	18.4	13.9
coefficient of variation (%)	8.3	5.0	9.6	23.8
values using recorded assays	16.3	51.4	18.9	13.3

hllh refers to high (h) and low (l) levels of elemental assays tested in the order silicon, aluminium, iron, magnesium; example represents Si_r + error, Al_r - error, Fe_r - error, Mg_r + error (X_r is recorded elemental assay). Recorded data used : 14.5% Si, 12.6% Al 2.6% Fe, 10.8% Mg, 14.79% H_2O, d spacings for chlorite : 14.3-14.2A.

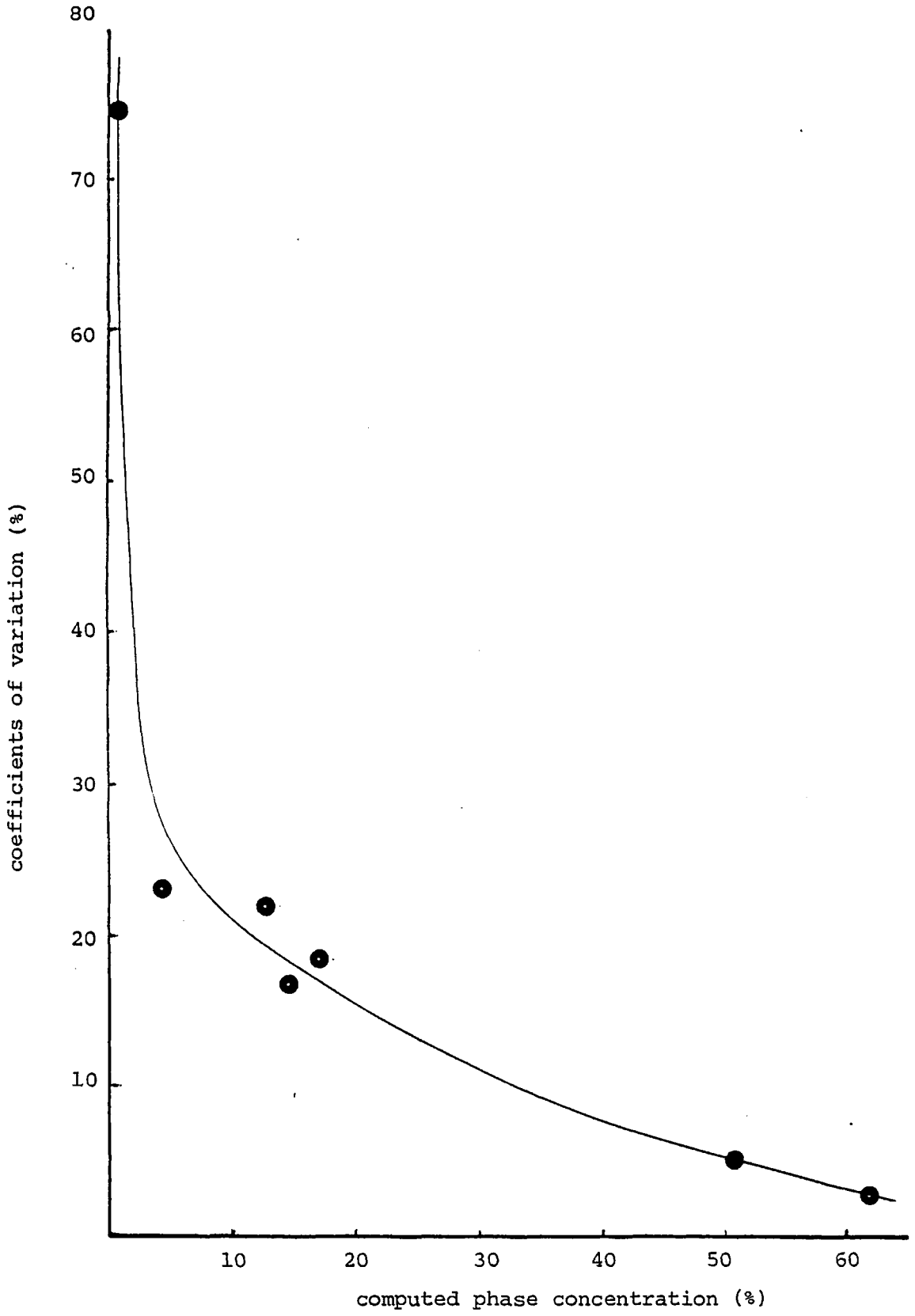


Figure 2.5.7 Relationship between computed phase concentration and associated coefficient of variation as attributable to chemical assay error (e_{cv})

of these figures were tested using the program, the four phase system being chl-verm-kand-Al-OH. The test conditions and results are shown in Table 2.5.2. From the table it can be seen that results of similar magnitude were obtained in each case. Thus chlorite ranged only from 13.9 to 17.7% over the extreme range of the standard deviations. The results indicated that the method was sufficiently stable to considerable variations in the elemental data input. The largest discrepancies occurred in the sink product which, in effect, was the least important of the four. The coefficient of variation decreased markedly as the magnitude of the phase proportions increase, falling from 23% for a mineral assay of 15% to 5% for an assay of 51%. The full relationship, based on the results featured in Table 2.5.2 and other similar investigations, is shown in Figure 2.5.7. This figure is employed in the next sub-section.

Reference-data selection error. The reliability of the method would be affected by the various literature values selected for the elemental assays of the minerals in each system. In certain cases these values had a large range of variation e.g. the iron assay for a chlorite (ripidolite) varied from 15 to 34% (Figure 2.5.5). Ideally the whole range of values between these limits should be taken into account, but this is costly in computing time. In order to assess the effect on precision and accuracy resulting from dealing only with the limits of reported assay values, a system was developed for incorporating 10-15 intermediate values in equal incremental steps for each elemental assay value involved. Thus in the case mentioned the value of the iron assay in chlorite tested could be 15.9, 17.8, 19.7... 34%. The input data used was the four head assays for the -75 μm product as listed in the explanatory note for Table 2.5.2. After all permutations within the system had been exhausted the results were presented as frequency

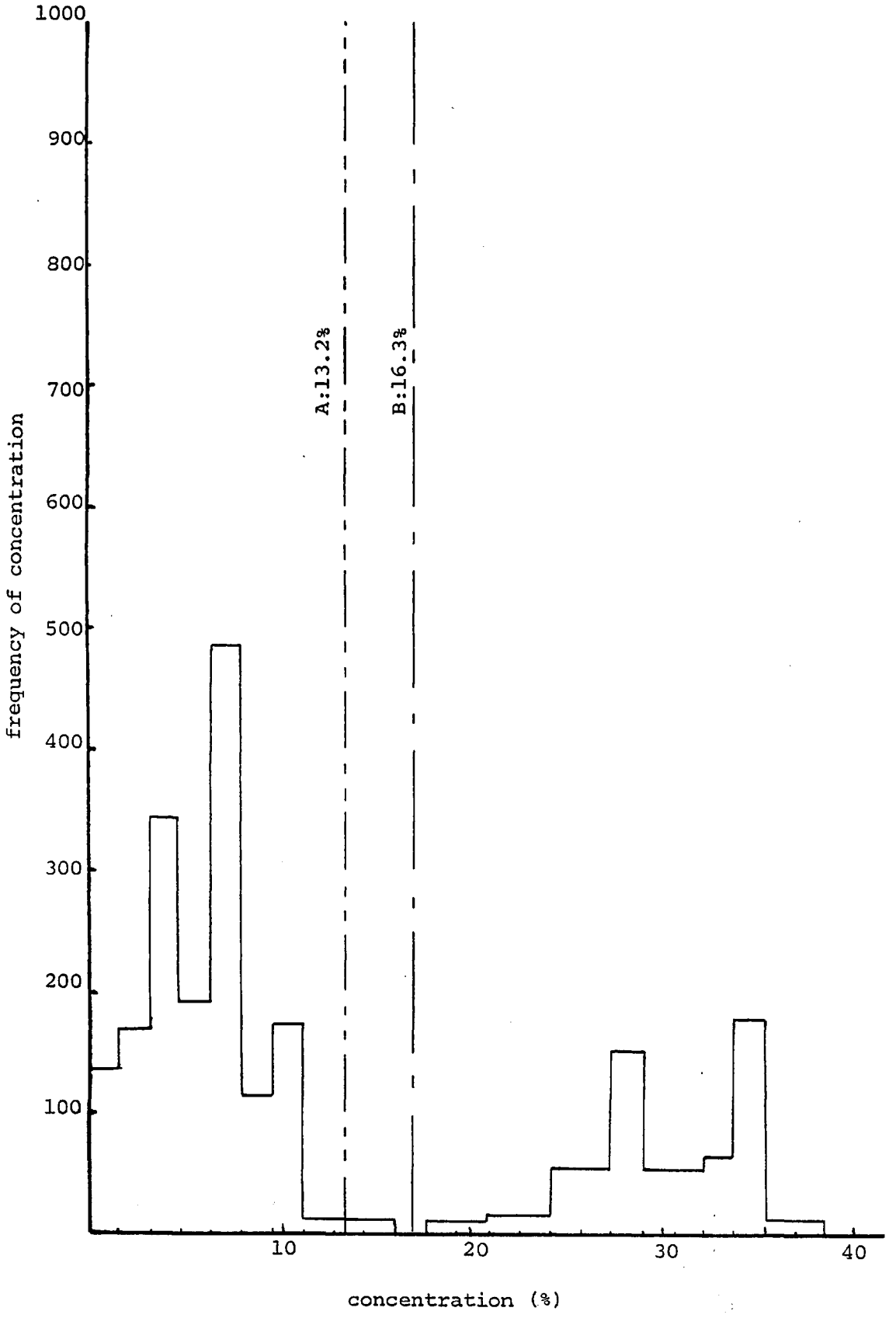


Figure 2.5.8 Frequency distribution chart for computed chlorite concentrations

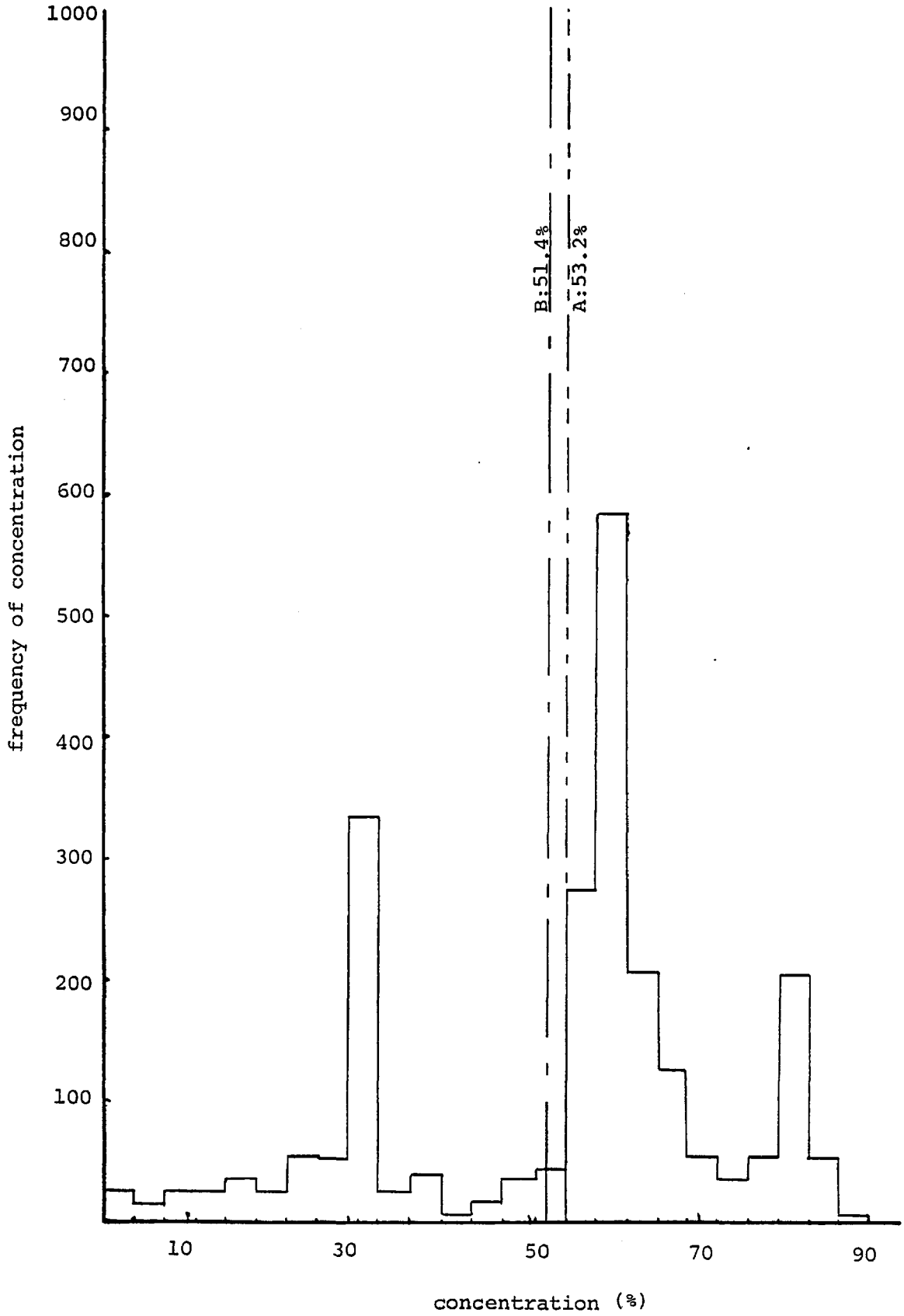


Figure 2.5.9 Frequency distribution chart for computed vermiculite concentrations

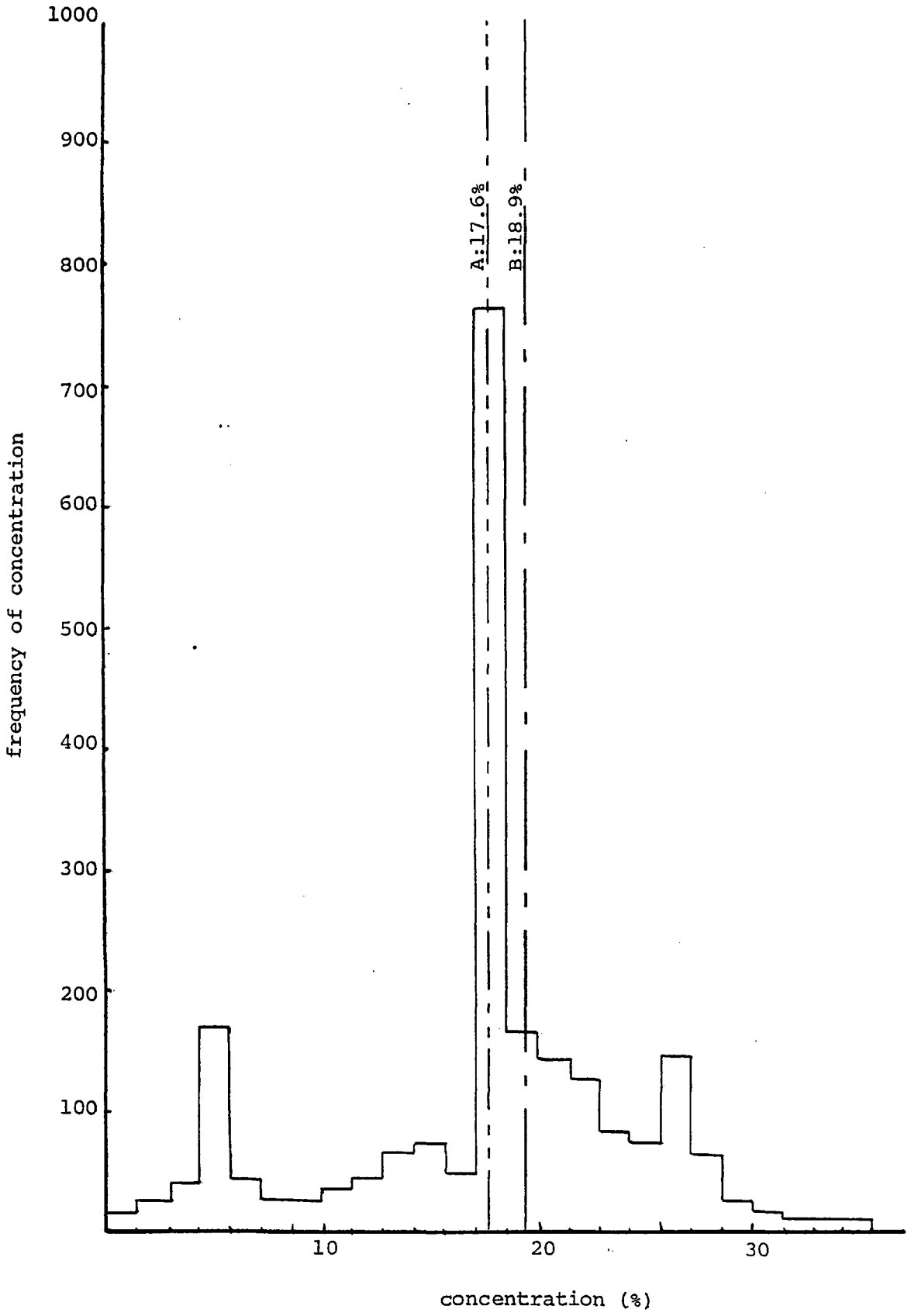


Figure 2.5.10 Frequency distribution chart for computed kandite concentrations

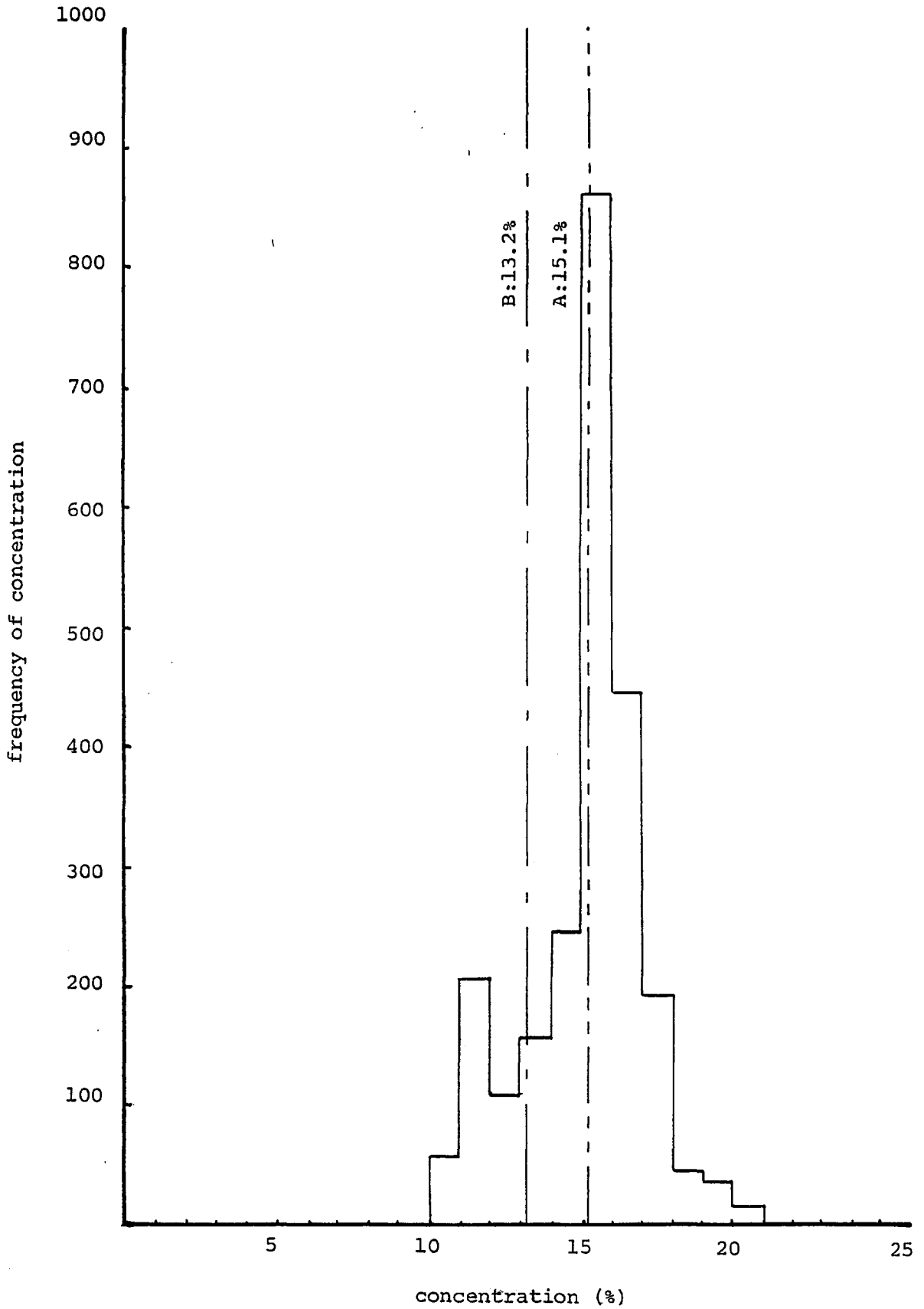


Figure 2.5.11 Frequency distribution chart for computed aluminium hydroxyoxides (gibbsite-boehmite) concentrations

distributions[238] of concentrations for each of the four phases, chlorite, vermiculite, kandite, aluminium hydroxide, as shown in Figures 2.5.8-11 respectively. In each diagram a weighted mean value for the total number of trials tested, i.e., 327678, is indicated by a line labelled A. This is compared with that using the simplified program approach as previously described, labelled B in the figures, which required only 1280 permutations. As can be seen, similar results were obtained. The meaned values approximated to the highest peaks of the distributions which represent the most commonly calculated concentration of the phase in question. The exception to this approximation was chlorite, though this was attributable to the unique manner of classifying the elemental data on the basis of the d spacing information. Summarising, it was apparent that the increase in permutations by 255 times had not produced a significantly different set of results.

To estimate the overall error for a particular phase concentration e_t the standard equation for the additivity of variances[238] was used as follows :

$$e_t^2 = e_{aa}^2 + c_{cv}^2 + c_{rd}^2 \qquad (2.5.8)$$

where e_{aa}, the error associated with AAS determination (i.e.,5.2%); e_{cv}, the error attributable to chemical assay variation as deduced from Figure 2.5.7; and e_{rd} is a reference data selection error deduced by comparing the values marked by A and B in Figures 2.5.8-11. (For vermiculite e_{rd} = 53.2-51.4/53.2 ≡ 3.5%.) By calculating e_t for the highest and lowest phase assays, an overall value for the precision of the method may be obtained.

For vermiculite (concentration = 51%),

$e_t^2 = 5.2\% + 3.2\% + 3.5\%$

$e_t = 7.1\%$ relative

For chlorite (concentration = 13%),

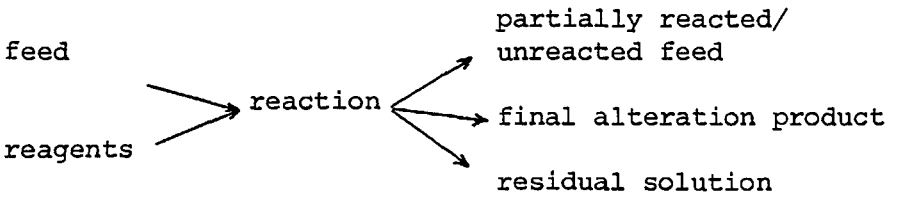
$e_t = 25.4\%$

Only the first of these terms (e_{aa}) can be considered as well established and the overall error e_t is perhaps the best estimate possible in the circumstances.

2.6 Discussion

The previous sections have firstly described how the kimberlite was analysed using well-established techniques. The advantages and limitations of these techniques were recognised (Section 2.2.3) and led to the development of two new methods of analysis (Sections 2.3 and 2.5) to provide the extra data required to elucidate alteration equilibria. Both methods were concerned with the rapid quantitative estimation of complex mineral phases, a field which has yet to be fully explored.

The alteration tests performed can be discussed in terms of the following scheme



(2.6.1)

To maximise and efficiently use the data obtained from these tests the various analytical methods had to be properly integrated.

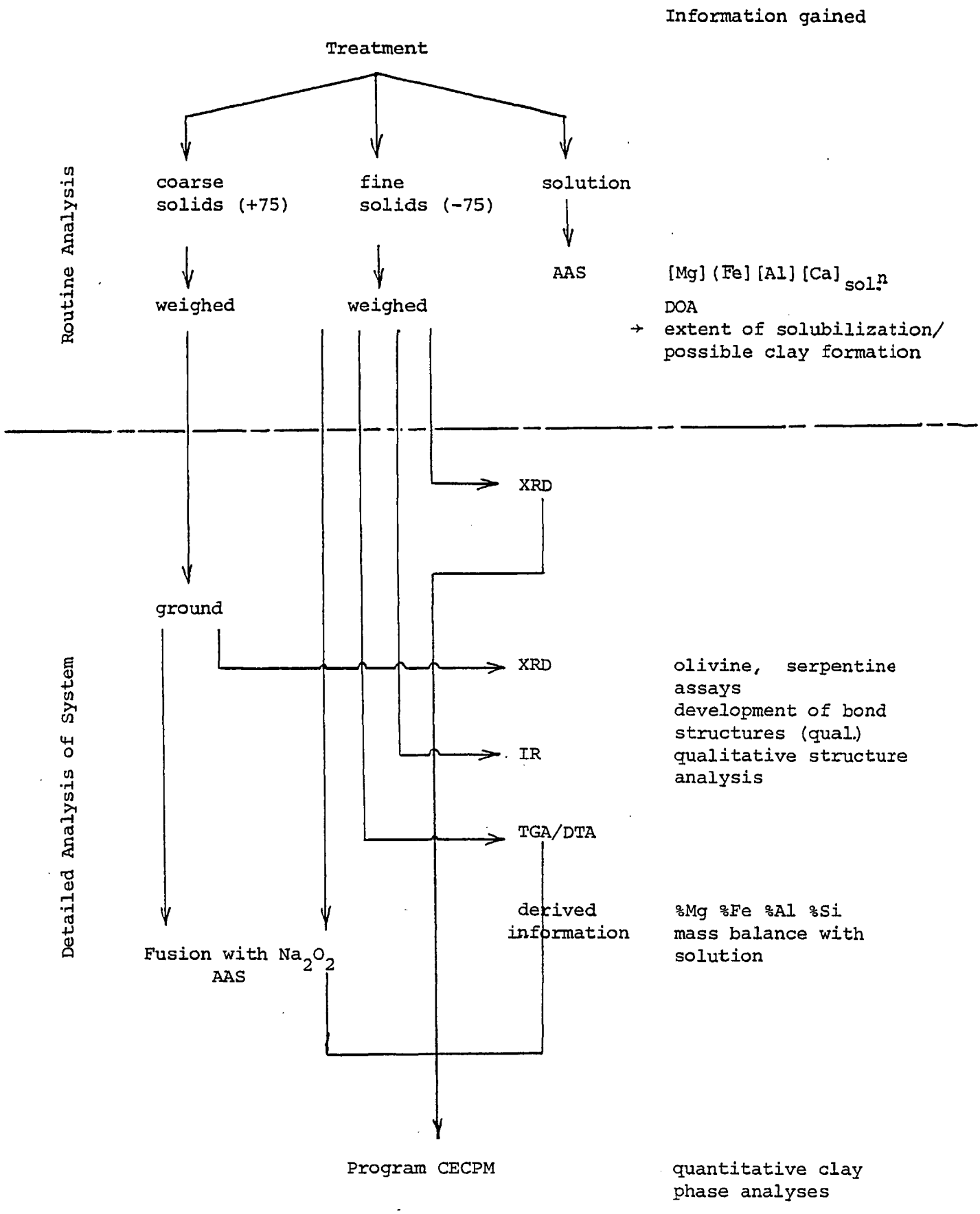


Figure 2.6.1 Scheme of analytical procedures employed in the testwork

The full analysis scheme adopted is shown in Figure 2.6.1. The figure shows a two-tier system. The first tier relates to analyses performed on every test performed, the object being to assess the significance of a particular treatment with regard to a) contributing to the physical breakup of the rock and/or b) stimulating the formation of degradation products. The degree of disintegration of the rock was initially assessed from the mass of residual solid material which was not considered as a final alteration product. The assumption made was that material passing 75 μm was fully altered. The measure of rock disintegration was termed the degree of alteration (DOA) and was defined as :

$$DOA = 100\ (m_f - m_{+75})/m_f \qquad (2.6.2)$$

where m_f is the mass of feed; m_{+75}, the mass of +75 μm residual product.

Although various models describing mineral liberation have been reported[239,240] they do not adequately cover the problems present in this particular case. One model refers to a binary system,[239] whereas the other requires quantification of particulate size distributions[240] which cannot be measured in the present system.

The progressive formation of clay minerals would be accompanied by a proportionate increase in -75 μm products and a simultaneous lowering of the cation concentration in the residual solution. Experimental procedures reported in Section 1.3 have demonstrated the worth of analysing the residual solution and this was practised in this study. Confirmation of the formation of a clay mineral from the solution was afforded by XRD.

The second tier in the analytical scheme involved more detailed analysis of alteration schemes of particular interest. The functions of

each method in Figure 2.6.1 have been discussed and the data contributed by each, when assessed together, were taken to be indicative of the environment and mechanism of alteration.

CHAPTER 3

ALTERATION OF KIMBERLITE : PHASE DIAGRAMS

3.1 Introduction

As mentioned in Chapter 1, Deer et al,[72] Korytkova et al[91] and Nagy and Bates[101] have shown that kimberlite minerals are susceptible to breakdown by acid hydrolysis reactions. It is also evident that the aluminium cation plays an important part in the generation of alteration products of this ultrabasic rock.[100] This chapter deals further with the effect of the H^+ and Al^{3+} ions as well as other readily available ions and reagents : Na^+, K^+, Cs^+, Cu^{2+}, Fe^{2+}, Fe^{3+}, $(COOH)_2$, F^-, Cl^-, $S_2O_4^{2-}$. A study of the nature and extent of the reactions that take place between these ions and the kimberlite, and the phase relationships between reagents and products are described. The aim was to obtain improved information concerning the physicochemical environment of kimberlite alteration.

The work has three main divisions : reactions at 70, 100 and 100-350°C. It should be noted that the research could not be an entirely straightforward physicochemical study because of the complexity of the kimberlite samples and the analytical uncertainties entailed. However, every effort was made, with the aid of analytical techniques specially developed (Chapter 2) to produce phase relationships and thermodynamic data of a semi-quantitative nature which might be compared with theoretically derived equations.

3.2 Reactions with 1-9M Sulphuric Acid at 70°C

3.2.1 Apparatus and procedures

The following conditions were typically employed. Four 10 g -1180+850 µm kimberlite samples were placed separately in four 100 ml flasks fitted with B19 Quickfit stoppers and agitated in a water bath maintained at a constant temperature of 70 ± 3°C. Aliquots of 40 ml of reagent containing various mixtures of Analar sulphuric acid and distilled water were added and the mixtures agitated, using a Griffin and George flask shaker, at a set rate for a specified time, usually 24 hours.

After the reaction, a standardised procedure, common to all the testwork, was employed. The flasks were cooled and where possible (i.e. at acid concentrations less than 1M) the pH was recorded using a Pye Unicam 401E7 electrode and 290 pH meter. The solution was diluted with distilled water to about 100 ml and the contents of the leach flask separately washed through a 75 µm monel wire screen (as supplied by Cadisch and Sons Ltd). The separated +75 and -75 µm fractions were filtered, washed, dried and weighed. The DOA was then calculated (Section 2.6). The filtrate was made up to a known volume, normally 500 ml, after sufficient Analar hydrochloric acid had been added to yield a final concentration of 5% acid. The solution was then analysed by AAS (Section 2.4.3) for the species Mg, Fe and Ca, and, where relevant, Al and Si also. Selected samples were analysed by XRD (Section 2.3.2).

Other reagents were tested in conjunction with the sulphuric acid medium. Species included were Na_2SO_4, K_2SO_4, $CuSO_4$, $FeSO_4$, $Fe_2(SO_4)_3$, $Al_2(SO_4)_3$, NaF, NaCl, and KCl, added in the solid form so that the total reagent volume was readily maintained at 40 ml. Testwork was also carried out under the similar conditions with 10 g samples of -6.18+3.18 mm kimberlite.

3.2.2 Results and discussion

The results for the experiments carried out using sulphuric acid and water alone are shown in Figures 3.2.1 and 3.2.2. Over a period of 24 hours, where equilibration was probably assured, an increased initial acid concentration resulted in greater degradation (as shown by the DOAs) up to a concentration of 9M H^+. Both the DOA plot in Figure 3.2.1 and the residual ion concentrations in Figure 3.2.2 reflect this trend. Initial acid concentrations greater than 9M H^+ caused substantially less degradation, a 12M H^+ solution producing a DOA of 27% as compared with the maximum of 54% at 9M H^+, for example. Although Figure 3.2.1 shows that half of the feed could be reduced to a fine-sized product, Figure 3.2.2 demonstrates that the extent of alteration was greater than that inferred by the DOA. Thus, in the optimum acid regime (9M H^+), more than 90% of the total magnesium and iron in the feed were leached. The same was probably true of calcium, this ion being reprecipitated as part of the white residue forming the -75 μm product. Quantitative XRD measurements substantiated these observations, no trace of olivine or serpentine being found in the diffractograms. They could only be detected (with difficulty) where acid concentrations greater than 10M H^+ had been employed. The XRD trace of the +75 μm product resulting from reaction with 4.5M sulphuric acid illustrated in Figure 3.2.3a, demonstrated that the kimberlite had been reduced to a silica framework devoid of the majority of its cationic constituents. As can be seen, peaks attributable to free silica were obtained whereas this mineral type is not present in the original rock. Calcium had been precipitated as the hydrated and anhydrous sulphates, gypsum and anhydrite, probably in the leached interstices. All the original minerals appeared to have been destroyed (cf. Figure 2.3.2a). The -75 μm product (Figure 3.2.3b) was apparently

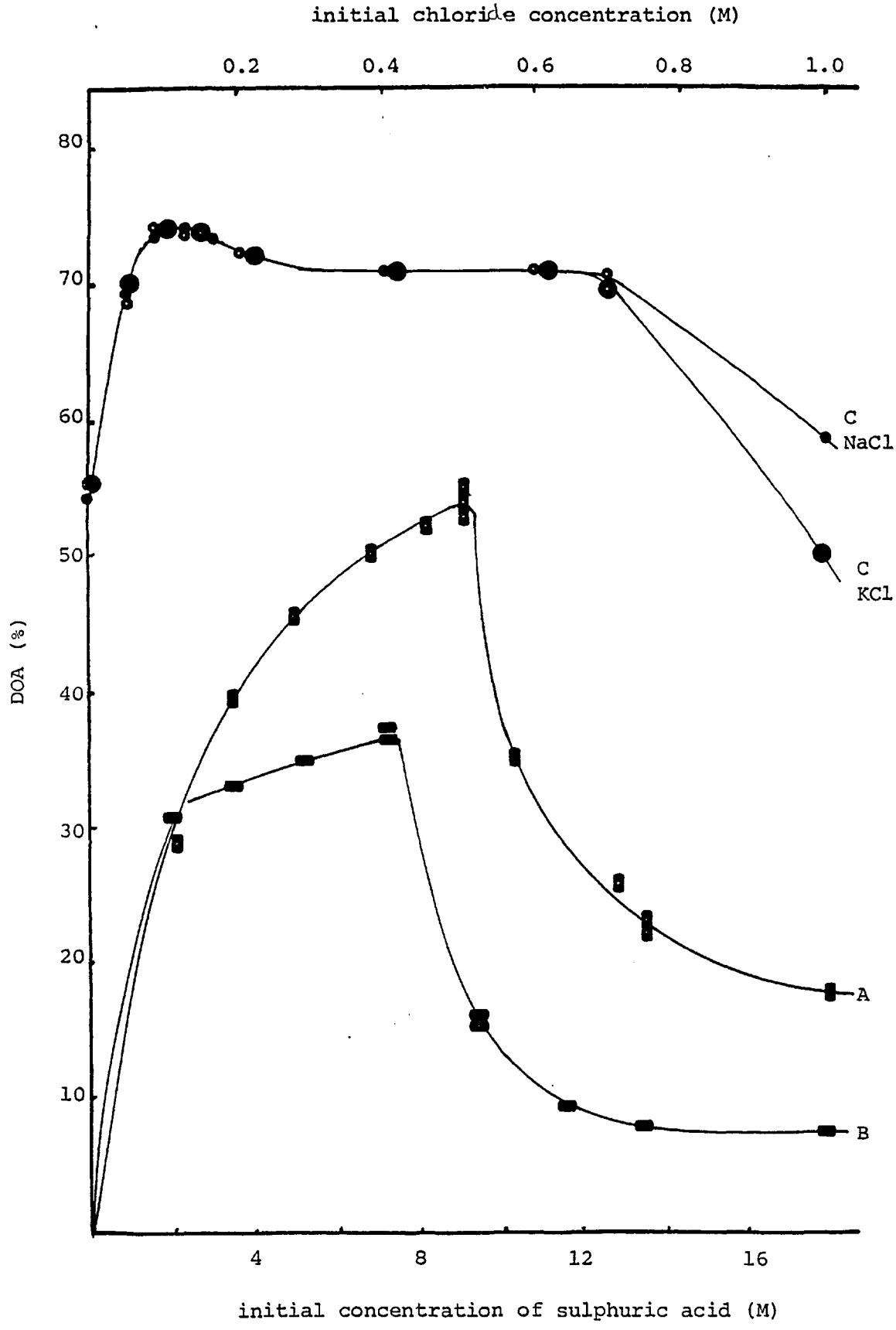


Figure 3.2.1 Relation between DOA and initial concentration of sulphuric acid for a feed agitated at 70°C for 24 h, the feed sizes being -1180+850 µm (A), -6.18+3.18 mm (B). The effect of various chloride concentrations, for a system involving a 10g -1180 +850 µm feed in a 9M sulphuric acid solution is shown above (C).

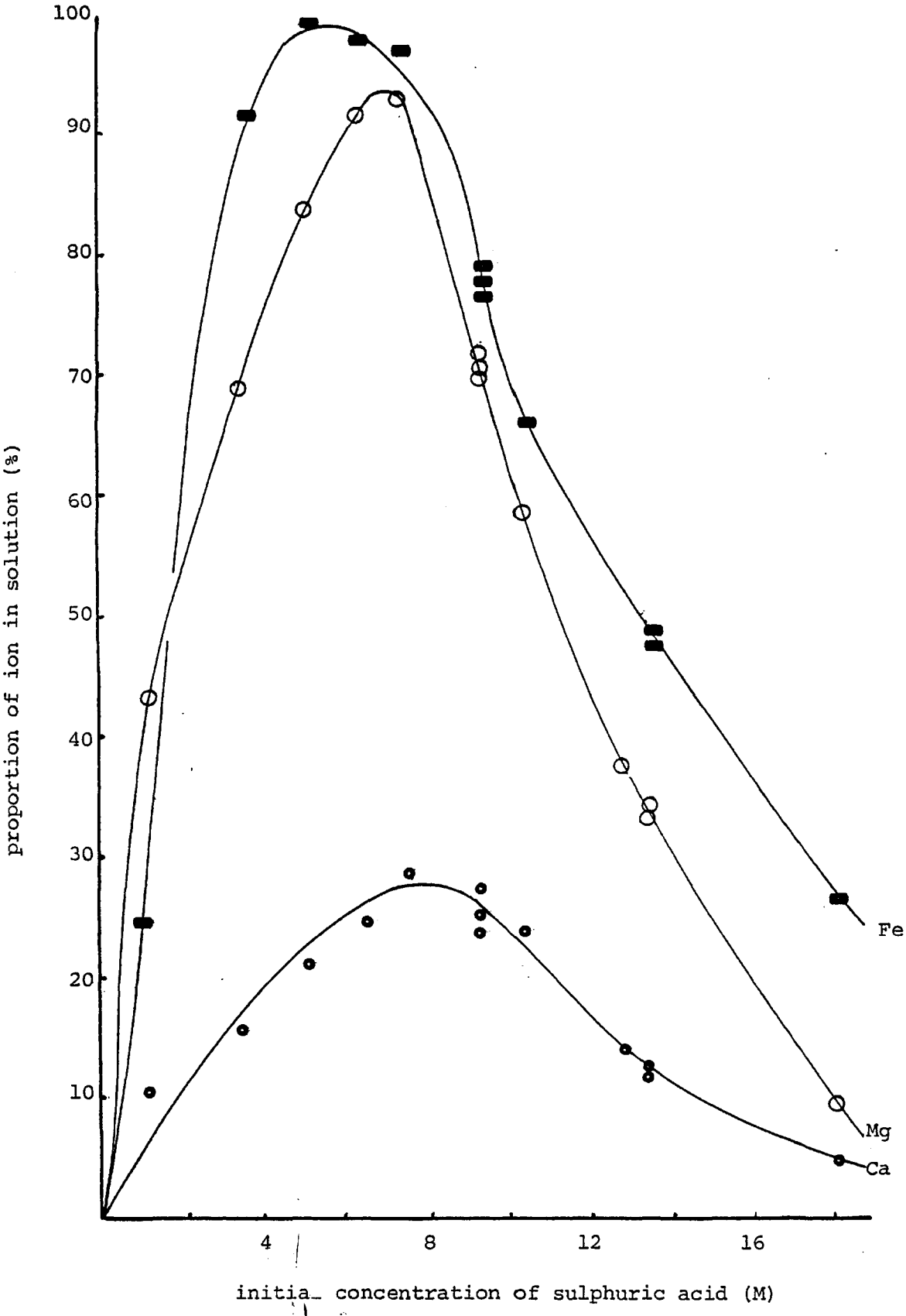


Figure 3.2.2 Relationship between the proportion of total magnesium, iron and calcium reporting to the residual solution and the initial sulphuric acid concentration for 10g -1180 +850 µm feed agitated at 70°C for 24 h.

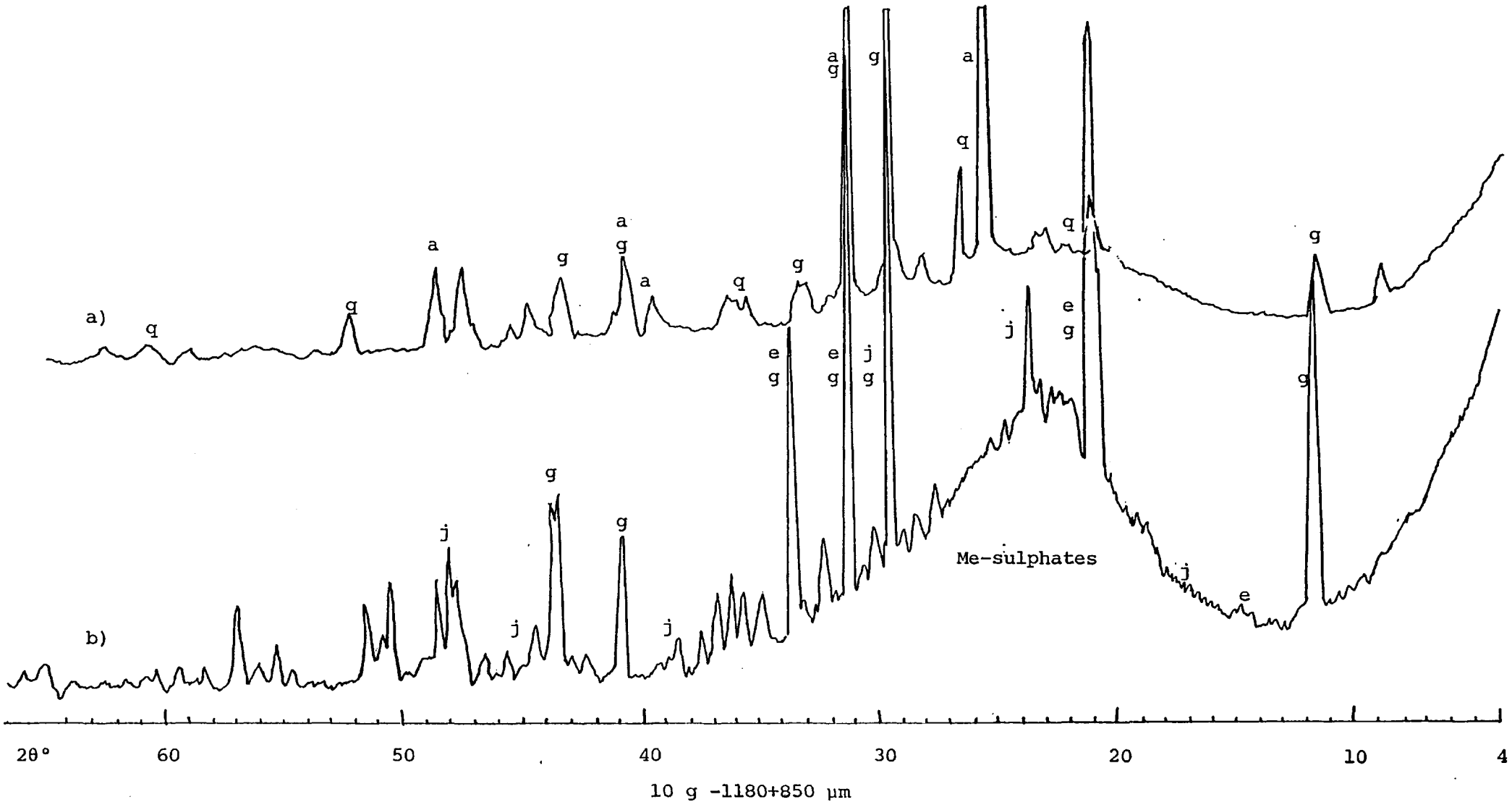


Figure 3.2.3 X-ray diffractograms for samples reacted with 4.5M sulphuric acid 70°C, 24h

a) +75 µm fraction
b) -75 µm fraction

a : anhydrite
e : epsomite
g : gypsum
j : jarosite
q : quartz

less crystalline in nature (reflected by the broad envelope at 2.63-4.92 Å). The only well crystallized compound was gypsum, though epsomite and jadeite were also detectable.

Reacting 10 g feed samples with 4.5M sulphuric acid for reaction times varying from 3 to 24 h resulted in the DOA and residual ion concentrations shown in Figure 3.2.4. As expected both criteria increased with reaction time. The general tendency for the curves to flatten parallel to the time axis showed the approach to equilibrium at approximately 24 h. These results were used to justify a similar reaction time in the experiments involving additional reagents.

Of the reagents tested with 4.5M sulphuric acid - listed in Table 3.2.1 - the only species found to have a positive effect was the chloride ion.

TABLE 3.2.1 ADDITIVES TESTED IN CONJUNCTION WITH 4.5M SULPHURIC ACID, 70°C, 24 h

Ionic species	Concentration range tested (M)
Na^{+}	0 - 1
K^{+}	0 - 1
Cu^{2+}	0 - 0.05
Fe^{2+}	0 - 0.35
Fe^{3+}	0 - 0.4
Al^{3+}	0 - 0.5
F^{-}	0 - 0.08
Cl^{-}	0 - 1

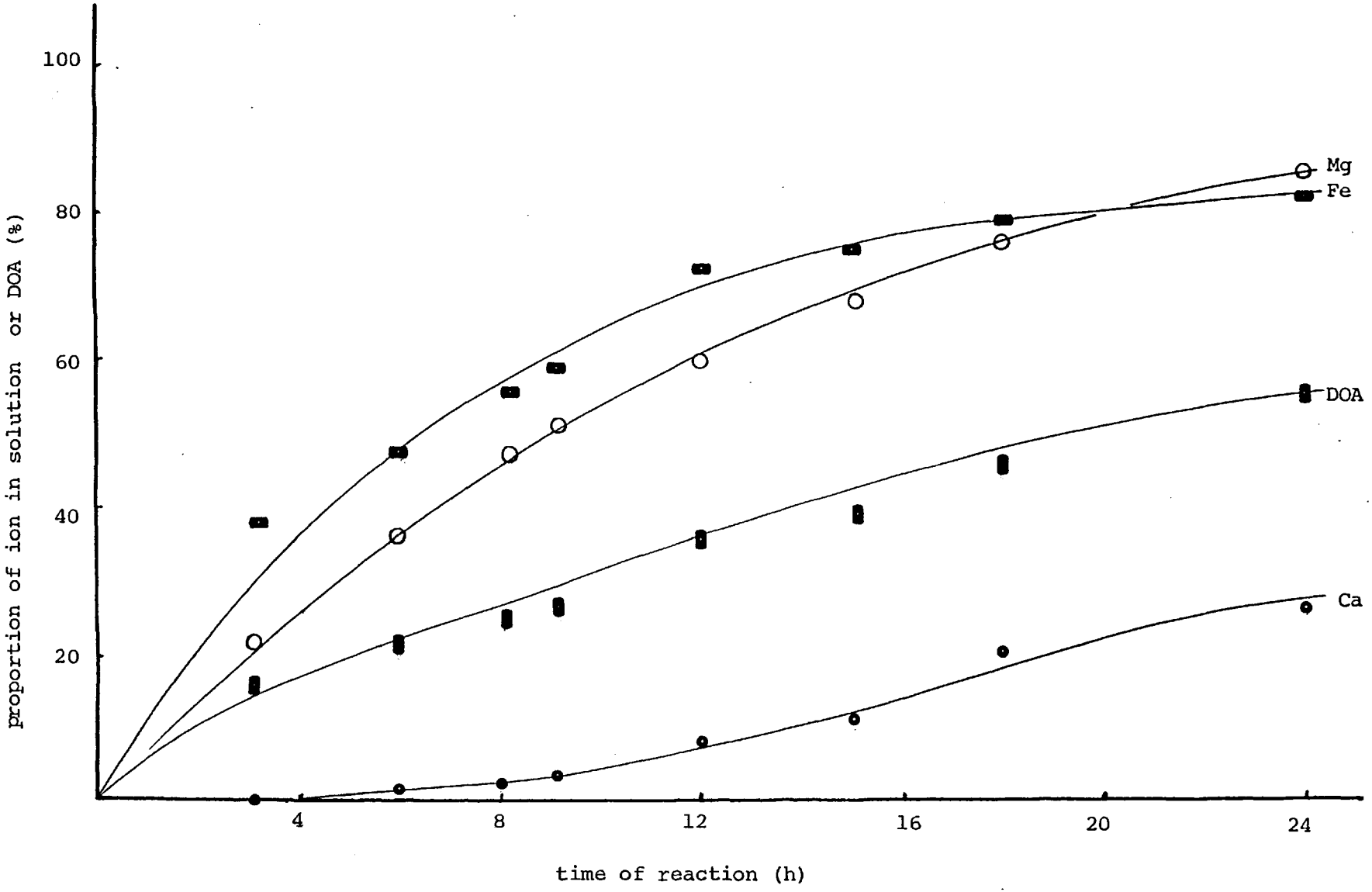


Figure 3.2.4 Relationship between DOA and the proportion of magnesium, iron and calcium reporting to the residual solution, and the time of reaction for 10g -1180 +850 µm kimberlite agitated with 40 ml 9M sulphuric acid at 70°C.

The effect of the chloride ion is shown in Figure 3.2.1 in which the previous DOA of 54% was increased to 74% where an initial concentration greater than or equal to 0.08M NaCl was employed. This result was verified to 99% confidence using standard factorial testing procedures.[238] Again, virtually all the magnesium, iron and calcium was extracted. Higher chloride concentrations were less effective (i.e.>0.7M). The effect of the chloride ion on DOA relates to the solubility of silica. The greater the solubilization of the residual silica in the +75 μm fraction, the larger the DOA. Marshall[241] states that the equilibrium between solid silica and silicilic acid can be written :

$$SiO_2.x\ H_2O_{(s)} + n\ H_2O \leftrightarrow H_4SiO_4 \qquad (3.2.1)$$

where n usually lies between 0 and 2 for amorphous silica and is proportional to the extent of hydration.

The equilibrium constant K_s can be written :

$$K_s = a_{H_4SiO_4} / (a_{solid}\ a^n_{H_2O}) \qquad (3.2.2)$$

where $a_{H_4SiO_4}$ is the activity of silicilic acid, similarly for the solid and water. By using $a = s.\gamma$ where s is the solubility, γ the activity coefficient, it can be found that

$$s_{H_4SiO_4} = K_s\ a^n_{H_2O} / \gamma_{H_4SiO_4} \qquad (3.2.3)$$

At 25°C it has been recorded that chloride ion concentrations of the order of 0.08 - 0.2M would substantially reduce the activity coefficient of silicilic acid.[242] With increasing hydration (n) the solubility would approach a maximum value. Increasing the chloride concentration above a specified value, results in a lowering of the solubility,[241]

partially due to an increase in the activity coefficient.[241] Marshall demonstrated that similar trends in solubility could be observed at elevated temperatures (up to 300°C). Hence it was likely that silica solubility was maximised for the chloride concentrations used.

Applying the optimum conditions deduced for the -1180+850 µm feed, namely 4.5M sulphuric acid, to the larger sized kimberlite particles tested produced a lower DOA than expected - 15%. The effect of treating this -6.18+3.18 mm feed with various concentrations of sulphuric acid at 70°C, 24 h, is shown in Figure 3.2.1 and 3.2.5. Referring to Figure 3.2.1, the DOAs were not only lower, but the maximum DOA (36% as compared to 54% for the smaller feed) also occurred at a lower acid concentration (7M H^+ cf. 9M H^+). Furthermore, the range of DOAs recorded for acid concentrations 2-7M H^+ differed for the two feed sizes tested. A range of 31-49% was noted for the smaller feed, whereas the DOA only increased from 31 to 36% where the -6.18+3.18 mm feed was employed. The significance of these findings is discussed below. Referring to Figure 3.2.5, which shows plots of the residual concentrations, complete leaching of magnesium and iron was attained using acid concentrations of about 6M H^+. The plots obtained mirrored that of the DOA (Figure 3.2.1).

Using the peroxide fusion/AAS method (Section 3.4.3) an elemental mass balance was carried out on the products of the reaction using 4.5M sulphuric acid in conjunction with -1180+850 µm feed. The elemental distributions are shown in Table 3.2.2.

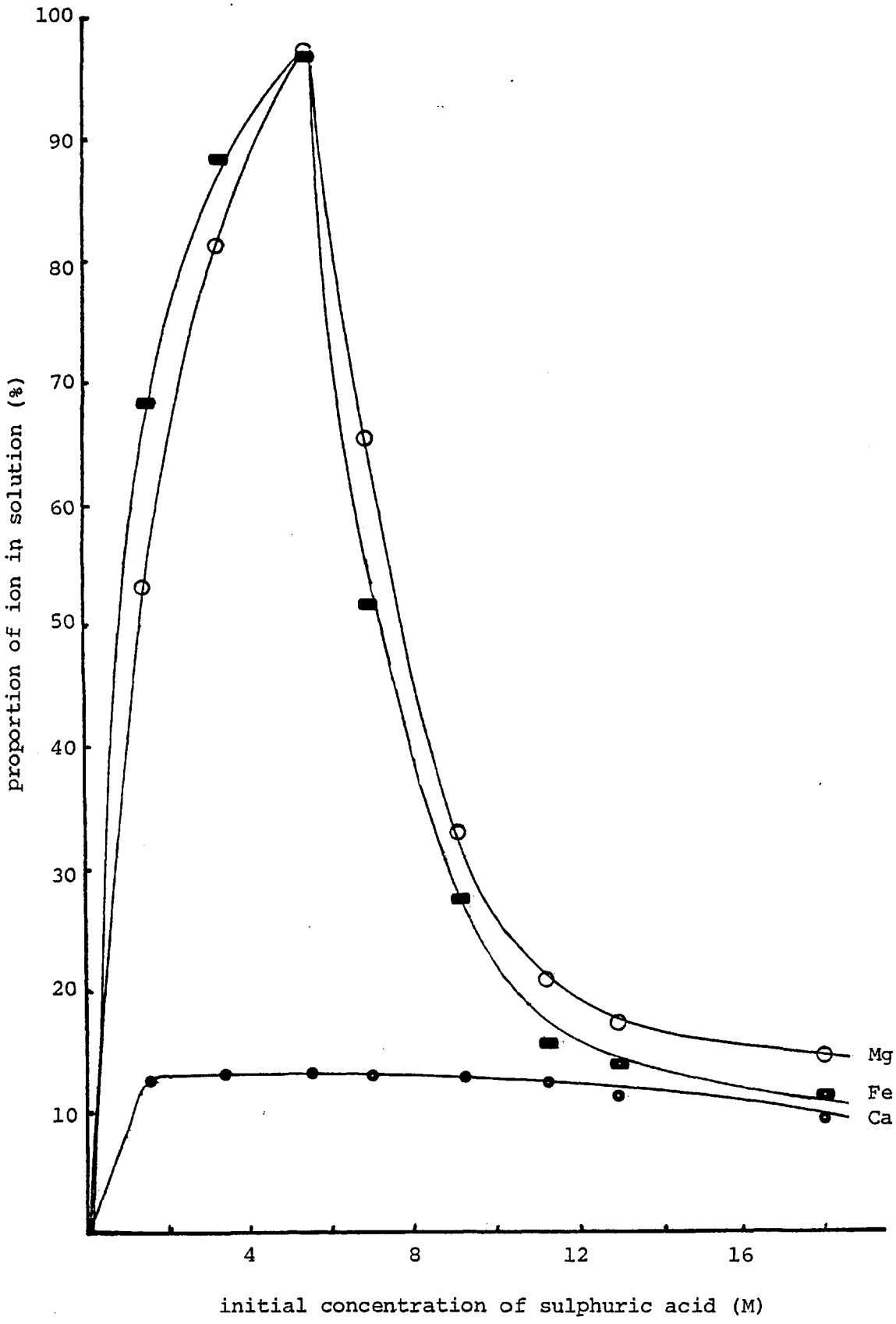


Figure 3.2.5 Relationship between the proportion of total magnesium ion and calcium reporting to the residual solution and the initial sulphuric acid concentration for a 10g -6.18+3.18mm feed agitated at 70°C for 24 h.

TABLE 3.2.2 PERCENTAGE ELEMENTAL DISTRIBUTIONS FOR THE REACTION WITH 4.5M SULPHURIC ACID

	Element			
Phase	Mg	Si	Fe	Ca
+75 μm	20	87	22	70
-75 μm	1	3	2	8
solution	79	10	76	22

The results, which are consistent with those featured in Figure 3.2.2, show that 79% of the total magnesium and 76% of the iron were leached by the H^+ ion from olivine, serpentine, and mica and entered the solution. Calcium was also leached but reacted with the SO_4^{2-} ion to produce anhydrite. Hydration subsequently led to the formation of gypsum, which was deposited in both solid phases (only 22% calcium reporting to solution). A majority reacted in situ, remaining in the residual +75 μm phase filling gaps in the skeletal silica structure. Further evidence for the leaching of mineral grains and the deposition of sulphate precipitation products in the cavities so formed was provided by scanning electron photomicrography (Plates 3.3 and 3.5). It would appear that the sulphuric acid extracted cations from the kimberlite mineral lattices by ion exchange with the H^+ ion. These cations were precipitated as the sulphates, where conditions were favourable. These reactions would preferentially take place along grain boundaries which would lead to the possibility of kimberlite particles being displaced from the feed (as observed in the -75 μm products).

Detailed equilibria consistent with the above description are

given below :

$$Ca_{.28}Mg_{1.8}Fe_{0.39}Al_{0.34}Si_2O_5(OH)_4 + 6H^+ \leftrightarrow$$

serpentine

$$0.28\ Ca^{2+} + 1.80\ Mg^{2+} + 0.39\ Fe^{2+} + 0.34\ Al^{3+} + 2SiO_2 + 5H_2O \qquad (3.2.4)$$

$$Ca_{.07}Mg_{1.62}Fe_{.21}Ni_{.10}Al_{.01}SiO_4 + 4H^+ \leftrightarrow$$

olivine

$$0.07\ Ca^{2+} + 1.62\ Mg^{2+} + 0.21\ Fe^{2+} + 0.10\ Ni^{2+} + 0.01\ Al^{3+} + SiO_2 + 2H_2O \qquad (3.2.5)$$

$$Ca\ CO_3 + 2H^+ \leftrightarrow Ca^{2+} + CO_2 + H_2O \qquad (3.2.6)$$

calcite

$$Ca^{2+} + SO_4^{2-} \leftrightarrow Ca\ SO_4 \qquad (3.2.7)$$

anhydrite

$$Ca\ SO_4 + 2H_2O \leftrightarrow Ca\ SO_4.2H_2O \qquad (3.2.8)$$

gypsum

$$Mg^{2+} + SO_4^{2-} + 7H_2O \leftrightarrow Mg\ SO_4.7H_2O \qquad (3.2.9)$$

epsomite

$$SiO_2 + 2H_2O \leftrightarrow Si(OH)_4(aq) \qquad (3.2.10)$$

The differences between the DOA trends in Figure 3.2.1 which, in turn, conflict with the ion concentrations in solution reflect the occurrence of the diffusion-controlled leaching reactions (equations 3.2.4 - 3.2.6 and 3.2.10). The effectiveness of these leaching reactions

was modified by the amount of acid available and the amount of water which would solvate the ions and remove them from the site of reaction. Consequently the reaction rate would be affected by the cavity volume through which the inward diffusing reagents and outward diffusing products would pass. The DOA and the optimum acid concentration would be, as a consequence, lower for a larger sized feed for the reactions at 70°C.

The importance of these reactions is discussed further in Chapter 5.

3.3 Reactions with 0.0001 - 1.5M Mineral Acids at 70 and 100°C

From Section 3.2 it was evident that kimberlites could be broken down rapidly and essentially completely using high concentrations of sulphuric acid at 70°C. Such conditions do not occur in natural systems in which kimberlite alteration is known to take place. This section considers the modelling of these alteration reactions, as it was thought the formation of layer lattice minerals would result in degradation of the kimberlite without the need for such large quantities of acid.

3.3.1 Apparatus and procedures

In the first set of about 30 experiments, 10 g samples of -1180+850 μm kimberlite were reacted with 40 ml aliquots of distilled water previously adjusted to a pH in the range 0.3-4.0 using hydrochloric, nitric, or sulphuric acids. The mixtures were allowed to react for 7 h at 70 or 100°C. The shaking flask equipment described in Section 3.2.1 was employed for the tests at the lower temperature. For reactions conducted at 100°C, the following conditions were typically employed : the feed and reagents were placed in a 250 ml conical flask, fitted with a Quickfit condenser and a side-arm, which provided for the sampling of the reaction solution and/or the admission of test gases (see later).

The flask was mounted on a Gallenkamp SWT-550-010 magnetic stirrer/ hotplate. After the reaction, the standardised solid-separation/AAS procedure described in Section 3.2.1 was employed. The stirring speed was adjusted so that the solution was gently swirled over the kimberlite particles to resemble the agitative action of the shaking flasks. To ensure that the results obtained were comparable with those obtained using the shaking flask apparatus, a 10 g sample was reacted with 40 ml sulphuric acid for 7 h at 70°C in the other equipment. The DOA obtained agreed with that indicated in Figure 3.2.4. Throughout the testwork involving this equipment, care was taken to maintain a constant stirring rate. (This was checked by recording and comparing the DOAs of samples reacted using a set of reagents, the effect of which had been previously established.)

A second set of experiments involved the use of various additives in conjunction with the hydrochloric acid medium. The aluminium ion was tested first; 4 g of hydrated aluminium chloride was dissolved in 40 ml of distilled water, the solution was adjusted to a pH of 0.5 with concentrated hydrochloric acid, added to a 10 g sample of kimberlite and the mixture reacted for 7 h at 100°C using the hotplate/stirrer apparatus. Similarly, 1-8 g of hydrated aluminium chloride and 2-12 g of hydrated aluminium nitrate were in turn reacted with the kimberlite.

The effect of other reagents at 100°C was investigated. The following species NaCl, KCl, CsCl, NaF, $Na_2S_2O_4$, $(COOH)_2$, $O_2(g)$, $CO_2(g)$ were added to a 40 ml solution containing 4 g hydrated aluminium chloride which was then adjusted to pH 0.5 using hydrochloric acid. Where gases were concerned, these were either added as water saturated with the gas or passed through the reacting mixture via a pipe equipped with a sintered disc.

A third set of experiments was concerned with the construction

of phase diagrams relating aluminium and hydrogen ion concentrations to the solid alteration products. Adopting the same experimental and standard analytical procedures as before, 1-8 g of hydrated aluminium chloride was reacted with 10 g samples of the -1180+850 μm kimberlite at 100°C for 7 h, the initial pH being 0.5. In some cases the reaction was buffered after 3.5 h by the addition of concentrated ammonia solution. Sampling of the reaction solution confirmed that the pH at 7 h was the same as that obtained on addition of the alkali.

This procedure was repeated for solutions containing a higher initial hydrochloric acid concentration (1.5M). This concentration was selected in accordance with concurrent designs which were being made for a bench scale apparatus which would provide for the semi-continuous alteration of kimberlite (Chapter 5). Such designs required the use of screening techniques at the site of the reaction, Monel alloy which proved to be the most resistant of the metal screen materials available having a maximum acid concentration tolerance of 1.5M H^+. This acid concentration was subsequently adopted in the testwork described here.

The fourth series of tests concerned an investigation of the effect of 40 ml solutions containing 0-4 g hydrated aluminium chloride and acid concentrations varying from 0.3-1.5M, at 100°C for 7 h. The experimental and analytical procedures were as before.

3.3.2 Results of reactions in the presence/absence of the Al^{3+} ion

Figure 3.3.1 shows the DOA obtained for the reaction between kimberlite and varying concentrations of sulphuric and hydrochloric acid at 70 and 100°C. The figure demonstrates that the DOA increased with a rise in temperature where a sulphuric acid medium was applied.

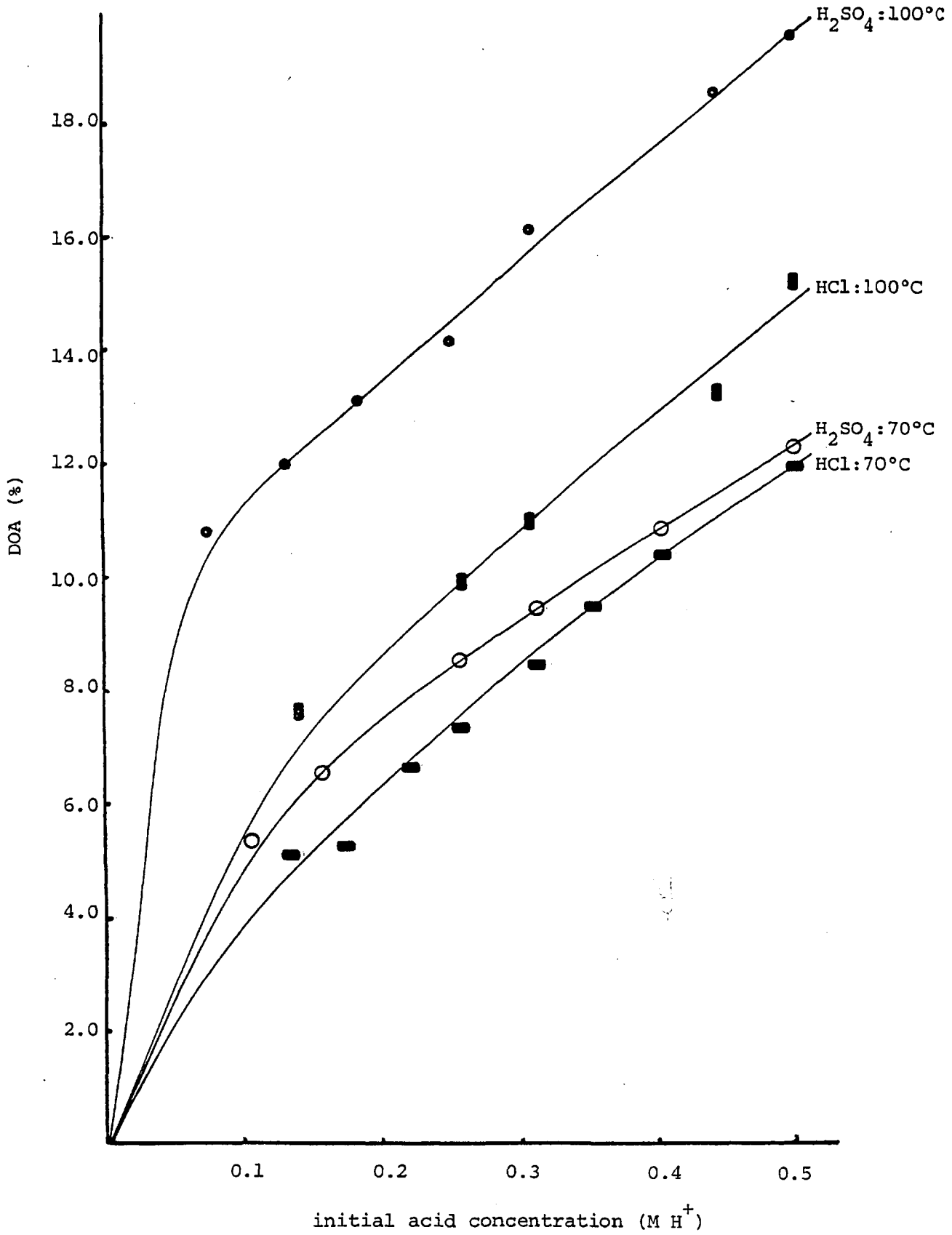


Figure 3.3.1 Relation between the DOA and the initial hydrochloric/sulphuric acid concentration for a 10g -1180+850 µm feed agitated/stirred at 70/100°C for 7 h.

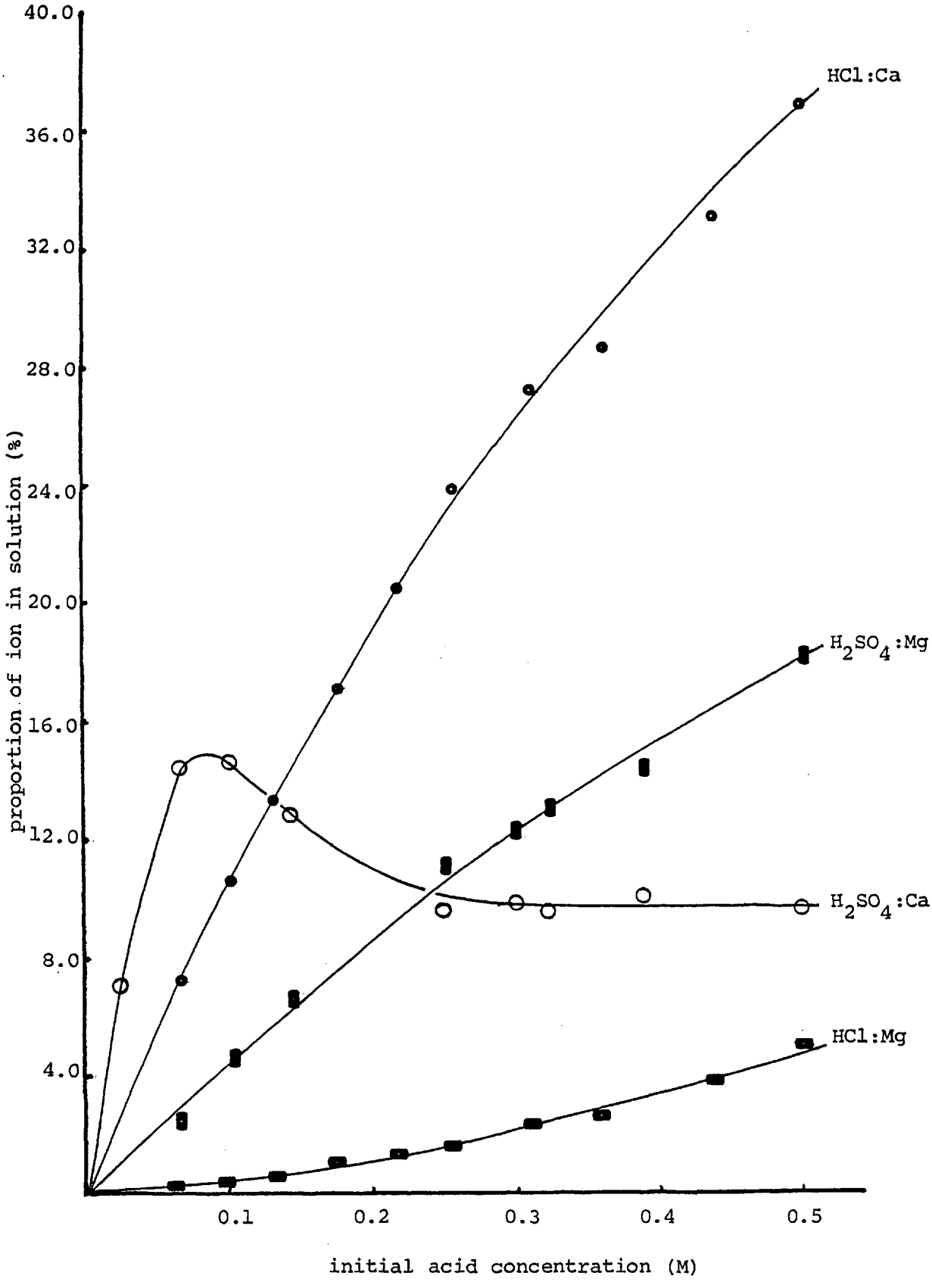


Figure 3.3.2 Relation between the proportion of total magnesium and calcium reporting to the residual solution and the initial hydrochloric/sulphuric acid concentration for a 10g -1180+850 µm feed agitated at 70°C for 7 h.

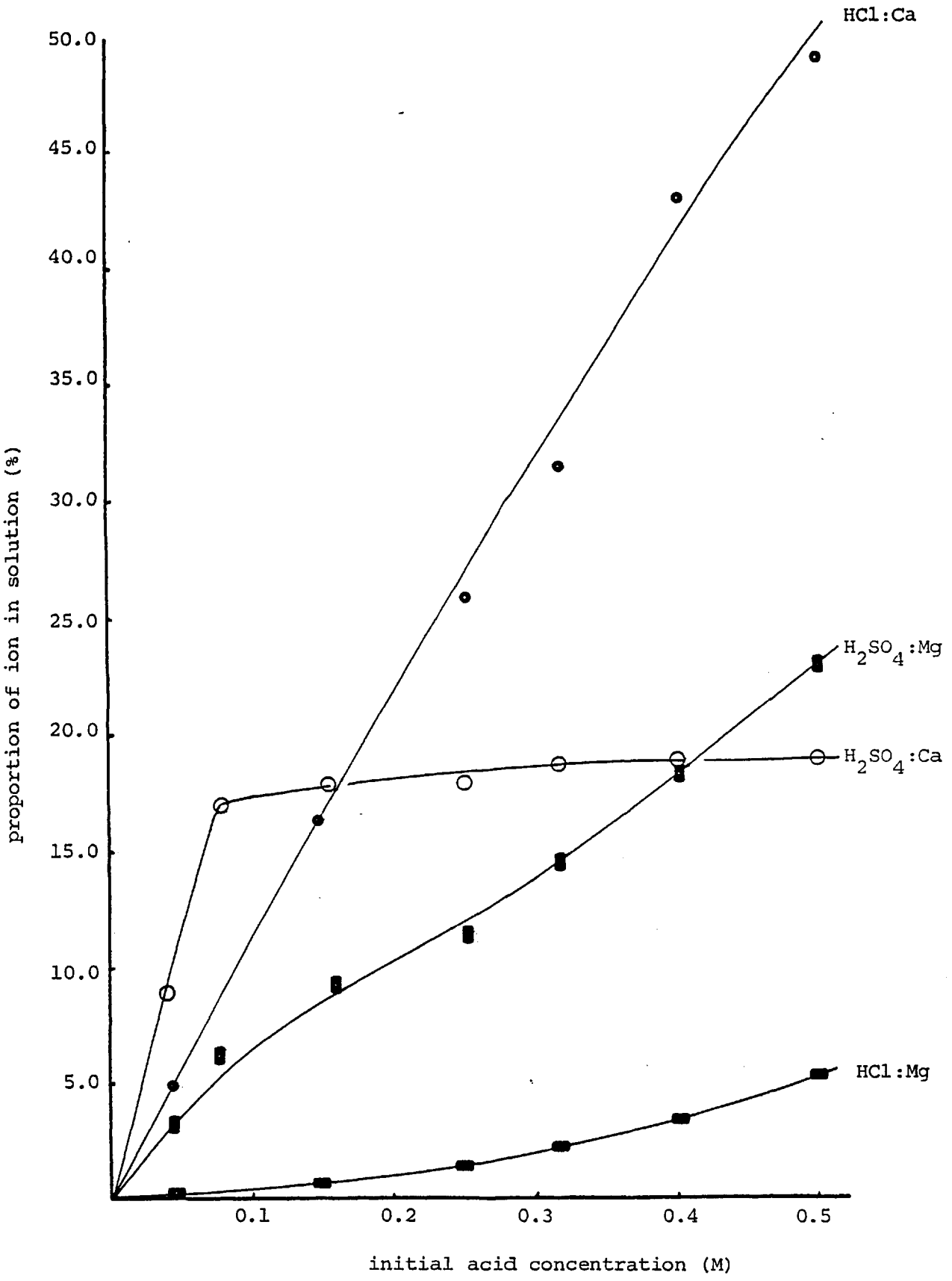


Figure 3.3.3 Relation between the proportion of total magnesium and calcium reporting to solution and the initial hydrochloric/sulphuric acid concentration for a 10g -1180+850 μm feed stirred at 100°C for 7 h.

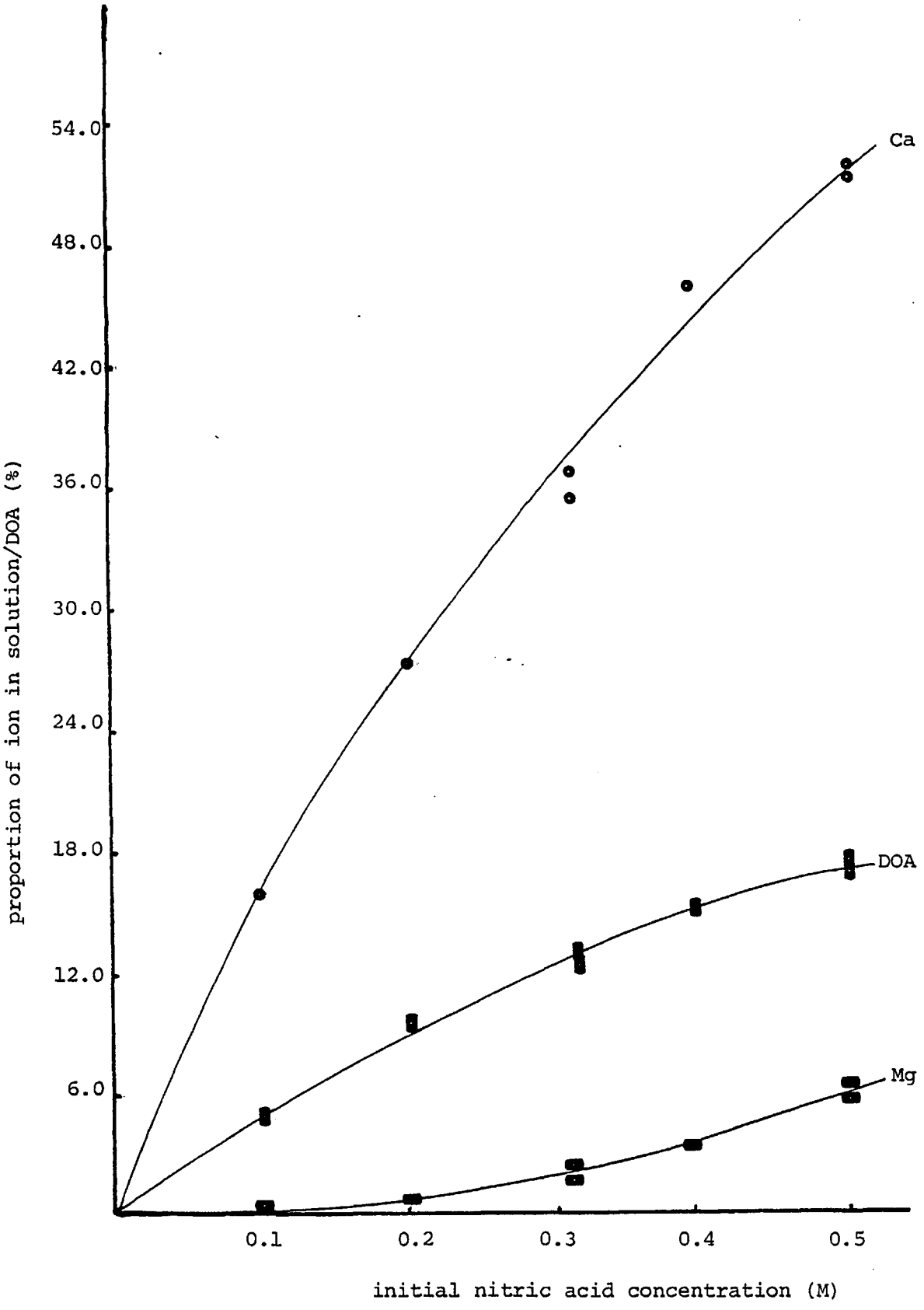


Figure 3.3.4 Relation between the proportion of total magnesium, iron and calcium reporting to solution and the initial nitric acid concentration for a 10g -1180 +850 µm stirred at 100°C for 7 h.

For example, increasing the temperature from 70 to 100°C increased the DOA from 11 to 17% at a sulphuric acid concentration at 0.4M. Larger masses of -75 μm product were also recorded, compared with those obtained employing hydrochloric and nitric acid. Figures 3.3.2 - 3.3.4 show the contrasting plots obtained for the residual ion concentrations recorded at 70 and 100°C respectively. In the case of the sulphuric acid, the magnesium progressively entered solution; for example, up to 18% of the total magnesium entered the solution for an initial acid concentration of 0.316M at 70°C; whereas 23% of the ion entered solution on raising the temperature to 100°C. The total proportion of calcium entering solution attained maximum values of 15% (70°C) and 17% (100°C) at low acid concnetrations of 0.06M H^+ above which a constant concentration of the ion was recorded : 0.04M (70°C), equivalent to 10% of that present in the system, or 0.07M (17% of the total at 100°C). From the results in Section 3.2 it appeared that similar cationic leaching reactions took place, the calcium ion concentration attaining an equilibrium with that precipitated as the sulphate. It was assumed that the hump in Figure 3.3.2 was due to a supersaturation effect.

The ion concentrations resulting from the hydrochloric acid treatment produced very different trends. Large amounts of calcium entered the solution phase; up to 40% of the total at 70°C for an acid concentration of 0.316M H^+, whereas 50% of the total calcium was solubilized at 100°C. The magnesium concentrations were considerably lower, no more than 5% of the total being dissolved. Similar trends were noted for the nitric acid reaction (Figure 3.3.4). It was clear that different types of reaction occurred in these cases.

Both the +75 μm and -75 μm products obtained using 0.3M solutions, at 100°C, of sulphuric and hydrochloric acids were analysed by XRD and the results are shown in Figure 3.3.5. Both products from

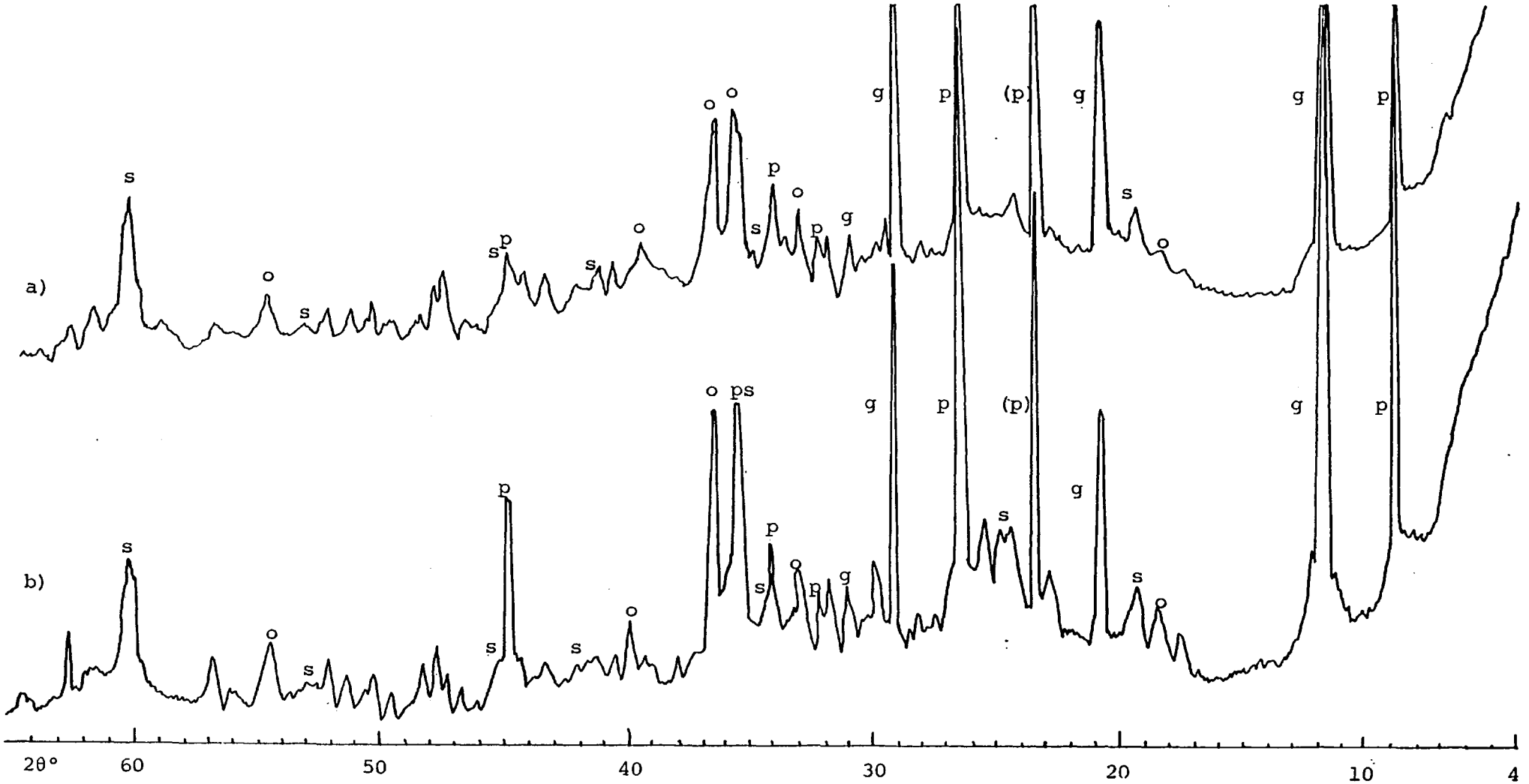


Figure 3.3.5 X-ray diffractograms of -1180+850 µm kimberlite reacted with 0.31M sulphuric acid, 100°C, 7 h.
a) +75 µm fraction
b) -75 µm fraction
g : gypsum p : phlogopite
o : olivine s : serpentine

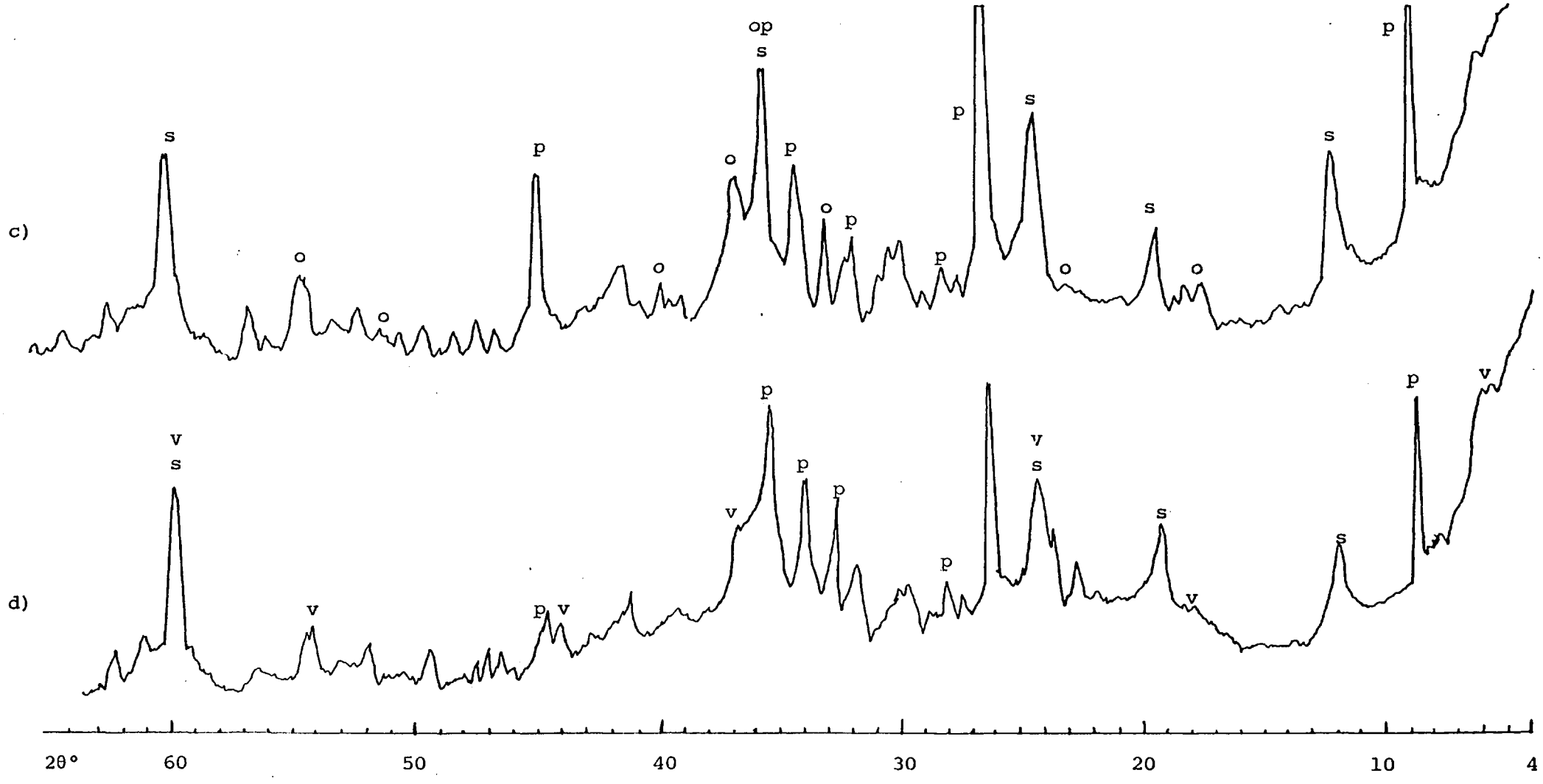


Figure 3.3.5 X-ray diffractograms of -1180+850 µm kimberlite reacted with 0.31M hydrochloric acid, 100°C, 7 h.
c) +75 µm fraction o : olivine s : serpentine
d) -75 µm fraction p : phlogopite v : vermiculite

the sulphuric acid experiments closely resembled the kimberlite head with the exception that gypsum was also present (Figures 3.3.5a,b). It was likely that the reactions proceeded according to equations 3.2.4 - 3.2.10, the dissolution of cations taking place along grain boundaries resulting in the liberation of individual kimberlite mineral grains. The +75 μm fraction, from the hydrochloric acid reaction, (Figure 3.3.5c), exhibited a mineralogy similar to the head. The -75 μm fraction (Figure 3.3.5d) differed in that olivine was clearly undetectable. Serpentine, mica and, for the first time, a 14 Å phase were present. Using glycolation and potassium saturation techniques this 14 Å phase was identified as vermiculite (Section 2.3.2). It appeared that the alteration involved complete reaction of the mineral grains as opposed to the sulphuric acid attack which was probably orientated along grain boundaries. This was shown in a series of scanning electron photomicrographs which are shown in the plates 3.6-3.11).

Further evidence for the difference in the nature of reaction induced by the two mineral acids is illustrated in Figure 3.3.6b,c which shows IR traces obtained for the -75 μm products. A recording for the head kimberlite (Figure 3.3.6a) is included for comparison, and as can be seen, was similar to that for the -75 μm product from the sulphuric acid reaction (Figure 3.3.6b). Figure 3.3.6c, which shows the IR result for the reaction with hydrochloric acid differed from the other two in several respects. A larger peak at 1630 cm^{-1} and an enhanced shoulder at 390 cm^{-1} inferred a greater concentration of minerals containing bonded water and hydroxide groups. The calcite 1420 cm^{-1} and 925 cm^{-1} peaks were absent. A broadening of the 1000-1100 cm^{-1} region was also noted which was probably associated with silicate structure disruption - as is discussed in Chapter 4.

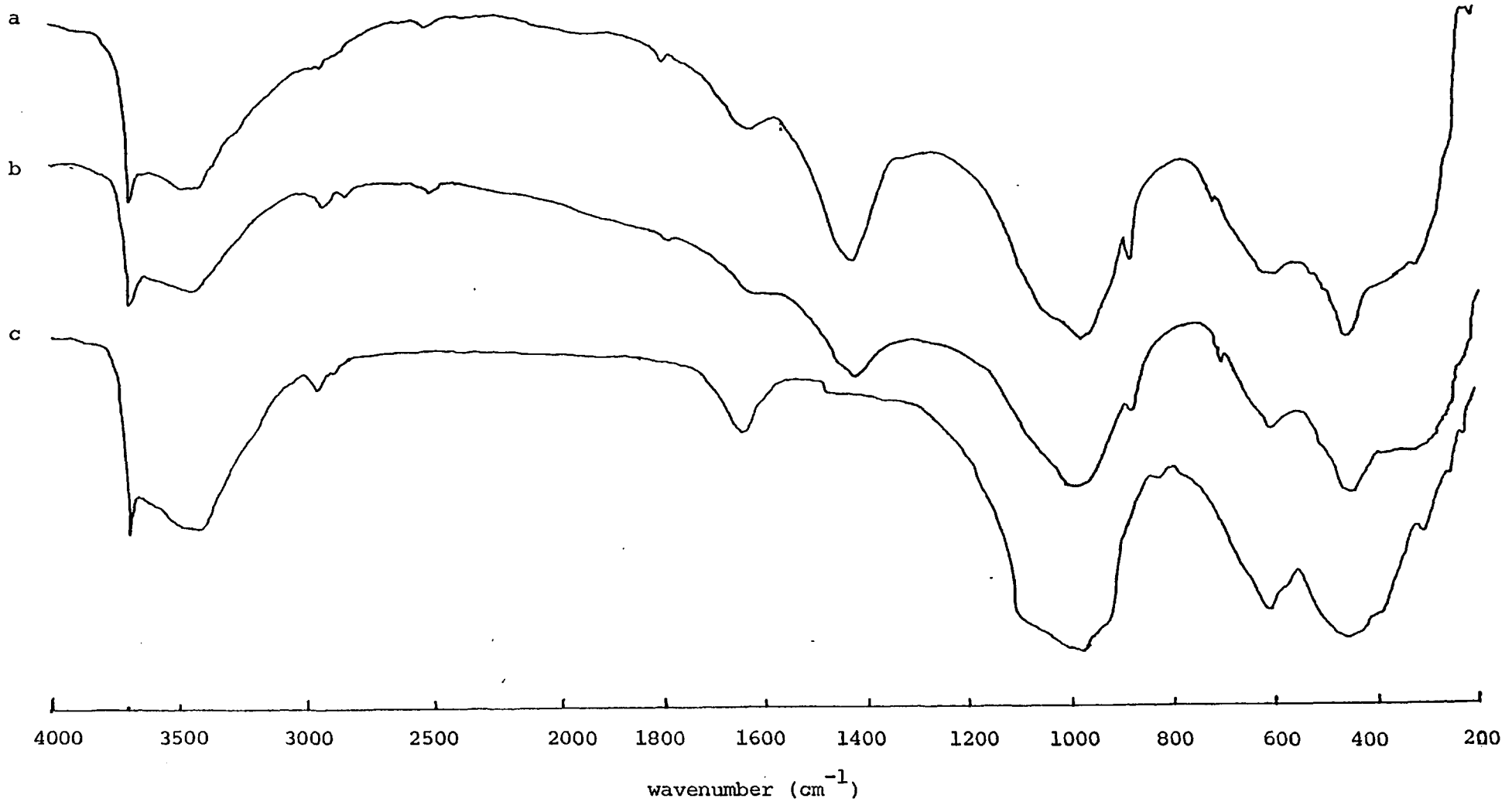


Figure 3.3.6 Infra red recordings for
a) kimberlite head
b) -75 µm fraction from reaction with 0.31M sulphuric acid at 100°C for 7 h.
c) As b; hydrochloric acid used instead.

Results were also obtained for elemental mass balances and these are described in Section 3.3.5.

3.3.3 Results of reactions in the presence of ions additional to the Al^{3+}, H^{+} species

The addition of 4 g of hydrated aluminium chloride to the hydrochloric acid medium produced a substantial increase from 10 to 21% in the DOA, as well as higher residual ion concentrations. Replications as part of a standard factorial experiment procedure,[238] combined with the testing of the effect of extra chloride ion in solution proved to 99% confidence that it was the aluminium ion which enhanced the kimberlite degradation. The -75 μm product was analysed by XRD, IR and DTA and the results are shown in Figure 3.3.7a-c. XRD revealed that the following minerals were present : chlorite, vermiculite, serpentine and mica. The variety or crystalline forms was greater than those generated from the hydrochloric acid reactions in the absence of the aluminium ion (Figure 3.3.5d), as indicated by the broad d spacing band at 3.07-3.67 Å. Broadening was also noted in the 7.1-7.4 Å region which inferred that the serpentine contained a higher aluminium content than before. The very strong peak at 1.53 Å however reflected the trioctahedral structure of the 14.2-14.4 vermiculite-chlorite and serpentine.

The IR recording in Figure 3.3.7b showed structures different to that featured in Figure 3.3.4d. Contrasting with the broad 995-1000 cm^{-1} of the latter, a comparatively sharper maximum was noted at 990-995 cm^{-1} as due to the replacement of silicon by aluminium in the tetrahedral lattice, typical of chlorites. Furthermore, there was evidence of increased concentrations of octahedrally-coordinated magnesium (shouldered peaks at 690 cm^{-1}, 400 cm^{-1} (Mg-OH bond)) and

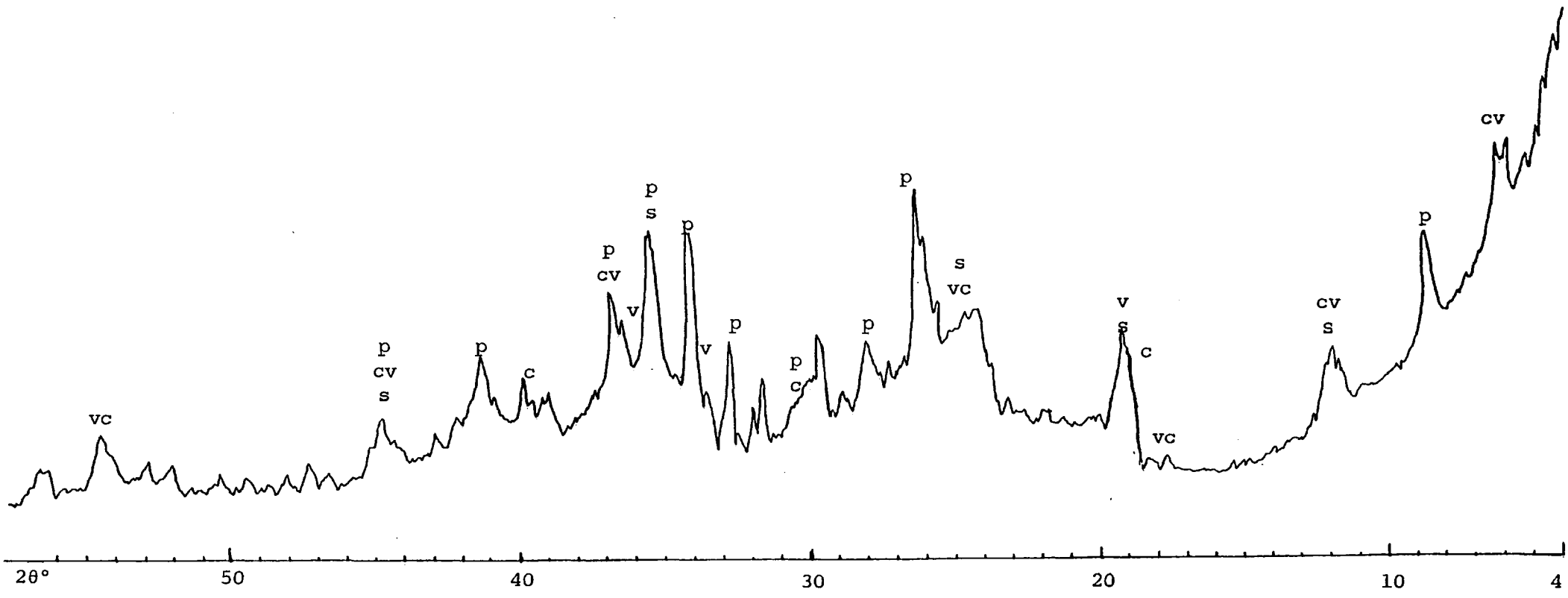


Figure 3.3.7a X-ray diffractogram for the residual -75 µm fraction from reacting 10g -1180+850 µm kimberlite with 40 ml 0.44M aluminium chloride, 0.31M hydrochloric acid at 100°C for 7 h.

c : chlorite s : serpentine
p : phlogopite v : vermiculite

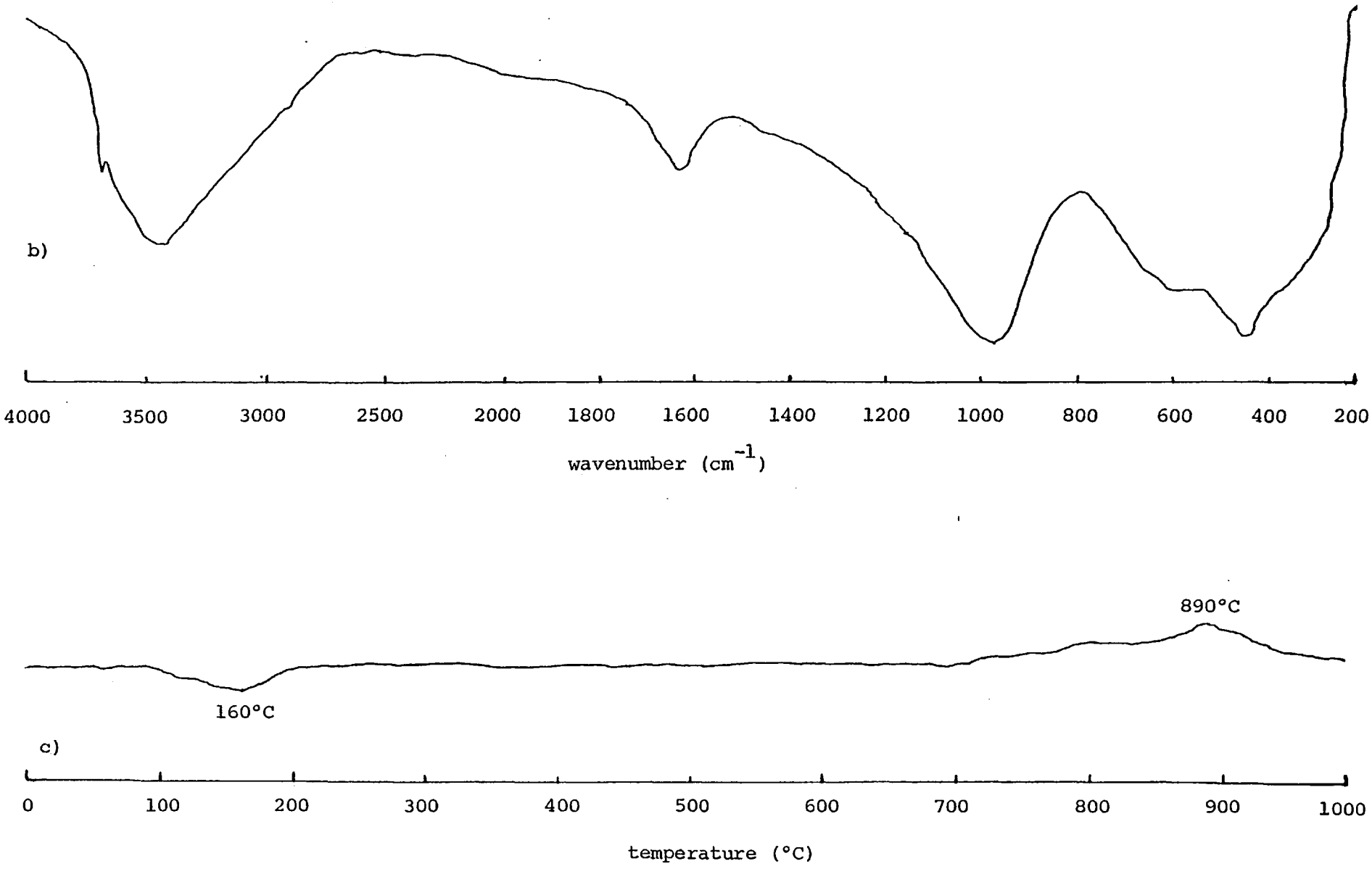


Figure 3.3.7 b) Infra red trace for the product noted in Figure 3.3.7a.
c) Differential thermal analysis of the same product.

aluminium (540 cm^{-1}). The sharp shoulder at 3600 cm^{-1} (Me-OH bond) was not as pronounced. This was due to larger amounts of associated water (i.e. due to vermiculite) indicated by the 3430 cm^{-1} peak.

The DTA trace (Figure 3.3.7c) served to confirm the identifications made. The first peak, an endotherm maximum at 160°C, was associated with the loss of free or adsorbed water from all the minerals. The width of the recorded deflection resulted from the differing peak temperatures for each mineral : 100°C, serpentine; 110°C, chlorite and 175°C, vermiculite. The exotherm at 750-950°C accounted for the losses of structural water and subsequent recrystallisation to neo- and ino-silicate forms (e.g. magnesium vermiculite → enstatite at 840°C; chrysotile → olivine 850°C).

The results of varying the quantities of aluminium nitrate and chloride added to the system, is shown in the diagram in Figure 3.3.8. This graph shows the relation between the DOA, the proportion of total magnesium and the proportion of total aluminium in solution compared with initial aluminium concentration in the system. As shown, the DOA increases up to an initial concentration of 0.4M Al^{3+} for both nitrate and chloride systems. Proportionately smaller rises were noted above this value. The amount of magnesium in solution increased from 3.5% (NO_3^- medium), 4.5% (Cl^- medium) in the absence of added aluminium, to 14% (NO_3^- medium) and 14.5% (Cl^- medium) at 0.4M Al^{3+}. The most important difference between the two plots was in the amount of aluminium remaining in solution. A majority of aluminium in the nitrate medium remained in solution (> 80%) whereas a substantial amount of the ion in the chloride medium reported to the solid phase (e.g. 71% at 0.41M Al^{3+}). Subsequently, aluminium was always added as the chloride in order to induce maximum precipitation of solid products which could yield aluminium rich clays, the natural alteration products of kimberlite. From the figure it was evident that

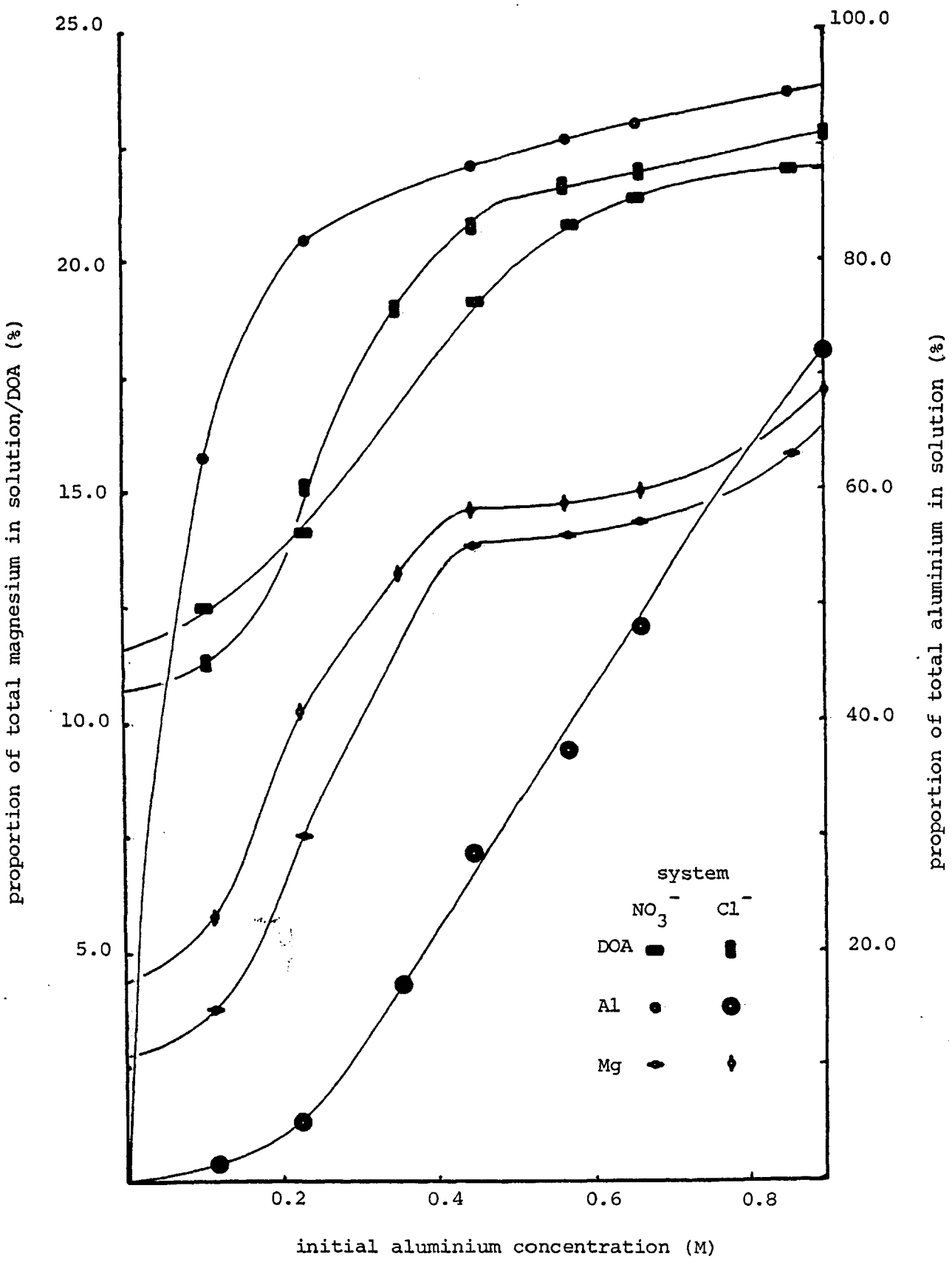


Figure 3.3.8 Relation between DOA, proportion of total aluminium and magnesium reporting to solution and the initial concentration of aluminium chloride/nitrate for 10g -1180+850 µm kimberlite reacted with a solution containing 0.31M hydrochloric/nitric acid at 100°C, for 7 h with various aluminium ion concentrations.

the optimum initial aluminium concentration for inducing alteration was 0.4M, for the conditions employed.

Table 3.3.1 lists the ions and their concentration ranges, tested in conjunction with solutions containing the concentrations 0.41M Al^{3+}, 0.31M H^{+}. None of these were found to have a positive effect as assessed by DOA and residual ion concentration data.

TABLE 3.3.1 ADDITIVES TESTED IN CONJUNCTION WITH 0.41M ALUMINIUM CHLORIDE, 0.31M HYDROCHLORIC ACID, 100°C, 7 h

Ionic/Gas species	Concentration range (M)
Na^{+}	0 - 1.0
K^{+}	0 - 0.5
Cs^{+}	0 - 0.07
F^{-}	0 - 0.3
Cl^{-}	0 - 1.0
$S_2O_4^{2-}$	0 - 0.12
$(COOH)_2$	0 - 0.4
O_2	0 - saturation
CO_2	0 - saturation

3.3.4 Results and discussion : Mass balances

Elemental mass balances were carried out using the peroxide fusion/AAS technique (Section 2.4.3) on the following three types of alteration reaction at 100°C and 7 h.

A : sulphuric acid medium, initial pH 0.5

B : hydrochloric acid medium, initial pH 0.5

C : As B; 4 g hydrated aluminium chloride added

The results are given in Table 3.3.2 where the systems are denoted A,B,C as above. The table is divided into four sections : firstly, the head assays of an unreacted -1180+850 µm sample; secondly, the assays of the +75,-75 and solution phases; thirdly, the percentage distributions derived from the measured concentrations and fourthly, calculated head assays which complete the mass balance.

Reaction A. The distribution values as measured for the +75 µm phase were of similar magnitude (ranging only from 69.3 to 78.7%). This showed that the acid attack was not directed preferentially at a particular mineral phase. The magnesium and calcium extracted from the kimberlite were found to be equally distributed between the -75 µm fraction and solution phases, whereas the silicon, iron and aluminium reported mainly to the solid phase. Mutually similar assays were also recorded for the +75 and -75 phases, though the -75 µm fraction had a reduced magnesium concentration. The similarity of these recorded assays and the distribution of the 'liberated' cations between the -75 µm solid and solution phases provided additional evidence for the hypothesis that the -75 µm product consisted of broken kimberlite particles incorporating hydrated calcium sulphates (as suggested from the XRD recordings - Figure 3.3.5a and b). Scanning electron photomicrographs of the +75 µm particles, which are illustrated in Plates 3.6-8 also indicated that the mineral acid attack was indeed orientated along planes of weakness. It was likely that the acid dissolved parts of the olivine and serpentine structures, as well as the calcite, where present on mineral grain boundaries. This resulted in the dissolution of magnesium (as inferred from Figure 1.4.1). Any 'liberated' iron and aluminium precipitated with the -75 µm product due to the final neutral pH attained (Figure 1.4.1).

TABLE 3.3.2 PARTIAL ELEMENTAL MASS BALANCES OF TYPICAL ALTERATION REACTIONS IN ACIDIC MEDIA

		Mg			Si			Fe			Ca			Al	
phase	A	B	C	A	B	C	A	B	C	A	B	C	A	B	C
head (%)		16.07			15.77			6.03			6.29			1.54	
Distribution Assay +75 µm (%)	16.3	16.9	15.5	16.5	17.3	18.8	6.3	6.7	6.5	6.1	4.7	6.3	1.2	2.0	3.1
Distribution Assay -75 µm (%)	9.9	14.7	5.0	18.5	17.5	12.9	7.4	7.1	3.3	7.5	1.7	1.8	2.5	4.0	13.0
Distribution Assay solution (M)	0.25	0.04	0.25	0.01	-	-	-	-	0.03	0.06	0.13	0.25	-	-	0.14
Distribution (%) +75 µm (%)	74.8	87.5	81.4	78.7	88.0	90.9	78.7	88.9	85.3	71.0	64.0	30.7	69.3	80.9	50.0
Distribution (%) -75 µm (%)	10.8	10.0	2.6	20.6	11.7	9.1	21.3	11.1	3.3	13.0	3.0	3.7	30.7	19.0	18.0
Distribution (%) solution (%)	14.4	2.5	16.0	0.6	0.3	0.0	0.0	0.0	11.5	16.0	33.0	65.6	0.0	0.0	32.0
calculated head (%) assay	16.7	16.0	15.6	16.0	16.3	16.1	6.2	6.3	6.1	6.1	6.3	6.2	1.3	1.5	1.0

Reaction A : sulphuric acid medium, initial pH 0.5

B : hydrochloric acid medium, initial pH 0.5

C : as B; 4 g hydrated aluminium chloride added

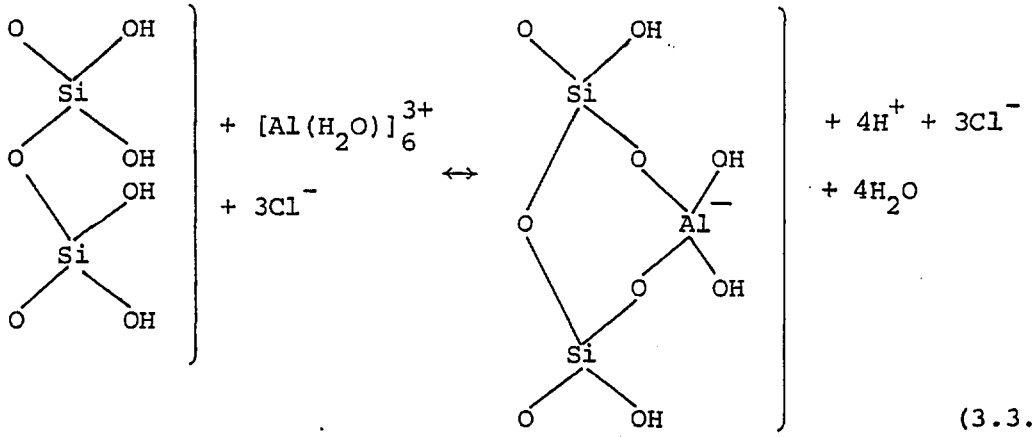
Silicon remained predominantly within the parent mineral structure. The entry of calcium ions into solution resulted in the precipitation of calcium sulphate and eventual establishment of the equilibrium between the gypsum product and the solvated ions. However, this alteration appeared to be restricted to the surfaces of the mineral grains as particles which retained a kimberlite mineralogy reported to the -75 μm phase.

Reaction B. The distribution values for the +75 μm phase were higher than those recorded for reaction A, which was consistent with the lower DOA recorded. In contrast to Reaction A, the majority of the 'liberated' calcium and magnesium reported to the solution and -75 μm solid phases respectively, otherwise the trends in the distribution values were similar to reaction A. As calcium was not precipitated, the proportion of the ion residual in the +75 μm fraction indicated that the penetration of reagents was greater than that inferred by the DOA (Figure 3.3.1). The precipitation of a magnesium-bearing mineral was inferred from the mass balance and previous XRD data (Figure 3.3.5d) and their poor crystallinity was shown in the scanning electron photo-micrographs obtained (Plate 3.10).

In contrast to reaction A, the alteration reactions were not restricted to dissolution along the surfaces of mineral grains, but extended throughout the kimberlite to completely transform the original olivine and serpentine to phyllosilicate minerals. Hence, for a certain concentration of reagents within a specified rock volume a smaller DOA resulted, together with a concentration of magnesium and other cations within the resultant -75 μm product, as shown by the mass balance figures in the table. These arguments are extended in Chapter 4.

Reaction C. The largest differences in the distribution values occurred between C and the other two reactions. The introduction of aluminium resulted in the formation of an aluminium-rich -75 μm product (13% Al). From the table it was possible that the ion had replaced magnesium and iron as the major cation, other than silicon involved in layer silicate formation. This was shown from the lower magnesium and iron assays (5.0% and 3.3% respectively), and the increasing proportion of these ions entering solution. The calcium distribution values indicated the extent of reagent penetration. From Figure 3.3.8 the DOA was 22%. The proportion of residual calcium suggested that 70% of the rock matrix had been exposed to the reagent solutions, the majority of this ion being liberated from calcite hydrolysis. This figure favourably contrasted with 6% as recorded for Reaction B where aluminium was not applied. These conflicting figures obtained for systems where the initial acid concentration was the same suggested that during the inter-reaction between the aluminium ion and the kimberlite further quantities of hydrogen ion were generated enhancing the degradation process. Two reactions which would result in hydrogen ion generation have been noted in the literature.

a) At pHs less than the precipitation value of aluminium, the ion can interact with surface silicate layers[124]



(3.3.1)

b) Precipitative formation of aluminium hydroxyoxides :

$$Al^{3+} + 3H_2O \leftrightarrow Al(OH)_3 + 3H^+ \qquad (3.3.2)$$

Evidence for the first type of reaction had been offered by the IR results (Figure 3.3.7b). The tetrahedral replacement of silicon by aluminium would be essential for chlorite and vermiculite formation and a reaction similar to equation 3.3.1 would probably take place. The large aluminium assay did suggest that the second type of reaction also took place. The end pH of the reaction was 3.20. A later experiment showed that aluminium did precipitate at the pH at 100°C in the absence of a kimberlite charge.

Equations describing the equilibrium relevant to the sulphuric acid reaction have been given in the previous section. For the other two systems the complex nature of the reactions required further data to be obtained before equations could be written. However, it was evident from the IR and elemental distribution data that the two-stage process discussed in Section 1.4.1 occurred, namely that a) the rock structure was disrupted and cations were released to solution and b) ion-exchange occurred after the attainment of a suitable pH for recrystallisation to occur. From the experiments conducted it was clear that vermiculites, chlorites and serpentines could be crystallised in weakly acidic environments i.e. pH $\sim$ 3. The work discussed in the following section delineated some of the pH limits for clay mineral crystallisation.

3.3.5 Results : Phase diagrams in the Al^{3+}-H^+ system I : Initial hydrochloric acid concentration 0.3l and 1.5M, at 100°C

The previous sections have considered individual reactions involving those agents which have affected kimberlite alteration and in

certain instances resulted in clay mineral formation (i.e. the ionic species Al^{3+}, H^{+}, Cl^{-}, NO_3^{-}). In order to examine further the range of reactions and products formed, it is appropriate to obtain results for a wide set of conditions such that phase diagrams may be constructed.[243] Such diagrams allow large quantities of data to be conveniently represented which provide a graphic summary of the mineral relationships that might be expected if equilibrium is attained.[243,244] However, with systems as complex as those involved in this particular study, it is not possible to deduce a fully quantitative description of the regions of stability for the various clay phases.

Phase predominance diagrams which resulted from the reaction of kimberlite samples in solutions initially containing 0-0.88M Al^{3+} equilibrating at differing pH values are shown in Figures 3.3.9 and 3.3.10. The former was obtained using an initial hydrochloric acid concentration of 0.31M H^{+}, the latter, 1.5M H^{+}. In both cases, the following conditions were used : a 10 g -1180+850 μm feed was reacted in a 40 ml reagent volume containing the species Al^{3+} and H^{+} for 100°C, 7 h. In certain instances, the pH was adjusted at 3.5 h by the addition of concentrated aqueous ammonia so as to further induce the formation of solid phases. The pH line (marked thus -●-) on each diagram marks the average residual hydrogen ion concentration in the absence of any adjustment. After the reaction was complete the solids separation/AAS analytical procedure (Section 3.2.1) was adopted as before. Solid products were analysed by XRD.

The phase predominance diagrams have as their axes initial aluminium concentration and equilibrium pH. The ordinate was chosen for convenience, as the precipitation of the clay phase and/or aluminium hydroxides caused the equilibrium aluminium concentration to be too low or too irregular to be employed as a reliable scale. To demarcate the phase regions shown, groups of points having similar major

products were sought. It was intended that the two phase diagrams should represent the full extent of the variation in the -75 μm products obtainable. The initial concentrations of acid used related to the limits of resistance of metal parts in the testwork (Section 5.3) and to the limits of precipitation of the clay phases (Section 3.3.1).

Phase diagram : $[H^+]_{initial}$ = 0.31M. Using XRD coupled with heating and interlayered saturation techniques[199,200] three regions of crystallisation could be outlined in Figure 3.3.9. At moderate to high pHs, where high initial aluminium concentrations had been applied, poorly crystalline 7.0-7.4 Å aluminium kandites were produced (Figure 3.3.11a). The second region in Figure 3.3.9, adjacent to the axes, represents the conditions in which phyllosilicates were synthesised. Between these two portions is a central zone representing amorphous hydroxyoxide products. The diagram interrelates the results of reactions that took place between the ions Al^{3+}, Mg^{2+}, Fe^{2+} and various silicate structure groups which resulted from acid hydrolysis of the kimberlite minerals.

The phyllosilicates produced in the region adjacent to the axes were not particularly well crystallized, and, as the diagram indicates, demarcation between the various phases could not be precise. There was a pronounced trend however that vermiculites and (aluminian) serpentines resulted when very low aluminium charges were introduced into the alteration system. At higher pHs (8-9) the product was principally kandite-like in nature. As the amount of aluminium employed increased, the proportion of chlorites tended to increase. Above concentrations of the order of 0.6M Al^{3+} (pH 2-3), however, 9-11 Å phases accompanied the vermiculite-chlorite products (Figure 3.3.11b).

IR analyses verified these findings in terms of the types of ion exchange that had occurred. The shift of the 1000 cm^{-1} band to lower

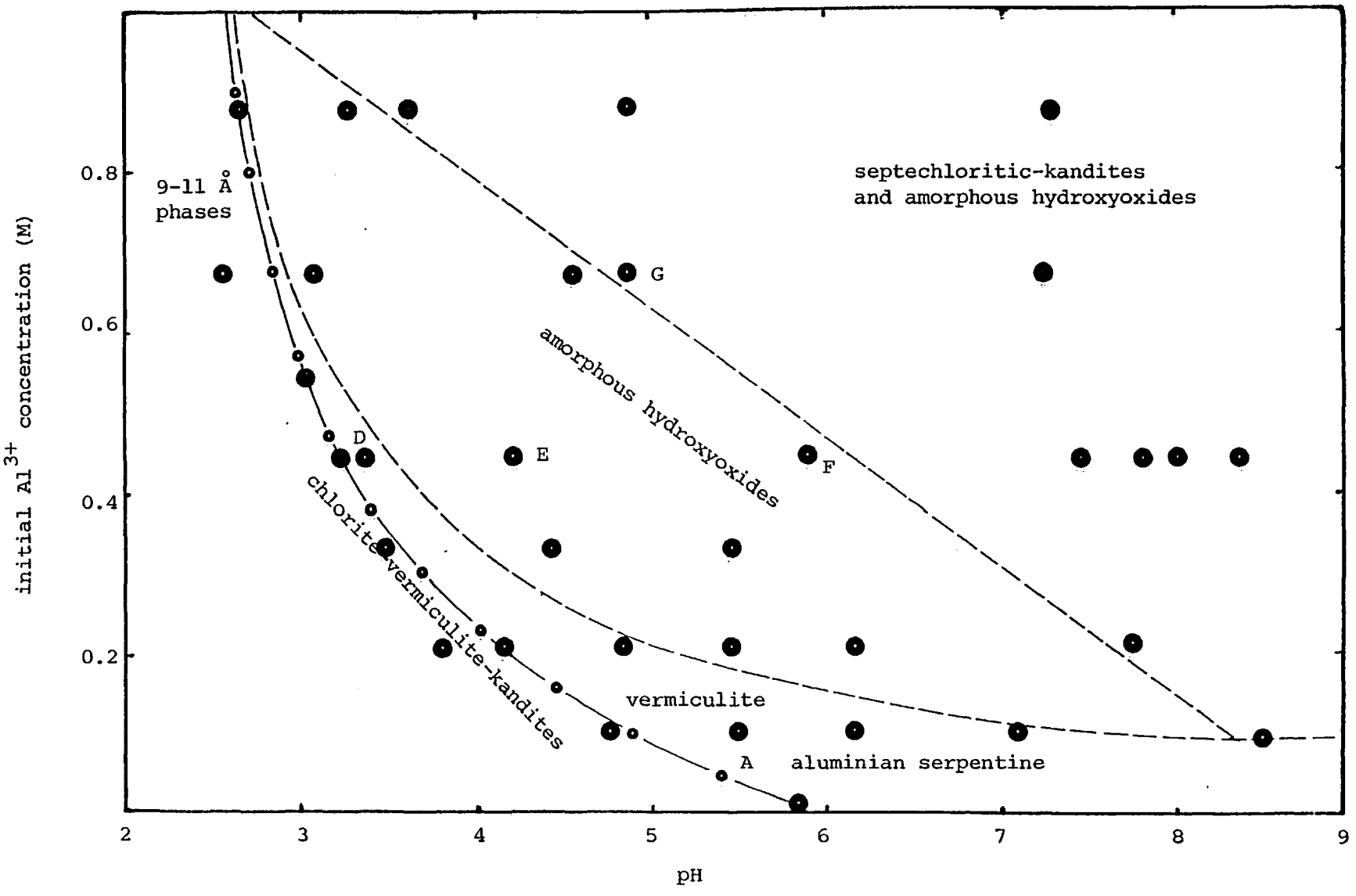


Figure 3.3.9 Phase predominance diagram showing the influence of initial aluminium concentration and the pH on the nature of the -75 µm product formed at 100°C, 7 h, initial acid concentration being 0.31M.

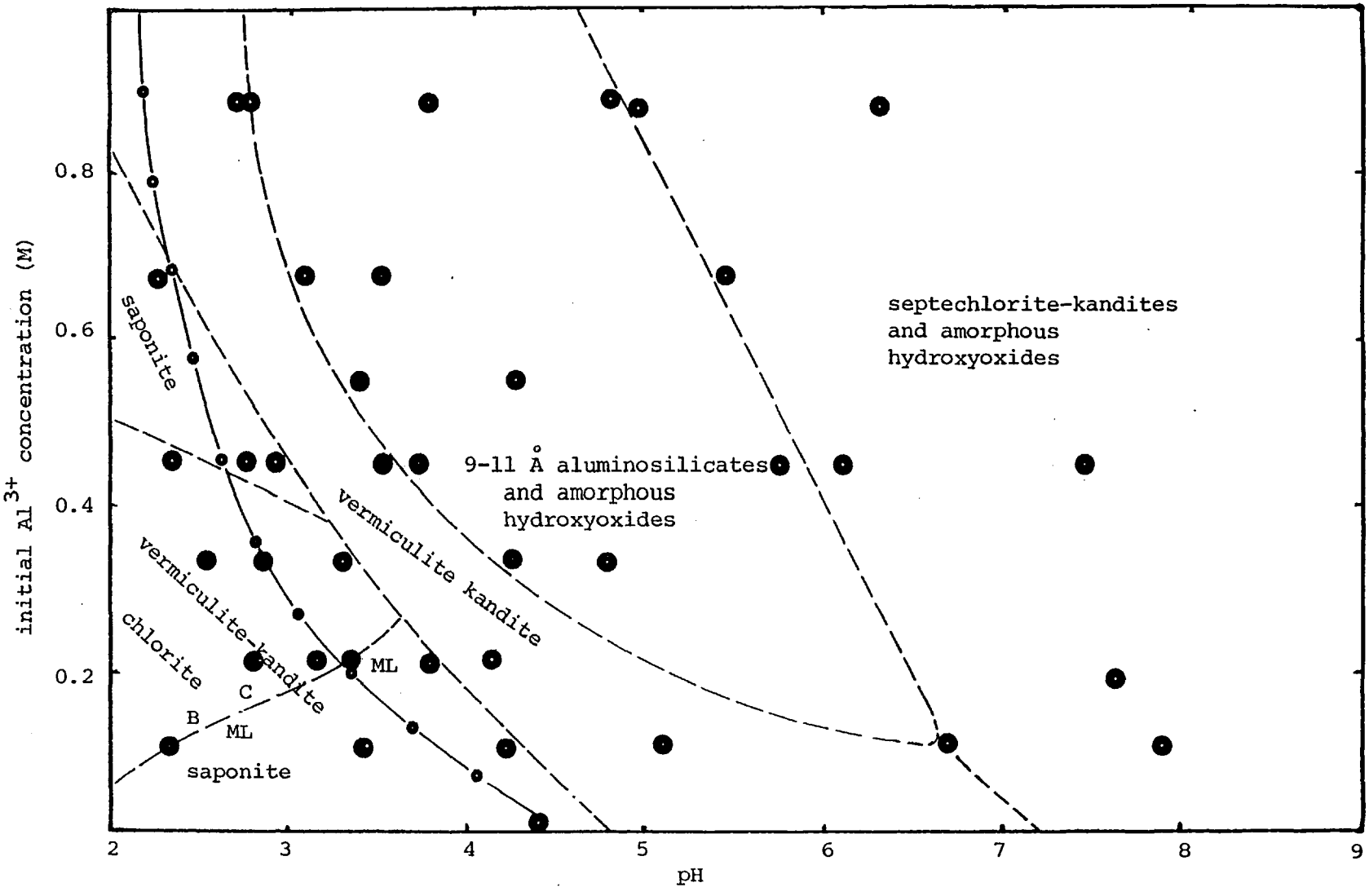


Figure 3.3.10 Phase predominance diagram showing the influence of initial aluminium concentration and the pH on the nature of the -75 µm product formed at 100°C, 7h, initial acid concentration being 1.5M.

frequencies, for the reactions conducted using 0.1-0.4M Al^{3+} solutions reflected the formation of chlorite-vermiculite rich products. The 540 cm^{-1} peaks could be interpreted as due to aluminium in octahedral coordination in all the minerals represented, though it was likely that the aluminium kandites and 9-11 Å phases were the predominant dioctahedral phases. The majority of the minerals produced at above 0.6M Al^{3+} appeared to retain a purely silicon tetrahedral layer.

On raising the pH of the solution beyond the pH 3-5 line (Figure 3.3.9) rapid precipitation of aluminium and iron hydroxyoxides occurred (as deduced from AAS analyses). Separate studies showed a ten-fold increase in the quantity of -75 μm product on crossing this pH line. These amorphous solids tended to obscure the XRD response of any smaller quantities of crystalline clay minerals previously formed. At higher aluminium concentrations (0.4-0.88M), these hydroxides tended to revert to aluminium-rich kandites or septechlorites. Measurement of the residual ion concentration by AAS also showed that as well as the concentrations of aluminium and iron being reduced by 90% as the pH was increased from 3 to 6, similar trends were noted for the DOA, and magnesium and calcium concentrations. For example, where an aluminium concentration of 0.4M Al^{3+} was applied, the DOA and other cation concentrations decreased from 21%, 0.249M Mg^{2+}, 0.029M Fe^{2+} (pH 3.2) to 17%, 0.155M Mg^{2+}, 0.0003M Fe^{2+} (pH 5.26).

Phase diagram : $[H^+]_{initial}$ = 1.5M. Using similar identification techniques to those used above, six phase regions were recognisable. At pHs 5.9, where aluminium concentrations lower than 0.6M had been employed, aluminium-rich septechloritic-kandites were present, whereas at higher concentrations of the ion, amorphous hydroxyoxides tended to mask these phases. The middle portion of the diagram was occupied by a region attributable to 9-11 Å

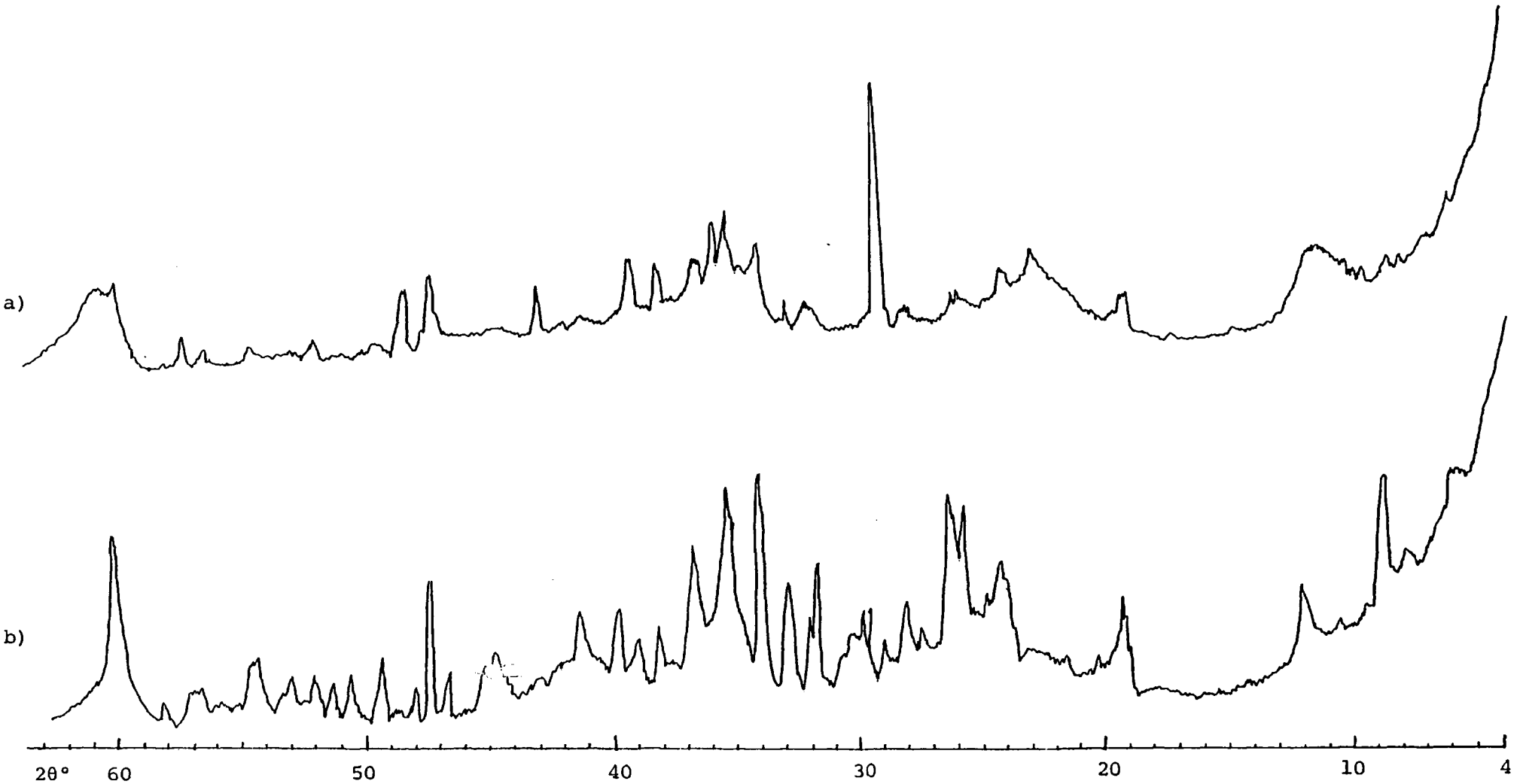


Figure 3.3.11 X-ray diffractograms of selected -75 μm products as featured in Figure 3.3.9
a) 7.0-7.4 Å aluminium kandites
b) mixed layer vermiculite-chlorite with residual mica

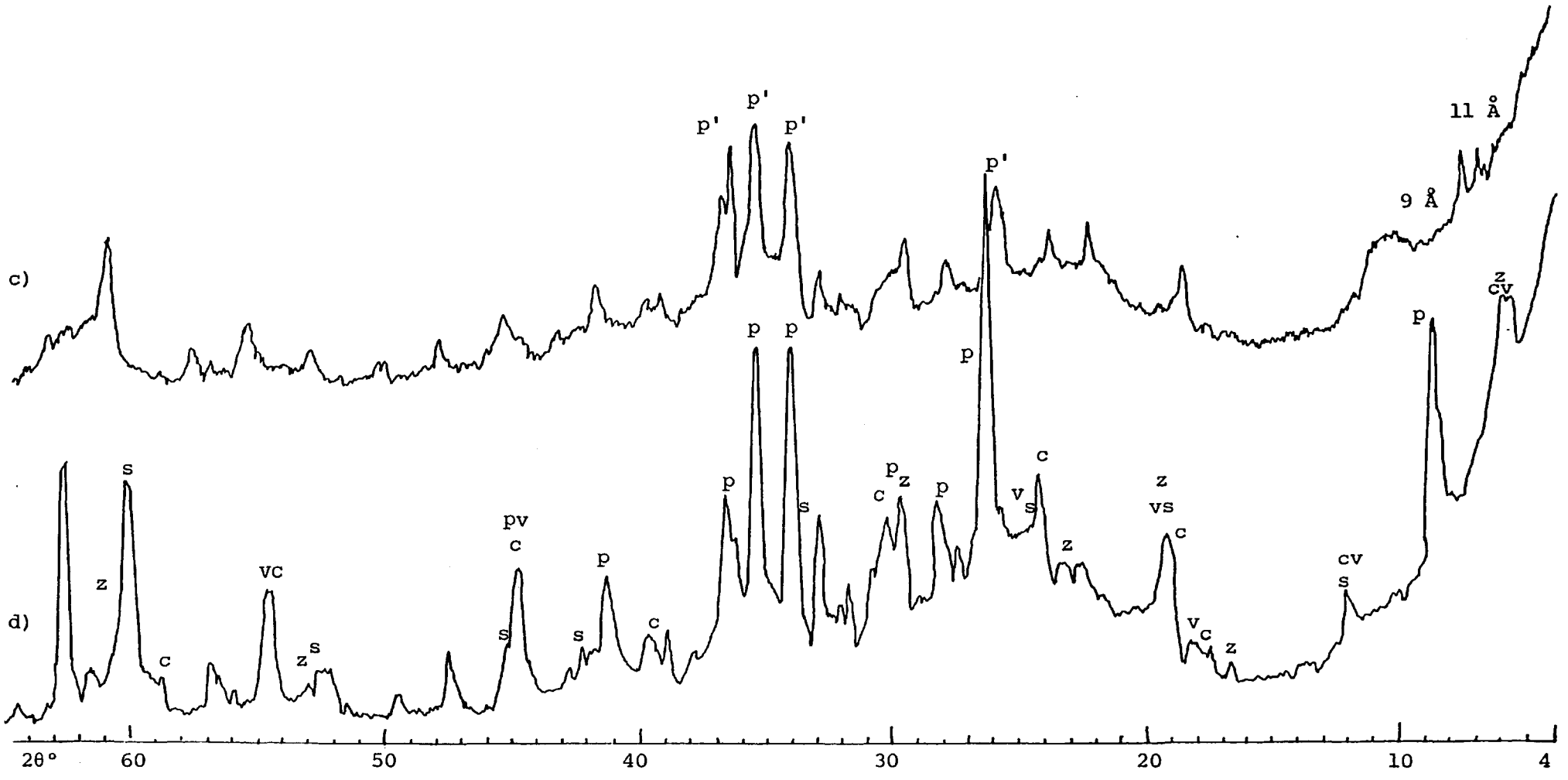


Figure 3.3.11 X-ray diffractograms of selected -75 µm products as featured in Figure 3.3.10.
c) 9, 11 Å aluminosilicate phases
d) mixed layer saponite-vermiculite-chlorite

c : chlorite v : vermiculite
p : phlogopite z : saponite
(p' probably residual mica)
s : serpentine

2:1 layered silicates (Figure 3.3.11c). These poorly crystalline compounds could not be further identified but their significance is discussed later (Chapter 4). At low pHs (< 4 for aluminium concentrations of 0.2M, < 2 for concentrations of 0.8M Al^{3+} a series of 14-15 Å phyllosilicates was produced which could be conveniently segregated into three phase predominance regions as shown. One region was characterised by the presence of chlorite whereas the other two were ascribable to saponitic smectites. Vermiculites and kandites were present in all three phase regions. In two instances a chlorite-vermiculite-smectite mixed layered product (Figure 3.3.11d) was formed as represented by ML on the diagram. The last region which was located between the previous and the 9-11 Å phases also represented vermiculite-kandite products, although the resolution of the peaks in the respective XRD diffractograms was reduced.

Infra red analysis of the 14-15 Å silicate fractions showed that they were principally trioctahedral in character. A concentration of Mg-OH and Mg^{VI}-O-Si bands (690 cm^{-1}) in preference to the Al^{VI}-O-Si and Al-OH bands was indicated by the respective smaller 540 and 350 cm^{-1} peaks. The reverse of this trend, however, was noted for the 9-11 Å phases. All products exhibited less tetrahedral substitution for silicon compared with those minerals featured in Figure 3.3.9, most Si-O bonds having a peak reading in the range 1000-1015 cm^{-1}. Hence, although the minerals formed were similar to those in Figure 3.3.9 their structures differed. In general it seemed that an increase in the concentration of acid employed resulted in a decrease in the extent of aluminium substitution in both tetrahedral and octahedral coordination, although it seemed that high initial aluminium concentrations could negate this effect. These differences in structure were attributable to differing relative amounts of reactants rather than differing types of reactions.

As expected the DOAs recorded were higher than in the previous phase diagram, a five-fold increase in acid concentration resulting in a

two-fold rise in the DOA. The largest values - 36-44% - were recorded, as before, where the pH had not been adjusted; although the effect was minor. The result of raising the pH beyond the line indicated on the diagram was to precipitate aluminium and iron as silicates and/or hydroxides. Only a 2-3 fold increase in the -75 μm product mass was noted in this case, on raising the pH to 6-8 in contrast to the 10 fold increase before. Furthermore, higher calcium and magnesium concentrations were recorded compared with those obtained under similar conditions using the weaker acid medium and decreased with increasing alkalinity.

These results are further discussed in Section 3.5.3.

Following the results obtained for the phase diagram (Figure 3.3.10) involving 1.5M acid concentrations, the most effective degradation environments were those where no pH adjustment was involved. The DOAs and residual ion concentrations measured for the alteration experiments concerned are shown in Figure 3.3.12. Although the proportionate increase in DOA with aluminium addition (36-44%) was not as great as that involving weaker acid media (10.5-22% - Figure 3.3.8), substantially more iron, magnesium and calcium entered the solution phase. For example, at an aluminium concentration at 0.3M, the proportions of the total ion available reporting to solution were 25% (Fe), 33% (Mg), 81% (Ca) in Figure 3.3.12, compared to 0% (Fe), 13% (Mg), 54% (Ca) in Figure 3.3.8. The high calcium assay indicated a similar extent of penetration by the reagents. Furthermore, magnesium and iron continued to enter solution with aluminium addition, in contrast to the analyses recorded for the weaker acid medium. This probably resulted from greater participation of the aluminium ions in the alteration transformations as a result of the greater disruption induced by the larger concentrations of acid added. The variation of aluminium was also different to that shown in the earlier figure. Figure 3.3.12 shows that for initial aluminium

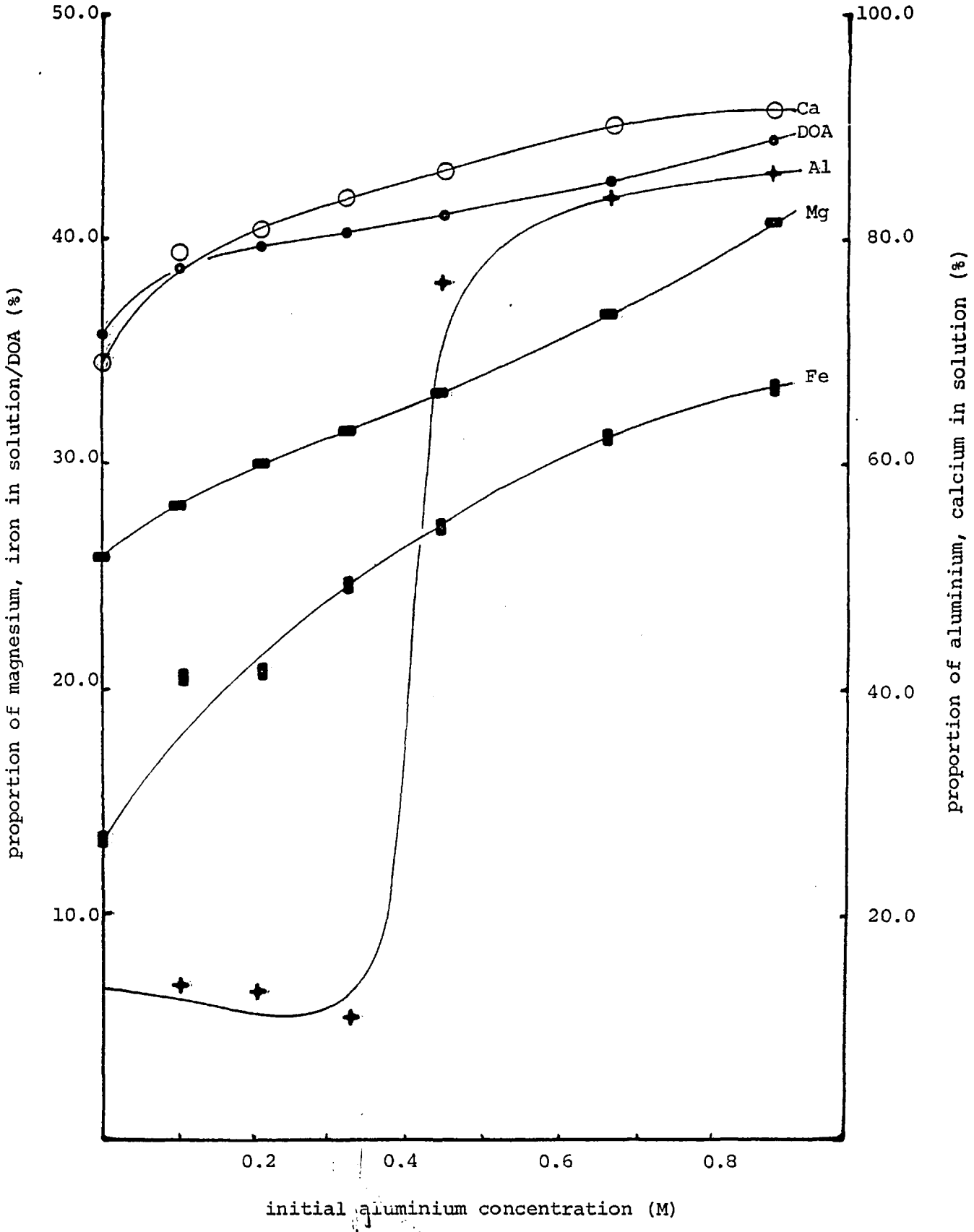


Figure 3.3.12 Relation between the DOA, proportion of total magnesium, aluminium, iron and calcium reporting to solution and the initial aluminium ion concentration for 10g -1180+850 µm kimberlite reacted with 1.5M hydrochloric acid at 100°C for 7 h.

concentrations less than 0.35M, less than 11% of the total present in the system entered solution. Above this concentration 80% or more was solubilised. As the pH of the residual solutions were less than 3, the aluminium in the solid phases was not a simple hydroxyoxide precipitate. Hence the use of aluminium concentrations $\sim$ 0.1-0.33M in conjunction with initial acid concentrations of 1.5M appeared to be the most effective and efficient from a consideration of the consumption of the reagents.

The progressive formation of the phases noted in Figure 3.3.10 could be observed by analysing various fields of view of sectioned + 75 µm grains using an electron microscope. Plates 3.12-19 relate to residual +75 µm products as resulting from alteration treatments represented in Figure 3.3.12. Plates 3.12-13 show the crystallisation of phyllosilicates on the cavity surfaces of kimberlite reacted with 1.5M hydrochloric acid. Addition of aluminium to the system results in more extensive clay mineral formation. Reagent attack could be localised or focussed on a certain part of the particle (Plate 3.15) and the presence of extra aluminium would facilitate crystallisation of the alteration product, sometimes within the mineral grain itself (Plate 3.17).

3.3.6 Scanning electron photomicrographs

To complement the XRD, IR and DTA analyses of the solid fractions obtained during the testwork, selected +75 µm residual products were analysed using a Vickers Stereoscan 600 electron microscope. A sample of the +75 µm fraction in question was mounted in deaerated araldite and presented as a polished section to the electron beam. The photomicrographs taken are shown in the following plates (3.1-3.19). Selected alteration conditions noted in Sections 3.2 and 3.3 are represented and the photomicrographs are grouped together for convenience even though

some are discussed elsewhere.

The photomicrographs show the differences possible in the nature of the attack by the reagents on the kimberlite as well as the type of alteration product. The plates are ordered according to the experimental procedures followed ranging from the sulphuric acid treatments to those conditions which induce a maximum amount of degradation through mineralogical transformations as well as acid leaching (i.e. Plates 3.15-19).

Plates 3.1 - 3.19 Scanning electron microphotographs

The following plates illustrate various aspects of the alteration of kimberlite. The effect of various sets of reagents on a 10 g -1180+850 µm feed at 70-100°C are presented here :

SEM 1 : Sulphuric acid, initial concentration 6.3M, 70°C, 24 h

SEM 2 : Sulphuric acid, initial concentration 3.6M, 70°C, 24 h

SEM 3 : Sulphuric acid, initial concentration 0.31M, 100°C, 7 h

SEM 4 : Hydrochloric acid, initial concentration 0.31M, 100°C, 7 h

SEM 5 : Hydrochloric acid, initial concentration 1.5M, 100°C, 7 h

SEM 6 : As SEM 5, 2 g hydrated aluminium chloride charge added

An approximate scale is indicated by the black bar on the bottom of each plate.

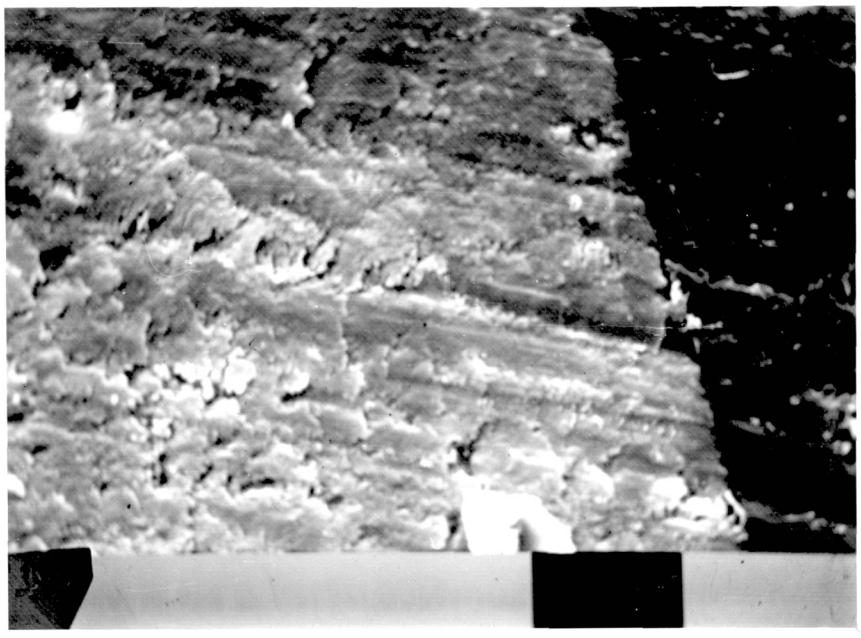


Plate 3.1 Unaltered head x8000. The unreacted kimberlite (grey) forms a distinct edge with the araldite (black) in which the particles were mounted.

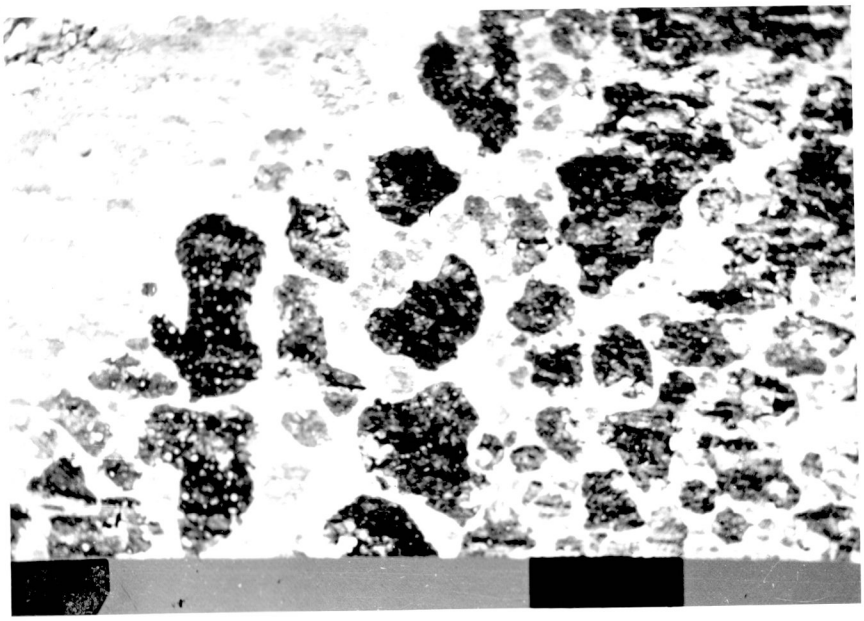


Plate 3.2 SEM 1 residual +75 fraction x 2000. Lower magnifications yield more confused views of the sectioned kimberlite grains. This plate, however, shows an amorphous product (grey) contrasting with the unreacted kimberlite grains (dark)

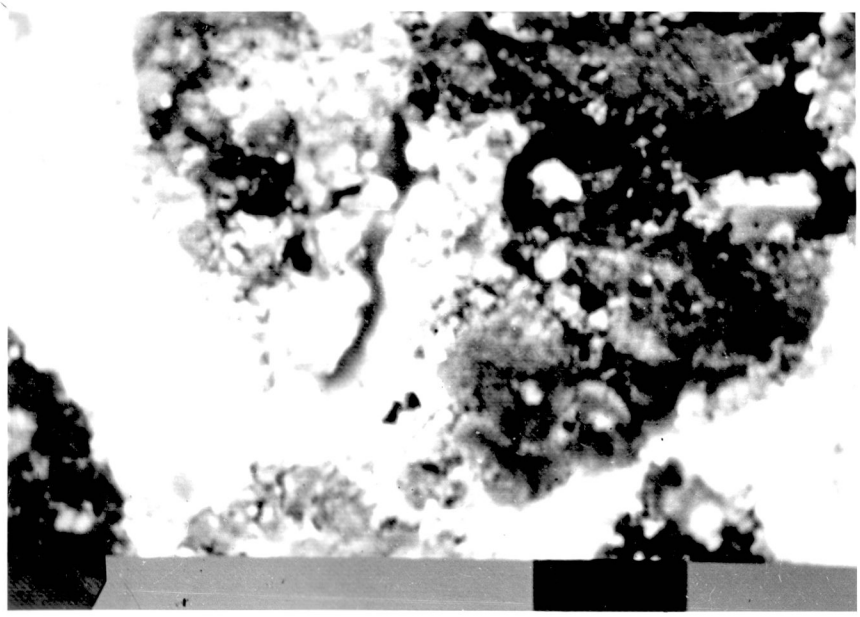


Plate 3.3 SEM 1 residual +75 fraction x 20000. Cavities are seen in this specimen and infilled by gypsum (left). Elsewhere the residual kimberlite appears as glassy or dull grey amorphous particulate aggregates.

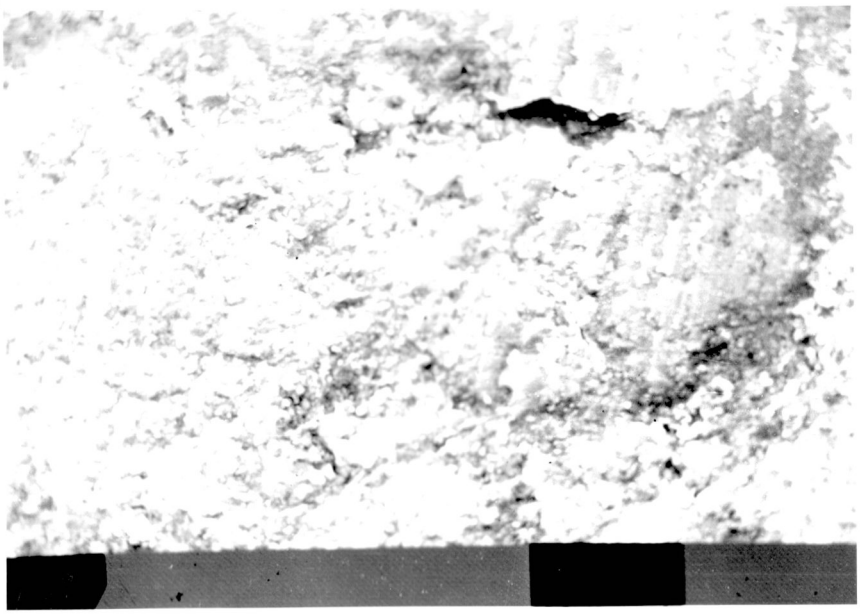


Plate 3.4 SEM 2 residual +75 fraction x 2000. Intensely altered kimberlite. The grain is just visible against the araldite mound and is covered with white sulphate precipitation products.

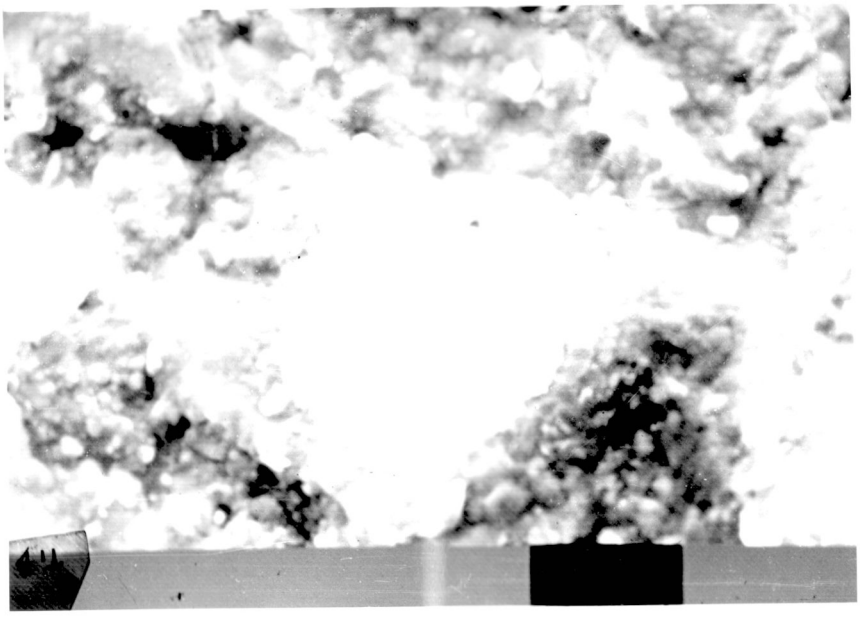


Plate 3.5 SEM 2 residual +75 fraction x 20000. Here the kimberlite has been reduced to a gelatinous, amorphous agglomerate cemented by large crystallites of gypsum (white).



Plate 3.6 SEM 3 : residual +75 µm fraction x 200. No evidence of bulk alteration (cf. Plate 3.9)

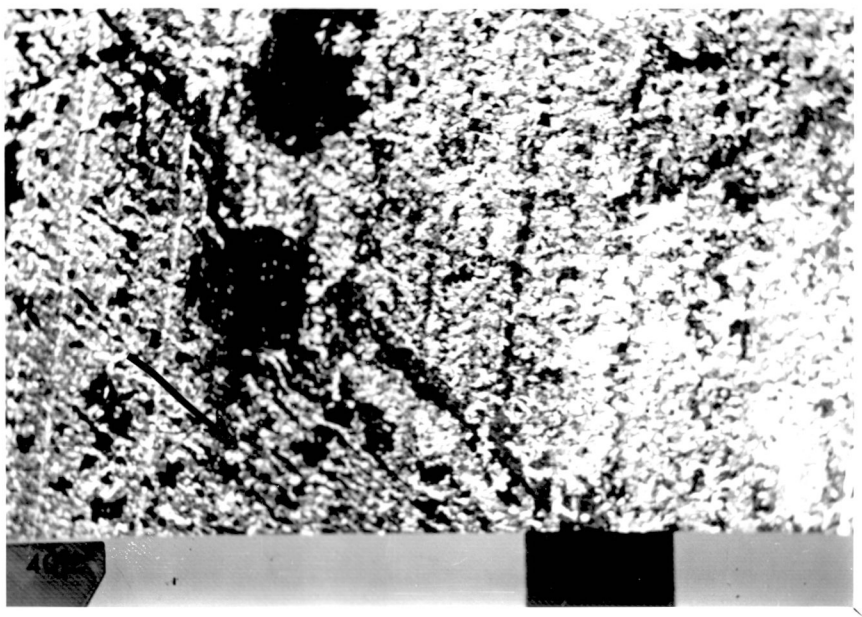


Plate 3.7 SEM 3 : residual +75 µm fraction x 2000. The pitted surface of the sectioned grain can be seen. In the lower left hand corner the pit marks are all orientated in the same direction ⟶ , whereas elsewhere no such pattern is seen. This reflects the heterogeneous nature of the dissolution reactions.

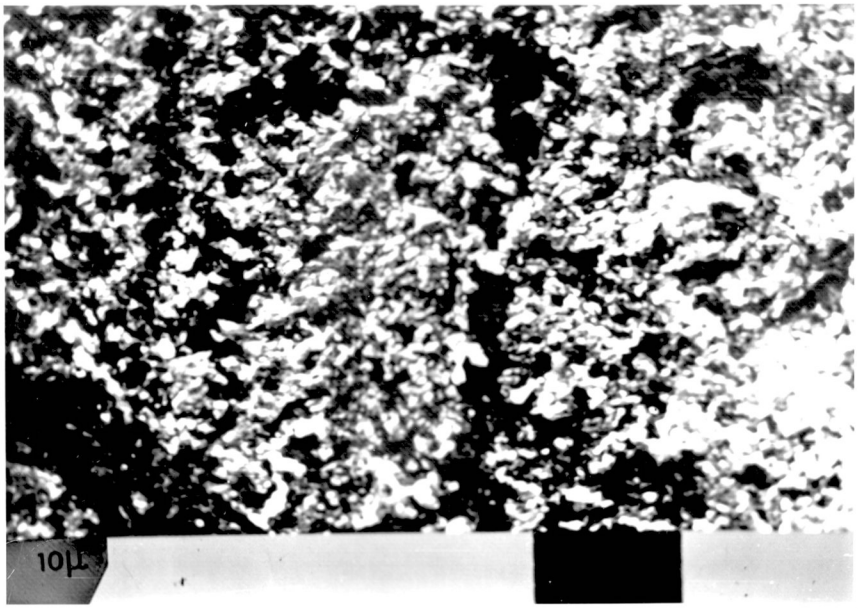


Plate 3.8 SEM 3 : residual +75 µm fraction x 8000. The higher magnification shows the residual kimberlite grains (grey) to be separated by cavities produced by the dissolution reaction. White gypsum crystallites are present in some cavities. The cavities are larger in certain directions indicating pathways along which the reaction was facilitated.

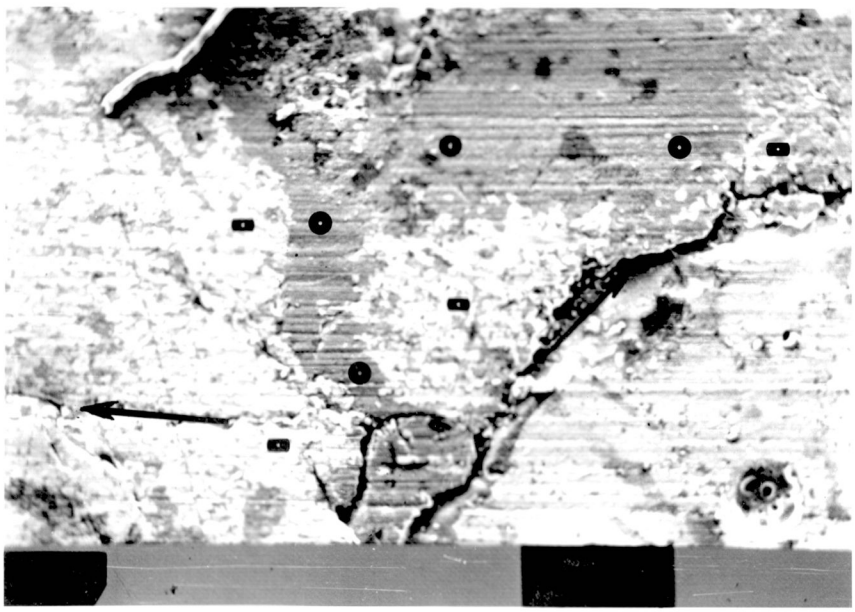


Plate 3.9 SEM 4 : residual +75 µm fraction x 800. Here the unaltered kimberlite (●) contrasts with the alteration product (▬) with which it has an intimate contact. Dissolution channels are indicated thus :⟶

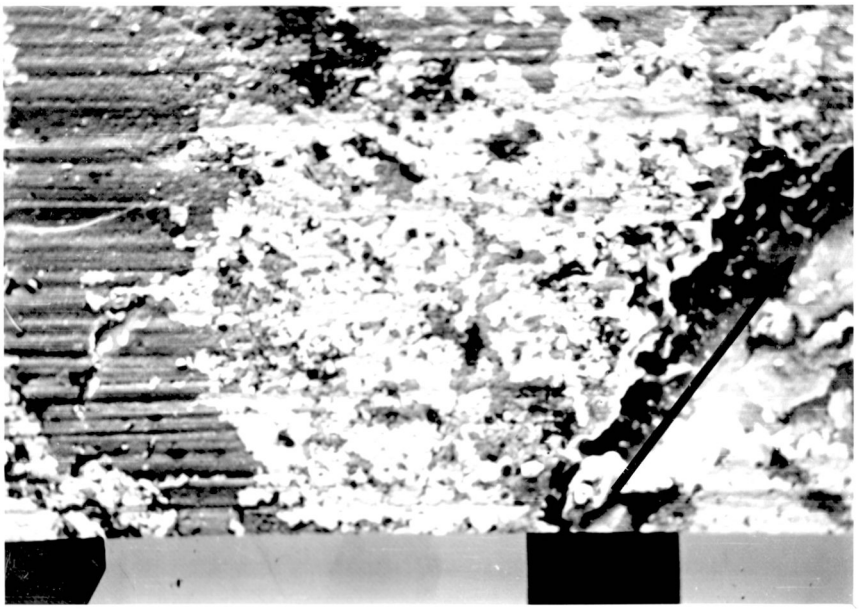


Plate 3.10 SEM 4 : residual +75 µm fraction x 2000. Lathe shaped minerals can be seen to develop on the edge of the reaction channel (⟶). The altered kimberlite is dissected by subsidiary channels and cavities.

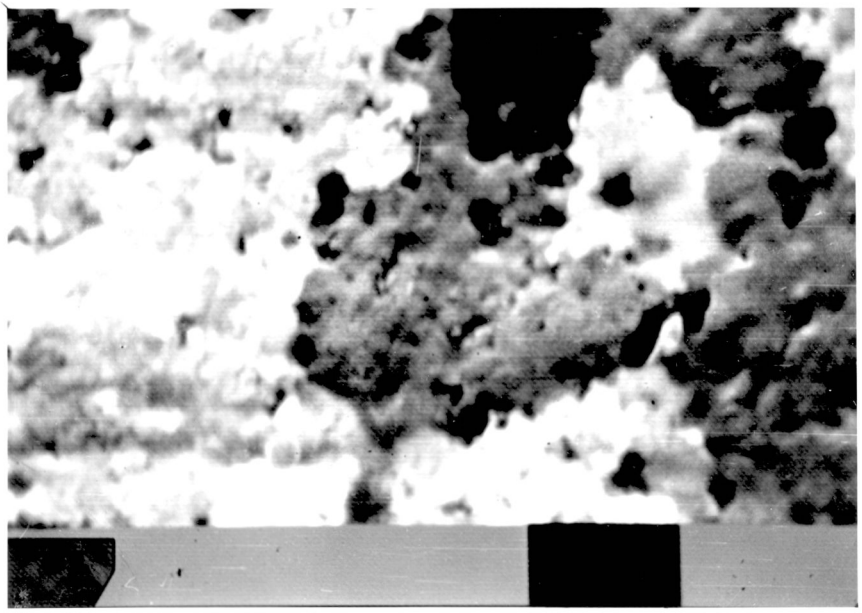


Plate 3.11 SEM 4 : residual +75 µm fraction x 20000. An example of a dissolution cavity in the kimberlite. No distinct phyllosilicate crystallization visible, however (cf. Plates 3.12-19)

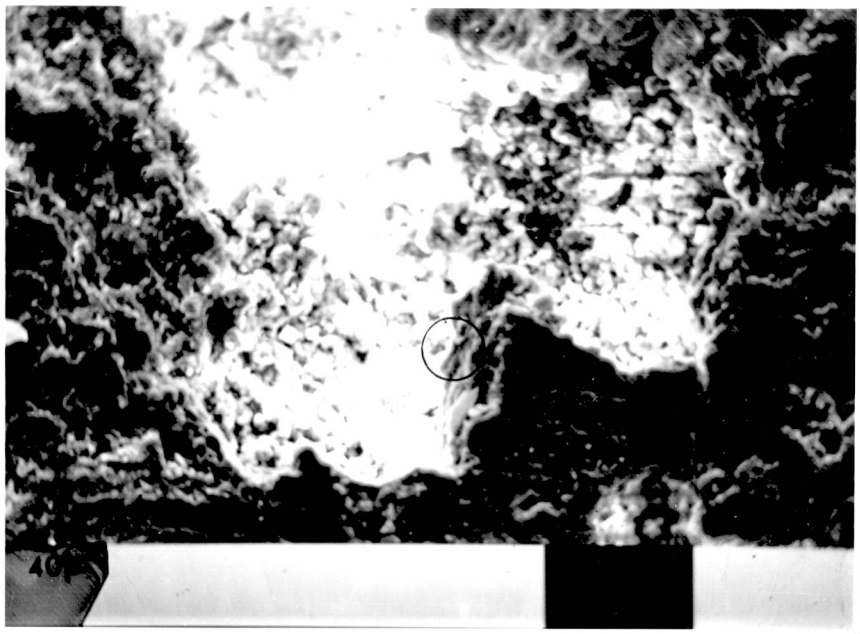


Plate 3.12 SEM 5 : residual +75 µm fraction x 2000. In contrast to Plate 3.1, white phyllosilicates crystallize in cavities produced by acid attack, at particle edge. At lower magnifications, a number of these cavities are observed on the particle edge as seen in Plate 3.15.

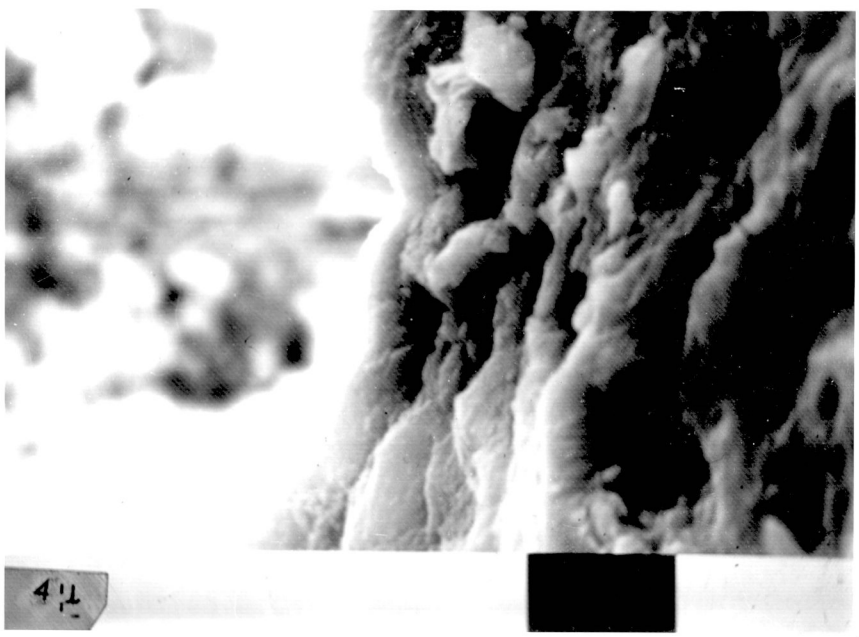


Plate 3.13 SEM 5 : residual +75 µm fraction x 20000. Magnification of reaction edge, circled in Plate 3.12 above. This shows the progressive development of phyllosilicate minerals from the kimberlite surface i.e. within the dissolution reaction zone.

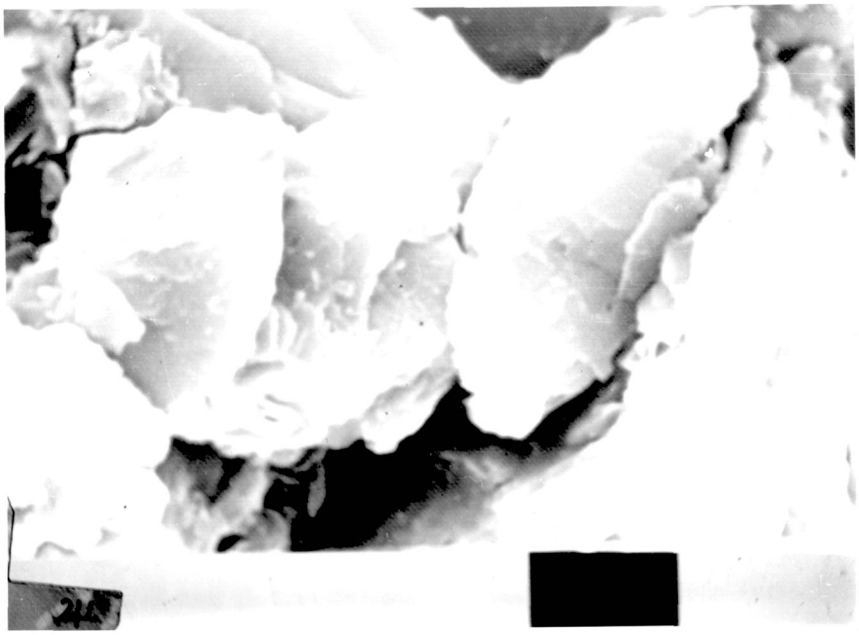


Plate 3.14 SEM 5 : residual +75 µm fraction x 40000. Free phyllosilicate minerals as present in the +75 µm fraction.

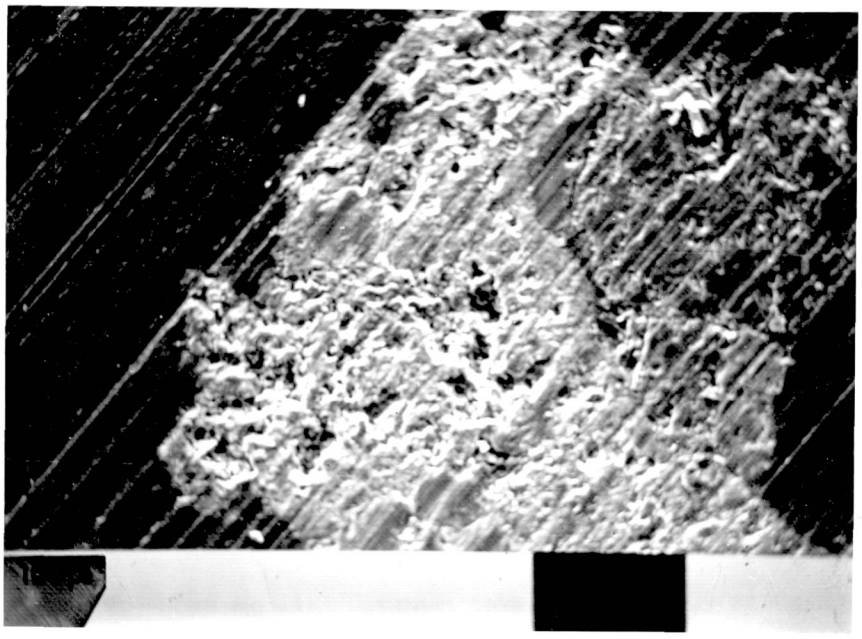


Plate 3.15 SEM 6 : residual +75 µm fraction x 800. This illustrates the localised nature of the attack of the reagents on the kimberlite. As shown, regions of extensive alteration border those which remain comparatively unreacted. A reacted layer concentric with the particle edge does not necessarily develop.

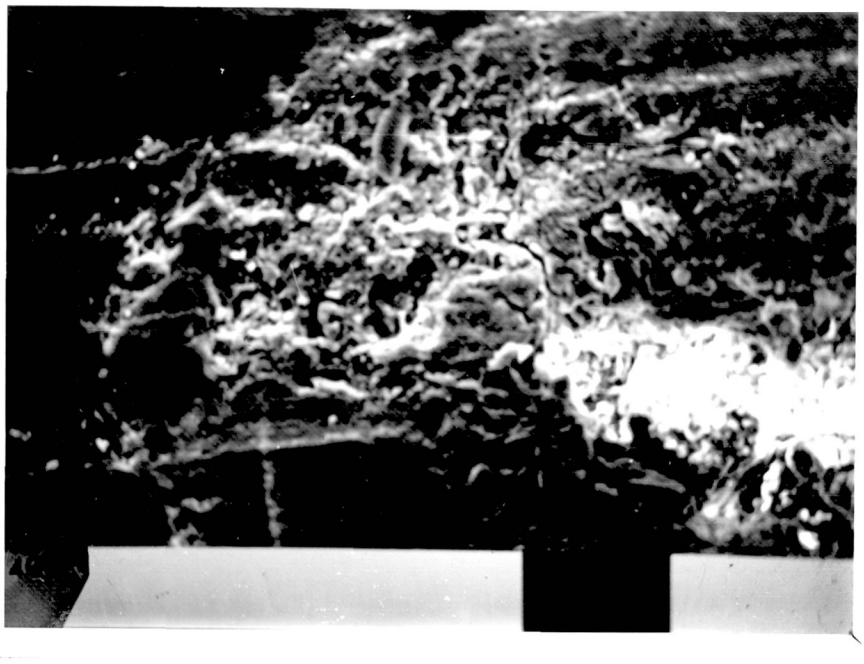


Plate 3.16 SEM 6 : residual +75 µm fraction x 2000. Penetration by the species Al^{3+} and H^{+} into the interior of a particle (no such case observed for SEM 5). Crystallization of clay minerals can occur within the particle.

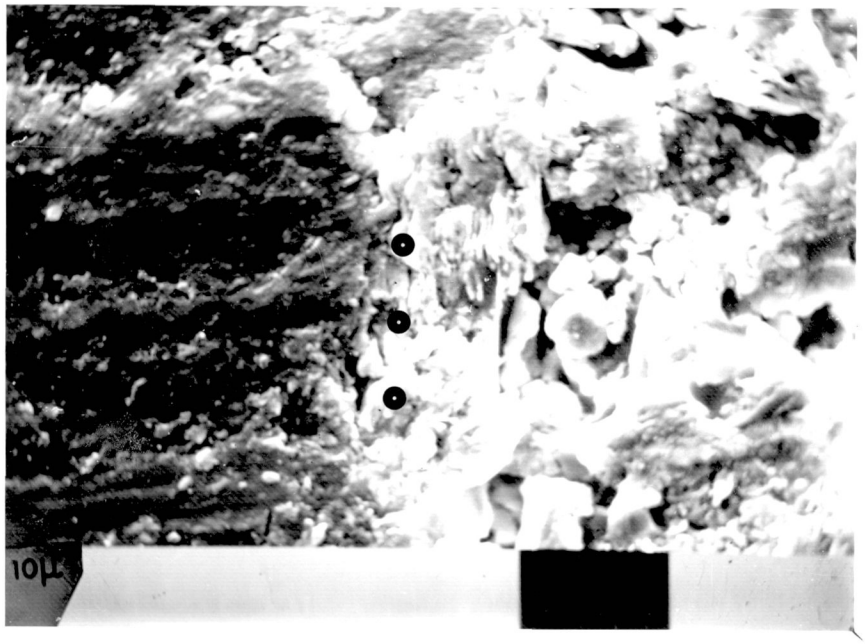


Plate 3.17 SEM 6 : residual +75 µm fraction x 8000. Development of phyllosilicates in contact with unreacted rock. A transitionary layer can be seen, as indicated : ⊙



Plate 3.18 SEM 6 : residual +75 µm fraction x 80000. Formation of phyllosilicate layers within transitionary layer adjacent to the reacted kimberlite surface (Plate 3.17).

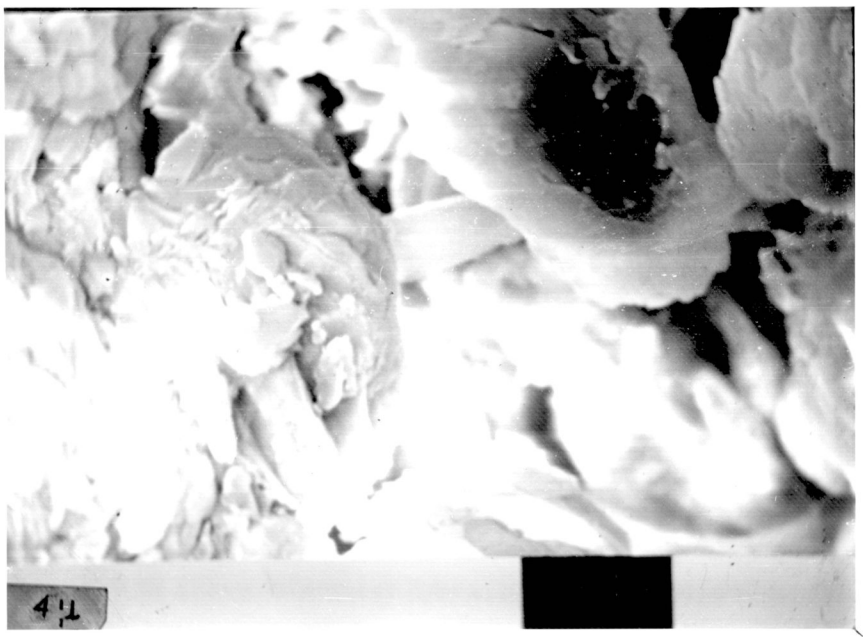


Plate 3.19 SEM 6 : residual +75 µm x 20000. Individual clay mineral crystallites. The concentration of these phases clearly exceeded that observed in SEM 5.

3.4 Reactions with 0.31M Hydrochloric Acid at 100-350°C

Preliminary testwork indicated that the reactions described in Section 3.3 were about 90% complete after 7 h at 100°C. To ensure more complete equilibration and to investigate the nature of other phases formed at elevated temperatures, specialised pressurised equipment was employed. The testwork described below relates to reactions carried out in hydrochloric acid media. Sulphuric acid was not used as no phyllosilicate formation had been previously observed in sulphate media (Section 3.3.2-4). The acid concentration employed, 0.31M H^+, was the highest possible - as larger values resulted in the metal apparatus involved being attacked at the higher temperatures. The reaction conditions differed from those in Section 3.3.5 in respect of the overall mass of feed and reagents and method of agitation. However, the systems used here and in Section 3.3 were comparable.

3.4.1 Apparatus and procedures

To investigate the effect of increased temperature on the alteration of kimberlite the apparatus illustrated in Plates 3.20 and 3.21 were used.[245] In a typical test, 2.5 g of -1180+850 µm kimberlite was placed in each of the four nickel-steel bombs shown in Plate 3.21. A total volume of 10 ml containing 0.5-2 g hydrated aluminium chloride (and adjusted to pH 0.5 using hydrochloric acid) was added and the bombs closed. The feed/reagent ratio was therefore equal to that used in the previous testwork, although the total masses were reduced by a factor of 4.

The bombs were concentrically mounted around the spindle (as shown) and driven at 36 rpm by a Parvalux 186W DC motor. The autoclave chamber was moved into position over the bombs and the assembly heated to desired temperature over 1 hour, using a hot air blower controlled by a Zenith 0-240V variac. Including the warmup time, the overall reaction

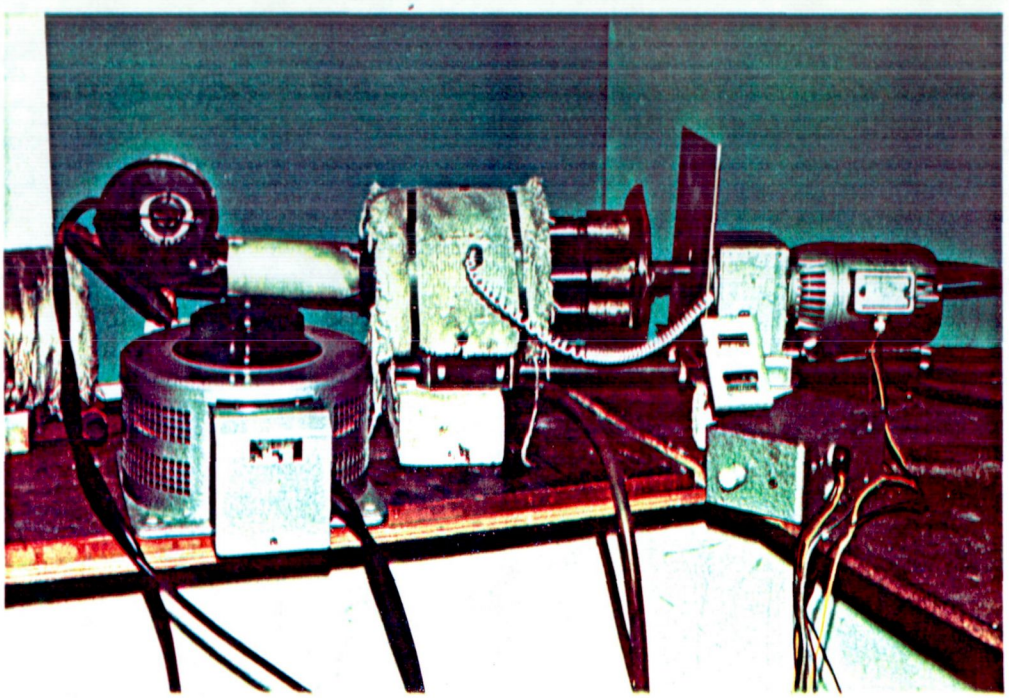


Plate 3.20 Autoclave apparatus used for testwork at 100-350°C

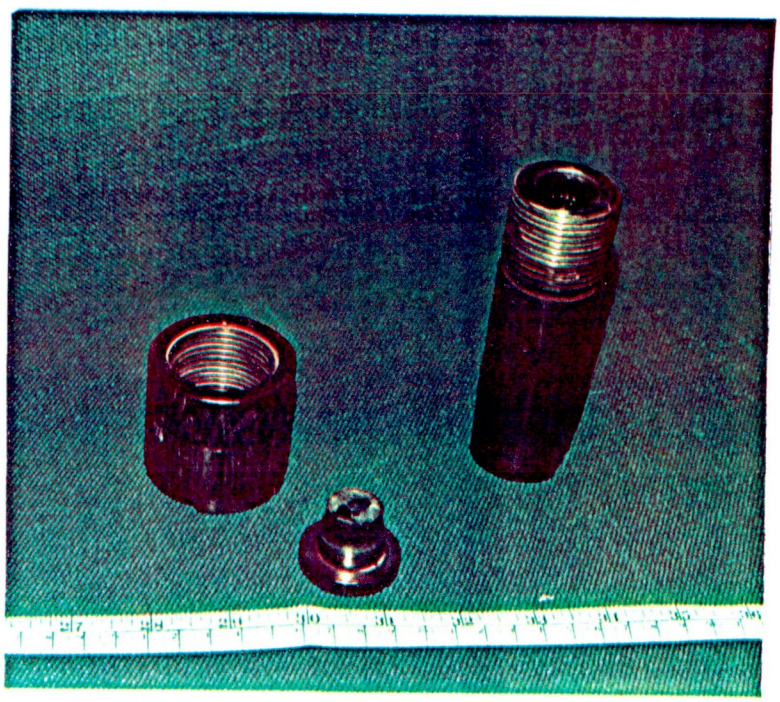


Plate 3.21 Detail of autoclave bomb.

time was 8 hours, the variac being adjusted throughout the experiment such that the temperature was ± 5% of the desired value. At the end of the reaction, the bombs were allowed to cool overnight and were carefully opened. The pH of the solution was recorded and the solids separation/AAS analytical procedure (Section 3.2.1) was then followed as before. In certain instances, the equilibrium pH was modified, 3.5 h after reaching the required reaction temperature by rapidly opening the bombs, adding a few drops of concentrated ammonia solution and quickly re-establishing the previous conditions for a further 3.5 h. In all these experiments, pressure remained an unrecorded variable, increasing with temperature in the range 0.1-10 MPa (as deduced from steam tables[246]).

This procedure employed at 100°C produced results comparable with those using the hotplate/stirrer apparatus at 100°C, as measured by the DOA and residual ion concentrations.

3.4.2 Results : Phase diagrams in the Al^{3+}-H^{+} system II : Initial acid concentration 0.31M at 100-350°C

Three phase predominance diagrams were constructed employing similar procedures to those described in Section 3.3.5 except that temperature replaced pH as the abscissa. Each diagram corresponded to a different pH regime. The first phase diagram described equilibria taking place without pH adjustment (terminal pH 2-5) and the two others where the pH attained values in the ranges pH 5-7 and pH 7-8 after adjustment. Of these, the first exhibited the greatest variety of crystalline forms and is shown in Figure 3.4.1.

Six regions of crystallisation were recognised from XRD and supplementary potassium saturation and glycolation techniques.[198-200] Amorphous hydrated oxides were formed at the lower temperatures (100-

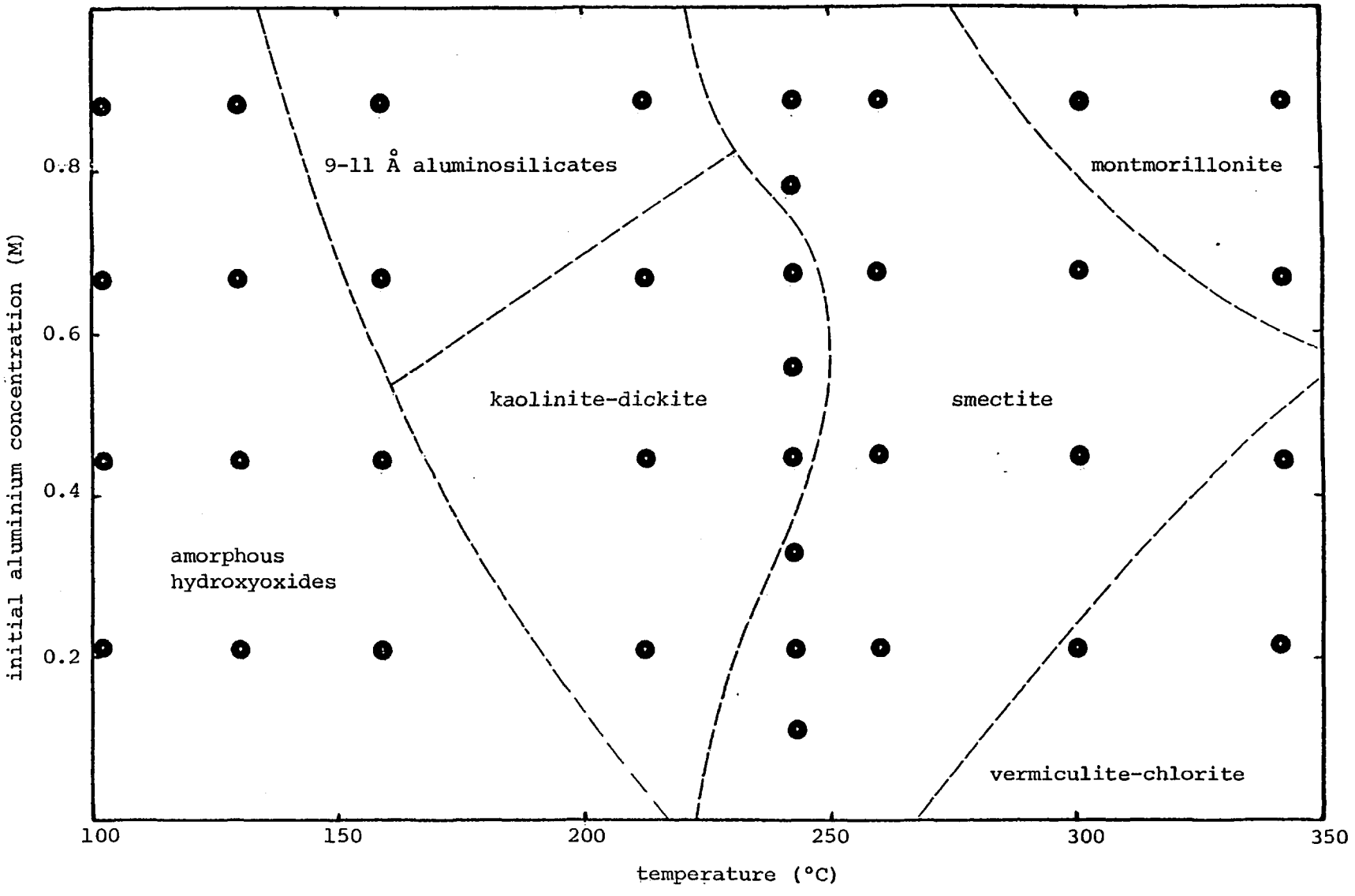


Figure 3.4.1 Phase predominance diagram showing the influence of initial aluminium concentration and the temperature on the nature of the -75 μm product formed after 8 h total reaction time, initial acid concentration being 0.31M.

150°C), though at higher aluminium concentrations poorly crystalline 9-11 Å aluminosilicate mineralisation could also be discerned (Figure 3.4.2a). This region in the figure corresponded to the amorphous region immediately to the right of the pH 3-5 line in Figure 3.3.9. A central portion in the figure is evident (at 170-250°C) in which the main products are 7 Å dioctahedral kandites, namely interlayered kaolinite and dickite (a good example of which is shown in Figure 3.4.2b). The portion grades into that at the higher temperatures, (250-350°C) where products consist mainly of vermiculite-smectite with kaolinite and dickite. These in turn grade into chlorite-vermiculites at low aluminium concentrations and montmorillonites at high aluminium concentrations at 270-350°C (Figure 3.4.2c,d). In general, the crystallinity of the phases improved markedly with temperature, as indicated by the well-defined peaks in the diffractograms given in Figure 3.4.2b-d.

The residual ion assays were consistent with the above observations. At low aluminium concentrations (∿ 0.1-0.4M) magnesium and iron concentrations progressively increased in the solution phase reaching a maximum at 200°C. Above this temperature, smaller concentrations were recorded as the -75μm became progressively more chloritic. At higher aluminium concentrations, the iron and magnesium concentration continued to increase above 200°C as dioctahedral smectites crystallised. The extent of degradation throughout the rock mass was reflected by the DOA and calcium concentration in the residual solution. The former ranged from 16% at 100°C, 0.2M Al^{3+}, to 42% at 350°C, 0.88M Al^{3+}. Calcium analysis inferred that 60-100% of the residual +75 μm fraction had been affected by the solutions. This is discussed later, with reference to reaction mechanisms.

Trends in the IR analyses of the -75 μm products, were not

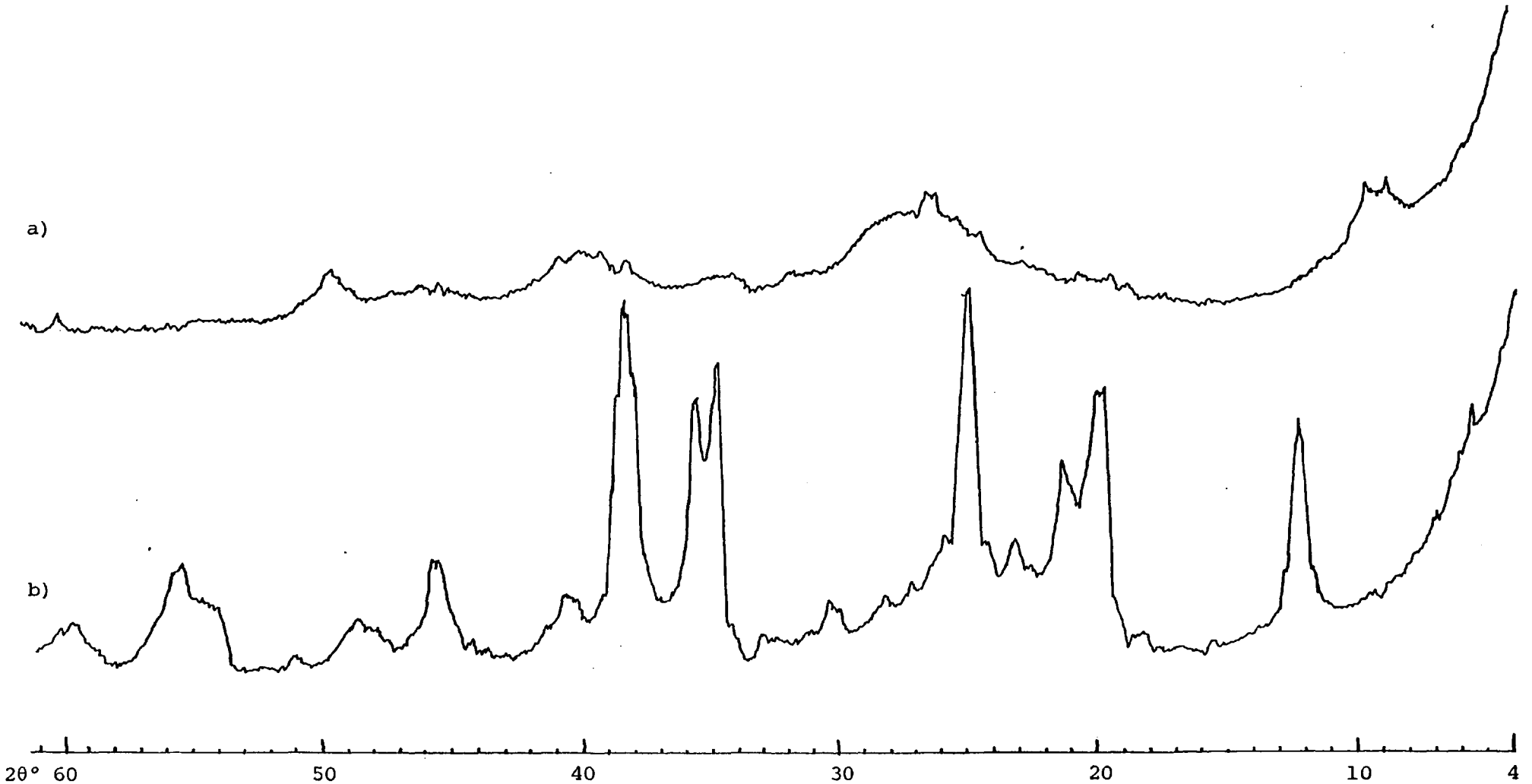


Figure 3.4.2 X-ray diffractograms of selected -75 μm products as featured in Figure 3.4.1
a) 9-11 Å aluminosilicate
b) kaolinite-dickite

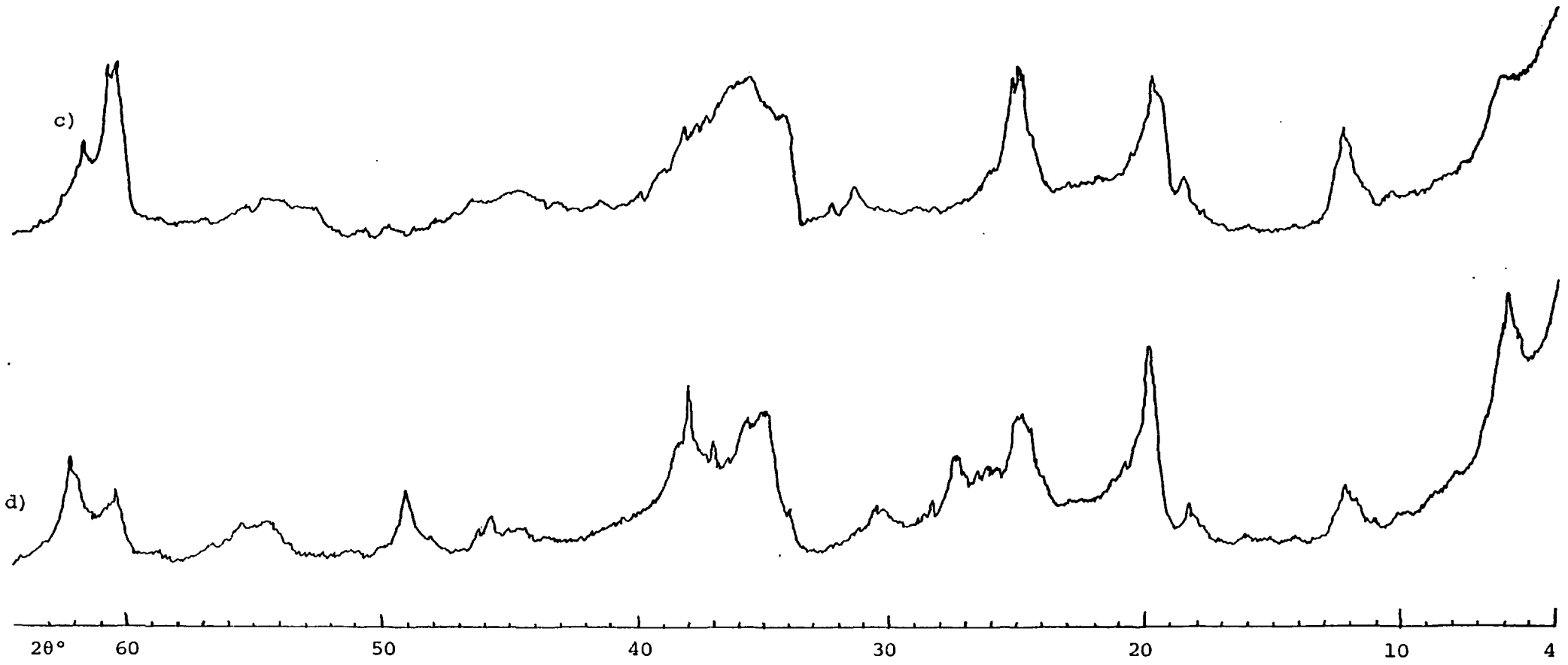


Figure 3.4.2 X-ray diffractograms for selected -75 µm products as featured in Figure 3.4.1.
c) vermiculite-chlorite
d) montmorillonite

immediately clear, partly owing to the general structural similarity of clay phases, and aluminium hydroxyoxide precipitation (due to the equilibrium pH exceeding 3.2) causing a lack of definition in the peaks in certain cases. Comparison between IR and the XRD results facilitated the interpretation in the former. Examples of the infra-red spectra are given in Figure 3.4.3a-d and correspond to the XRD traces recorded in the previous figure.

The broad square-shaped peaks in Figure 3.4.3a (with accentuated shoulders at 1200, 940, 780 and 350 cm^{-1}) were assumed to characterise the 2:1 9Å type mineral synthesised at 150°C. These shouldered peaks indicated a high concentration of Al-OH bonds associated with a silicon-rich basal structure which would be expected from the high aluminium concentrations applied to the system.[139] The IR spectrum in Figure 3.4.3b was similar to that of well-crystallised kaolinite (reported in the literature[217,230]) but contained less well defined peaks. Figures 3.4.3c and d represent vermiculite-chlorites and montmorillonite type smectites, respectively. The former exhibit a strong shouldered peak at 690 cm^{-1} which appears to be characteristic of Mg-OH bonding. The subsequent inference of a dominantly trioctahedral structure was confirmed from XRD evidence (1.53 Å). A similar shoulder was noted in the IR traces of chlorites synthesised at 100°C (Figure 3.3.9) but their poorer crystalline state caused the infra-red peak intensity to be reduced. In contrast to this trace, Figure 3.4.3d showed the development of peaks at 3100 cm^{-1}, 785 cm^{-1}, 730 cm^{-1} characteristic of smectites.

Raising the pH midway through the reaction resulted in widespread precipitation of the ions as hydroxyoxides and septechlorites. No separate phase regions could be discerned. Amesite and chamosites were the principal septechlorites formed at 150-350°C, though very

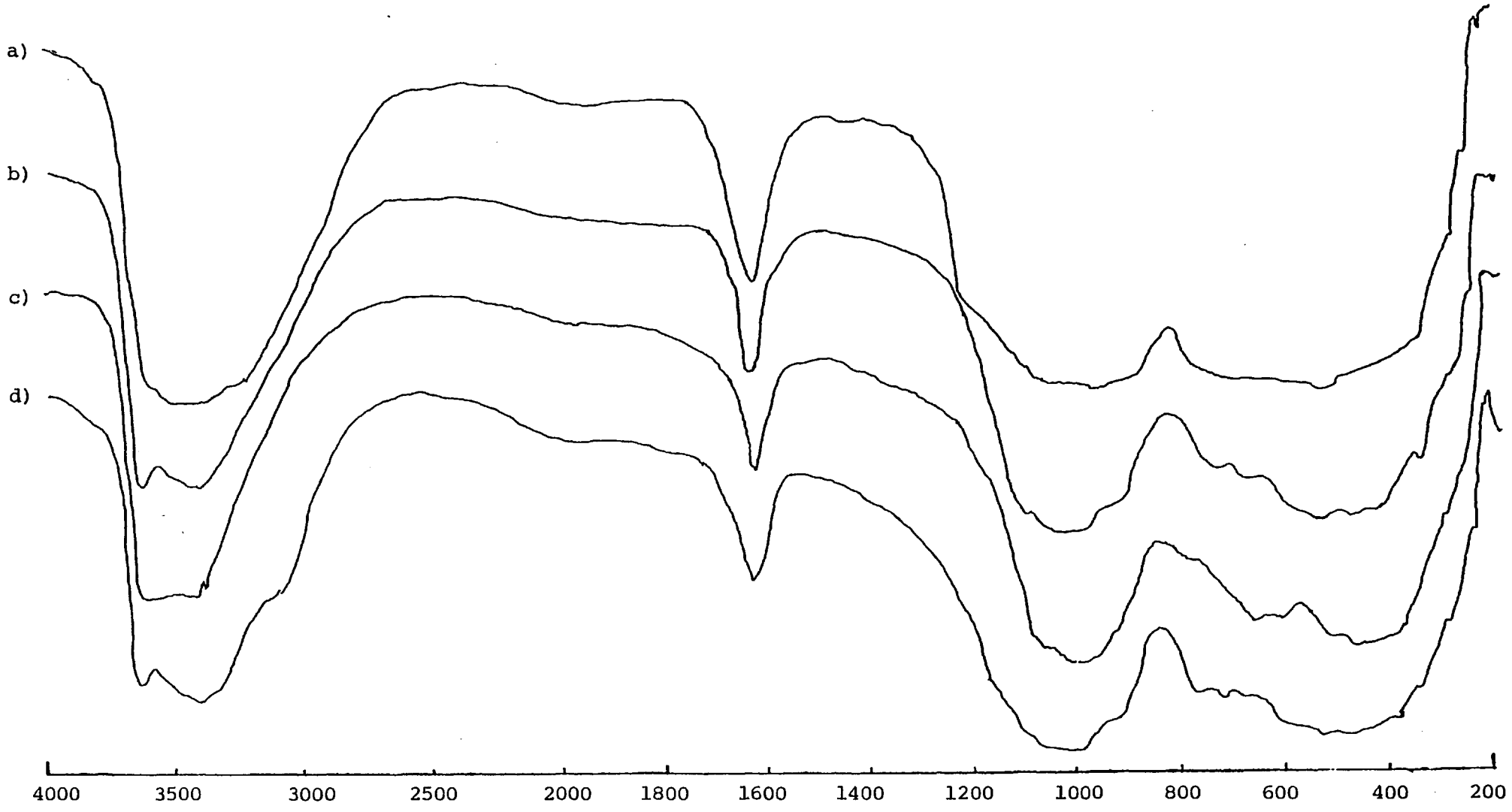


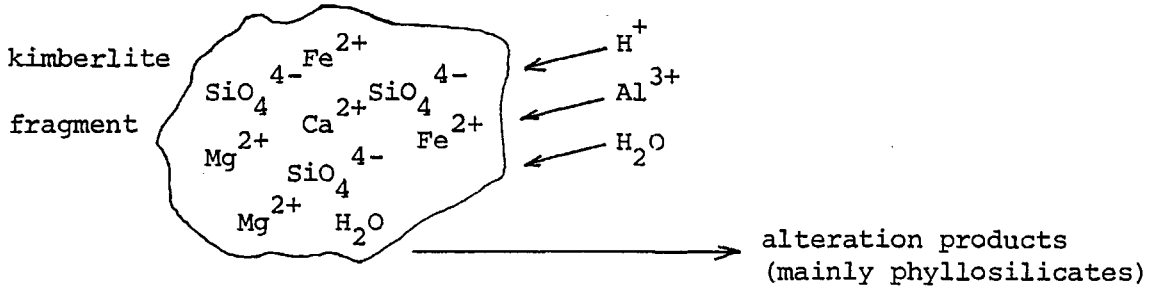
Figure 3.4.3 Infra-red traces for selected -75 μm products featured in Figure 3.4.1
a) 9-11 Å aluminosilicate
b) kaolinite-dickite
c) vermiculite-chlorite
d) montmorillonite

poorly crystalline 10 Å aluminosilicates appeared to develop at lower temperatures at pHs greater than 7. For these reasons the other two phase diagrams mentioned are not considered in detail.

3.5 Discussion : Comparison of Experimental Results with Theoretical Reaction Equilibria and Phase Diagrams

The previous sections have described the various experimental conditions under which the alteration of kimberlites to form clay minerals may be effected. The aim of this section is to discuss the different reactions that have been observed in comparison with theory. As details of reaction path are not discussed until Chapter 4 the formation of clay minerals is discussed in simple terms : namely, the inter-reaction of ionic species. Two forms of presentation are described, each based on averaged clay structural formulae deduced from products analysed using Program CECPM (Section 2.5.4).

a) The addition of hydrogen and aluminium ions to a system where the minerals are considered as solid aggregates of the constituent ionic species : Mg^{2+}, Fe^{2+}, Fe^{3+}, Ca^{2+} and SiO_4^{4-} and water as shown in the diagram :



In the reaction equilibria that follow (equations 3.5.1-12, 3.5.17-24) species considered to be part of the mineral lattices are shown in inverted commas i.e. 'Mg^{2+}', 'SiO_4^{4-}' etc. The overall

equilibrium considers the ion requirements of each clay phase - the aluminium, hydrogen and water (as reagents) and the ionic species derived from the kimberlite. These reactions (discussed in Sections 3.5.1 and 3.5.2) do not assume that the ions react in the proportions of, or originate entirely from, a specific mineral. The equilibria permitted comparison between the ion requirements of each product phase and, subsequently, a partial theoretical interpretation of Figures 3.3.9, 3.3.10, 3.4.1; and it was for these purposes that they were designed.

b) The formation of phyllosilicate minerals from solution are considered. This presentation assumes an initial hydrolysis reaction to have taken place and the constituent ions of the kimberlite minerals to have entered solution as Mg^{2+}, Fe^{2+}, Fe^{3+}, Ca^{2+} and $Si(OH)_4$. This allows mineral-solution phase diagrams to be constructed for a thermodynamic description of the synthesis of the phyllosilicate minerals (as given in Sections 3.5.3 and 3.5.4).

3.5.1 Phase diagrams in the Al^{3+}-H^{+} system III : Reaction equilibria at 100°C

These equilibria considered the formation of the phyllosilicates shown in Figures 3.3.9 and 3.3.10, from the reaction of aluminium and hydrogen ions with the kimberlite. Equilibria which relate exclusively to Figure 3.3.9 are equations 3.5.6 and 3.5.12. Equations 3.5.5 and 3.5.7 relate only to Figure 3.3.10.

The equilibria represent the different products expected to predominate at particular ratios of solution reactants, based on reactant ion abundance. The formulae of most of the clay minerals arise directly from computed phase analyses of -75 μm products using Program

CECPM (Section 2.5.4). Exception were the septechlorites, which were noted (by XRD) to form at pH values higher than those considered in Program CECPM.

$$1.2\ Al^{3+} + 6.64\ H^{+} + 4.98\ H_2O \leftrightarrow Al_{.78}\ Mg_{1.19}\ Fe_{.57}$$
$$1.19\ 'Mg^{2+}' + 0.57\ 'Fe^{3+}' + 3.58\ 'SiO_4^{4-}' \quad (Al_{.42}\ Si_{3.58})\ O_{10}\ (OH)_2\ 7.3\ H_2O$$
9-11 Å aluminosilicate I (3.5.1)

$$1.6\ Al^{3+} + 2\ H^{+} + H_2O + \leftrightarrow Al_{1.6}\ Mg_{.3}\ Fe_{.3}\ Si_2O_5(OH)_4$$
$$0.3\ 'Mg^{2+}' + 0.3\ 'Fe^{2+}' + 2\ 'SiO_4^{4-}'$$ aluminian serpentine (3.5.2)

$$0.3\ Al^{3+} + 2\ H^{+} + H_2O + 1.25\ 'Mg^{2+}' \leftrightarrow Al_{.3}\ (Mg_{1.25}\ Fe_{1.25}\ Si_2O_5(OH)_4$$
$$1.25\ 'Fe^{2+}' + 2\ 'SiO_4^{4-}'$$ magnesian serpentine (3.5.3)

$$0.93\ Al^{3+} + 3.10\ H^{+} + 2.86\ H_2O + \leftrightarrow Ca_{.16}\ Al_{.09}\ Mg_{2.42}\ Fe_{.53}\ (Al_{.84}Si_{3.16})$$
$$2.42\ 'Mg^{2+}' + 0.53\ 'Fe^{3+}' + \quad O_{10}\ (OH)_2\ 3.6\ H_2O$$
$$0.16\ 'Ca^{2+}' + 3.16\ 'SiO_4^{4-}'$$ (saponite) smectite I (3.5.4)

$$1.22\ Al^{3+} + 2.78\ H^{+} + 4\ H_2O + \leftrightarrow Ca_{.09}\ Al_{.26}\ Mg_{2.58}\ Fe_{.28}(Al_{.96}Si_{3.04})$$
$$2.58\ Mg^{2+} + 0.28\ 'Fe^{3+}' + 0.09\ 'Ca^{2+}' \quad O_{10}\ (OH)_2\ 4.3\ H_2O$$
$$+ 3.04\ 'SiO_4^{4-}'$$ vermiculite II (3.5.5)

$$1.28\ Al^{3+} + 0.32\ H^{+} + 4.84\ H_2O + \leftrightarrow Ca_{.28}\ Al_{.08}\ Mg_{2.51}\ Fe_{.44}\ (Al_{1.21}Si_{2.79})$$
$$2.51'Mg^{2+}' + 0.44\ 'Fe^{3+}' + \quad O_{10}\ (OH)_2\ 4.6\ H_2O$$
$$0.28\ 'Ca^{2+}' + 2.79\ 'SiO_4^{4-}'$$ vermiculite I (3.5.6)

$$1.73\ Al^{3+} + 4.16\ H_2O + 2.76\ 'Mg^{2+}' + 1.79\ 'Fe^{2+}' + 3.46\ 'SiO_4^{4-}' \leftrightarrow Al_{1.19}\ Mg_{2.76}\ Fe_{1.79}\ (Al_{.54}Si_{3.46})\ O_{10}\ (OH)_8 \text{ chlorite II} + 0.45\ H^+ \quad (3.5.7)$$

$$3.42\ Al^{3+} + 9.3\ H_2O + 0.5\ 'Mg^{2+}' + 0.25\ 'Fe^{2+}' + 2.5\ 'SiO_4^{4-}' \leftrightarrow Al_{1.92}\ Mg_{.50}\ Fe_{.25}\ (Al_{1.5}Si_{2.5})\ O_{10}\ (OH)_2\ 7.3\ H_2O \text{ 9-11 Å aluminosilicate II} + 2\ H^+ \quad (3.5.8)$$

$$Al^{3+} + .3\ OH^- \leftrightarrow Al\ (OH)_3 \text{ gibbsite} \quad (3.5.9)$$

$$4\ Al^{3+} + 4\ OH^- + 2\ H_2O + 2\ (Mg,Fe)^{2+} + 3\ SiO_4^{4-} \leftrightarrow Al_3\ (Mg, Fe)_2\ (Al\ Si_3)\ O_{10}\ (OH)_8 \text{ septechlorite-kandite I} \quad (3.5.10)$$

$$Al^{3+} + 4\ OH^- + 2\ H_2O + 6.5\ (Mg,Fe)^{2+} + 3\ SiO_4^{4-} \leftrightarrow (Mg,Fe)_{6.5}\ (Al\ Si_3)\ O_{10}\ (OH)_8 \text{ septechlorite-kandite II} \quad (3.5.11)$$

$$2.50\ Al^{3+} + 6.88\ H_2O + 4.04\ 'Mg^{2+}' + 0.73\ 'Fe^{2+}' + 2.78\ 'SiO_4^{4-}' \leftrightarrow Al_{1.28}\ Mg_{4.04}\ Fe_{.73}\ (Al_{1.22}\ Si_{2.78})\ O_{10}\ (OH)_8 \text{ chlorite I} + 5.76\ H^+ \quad (3.5.12)$$

The twelve equations are arranged in the order of decreasing stoichiometric hydrogen ion (or increasing hydroxyl ion) requirement per '$(Al,Si)_4\ O_{10}$' unit for the clay mineral structures. From the first six equations it can be deduced that smectites, aluminian serpentines, vermiculites and certain 9-11 Å phases were stable in acidic media, as found experimentally. Gibbsite and septechlorite kandites (equations 3.5.9-11) would be expected to precipitate at higher pH values. This was

also observed experimentally (Figures 3.3.9 and 10), these phases being stable in pH regimes 4 and above.

The reactions relating to the formation of chlorite and other 9-11 Å phases (equations 3.5.7, 3.5.9 and 3.5.12) either require alkaline conditions for their crystallization or generate hydrogen ions through their formation. As chlorites were detected in acidic pH regimes (Figures 3.3.9 and 3.3.10) it would appear that the latter applied in this case, the extra hydrogen ions generated being consumed through the formation of other clay phases, such as smectites.

Comparing the equations it became apparent that the majority of the reactions could be further distinguished from each other by the extent of aluminium substitution in the tetrahedral lattice. Indeed, it was evident that, as the extent of such substitution increased, the hydrogen ion requirement correspondingly decreased, as shown graphically in Figure 3.5.1.

The figure consists of two linear plots each point representing a datum deduced from one of the above equilibria. The plotted lines are parallel to each other, one linking points attributable to smectites, vermiculites and 9-11 Å phases, the other to chlorites, kandites, and septechlorites. It is suggested that the demarcation between the two plots relates to the nature of the fundamental chemical groupings of each mineral. Smectites, vermiculites and 9-11 Å phases are all based on the 2:1 (9 Å) layer lattice (Plate 1.7) whereas chlorite structures can be envisaged, from the point of view of chemical composition, to be multiples of the 1:1 (7 Å) layer lattice attributable to kandites and septechlorites (Plate 1.6). From the nature of the equilibria and experimental data afforded by infra-red spectroscopy it could be seen that the extent of tetrahedral substitution by aluminium increased to a certain extent with initial aluminium dosage, though this effect was

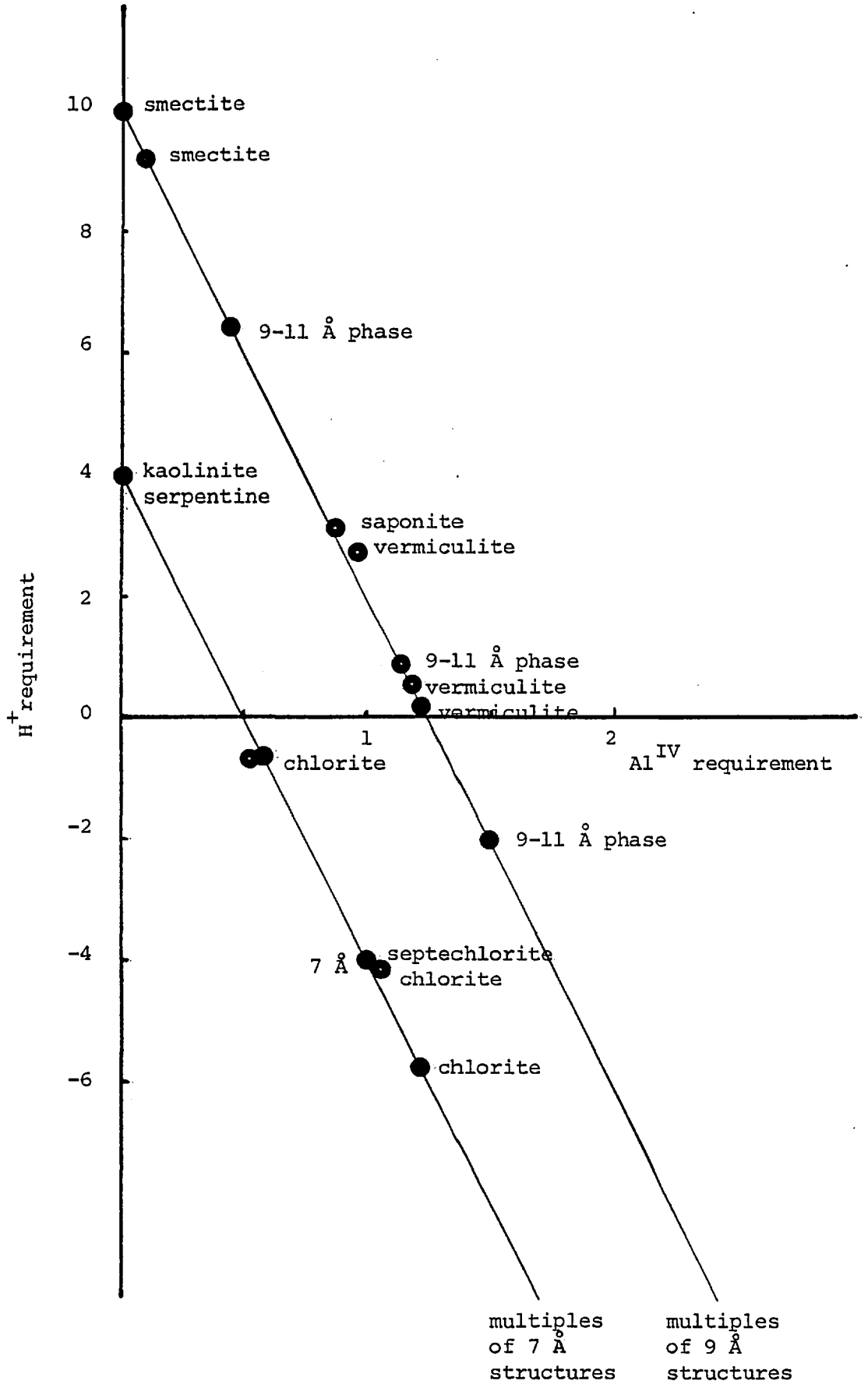


Figure 3.5.1 Relation between hydrogen ion requirement/ regeneration and the extent of aluminium substitution in the tetrahedral lattice for phyllosilicates.

partially negated by increased initial acid concentration (Figure 3.5.1).

These observations explain why a larger proportionate increase in the DOA and ion concentration levels was recorded where aluminium ions were added to dilute acid systems, (i.e. 0.31M H^+ : Figure 3.3.8) rather than to more concentrated ones (e.g. 1.5M H^+ : Figure 3.3.12). Namely, the extent of tetrahedral substitution, and hence hydrogen ion regeneration, was larger in the case of the former. The nature of the phyllosilicate phase formed was obviously dependent on the availability of the ionic species derived from the kimberlite, which was in turn dependent on the concentrations of aluminium and hydrogen ions added to the system. In the case of silicon, the number of ions needed for reaction was moderated by the presence of tetrahedrally coordinated aluminium ions. A relationship between silicon and hydrogen ion requirement is now deduced, From Figure 3.5.1 :

$$Al_{no}^{IV} = 0.497 - 0.1258\ H_{no} \text{ for 7 Å based phases}$$

$$Al_{no}^{IV} = 1.261 - 0.1258\ H_{no} \text{ for 9 Å based phases} \qquad (3.5.13)$$

where Al_{no}^{IV}, H_{no} are the number of tetrahedrally coordinated aluminium ions and the number of hydrogen ions, respectively.

Hence, as the sum of silicon (Si_{no}) and tetrahedrally coordinated aluminium ions is a constant, the following equations hold for phyllosilicates whose structure is based on the '$(Al,Si)_4O_{10}$' unit.

$$Si_{no} = 4 - Al_{no}^{IV}$$

$$\doteq 3.502 + 0.1258\ H_{no} \text{ for 7 Å based phases}$$

$$= 2.739 + 0.1258\ H_{no} \text{ for 9 Å based phases} \qquad (3.5.14)$$

A measure of the number of the octahedrally coordinated ions

(Mg^{2+},Fe^{2+},Fe^{3+},Ca^{2+}) in a phase may be obtained in terms of Al_{no} and H_{no} where Al_{no} is the sum of tetrahedrally coordinated (Al^{IV}_{no}) and octahedrally coordinated (Al^{VI}_{no}) aluminium ion requirements.

For 7 Å phases and chlorite, adopting a similar notation to that above for the species Mg^{2+},Fe^{2+},Fe^{3+},Ca^{2+}, the charge balance for the octahedral layer would be as follows :

$$2\ (Mg_{no} + Fe_{no} + Ca_{no}) + 3\ Al^{VI}_{no} = 12 + Al^{IV}_{no}$$

substituting $Al_{no} = Al^{VI}_{no} + Al^{IV}_{no}$ and equation 3.5.13.

$$2\ (Mg_{no} + Fe_{no} + Ca_{no}) = 14 - 3\ Al_{no} - 0.503\ H_{no} \qquad (3.5.15)$$

Similarly for 9 Å based phases

$$2\ (Mg_{no} + Ca_{no}) + 3\ Fe_{no} = 11.04 - 3\ Al_{no} - 0.503\ H_{no} \qquad (3.5.16)$$

These equations assume that the iron is present as the Fe^{2+} ion in kandites, septechlorites and chlorites, and as the Fe^{3+} ion in smectite, vermiculite and 9-11 Å phases.

These equations were used to construct the (theoretical) phase diagram shown in Figure 3.5.2 which indicates the regions of phyllosilicate stability in terms of Al_{no} and H_{no} stoichiometric requirement. Hydrogen ion requirements were calculated for the individual clay phases using equation 3.5.13. Other limits of formation (dotted in the diagram) were deduced from equations 3.5.15 and 3.5.16 using the structural formulae computed i.e. Mg_{no}, Fe_{no}, Ca_{no} and Al_{no}. A region of stability for a particular phase was hence indicated (a) by the cluster of theoretical phase points as arising from the Al_{no} and H_{no} requirements,

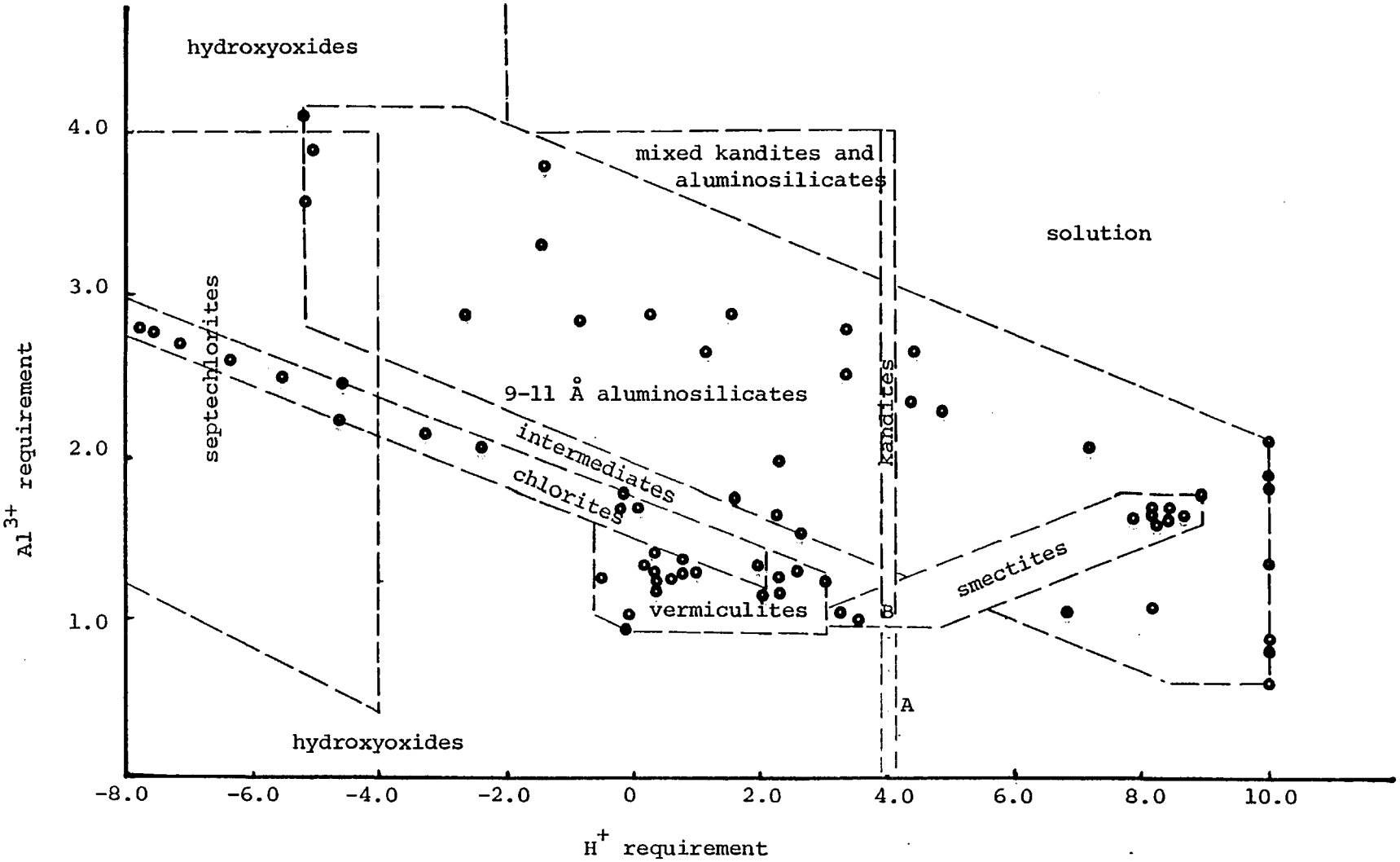


Figure 3.5.2 Theoretical relationship between the aluminium and hydrogen ion requirement and the nature of the product formed from the alteration of kimberlite.

and (b) the constraints imposed by the electroneutrality of the molecule (equations 3.5.15 and 3.5.16). Taking the 9-11 Å aluminosilicates as an example, the highest and lowest H_{no} recorded in this work were 10 and -5.2, respectively and for Al_{no}, 4.1 and 0.6 respectively. Using equations 3.5.16 diagonal parallel lines could be drawn through each point. Those lines bordering or enclosing all the experimental points marked the known limits of formation of the phase. Intermediate regions were assumed to represent amorphous phases and the remainder, solution phases (where H_{no} was high).

Figure 3.5.2 summarises the effect of aluminium and hydrogen ion requirement on the formation of phyllosilicates from kimberlite. It should be noted that the diagram is independent of temperature - products of similar composition were observed at temperatures greater than 100°C (i.e. up to 350°C). Furthermore the construction of the diagrams was independent of experimental work other than for the chemical compositions deduced for the phases of interest.

Where the hydrogen ion requirement was low (0-4), a variety of phases could be formed on stoichiometric grounds, as indicated in Figure 3.5.2, including kandites, vermiculites, chlorites and 9-11 Å phases. This compares well with the experimental results (Figure 3.3.9) where a mixture of just these minerals commonly formed the majority of the -75 μm product where no pH adjustment was made. For example, where initial aluminium and hydrogen ion concentrations of 0.046M and 0.31M respectively had been used, an aluminian serpentine formed as indicated by the point A in the figure. Applying the Al_{no} and H_{no} requirements for this kandite yields the equivalent point A in Figure 3.5.2. In the cases of vermiculite, chlorite and the 9-11 Å phases the Al_{no}/H_{no} requirement ratios were greater than those for smectites, as indicated in the theoretical phase diagram. This compares favourably with Figure 3.3.9

where these phases are ascertained to form with an increase in initial aluminium concentration in the order vermiculite, chlorite, 9-11 Å phase. Typical reactions which describe these transformations are given by equations 3.5.3 (kandite), 3.5.6 (vermiculite), 3.5.12 (chlorite) 3.5.8 (9-11 Å aluminosilicate).

The effect of adjustment of the pH towards alkaline values as illustrated in Figure 3.3.9, is modelled in Figure 3.5.2 by considering negative H_{no} values. The resultant products which could form are dependent, in the main, on Al_{no} requirement. Hydroxyoxides and 7 Å septechlorites can form for various Al_{no} values whereas, chlorites and 9-11 Å phase formation have Al_{no} requirements greater than 2. The phase diagram in Figure 3.3.9 suggests that aluminium ion availability was insufficient for the latter two phases to form since 7 Å phases and hydroxyoxides were solely detected.

Alteration system employing higher initial acid concentrations (Figure 3.3.10) would favour the formation of minerals which have a larger H_{no} requirement than those discussed previously. At these higher acidities the extent of tetrahedral substitution in the clay mineral lattices would be reduced. From Figure 3.5.2, this would render possible the formation of saponitic smectites and kandites which are also observed in practice (Figure 3.3.10), the equivalent regions in both diagrams being marked B. Increasing the aluminium ion concentration at high initial acid values would result in vermiculite and chlorite formation according to the theoretical diagram. This is consistent with Figure 3.3.10 where chlorite and vermiculite are the principal products for initial aluminium concentrations of 0.2-0.4M, where no pH adjustment was applied. 9-11 Å phases appear to be the only clay phases forming to have Al_{no} requirements greater than 2 for H_{no} values larger than 0. Referring to Figure 3.3.10 it was evident that smectites and

vermiculites formed instead, these minerals having lower Al_{no} requirements than 9-11 Å phases. This apparent inconsistency may be explained in terms of localised reactions which are discussed in Chapter 4, in that the actual aluminium ion availability was less than that inferred from the bulk concentration.

On increasing the pH of the solution after an initial 3.5 h interval (Section 3.3.4) minerals with lower H_{no} requirement should form. Immediately to the right of the pH line drawn in the experimental phase diagram, vermiculites and kandites were recorded as the principal crystalline compounds although they were accompanied by poorly crystalline 9 and 11 Å phases. The presence of the latter, coupled with the less well resolved peaks obtained in the diffractograms, suggested that the vermiculites and kandites were first-formed products in the initial 3.5 h experimental period and were subsequently diluted by the precipitation of 9-11 Å phases and hydroxyoxides, after pH adjustment (as indicated by the theoretical diagram). Indeed, 9-11 Å phases appeared to predominate with increasing initial aluminium concentration (Figure 3.5.1). As the Al^{3+}/H^{+} ratio increased with increasing pH, 9-11 Å forms would be expected at Al_{no} requirements > 2-2.8 and/or hydroxyoxides at lower Al_{no} values. Both could be accompanied by septechloritic-kandite minerals. This theoretical deduction agrees with the experiment, though, in contrast to low-acid-charged systems (Figure 3.3.9), 9-11 Å phases are present in greater concentration. This would be expected from the more penetrative leaching conditions afforded by the higher initial acid concentration used.

From the foregoing comparisons between the experimental phase diagrams and that based on theory in Figure 3.5.1 there appears to be some justification in modelling the kimberlite as an ion aggregate. According to the model, the aggregate reacts with aluminium and hydrogen

ions, the nature of products being determined by their stoichiometric requirements and the actual availability of the reagent cations added. Such a model, which in effect assumes homogeneity of ion distribution, works to a degree, namely where alteration can be considered to occur by surface/bulk solution interaction only followed by clay precipitation once a certain pH is reached. (The scanning electron photomicrographs obtained for low acid systems (Plates 3.9-10) are consistent with surface reactions of this type.) In some cases the disagreement between practice and theory may be explained in terms of reactions taking place within cavities in the kimberlite which would lead to a restriction of ion availability. This appeared to be the case for high-acid-charged systems (as indicated by the scanning electron photomicrographs, Plates 3.15-17). Such reactions have to be explained in terms of the micro- rather than macro-scale and are dealt with in Chapter 4.

3.5.2 Reaction equilibria at 150-350°C

Adopting the same approach as in Section 3.5.1 the following equilibria were deduced :

$$2\ Al^{3+} + 10\ H^{+} + 4\ 'SiO_4^{4-}' \leftrightarrow Al_2\ Si_4\ O_{10}\ (OH)_2 \text{ pyrophyllite} + 4\ H_2O \qquad (3.5.17)$$

$$1.62\ Al^{3+} + 9.44\ H^{+} + 0.39\ 'Mg^{2+}' + 0.13\ 'Fe^{3+}' + 0.125\ 'Ca^{2+}' + 3.93\ 'SiO_4^{4-}' \leftrightarrow Ca_{.125}\ Al_{1.55}\ Mg_{.39}\ Fe_{.13}\ (Al_{.07}\ Si_{3.93})\ O_{10}\ (OH)_2\ 3.5\ H_2O \text{ smectite III} + 0.22\ H_2O \qquad (3.5.18)$$

$$2\ Al^{3+} + 2\ H^{+} + H_2O + 2\ 'SiO_4^{4-}' \leftrightarrow Al_2\ Si_2\ O_5\ (OH)_4 \text{ kaolinite-dickite} \qquad (3.5.19)$$

$2.70\ Al^{3+} + 0.76\ H^{+} + 16.9\ H_2O + 0.46\ 'Mg^{2+}' + 0.54\ 'Fe^{3+}' + 2.85\ 'SiO_4^{4-}' \leftrightarrow Al_{1.55}\ Mg_{.46}\ Fe_{.54}\ (Al_{1.15}\ Si_{2.85})\ O_{10}\ (OH)_2\ 16.3\ H_2O$

9-11 Å aluminosilicate III (3.5.20)

$1.36\ Al^{3+} + 0.48\ H^{+} + 4.76\ H_2O + 2.44\ 'Mg^{2+}' + 0.38\ 'Fe^{3+}' + 0.31\ 'Ca^{2+}' + 2.81\ 'SiO_4^{4-}' \leftrightarrow Ca_{.31}\ Al_{.17}\ Mg_{2.44}\ Fe_{.38}\ (Al_{1.19}\ Si_{2.81})\ O_{10}\ (OH)_2\ 4\ H_2O$

vermiculite III (3.5.21)

$Al^{3+} + 3\ OH^{-} \leftrightarrow AlOOH + H_2O$ (3.5.22)

$2.31\ Al^{3+} + 6\ H_2O + 2.31\ 'Mg^{2+}' + 2.21\ 'Fe^{2+}' + 3\ 'SiO_4^{4-}' \leftrightarrow Al_{1.31}\ Mg_{2.31}\ Fe_{2.21}\ (Al\ Si_{3.0})\ O_{10}\ (OH)_8$

chlorite III + $4\ H^{+}$ (3.5.23)

$4\ Al^{3+} + 12\ OH^{-} + 4\ '(Mg,Fe)^{2+}' + 2\ SiO_4^{4-} \leftrightarrow Al_2\ (Mg,Fe)_2\ (Al_2Si_2)\ O_{10}\ (OH)_8$

amesite-chamosite (3.5.24)

The above equations were written for the system described in Section 3.4.1 and 3.4.2. A low hydrochloric acid dosage was employed ($0.31M\ H^{+}$) throughout as the equipment would not withstand attack by higher acid concentrations at the temperatures used.

The equations, which are arranged once again in order of decreasing stoichiometric hydrogen ion requirement per $'(Al,Si)_4O_{10}'$ unit show that minerals formed at higher temperatures continue to depend upon aluminium and acid requirement.

The phase diagram shown in Figure 3.4.1 represents the effect of temperature on the nature of crystallisation of clays rather than the effect of different concentrations of hydrogen ions. As described earlier, amorphous cationic (predominantly aluminian) hydroxyoxides

formed the majority of the -75 μm product at 100°C and 150°C. 9-11 Å aluminosilicates preferentially formed at 150°C where high aluminium concentrations were used. These products recrystallised at increasingly higher temperatures to form kaolinite at 200-250°C, aluminian smectites at 220-320°C, vermiculite, chlorites and montmorillonite above 300°C. Of the latter two, montmorillonite crystallised where high aluminium concentrations were employed.

The equilibria above mirror certain of the trends that occur with increase in temperature. Firstly, the proportion of amorphous hydroxyoxides (equation 3.5.22) decreases with increasing temperature, being replaced by the phyllosilicate minerals according to equations 3.5.17-21, 3.5.23. Secondly, the proportion of aluminium entering tetrahedral coordination increases with temperature although this effect is negated where the concentration of the ion is sufficiently high. Thus at 200-250°C octahedrally coordinated aluminium minerals predominate (namely pyrophyllite, aluminian smectites and kaolinite group minerals, — equations 3.5.17-19) as shown in Figure 3.4.1, and as reported in the literature.[133,138,139] Above 250°C it is apparent that minerals containing tetrahedrally coordinated aluminium are formed (namely trioctahedral vermiculites and chlorites, equations 3.5.21 and 3.5.23), where low aluminium reagent concentrations were used, though montmorillonite smectites in the case of higher ones. The latter, which are characterised by a relatively small proportion of tetrahedral aluminium may be explained with regard to the concentration of aluminium ion as added to the system. High concentrations of the cation tend to stabilise the octahedral coordinate state of aluminium.

3.5.3 Phase diagrams in the Al^{3+}-H^{+} system IV : Mineral solution equilibria at 100°C

The phase diagrams shown in Figure 3.3.9, 3.3.10 and 3.4.1

indicated the phases formed in practice from kimberlite alteration induced by the addition of the ions Al^{3+} and H^{+} at differing concentrations at 100-350°C. As an additional means of interpreting these complex results (at the lower temperature), a theoretical phase diagram can be calculated on the basis of free energy of formation under standard conditions. This is now attempted.

Thermodynamic stability relationships are normally obtained by considering dissolution equilibria for the individual minerals concerned.[244,247-9] In the present context this requires the assumption that clay minerals come to reversible thermodynamic equilibrium with their constituent ions in solution and that the original dissolution of the kimberlite need not be considered. Although thermodynamic data for silicates are sparse it is possible to estimate the Gibbs free energies of formation of phyllosilicate minerals[243,250] by the method of Tardy and Garrels.[250] This method considers the free energy of formation of clay minerals as the stoichiometric sum of the free energies of the component 'oxides' represented in each silicate structure. This procedure is adopted for all elemental oxides, save magnesium (which is treated, insofar as possible, as the hydroxide in all silicates). The free energies of the 'silicated' cationic oxides are shown in Table 3.5.1 for 100°C together with values for higher temperature deduced in the present work. An example of the procedure is given below.[250]

Consider the montmorillonite phase $H_{.4}\ Al_{1.52}\ Fe_{.22}\ Mg_{.29}\ (Al_{.19}Si_{3.81})\ O_{10}\ (OH)_2$

$$\Delta G^{o}_{f25}[\text{mont}] = 0.2\ \Delta G^{o*}_{f25}[H_2O]_{\text{inter}} + 3.81\ \Delta G^{o*}_{f25}[SiO_2] + 0.86\ \Delta G^{o*}_{f25}[Al_2O_3] + 0.29\ \Delta G^{o*}_{f25}[Mg(OH)_2] + 0.11\ \Delta G^{o*}_{f25}[Fe_2O_3] + 0.71\ \Delta G^{o*}_{f25}[H_2O] \qquad (3.5.25)$$

In this equation $\Delta G^{o*}_{f25}[X]$ is the Gibbs free energy of formation at 25°C of X as present in the main silicate structure and 'inter' represents water in the interlayer. Substitution of values from Table 3.5.1 gives :

$$\Delta G^{o}_{f25}[\text{mont}] = 5191 \text{ kJ mol}^{-1}$$

This is in good agreement with solubility measurements which yield values of 5190 kJ mol^{-1}.

In the present work free energies of formation were required for clay minerals formed at 100°C (and, if possible, higher temperatures). Suitable data were available for certain minerals[251] but these did not take account of compositional variations in these minerals. Hence, the free energies of formation of the chlorites, vermiculites and other synthesised minerals had to be calculated by (a) re-evaluating (for 100°C) the Gibbs energies of formation of the oxides of cations as present in the phyllosilicate structures, and (b) evaluating the stoichiometric sum of the free energies of these 'silicated' oxides. Thus by adopting the procedure of Tardy and Garrels[250], new free energy values (ΔG^{o*}_{ft} [oxide]) were calculated and are also shown in Table 3.5.1 for 100, 150, 200, 250 and 350°C. Briefly, the procedure involved setting up and solving a number of simultaneous equations (for each temperature) which related the recorded free energies of formation of the various minerals with the (unknown) free energies of formation of the constituent silicated oxides, so that the latter could be determined. This procedure was carried out for minerals of idealised chemical composition including serpentine, kaolinite, pyrophyllite, chlorite and smectite. An example of the form of simultaneous equations is given below :

TABLE 3.5.1 GIBBS FREE ENERGIES OF FORMATION FOR CATIONIC OXIDES AND HYDROXIDES AS PRESENT IN SILICATES (kJ mol^{-1})

Component	ΔG^{o*}_{f25}	ΔG^{o*}_{f100}	ΔG^{o*}_{f150}	ΔG^{o*}_{f200}	ΔG^{o*}_{f250}	ΔG^{o*}_{f300}
CaO	- 765.4	- 730.6	- 671.4	- 675.8	- 683.7	- 687.9
MgO	- 624.7	- 614.2	- 613.4	- 605.9	- 598.7	- 590.8
$Mg(OH)_2$	- 851.2	- 821.9	- 806.8	- 791.8	- 776.7	- 761.2
FeO	- 268.4	- 252.4	- 250.0	- 245.8	- 242.0	- 237.8
Fe_2O_3	- 744.0	- 737.7	- 723.5	- 711.0	- 698.0	- 685.8
Al_2O_3	-1601.1	-1542.1	-1550.4	-1531.6	-1511.1	-1488.5
SiO_2	- 856.6	-849.9	- 838.2	- 829.4	- 820.7	- 812.7
H_2O	- 247.8	-229.0	- 209.4	- 200.1	- 192.6	- 184.6
H_2O_{inter}	- 245.3					

Notes

a) A more extensive list for ΔG^{o*}_{f25} is given in the paper by Tardy and Garrels for other cations.

b) Data produced in columns 2-6 verified using data from Barner and Scheuermann e.g. for a montmorillonite at 100°C $Mg_{.16}\ Al_{2.33}\ Si_{3.67}\ O_{10}\ (OH)_2$ calculated ΔG^{o}_{f100} was 5242 kJ mol^{-1} (cf. 5246 kJ mol^{-1} as tabulated).

$$\Delta G^{o}_{f\,100}[\text{serpentine}] = 2\Delta G^{o*}_{f\,100}[Mg(OH)_2] + \Delta G^{o*}_{f\,100}[MgO] + 2\Delta G^{o*}_{f\,100}[SiO_2] \quad (3.5.26)$$

where serpentine is taken to be $Mg_3\ Si_2O_5(OH)_4$.

From the newly determined free energies of the 'oxides' of the idealised phyllosilicates above and the structural formulae computed for the real clay minerals produced (Section 2.5.4), Gibbs free energies of formation could be calculated for the products given in equilibria 3.5.1-12. These final values are given in Table 3.5.2 together with the free energies of formation of the constituent ions at elevated temperatures.

To produce a theoretical mineral-solution phase diagram based on the phases produced in the present work the following procedure was used. Equilibria were first written in the convenient form of dissolution equations for all the minerals in Table 3.5.2; an example being that of vermiculite I (originating in Figure 3.3.9).

$$Ca_{.28}\ Al_{.08}\ Mg_{2.51}\ Fe_{.44}\ (Al_{1.21}\ Si_{2.79})\ O_{10}\ (OH)_2 + 10.8\ H^{+}$$

$$\leftrightarrow\ 0.28\ Ca^{2+} + 1.29\ Al^{3+} + 2.51\ Mg^{2+} + 0.44\ Fe^{3+} + 2.79\ Si(OH)_4 + 0.8\ H_2O \quad (3.5.27)$$

The free energy change for each dissolution reaction ($\Delta G^{o}_{diss\ 100}$) was determined in the usual way; for the example given :

$$\Delta G^{o}_{diss\ 100} = \Sigma\Delta G^{o}_{f\,100}\ (\text{products}) - \Sigma\Delta G^{o}_{f\,100}\ (\text{reactants}) = +\ 15.7\ kJ \quad (3.5.28)$$

TABLE 3.5.2 GIBBS FREE ENERGIES OF FORMATION FOR MINERALS AT 100°C AND AQUEOUS SPECIES IN SOLUTION AT 100-300°C (kJ mol^{-1})

Mineral	ΔG°_{f100}
chlorite I	-7774.8
chlorite II	-7279.1
vermiculite I	-5504.2
vermiculite II	-5518.4
smectite I	-5307.8
kaolinite	-3700.0
serpentine	-3790.5
9-11 Å phase I	-5219.5
9-11 Å phase II	-5686.5
septechlorite I	-7395.2
septechlorite II	-6984.0

Aqueous species	ΔG°_{f100}	ΔG°_{f150}	ΔG°_{f200}	ΔG°_{f250}	ΔG°_{f300}
Ca^{2+}	-556.4	-558.1	-559.4	-560.6	-561.5
Mg^{2+}	-452.6	-450.9	-449.7	-448.4	-447.2
Fe^{2+}	- 76.6	- 75.4	- 74.5	- 73.3	- 72.4
Fe^{3+}	+ 6.3	+ 13.4	+ 20.1	+ 26.8	+ 33.5
Al^{3+}	-474.4	-467.3	-460.3	-453.0	-445.9
$Si(OH)_4$	-1221.2	-1192.9	-1167.8	-1142.6	-1119.6
H_2O	-225.3	-217.7	-210.2	-202.7	-196.0

Notes

a) ΔG°_{ft} values for all the species save $Si(OH)_4$ were taken from Barner and Scheuerman.[251]

b) ΔG°_{ft} values for $Si(OH)_4$ were calculated from equilibrium constant-temperature relationships given by Rimstadt and Barnes.[252]

making use of the equilibrium isotherm with the usual notation

$$\Delta G^{o}_{T} = -RT \ln K$$

and K_{100} (vermiculite I) = $10^{-2.20}$

From the equilibrium law

$$K_{100} \text{ (vermiculite I)} = (a^{.28}_{Ca^{2+}} \; a^{1.29}_{Al^{3+}} \; a^{2.51}_{Mg^{2+}} \; a^{.44}_{Fe^{3+}} \; a^{2.79}_{Si(OH)_4})/ (a^{10.8}_{H^{+}}) \qquad (3.5.29)$$

where a_X represents the activity of species X; the activity of water and vermiculite being taken as unity. Taking logarithmic values :

$$\log K = -2.20 = 0.28 \log a_{Ca^{2+}} + 1.29 \log a_{Al^{3+}} + 2.51 \log a_{Mg^{2+}} + 0.44 \log a_{Fe^{3+}} + 2.79 \log a_{Si(OH)_4} - 10.8 \log a_{H^{+}} \qquad (3.5.30)$$

This linear equation interrelates the permissible activities of the constituent ion species in solution when the solid phase is at reversible equilibrium with the solution. Such an equation cannot, however, be conveniently plotted unless three of the variables, namely $\log a_{Ca^{2+}}$, $\log a_{Si(OH)_4}$, $\log a_{Fe^{3+}}$ are suppressed. Previous sections have indicated the main ionic species to control the nature of the phyllosilicate/hydroxide product are Al^{3+}, Mg^{2+}, H^{+}; the others, Ca^{2+}, Fe^{2+}, Fe^{3+}, $Si(OH)_4$ are of subsidiary importance and consequently were

ascribed set values.

Activities were calculated by multiplying typical analytical concentrations by the activity coefficient, γ, estimated from the calculated ionic strength and the extended Debye-Hückel Law :

$$\log \gamma = -Az^2 I^{\frac{1}{2}}/(1 + \mathring{a} B I^{\frac{1}{2}}) \qquad (3.5.31)$$

where A and B are constants characteristic of the solvent (water) at the specified temperature and pressure; $\mathring{a}$ is based on the 'effective diameter' [243] of the ion; z, the valence of the ion; and I, the ionic strength of the solution. At 100°C the values of A and B were estimated as 0.589 and 0.3411×10^{-8} from extrapolation of data given by Garrels. Values of $\mathring{a}$ used were as follows : Ca : 6×10^{-8}; Fe : 7.5×10^{-8}; Mg : 8×10^{-8}; Al^{3+} and H^+ : 9×10^{-8}.[243,244] In the case of silicon, the activity coefficient could be assumed to be unity.[244]

Having completed all the calculations for the written equations of the form of 3.5.30 for all the minerals of interest, a three variable activity phase diagram was constructed, as is shown in Figure 3.5.3. The equations employed are given in their full form below, but the planes drawn relate only to the variable $\log a_{Al^{3+}}$, $\log a_{Mg^{2+}}$ and $\log a_{H^+}$; the other activities for Ca^{2+}, Fe^{2+}, Fe^{3+} and $Si(OH)_4$ being ascribed the values as noted in the diagram.

chlorite I (Figure 3.3.9) $Al_{1.28}\ Mg_{4.04}\ Fe_{.73}\ (Al_{1.22}Si_{2.78})\ O_{10}\ (OH)_8$

$$31.53 = 2.5 \log a_{Al^{3+}} + 4.04 \log a_{Mg^{2+}} - 16.88 \log a_{H^+} + 0.73 \log a_{Fe^{2+}} + 2.78 \log a_{Si(OH)_4} \qquad (3.5.32)$$

chlorite II (Figure 3.3.10) $Al_{1.19}\ Mg_{2.76}\ Fe_{1.79}\ (Al_{.54}Si_{3.46})\ O_{10}\ (OH)_8$

$$13.30 = 1.73 \log a_{Al^{3+}} + 2.76 \log a_{Mg^{2+}} - 14.3 \log a_{H^+} + 1.79 \log a_{Fe^{2+}} + 3.46 \log a_{Si(OH)_4} \quad (3.5.33)$$

vermiculite I (Figure 3.3.9) $Ca_{.28}\ Al_{.08}\ Mg_{2.51}\ Fe_{.44}\ (Al_{1.21}Si_{2.79})\ O_{10}\ (OH)_2\ 4.6\ H_2O$

$$-2.201 = 1.29 \log a_{Al^{3+}} + 2.51 \log a_{Mg^{2+}} - 10.8 \log a_{H^+} + 0.44 \log a_{Fe^{3+}} + 0.28 \log a_{Ca^{2+}} + 2.79 \log a_{Si(OH)_4} \quad (3.5.34)$$

vermiculite II (Figure 3.3.10) $Ca_{.09}\ Al_{.26}\ Mg_{2.58}\ Fe_{.28}\ (Al_{.96}Si_{3.04})\ O_{10}\ (OH)_2\ 4.3\ H_2O$

$$-2.93 = 1.12 \log a_{Al^{3+}} + 2.58 \log a_{Mg^{2+}} - 9.54 \log a_{H^+} + 0.28 \log a_{Fe^{3+}} + 0.09 \log a_{Ca^{2+}} + 3.04 \log a_{Si(OH)_4} \quad (3.5.35)$$

saponite (Figures 3.3.9 and 3.3.10) $Ca_{.16}\ Al_{.09}\ Mg_{2.42}\ Fe_{.53}\ (Al_{.84}Si_{3.16})\ O_{10}\ (OH)_2\ 3.6\ H_2O$

$$5.1025 = 0.93 \log a_{Al^{3+}} + 2.42 \log a_{Mg^{2+}} - 9.33 \log a_{H^+} + 0.21 \log a_{Fe^{2+}} + 0.32 \log a_{Fe^{3+}} + 0.16 \log a_{Ca^{2+}} + 3.16 \log a_{Si(OH)_4} \quad (3.5.36)$$

aluminian serpentine $Al_{1.6}\ Mg_{.3}\ Fe_{.3}\ Si_2O_5(OH)_4$

$$4.705 = 1.6 \log a_{Al^{3+}} + 0.3 \log a_{Mg^{2+}} - 6 \log a_{H^+} + 0.3 \log a_{Fe^{2+}} + 2 \log a_{Si(OH)_4} \quad (3.5.37)$$

serpentine $Ca_{.28}\ Al_{.34}\ Mg_{1.8}\ Fe_{.39}\ Si_2O_5\ (OH)_4$

$$4.541 = 0.34 \log a_{Al^{3+}} + 1.8 \log a_{Mg^{2+}} - 6 \log a_{H^+} + 0.39 \log a_{Fe^{2+}} + 0.28 \log a_{Ca^{2+}} + 2 \log a_{Si(OH)_4} \quad (3.5.38)$$

9-11 Å aluminosilicate $Al_{0.66}\ Mg_{1.54}\ Fe_{.63}\ (Al_{.95}Si_{3.05})\ O_{10}\ (OH)_2$

$$-6.686 = 1.61 \log a_{Al^{3+}} + 1.54 \log a_{Mg^{2+}} - 10.2 \log a_{H^+} + 0.63 \log a_{Fe^{3+}} + 3.05 \log a_{Si(OH)_4} \quad (3.5.39)$$

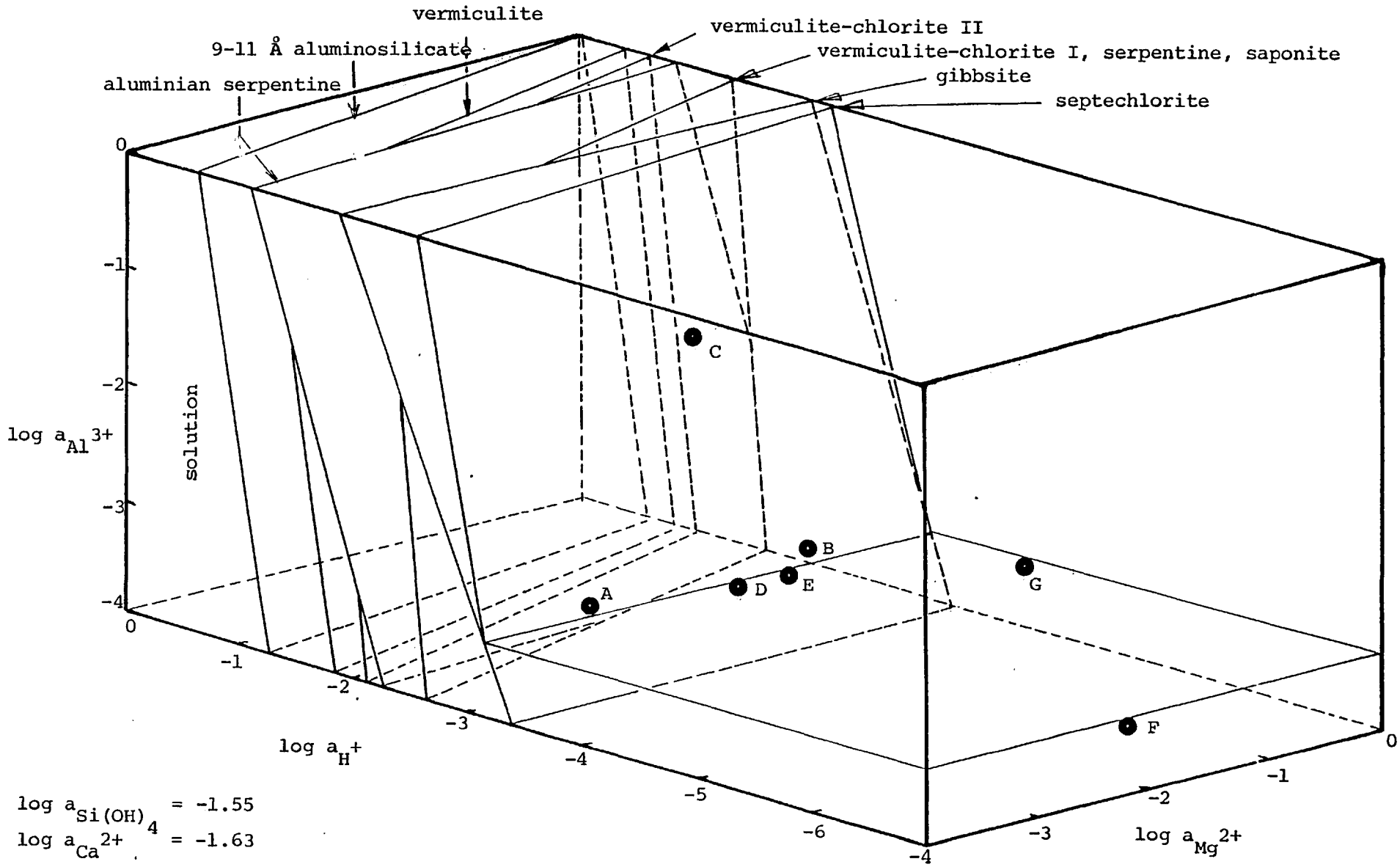
septechlorite $Al\ Mg\ Fe\ (AlSi)\ O_5\ (OH)_4$

$$17.75 = 2 \log a_{Al^{3+}} + \log a_{Mg^{2+}} - 10 \log a_{H^+} + \log a_{Fe^{2+}} + \log a_{Si(OH)_4} \quad (3.5.40)$$

gibbsite $Al(OH)_3$

$$-5.68 = 3 \log a_{H^+} - \log a_{Al^{3+}} \quad (3.5.41)$$

The thermodynamic data available and the method used to calculate free energies of formation was extended to evaluate similar values for interlayered chlorite-vermiculite clay species as observed in Figures 3.3.9 and 3.3.10. (These products produced X-ray diffractograms which bore favourable comparison to other interlayered chlorite-vermiculites analysed elsewhere.[253,254]) From the computed results of the -75 μm products (Section 2.5.4) the ratios of vermiculite:chlorite were calculated and the data relating to equations 3.5.32-35 combined accordingly to produce equations 3.5.42 and 3.5.43. These equations were derived by assuming a linear relationship between the free energy of formation and the fraction of chlorite as present in the interlayered chlorite-vermiculite.



log $a_{Si(OH)_4}$ = -1.55
log $a_{Ca^{2+}}$ = -1.63
log $a_{Fe^{2+}}$ = -2.29
log $a_{Fe^{3+}}$ = -3.03

Figure 3.5.3 Theoretical mineral-solution phase diagram for kimberlite alteration products at 100°C.

vermiculite-chlorite I (2/1 ratio) (Figure 3.3.9)

$$9.034 = 1.692 \log a_{Al^{3+}} + 3.183 \log a_{Mg^{2+}} - 12.81 \log a_{H^{+}} + 0.293 \log a_{Fe^{3+}} + 0.022 \log a_{Fe^{2+}} + 0.186 \log a_{Ca^{2+}} + 2.78 \log a_{Si(OH)_4} \quad (3.5.42)$$

vermiculite-chlorite II (6/1 ratio) (Figure 3.3.10)

$$-0.611 = 1.207 \log a_{Al^{3+}} + 2.606 \log a_{Mg^{2+}} - 10.22 \log a_{H^{+}} + 0.256 \log a_{Fe^{2+}} + 0.24 \log a_{Fe^{3+}} + 0.07 \log a_{Ca^{2+}} + 3.10 \log a_{Si(OH)_4} \quad (3.5.43)$$

Figure 3.5.3 consists of a series of inclined planes, each of which represents the boundary between solvated ions and a precipitated (clay) phase. In all cases these planes were assumed to form once the $\log a_{H^{+}}$ had decreased to a certain value in a theoretical leach of kimberlite.

The seven phase types in Figure 3.3.9 and 3.3.10 are represented - 9-11 Å aluminosilicate; aluminian serpentine; saponite; vermiculite; vermiculte-chlorite; gibbsite; septechlorite-kandite. In certain instances the solution-solid boundaries for two or more different minerals coincided; as in the case of vermiculite-chlorite I, serpentine and saponite. This indicated that simultaneous formation of the mineral phases was likely on thermodynamic grounds. The segments in the diagram do not represent a single homogeneous phase. A complex mixture of mineral phases could crystallise as the pH increased above the limits set by each plane. For example, consider a system where $\log a_{Al^{3+}} = \log a_{Mg^{2+}} = -4$, then at pH 0 ions would remain in solution. Increasing the pH to 1.2 precipitates a 9-11 Å phase, whereas at pH 1.8 both a vermiculite and a

9-11 Å phase could crystallise. At pH 3 the product could include all or some of the clay minerals shown in equations 3.5.32-39.

Attempts were made to interrelate the theoretical phase diagram with the experimental results in Figures 3.3.9 and 3.3.10. Although it was unlikely that true reversible equilibrium was ever established under the laboratory conditions involved, it was assumed that their equilibration states were closely approached so that useful comparisons could be made.

Particular points of comparison are labelled A-G in Figures 3.3.9, 3.3.10, 3.5.3. The correspondence was achieved as follows : the residual concentrations of the species Ca^{2+}, (Fe^{2+} and Fe^{3+}), Cl^{-}, $Si(OH)_4$, Al^{3+}, H^{+}, Mg^{2+} in the residual solution were measured, the last three being converted to activities through multiplying by the appropriate activity coefficient. (The first four allowed an estimate of the ionic strength of the solution to be made.) The calculated activities were used to plot a point on the phase diagram. For example, point C in Figure 3.5.3 suggests the presence of chlorite-vermiculite interlayered products with associated 9-11 Å phases. The former certainly characterise the phase region marked by C in Figure 3.3.10. The other points A-G could be similarly related.

In comparing theory and practice two difficulties arise with regard to the discussion of Figure 3.5.3. Firstly, insufficient thermodynamic data exists with regard to the formation of interlayered clay phases. The planes drawn represent approximate positions for intimately mixed chlorite-vermiculites and further data would be necessary to delinate their position on the phase diagram with greater accuracy. Secondly inconsistencies arose between the position of areas of stability for vermiculites and 9-11 Å aluminosilicates in the experimental phase diagram (Figure 3.3.10) and that inferred from the

theory. This may be partly resolved by assuming the vermiculite to be formed prior to pH adjustment and persisted despite dilution by precipitation of hydroxides of residual ions in solution after pH adjustment.

As in Section 3.5.1, theory and practice are consistent up to a point in that kimberlite alteration can be considered as the description of an ion aggregate coupled with the inter-reaction of leached ions to form a clay mineral product. However, the irregularities noted suggested that further investigation into the alteration system was necessary, as is described in Chapter 4.

3.5.4 Free-energy-temperature relationships for mineral-solution equilibria at 100-300°C

In a similar manner to that described above (Section 3.5.3) a comparison was made between experimental results (Figure 3.4.1) and derived thermodynamic data (Table 3.5.1 and 3.5.3). However as the residual concentration of aluminium and silicon in the reaction solutions were too small for precise measurements to be made at higher temperatures, certain thermodynamic data could not be reliably estimated. A simpler form of diagramatic representation concerning mineral stability had to be employed (cf. Figure 3.5.3) and was developed in the following manner.

The diagram (Figure 3.5.4) produced shows the variation of free energy of formation from solution with temperature for the minerals discussed in Section 3.5.2. To estimate the free energies of formation of the minerals therein, at elevated temperatures, the method due to Tardy and Garrels[250] was again employed. This necessitated the calculation of the free energies of formation of the constituent elemental oxides (and hydroxides in the case of magnesium) which were

TABLE 3.5.3 CALCULATED STANDARD GIBBS FREE ENERGIES OF FORMATION FOR MINERALS FROM SOLUTION AT VARIOUS TEMPERATURES (150-300°C)

Mineral	Formula	Temperature (°C)	ΔG^{o}_{ft} (kJ mol^{-1})	ΔG^{o}_{fts} (kJ mol^{-1})
chlorite III	$Al_{1.31}\ Mg_{2.31}\ Fe_{2.21}\ (Al_{1.0}Si_{3.0})\ O_{10}(OH)_8$	300	-6753.2	- 4.4
		250	-5313.7	- 4.1
vermiculite III	$Ca_{.31}\ Al_{.18}\ Mg_{2.44}\ Fe_{.38}\ (Al_{1.18}Si_{2.82})\ O_{10}\ (OH)_2$	300	-5248.4	- 25.6
smectite II	$Ca_{.18}\ Al_{1.47}\ Mg_{.39}\ Fe_{.22}\ (Al_{.21}Si_{3.79})\ O_{10}\ (OH)_2$	250	-4999.7	-278.4
smectite III	$Ca_{.13}\ Al_{1.55}\ Mg_{.39}\ Fe_{.13}\ (Al_{.07}Si_{3.93})\ O_{10}\ (OH)_2$	300	-4943.1	-306.6
kaolinite	$Al_2\ Si_2\ O_5\ (OH)_4$	150	-3642.7	-107.6
		200	-3591.6	-125.6
		250	-3537.6	-143.6
		300	-3483.2	-156.1
9-11 Å phase III	$Al_{1.55}\ Mg_{.46}\ Fe_{.54}\ (Al_{1.15}Si_{2.85})\ O_{10}\ (OH)_2$	200	-5067.3	-174.5
9-11 Å phase IV	$Al_{1.83}\ Mg_{.51}\ Fe_{.32}\ (Al_{1.45}Si_{2.55})\ O_{10}\ (OH)_2$	250	-5173.0	-188.4
9-11 Å phase V	$Al_{1.97}\ Mg_{.47}\ Fe_{.32}\ (Al_{1.77}Si_{2.23})\ O_{10}\ (OH)_2$	300	-5161.1	-193.7
boehmite	AlOOH	150	-1764.0	-861.27
		200	-1738.9	-858.3
		250	-1713.7	-854.1
		300	-1688.2	-850.4

Table 3.5.3 contd

Mineral	Formula	Temperature (°C)	ΔG^{o}_{ft} (kJ mol^{-1})	ΔG^{o}_{fts} (kJ mol^{-1})
silica	SiO_2	150	- 834.5	- 73.1
		200	- 825.3	- 77.0
		250	- 816.0	- 78.8
		300	- 807.3	- 79.6

Notes

a) ΔG^{o}_{ft} is the Gibbs free energy of formation at temperature t from the elements in their standard states;

ΔG^{o}_{fts} is the free energy of formation at temperature t from the solution.

b) Pressure had a negligible effect on the calculations.

computed at 150, 200, 250 and 300°C as described before, and are listed in Table 3.5.1. Using this data and the computed structural formulae of the various phyllosilicate minerals (employing Program CECPM, Appendix 5), free energies of formation for these synthesised phases were deduced. Following the procedures outlined in Section 3.5.4 the free energies for the formation of the clay minerals from solution were calculated and are shown below in Table 3.5.3. These free energy values (ΔG^{o}_{fts}) were plotted against temperature to give Figure 3.5.4.

The diagram shows the relative thermodynamic stability of the mineral types noted in equations 3.5.18-23 together with silica and gibbsite. If true reversible thermodynamic equilibrium was achieved, the principal product expected to form would be that which has the highest negative free energy of formation from solution (ΔG^{o}_{fts}). From the diagram this product would appear to be boehmite, but in practice other phases are detected. It would appear that these products form more rapidly and such comparatively metastable phases can persist for long periods of time. The amorphous hydroxyoxides recorded in the experimental phase diagram were hence attributed to structureless gels consisting of silicilic acid species and cationic hydroxides. These would then recrystallise to form the more stable products; that is clay minerals and less hydrated oxides.

As a consequence of the above discussion, and in accordance with Figure 3.5.4, the most stable products expected to form from alteration reactions conducted at 100-200°C would be kandites and 9-11 Å aluminosilicates. In the case of the former a change in the chemical and structural composition - from a magnesian (trioctahedral) to an aluminian (dioctahedral) kandite results in a five-fold increase in the ΔG^{o}_{fts} value from 100 to 150°C. In accordance with theory, kaolinite and the 9-11 Å products were the main products detected at 150-200°C in

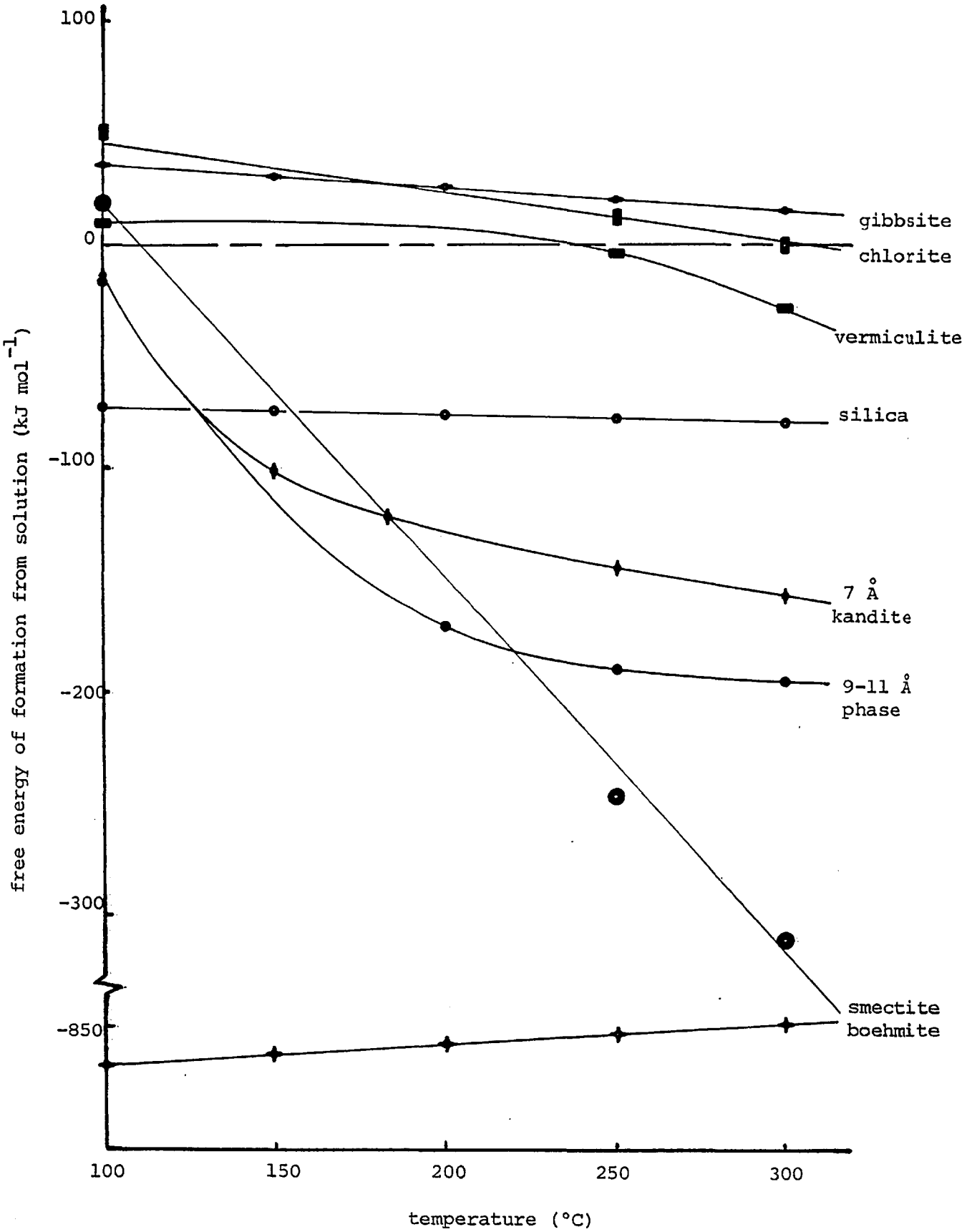


Figure 3.5.4 Free energy of formation-temperature relationships for alteration products of kimberlite.

Figure 3.4.1.

The agreement between theory and practice extended to the higher temperatures. Figure 3.5.4 shows that above 230-250°C smectites become the most stable phases in preference to the 7 and 9-11 Å forms above. The increasing (negative) free energy of formation from solution with temperature resulted from the increasing dioctahedral character of the smectite produced. 7 and 9-11 Å silicates would still be stable at these temperatures.

An increase in temperature also renders vermiculites and chlorites more stable compared with the solution phase. Negative ΔG^{o}_{fts} values occur at temperatures greater than 230°C (vermiculite) and 300°C (chlorite). These values infer a comparable range of stability for these phases, as obtained experimentally. Although vermiculite-chlorites are not observed in the system studied until the temperature reached 300°C, these minerals can crystallise at temperatures as low as 100°C as discussed in the previous section, despite their positive ΔG^{o}_{fts} values. It would appear that the diagram in Figure 3.5.4 gives an indication of likely predominance of the solid phases as compared to their constituent ions in the solution or the amorphous solid phase. For example, at 100°C the yield of vermiculite-chlorite was low (Section 3.5.3) and the clay products were diluted by the amorphous metastable gels. However, at higher temperatures the yield and degree of crystallinity increased with more negative ΔG^{o}_{fts} values such that the clay phases could be clearly identified in the XRD trace.

In conclusion, it should be noted that there is good agreement between products formed in practice and those predicted to form (in analysable quantities) on theoretical grounds. The comparison, however, remains incomplete due to the lack of reliable thermodynamic data. In particular, data was not available for those 14-16 Å phases such as

vermiculite in the temperature range 150-200°C where they could not be detected experimentally. Although the presentation was basically theoretical in nature, it does rely on the use of computed structural formulae of the phases in question; the smectites are a case in point.

CHAPTER 4

ALTERATION OF KIMBERLITE : KINETICS AND MECHANISMS OF REACTIONS IN CHLORIDE MEDIA

4.1 Introduction

This chapter describes testwork to identify the steps and sequences in the alteration of kimberlite. The kinetic studies were carried out using chloride media only, as this gave the most extensive alteration and had many characteristics in common with geological systems.

The data is used to outline a scheme of elementary reactions for the formation of phyllosilicate minerals from their constituent ionic species. An equation is derived expressing the overall rate of kimberlite reaction in terms of the principal variables - which are the initial concentrations of aluminium and hydrogen ion and temperature. Finally, the rate determining step is discussed as a prerequisite to the process design study described in Chapter 5.

4.2 Systems Containing 0.45M Al^{3+} and 0.31M H^{+}; 0.22M Al^{3+} and 1.5M H^{+} at 100°C

4.2.1 Procedures

Two alteration systems were studied, which will be referred to as A and B. The initial concentrations of aluminium and hydrogen ion, in 40 ml aliquots, employed in the alteration experiments were as follows :

System A : 0.45M Al^{3+}, 0.316M H^{+}

System B : 0.22M Al^{3+}, 1.50M H^{+}

The former had been found to give the greatest alteration at very low acid concentrations (Section 3.3.3-5) whereas the latter appeared to produce the most extensive physical degradation possible at the temperature employed (100°C) (Figure 3.3.12). Experiments used the hotplate-stirrer apparatus described in Section 3.3.1. 10 g samples of -1180+850 µm kimberlite were reacted at 100°C for reaction times varying from 1 to 24 h. The same product separation/AAS analysis procedure was applied. The +75 µm products were ground in ethanol for XRD quantitative analysis and elemental mass balance determination, while the -75 µm fractions were analysed by XRD and IR analysis. Chemical assay was carried out by the fusion/AAS technique (Section 2.4.3) and used to obtain mass balances as well as estimates of the clay phase concentration based on XRD identifications (Section 2.5).

4.2.2 Results : DOA, residual olivine and serpentine proportions and residual solution concentrations

The plots obtained with time for the DOA and residual metal ion concentrations are shown in Figures 4.2.1 and 4.2.2. In all cases there was an initial rapid increase in alteration (over the first 1-2 h) after which reaction occurred at a much slower rate. The largest proportions of ions entering solution were those recorded for calcium, the values for systems A and B being respectively : 70 and 74% (2 h); 70 and 78% (7 h) and increasing to 79 and 81% (24 h). The initial high values would be a result of the acid dissolution of calcite, which would have consumed the bulk (i.e. ∿ 90%) of the acid initially added in system A. The plot obtained for iron was similar to that described

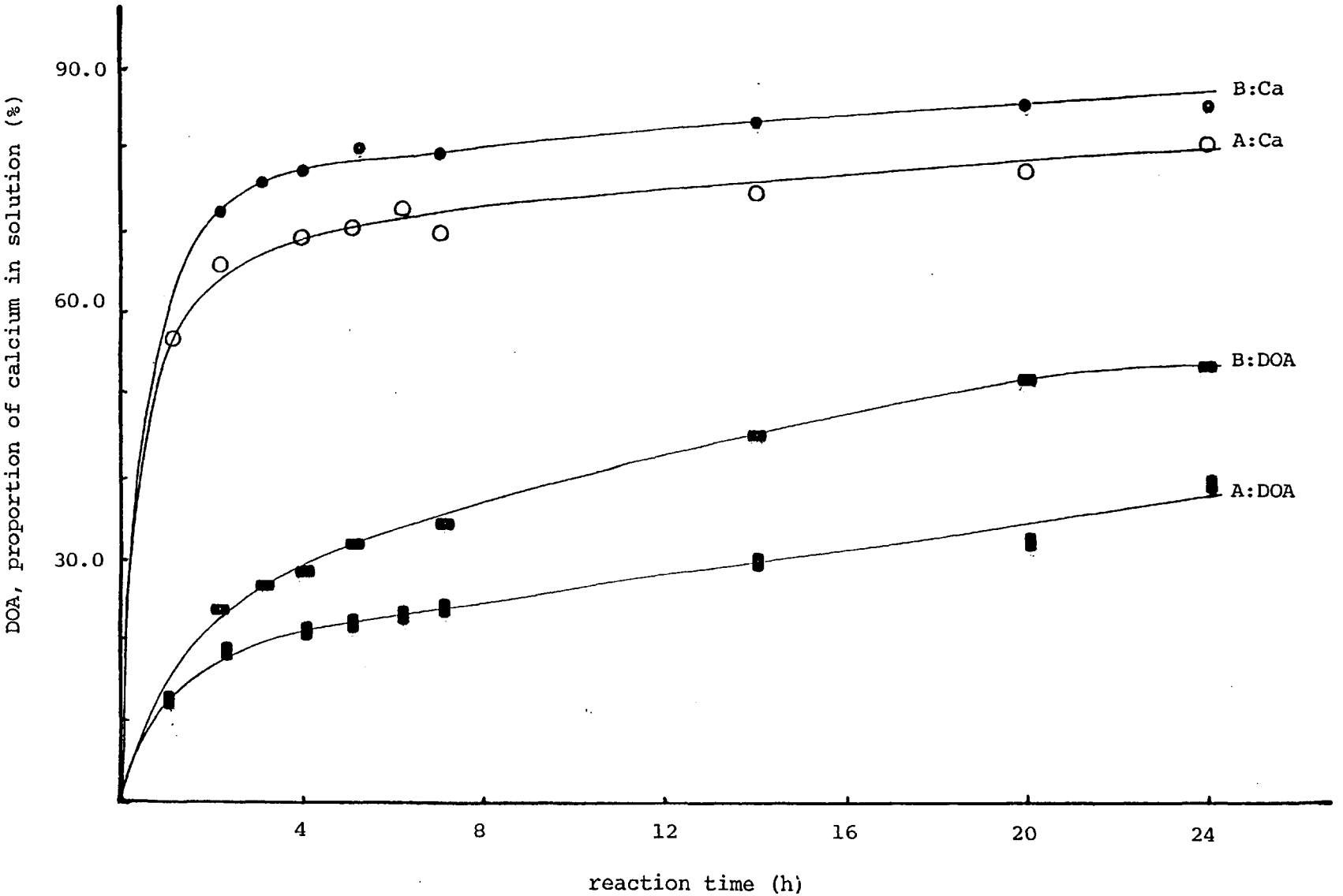


Figure 4.2.1 Relation between DOA, proportion of calcium entering solution and reaction time for systems A and B

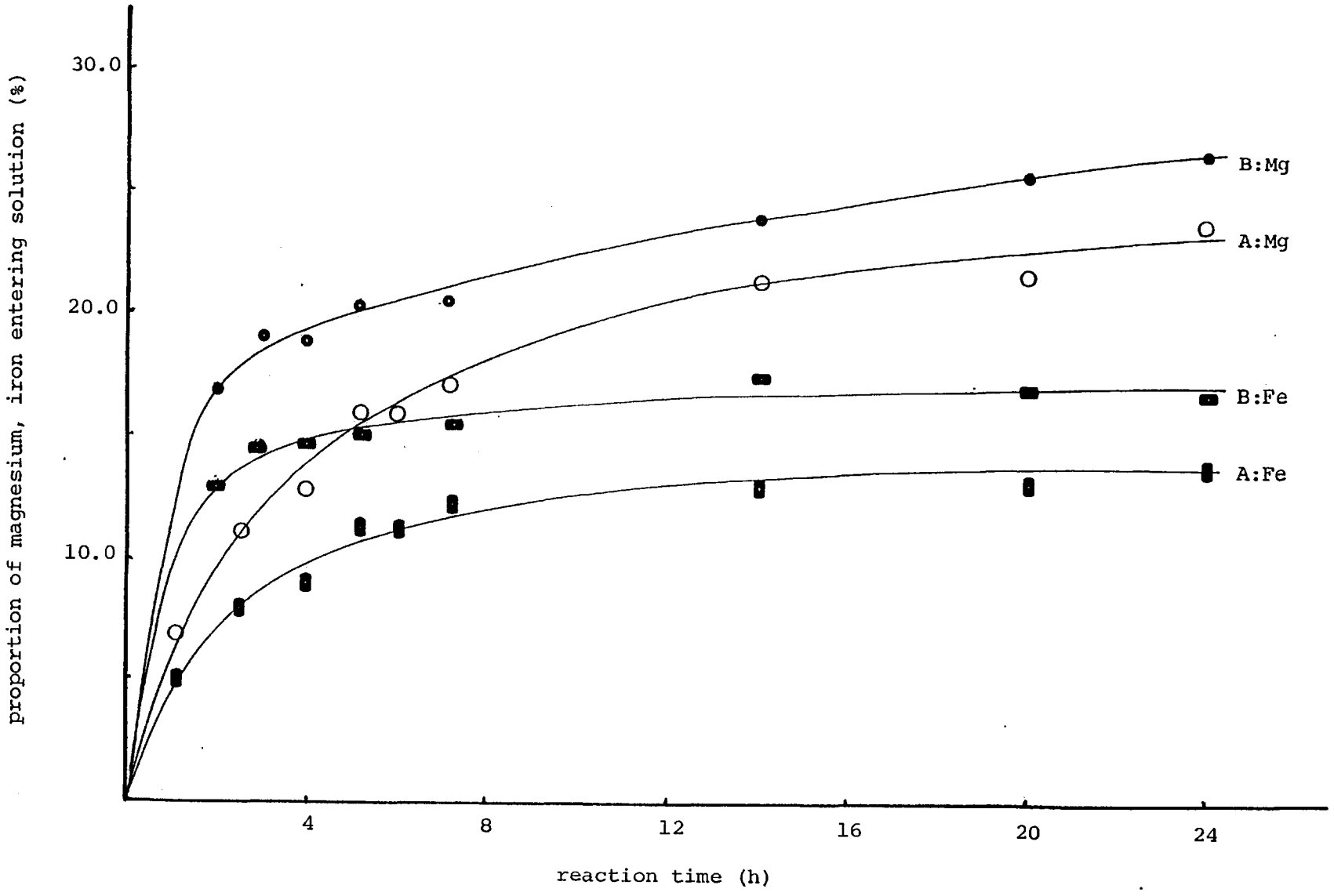


Figure 4.2.2 Relation between proportion of magnesium and iron entering solution and reaction time for Systems A and B.

for calcium, although the overall quantities involved were lower and the metal was assumed to originate from serpentine. For example, the respective values for Systems A and B were 12.5 and 15.5% (7 h), 13.5 and 16.5% (24 h). Although iron and calcium concentrations appeared to approach equilibrium values after 5 h, the plots of the former indicated a difference in the rate of reaction for the two systems from the gradients of the lines drawn. Similar findings were made for the magnesium concentration, the inference being that the reaction in the system with the higher initial acid concentration took place at a faster rate; as would be expected. In contrast to the iron and calcium plots, those for magnesium and the DOA continued to rise with time beyond the initial period, respective values for systems A and B being 10%, 17% (Mg); 16%, 25% (DOA) at 2 h; 16.5%, 21% (Mg); 22%, 32% (DOA) at 7 h; 23%, 25.5% (Mg); 37%, 52% (DOA) at 24 h. These parallel trends were indicative of a continuing overall reaction after the initial dissolution attack by the acid.

The pH of the solution on extraction and the proportion of aluminium entering the solid phases are shown on a combined diagram in Figure 4.2.3. In both systems the pH rapidly increased in the first hour of reaction to a value $\sim$ 3. In the case of System A the pH continued to increase thereafter, though at a substantially slower rate, crossing the line (shown) at which aluminium hydroxide precipitation would occur, after 6 h, and giving a final pH of 4.5 after 24 h. The precipitation pH was not exceeded until 14-20 h in the case of System B however.

The pH values yielded useful information on the nature of the aluminium-rich solid products produced, as follows. Figure 4.2.3 shows that in both systems similar proportions of the total aluminium present reported to either the +75 or -75 μm phases (the curves are virtually coincident). Noting the time at which the pH line was intersected (i.e.

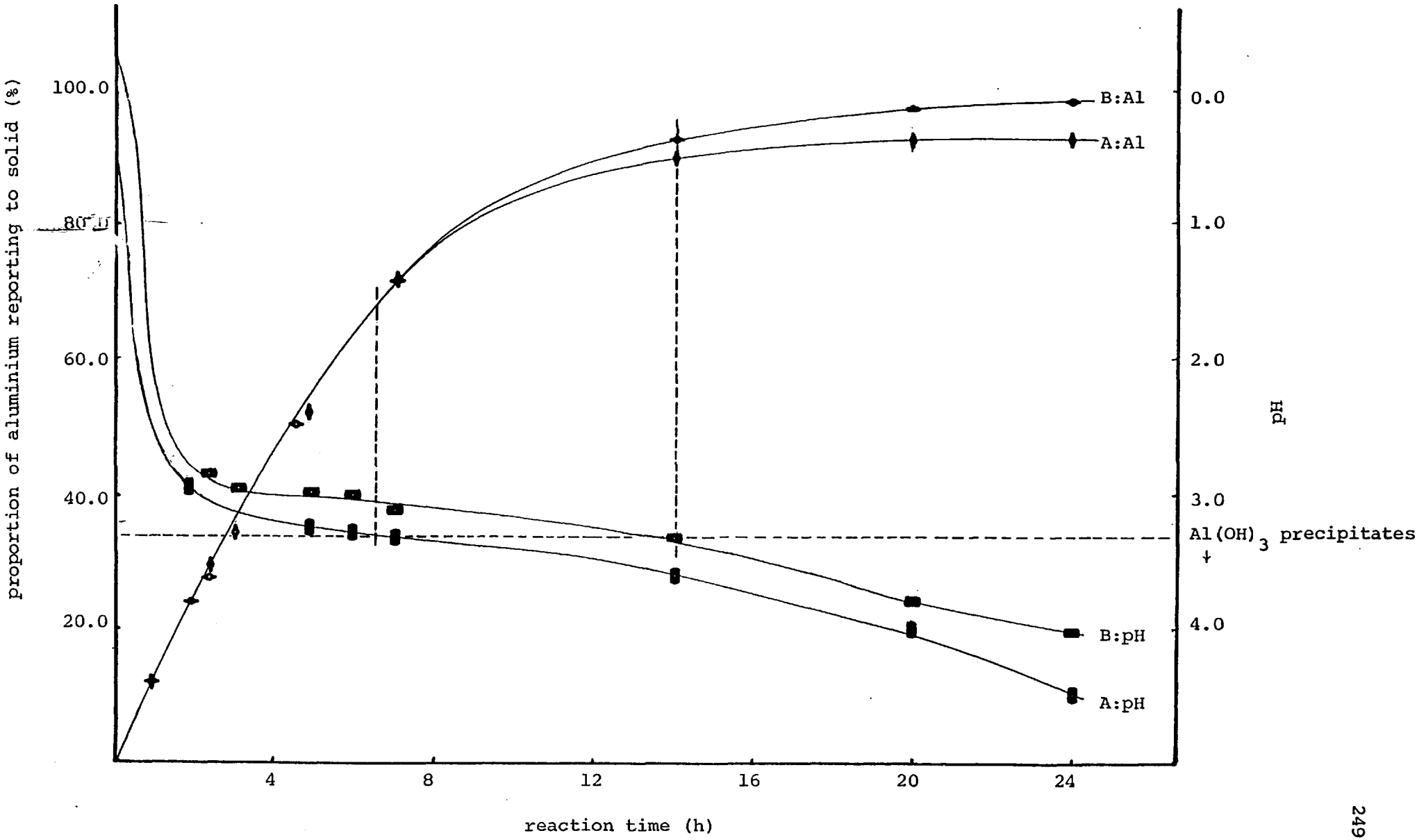


Figure 4.2.3 Relation between proportion of total aluminium reporting to a solid +75/-75 µm fraction, pH and reaction time for systems A and B.

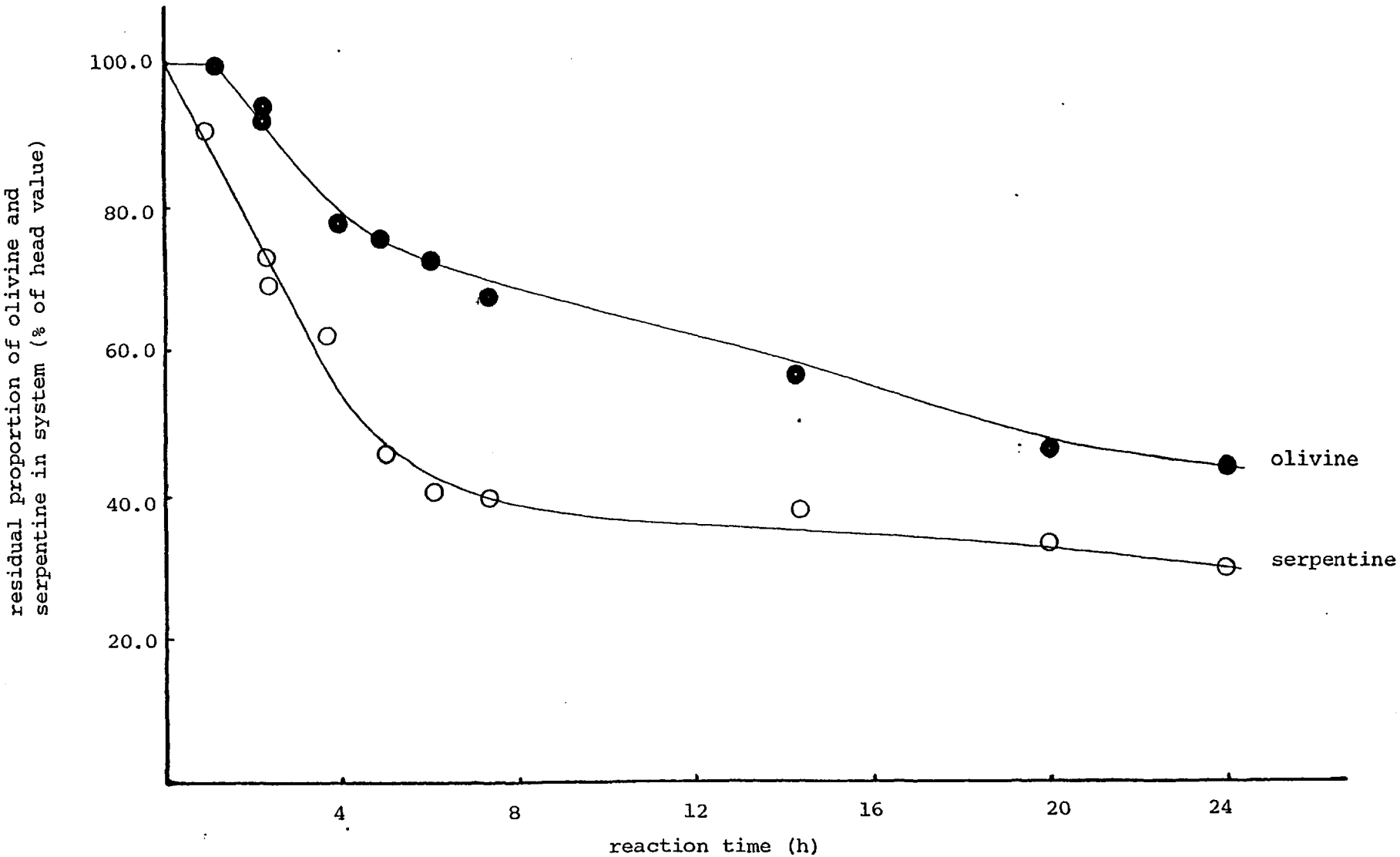


Figure 4.2.4 Relationship between residual concentrations of olivine and serpentine in the final +75 μm fraction and time of reaction for system A, the mineral assays being expressed as a percentage of their head values.

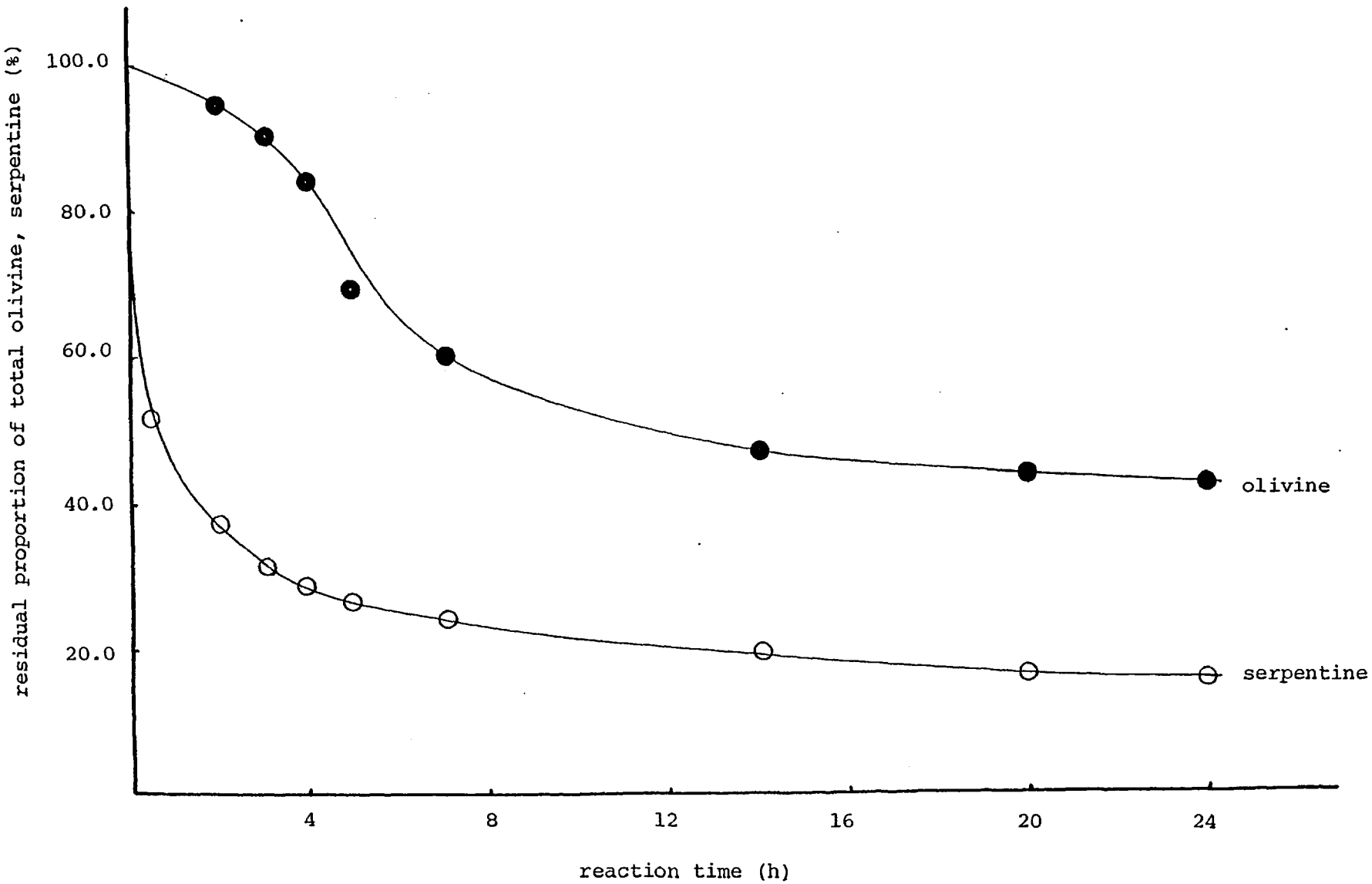


Figure 4.2.5 Relationship between residual concentrations of olivine and serpentine in the final +75 μm fraction and reaction time for system B, the mineral assays being expressed as a percentage of their head values.

at pH 3.2), the corresponding proportion of aluminium reporting to the solid fractions at pHs greater than 3.2 were deduced; namely 40% for System A, 5% for System B. These are indicated on the figure by dotted lines. As the product precipitated at pHs greater than 3.2 was most likely to consist of aluminium hydroxyoxide gel (whereas any precipitated below this pH should be predominantly clay mineral), it was apparent from Figure 4.2.3 that the majority (95%) of the aluminium ion fed to System B was involved in clay mineral formation whereas only 60% was so used in System A. This is consistent with Figures 3.3.9 and 3.3.10.

The changing extent of degradation with time was more clearly shown by Figures 4.2.4 and 4.2.5 which illustrate the relationship between the residual fraction of the total olivine and serpentine present in the +75 μm fraction and the reaction time. This ordinate scale was preferred to that of assay proportions, as in certain cases particularly for low reaction times, the assay actually exceeded the head value. This resulted from the dissolution of calcite prior to reaction with the olivine/serpentine. Both figures show that equilibrium was closely approached after 20 h. At this point the amount of residual unaltered serpentine in the +75 μm fraction was substantially smaller in System B (16%) compared to System A (30%). However, over the same period the amounts of residual olivine were the same (42%).

In both systems, the chemical attack was directed preferentially towards serpentine, rather than olivine, particularly in the case of B where the proportion of serpentine present fell to 38% in the first 2 h of reaction.

4.2.3 Results : Mass balances

Using the peroxide fusion/AAS procedure, described in Section

2.4.3, elemental mass balances were determined for each of the sets of three phases (+75 μm, -75 μm and solution) generated in the kinetics experiments for the elements Ca, Si, Fe, Mg, Al. Magnesium and aluminium are considered first.

The percentage distributions of the magnesium and aluminium present in Systems A and B are shown in Figures 4.2.6 and 4.2.7 respectively. Comparing the two figures it can be seen that the magnesium proportion in the +75 μm fraction falls to 63% (System A) and 53% (System B) after 24 h : the rate of reaction was thus greater in the case of the latter, as also indicated by the difference in the gradient of the graph at low reaction times. Magnesium progressively entered both the solution and solid -75 μm phase : in System B an equilibrium solution concentration containing 24-26% of the total magnesium was established at 5 h and a similar amount was also deposited in the -75 μm fraction at 24 h. In System A however, such a solution equilibrium was only approached after 24 h, the increase in the proportion of ions entering the -75 μm product and solution phases being low in comparison.

The aluminium distributions are plotted on the same scales so that the interaction of the two elements could be compared. Unlike other ionic species, the majority of the aluminium originated from the solution phase, and decreased sharply in concentration for reaction times 1-7 h while the -75 μm content proportionately increased. After 24 h very little aluminium remained in solution. Aluminium also apparently entered the +75 μm phase, at least, temporarily : the proportion increased from 38% (0 h) to 47% (5 h) and then decreased to 34% (14 h) for System B. The ion seemed to be retained in the kimberlite for a longer period of time in System A, where the initial proportionate value was raised from 25 to 44%. The importance of these

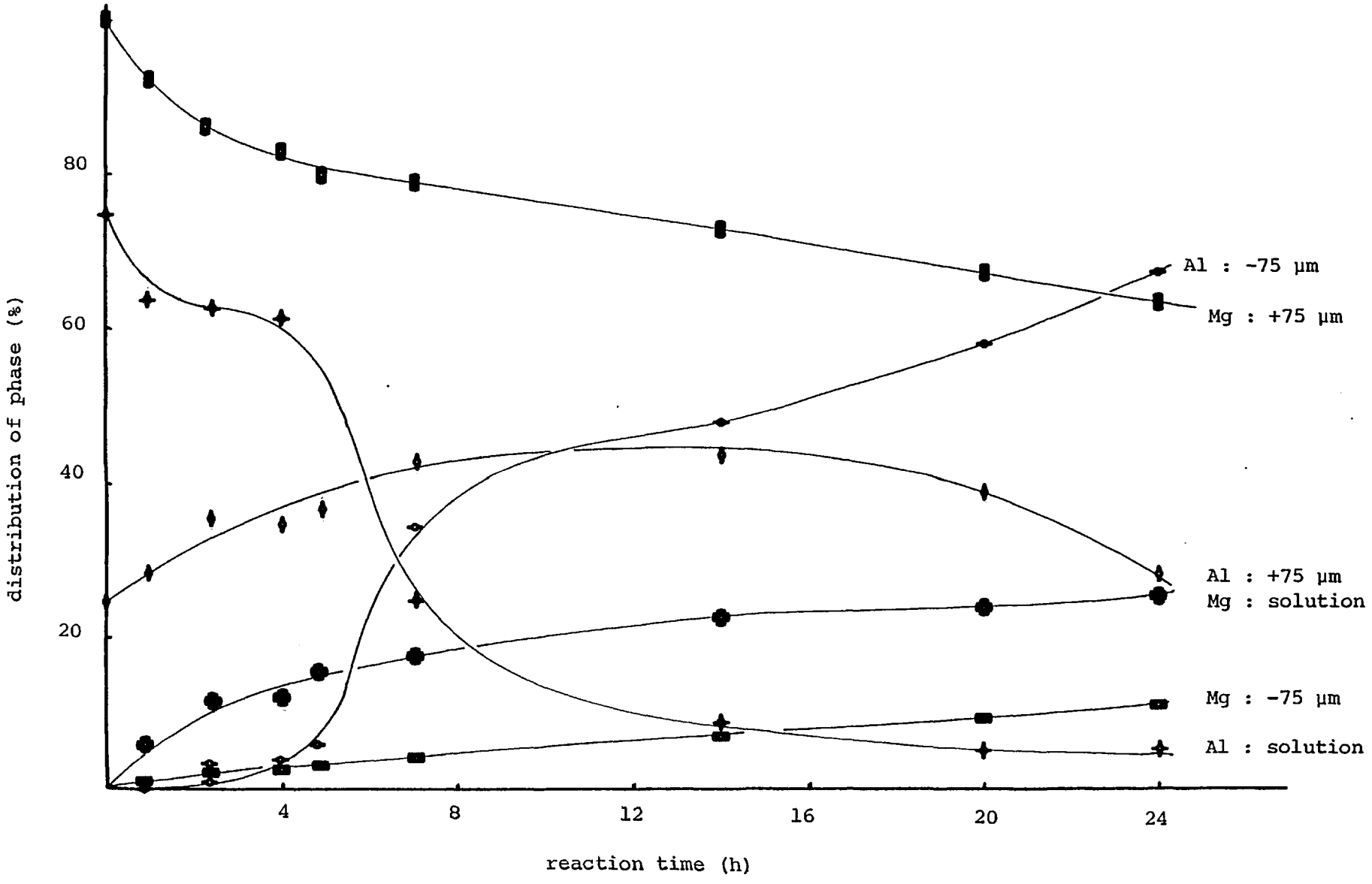


Figure 4.2.6 Elemental mass distributions for the +75 µm, -75 µm and solution phases generated at various reaction times for system A.

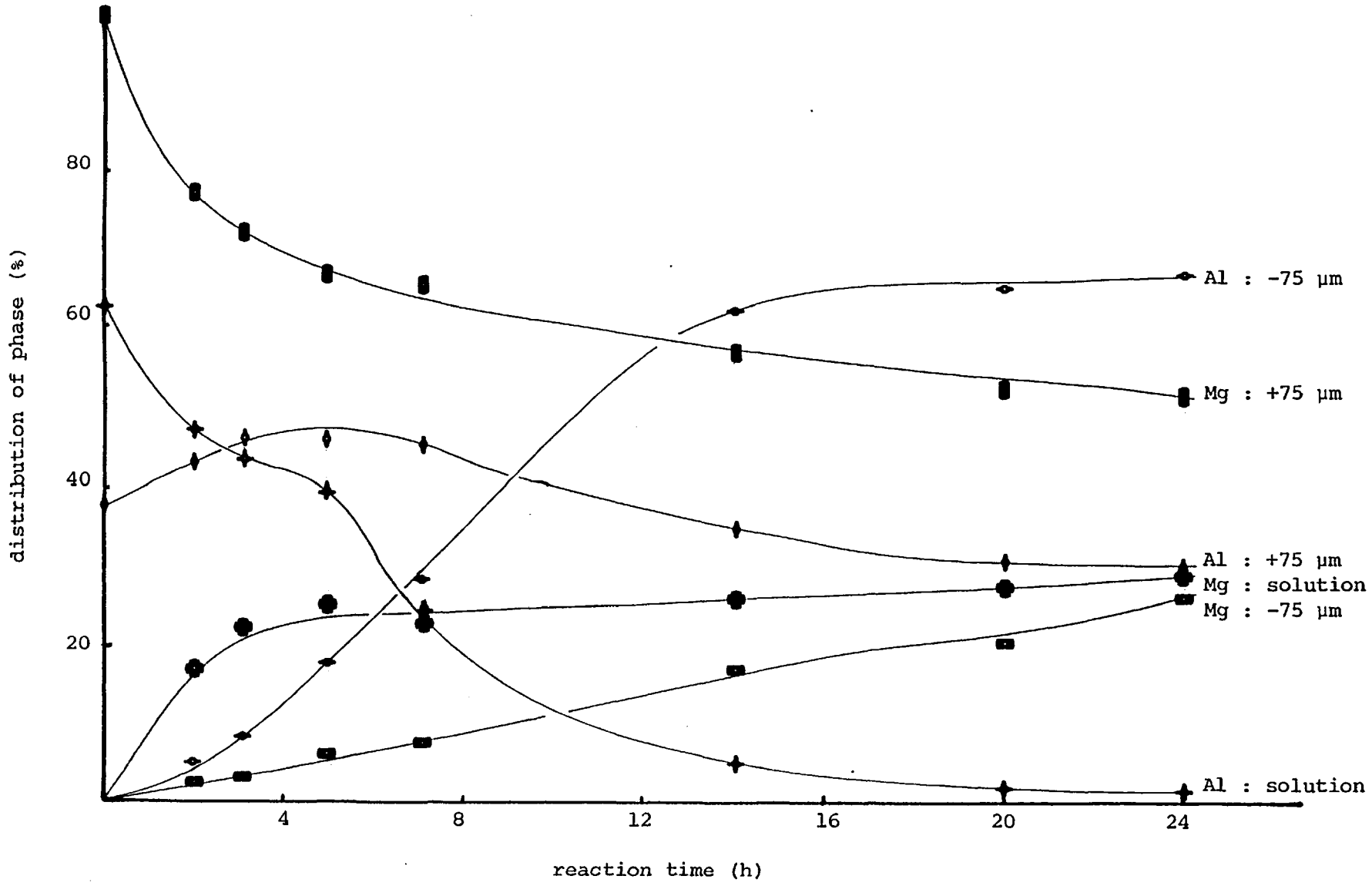


Figure 4.2.7 Elemental mass distributions for the +75 µm, -75 µm and solution phases generated at various reaction times for system B.

trends is discussed in Section 4.5.1.

The mass balance distributions for calcium, iron and silicon were mutually similar in trend, for both systems. The proportion of each cation concerned in the +75 μm fraction progressively decreased with time. The amount of ion entering the -75 μm fraction and/or the solution phase correspondingly increased. Apart from this general trend the following observations were made.

The majority of the 'liberated' calcium reported to the solution phase. However, in the case of System B the proportion being preferentially precipitated in the -75 μm product was greater (e.g. 17% at 24 h). It would appear that this trend reflected the progressive formation of a calcium-interlayered mineral, namely vermiculite. The -75 μm products were also shown to have iron as an important constituent.

Little silica was found to remain in solution. As much as 38% of the total silica could be extracted from the kimberlite (System B, 24 h) but this presumably remained as a solid mixed phase of silica gel and partially formed phyllosilicates.

4.2.4 Results and interpretation : Infra-red analyses

The -75 μm products were also analysed by IR spectroscopy to investigate the nature of the reactions taking place. The 1200-200 cm^{-1} regions of the IR spectrograms obtained for each product are shown in Figures 4.2.8 and 4.2.9. Vertical lines are drawn to highlight wavenumbers of particular interest. In the case of System A, IR analysis of the -75 μm products obtained after 1-4 h was not possible owing to the small masses obtained. The IR traces obtained for those products formed after 5 and 6 h were indicative of a phyllosilicate mineral mixture, though at 7 h and thereafter, the details of the spectrogram

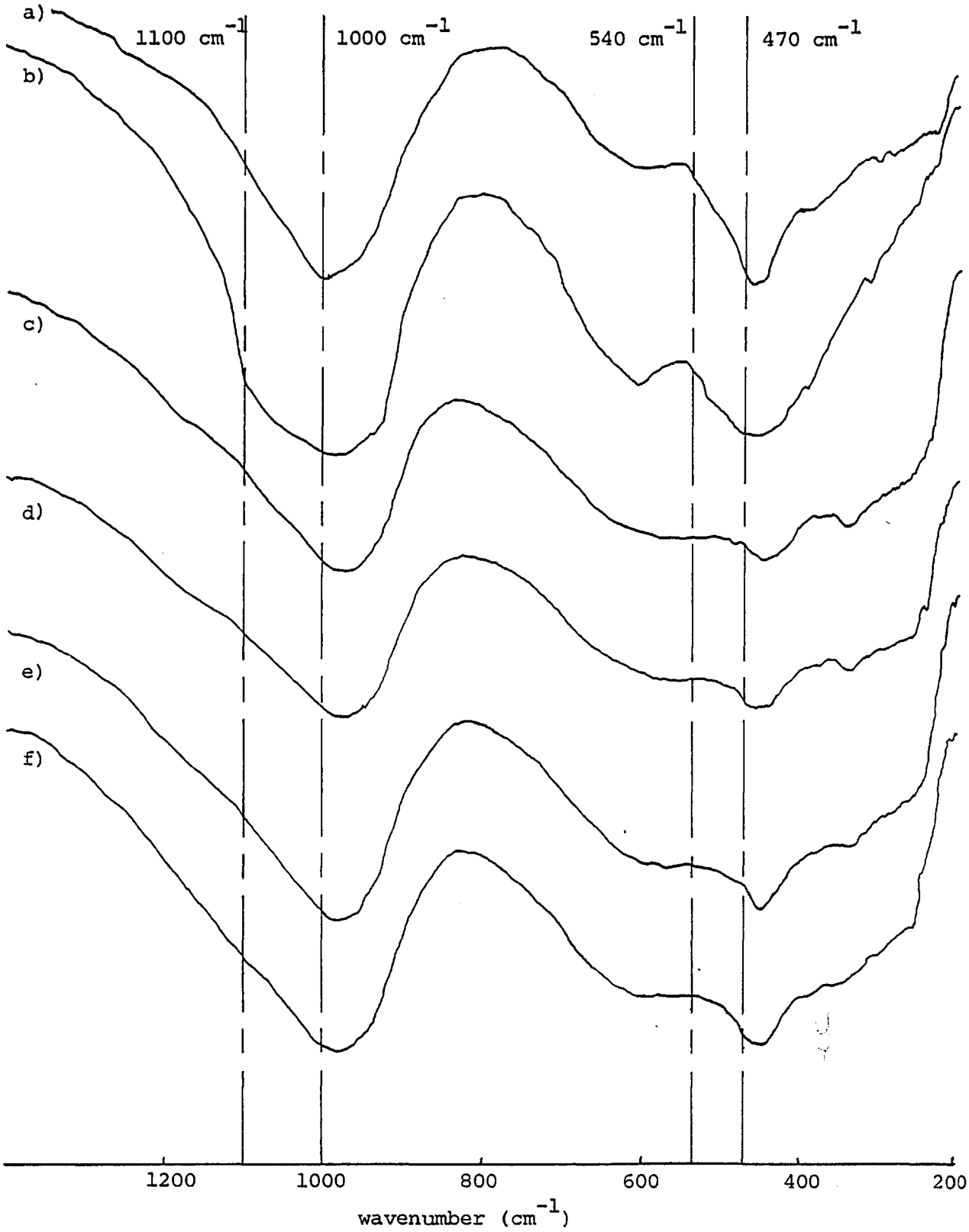


Figure 4.2.8 Infra-red spectrograms for -75 μm products obtained from System A reacted at 100°C for

a) 5h; d) 14h;
b) 6h; e) 20h;
c) 7h; f) 24h.

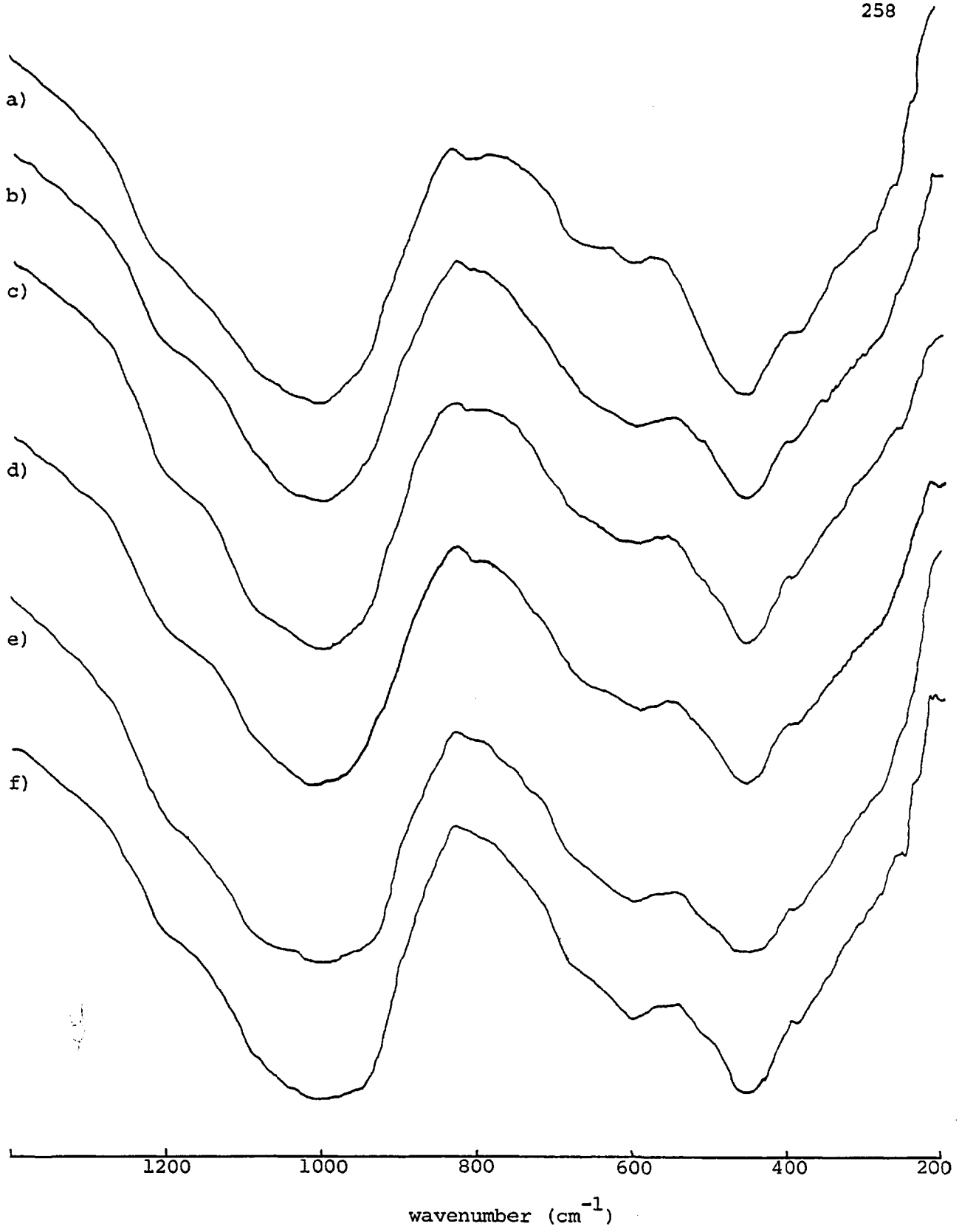


Figure 4.2.9 Infra-red spectrograms for -75 μm products obtained from system B reacted at 100°C for a) 2 h; b) 4 h; c) 7 h; d) 14 h; e) 20 h; f) 24 h.

were partially obscured owing to hydroxyoxide precipitation (Figure 4.2.3). Thus, the traces for 7-24 h showed an increase in peak width and intensity, particularly in the 250-400 cm^{-1} region which was indicative of the formation of Al-OH bands (Figure 4.2.8c).[233] However, the product retained a pronounced silicate character as opposed to a simple hydroxyoxide one as shown by the peaks at 980-1000 cm^{-1} and 470 cm^{-1}.[255] Al-OH bonding in System B was not developed to the same extent.

In both systems three peaks were selected for further investigation as these were expected to be characteristic of specific band groups of interest.

a) 540 cm^{-1} : the intensity of this peak increased in proportion with Al^{VI}-O-Si bands in the sample.[232,233]

b) 980-1000 cm^{-1} : movement of the peak to lower wavenumbers represented a proportionate increase in tetrahedrally coordinated aluminium.[233]

c) 1100 cm^{-1} : this represents silica bonding which is associated with gelatinous phases.[255]

To detect changes in the octahedral and 'Si-O ordered' character of the products, the peak intensities of the 540 cm^{-1} and 1100 cm^{-1} wavenumbers were expressed as ratios compared to that of the Si-O bond (1000 cm^{-1}) in the same IR trace (Section 2.4.2). The intensity of the latter served as a reference against which interactions between ions and the silicate tetrahedral lattice could be studied. (Other authors have used such a ratio technique but have restricted it to comparing the peaks of two samples of interest.[189]) The relative

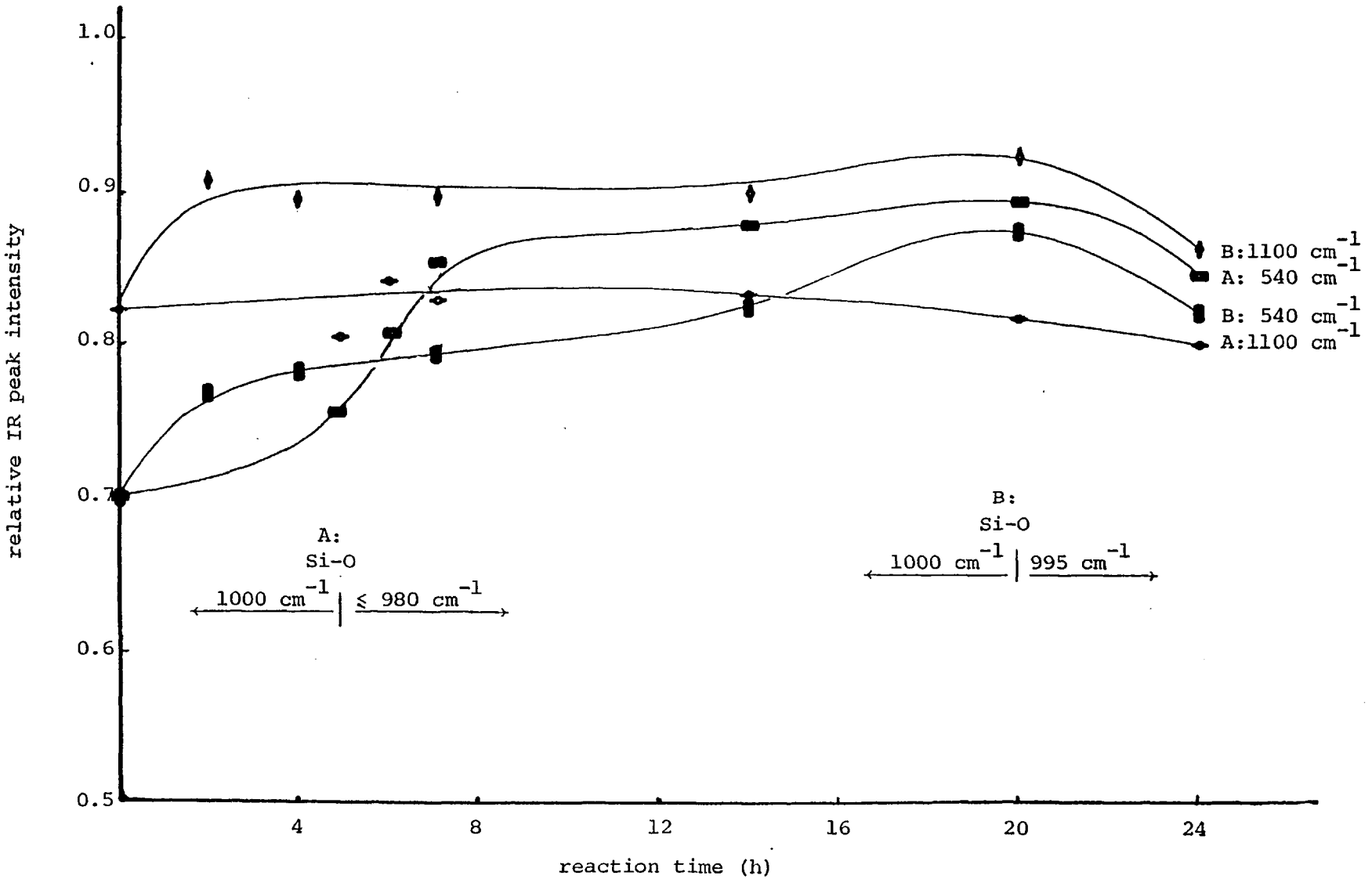


Figure 4.2.10 Relation between relative IR peak intensity and reaction time for -75 μm products generated in systems A and B.

peak intensities for the 540 cm^{-1} and 1100 cm^{-1} wavenumbers are shown plotted in Figure 4.2.10. Replicate analyses that the ratios obtained had an error of 5%.

The ratios were compared with those for the serpentine standard which represented a comparatively well-crystallised trioctahedral silicate. In both systems the 540 cm^{-1} relative intensities increased with time. The result was more immediate in System B. The replacement of divalent cations by aluminium to form Al^{VI}-O-Si bonds was complemented by tetrahedral substitution by the ion. In System A the peak shift from 1000 to 980 cm^{-1} was noted at a reaction time of 5 h whereas in System B a smaller shift was only detectable for a reaction time between 14 and 20 h. The degree of crystallinity in System B appeared to have been partly disrupted. An increase in the 1100 cm^{-1} peak intensity was noted for most samples whereas for System A values similar to the 'head' were noted.

4.3 Systems Containing 0.22/0.45M Al^{3+} and 0.31M H^{+} at 215,260,300°C

4.3.1 Procedures

Four alteration systems were considered initially. One consisted of a 2.5 g -1180+850 μm feed reacted with 10 ml solution containing 0.5 g hydrated aluminium chloride conditioned at a pH of 0.5. The other three differed solely in the quantity of aluminium added; the others involved 1 g, 1.5 g and 2 g $AlCl_3.6H_2O$. The experimental procedure was as described in Section 3.4.1. The reagents were agitated in the nickel-steel bombs at 36 rpm and heated to one of five temperatures : 100, 150, 215, 260 and 300°C. Total reaction times of 1-8 h were employed after which the bombs were quenched and the products removed and analysed according to the procedures outlined in Section 3.2.1.

4.3.2 Results : DOA and residual solution concentrations

The variation in % DOA with overall reaction time is shown graphically in Figures 4.3.1 and 4.3.2 for the systems involving 0.5 and 1.0 g hydrated aluminium chloride, and these will be referred to as C and D (cf. Systems A and B in Section 4.2). The other two systems (having 1.5 and 2.0 g hydrated aluminium chloride) are not considered in detail here because of the masking effect observed, which resulted from precipitating aluminium hydroxyoxide phases.

For reference, the sets of physicochemical conditions finally employed, denoted as Systems A-E, are given below in Table 4.5.1.

TABLE 4.3.1 THE PHYSICOCHEMICAL CONDITIONS TESTED AS REPRESENTED BY SYSTEMS A, B, C, D, E

Property	System				
	A	B	C	D	E
Feed (g)	10.0	10.0	2.5	2.5	2.5
Initial acid concentration (M)	0.31	1.50	0.31	0.31	0.31
Initial aluminium concentration (M)	0.41	0.20	0.20	0.41	0.88
Temperature (°C)	100	100	100-300	100-300	100-300
Apparatus	Hotplate/stirrer		autoclave		

As shown in Figures 4.3.1 and 4.3.2, the majority of the degradation occurred during the first 3 h of reaction. For temperatures

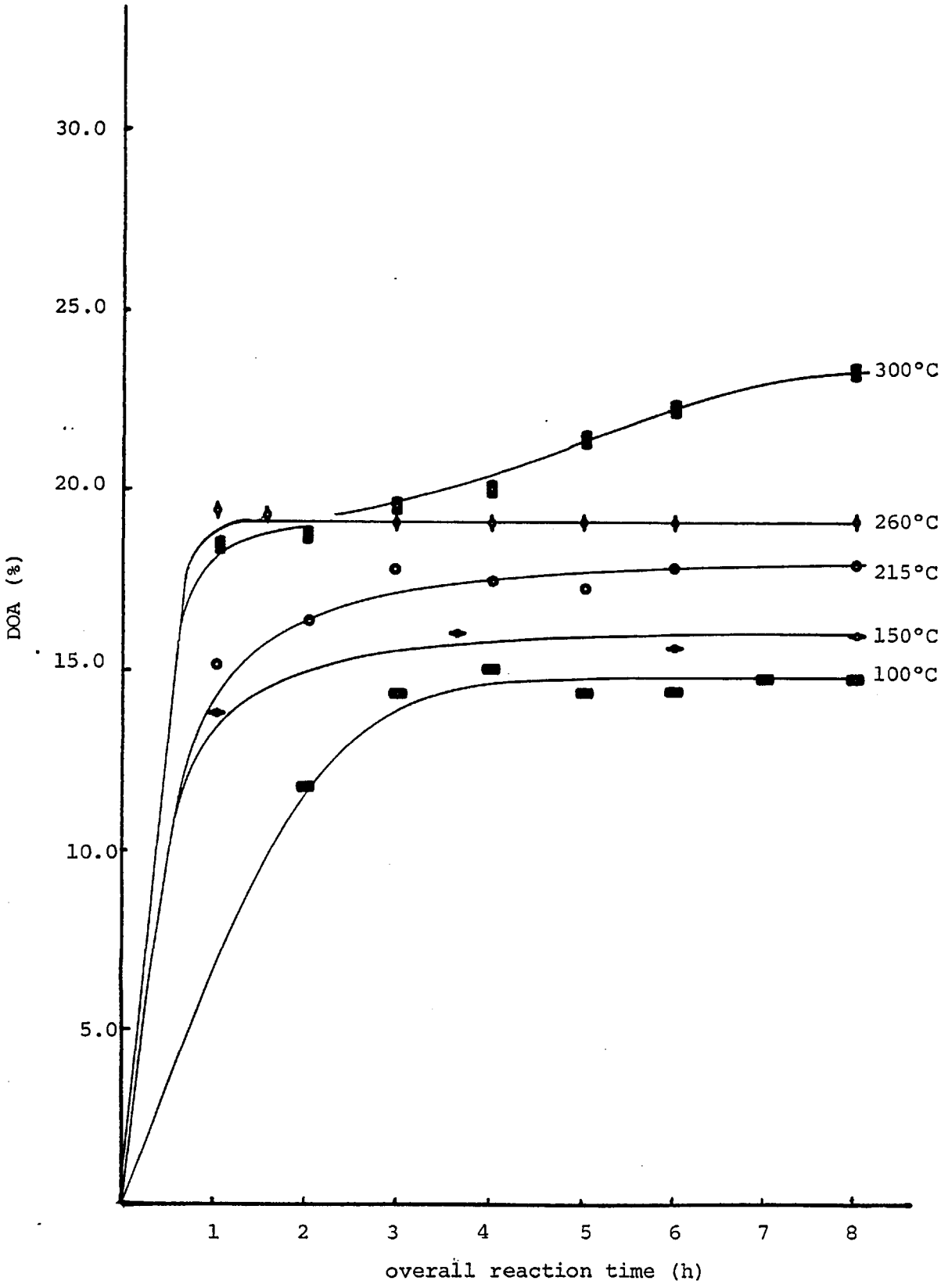


Figure 4.3.1 Relation between DOA and reaction time for system C at various temperatures.

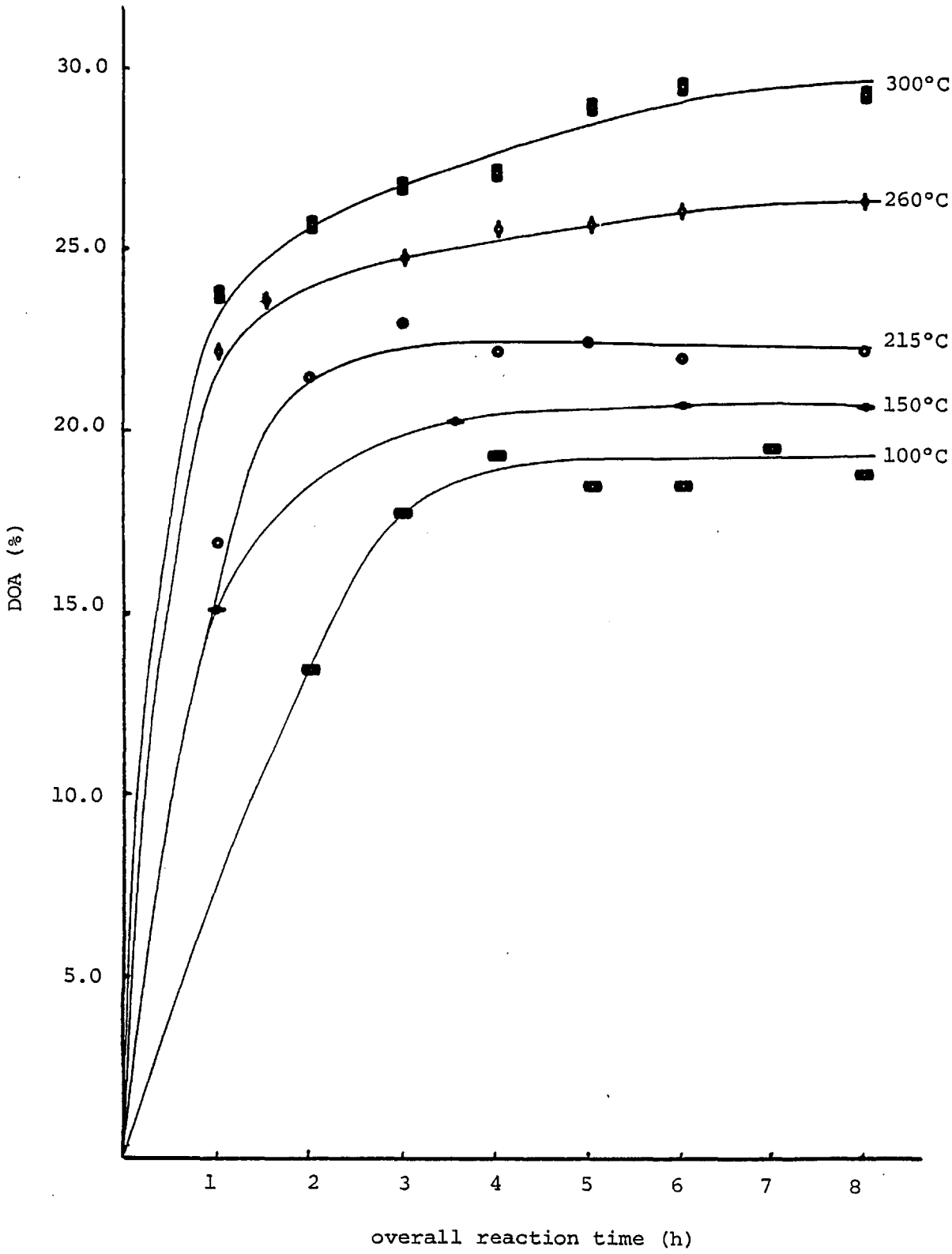


Figure 4.3.2 Relation between DOA and reaction time for system D at various temperatures.

below 260°C (System C) and 215°C (System D) no significant further degradation was recorded after this time. However, at higher temperatures, the DOAs continued to increase, though at a lower rate.

Figures 4.3.3-7 illustrate the relationships between residual concentration (or proportion of total ion) and the overall reaction time for magnesium, iron and calcium. In respect of the magnesium concentrations it is apparent that System C exhibited more complex behaviour than D : in the latter case, there is an increasingly rapid rate of solvation with increasing temperature followed by equilibration; this pattern being disrupted at the higher temperatures by precipitation of magnesium towards the end of the reaction. In the case of System C, reprecipitation appears to be more extreme. Furthermore, the rate and amount of magnesium entering solution increased with the initial aluminium concentration. For example, for System C the magnesium concentration was 0.05M at 1 h which rose to 0.33M at 7 h; whereas at 300°C a peak concentration 0.5M was noted at 1 h.

The changes in the iron concentration (Figures 4.3.5 and 4.3.6) differed in several respects from those observed for magnesium. In both systems a lower proportion of iron than magnesium was extracted from the kimberlite (e.g. 23% at 300°C, System D at 2 h, compared with 31% magnesium under the same conditions). Less clear trends were also observed. The initial reaction rate increased with temperature and with the concentration of aluminium employed. After rapid solvation of iron, reprecipitation of the ion occurred, the rate increasing with temperature up to 215°C. Above 215°C, the temperature had a progressively less important effect on the iron reprecipitation rate, such that at 300°C the recorded concentrations approached equilibrium values similar to the peak concentrations at 2-3 h.

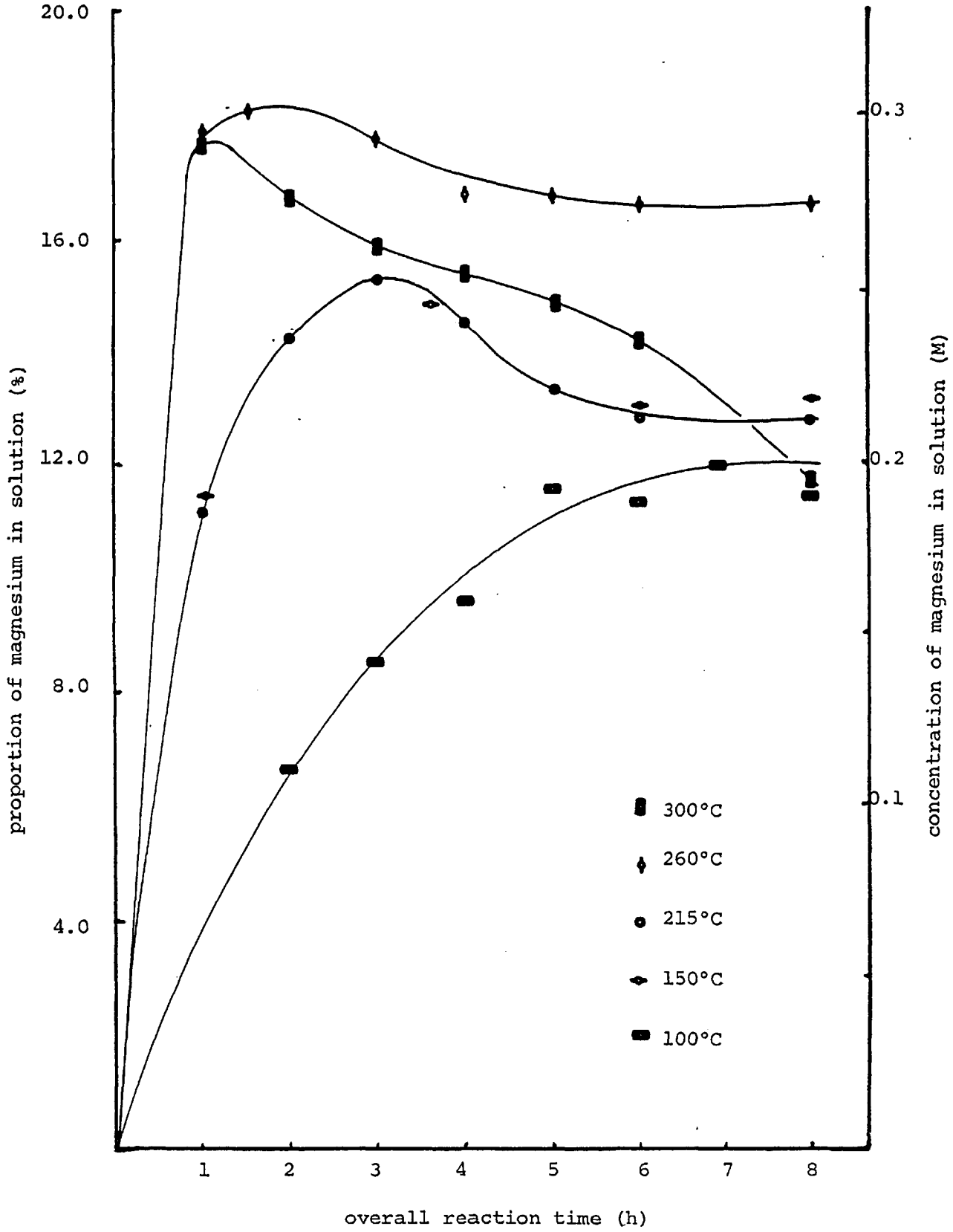


Figure 4.3.3 Relation between proportion and concentration of magnesium entering solution and reaction time for system C at various temperatures.

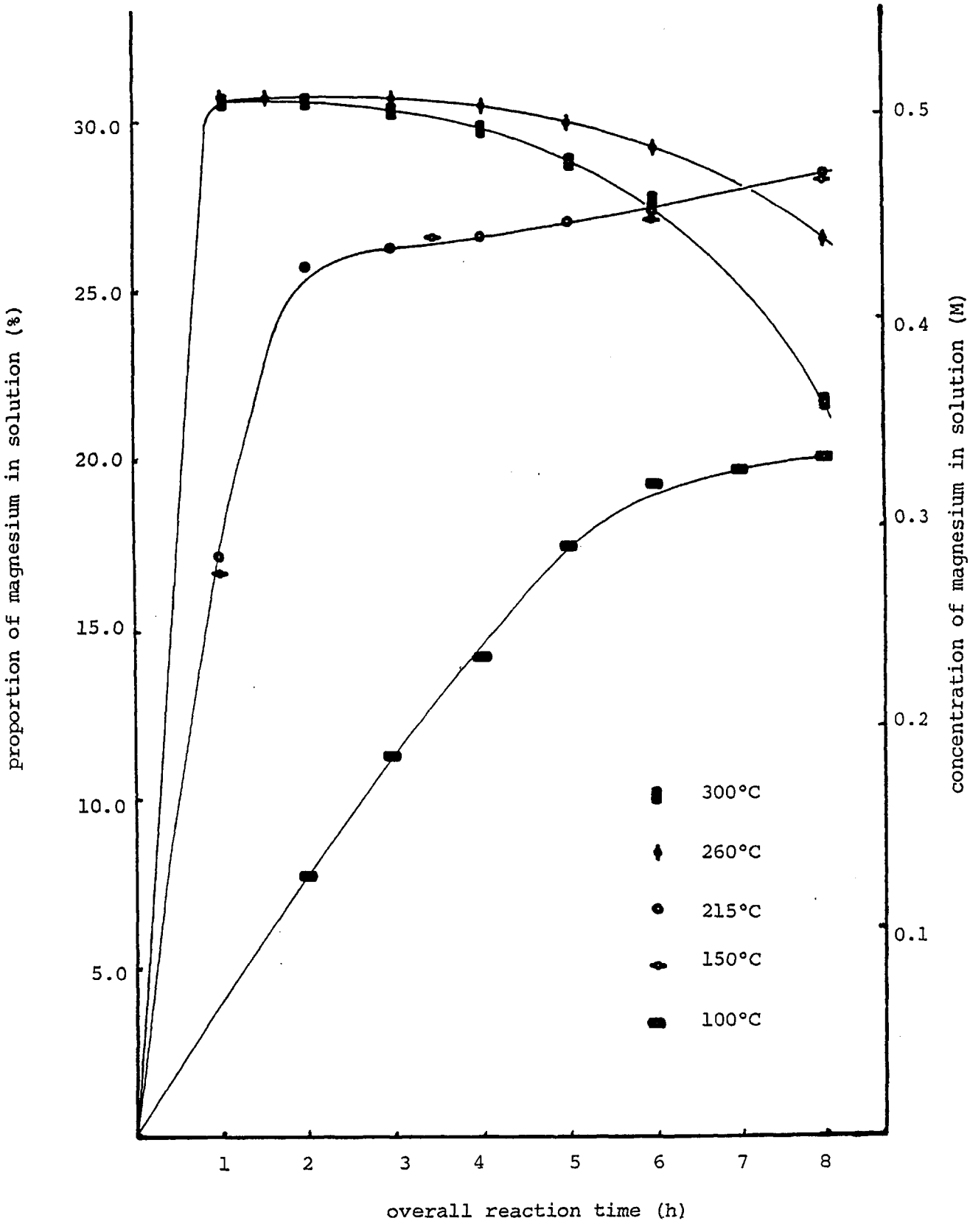


Figure 4.3.4 Relation between proportion and concentration of magnesium entering solution and reaction time for system D at various temperatures.

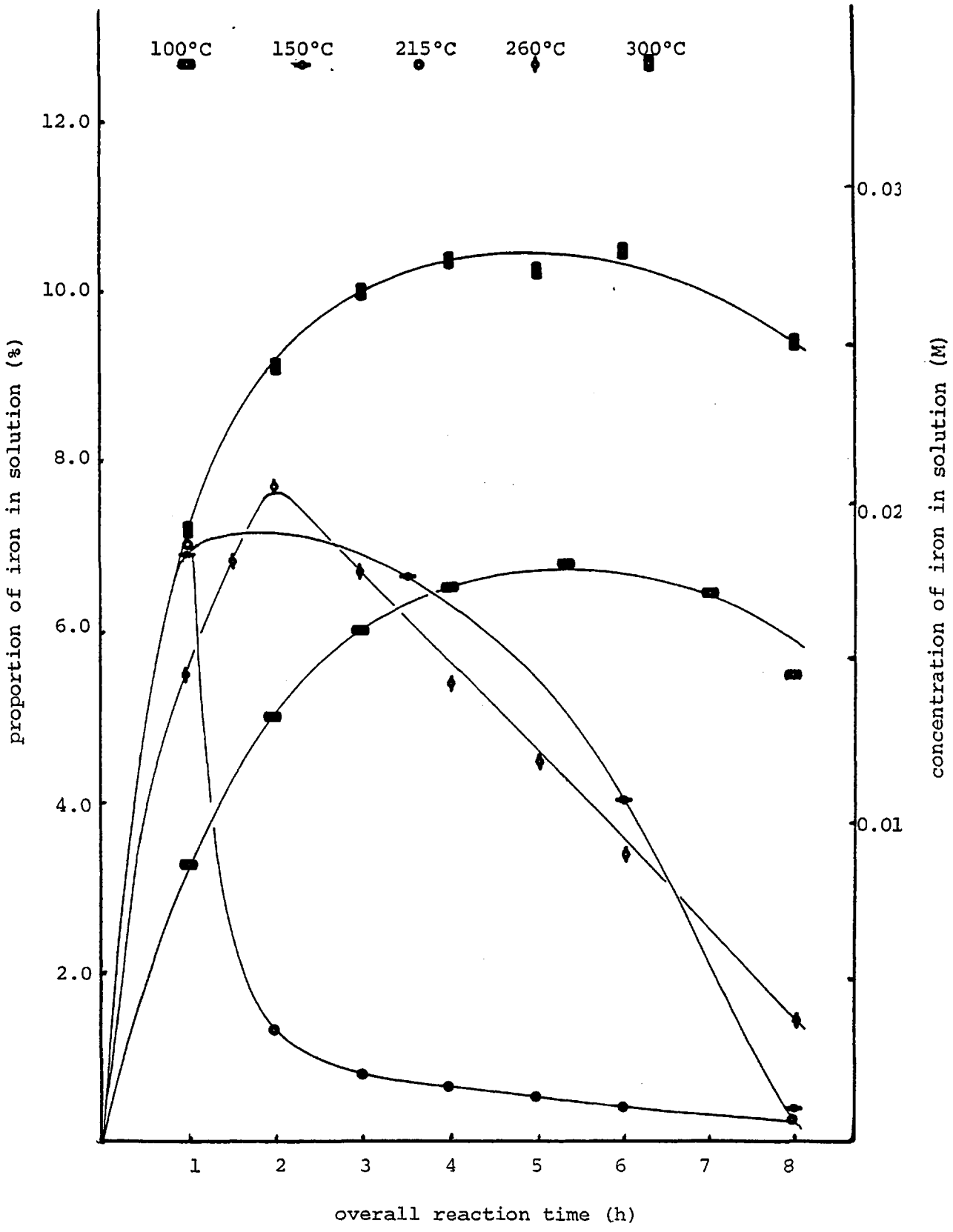


Figure 4.3.5 Relation between proportion of iron entering solution and reaction time for system C at various temperatures.

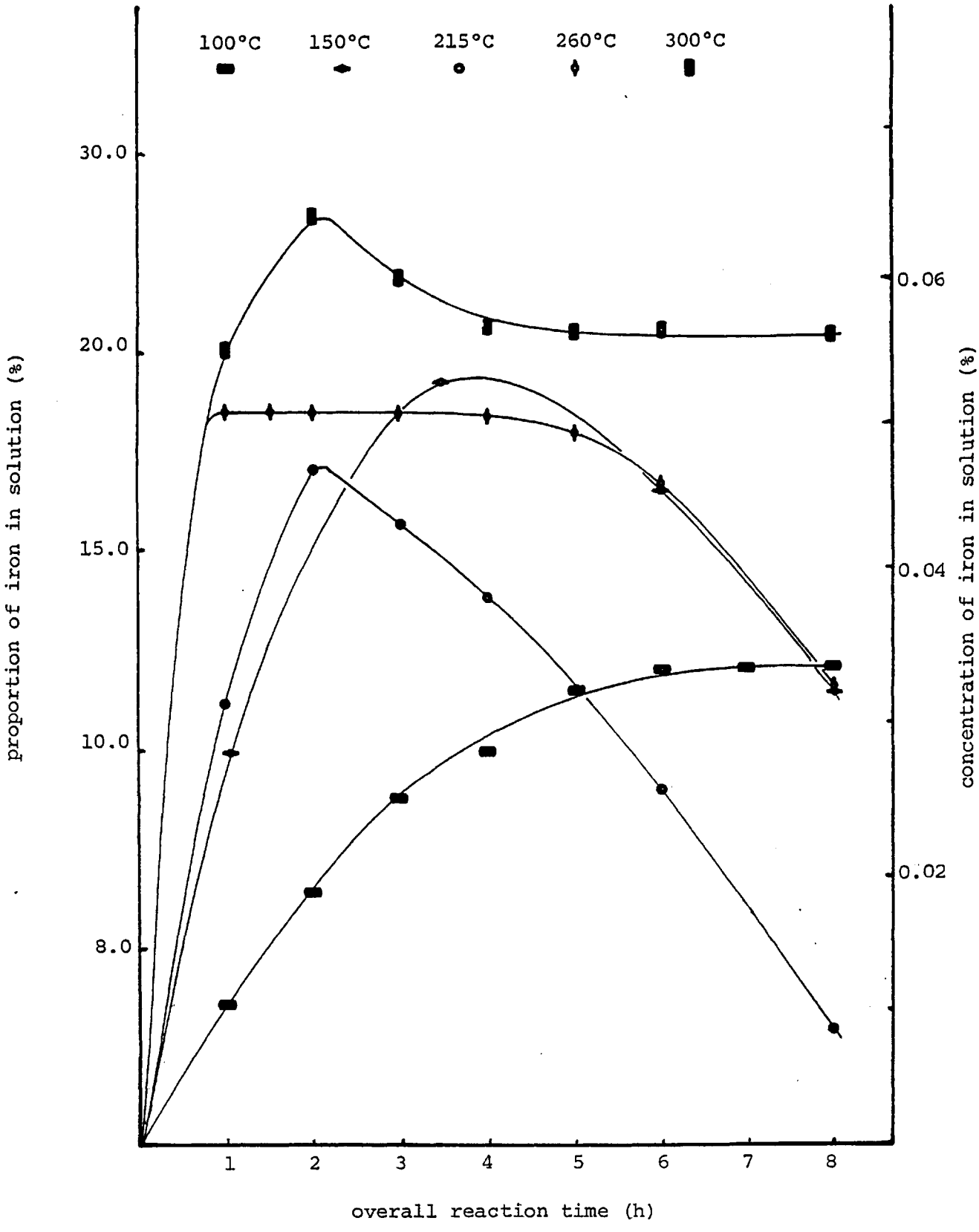


Figure 4.3.6 Relation between proportion and concentration of iron entering solution and reaction time for system D at various temperatures.

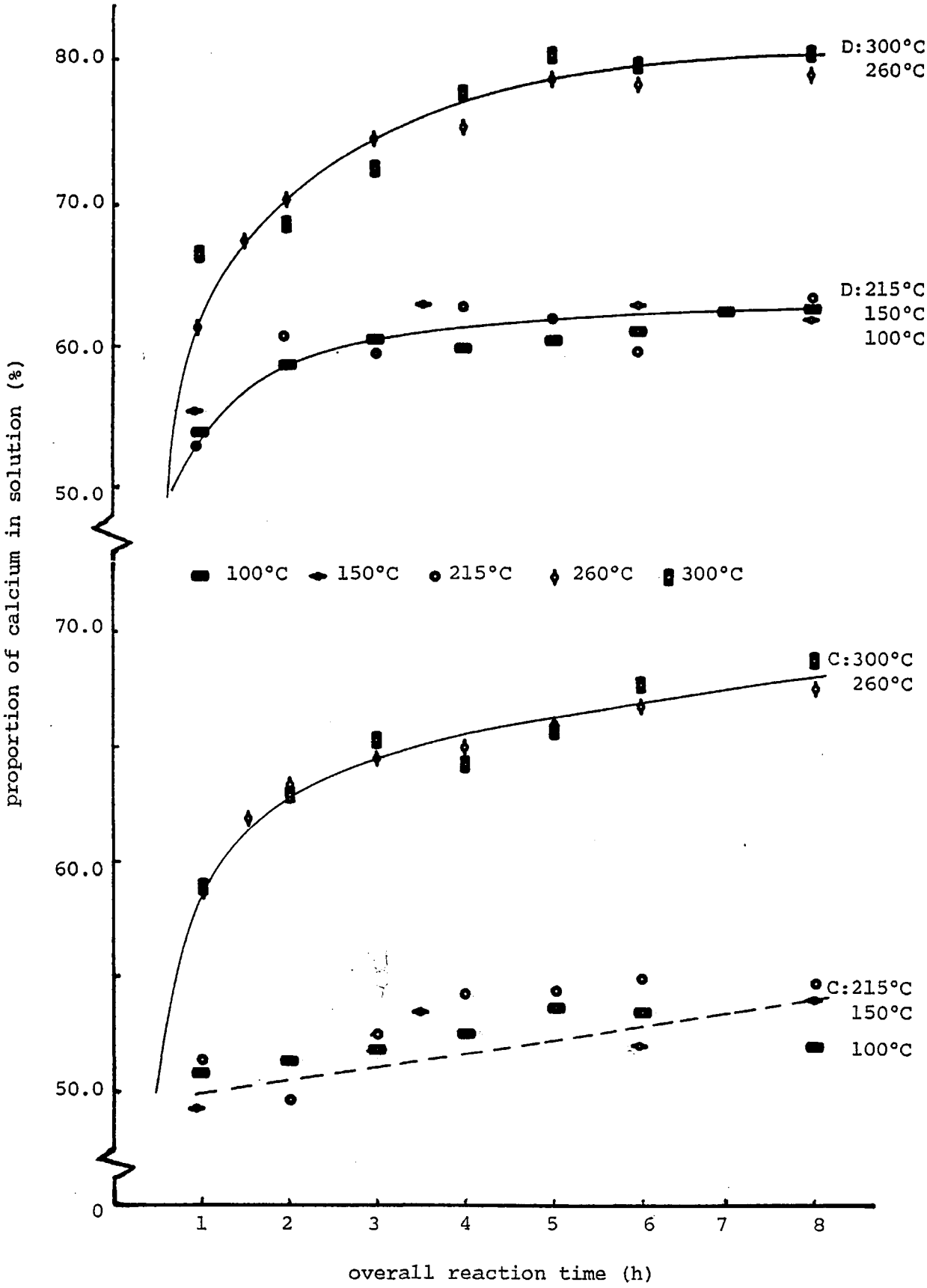


Figure 4.3.7 Relation between proportion of calcium entering solution and reaction time for systems C and D at various temperatures.

Examples of the wide extent of variation in iron concentration are those measured for System C at 4 h; namely 100°C, 0.017M; 150°C, 0.016M; 215°C, 0.002M; 260°C, 0.015M; 300°C, 0.028M. (There appears to be no reference in the literature to this unusual type of solubility behaviour for iron. Consequently it was assumed that the trends observed were unique to rock alteration systems involving secondary mineral formation.)

The proportions of calcium entering the solution phase for the two systems are shown in Figure 4.3.7. The spread of data points permitted only two plots to be drawn for both systems and are grouped for the temperatures 100-215°C, and 260-300°C. The majority of solubilised calcium was obtained during the first hour (50-70% of the total), as would be expected on the basis of calcite dissolution, after which the increase in concentration was small. The proportion of calcium entering solution increased with temperature and aluminium dosage.

In most cases, little or no aluminium or silicon could be detected in the solutions analysed.

4.3.3 Results : Mass balances

Examples of elemental mass balances for magnesium, silicon and iron at 215 and 300°C (System C) are shown in Table 4.3.2. Similar results were obtained at other temperatures and for System D but these are not shown here. In the case of the latter any trends in the mass balance data were masked, owing to loss of sensitivity due to the precipitation of aluminium hydroxyoxide phases.

The data in Table 4.3.2 are presented in terms of percentage elemental distributions. These were calculated after deducing the mass of the ion in question in each of the +75 μm, -75 μm

TABLE 4.3.2 PERCENTAGE ELEMENTAL DISTRIBUTION AT VARIOUS REACTION TIMES FOR SYSTEM C AT 215°C and 300°C

	215°C				300°C			
Phase	Reaction Time (h)	Element Mg	Si	Fe	Reaction Time (h)	Element Mg	Si	Fe
+75 μm		88.5	97.0	93.1	1	81.4	96.0	69.2
-75 μm	1	0.5	2.0	0.6	1	1.2	4.0	1.6
solution		11.0	1.0	6.3		17.4	0.0	29.2
+75 μm		83.9	93.2	95.8		82.7	95.0	82.8
-75 μm	2	1.0	6.8	4.2	2	1.2	5.0	2.0
solution		15.1	0.0	0.0		16.1	0.0	15.2
+75 μm		86.2	92.0	95.1		82.0	91.7	73.7
-75 μm	4	1.1	8.0	4.3	3	2.0	8.3	1.9
solution		12.7	0.0	0.6		16.0	0.0	19.4
+75 μm		84.4	91.7	92.8		82.9	90.2	88.2
-75 μm	5	2.0	8.3	6.5	5	2.2	9.8	2.0
solution		13.6	0.0	0.7		14.9	0.0	9.8
+75 μm		84.4	89.2	89.9		80.3	90.0	74.2
-75 μm	6	3.2	10.8	9.5	8	7.7	10.0	18.7
solution		12.4	0.0	0.6		12.0	0.0	1.1

and solution phases (Section 2.4.3).

The table indicates the progressive incorporation of magnesium, silicon and iron in the -75 μm altered solid phase. For short reaction times (1-2 h) the majority of magnesium and iron extracted reported to the solution phase, whereas at 5-8 h these ions progressively precipitated (with increasing temperature) in the -75 μm fraction (in particular at 8 h, 300°C). Silicon, where liberated, entered the -75 μm phase.

Further to the comments at the end of the last section, the distributions for aluminium and calcium did not exhibit any significant variation with time. No aluminium remained in the solution phase, though as much as 70% of that present remained in the +75 μm phase. Any liberated calcium (56-65%) remained in solution.

The significance of these mass balances will be considered in Section 4.5.

4.3.4 Results and interpretation : Infra-red analyses

In consideration of the XRD results to be described in Section 4.4.1, the most useful IR recordings were those obtained at 215, 260 and 300°C where discernible crystalline phases were generated (for Systems C and D). These will be described here. IR recordings will also be interpreted for the system employing 2 g hydrated aluminium chloride (Section 4.3.1), which will be denoted as System E. The IR recordings are shown in Figures 4.3.8-14 and it is convenient to discuss System E (215°C) first, as the greatest variation in peak intensity was observed in this case. The treatment is somewhat more detailed than in previous sections on IR in an attempt to follow structural transformations taking place as the reactions proceeded.

215°C Figure 4.3.8a shows the trace for the -75 μm product obtained from System E after 1 h at 215°C. The peak at 970 cm^{-1} was taken as indicative of a tetrahedral lattice structure containing both aluminium and silicon. The high aluminium concentration was reflected by Al-OH groups at 250 cm^{-1}, 340 cm^{-1} (and part of the) 540-600 cm^{-1} bands. The spectrum resembled that of an imogolite. This mineral type is described by Farmer et al[255] as consisting of orthosilicate groups attached to fragments of gibbsite-like sheets of aluminium hydroxide. The structure would appear to have similarities to kaolinite, though, of course a considerable concentration of simple hydroxyoxides (such as boehmite[233]) was present. As the reaction progressed (2-4 h) the introduction of a shouldered peak was observed at 360-370 cm^{-1} at the expense of the 340 cm^{-1} peak. The bands also became broader, occupying the 900-1100 cm^{-1} (Al-OH, Si-O) and 470-790 cm^{-1} (Al^{VI}-O-Si, Si-O) regions[233] (Figures 4.3.8b,c). Of particular interest was the peak at 1070 cm^{-1} for the 4 h product. Whereas the shape of the recorded spectrum was indicative of a 2:1 layered silicate mineral,[204,228] the 1070 cm^{-1} peak, in conjunction with the broad shoulder at 1200 cm^{-1} and the peak at 460 cm^{-1} was suggestive of a 1:1 silicon-aluminium gel being also present.[255] As the reaction proceeded to 8 h, the shouldered peaks at 900 cm^{-1} and 200-250 cm^{-1} decreased in intensity. These groups of peaks are associated with aluminium hydroxyoxides. This decrease was probably the result of the increasing silicon proportion in the -75 μm product which resulted in the incorporation of hydroxyoxide groups in the silicate lattice. The resultant spectra shown in Figures 4.3.8d,e are representative of a 2:1 layered silicate (cf. Figure 4.4.3).

From the results obtained for System E, the data for Systems C and D could be more readily interpreted. The trace shown in Figures

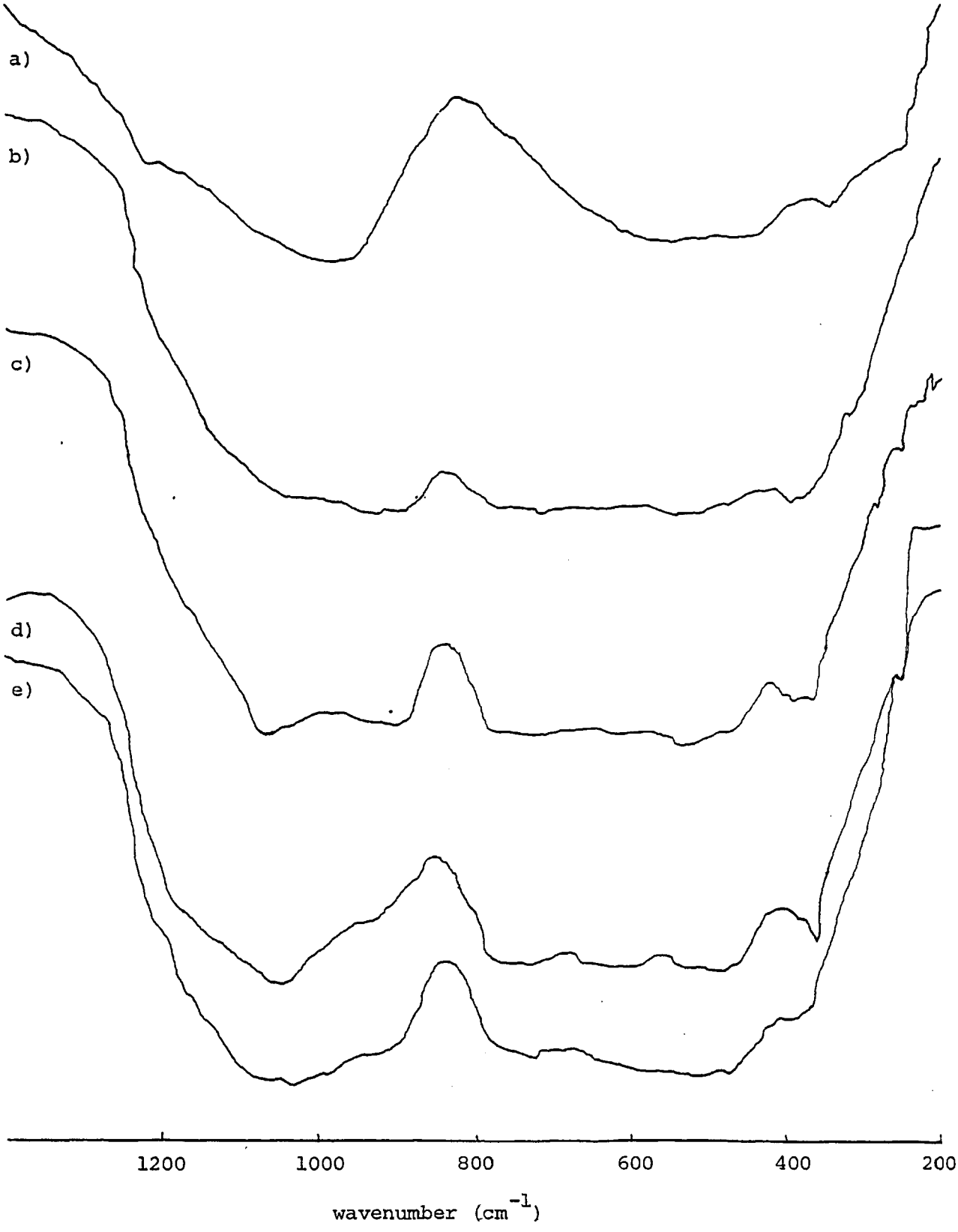


Figure 4.3.8 Infra-red spectrograms for -75 μm products obtained from system E reacted at 215°C for

a) 1h;
b) 2h;
c) 4h;
d) 6h;
e) 8h.

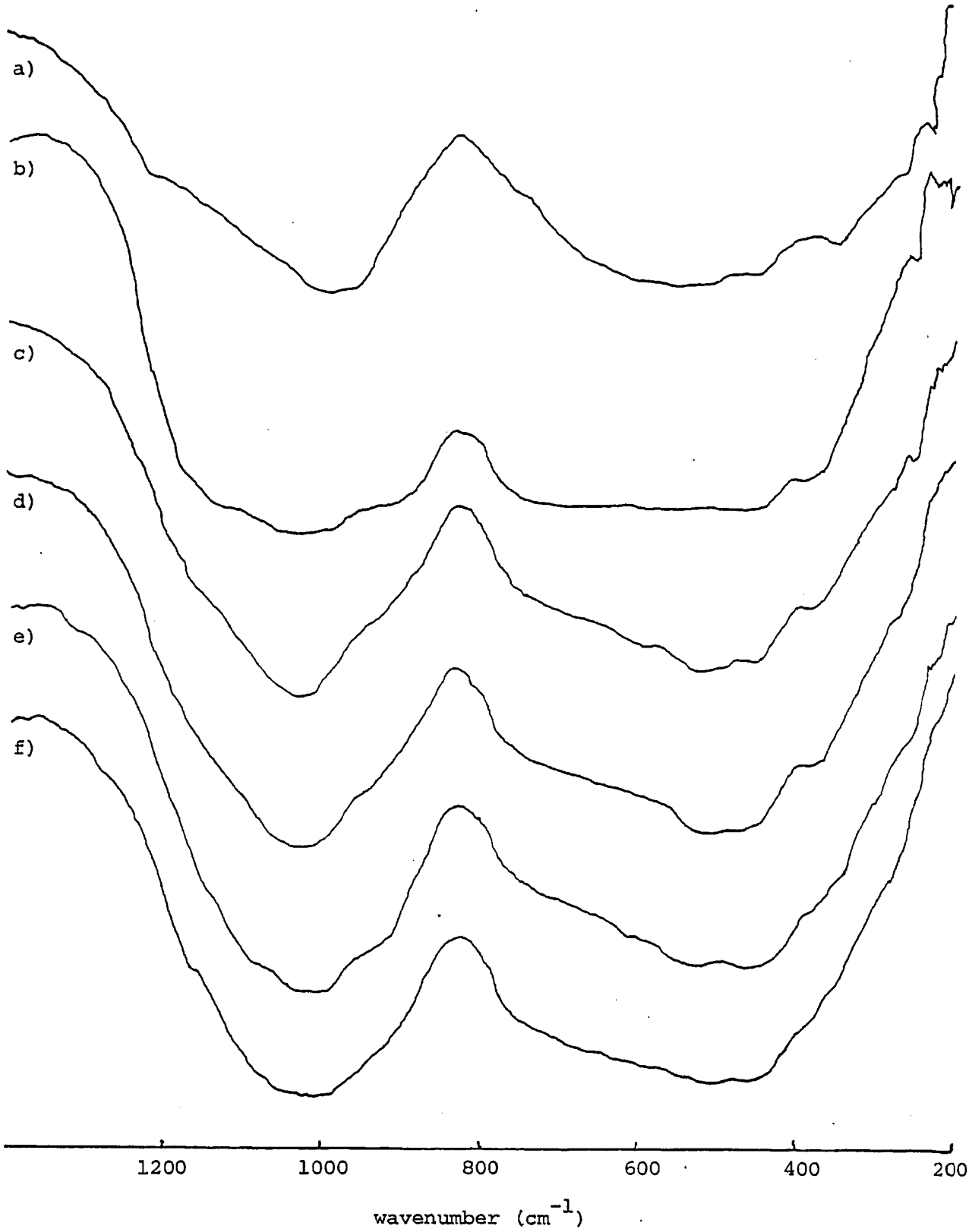


Figure 4.3.9 Infra-red spectrograms for -75 μm products obtained from system C reacted at 215°C for

a) 1h; d) 5h;
b) 2h; e) 6h;
c) 3h; f) 8h.

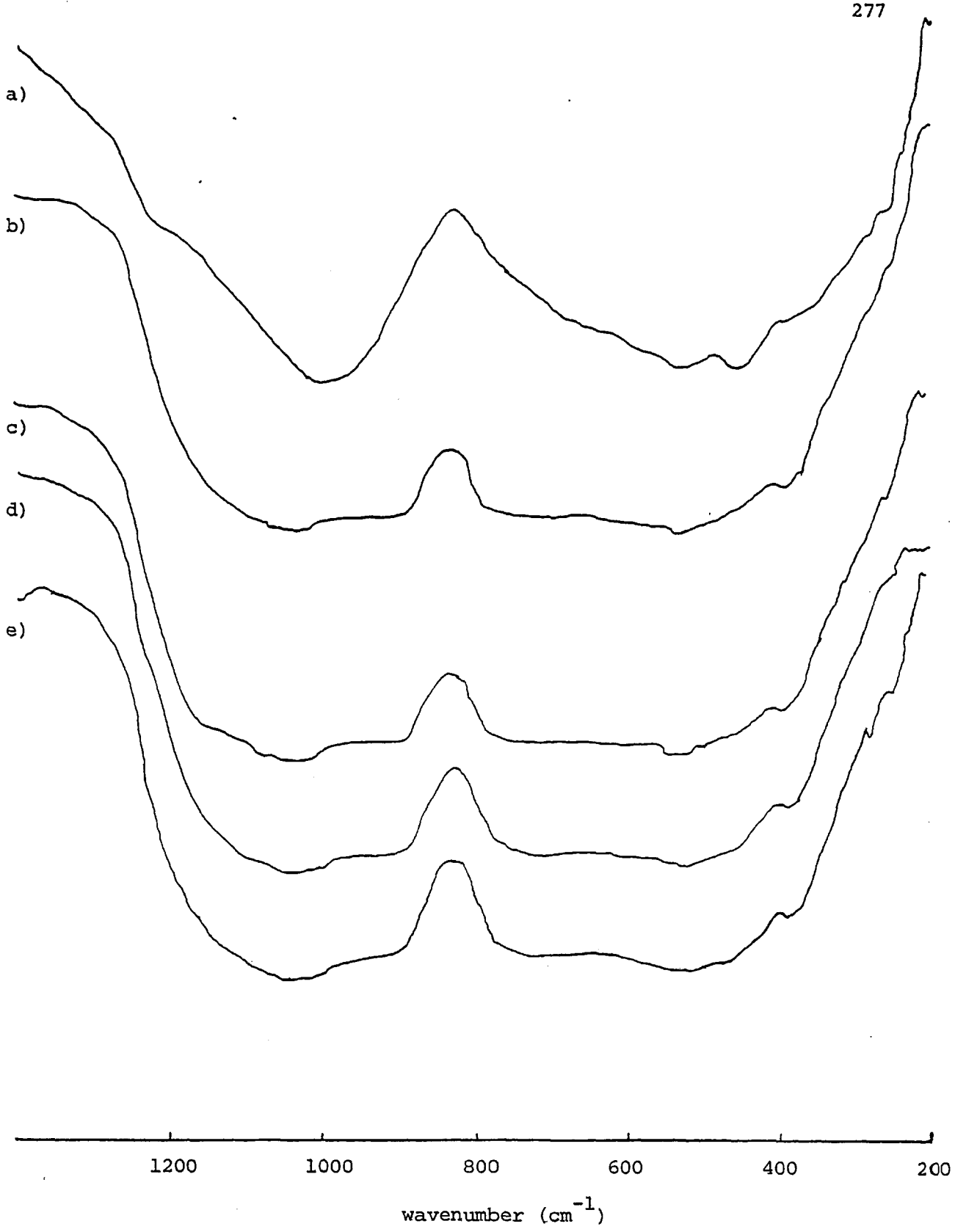


Figure 4.3.10 Infra-red spectrograms for -75 μm products obtained from system D reacted at 215°C after

a) 1h;
b) 2h;
c) 4h;
d) 6h;
e) 8h.

4.3.9a resembled 4.3.8a. This imogolite-type phase was replaced by a disordered alumino-silicate mixture at 2 h. By 4 h the broad 940-1200 cm^{-1} and 400-800 cm^{-1} bands had sharpened and peaks at 450 cm^{-1} (Si-O), 540 cm^{-1} (Al^{VI}-O-Si) and 1000 cm^{-1} (Si-O) had emerged. This product was identifiable with 1:1 kandites (Figures 4.3.9c,d). The resolution of the first two peaks decreased as the reaction time increased and the 770 cm^{-1} shouldered peak became more prominent. It appeared that the concentration of 2:1 silicate phases increased in the latter stages of reaction (Figures 4.3.9e,f. cf. Figure 4.3.8e).

In the case of System D (Figure 4.3.10), a series of peak shifts comparable with those in System E were observed.

260°C The IR trace of the first formed product obtained using System C at 260°C was also similar to those in Figures 4.3.8a and 4.3.9a. This imogolite-kandite phase was apparently replaced by a poorly crystalline 2:1 layer silicate at 2-3 h, as typified by the broad peaks in Figure 4.3.11b; (cf. 4.3.9e,f); and the movement of the 340 cm^{-1} peak to 360 cm^{-1}. At 4 h a different set of peaks was observed, as seen in Figures 4.3.11d-g. These peaks were at 3640 cm^{-1} (Me-OH), 1020 cm^{-1} (Si-O), 540 cm^{-1} (Al^{VI}-O-Si), 470 cm^{-1} (Mg^{VI}-O-Si, Si-O) and shoulders at 930 cm^{-1} (Al-OH), 770 cm^{-1} (Al^{VI}-O-Si), 700 cm^{-1} (Si-O), 620 cm^{-1} (Mg^{VI}-O-Si, Si-O) and 360 cm^{-1} (Al-OH)[232,233] The introduction of peaks at 540 cm^{-1}, 620 cm^{-1} and 3640 cm^{-1} indicated the presence of a stable octahedral aluminium/magnesium hydroxide layer in the lattice. The resolution of these peaks increased with time. The movement of the (Si-O) peak from 1000 cm^{-1} to 1020 cm^{-1} was also associated with the stabilisation of the clay mineral structure.

A similar set of traces was obtained for System D (Figure

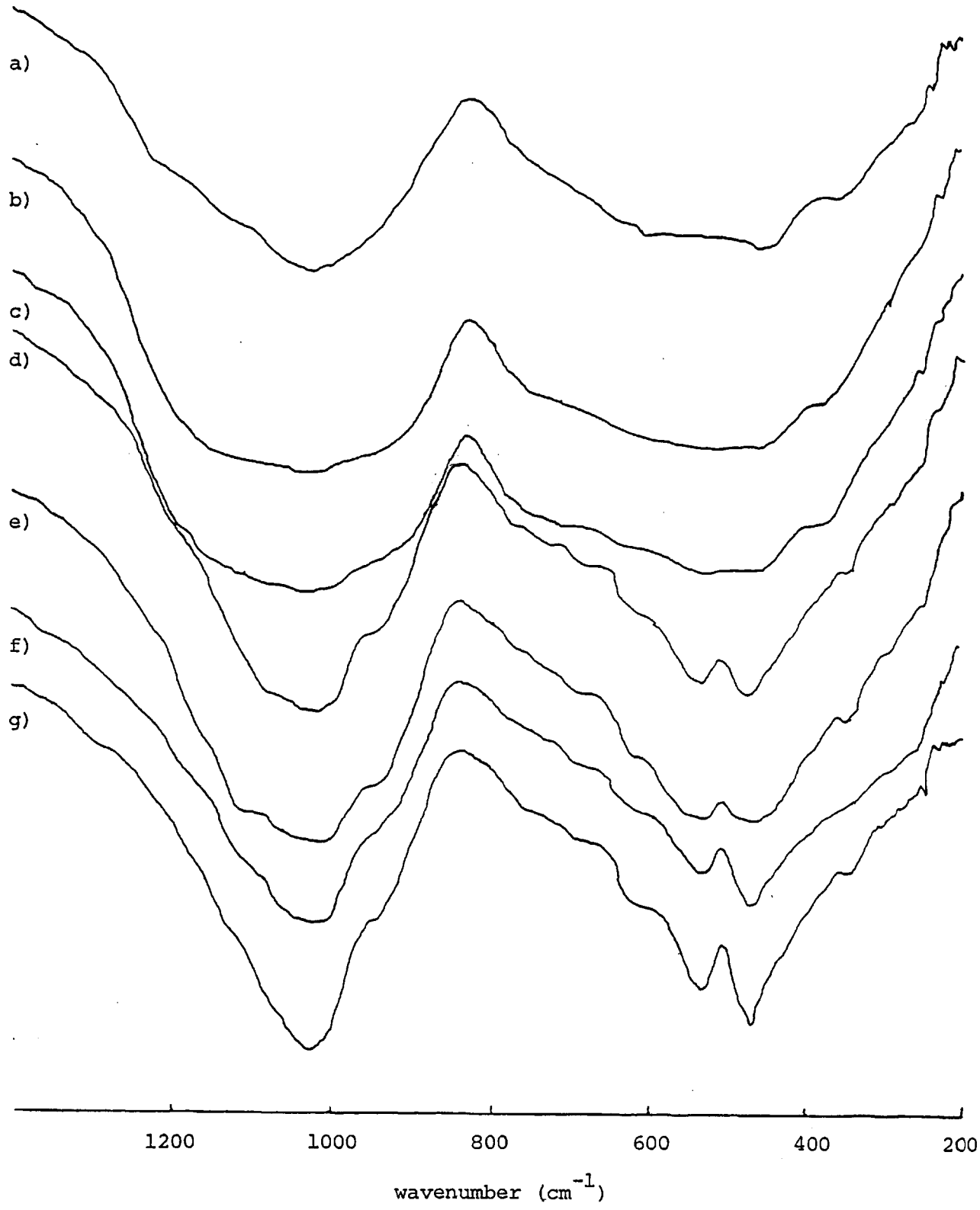


Figure 4.3.11 Infra-red spectrograms for -75 μm products obtained from system C reacted at 260°C for

a) 1h;
b) 2h;
c) 3h;
d) 4h;
e) 5h;
f) 6h;
g) 8h.

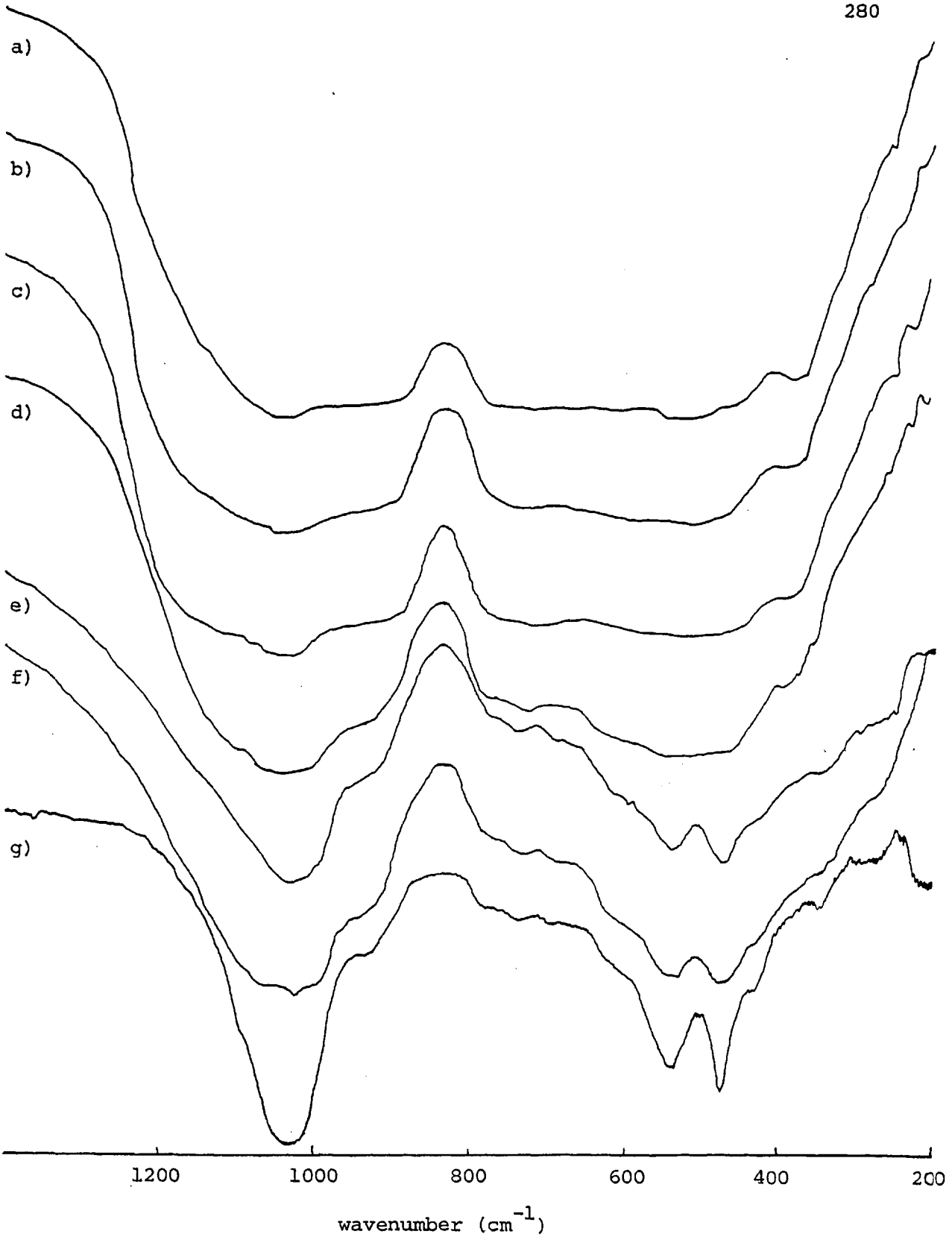


Figure 4.3.12 Infra-red spectrograms for -75 μm products obtained from system D reacted at 260°C for

a) 1h;
b) 2h;
c) 3h;
d) 4h;
e) 5h;
f) 6h;
g) 8h.

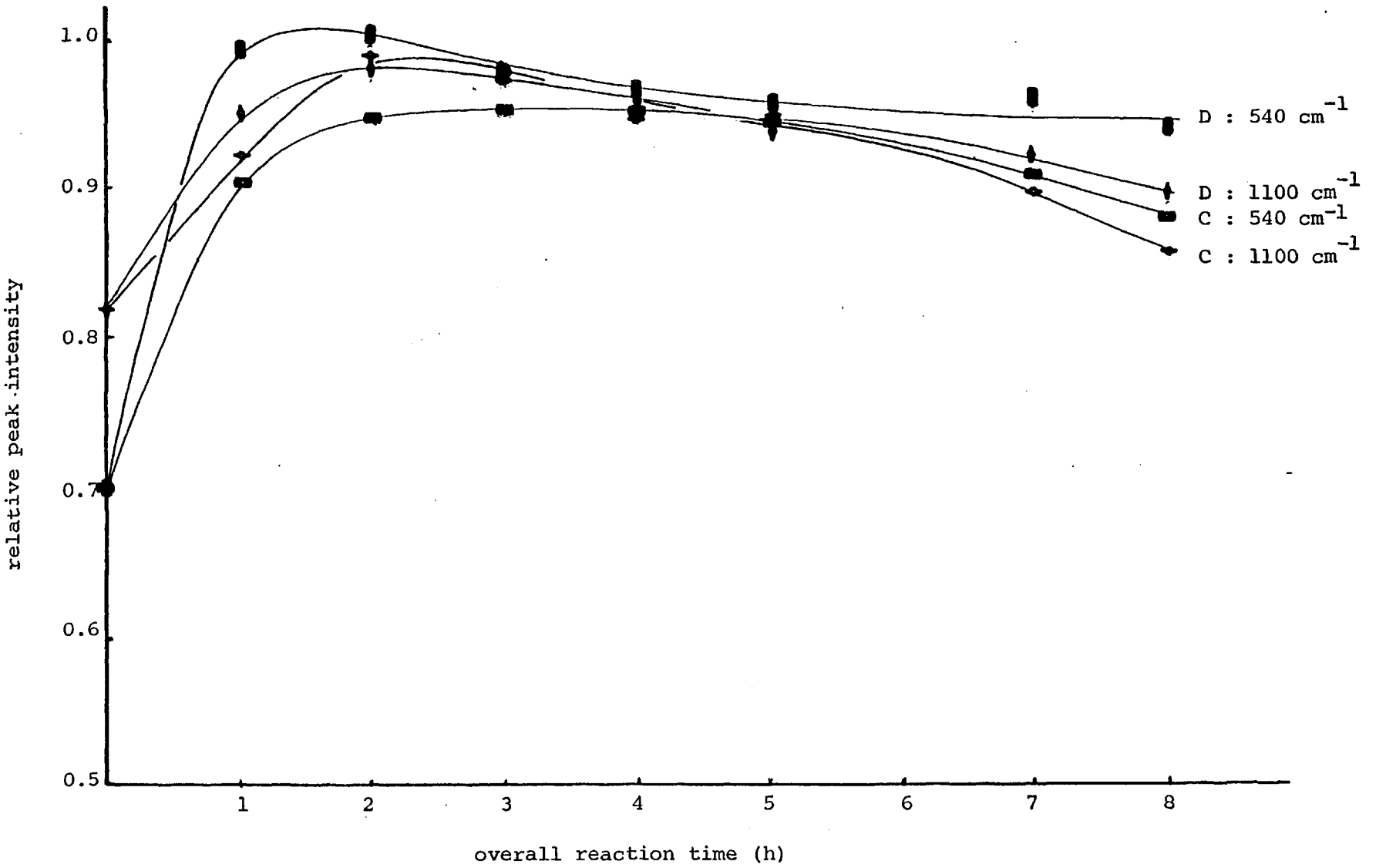


Figure 4.3.13 Relation between relative IR peak intensities reaction time for -75 μm products generated in systems C and D at 260°C

4.3.12 a-g). Here, 2:1 layered type silicates appeared as the first formed products (Figures 4.3.12 a-c). At 4 h a structural transformation began, which, by 5 h had resulted in the sharpening of the broad peaks in the 900-1100 cm^{-1} and 400-800 cm^{-1} regions. The resultant products (Figures 4.3.12 e-g) had well resolved peaks at 540 cm^{-1}, 770 cm^{-1}, 940 cm^{-1} (Al-OH) and 1020 cm^{-1} which were found to typify diactahedral smectites.

The data illustrated in Figure 4.3.11 and 4.3.12 were further analysed by measuring peak heights relative to the 1000 cm^{-1} peak after the procedure described in Section 4.2.4. As can be seen (Figure 4.3.13) the proportion of amorphous silica species and octahedrally coordinated aluminium increased to maximum values at 1-2 h for both systems. The 1100 cm^{-1} peak ratios decreased after 2 h for System C and after 4 h for System D. These times marked the transition from a relatively amorphous to a relatively crystalline state in agreement with the general trends observed in Figures 4.3.11 and 4.3.12. The ratios for the 540 cm^{-1} band also decreased with time for System C which indicated the progressive entry of divalent ions into the octahedral lattice of the newly-forming phyllosilicates. In the higher aluminium concentrations of System D, however, dioctahedral forms continued to predominate as inferred from Figure 4.3.13.

300°C The IR recordings obtained for the -75 μm fractions produced using Systems C and D at 300°C are shown in Figures 4.3.14 and 4.3.15 respectively. As can be seen, the resolution of the peaks was improved at the higher temperatures. For System C, the initial product (Figure 4.3.14a) appeared to resemble a kandite - 2:1 layer silicate of the type reported in Figure 4.3.9f. At 2 h a crystalline phyllosilicate comparable with that obtained after 6 h at 260°C (Figure 4.3.11f) was

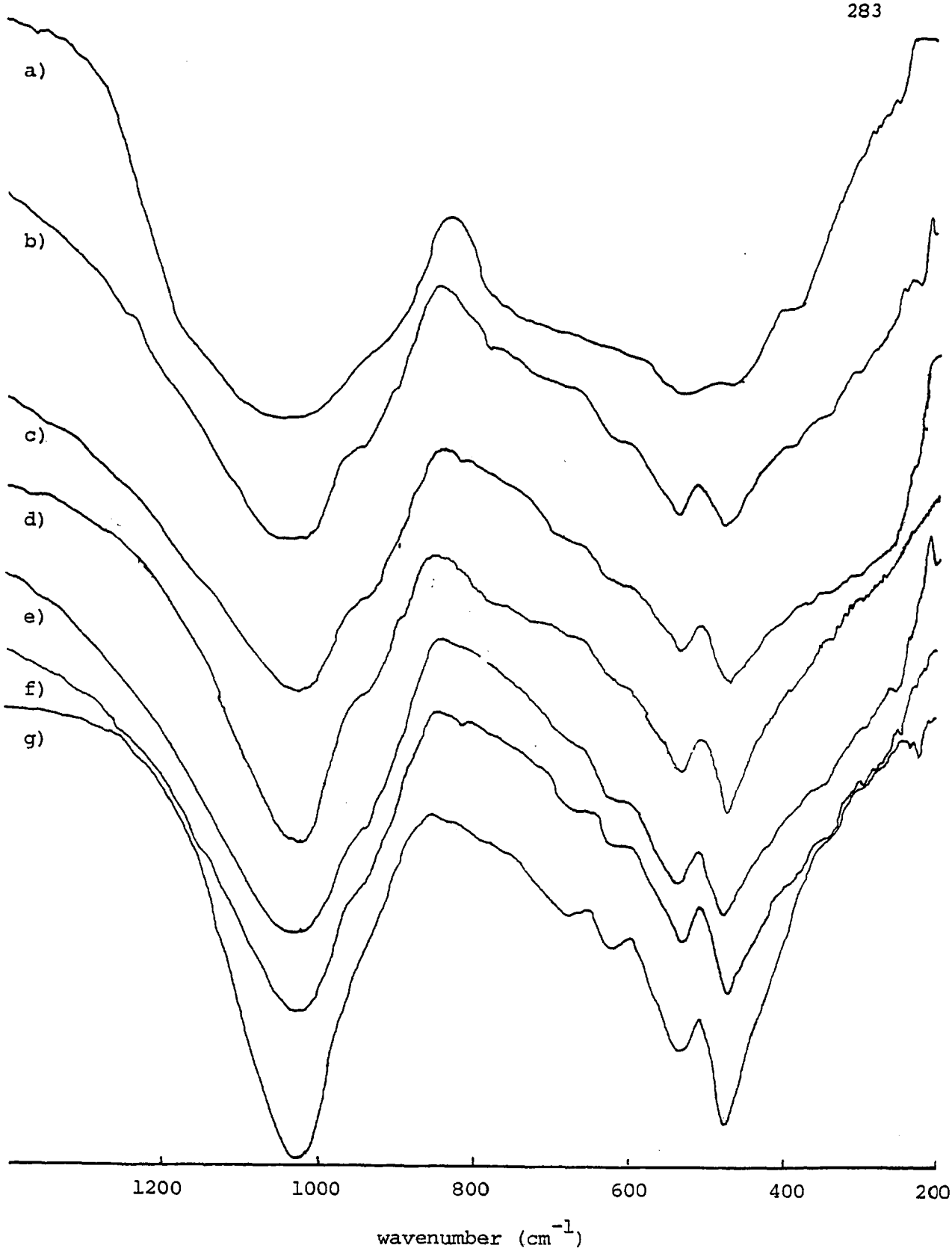


Figure 4.3.14 Infra-red spectrograms for -75 μm products obtained from system C reacted at 300°C for

a) 1h;
b) 2h;
c) 3h;
d) 4h;
e) 5h;
f) 6h;
g) 8h.

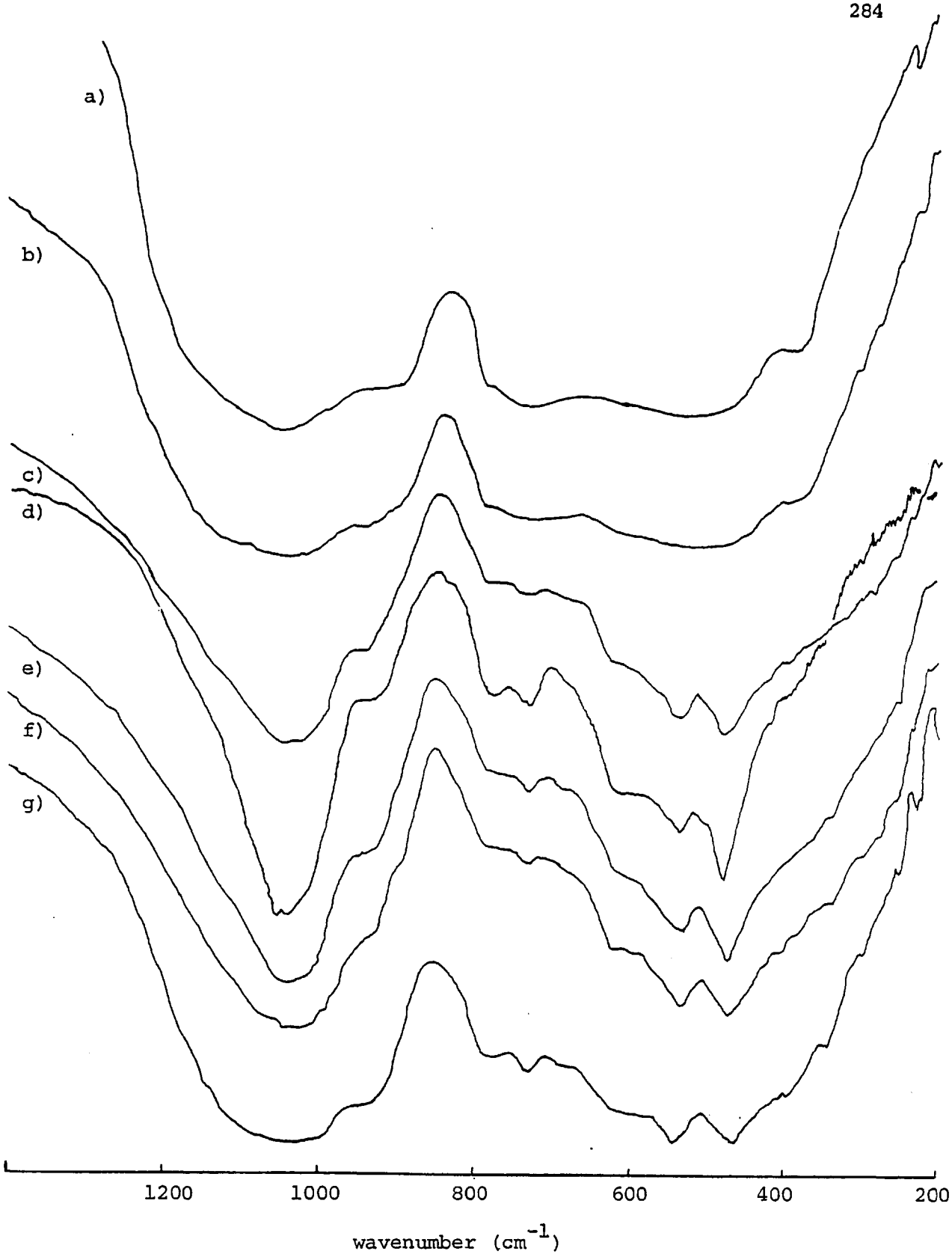


Figure 4.3.15 Infra-red spectrograms for -75 μm products obtained from system D reacted at 300°C for

a) 1h;
b) 2h;
c) 3h;
d) 4h;
e) 5h;
f) 6h;
g) 8h.

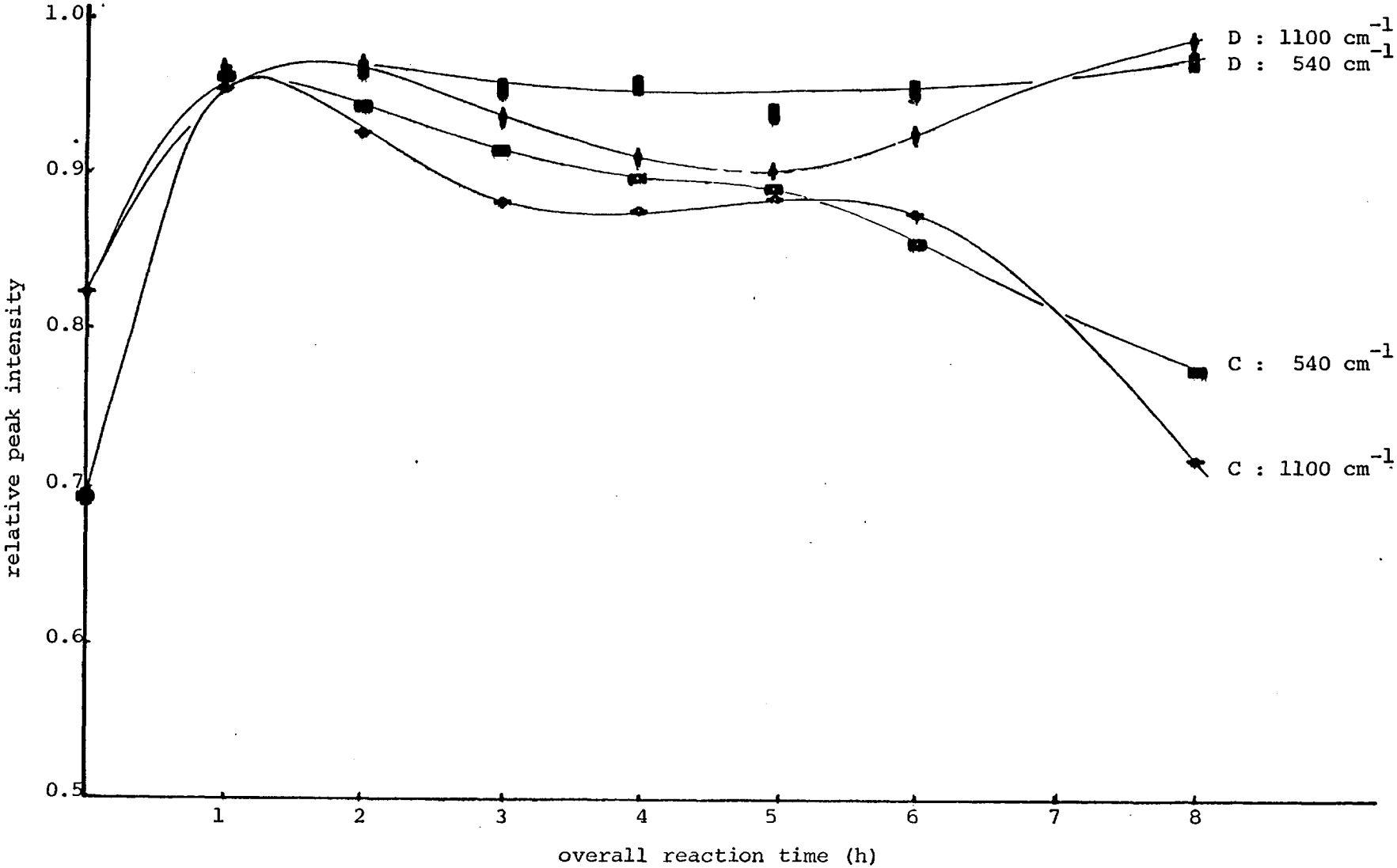


Figure 4.3.16 Relation between relative IR peak intensities and reaction time for -75 μm products generated in systems C and D at 300°C.

recognisable. For reaction times greater than 2 h, the peak intensities increased, save for those associated with certain free Al-OH groups, notably at 340 and 940 cm^{-1}, which disappeared completely by 8 h. Figures 4.3.14 e-g show the progressive crystallisation of the final vermiculite-chlorite product (see Section 4.4.1).

The sequence of IR traces obtained for System D was very similar to that of System C except peaks associated with aluminium groupings persisted (as expected). The first formed product was clearly an aluminium-rich 2:1 silicate (Figure 4.3.15a) which recrystallised slowly at 2-4 h into a predominantly dioctahedral smectite (Figure 4.3.15g).

The peak intensities of 540 and 1100 cm^{-1} expressed relative to that at 1000 cm^{-1} were also plotted as shown in Figure 4.3.16. The figure showed strong similarities with that in Figure 4.3.13, the difference being the larger drop in the 540 and 1100 cm^{-1} ratios for system C after the initial increase at 1 h. In contrast to Figure 4.3.13 the 1100 cm^{-1} ratio continued to increase. This apparent increase in the amorphous siliceous character in the product may be interpreted as resulting from the continuation of the alteration reaction after the establishing of the first final crystalline product at 5-6 h (Figures 4.3.15e,f).

4.4 Estimation of Clay Phases Formed at 100-300°C

4.4.1 Results and discussion : Qualitative X-ray diffraction analyses

Each of the -75 μm products obtained (Sections 4.2.1 and 4.3.1) were analysed by XRD (Section 2.3.2) and the 4-20 '2θ' regions representing the diffractograms are shown in Figures 4.4.1-7. These were drawn to indicate the progress of the reactions with time. It should be again noted, however, that the intensity of X-rays diffracted

by clay minerals can greatly vary according to crystallinity, packing, orientation and other effects noted in Section 2.3.4. By analysing the products within a short space of time and adopting the same sample preparation procedure throughout, extraneous effects were assumed to be sufficiently suppressed such that trends in reaction could be observed; at least, in part.

Products synthesized at temperatures of 100, 130 and 150°C for reaction times of less than 7 h were relatively poorly crystalline, particularly in the cases of Systems C and D. In System A however, where the masking effects of precipitated hydroxides were less, peaks attributable to vermiculite-chlorite and kandite type minerals were observed with some residual mica. An example is shown in Figure 3.3.11b. A similar suite of minerals was detected for System B and the diffractogram peaks of the clay minerals (e.g. Figure 3.3.11d) were somewhat better resolved. In these products broad small 7.2 Å and 9.8 Å peaks were also observed. The low order of crystallinity of these products obtained at temperatures at or below 150°C resulted in poor peak resolution masking any trends in the proportions of mineral phases. Hence data for these systems at lower temperatures are not included.

Reactions using similar conditions (Systems A or B) produced similar results when tested with the serpentine standard. In the case of the olivine standard, gels resulted in most cases. However where the pH exceeded 3.5 a fine alteration product was obtained (see later).

The degree of definition (and thus the crystallinity) of important clay mineral diffraction peaks improved with a rise in reaction temperature. Identifiable crystalline products were obtained at 215°C. Consequently, the technique of XRD analysis could be employed directly to investigate phase changes, and to make inferences with respect to lower temperature reactions.

The XRD results of the sequence of kinetic experiments performed at 215°C are given in Figure 4.4.1 a-d (System C) and 4.4.2 a-e (System D). In System C, a broad band was observed in the 7.3-11 Å region after 1 h (Figure 4.4.1a). The recorded peaks related to poorly crystalline silicate phases, rather than amorphous hydroxyoxides as can be seen from comparing the diffractogram with the smooth trace obtained for hydroxyoxide minerals in Figure 2.3.2f. The first-formed products in System C at 215°C were attributed to a mixture of disordered 1:1 and 2:1 layered silicates. As the reaction progressed, crystal ordering these silicates evidently occurred to form a 7.2-7.6 Å 1:1 layered silicate at 6 h (figure 4.4.1d). In System D the 9-11 Å phase (barely seen in System C) had much enlarged peaks which diminished in intensity with reaction time (Figures 4.4.2 a-e). After 8 h the major final products were 7 Å kaolinite and 9-11 Å silicates.

The 9-11 Å phases formed could not be readily identified from the XRD traces. A well crystallised product was obtained however, using System E at 215°C (presumably owing to the more extensive degradation of the original kimberlite in this case). The XRD trace is shown in Figure 4.4.3a which was similar to that of the 9-11 Å product obtained from olivine standard alteration (Figure 4.4.3b). Although the water content (19.5%) of the former, as evaluated by TGA, was greater than that expected for most phyllosilicate minerals (∿ 14%), the suite of peaks did infer that the basic structure was attributable to a 2:1 silicate. The closest agreement between the tabulated XRD data and that experimentally found was obtained for pyrophyllite and talc; the present 9-11 Å silicates were assumed to have the same basic structure. It was therefore hypothesized that such 9-11 Å phases consisted of hydrated 2:1 layered aluminosilicates of the form

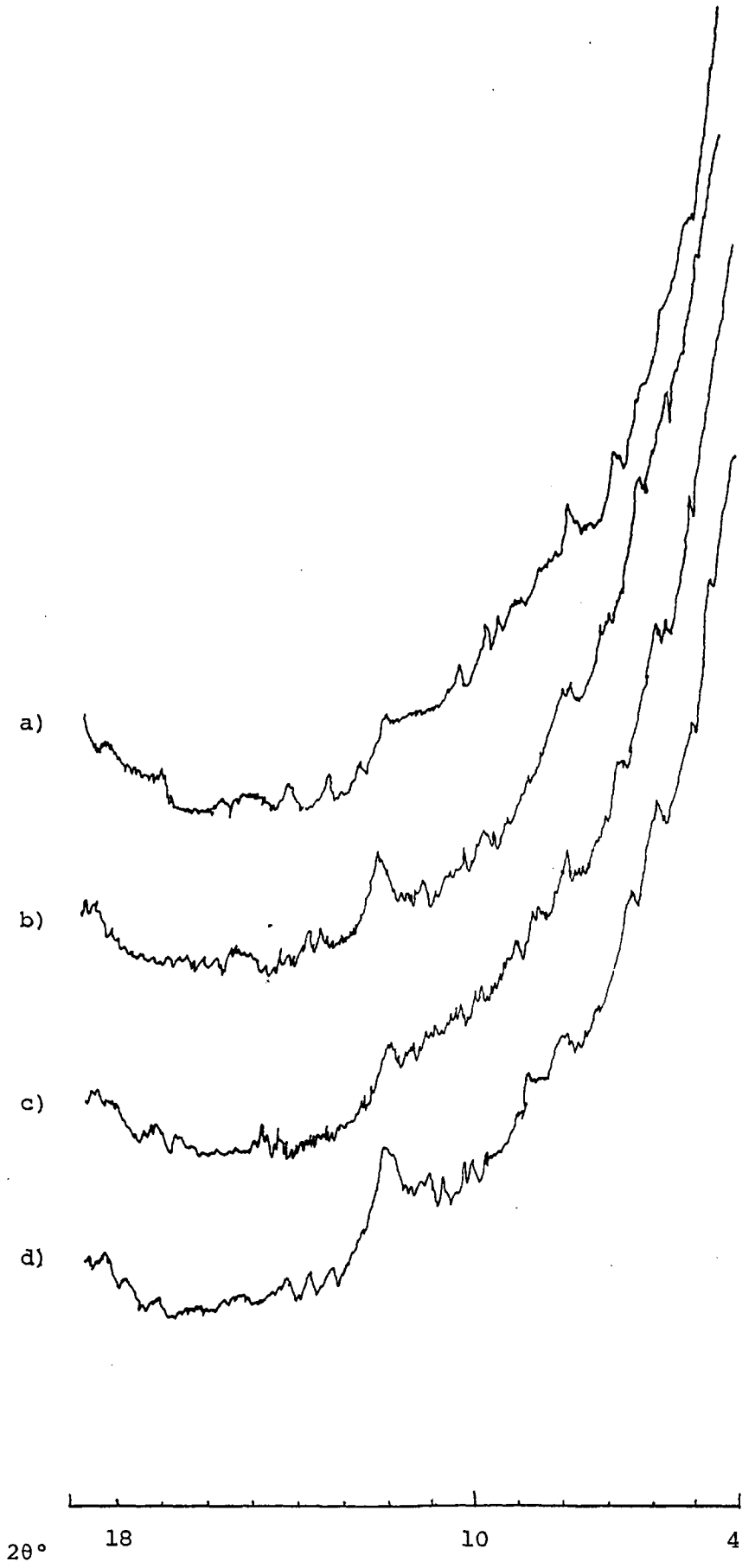


Figure 4.4.1 X-ray diffractograms for -75 μm products obtained from system C reacted at 215°C for

a) 1h; c) 5h;
b) 2h; d) 6h.

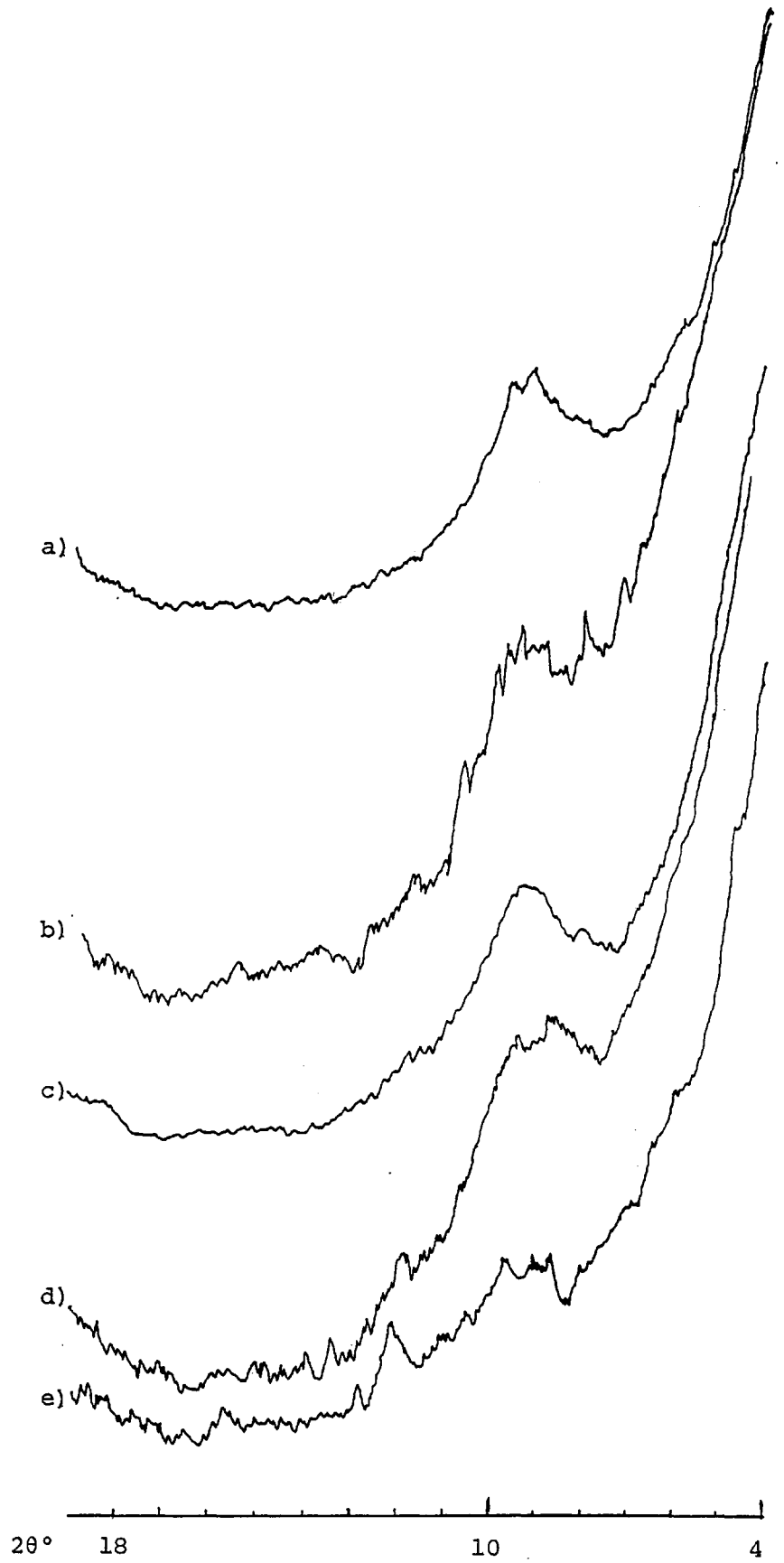


Figure 4.4.2 X-ray diffractograms for -75 μm products obtained from system D reacted at 215°C for

a) 1h;
b) 3h;
c) 4h;
d) 6h;
e) 8h.

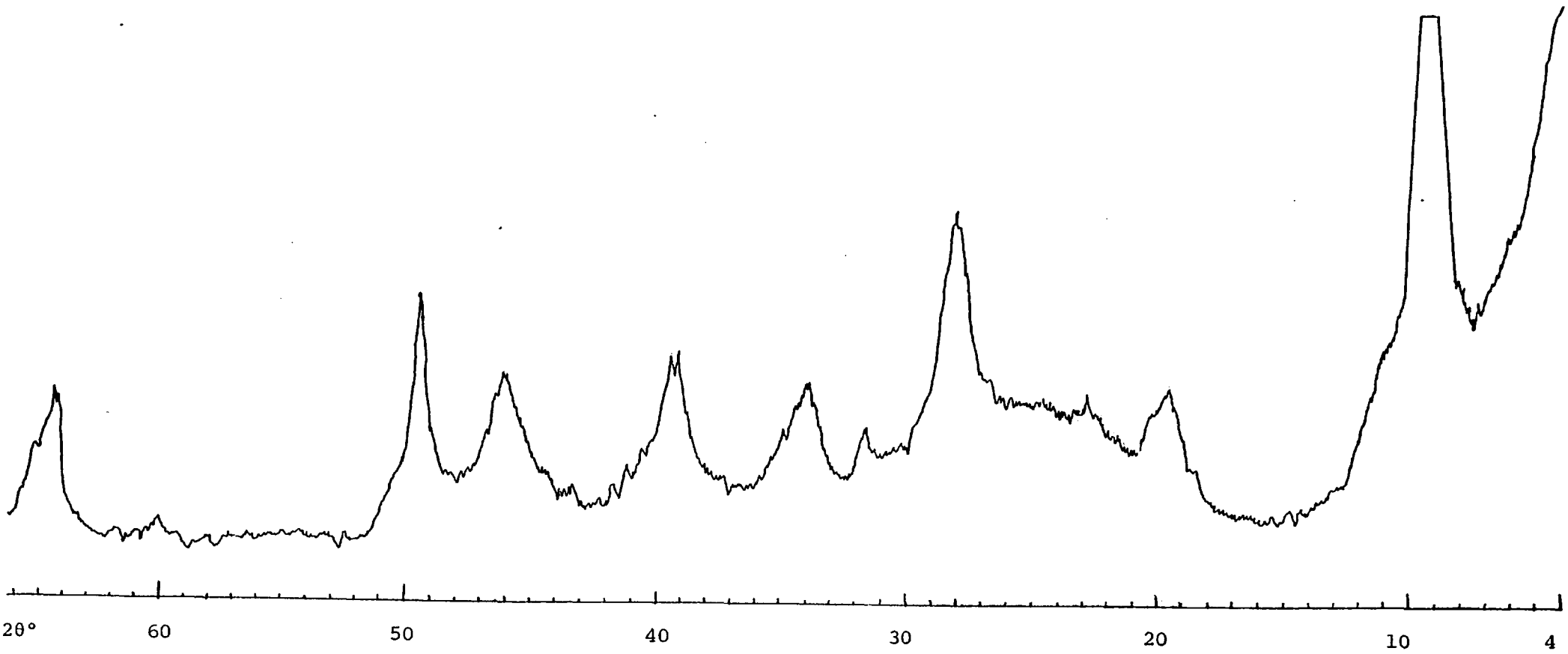


Figure 4.4.3a X-ray diffractogram of 9-11 Å aluminosilicate obtained using system E at 215°C after 5h.

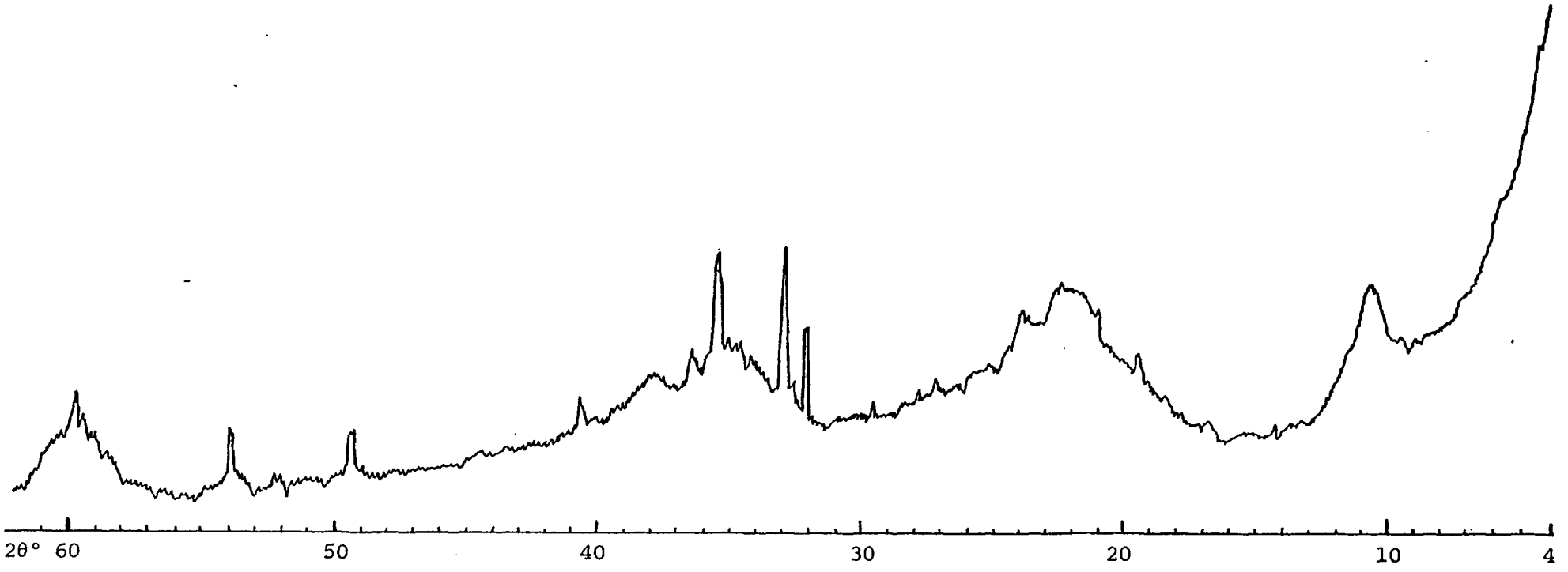


Figure 4.4.3b X-ray diffractogram of 9-11 Å aluminosilicate obtained from reaction of 1 g olivine standard with 0.31M hydrochloric acid at 100°C for 24 h.

$$(Al_a\ Mg_b\ Fe^{II}_c\ Fe^{III}_d)\ (Al_t\ Si_{4t}\ O_{10})\ (OH)_2\ nH_2O$$

where $3(a+d) + 2(b+c) = 6+t$

and n is variable.

A comparable 10 Å phase has been discussed recently by Bauer and Sclar [256] in the $MgO-SiO_2-H_2O$ system. The compositions of the 9-11 Å silicates as discussed in Sections 4.4.2 and 4.4.3 subsequently based on the representation above.

The results for the series of products generated at 260°C are illustrated in Figure 4.4.4 a-g (System C) and Figure 4.4.5 a-g (System D). In System C the improved crystallinites was immediately evident in the sharper peaks recorded. Products and trends similar to those noted at 215°C were seen except that 14-15 Å minerals now became observable. The first-formed disordered silicates (Figure 4.4.4a) re-crystallized to form 7.1 Å, 9.8 Å and 14.7 Å minerals at approximately 3 h (Figure 4.4.4c). Figure 4.4.4d shows an increase in the prominence of the 7 Å and 14 Å (vermiculite) phases at the expense of the 9.8 Å one. As the reaction proceeded the 4.7 Å and 14 Å basal reflections broadened to include 4.9 Å and 15 Å peaks respectively. These observations coupled with marked rises in the intensity of the 1.49 Å peak (not shown) demonstrated an increasing proportion of dioctahedral smectite in the sample (Figues 4.4.5 e-g).

The first-formed products in System D at 260°C were 9.2-9.8 Å aluminosilicates (Figure 4.4.5a), also noted at 215°C. At 2-3 h the peak broadened to include an 11.4 Å peak, which later diminished in intensity. Furthermore 7.2-8 Å 1:1 layered silicates started to develop, also noted at 215°C (Figures 4.4.5 b-c). By 4 h, the first-formed products had been replaced by these kandites, as well as a

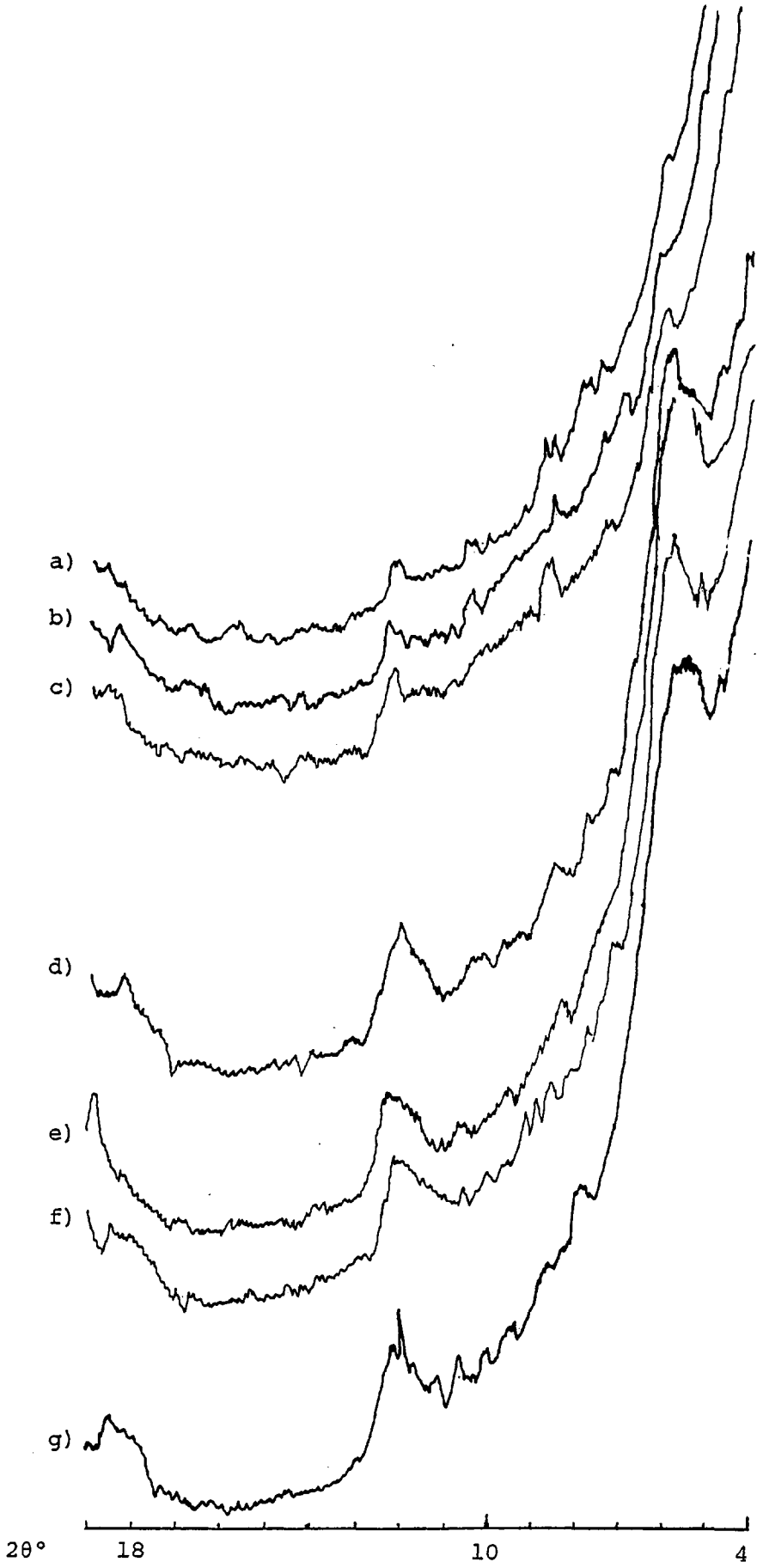


Figure 4.4.4 X-ray diffractograms for -75 μm products from system C reacted at 260°C for

a) 1h;
b) 2h;
c) 3h;
d) 4h;
e) 5h;
f) 6h;
g) 8h.

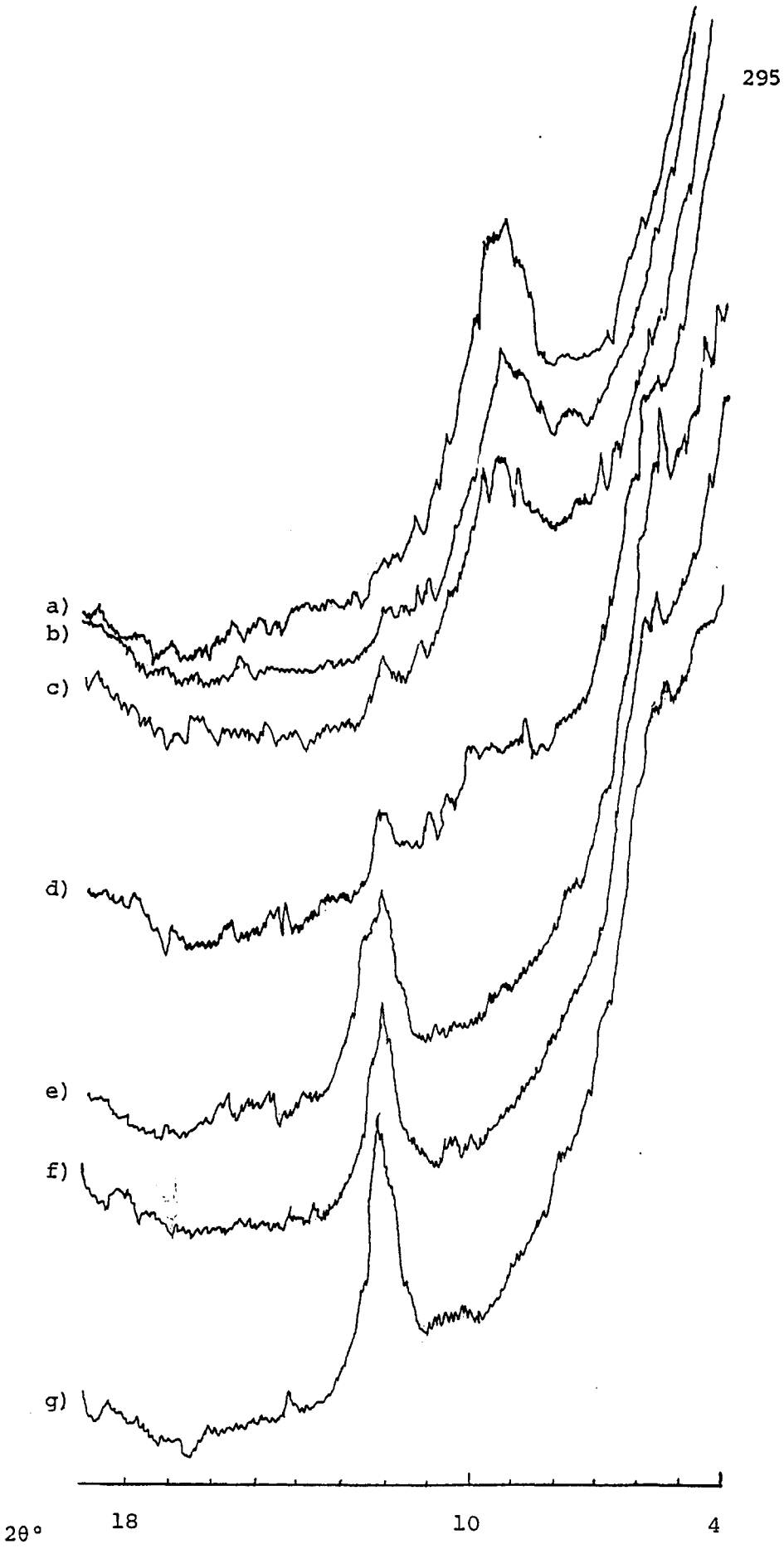


Figure 4.4.5 X-ray diffractograms for -75 μm products obtained from system D reacted at 260°C for

a) 1h; c) 3h; e) 5h;
b) 2h; d) 4h; f) 6h; g) 8h.

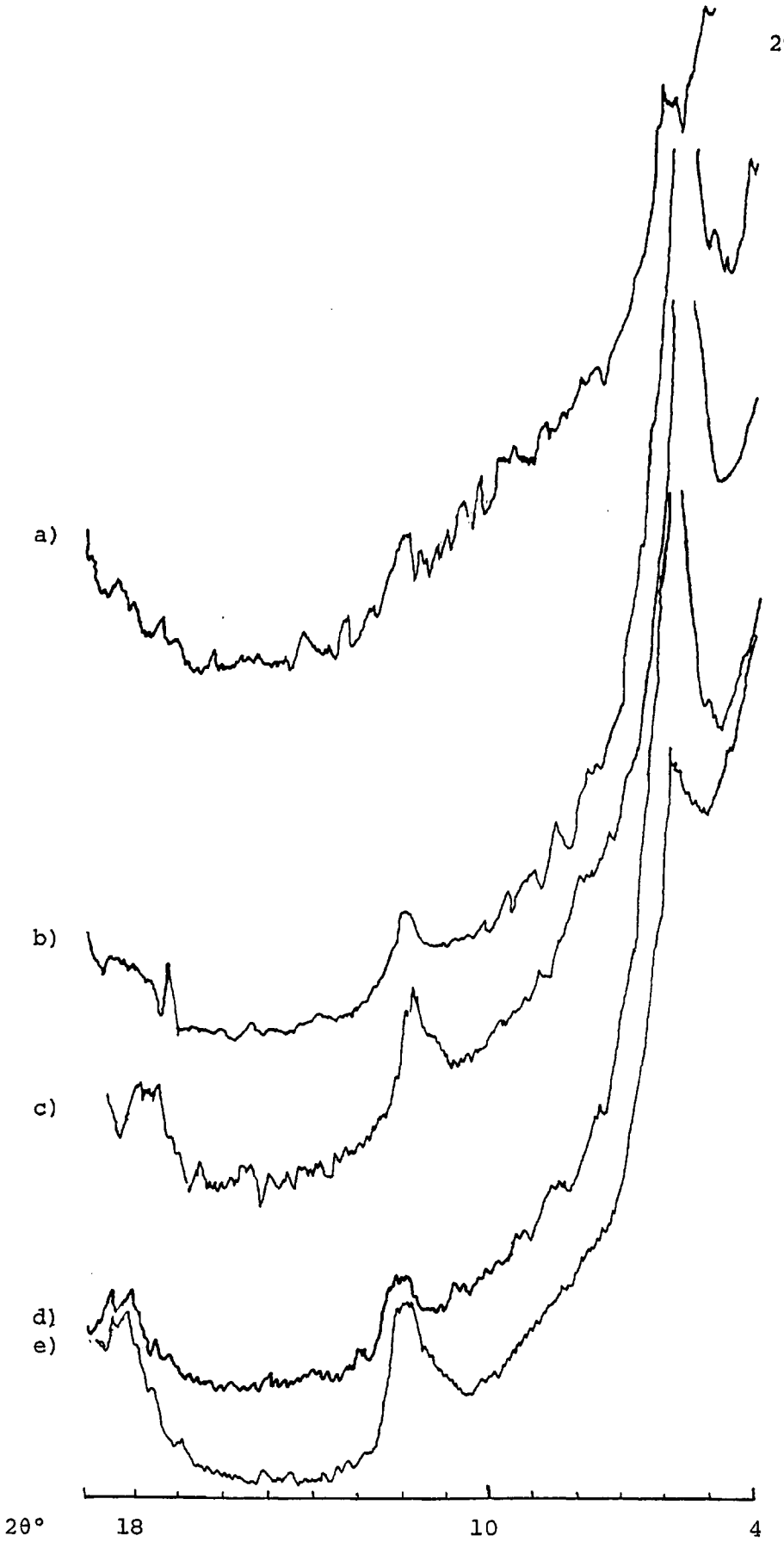


Figure 4.4.6 X-ray diffractograms for -75 μm products obtained from system C reacted at 300°C for

a) 1h;
b) 2h;
c) 4h;
d) 6h;
e) 8h.

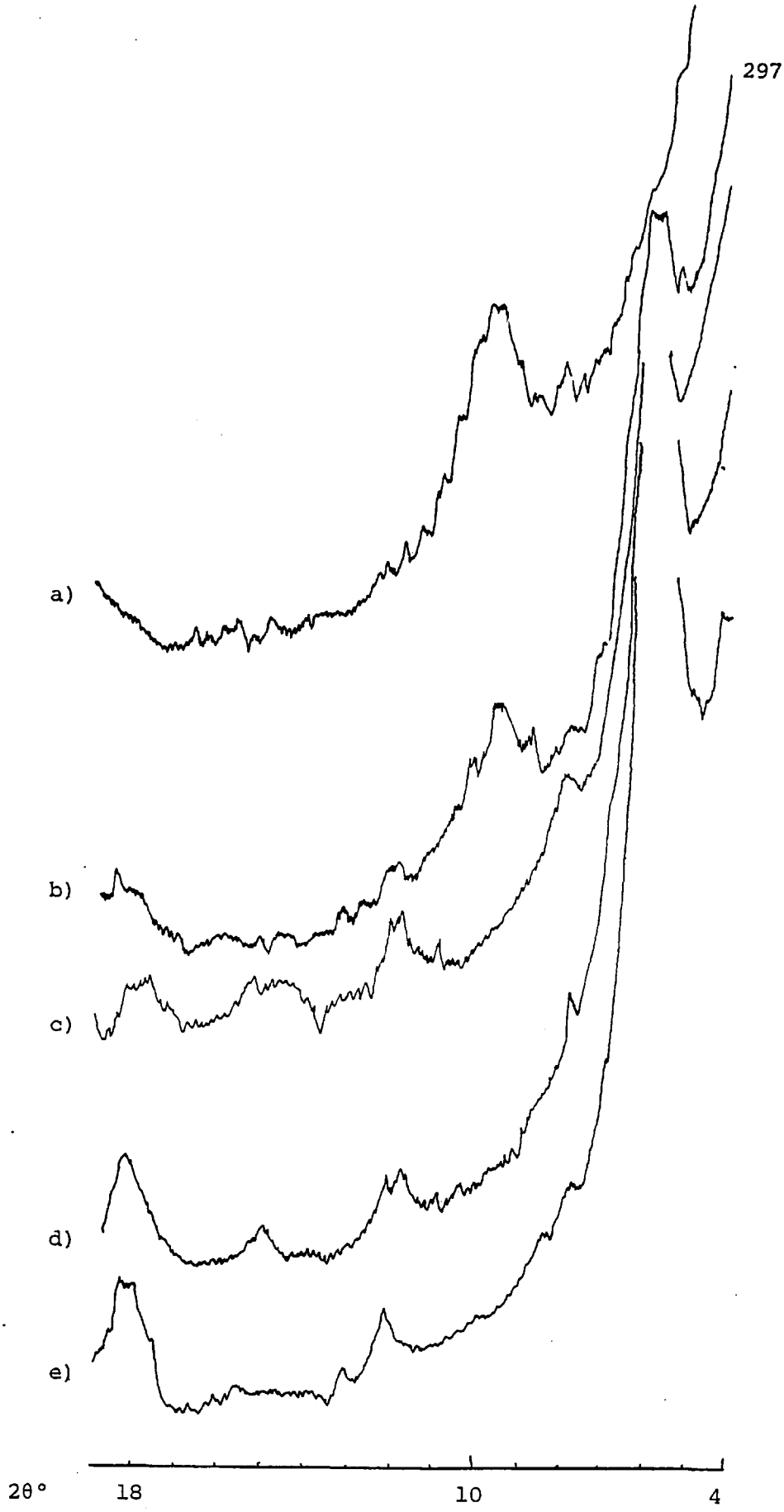


Figure 4.4.7 · X-ray diffractograms for -75 μm products obtained from system D reacted at 300°C for

a) 1h;
b) 2h;
c) 4h;
d) 5h;
e) 8h.

vermiculite-smectite phase (Figure 4.4.5d). The peak intensity of the 14-15 Å vermiculite-smectite remained relatively constant, unlike the kaolinite peak which progressively increased in intensity.

Similar trends were obtained at 300°C. The results are shown in Figure 4.4.6 a-g (System C) and Figures 4.4.7 a-g (System D). In Figure 4.4.5a a very broad 8-11 Å peak was initially discernible. A minor 14.2 Å peak was also present. After only 2 h the metastable 9-11 Å hydrated aluminosilicate had disappeared. However, new peaks at 7.2-7.3 Å and 14.7 Å representing both trioctahedral and dioctahedral kandites and vermiculite-smectite had appeared, as before (Figure 4.4.6b). As the reaction proceeded the dioctahedral character and smectite content of the majority of the products increased as indicated by 1.49 Å peak (not shown) and 15 Å peak respectively (Figure 4.4.6c). Trioctahedral minerals were also present according to the peak observable at 1.54 Å. The presence of a shouldered peak at 2.46 Å (not shown) and 4.84 Å indicated the formation of a chloritic phase as well (Figure 4.4.6e) in the later stages of the reaction.

In contrast to the initial product formed in System C, Figure 4.4.7a (System D) illustrates a well-developed 9.3 Å alumino-silicate phase. As above however, the proportion of this phase rapidly decreased with the production of a vermiculite-smectite at 2 h (Figure 4.4.8b). The final major products after 8 h appeared to be smectite, vermiculite and kaolinite (Figure 4.4.7e).

4.4.2 Computed proportions of phases produced at 100°C

Careful examination of the X-ray diffractograms and the use of glycolation and potassium saturation techniques demonstrated tnat the principal phyllosilicate phases formed were chlorite, vermiculite,

and aluminian serpentine, albeit poorly crystalline. Infra-red data and observations at higher temperatures showed that a fourth phase, a hydrated 9-11 Å aluminosilicate, was also likely to be present. These four phases were incorporated in the Program CECPM (system code 1 0 Table 2.5.1) employing the methods developed in Section 2.5. The modelling of chlorite, vermiculite and kandites has been discussed previously. To estimate the chemical composition of the 9-11 Å aluminosilicates for which tabulated data was unavailable, the following assumptions were made.

Referring to the structural formula given in Section 4.4.1 :

a) The relative ratios of the species Al:Fe:Mg were the same as those for the chemical assay of the -75 µm fraction analysed (this reduced the number of permutations to be tested).

b) The number of water molecules present, n, could range from 0 to 30 (the upper limit was taken to be 6 times that normally occurring in smectites and vermiculites, the most hydrated of clay minerals) in view of the high water content observed.

c) Aluminium could substitute for silicon in the tetrahedral lattice where t (as given in the formula above) ranged from 0 to 2.

d) The water content and elemental assay could be inter-related by the use of suitable algorithms in Subroutines KFIX1 and KFIX2 (Appendix 5).

e) By careful incrementation of the number of water molecules and tetrahedrally coordinated aluminium ions per $(Al,Si)_4O_{10}$ unit cell, various types of 9-11 Å silicate could be modelled and 'acceptable' solutions to the computation found.

The results obtained from the various kinetic experiments

conducted using Systems A and B are shown graphically in Figures 4.4.8 and 4.4.9. Meaned computed data for the 9-11 Å aluminosilicates are given in Table 4.4.1 The figures and tables provide complementary information.

During the first six hours of the reaction using System A, serpentine, vermiculite, chlorite and 9-11 Å aluminosilicates formed the majority of the product as shown in Figure 4.4.8. Serpentine predominated at first (46% of the -75 μm reaction at 1 h) to be superseded later by vermiculite (50% at 4 h) combined with an increasing proportion of chlorite (21%). The proportion of 9-11 Å aluminosilicates attained a constant value of 8-12% 1-4 h after which it steadily increased up to 68% at 6 h, whereas those of the other phyllosilicates correspondingly decreased; the proportion of vermiculite falling from 50% (4 h) to 12% (8 h) and serpentine being replaced by kaolinite. As shown in Table 4.4.1, the increase in proportion of the 9-11 Å phases was mirrored by an increase in the aluminium content which would be expected from the precipitation of aluminium hydroxyoxides noted before (Figure 4.2.3). It was likely that the 9-11 Å form recorded consisted of the original 9-11 Å phase structure formed in the first 1-4 h of the reaction, with associated cationic hydroxyoxides. The proportion of this 'combined' phase decreased with reaction time which was suggestive of a form of recrystallization to another product, probably vermiculite according to the diagram; the concentration of chlorite and kaolinite remained 8-12%.

In System B (Figure 4.4.9) the maximum concentration of the 9-11 Å aluminosilicate (46%) was attained in the first 3 h of reaction. The concentration of vermiculite and chlorite, however, continued to increase up to 5 h (being 72 and 10% respectively). After this time, the clay phases came to apparent equilibrium values of 58% vermiculite,

TABLE 4.4.1 COMPOSITIONAL DATA FOR 9-15 Å ALUMINOSILICATES I : SYSTEMS A AND B

System A [initial concentrations : 0.44M Al^{3+}, 0.316M H^{+}; 100°C]

Mineral	Reaction time	Assay (%)					Stoichiometric coefficient				
		Si	Al	Fe	Mg	H_2O	Si	Al	Fe	Mg	nH_2O
	1	13.1	6.3	5.6	5.6	42.6	3.1	1.6	0.6	1.5	14.5
	4	12.7	6.5	5.4	5.6	43.5	3.0	1.6	0.7	1.6	15.3
	5	16.5	16.1	9.1	10.6	4.4	2.4	2.4	0.6	1.8	-
9-11 Å	7	7.1	10.9	2.2	2.1	57.6	2.3	3.5	0.2	0.8	26.6
phases	14	9.1	14.1	2.8	2.7	45.4	2.2	3.6	0.3	0.8	16.1
	20	8.1	13.6	2.9	2.5	48.6	2.1	3.6	0.4	0.8	18.6
	24	8.2	9.7	3.3	3.1	54.4	2.4	2.9	0.6	1.0	24.2
chlorite	1-24	13.6	11.7	6.8	16.8	11.7	2.8	2.5	0.7	4.0	-
vermiculite	1-24	16.9	7.5	4.8	13.0	20.1	2.8	1.3	0.4	2.5	4.2

System B [initial concentrations : 0.22M Al^{3+}, 1.5M H^{+}; 100°C]

	2	25.7	3.6	7.5	7.0	16.1	4.0	0.6	0.5	1.3	2.9
	3	20.7	3.4	5.9	5.0	32.4	4.0	0.7	0.6	1.1	8.8
	5	29.2	4.5	8.6	7.3	4.7	4.0	0.6	0.7	1.1	0
9-11 Å	7	20.3	11.8	7.1	7.0	12.6	3.1	1.8	0.5	1.3	2.0
phases	14	17.9	5.2	4.8	4.6	37.9	3.7	1.1	0.6	1.1	11.5
	20	14.5	8.5	5.7	5.0	36.6	3.0	1.9	0.6	1.2	11.0
	24	15.3	4.9	4.7	4.2	44.4	3.6	1.2	0.6	1.1	15.4
chlorite	1-24	15.8	7.6	16.7	10.9	11.7	3.4	1.7	1.8	2.7	-
vermiculite	1-24	17.9	6.9	3.6	13.4	20.1	3.0	1.2	0.3	2.6	4.2

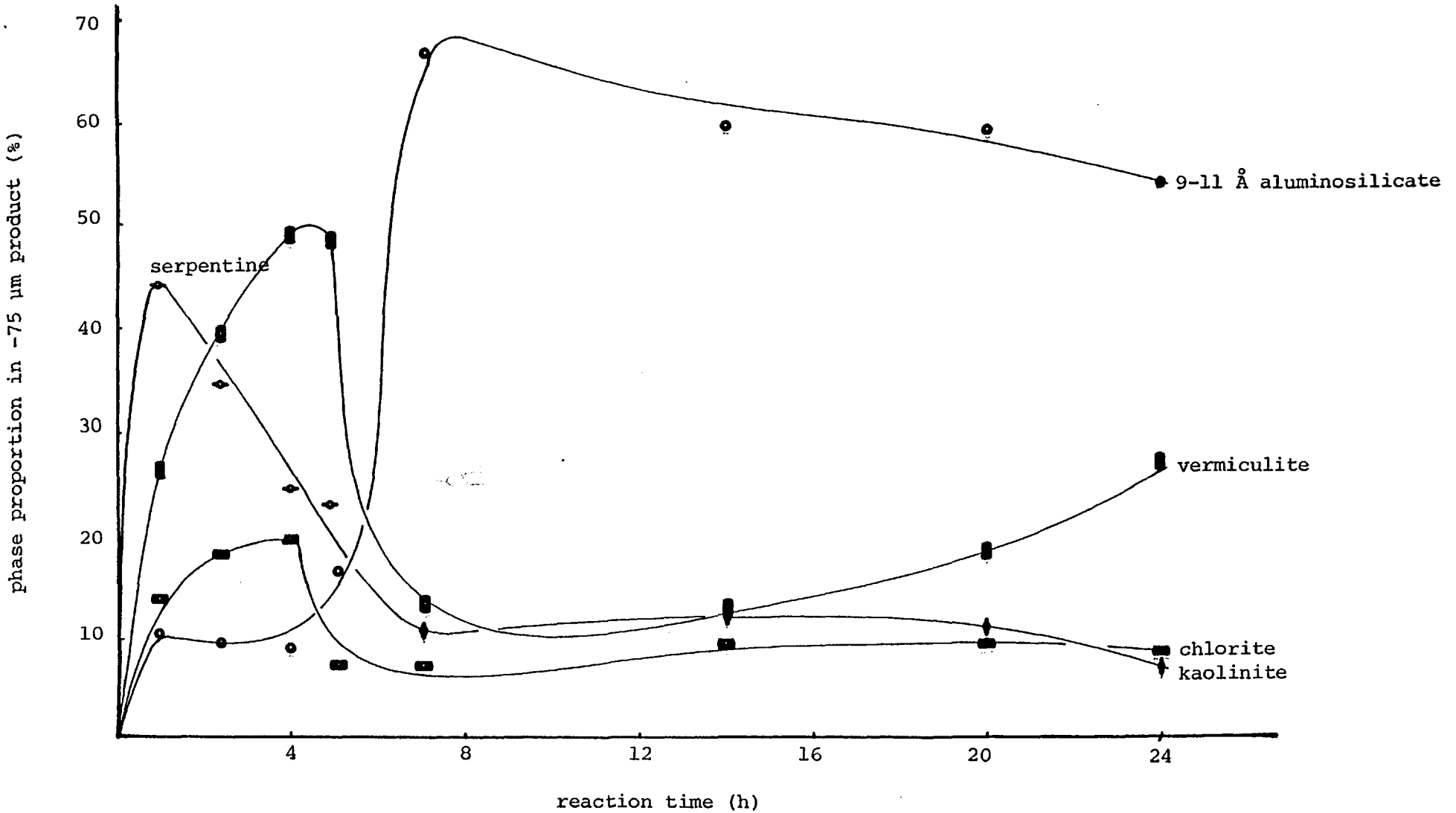


Figure 4.4.8 Computed proportions of phases in the -75 µm product generated at various reaction times for system A at 100°C.

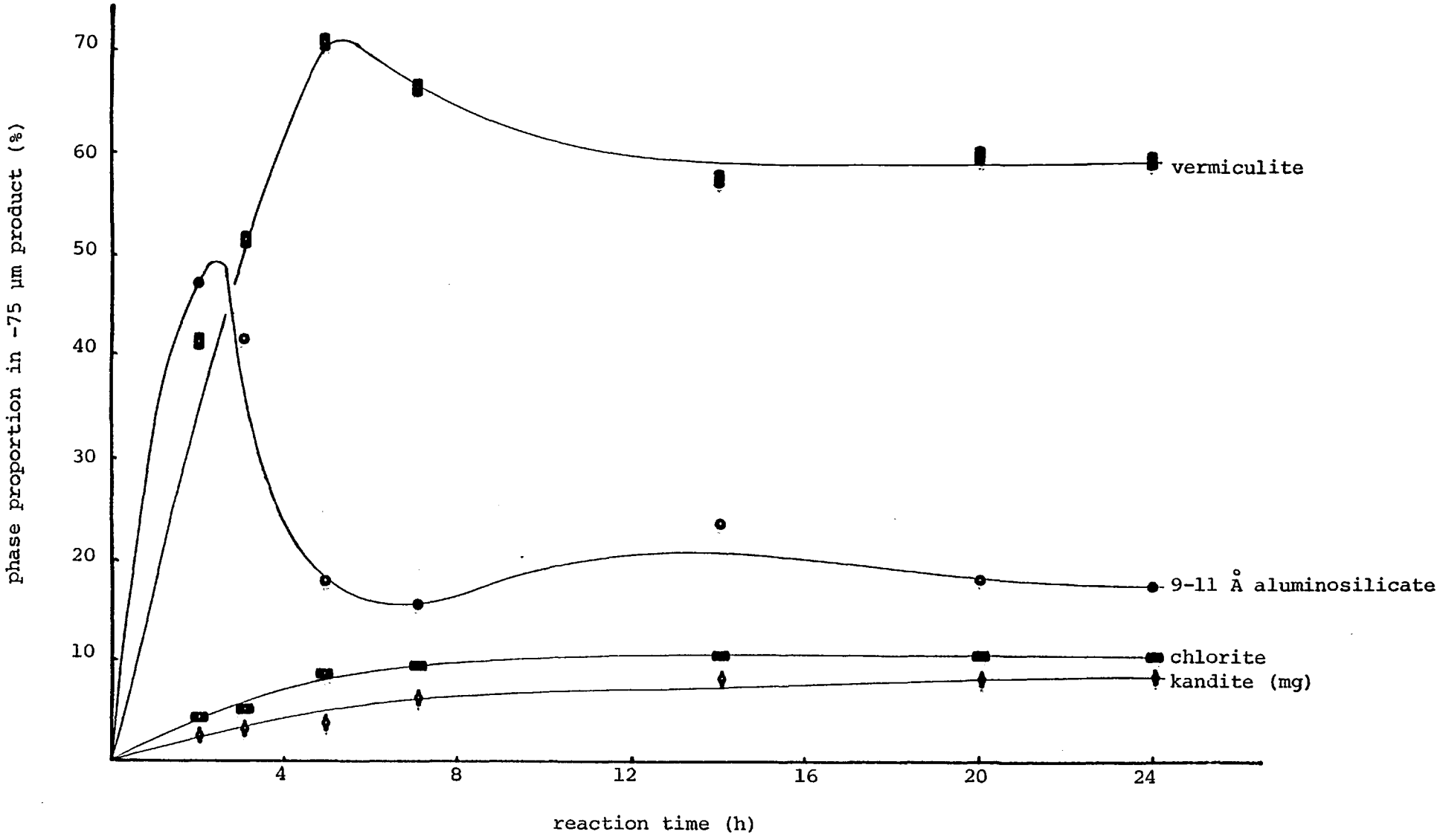


Figure 4.4.9 Computed proportions for phases in the -75 µm product generated at various reaction times for system B at 100°C/

∿ 23% 9-11 Å aluminosilicate, 10% chlorite and 9% magnesian kaolinite.

Table 4.4.1 includes meaned structural formulae data for the vermiculites and chlorites obtained in both systems. Comparing these with the formulae deduced (i.e. from the stoichiometric coefficients) for the 9-11 Å aluminosilicates showed that the extent of tetrahedral substitution was similar at 4-5 h (System A) and 14-20 h (System B) i.e. at pHs 2.5-3 (Figure 4.2.3). It was apparent that aluminium entered into tetrahedral rather than octahedral coordination at such pH levels making possible the formation of chlorites and vermiculites. (This is discussed later in terms of reaction mechanism.)

4.4.3 Computed proportions of phases produced at 215, 260 and 300°C

215°C : Systems C and D At 215°C, the degree of crystallinity of the -75 μm products was greater than at 150°C. XRD analysis (Section 2.3.2) and residual solution ion analysis (Section 4.3.2) showed that aluminosilicates depleted in magnesium and iron were the major products. The same computer method as described in Section 4.4.2 with the exception that the mineral system, identified by code 2 0, was employed. In this particular system, the following suite of minerals was considered : kaolinite-halloysite, 9-11 Å aluminosilicates, aluminium and iron hydroxides and serpentine-magnesian carbonate. The results obtained are shown in Figures 4.4.10 and 4.4.11.

In both systems the principal hydroxyoxides of aluminium and iron were boehmite (Al OOH) and lepidocrocite (FeOOH) respectively. This conclusion was reached on the basis both of these minerals giving suitable mass balance solutions and those most likely to exist at the temperature in question (Figure 1.4.3). For the purpose of computation they were considered as a mineral mixture forming one phase; the ratio

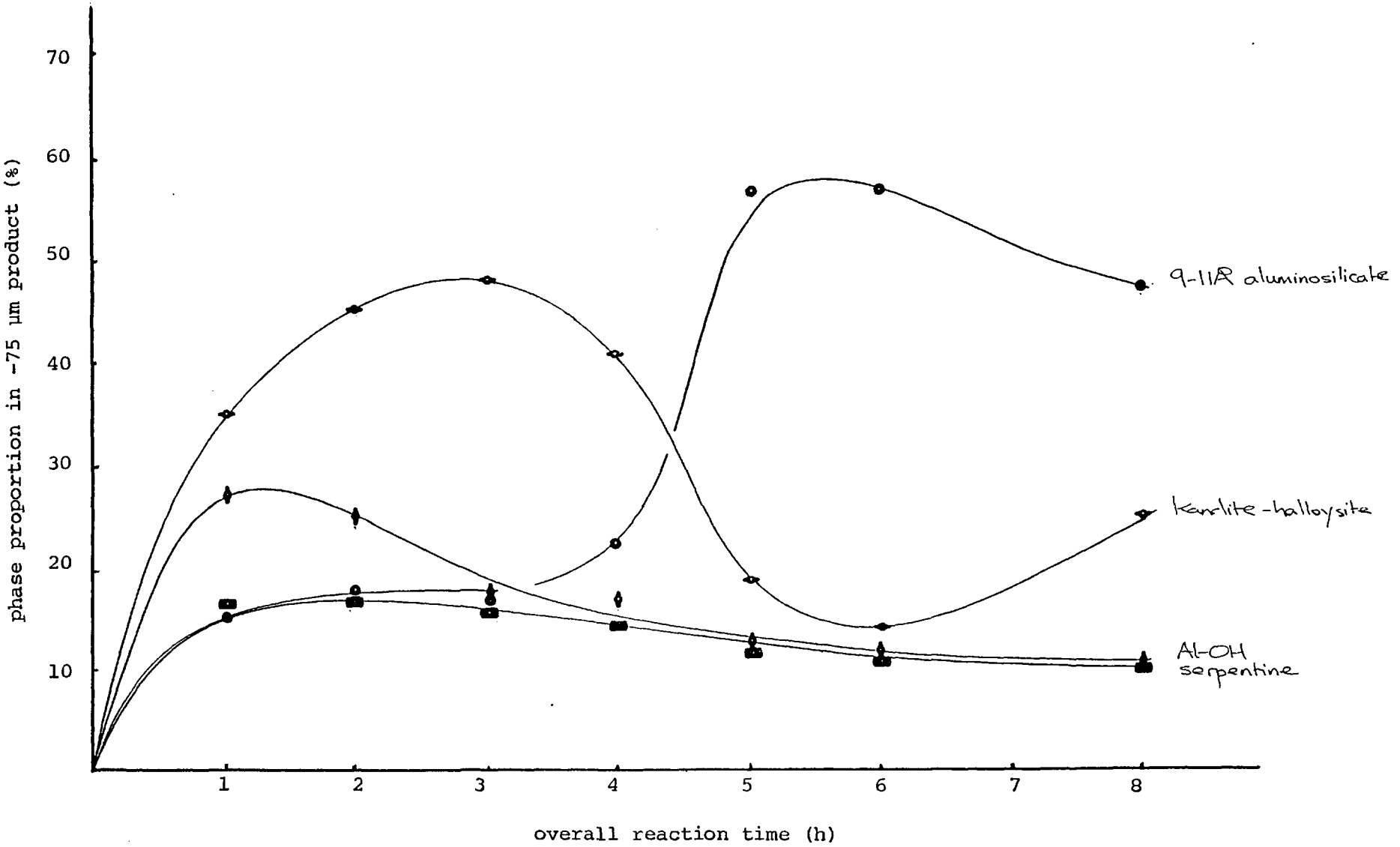


Figure 4.4.10 Computed proportions of phases in the -75 µm product generated at various reaction times for system C at 215°C.

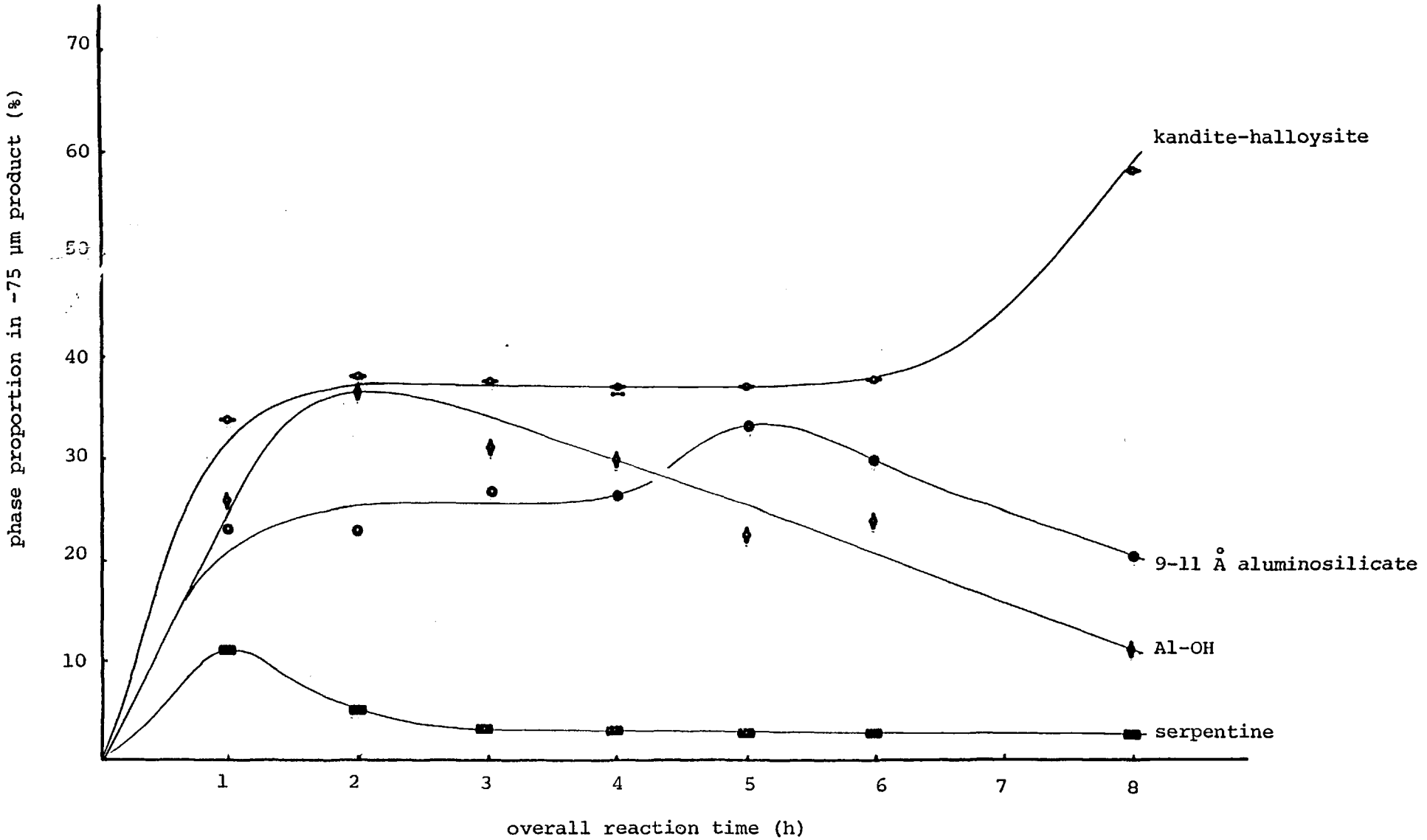


Figure 4.4.11 Computed proportions of phases in the -75 µm product generated at various reaction times for System D at 215°C.

of aluminium and iron assay being the same as that in the assay of the -75 μm product. (None of the calculations suggested the presence of gibbsite ($Al(OH)_3$) or an iron equivalent, $Fe(OH)_3$.)

In System C, the three aluminium rich products were formed simultaneously and maximum concentrations reached after different time periods; the first being boehmite-lepidocrocite (28%) after 1 h. As the reaction time increased, the hydroxyoxide proportion progressively decreased, reaching 12% at 8 h. The concentration of the kaolinite-halloysite continued to increase up to 3 h (maximum 49%). After 4 h the 9-11 Å aluminosilicates became increasingly the dominant phase. The proportion of serpentine changed little throughout.

System D exhibited similar behaviour. The boehmite-lepidocrocite was precipitated in increasing concentrations up to 2 h, after which it decreased to an overall assay of 12% as before. The kaolinite-halloysite and 9-11 Å aluminosilicate phase proportions varied little from 1-6 h, the values recorded being 38-40% and 25-35% respectively. The elemental concentrations of the phases suggested that a dioctahedral type of mineral predominated which was likely in view of the relatively large quantities of the aluminium applied. This change was mirrored by the increase in the kaolinite-halloysite concentration from 39 to 58% at 8 h and a decrease in that for the 9-11 Å silicate from 30 to 18%.

260°C : Systems C and D The increase in reaction temperature improved the crystallinity of the products, facilitating their identification, the minerals formed being : vermiculite, smectite, (instead of halloysite), kaolinite, serpentine and 9-11 Å aluminosilicates. Their proportions were evaluated using the mineral system for which the code was 3 0 (Table 2.5.1). In certain instances, both at 260 and 300°C, a

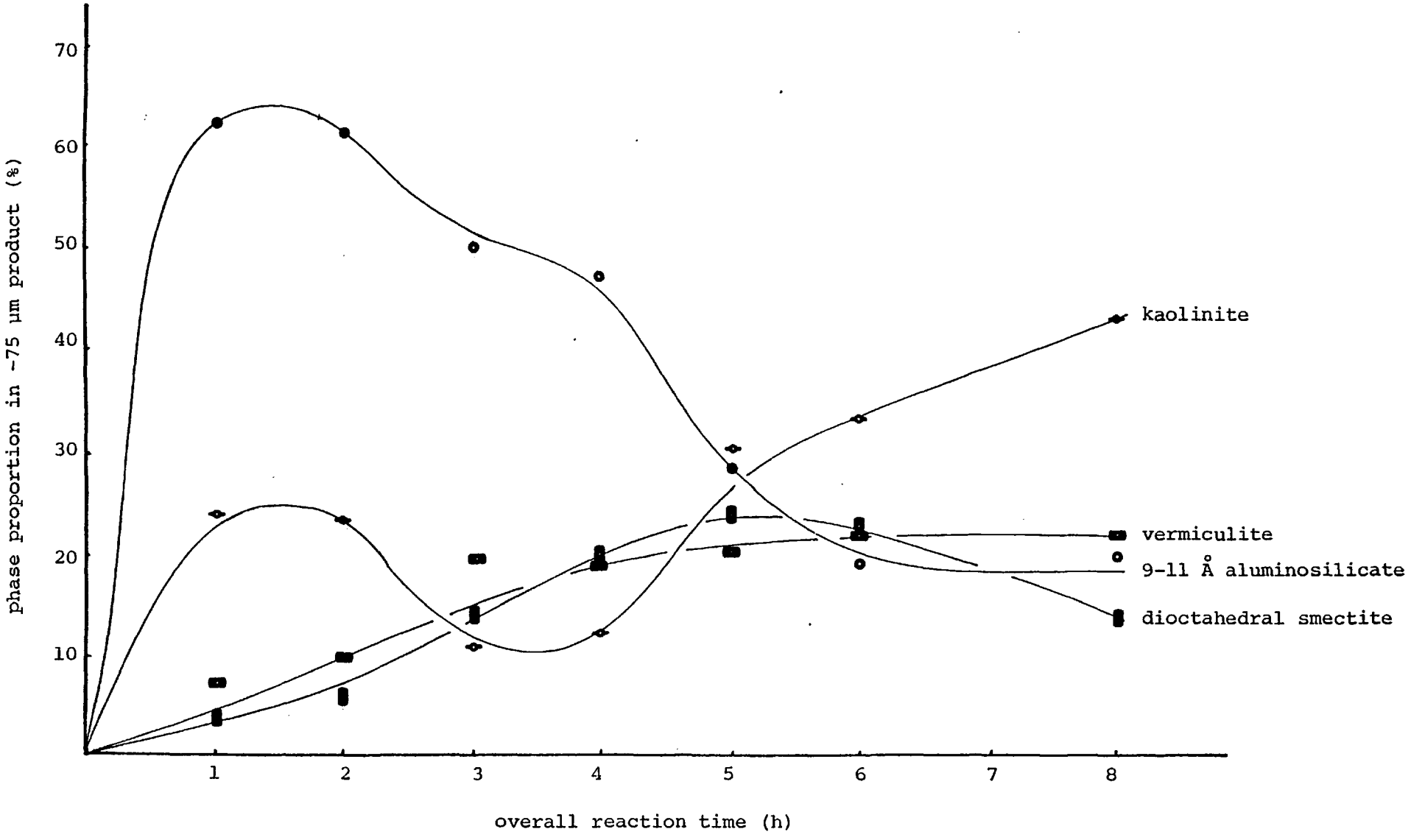


Figure 4.4.12 Computed proportions of phases in the -75 µm product generated at various reaction times for system C at 260°C.

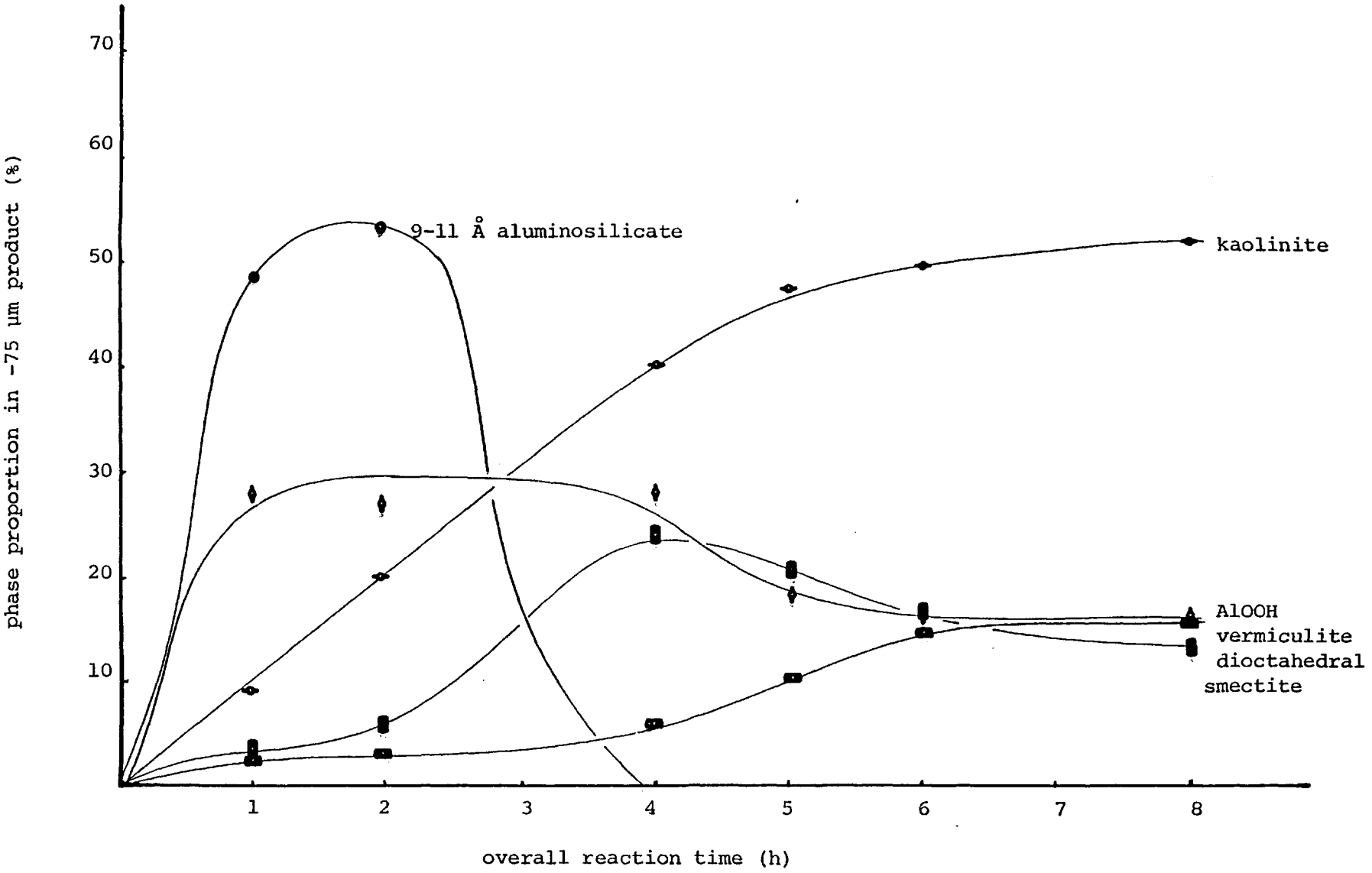


Figure 4.4.13 Computed proportions of phases in the -75 µm product generated at various reaction times for system D at 260°C.

five mineral suite (code 3 2) had to be employed due to the significant proportion of aluminium and iron hydroxyoxides present (as inferred from the -75 μm fraction elemental assays). The results are shown in Figures 4.4.12 and 4.4.13.

System C (Figure 4.4.12) illustrated that the 9-11 Å alumino-silicates represent the principal first-formed phases (62% of total) at 1 h. The concentration of this mineral progressively decreased with time (48% at 3 h, 20% at 6 h) but was still detectable after 8 h. Vermiculite and smectite increased slowly in proportion for most of the reaction period mirroring the larger 14-15 Å peaks recorded with time in the XRD analyses. Unlike the 9-11 Å aluminosilicates, these minerals were readily identifiable by XRD. By 8 h the concentrations of these three phases were virtually equal (∿ 20%). The kaolinite concentration, in general, increased with time in concert with the 14-15 Å minerals, despite an apparent reduction at 3-4 h. At 5 h kaolinite became the predominant phase.

Similar trends were observed for System D. However because of the presence of a larger quantity of aluminium, more precipitated as the hydroxyoxide and constituted as much as 30% of the product in the initial stages of the reaction. Smaller quantities of the 9-11 Å silicate, vermiculite and smectite were formed, compared with those in Figure 4.4.12 owing to the dilution effect of the hydroxyoxide. In contrast to System C, there was no trace of the 9-11 Å aluminosilicate after 4 h (cf. Figure 4.4.5). The proportion of the aluminium hydroxyoxide decreased to 18% (5-8 h) whereas those of vermiculite and kaolinite increased, the latter forming the most predominant phase (50%) in the -75 μm product. The concentration of smectite reached a maximum of 25% at 4 h but decreased to 15% by 8 h.

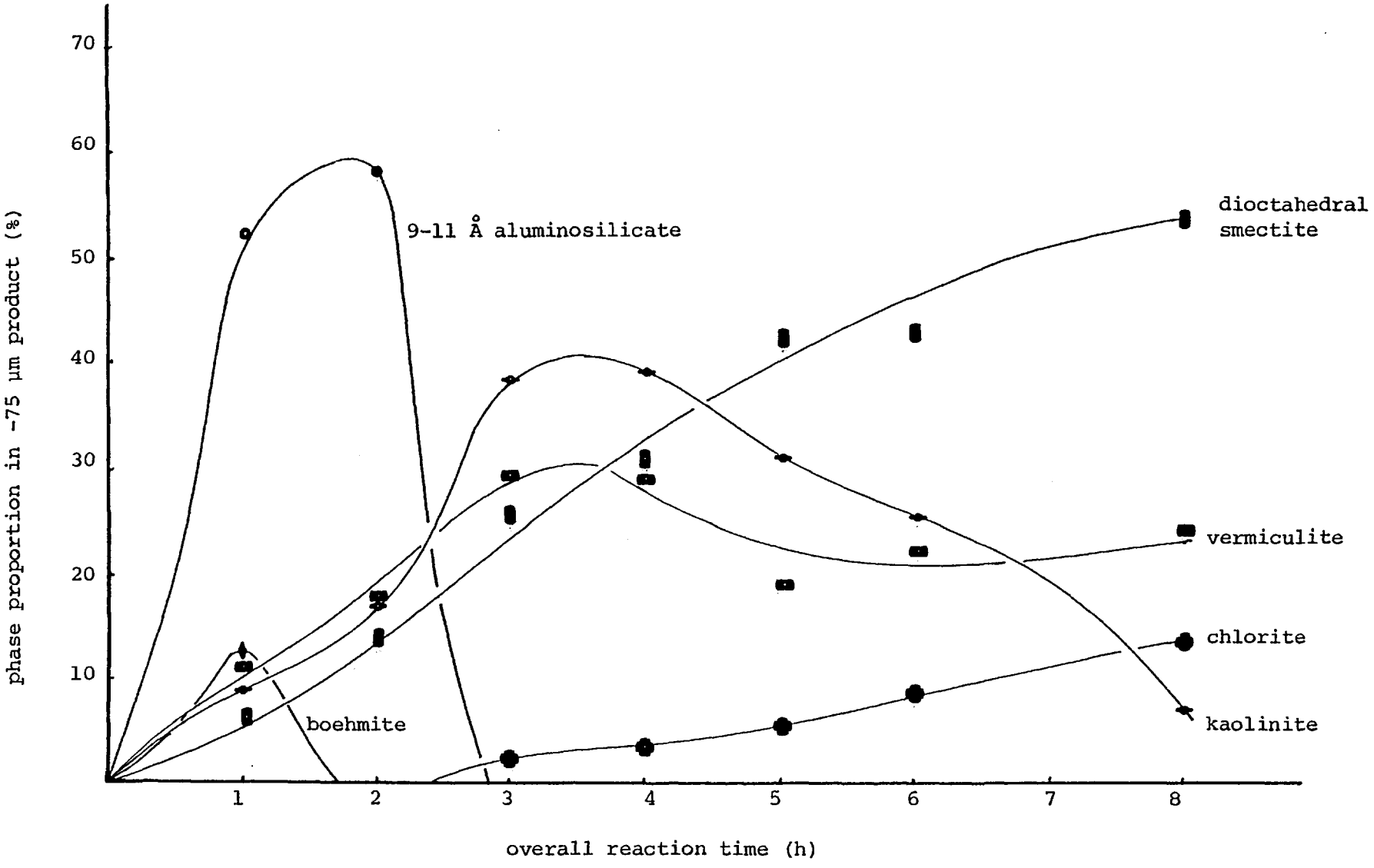


Figure 4.4.14 Computed proportions of phases in the -75 µm product generated at various reaction times for system C at 300°C.

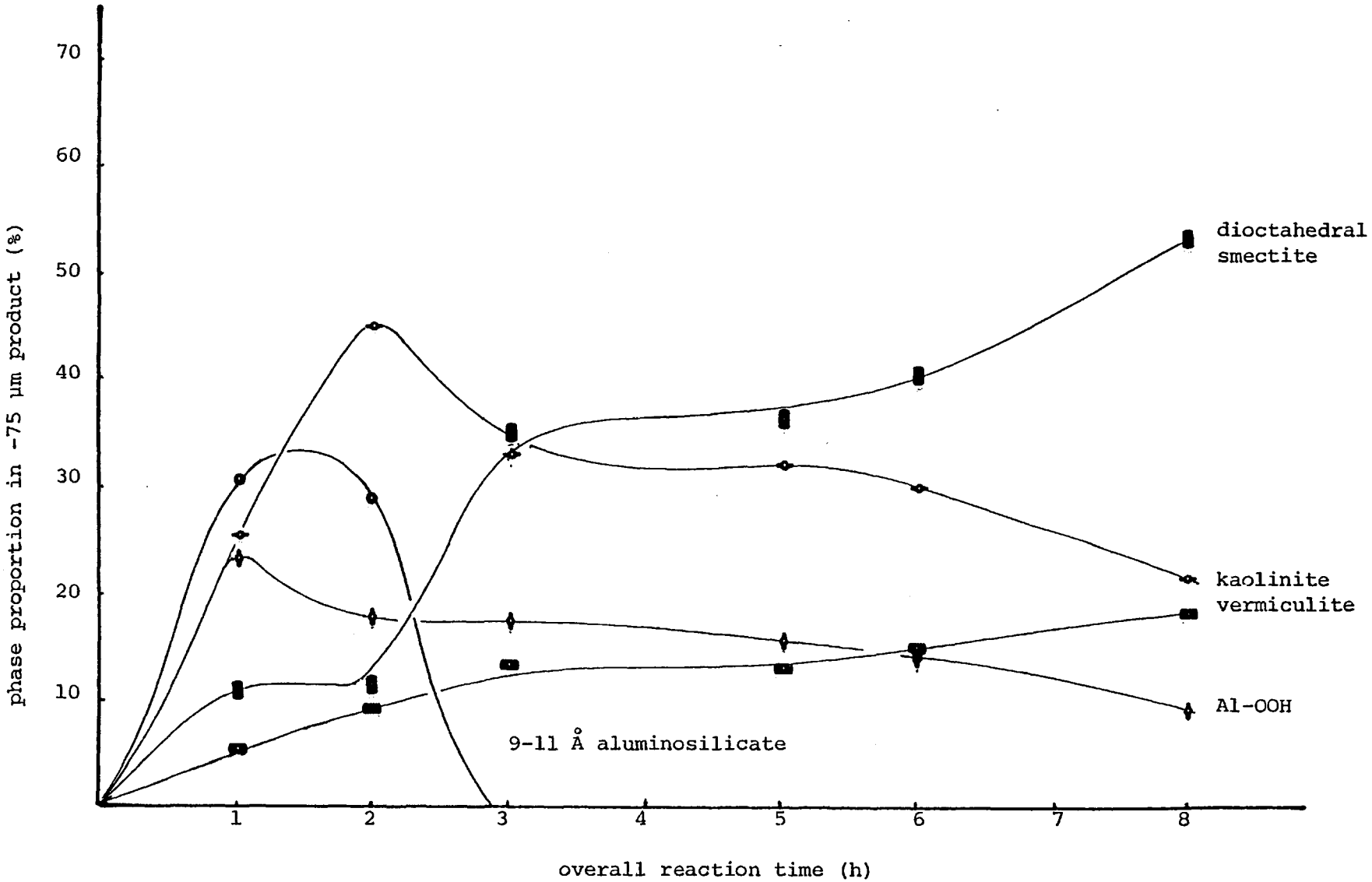


Figure 4.4.15 Computed proportions of phases in the -75 µm product generated at various reaction times for system D at 300°C.

300°C : Systems C and D The mineralogy of the -75 μm products became more complex at this temperature. XRD analysis had demonstrated the presence of vermiculite, smectite (montmorillonite) and kandite (kaolinite/serpentine) at experiments conducted at 8 h (Figure 3.4.1). System C differed from D in that there was evidence for the presence of chlorite as well. It was necessary to employ different mineral suites in Program CECPM at different stages of the reaction viz : System C - code 3 2, 1-2 h; code 4 0, 3-8 h; System D - code 3 2, 1-2 h; code 3 1, 3-8 h.

The computed results for the kinetic experiments at 300°C for System C are shown in Figure 4.4.14. The graph shows an abrupt increase in the concentration of the 9-11 Å aluminosilicates to 52-58% during 1-2 h. After 3 h, however, the phase was undetectable, and had been replaced by vermiculite, dioctahedral smectite, kaolinite, and chlorite, the latter in relatively small proportions. In contrast to Figure 4.4.12, kaolinite concentration reached a maximum (40%) at 3-4 h after which it progressively decreased to 8% at 8 h. This mineral was replaced by smectite (montmorillonite) as the major phase (40% at 5 h, 54% at 8 h); together with vermiculite and chlorite, the former reaching an equilibrium value of 22% by 8 h and the latter rising to a concentration of 14% of the total.

In System D (Figure 4.4.15) no chlorite was detected. The mass balance was made up of smectite, vermiculite, 9-11 Å aluminosilicates and aluminium and iron hydroxyoxides (boehmite-lepidocrocite) as before. The trends were similar to those noted in System C, a 9-11 Å phase being initially formed and replaced by the other phyllosilicate species. The former however, assumed smaller proportions than before (only 30%) and was undetectable after 3 h. At 2 h the kaolinite concentration reached a maximum (46%) after which it tended to decrease (cf. Figure 4.4.14) to 20% after 8 h. At 3 h smectite replaced kaolinite as the most common

phase formed. The concentration of the former increased with time reaching 52% after 8 h. The proportion of vermiculite also increased with time as in Figure 4.4.15. The proportion of the hydroxyoxides however, decreased from a maximum of 22% (1 h) to 10% (8 h).

Compositional data for the 9-11 Å aluminosilicates The compositions of the 9-11 Å aluminosilicates as well as for the 14-15 Å phases formed are shown in Tables 4.4.2 and 4.4.3. These tables indicate that the majority of the 9-11 Å phases contained more than 32% water. However, in the cases named below the water content was less and approached that tabulated for vermiculites and smectites[72] : System C : 215°C (5-8 h), 260°C (4 h); System D 300°C (2 h). There appeared to be a general trend : as the time or temperature of reaction increased the water content decreased. This would be expected if these 9-11 Å aluminosilicates later recrystallized as 14-16 Å phyllosilicates.

All the 9-11 Å phases had a dioctahedral character, the iron and magnesium assays being less than 7.5 and 2.2% respectively. However, it was seen that the assays of these elements increased with reaction time for System C. Other trends noted were that as the temperature increased, the aluminium assay and the extent of tetrahedral replacement of silicon increased for both systems studied. These trends can be summarised by Figure 4.4.16.

TABLE 4.4.2 COMPOSITIONAL DATA FOR 9-15 Å ALUMINOSILICATES II : SYSTEM C

System C [initial concentrations : 0.22M Al^{3+}, 0.31M H^{+}]

Mineral	Reaction time	Assay (%)					Stoichiometric coefficient				
		Si	Al	Fe	Mg	H_2O	Si	Al	Fe	Mg	H_2O
215°C	1	13.1	10.6	1.4	1.6	47.3	4.0	1.8	0.2	0.4	16.9
	2	12.3	11.2	2.8	0.7	47.4	2.9	3.0	0.4	0.2	17.3
	3	14.1	8.4	2.9	1.3	47.7	4.0	1.6	0.4	0.4	17.4
9-11 Å	4	15.9	10.3	3.8	1.1	39.2	3.3	2.4	0.4	0.3	12.0
phases	5	17.7	17.6	6.2	2.2	16.4	2.8	2.9	0.5	0.4	3.0
	6	18.5	15.4	7.3	2.8	16.3	2.9	2.5	0.6	0.5	3.0
	8	20.4	13.4	4.1	2.0	22.0	3.3	2.3	0.4	0.4	4.7
260°C	1	9.9	17.0	2.2	1.0	41.9	2.2	4.0	0.2	0.3	13.6
	2	9.7	18.5	1.6	1.1	40.3	2.1	4.2	0.1	0.3	12.5
	3										
9-11 Å	4	12.3	21.4	4.2	2.9	22.3	2.1	3.8	0.1	0.6	4.7
phases	5	12.7	12.4	2.5	1.7	42.8	2.8	2.9	0.4	0.5	14.3
	6	13.7	15.1	4.4	2.2	32.0	2.6	3.1	0.4	0.5	8.6
	8	13.2	16.6	3.0	2.2	32.5	2.5	3.3	0.4	0.5	8.9
300°C	1	9.3	16.3	2.9	2.0	41.8	2.0	4.2	0.2	0.4	13.6
9-11 Å phases	2	8.7	14.3	2.5	1.6	48.3	2.2	3.7	0.4	0.5	18.3

TABLE 4.4.3 COMPOSITIONAL DATA FOR 9-15 Å ALUMINOSILICATES III : SYSTEMS C AND D

System D [initial concentrations 0.44M Al^{3+}, 0.31M H^{+}]

Mineral	Reaction time	Assay (%)					Stoichiometric coefficient				
		Si	Al	Fe	Mg	H_2O	Si	Al	Fe	Mg	H_2O
215°C											
	1	14.7	11.5	1.8	1.1	42.4	4.0	1.9	0.2	0.3	13.6
	2	12.2	10.8	0.7	0.4	51.7	3.3	2.8	0.1	0.1	19.9
9-11 Å	3	15.2	13.9	1.0	0.5	38.9	4.0	2.1	0.1	0.1	11.5
phases	4	17.1	15.9	1.0	0.5	31.2	3.2	3.0	0.1	0.1	7.9
	5	18.8	15.8	1.6	0.6	26.6	3.2	2.8	0.1	0.1	6.0
	6	15.2	7.3	0.8	0.3	52.2	4.0	2.0	0.1	0.2	20.4
	8	15.6	12.3	1.3	0.7	40.3	3.3	2.7	0.1	0.2	12.2
260°C											
9-11 Å	1	10.7	19.4	2.9	0.9	36.3	2.0	4.2	0.3	0.2	10.6
phases	2	11.3	20.6	0.9	0.6	34.6	2.1	4.2	0.2	0.1	0.6
300°C											
9-11 Å	1	13.7	20.5	2.5	0.9	26.8	2.4	3.6	0.4	0.2	6.5
phases	2	13.0	25.1	2.0	1.4	19.6	2.2	4.0	0.2	0.2	3.9
Systems C and D											
260°C											
smectite		24.6	10.5	2.8	2.1	19.1	3.79	1.68	0.22	0.38	3.6
vermiculite		16.9	7.9	4.6	12.7	20.1	2.81	1.36	0.38	2.44	4.2
300°C											
smectite		25.7	10.2	1.7	2.2	19.1	3.93	1.62	0.13	0.39	3.6
chlorite		13.5	10.0	19.8	9.0	11.7	3.00	2.31	2.21	2.31	-
vermiculite		16.8	7.9	4.2	12.8	20.1	2.84	1.36	0.35	2.45	4.2

300°C 260°C	t = 2, trioct	t = 2, dioct
215°C	t = 0-1, dioct 0.2M Al^{3+}	t = 0-1, dioct 0.4M Al^{3+}

t represents the number of aluminium ions in tetrahedral coordination per unit cell ($Al_t\ Si_{4t}\ O_{10}$)

Figure 4.4.16 Trends in the octahedral and tetrahedral structure of the 9-11 Å silicates formed in aluminium rich conditions at 215-300°C

These trends mirrored those reported for the 14-15 Å minerals portrayed in the phase diagram in Figure 3.4.1. This would be expected if the 9-11 Å aluminosilicates were metastable transitionary products from which smectites, vermicultes and chlorites eventually crystallised. Indeed, similar compositional variations with increasing temperature have been noted for 14-16 Å silicate synthesis.[162-169]

4.5 Discussion : Reaction Mechanisms

It was evident that the alteration reactions (Sections 4.2 and 4.3) yielded a variety of different products some of which were metastable or could not be identified at the lower temperatures studied i.e. 100 and 150°C. The purpose of this section is to attempt a general correlation of the different reactions occurring with the data obtained and to postulate an overall reaction mechanism. As each of the temperatures employed yielded particular mechanistic information, it has been convenient to consider each temperature range in sequence, so as to build up progressively a scheme of elementary equilibria, and to introduce background information as required.

4.5.1 Reactions at 100°C

The observations discussed below relate principally to Systems A and B.

The results and discussion in previous sections (Sections 3.3.6, 3.5.1, 3.5.3, 4.2.2, 4.2.3) implied that the alteration reactions took place, at least in part, within the kimberlite particles and not just at the surface. For this reason, alteration of the material can be associated with the classic shrinking core model when account is taken of the different inter-reaction possible, due to the heterogeneous kimberlite petrology. The main evidence for 'cavity' reactions was obtained from the scanning electron photomicrographs (Plates 3.9-3.19).

Plates 3.9-3.11 show the bulk alteration of kimberlite induced by 0.31M hydrochloric acid. Cavities were observed within the reacted portion (Plate 3.11) although the phyllosilicate product could not be readily distinguished from the rock matrix. Plates 3.12-14 illustrate the effect of 1.5M hydrochloric acid on the kimberlite. Cavities adjacent to the surface were commonly observed (Plate 3.12), in which lathe-shaped clay crystallites developed (Plate 3.14), part of their growth originating from the reaction interface with the comparatively unaltered kimberlite. The introduction of aluminium to the system resulted in more penetrative alteration (Plates 3.15,3.16), making possible the crystallisation of phyllosilicates in the solution cavities within the kimberlite (Plate 3.17).

The kinetic data (Sections 4.2.2-4) have indicated that the alteration processes occurred in two stages : dissolution of the kimberlite followed by precipitation of solvated/liberated ionic species.

The initial period of acidic dissolution was very short compared with the overall reaction periods employed, as indicated by the rapid increase in metal ion concentration in solution (especially

that of calcium), as shown in Figures 4.2.1 and 4.2.2. After the bulk of the acid added had been consumed, (1-2h, Figure 4.2.3) interactions between aluminium and liberated ionic species followed. It was assumed that such reactions were similar in both surface and cavity zones though different time scales could have been involved. That this two-stage alteration mode accounted for the degradation of the kimberlite was supported by the plots obtained from the DOA, residual pH, olivine and serpentine analyses (Figures 4.2.1, 4.2.3-5). The extent of physical degradation increased with the breakdown of olivine and serpentine which was attributable not only to acid consumption (i.e. 0-1 h) but also to aluminium inter-reactions. The steady increase in the -75 μm product reflected the formation of clay phases (as detected by XRD) which constituted the second stage of the alteration process.

The mass balance results (Section 4.2.3) confirmed that the alteration induced involved the progressive formation of a magnesium-iron-aluminium silicate as the -75 μm product. Whereas simple trends were recorded for the calcium, silicon, iron and magnesium (the +75 μm distribution values decreased with time and those due to the -75 μm fraction and solution phase increased), those for aluminium showed a different type of behaviour. Between 3-5 h, the aluminium concentration in solution apparently achieved a temporary steady state, during which the cation was in some way interchangeable between the +75 μm and -75 μm fractions. These observations were consistent with the introduction of aluminium into tetrahedral and octahedral coordination states, as noted from IR analyses (Section 4.2.4), to form phyllosilicate minerals.

The principal clay minerals produced as identified by XRD were vermiculite-chlorite (presumably a poorly-formed mixed-layered phase), kandites (serpentine-kaolinite) and ill-defined 9-11 Å aluminosilicates.

The latter products, whatever their precise composition, were a major constituent in the reaction products at 100°C which once formed, persisted under the conditions employed. It was assumed, however, that they were basically metastable in nature.

Little more can be stated for reactions at 100°C except by inference from higher temperature reactions (see later).

4.5.2 Reactions at 150 and 215°C

This section considers the intermediate temperatures, 150 and 215°C for Systems C and D, but concentrates mainly on the latter as these reactions yielded the best information on first formed metastable products.

As noted previously, the first stage of the alteration process was considered as the dissolution of the kimberlitic minerals. The main active agent was the hydrogen ion, the liberated silicon being considered to enter solution as monomeric silicilic acid as noted previously.[71]

$$\underset{\text{olivine}}{M_2\,SiO_4} + 4H^+ \leftrightarrow 2M^{2+} + Si(OH)_4 \qquad (4.5.1)$$

$$M_3\,Si_2\,O_5(OH)_4 + 6H^+ \leftrightarrow 3M^{2+} + 2Si(OH)_4 + H_2O \qquad (4.5.2)$$

where M represents Mg^{2+},Fe^{2+},Ni^{2+},Ca^{2+}.

Such dissolution reactions are considered to involve rapid ion exchange between the M^{2+} and H^+ ions combined with a slower rate of incongruent dissolution of the silicate structure.[257] Whereas the majority of the M^{2+} ions would become readily solvated, the conditions were not favourable for formation of concentrated silica solutions as shown by the data in Sections 4.3.2 and 4.3.3. The subsequent

polymerization of silica monomers and the interaction of the aluminium ions to form the residual clay minerals[108] appeared to constitute the second stage of the alteration process.

The polymerization/precipitation of released silica may have been induced by three agencies :

a) pH. The equilibrium pH recorded was in the range 3-4 (Section 4.3.2) in which silica solubility is low (Figure 1.4.2).
b) the presence of the ions Ca^{2+} and Mg^{2+} would increase the activity coefficient of the dissolved silica[242] resulting in a reduction in the solubility[241,258] (Section 3.2.2), and
c) the addition of aluminium ions induces silica coprecipitation with this ion.[120,124,259]

Hence the effect of the constituent cations in solution predominated over that of the temperature which would otherwise have induced further silica dissolution.[259]

The first-formed products were identified by IR analyses (Figures 4.3.8a, 4.3.9a, 4.3.10a) as being similar to proto-imogolite[255] despite difficulties in interpretation of the complex traces involved. XRD analysis (Figures 4.4.1a, 4.4.2a) indicated a mixture of 7 and 9 Å silicate forms, the latter being preferentially produced where larger initial aluminium ion concentrations had been employed. As stated before this product consisted largely of orthosilicate units bonded to an aluminium hydroxide lattice. Three types of polymerization could be considered in relation to the possible interactions between the ionic species in solution.

Firstly, dimerization of silicilic acid[126] occurs at an increasing rate as the pH increased from 2 to 4[124] (Figure 1.4.1).

$$2Si(OH)_4 \leftrightarrow (HO)_3Si\text{-}O\text{-}Si(OH)_3 + H_2O \qquad (4.5.3)$$

Further polymerization of the dimer would result in the formation of free silica.[124]

$$\underset{\text{dimer}}{Si_2O(OH)_6} + \underset{\text{monomer}}{Si(OH)_4} \leftrightarrow \underset{\text{trimer}}{((HO)_2SiO)_3} + 2H_2O$$

$$n[((HO)_2SiO)_3] \leftrightarrow \underset{\text{silica}}{Si_{3n}O_{6n}} + 3n\ H_2O$$

However as silica was not formed, such silica interactions beyond the dimeric stage are not considered.

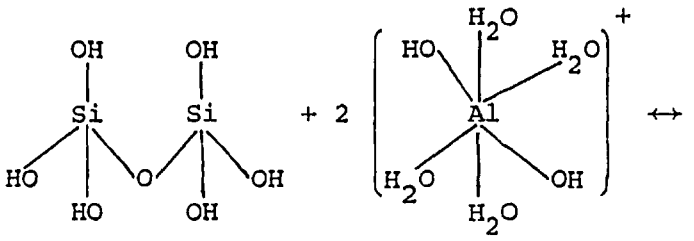
Secondly, the aluminium ions solvate, adopting an octahedral coordination state due to the high initial concentration and low pH.[139,153] In the final event boehmite is produced[132] (the phase always detectable after 1 h at 215°C).

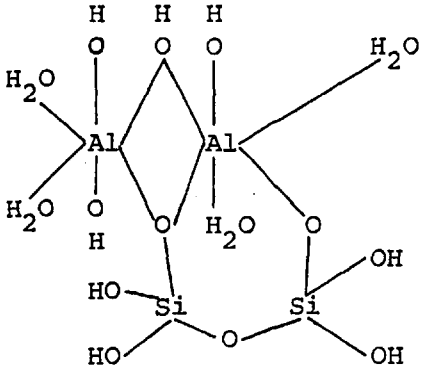
$$Al^{3+} + 6H_2O \leftrightarrow [Al(OH)_2(H_2O)_4]^+ + 2H^+$$

$$[Al(OH)_2(H_2O)_4]^+ \leftrightarrow Al(OH)_3 + H^+ + 3H_2O$$

$$Al(OH)_3 \leftrightarrow AlOOH + H_2O \qquad (4.5.4)$$

Thirdly the two elementary forms condense to produce a mixed elementary structure relatable to a kandite, detected as an imogolite.



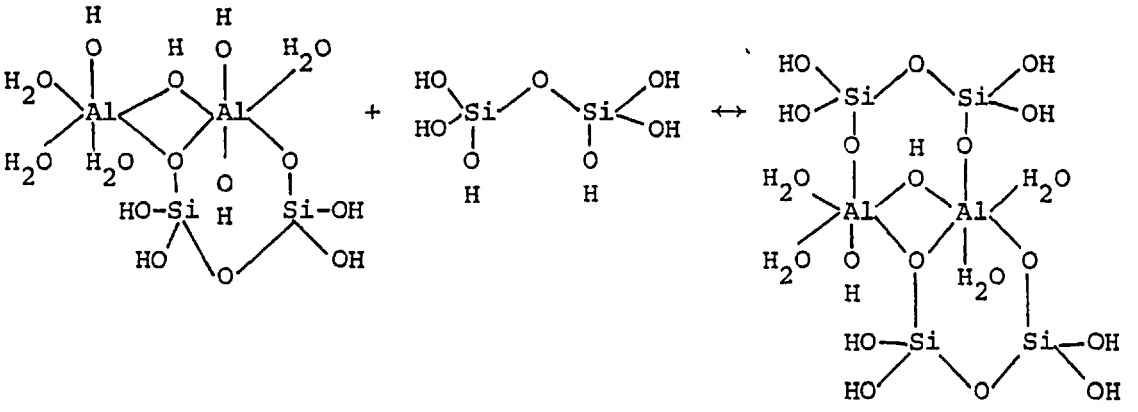


'imogolite' I

$$+ 4H_2O + 2H^+ \qquad (4.5.5)$$

The production of hydrogen ions in the alteration process in this way would explain continuation of the degradation recorded (Figures 4.3.1, 4.3.2 and 4.3.7) after 1 h, when the acid concentration had decreased to less than 0.1% of its initial value.

The formation of 9-11 Å elementary structures (as indicated by 4.3.8a, 4.3.10a as well as alteration tests conducted using the olivine standard) can then be considered as a continuation of the reaction described in equation 4.5.5.



+ $2H_2O$ (4.5.6)

It was from these two basic structural types shown on the right hand side of equations 4.5.5 and 4.5.6 that the clay phases were thought to be formed. Further polymerization of the 'imogolite I' products with the removal of water resulted in kaolinite formation (this process with the previous inter-reactions compares favourably with previous syntheses[133,134,137,138,145-147,152,153]) :

$$n\ (H_2O)_4\ (HO)_4\ Al_2\ O_3\ Si_2(OH)_4 \leftrightarrow [Al_2\ Si_2O_5(OH)_4]_n + 6n\ H_2O \quad (4.5.7)$$

'imogolite I' kaolinite

In the above equation n unit cells of imogolite were considered to react to form a clay phase, the simple stoichiometric formula of which is given on the right hand side. This convention is used in other equations which follow.

Similarly, by polymerization of the products shown in equations 4.5.6 9-11 Å hydrated aluminosilicates (akin, but not the same as pyrophyllite or talc) formed. Metallic cations, Ca^{2+}, Mg^{2+} (represented as M^{2+} below) were incorporated in the forming structure, to stabilise the water molecules in the octahedral interlayers which

develop.

$$n\ [(HO)_4\ Si_2O_3\ (H_2O)_4\ Al_2(OH)_2O_3\ Si_2(OH)_4] + xn\ M^{2+}$$

$$\leftrightarrow [M_x\ [Al_2\ Si_4\ O_{10}\ (OH)_2]\ 8H_2O]_n \qquad (4.5.8)$$

Although the first-formed products exhibited no detectable tetrahedral substitution of aluminium for silicon, this was not the case for the products obtained from 2 h onwards (Table 4.4.2 and 4.4.3 for the 9-11 Å aluminosilicates). At this stage of the reaction the 'free' aluminium existed as 'boehmite'. The hydroxyoxide was considered to react with liberated monomeric silica as follows (cf. equation 4.5.3) :

$$\text{'AlOOH'} + Si(OH)_4 \leftrightarrow (HO)_3\ Al\text{-}O\text{-}Si(OH)_3 + H_2O + H^+ \qquad (4.5.9)$$

from which an aluminium-rich imogolite product was produced, excess aluminium entering octahedral coordination :

$$(HO)_3\ Al\text{-}O\text{-}Si(OH)_3 + 2\text{'AlOOH'} + 4H_2O \leftrightarrow (H_2O)_4\ (HO)_4\ Al_2O_2\ AlSiO(OH)_4 \quad \text{imogolite II} \qquad (4.5.10)$$

(A similar reaction relating to imogolite is given by Farmer et al.[255]) The 9-11 Å aluminosilicate would then develop from imogolite II species and aluminium-silicilic acid dimers according to equilibria similar to those in equations 4.5.8 and 4.5.9. The development of a 7 Å 1:1 layered kaolinite structure as opposed to 9-11 Å 2:1 layered aluminosilicates would be dependent on the localised availability of silica[105]

(as indicated in Figure 3.5.1). It was likely that in the final stages of reaction the concentration of free monomeric or dimeric silica would have substantially decreased owing to consumption of the regenerated hydrogen ions. 7 Å structures which have a higher aluminium assay would preferentially form as indicated by the XRD traces and the computed phase proportions.

Although it was not certain that reactions of this type occur at lower temperatures it was assumed that less crystalline and hence undetectable structures formed in Systems C and D at 100-150°C.

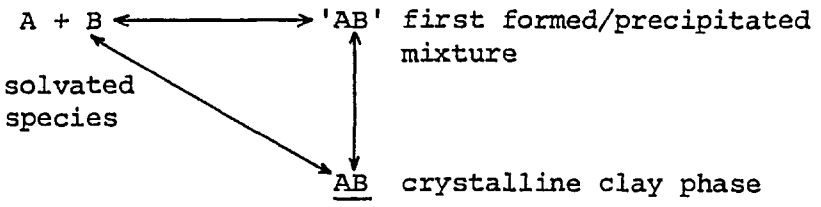
4.5.3 Reactions at 260°C and 300°C

The reactions at 260 and 300°C (Systems C and D) were similar to those at lower temperatures, but reaction trends were clearer in that the -75 μm products were better crystallised and could then be identified more readily. From the compositional data in Tables 4.4.2 and 4.4.3, additional effects were considered to take place, in particular :

a) the introduction of magnesium and iron into the octahedral lattice of the clay mineral structures
b) the substitution of aluminium for silica in tetrahedral coordination and
c) the formation of larger crystal lattices i.e. 14-16 Å minerals.

As a consequence of the improved mineral form it became possible to interpret XRD spectra in more detail, in particular, to relate changes in peak breadth and height to particular types of reaction mechanism. In this respect, two limiting possibilities can be identified for the production of well crystallised clay minerals from

first-formed poorly crystalline mixtures (cf. Figures 4.4.8-15). These are shown in the scheme below :



One possibility shown is that the first-formed poorly crystalline mixture 'AB' is in equilibrium with the solution phase ions A and B, which are silicon and aluminium species respectively, of whatever nature. Recrystallisation subsequently occurs via these to form clay phase(s) represented by AB. Alternatively the product 'AB' may undergo a solid state transformation to form(s) AB directly. Although both may occur, the predominant type of transformation appeared to be via the solution phase. This was inferred by the detectable (though small) aluminium and silicon concentrations (at 1-2 h) in the residual reaction solutions. It also appeared less likely that the extent of structural reorganisation required could occur in the solid phase. This hypothesis is in agreement with previous observations.[143]

Reference to the IR, XRD and computer interpreted phase analyses showed that the mineralogical compositions of the -75 μm fractions obtained at 1-2 h at 260°C were similar to those recorded at 5-6 h at 215°C (cf. Figures 4.3.9d, 4.3.11b; 4.3.10d, 4.3.12b; 4.4.1c, 4.4.4b; 4.4.2d, 4.4.5b; 4.4.10, 4.4.12; 4.4.11, 4.4.14). Whereas 9-11 Å aluminosilicates progressively formed at 215°C, the higher temperature induced, in comparison, rapid precipitation of a series of aluminosilicates which produced the XRD spectra shown in Figures 4.4.4a-c, 4.4.5a-c. In contrast to the reactions at 215°C, tetrahedrally substituted forms were thought to form at the outset as follows :

$$Si(OH)_4 + [Al(OH)_2(H_2O)_4]^+ \leftrightarrow (HO)_3Al^-\text{-}O\text{-}Si(OH)_3 + 2H^+ + 3H_2O \quad (4.5.11)$$

$$2(HO)_3\,Al^-\text{-}O\text{-}Si(OH)_3 + 2[Al(OH)_2(H_2O)_4]^+ \leftrightarrow (HO)_4\,Al^-Si\,O_3(H_2O)_4\,(HO)_2\,Al_2\,O_3\,Al^-Si(OH)_4 + 2H^+ + 6H_2O \quad (4.5.12)$$

Finally, polymerization yielded the observed product :

$$n\,(HO)_4\,Al\,Si\,O_3(H_2O)_4(HO)_2\,Al_2\,O_3\,Al\,Si(OH)_4 \leftrightarrow [Al_2\,(Al_2Si_2)\,O_{10}\,(OH)_2.8H_2O]_n$$

9-11 Å intermediary (4.5.13)

The 9-11 Å products obtained (according to the computing procedure Section 2.5.4) at 1-2 h/Tables 4.4.2 and 4.4.3) represented metastable forms which contained the highest proportions of aluminium possible in a silicate structure. The extent of tetrahedral replacement of silicon by aluminium was affected partly by the localised availability (Section 3.5.1) of the latter (the Al^{3+} cation only entering tetrahedral coordination when the $Al_2O_3/(Al_2O_3+SiO_2)$ ratio at the reaction site, fell below 0.3-0.4[139]) and partly by the aluminium avoidance principle.[124,260] This principle states that the introduction of a negative charge into a tetrahedral lattice destabilises any further Al^{IV}-O-Si bonding owing to the mutual repulsion of negative changes. It was evident that the higher temperature (260°C) stabilised the tetrahedral form of aluminium (as recorded elsewhere[127]) and that the pH at the zone of reaction ($\sim$ 5) was favourable for the substitutions to be made.

The 9-11 Å form was unstable over the reaction time investigated. TGA analysis showed that progressive removal of interlayer water occurred.

IR and XRD confirmed that these hydrated forms were replaced by less hydrous ones. The 9-11 Å forms were assumed to break down according to the reversal of the equilibria in equations 4.5.11-13; other silicates, which formed simultaneously with the 9-11 Å phases, namely kaolinite at 260°C (Figures 4.4.12 and 4.4.13) or vermiculite and smectite at 300°C (Figures 4.4.14 and 4.4.15), remaining stable. The remainder of clay phases observed were then slowly formed from the re-solvated monomeric and dimeric aluminosilicilic species originating from the 9-11 Å phases. The synthesis of kaolinite has been discussed above (equations 4.5.5 and 4.5.7). Smectite formation however, can be represented by the equations below. As 9-11 Å structures had formed readily earlier in the reaction, it was likely the formation of the smectite would involve a product comparable with that shown in equation 4.5.6.

$$0.8(HO)_3\,Si\text{-}O\text{-}Si(OH)_3 + 0.2(HO)_3\,Al\text{-}O\text{-}Si(OH)_3 + (H_2O)_4\,(HO)_4\,Al_2O_3Si_2(OH)_4$$

imogolite I

$$\leftrightarrow (HO)_4\,Al_{0.2}\,Si_{1.8}\,O_3\,(H_2O)_4\,(HO)_2\,Al_2O_3Si_2(OH)_4 + 2H_2O$$

intermediate (4.5.14)

Polymerisation of the intermediate produced the smectite; the introduction of metallic cations stabilising the hydrous interlayers :

$$n\,(HO)_4\,Al_{0.2}\,Si_{1.8}\,O_3\,(H_2O)_4\,(HO)_2\,Al_2O_3Si_2(OH)_4 + n\,M^{2+}$$

$$\leftrightarrow [M\,Al_2\,(Al_{0.2}Si_{3.8})\,O_{10}\,(OH)_2.3.5H_2O]_n + 4.5n\,H_2O$$

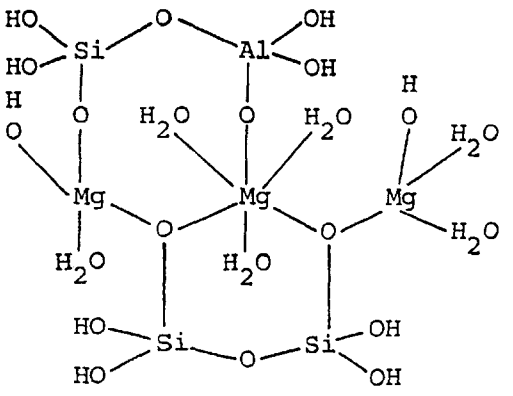
smectite (4.5.15)

The formation of vermiculite involved the inter-reaction of

aluminium-silicon dimers and solvated magnesium and iron hydroxides[261] to form an intermediary product having structural similarities to that in equation 4.5.6.

$$(HO)_3\,Al\text{-}O\text{-}Si(OH)_3 + (HO)_3\,Si\text{-}O\text{-}Si(OH)_3 + 3[(Mg,Fe)(OH)(H_2O)_3]^+$$

$\leftrightarrow$



$$+ 3H^+ + 4H_2O \qquad (4.5.16)$$

Polymerisation led to the synthesis of vermiculite, metallic cations (M^{2+}) stabilising the associated water interlayers :

$$n\,(HO)_4\,AlSiO_3(H_2O)_6\,(HO)_2\,(Mg,Fe)_3\,O_3Si_2(OH)_4 + 0.5n\,M^{2+}$$
$$\leftrightarrow [M_{0.5}(Mg,Fe)_3(AlSi_3)O_{10}(OH)_2.4.5H_2O]_n + 5.5n\,H_2O \qquad (4.5.17)$$

As indicated by the residual ion analyses (Figures 4.3.3-7), IR analyses (Figures 4.3.13 and 4.3.14), XRD analyses (Figures 4.4.6 and 4.4.7) and computed phase analyses (Figure 4.4.14 and 4.4.15) the alteration reactions at 300°C were similar to those observed at 260°C. The principal differences were in the smaller proportions of the metastable 9-11 Å minerals (as expected) and in the formation of chlorite.

The formation of chlorite has similarities to the synthesis

of vermiculite, particularly in the case of tetrahedral replacement. Equations for the synthesis of chlorite are given below (as based on the structural formulae in Table 4.4.3) :
following reactions comparable to those described in equations 4.5.9, 4.5.10 and 4.5.16

$$(HO)_3\,Al\text{-}O\text{-}Si(OH)_3 + (HO)_3\,Si\text{-}O\text{-}Si(OH)_3 + 0.6\ 'AlOOH' + 2.3[(Mg,Fe)(OH)(H_2O)_3]^+ \leftrightarrow (HO)_4\,AlSiO_3(H_2O)_6(OH)_2\,Al_{0.6}(Mg,Fe)_{2.3}O_3Si_2(OH)_4 \quad \text{intermediate} + 1.9H^+ + 2.4H_2O \qquad (4.5.18)$$

the intermediate with a precipitating solvated magnesium-aluminium-iron hydroxide polymerizes to form the final chloritic product

$$n[(HO)_4AlSiO_3(H_2O)_6(OH)_2\,Al_{0.6}(Mg,Fe)_{2.3}O_3Si_2(OH)_4] + 2.2n\,[(Mg,Fe)(OH)(H_2O)_3]^+ + 0.7n\ 'AlOOH' \leftrightarrow [(Mg,Fe)_{4.5}\,Al_{1.3}\,(AlSi_3)O_{10}(OH)_8]_n \quad \text{chlorite} + 14.2n\,H_2O + 1.6n\,H^+ \qquad (4.5.19)$$

It is appreciated that these above equilibria (equations 4.5.1-19) are very complex and are far from fully established. These equilibria do appear to be consistent with the analytical data obtained and the mass balances in the following section were intended to provide further comfirmatory evidence for the proposed mechanism.

4.5.4 Overall mineral equilibria : confirmatory mass balances

The purpose of this section was to undertake a check on the internal consistency of the experimental data and derived mechanistic data. Such a check was of particular significance in a system as complicated as kimberlite alteration. The method adopted is outlined in the scheme in Figure 4.5.1 and is explained in detail in Appendix 6. The technique was to employ solid phase elemental and mineralogical assay data, in conjunction with overall mineral equilibria deduced from the reaction mechanism, to predict the residual concentrations of the elements Mg, Fe, Al and Si in solution and compare the figures with those determined experimentally.

Figure 4.5.1 is now discussed briefly in terms of the assumptions made. The first assumption was that the elements Mg, Fe and Si originated solely from olivine and serpentine (which with calcite formed 92% of the kimberlite). Olivine and serpentine were consequently considered as the only phase inputs with respect to the cations of interest. XRD analysis showed that 64% of the +75 μm fraction consisted of head minerals. By assuming the remainder (which formed an alteration crust to consist of minerals similar to those present in the -75 μm fraction) a mineralogical composition could be deduced using Program CECPM. To model the overall mineral equilibria, the separate reaction steps discussed in the reaction mechanism (Sections 4.5.1-3) were added algebraically, taking account of experimentally based determinations of clay proportions and formulae, and assays of olivine and serpentine standards, to give the following equation form :

$$\begin{matrix}\text{4.olivine/} \\ \text{2.serpentine}\end{matrix} + aH^{+} + bAl^{3+} \leftrightarrow \text{clay phase } (Al,Si)_4O_{10} \text{ unit)} + \sum_{1}^{n} c_i M_i^{x+} + d\ Si(OH)_4$$

where M is Mg^{2+},Fe^{2+},Fe^{3+},Ca^{2+},Ni^{2+}

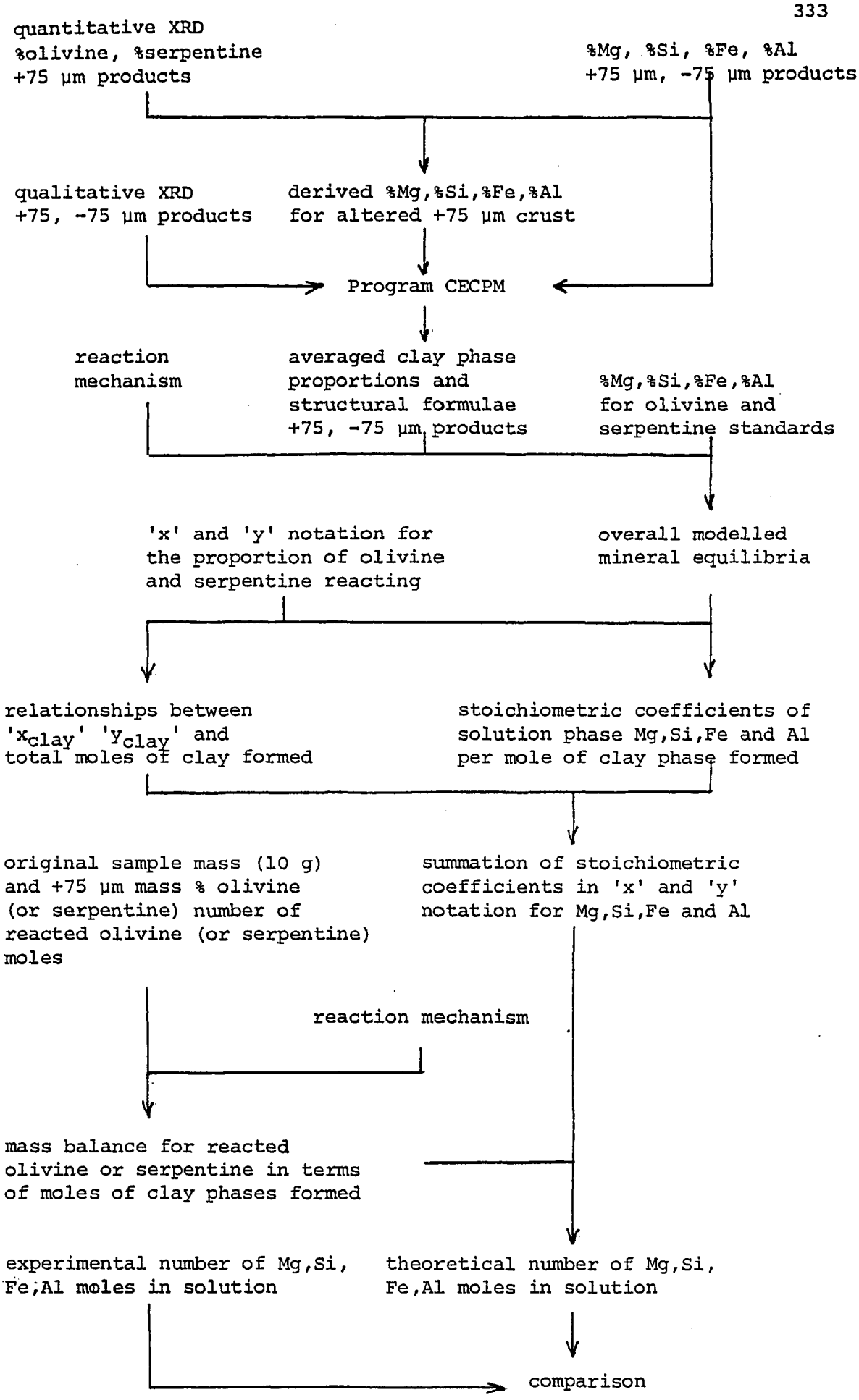


Figure 4.5.1 Scheme for calculating moles of ions residual in solution.

An example is the transformation of olivine to chlorite :

$$4\ Ca_{.07}\ Mg_{1.62}\ Fe_{.21}\ Ni_{.1}\ Al_{.01}\ SiO_4 + 2.76\ Al^{3+} + 7.72H_2O$$

olivine

$$\leftrightarrow Al_{1.37}\ Mg_{3.98}\ Fe_{.77}\ (Al_{1.43}\ Si_{2.57})\ O_{10}\ (OH)_8$$

chlorite

$$+ 0.28Ca^{2+} + 2.50Mg^{2+} + 0.07Fe^{2+} + 0.40Ni^{2+} + 1.72H^{+}$$

$$+ 1.43Si(OH)_4$$

Direct calculation through the steps shown produced the theoretical number of moles of the elements Mg, Si, Fe and Al which could be compared directly with the experimental solution concentrations.

As given in Appendix 6, the theoretical and experimental figures for the example are shown below :

	Number of Moles			
	Mg	Si	Fe	Al
theoretical	0.0129	0.0024	0.0011	0.0139
experimental	0.0102	0.0023	0.0009	0.0140

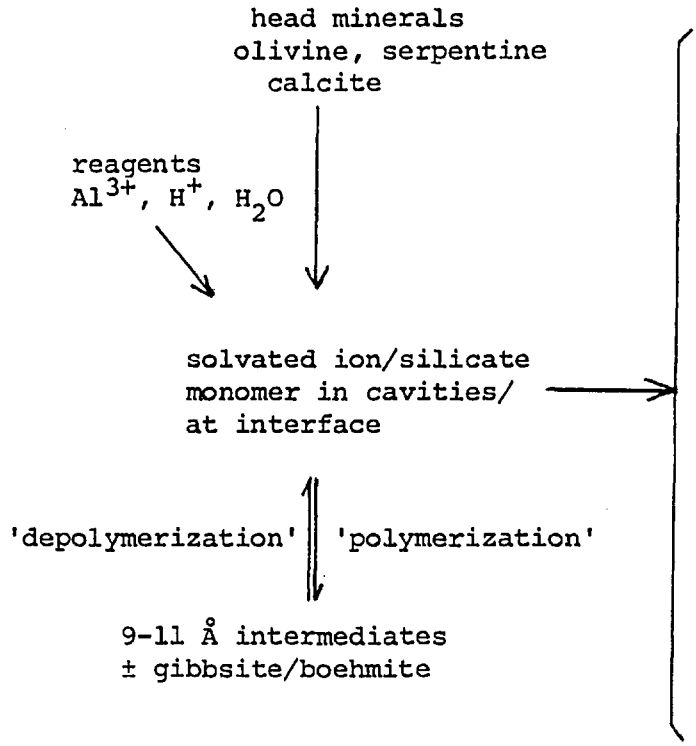
The agreement was seen to be well within experimental error. Similarly favourable results were obtained for the other systems investigated and hence it was possible to have extra confidence in both the analytical techniques and the proposed reaction mechanism. Hence, alteration could occur in aqueous media[62-67] the greatest degradation most readily taking place where aluminium and hydrogen ions were present in aqueous chloride media. Although water can be instrumental in solubilizing minerals over long periods of (geological) time, in the

present work it solely acted as a medium in which ion interactions and structural organisations could take place, as well as providing for the formation of hydrous polymeric complexes from which clay minerals developed. It was the hydrogen ion which liberated ionic species from the kimberlite. In contrast to suggestions previously made[64,67,72,95] the addition of silica was not required. Indeed, the mechanism appeared to model the geological fenitization processes[108] (section 1.3.5) which have been reported to affect kimberlite degradation and replacement by secondary minerals.

4.6 Alteration Reaction Kinetics

4.6.1 Alteration stages and products

The generalised two-stage alteration mechanism described in Sections 4.5.1-3 can be considered again in the form of the schematic diagram shown in Figure 4.6.1. In the figure the head minerals, modelled as olivine, serpentine and calcite, are considered to interact with the ions Al^{3+}, H^{+} and water at pHs below 1. Solvated ions and siliceous gels are generated in dissolution cavities and at the solid/liquid interface of the kimberlite particles (and <u>not</u> primarily in the bulk solution). These primary species are rapidly precipitated to form highly hydrous 9-11 Å intermediates which are presumably colloidal polymers which are stable over 7 h at 100-215°C but depolymerize at higher temperatures (≥ 260°C). Some gibbsite/boehmite also precipitates where high aluminium concentrations are present; magnesium, iron and calcium entering solution. However, given time, the solubilized cations condense on to depolymerized primary species - repolymerizing alumino-silicilic structures to crystallize clay minerals. The type of clay phase formed depends on the aluminium and hydrogen ion concentrations at the site of reaction (which in turn is controlled by



		Al^{3+}	H^+	T_1	T_2	T_3
kandite	dioct	1	3	4	1	1
	trioct	1	3	1	2	3
smectite	dioct	3	1	4	3	1
	trioct	4	2	2	5	4
vermiculite		2	4	3	4	2
chlorite		2	5	4	5	3

Notes : The numbers 1→4 or 5 give the order of preferential formation for an increase in Al^{3+} or H^+ ion concentration or at 100°C (T_1), 200°C (T_2) or 300°C (T_3)/

Figure 4.6.1 Schematic representation of alteration reaction mechanism which relates to microscale inter-reactions

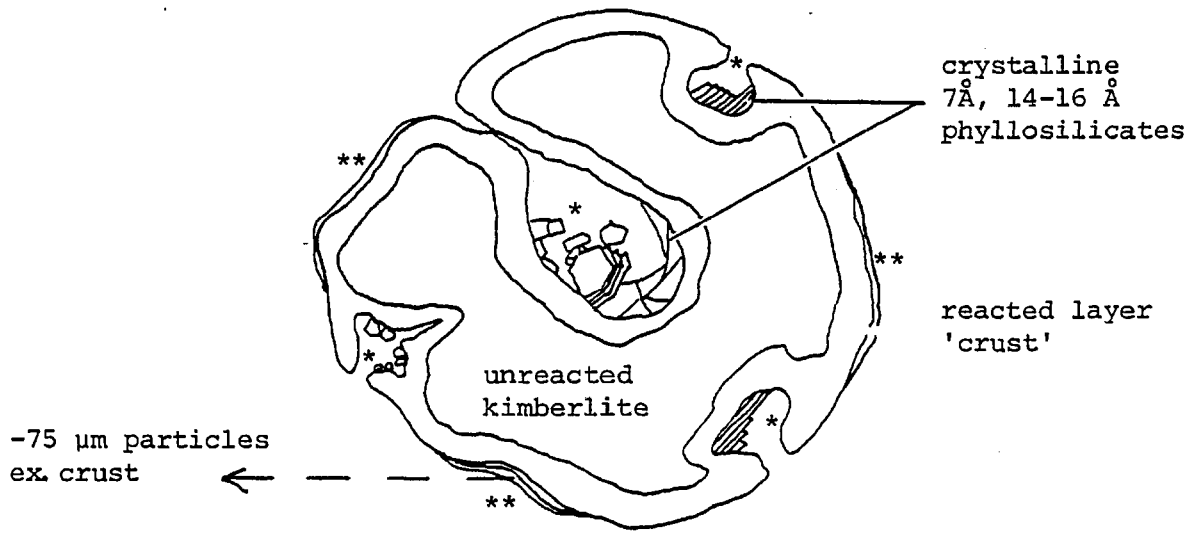


Figure 4.6.2 The nature of the degradation induced in the kimberlite in accordance with the proposed reaction mechanism.

the initial reagent concentrations employed and temperature). An approximate order of preferential formation is given in Figure 4.6.1; for example dioctahedral kandites will preferentially form where aluminium concentrations are high (∿ 0.4M Al^{3+}, Figure 3.4.1) and the temperatures are ∿200°C or above. Chlorites however form in weakly acidic pHs (∿ 4.5), moderate aluminium concentrations (∿ 0.2-0.3M Al^{3+}, Figures 3.3.9 and 3.3.10) and proportionately increase in concentration with temperature.

As mentioned above, the temperature and the concentrations of aluminium and hydrogen ions at the site of the reaction control the nature of the phyllosilicate product. The concept of localised availability (Section 3.5.1) is important as reactions appear to occur either within solution cavities in the kimberlite (*) or at the solution/solid interface (**) as indicated in the schematic diagram in Figure 4.6.2.

On addition of the reagents, dissolution occurs, the reaction being orientated along paths of physical weakness (e.g. grain boundaries) or via minerals of greater reactivity (according to the sequence calcite > serpentine > olivine). A reacted layer or 'crust' is subsequently produced as shown in Figure 4.6.2 which extends further into the particle with time through the formation of cavities (Plate 3.17). This action is limited by the concentration of hydrogen ions available via diffusion channels. Although further penetration follows from hydrogen ion regeneration (Sections 4.5.2 and 4.5.3) a substantial proportion of the head mineral dissolution occurs during the period of initial contact between the acidic solutions and the kimberlite over 0.25 - 2 h. The resultant reacted layer consists largely of 9-11 Å intermediary phases (Section 4.5.4, Appendix 6) which with kaolinite, are the phases most rapidly formed (but not necessarily

the most stable (Figures 4.4.9-15)). Whereas kandites once formed are relatively stable, 9-11 Å phases re-solvate and magnesium, iron and other aluminium cations within the solution reaction zone interact to precipitate clay mineral phases (Figure 4.6.1). The maintenance of a relatively high aluminium concentration in the bulk solution is important in driving the cation to the sites of reaction. However excess (> 0.5M in the tested systems) results in widespread precipitation of simple hydroxyoxides rather than phyllosilicate minerals. The resultant phyllosilicate products which crystallize within cavities (Plate 3.17) or the particle surface (as generally observed) are assumed only to be removed through mechanical disruption only (i.e. attrition between particles).

A comparison will now be made with geological systems. The proposed reaction mechanism (that necessitating the addition of the ions Al^{3+}, H^{+} and water to induce kimberlite alteration) appears to explain not only the mineral transformations noted in the laboratory but also those 'fenitization' reactions observed in the field.[108] The present scheme allows for in situ replacement of kimberlitic rocks by their natural alteration products, which include chlorites,[64,75] vermiculates,[79] smectites,[81,99] and kandites[64-74] as synthesised in the present work. Kimberlites also contain 9 Å talc phases as an important alteration product.[61,64,97] Dehydration rather than re-solvation of the 9-11 Å intermediates shown in Figure 4.6.1 would yield talc-pyrophyllite products. Indeed, the talcose products observed at Premier Mine were considered to be intermediary products prior to chlorite/vermiculite/nontronite/saponite/stevensite formation.[61] As shown in Plates 1.4 and 1.5 some alteration occurred during consolidation of the pipe, the transformation of primary minerals (olivine serpentine, pyroxene) to secondary ones being especially induced during

the gas-liquid fluidized stage[8] if the temperatures were sufficiently low to permit phyllosilicate formation (cf. temperatures used in the testwork : 100-300°C). Water and carbon dioxide were entrained within the pipe[8] and these would induce re-solubilization of ferromagnesian minerals[96] (cf. acidic aqueous solutions in the testwork). The formation of the clay minerals observed was however also dependent on aluminium availability in the same way it was in the laboratory. It is proposed that in contrast to other kimberlites those at Premier were formed from sites in which unusually high concentrations of aluminium rich liquors were locally injected and carried up with the fluidized intrusion. However, the origin of the aluminium which is required to produce the alteration products of kimberlite, as observed in the field, remains a subject of debate.[61,62]

4.6.2 Overall rate equations

In accordance with the classic approach to kinetics, attempts have been made to model kimberlite degradation in terms of a rate equation. The main factors controlling the reaction studied in the present work were hydrogen and aluminium ion concentration, temperature, feed size and the degree of agitation. These were considered for the deduction of rate equations based on experiments using Systems A and B (Section 4.2.1) involving -1180+850 μm samples of kimberlite (though other size fractions also used were -420+300 μm, -1700+1180 μm, -3.18+1.70 mm, -6.18+3.18 mm, -15+9.5 mm). Suitable criteria of alteration were the numbers of unreacted moles of olivine and serpentine (denoted ξ_{ol} and ξ_{sp} respectively) which were deduced from XRD analysis of the +75 μm fractions. For a typical head grade feed of 10 g kimberlite initial values of ξ^{o}_{ol} and ξ^{o}_{sp} were 0.0227 and 0.0163 respectively. Each of the factors above will be discussed in turn.

Effects of hydrogen and aluminium ion concentrations : These were deduced from a series of initial rate experiments. Ten gramme quantities of -1180+850 μm feed samples were reacted with various initial concentrations of the two ions for 0.25 h under the conditions described previously. Examples of the results, plots of ξ_{ol} and ξ_{sp} as functions of initial hydrogen and aluminium concentrations, are shown in Figure 4.6.3. As can be seen, serpentine was preferentially attacked by the reagents, the latter only affecting the olivine significantly where the reagent concentrations exceeded 0.4M Al^{3+}, 1.3M H^+ or 0.2M Al^{3+}, 1.5M H^+. Although both the H^+ and Al^{3+} ions evidently interact with both serpentine and olivine, by far the most reactive combination was the H^+ ions and serpentine.

Initial rates of reaction $d\,\xi_{ol}/dt$ and $d\,\xi_{sp}/dt$ were expressed as functions of initial acid and aluminium ion concentrations by using a multiple linear regression procedure. (The initial ion concentrations produced more significant correlations than those involving either ion consumption or final ion concentration.) By assuming the initial rates to be constant with time over 0.25 h the number of moles of olivine and serpentine reacting per second could be evaluated. For example, for $\xi_{sp} = 0.0009$, $d\,\xi_{sp}/dt = (0.0163-0.009)/900$ moles s^{-1}, for the 0.25 h period. Moreover by introducing various types of function into the multiple linear regression routine, the following equations could be deduced :

$$\left(\frac{d\,\xi_{ol}}{dt}\right)'_{initial,100°C} = \phi_{ol} = 5.19 \times 10^{-11} [H^+]^{0.26}_{initial}$$

$$\exp(6.55[H^+]_{initial} + 2.41[Al^{3+}]_{initial})$$

$$R^2 = 1.00 \qquad (4.6.1)$$

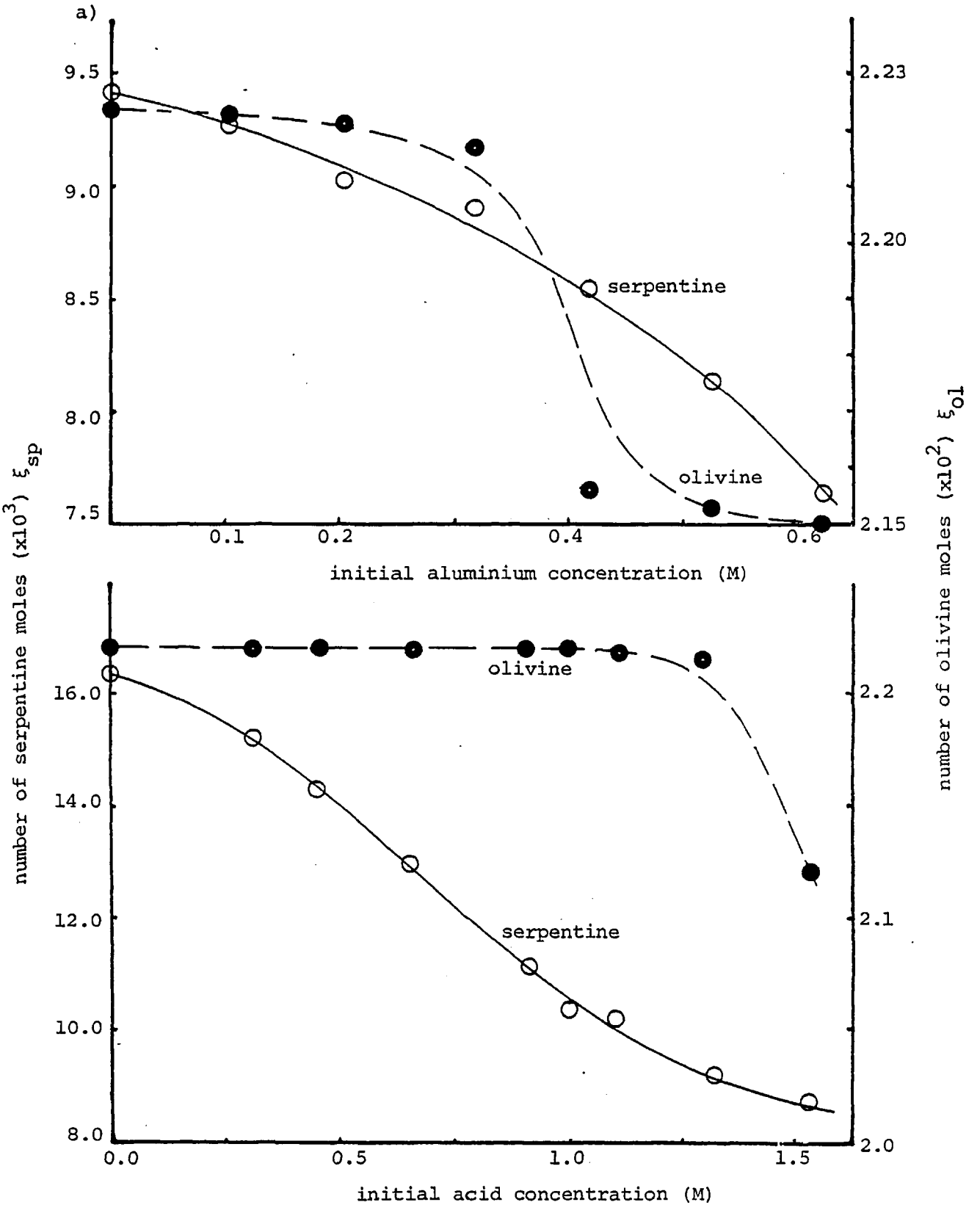


Figure 4.6.3 Initial-rate kinetics : Residual number of moles of olivine and serpentine after 0.25 h for systems having :

a) initial acid concentration 1.3M, initial aluminium concentration variable
b) initial aluminium concentration 0.2M, initial acid concentration variable

at 100°C.

$$\left(\frac{d\,\xi_{sp}}{dt}\right)'_{initial,100°C} = \phi_{sp} = -9.52 \times 10^{-7} + 6.21 \times 10^{-6}[H^+]_{initial}$$

$$+ 3.97 \times 10^{-6}\,[Al^{3+}]_{initial}$$

$$R^2 = 0.97 \qquad (4.6.2)$$

where R is the correlation coefficient.

These equations will be considered later.

Effect of temperature : The activation energies, Ea, for the alteration reactions of olivine and serpentine, and the associated frequency factors M, were calculated from the linearized form of the Arrhenius equation :

$$\ln k = -Ea/RT + \ln M \qquad (4.6.3)$$

where k is the rate constant; T, the temperature and R, the gas constant.

To determine the nature and magnitude of the rate constant, correlations were sought between various functions of ξ_{ol} and ξ_{sp} and the reaction time, with the objective of finding a linear response. Only one such linear plot was obtained (Figure 4.6.4) for the entire reaction period investigated (0-24 h) i.e. ξ_{ol}^{-1} in System A.

$$\text{s.t.} \quad \xi_{ol} = kt + N \qquad (4.6.4)$$

where t is the time (s) and N a constant. The other data were plotted in a similar manner as shown in Figures 4.6.4 and 4.6.5, but gave curved plots indicating variable kinetics. Straight lines could be regressed for portions of the data such that values of the rate constant could be evaluated (equation 4.6.4). This procedure was

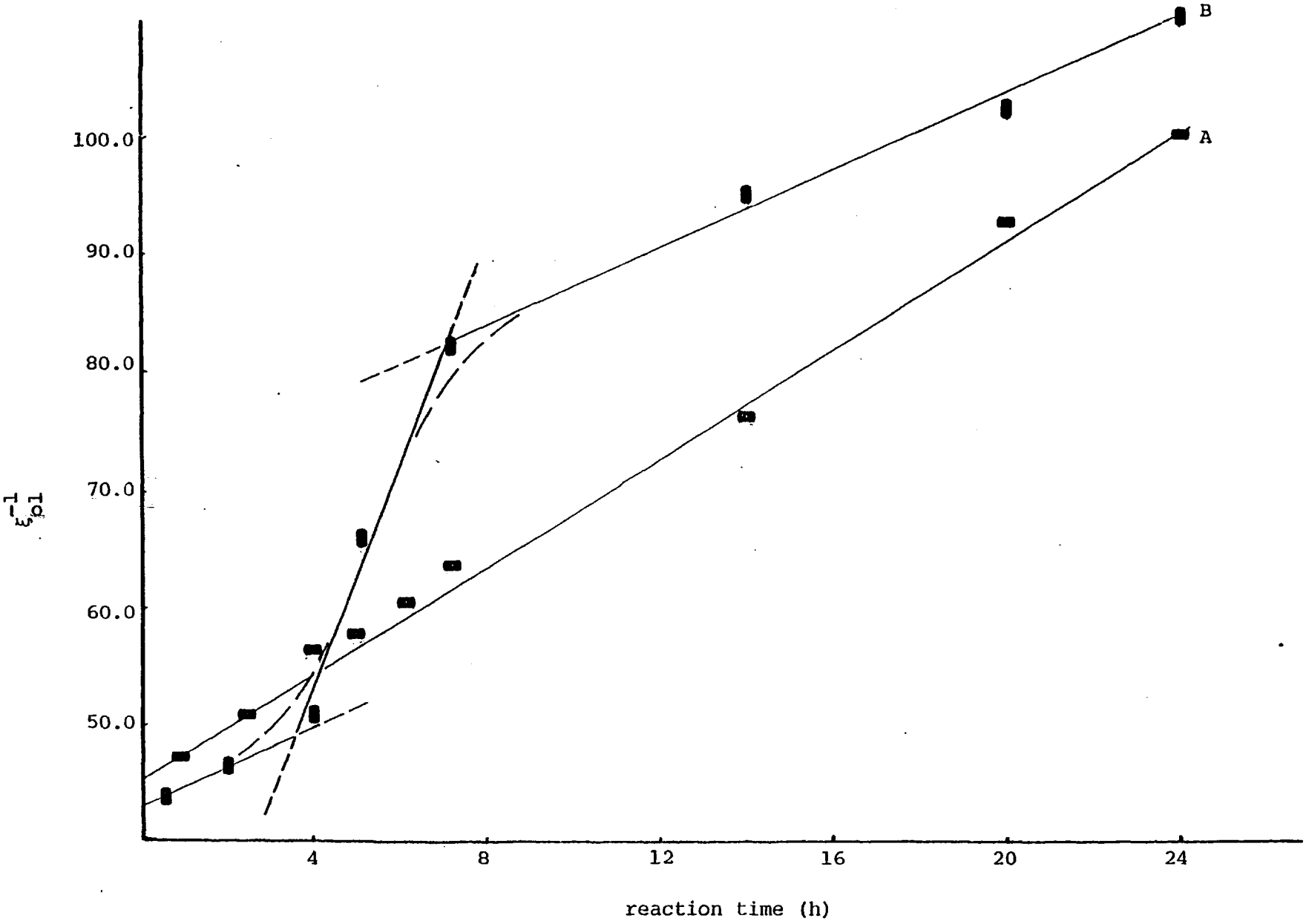


Figure 4.6.4 Relation between the reciprocal for the residual moles of olivine in the +75 μm fraction, ξ_{ol}^{-1} and the reaction time for systems A and B.

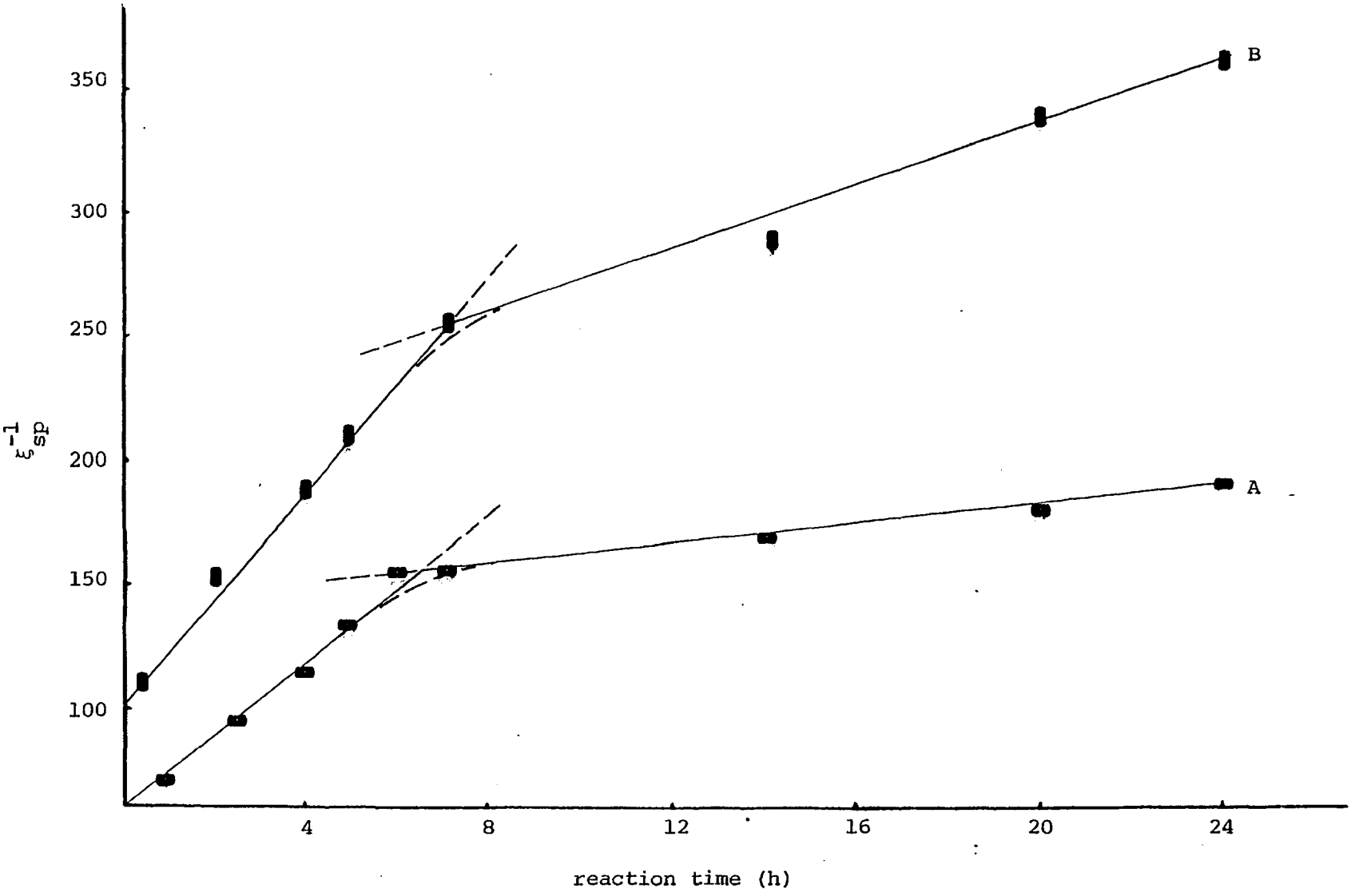


Figure 4.6.5 Relation between the reciprocal of the residual moles of serpentine in the +75 μm fraction, ξ_{sp}^{-1}, and the reaction time for systems A and B.

adopted in the absence of a better method at various temperatures for the two systems used for reaction time 0-7 h - System A : 25°C, 65°C, 100°C, 215°C, 260°C, 300°C; System B : 25°C, 65°C, 70°C, 100°C. In System B investigations were limited to $\lesssim$ 100°C owing to the low acid tolerance of the autoclave bombs (Section 3.4.1). Further constraints were : no ξ_{sp} values could be recorded where reaction temperatures $\gtrsim$ 100°C were employed because well-crystallized 7 Å products deposited on the +75 μm fraction confused the XRD analysis. This effect was not apparent below 100°C. In view of these difficulties the results should be treated with caution.

As an example of the method, the values of ξ_{ol}^{-1} are plotted against the reaction time (0-8 h) for System A at various temperatures in Figure 4.6.6. The reaction rates were calculated (i.e. the gradients of the lines a-d) and their logarithmic values plotted against the reciprocal of the temperature (Figure 4.6.7). Values of Ea and M were evaluated from the slope and intercept according to equation 4.6.4. This procedure was repeated for both systems. The calculated constants Ea and M are given in Table 4.6.1 below.

TABLE 4.6.1 VALUES OF THE ARRHENIUS EQUATION CONSTANTS FOR SYSTEMS A AND B

	System A		System B	
	olivine	serpentine	olivine	serpentine
Ea (kJ mol^{-1})	25	10	35	25
M (mol^{-2} s^{-1})	2.8	0.1	165	15

As expected, the activation energies for serpentine were lower

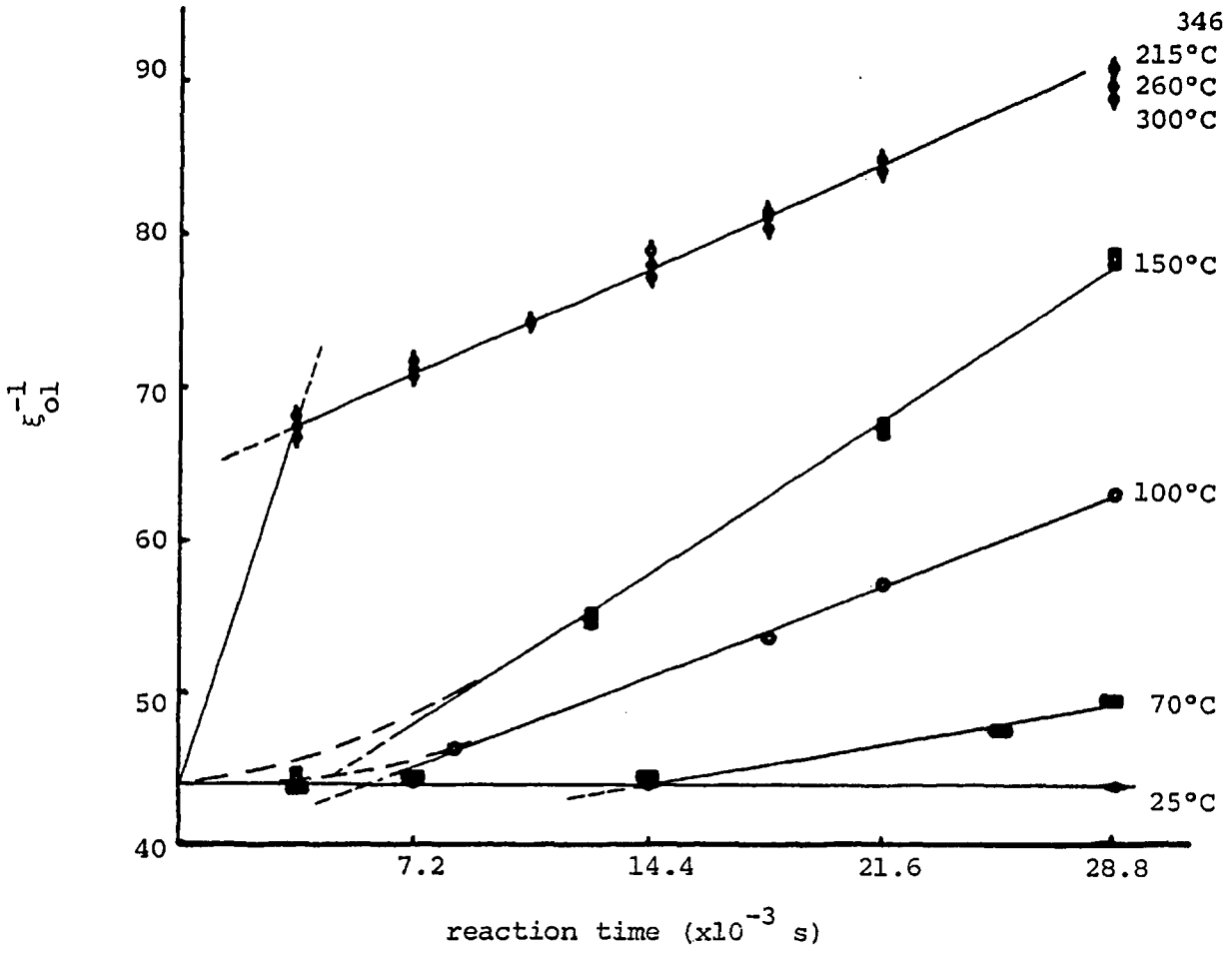


Figure 4.6.6 Relation between ξ_{ol}^{-1} and reaction time at various temperatures for system A.

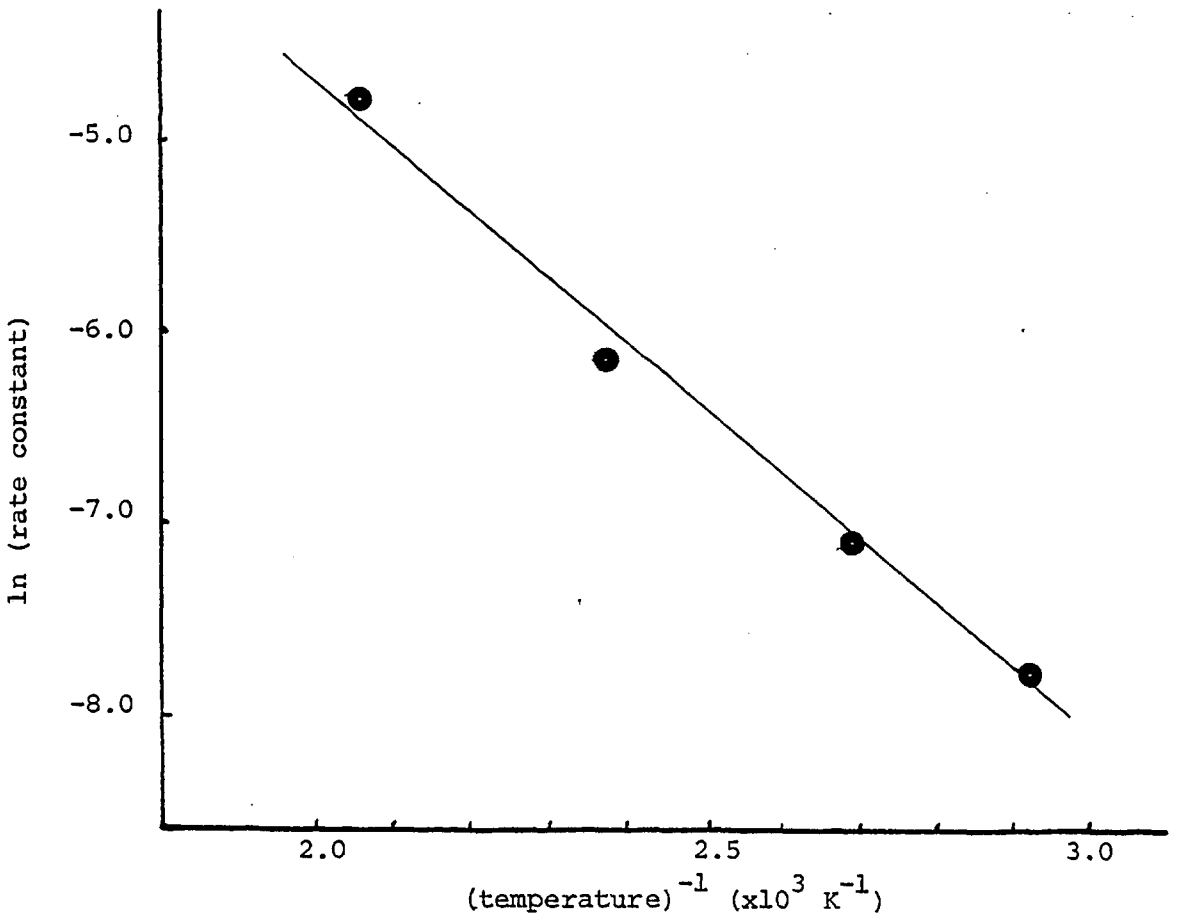


Figure 4.6.7 Arrhenius plot for system A : olivine reaction.

than those for olivine. However, the system with the higher acid concentration (B) yielded higher activation energies than System A. In view of the rapid loss of acid it was evident that a more complex interpretation was necessary in the case of System B, i.e. the precise determination of two activation energies (one for acid dissolution, the second for aluminium interaction). The complexity of the alteration reactions made such a sophisticated approach untenable under the available conditions.

Despite these difficulties, the simple composite constants calculated were thought to be acceptable for their inclusion in a semi-quantitative description of the rate processes involved.

Effect of agitation : Replicate factorial experiments[238] demonstrated at the 99% confidence level that the stirring rate had a significant effect on the extent of degradation. This was indicative of mass transfer and/or surface interaction control of the reaction rate as far as solution/mineral equilibria were concerned. However, as porous diffusion through an altered layer appears to occur then mechanical attrition of the surfaces of the reacted particles would be an important factor. As the precise effect of these combined processes could not be evaluated, a constant stirring rate had to be adopted so that the relevant parameter was reduced to a constant in the overall rate equation.

Effect of surface area : As the investigations related to the degradation of coarse particles, the exposed reacting surface area had to be treated in terms of particle screen fraction size. To estimate the effect of feed size on the extent of reaction for a given time 10 g portions of various sized fractions (from the sampling scheme Figure

2.2.1) were reacted using System B at 100°C for 2 h. (This time was approximately the period employed in each cycle for the semi-continuous alteration equipment - Chapter 5.) Olivine and serpentine assays of the residual +75 μm fraction were measured as before.

By noting the extent of reaction using System B at 2 h for the 1180+850 μm feed, the rate equation adopted the following form :

$$\frac{d\xi}{dt} = \frac{\Omega}{\Delta\xi'} \left(\frac{d\xi}{dt}\right)_{i,t} \qquad (4.6.5)$$

where $d\xi/dt$ represents the general reaction rate; Ω a function relating the size of particle to the extent of reaction $\Delta\xi$; $\Delta\xi'$ the extent of reaction given by the difference between the original number of moles of the head mineral and the residual number of unreacted moles ξ, and $(d\xi/dt)_{i,t}$ the rate equation in terms of initial rate and temperature only (and other constants).

From the results obtained the following correlations were deduced :

$$\left.\begin{aligned} \Omega_{ol} &= 5.37 \times 10^{-4}\ S^{-1.08} \\ \Delta\xi'_{ol} &= 6.81 \times 10^{-4} \end{aligned}\right) \qquad (4.6.6)$$

$$\left.\begin{aligned} \Omega_{sp} &= 1.03 \times 10^{-2} - 7.02 \times 10^{-4}\ (S) \\ \Delta\xi'_{sp} &= 9.94 \times 10^{-3} \end{aligned}\right) \qquad (4.6.7)$$

where S is the cube root of the size used by Barbery (Appendix 2) namely $((d_1^3 + d_2^3)/2)^{1/3}$, d_1 and d_2 being the screen-fraction sizes.

Overall rate equation : The previous discussions in Chapters 3 and 4 have modelled the alteration process as a two-stage reaction, the first stage being the liberation of ions from the matrix, predominantly by acid hydrolysis reaction, the second, inter-reaction of those liberated ions with added aluminium to form the clay minerals. The overall rate equations deduced below are thus presented as a two-stage series :

a) Initial rate kinetics. The period involved considers the first 0.25 h of the reaction. The equation below was deduced from the relations expressed in equations 4.6.1-7.

$$\left(\frac{d\xi_x}{dt}\right)_{initial} = C\,\Omega_{x,initial}\,\phi_x \exp-(Ea_{initial}/RT) \qquad (4.6.8)$$

where x relates to olivine or serpentine and C is a constant.

In the above equation ϕ_x is the only function which has been quantified directly from initial rate experiment(equations 4.6.1 and 4.6.2). Difficulties were encountered in deducing Ω for larger particle sizes owing to the small values of $\Delta\xi$ recorded over the time period (0.25 h) employed. Consequently $\Omega_{initial}$ could be treated as being equivalent to Ω as described in equations 4.6.6 and 4.6.7. As the warm-up time required for the autoclave apparatus was about four times the initial reaction time period, it was difficult to obtain accurate values of the Arrhenius constants.

As a majority of the reactions which would be applied to process designs took palce at 100°C, equation 4.6.9 below became the best available, (as a special case of that immediately above) :

$$\left(\frac{d\xi_x}{dt}\right)_{initial} = C\,\Omega_{x,initial}\,\phi_x \qquad (4.6.9)$$

b) Clay formation kinetics. These rate equations were based on the form in equation 4.6.8. From the empirical derived relationship in equation 4.6.4, the experimental reaction rate was obtained by differentiation i.e.

$$\frac{d\xi_x}{dt} = k_x \xi_x^2 \qquad (4.6.10)$$

where k is the experimentally derived rate constant and x relates to either olivine and serpentine. By using the data, as presented in Figures 4.2.4 and 4.2.5, and the rate constants given by equation 4.6.4, experimental reaction rates for Systems A and B could be calculated. From the results obtained, lower rates of reaction were recorded for System B at times greater than 2 h compared with System A. This was a consequence of the more extensive alteration induced at the start of the reaction. It was surmised that the overall rate of reaction was best expressed in terms of the difference between a 'theoretical' initial reaction rate and that deduced from equations 4.6.1 and 4.6.2 (i.e. (ϕ_{theory} - ϕ_x). If a system was considered where the initial reaction rate was low (System A), this difference would be large, leading to larger rates of reaction being recorded at times 10-24 h, compared with those involving higher rates of reaction. The theoretical initial rate employed was that expected if all the minerals were liberated and allowed to react immediately. The values adopted for olivine and serpentine were 2.52×10^{-5} and 1.81×10^{-5} mol s^{-1} respectively (i.e. the total number of moles of the head minerals in a 10 g feed which would react over a 0.25 h period as used in initial rate experiments).

It was also apparent that the experimental rates had an inverse proportionality with respect to time. After testing various types of function, that which described most closely the decrease in the

rate of reaction was the exponential decay function exp-(pt). The resultant rate equation was concluded to have the form

$$\frac{d\xi_x}{dt} = C\frac{\Omega}{\Delta\xi'} M(\phi_{theory}-\phi_x)\ \text{exp-(Ea/RT).exp-pt} \qquad (4.6.11)$$

where C and p are constants and M the frequency factor. By carrying out a regression analysis of the experimentally determined rate values in terms of exp-(pt) the following equations were deduced for olivine and serpentine, (the correlation coefficient is given under each equation) :

System A : olivine

$$\frac{d\xi_{ol}}{dt} = 19.5\ \frac{\Omega}{\Delta\xi'_{ol}} M(\phi_{theory}-\phi)_{ol}\ \text{exp-(Ea/TR} + 1.89 \times 10^{-5}\ t)$$

$$R^2 = 0.92 \qquad (4.6.12)$$

System B : olivine

No significant correlation could be obtained owing to the complexity of the reaction kinetics (see later).

System A : serpentine

$$\frac{d\xi_{sp}}{dt} = 5.65\ \frac{\Omega}{\Delta\xi'_{sp}} M(\phi_{theory}-\phi_{sp})\ \text{exp-(Ea/RT} + 5.64 \times 10^{-5}\ t)$$

$$R^2 = 0.90 \qquad (4.6.13)$$

System B : serpentine

$$\frac{d\xi_{sp}}{dt} = 5.65\frac{\Omega}{\Delta\xi'_{sp}} M(\phi_{theory}-\phi_{sp})\ \text{exp-(Ea/RT} + 4.01 \times 10^{-5}\ t)$$

$$R^2 = 0.95 \qquad (4.6.14)$$

where R is the correlation coefficient and the values of Ea and M for

each system given in Table 4.6.1.

In principle these equations described the overall rate of decomposition of the kimberlite, as the initial dissolution stage was relatively fast. In practice, certain question marks are held against them for the reasons discussed earlier. However they do indicate that the proportion of unreacted material effectively controls the rate of alteration. Furthermore, the inclusion of the exponential function in time (as distinct from temperature) is consistent with a shrinking core model type in which a reaction product diffusion layer is steadily built up to progressively reduce the overall reaction rate[262] (by increasing the necessary path length of diffusion prior to reaction).

4.6.3 Determination of the rate determining step

The magnitude of the calculated activation energies in the previous section inferred that the overall rate of reaction was, in the main, controlled by mass transfer processes[263] (i.e. the values were within the range 10.5 - 27.2 kJ mol^{-1} which implied diffusion controlled mechanisms[264]). This section briefly considers other models relating to rate determining processes which may be applicable to kimberlites.

Several models have been discussed with respect to mass transfer be ween silicates and solutions.[265-7] Adopting the techniques discussed by Helgeson,[265] the residual solution concentrations of magnesium, iron and calcium for Systems A and B were plotted against the square root of the reaction time as shown in Figures 4.6.8 and 4.6.9. Correlating the data for magnesium (Figure 4.6.9), iron and calcium by a series of straight lines, in accordance with Helgeson's procedure[265] indicated that diffusion controlled transfer of the ions occurred as they migrated from the reaction zone through surface layers of reaction

products into the bulk solution. The linearity of the plot for magnesium in Figure 4.6.8 suggested a different type of control.[268] Here, the reaction appeared to be diffusion controlled with respect to the diffusion of reactants to the site of the reaction and subsequent ion-exchange (this would be expected in the case of System A where a weaker acid concentration was used and hence the driving potential for the reaction was lower compared to System B). High initial rates of reaction of the type noted in System B have been attributed to various causes,[268] in the present work these would appear to be the presence of reactive sites (i.e. calcite, serpentine phenocrysts) and possibly mechanically strained surfaces.

A recently developed theoretical model has related laws governing molecular species detachment, mass transfer and crystal growth to non-equilibrium water/rock interactions.[262] The workers attribute results similar to those presented in Figures 4.6.8 and 4.6.9 to slow (physical) interface detachment processes which become an integral part of the dissolution reactions. More detailed data would be required in the present work investigating the system further with respect to the effect of microstructures on the reaction rate.

Although the activation energy for the alteration of olivine using System B and the difficulties in deducing a rate equation suggested an additional mechanism, the rate controlling step for kimberlite alteration was attributable to diffusion processes. During alteration a progressively thicker altered 'crust' was built up which would hinder the passage of reactant/product ions to/from the site of reaction at the interface between the altered and unaltered kimberlite. This was apparent from observations made using the semi-continuous alteration apparatus (Chapter 5) and the results described above. Although hydrogen ions would most readily diffuse to the reaction site (due to their small size)

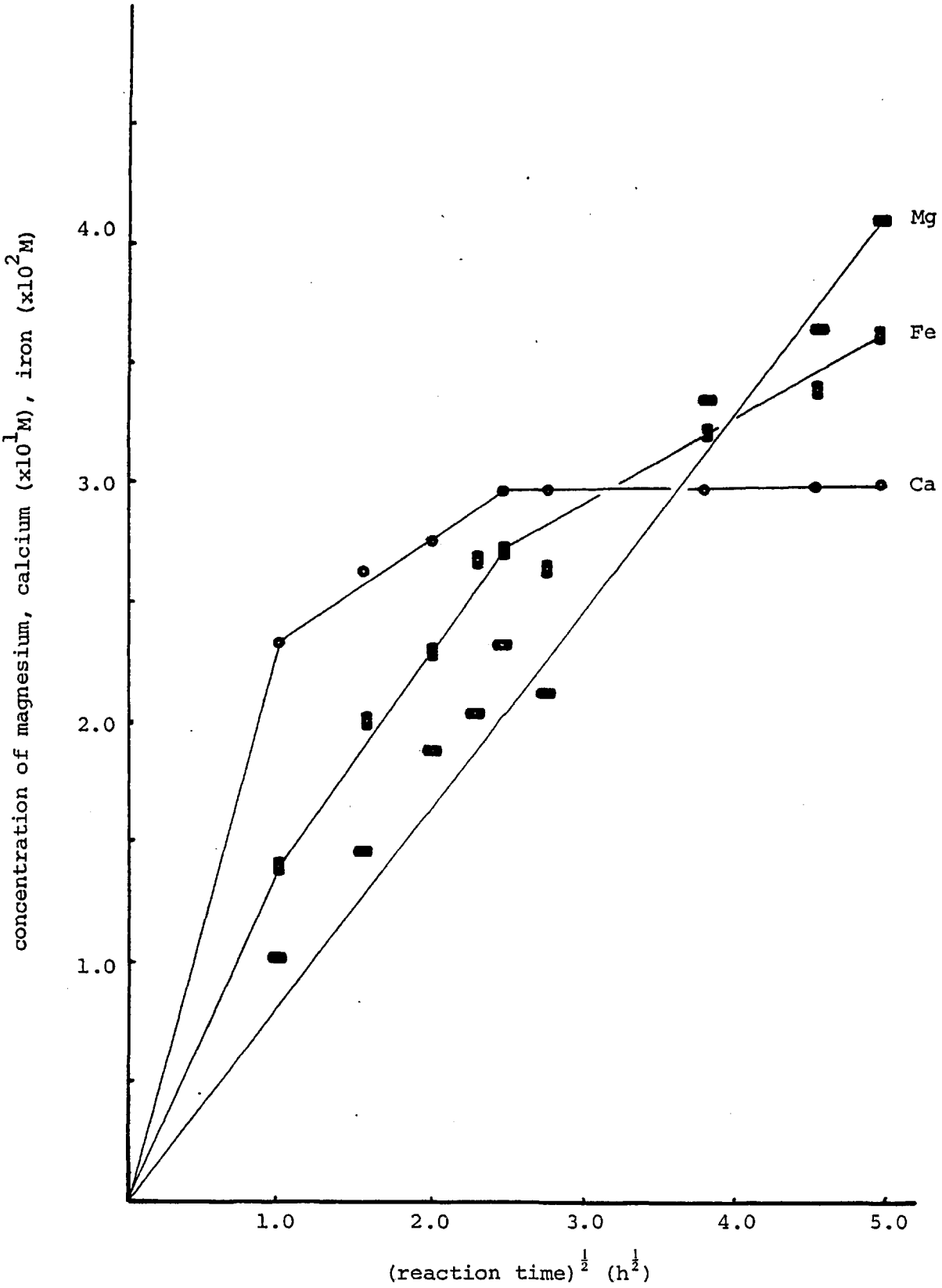


Figure 4.6.8 Relation between residual concentrations of magnesium, iron and calcium in solution and the square root of the reaction time for system A.

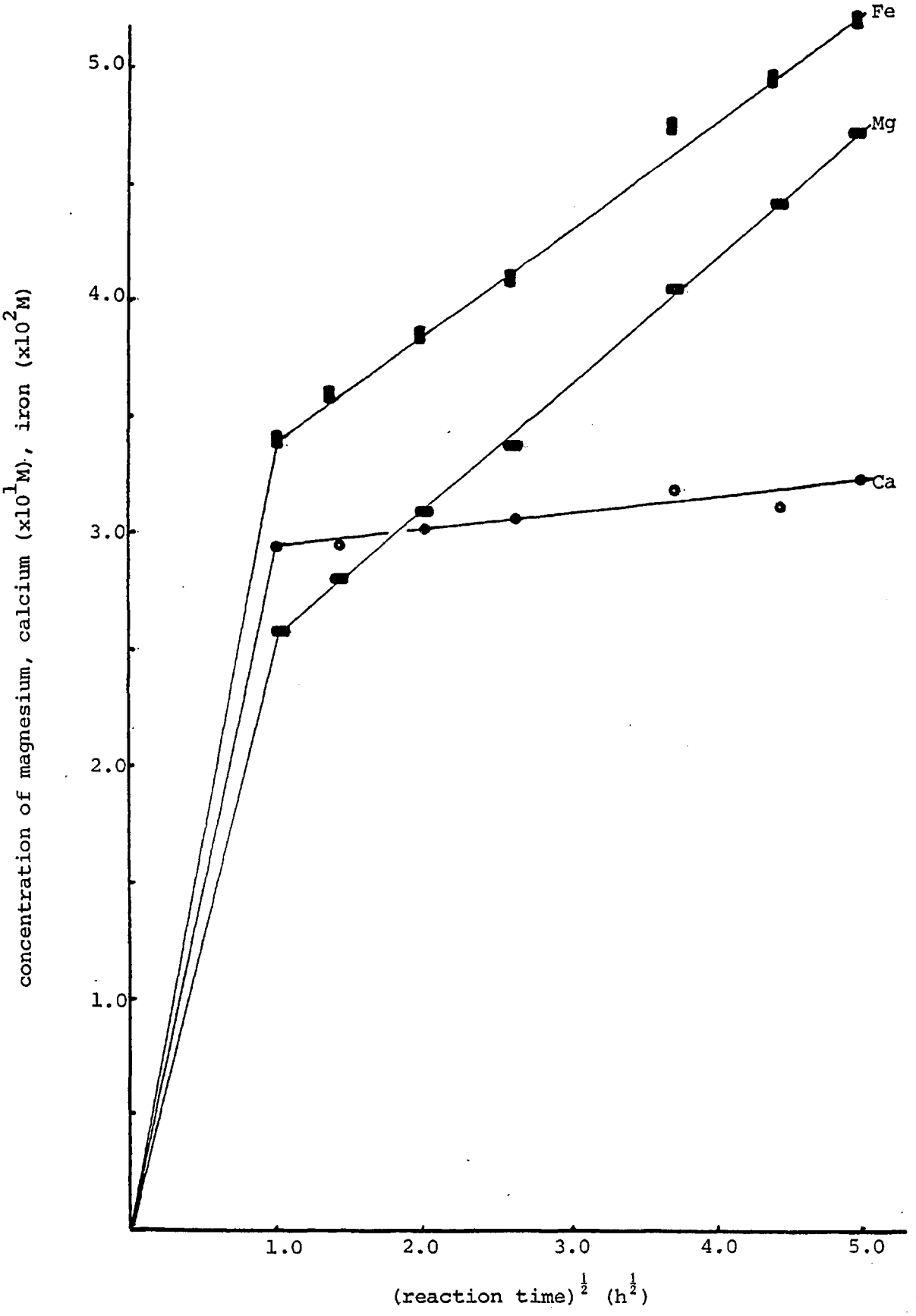


Figure 4.6.9 Relation between residual concentrations of magnesium, iron and calcium in solution and the square root of the reaction time for system B.

the rate was controlled by the hydrogen ion concentration (cf. the results for the magnesium ion, Figure 4.6.8). This argument can also be extended to the (larger) aluminium cations. Here, the presence of a large aluminium concentration to provide a diffusion potential (so as to induce the cations to move to the site of reaction), was particularly evident (as shown by the minimum aluminium concentration required to produce an alteration effect in addition to that due to hydrogen ions, Figures 3.3.8 and 3.3.12). In conclusion, the rate of the alteration reaction was limited by the build up of products. The removal of such products (by attrition) would subsequently provide new surface areas for reaction.

CHAPTER 5

PRELIMINARY PROCESS DESIGN

5.1 Introduction

The testwork in Chapters 3 and 4 showed that the ionic species Al^{3+} and H^{+}, and their relative proportions, controlled the nature and extent of kimberlite degradation at various temperatures and the clay minerals formed as alteration products. Making use of the data obtained from the experimental work and derived kinetics of reaction, a preliminary process design study has been made for a new method of diamond liberation from kimberlite. The study involved the construction of new laboratory apparatus to provide for semi-continuous alteration of a kimberlite charge. These considerations together with process requirements and a brief comparison with current diamond extraction technology, form the content of this chapter.

5.2 Effect of Variation of Al^{3+} and H^{+} Ion Concentrations on Degradation

Although fundamentally interesting and rapid mineralogical transformations occurred in superheated aqueous media at temperatures greater than 100°C (Section 3.4), from a practical engineering point of view it would obviously be preferable, wherever possible, to recommend reactions at low temperatures and pressure for any process leading ultimately to bulk mineral (i.e. diamond) production. This section considers the optimum combination of temperature, aluminium concentration and hydrogen ion concentrations for systems reacting at atmospheric

pressure.

A temperature of 100°C was found to be the most effective in inducing alteration. Not only was the alteration most rapid at 100°C under conditions of ordinary atmospheric pressure in comparison with lower temperatures, but also the most extensive with respect to the solubilization of all the ionic species (including silica) at the site of reaction and later precipitation as clay minerals.

The highest initial aluminium and hydrogen ion concentrations employed were 0.4M and 1.5M respectively. The latter was limited mainly by the tolerance of Monel alloy (used in the new apparatus) to acids at 100°C, but also by the rate of acid consumption by the kimberlite so as to reach the pH suitable for clay mineral precipitation. (From Figure 4.2.3 it is clear that higher initial acid concentrations lead to longer periods before clay minerals precipitate.) Aluminium ion concentrations in the range 0-0.4M were the most effective as indicated by Figures 3.3.8 and 3.3.12, higher concentrations being subject to simple hydrolysis. Consequently from testwork carried out as described in Section 3.3.1, the effect of variation of the initial concentrations of these ions was quantified in terms of DOA (Figure 5.2.1), residual magnesium, iron and calcium concentrations (Figure 5.2.2), proportion of aluminium entering solid phases (Figure 5.2.3) and the residual proportion of olivine and serpentine in the alteration system (Figure 5.2.4).

The axes of the diagram in Figures 5.2.1-4 refer to the initial aluminium and hydrogen ion concentration. Each point on the figures represents an experimental test, for which the DOA, residual solution concentration of the ions Mg^{2+}, (Fe^{2+} and Fe^{3+}), Ca^{2+}, Al^{3+}, and olivine and serpentine assays in the +75 μm fraction were made. The magnitudes of the various assays were indicated semi-quantitatively by contoured lines interpolated between the recorded data points. The

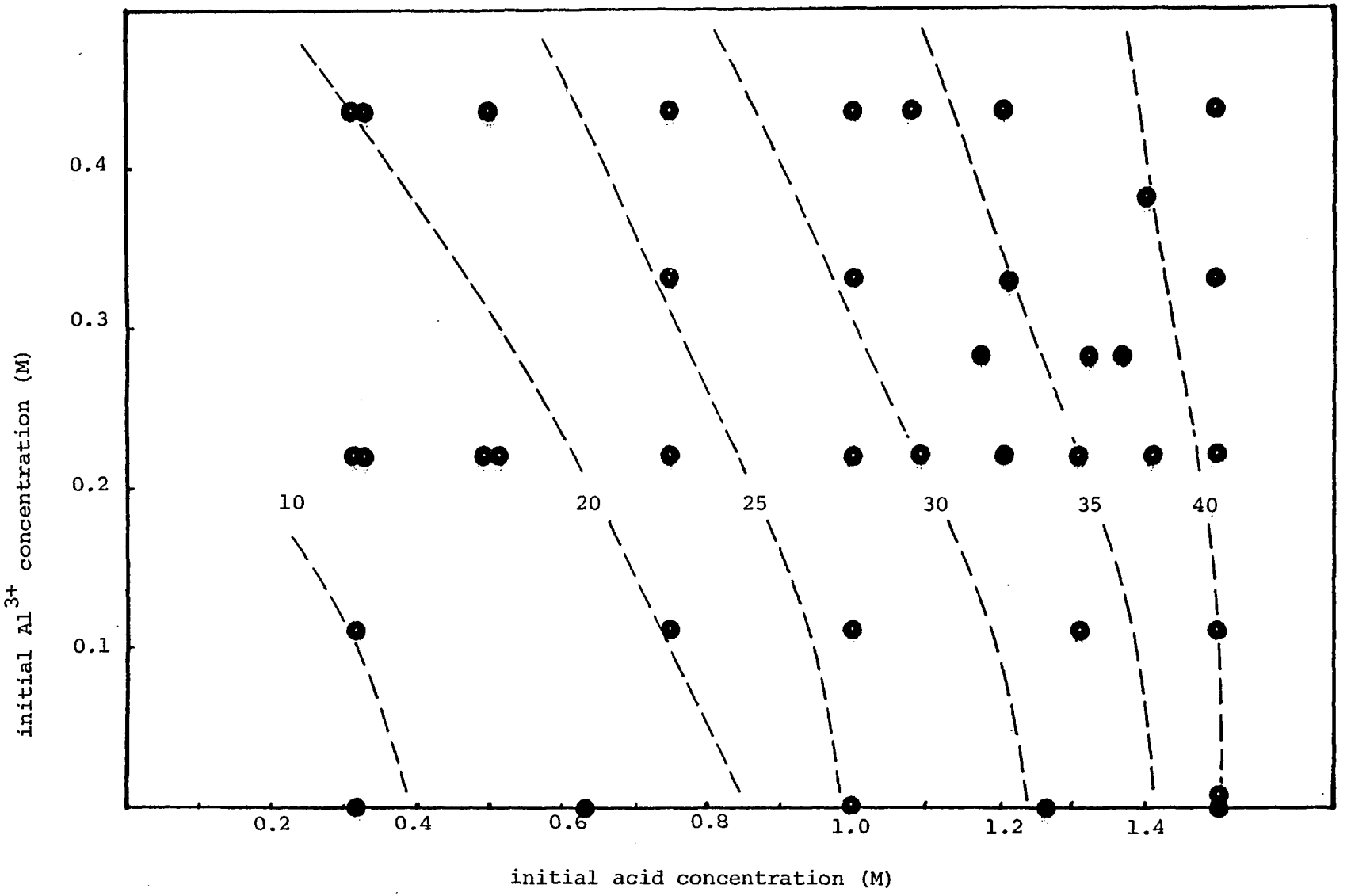


Figure 5.2.1 Diagram showing the effect of the initial aluminium and hydrogen ion concentrations on the DOA (%) for a 10 g -1180+850 µm feed reacted at 100°C for 7 h.

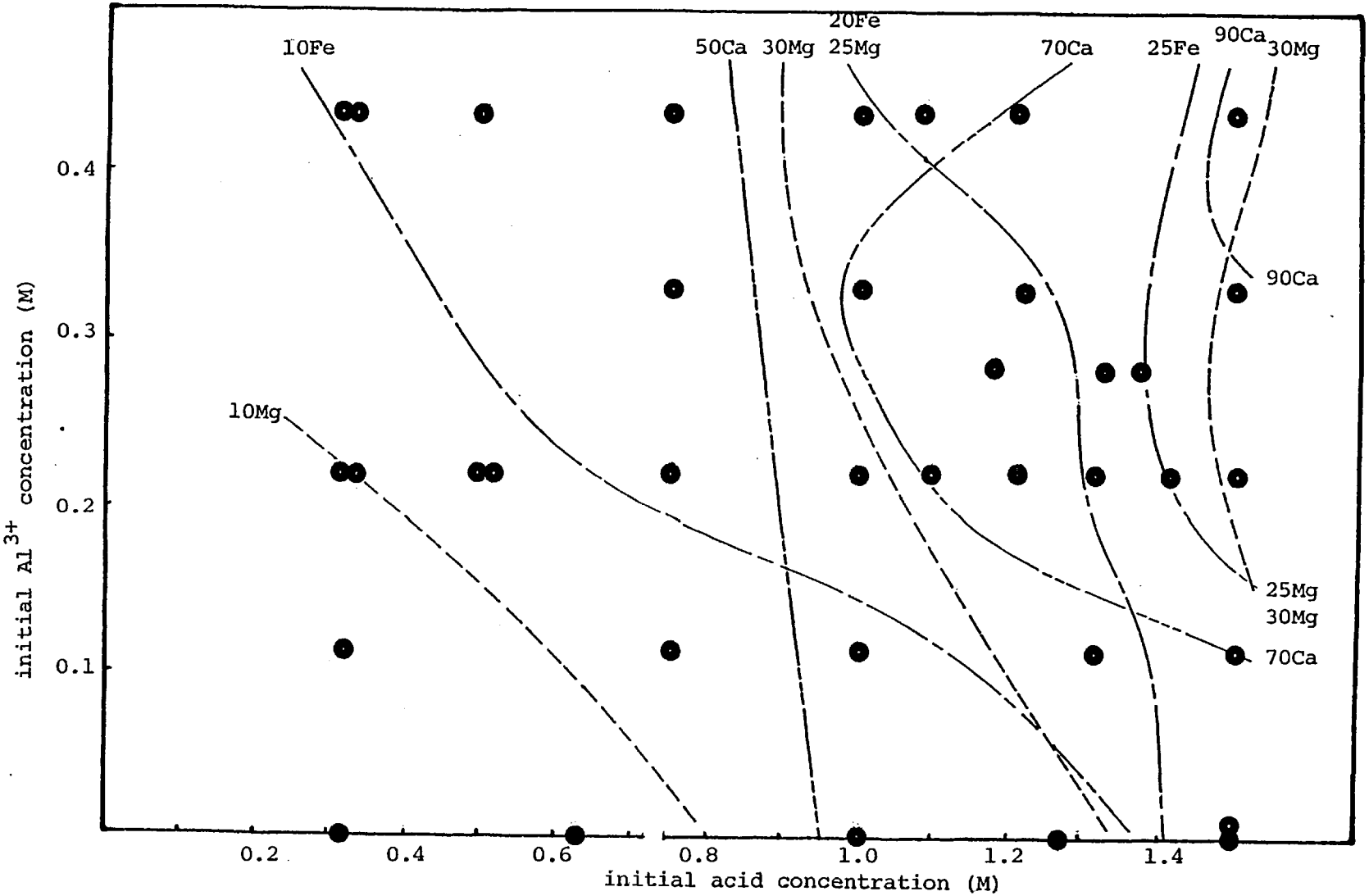


Figure 5.2.2 Diagram showing the effect of the initial aluminium and hydrogen ion concentration on the proportion of total magnesium, iron and calcium entering solution (%).

positions of the points were the same in each figure but, of course, the contours differed according to the assay in question.

The DOA values in Figure 5.2.1 were seen to be more strongly affected by the aluminium concentration at low acid levels; the contour slopes being steeper. As the acid concentration increased, the effect of aluminium was progressively reduced and became barely detectable at acid concentrations greater than 1.5M H^+, where the DOA was 40%.

Figures 5.2.2 and 5.2.3 represent the proportions of magnesium, iron and calcium entering solution, and of aluminium entering a solid phase (+75 μm or -75 μm fractions). Conclusions similar to those of the DOA plots could be made for magnesium and iron, with the exception that an enclave was outlined for 30% magnesium and 25% iron in the top right hand side of the diagram. This formation of an enclave was mirrored by the results for calcium and aluminium. Whereas the contour for 50% calcium was essentially linear, those for 70% and 90% calcium were enclaved and indicated a similar set of conditions where the reagent penetration (Section 3.3.4) was a maximum. In the case of aluminium high values (∿ 90% aluminium entering a solid phase) were recorded either adjacent to the abscissa or on the top right hand side margin. The former were attributable to the formation of simple aluminium hydroxyoxides as indicated by the residual pH measured after 7 h (cf. Figure 4.2.3). However, the other high values recorded indicated efficient use of the aluminium ions in clay mineral formation as the pH remained below the hydroxide precipitation level after 7 h.

The proportions of olivine and serpentine in Figure 5.2.4 served to confirm the deductions made from Figure 5.2.3. The extent of alteration of the head minerals increased from the bottom left to the top right hand side section of the diagram, the residual kimberlite

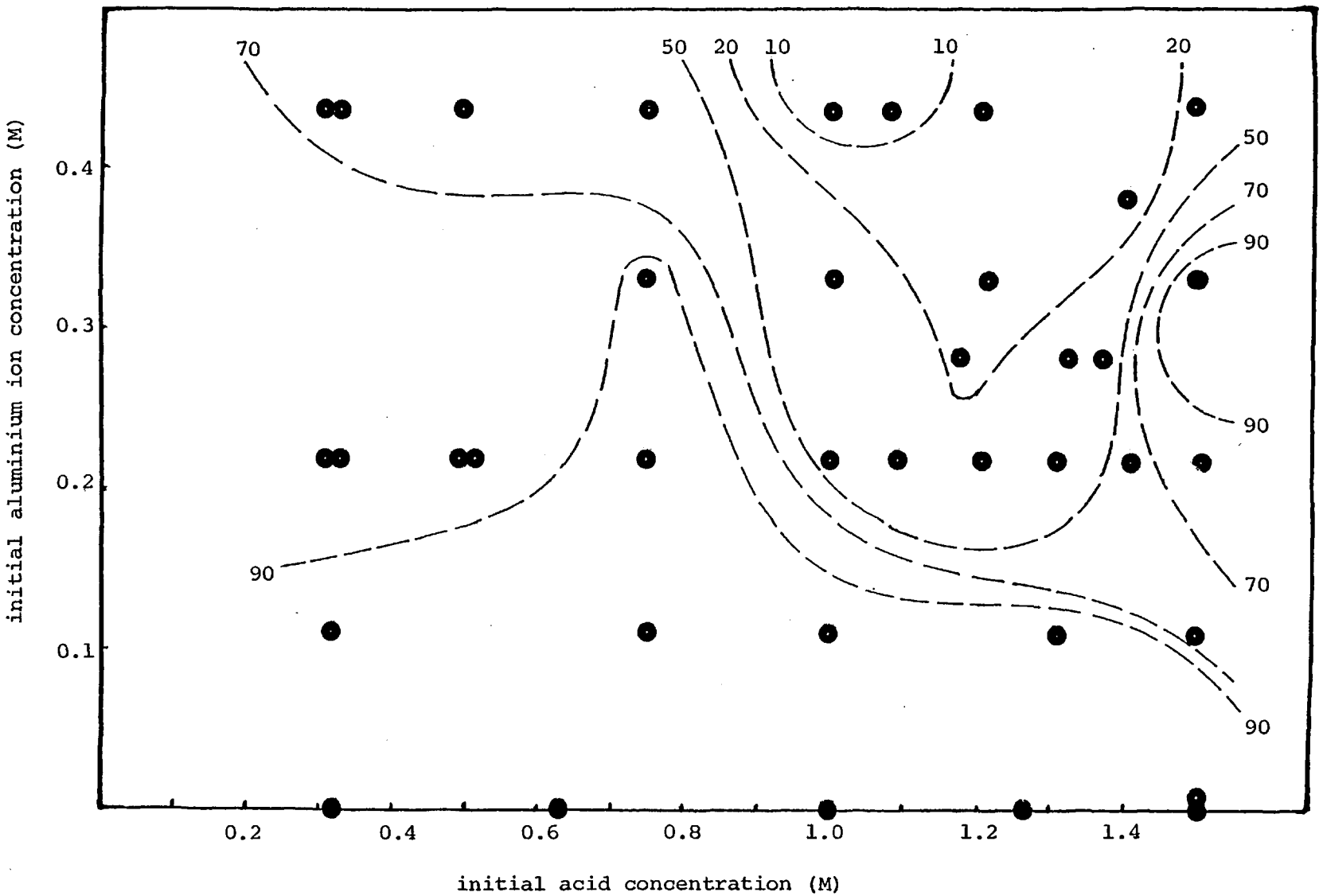


Figure 5.2.3 Diagram showing the effect of the initial aluminium and hydrogen ion concentrations on the proportion of aluminium reporting to a solid product (%).

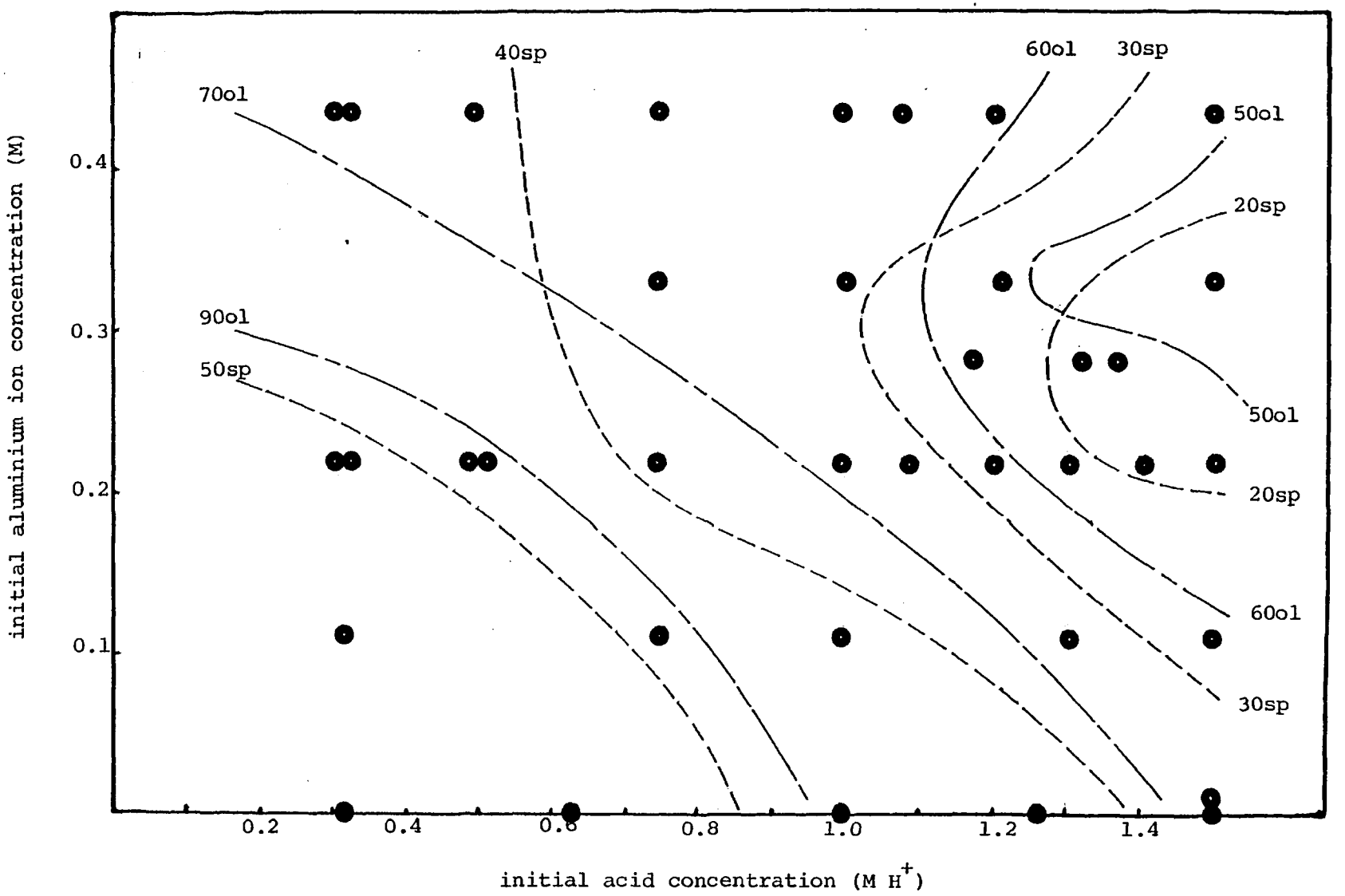


Figure 5.2.4 Diagram showing the effect of the initial aluminium and hydrogen ion concentrations on the residual proportion of olivine and serpentine in the system (% of head value).

containing as little as 17% olivine and 9.5% serpentine in the latter case. The clay minerals formed in the tests employing 1.4-1.5M hydrochloric acid and 0.25-0.35M aluminium chloride were vermiculite-chlorites. These would be expected as their formation would

a) maximise the exsolution of magnesium and iron causing dissolution equilibria to proceed further (Section 4.5) and
b) maximise the amount of regenerated hydrogen ion owing to the tetrahedral substitutions of aluminium for silicon in the layer lattices (Sections 3.3.4 and 4.5).

In conclusion, the optimum conditions for kimberlite alteration were 1.4-1.5M H^+, 0.25-0.35M Al^{3+} for a 10 g -1180+850 µm feed reacted at 100°C for 7 h.

5.3 Semi-Continuous Alteration of Kimberlite at 100°C

5.3.1 Apparatus and procedures

In designing the new apparatus particular consideration was given (Section 5.4.2) to :

a) the continuous removal of altered product from the site of the reaction
b) the continuous monitoring of the pH of the solution, and
c) the minimisation of the solution/feed ratio.

The apparatus employed is shown in Figures 5.3.1, 5.3.2 and

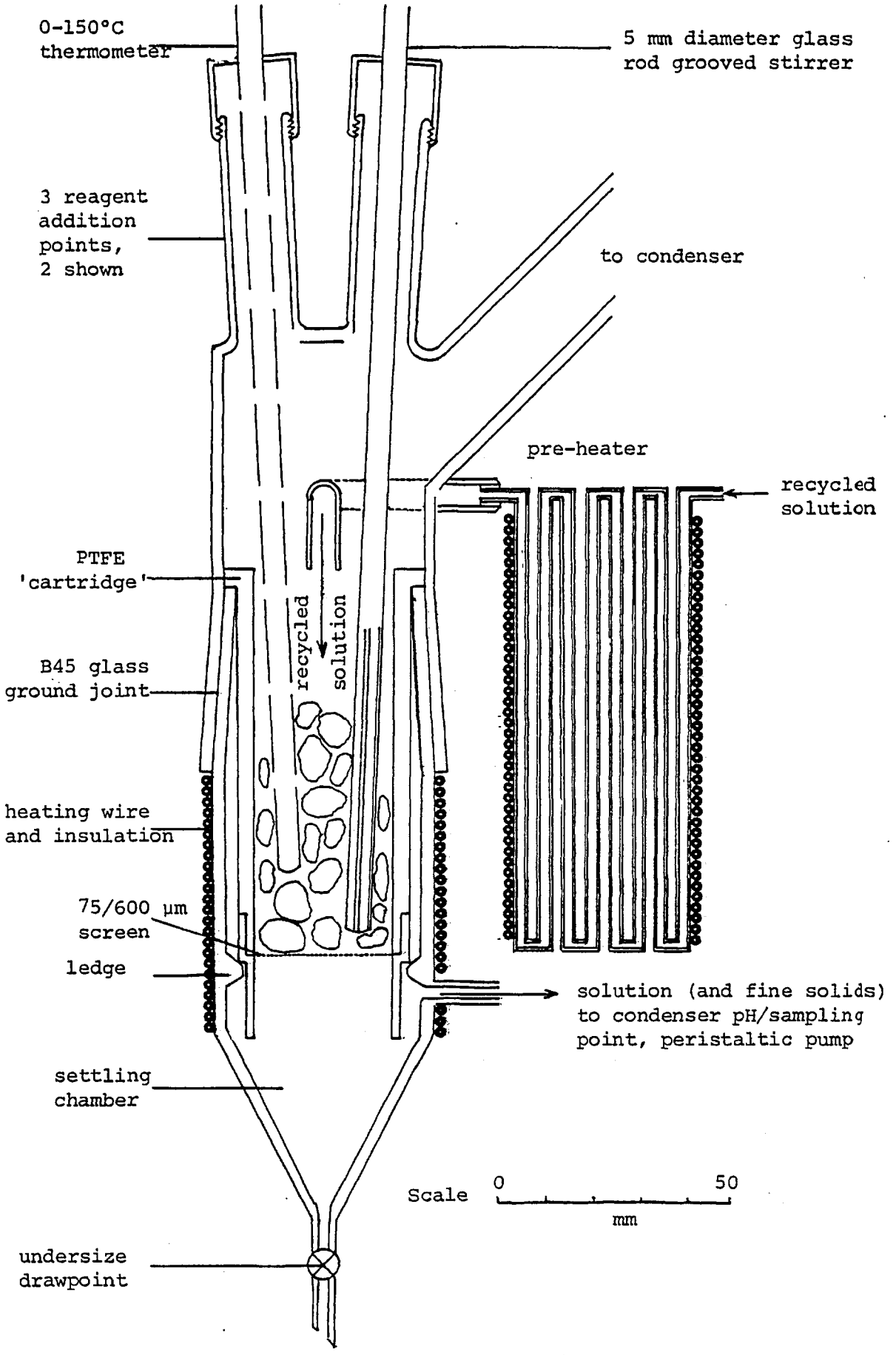


Figure 5.3.1 Semi-continuous alteration apparatus

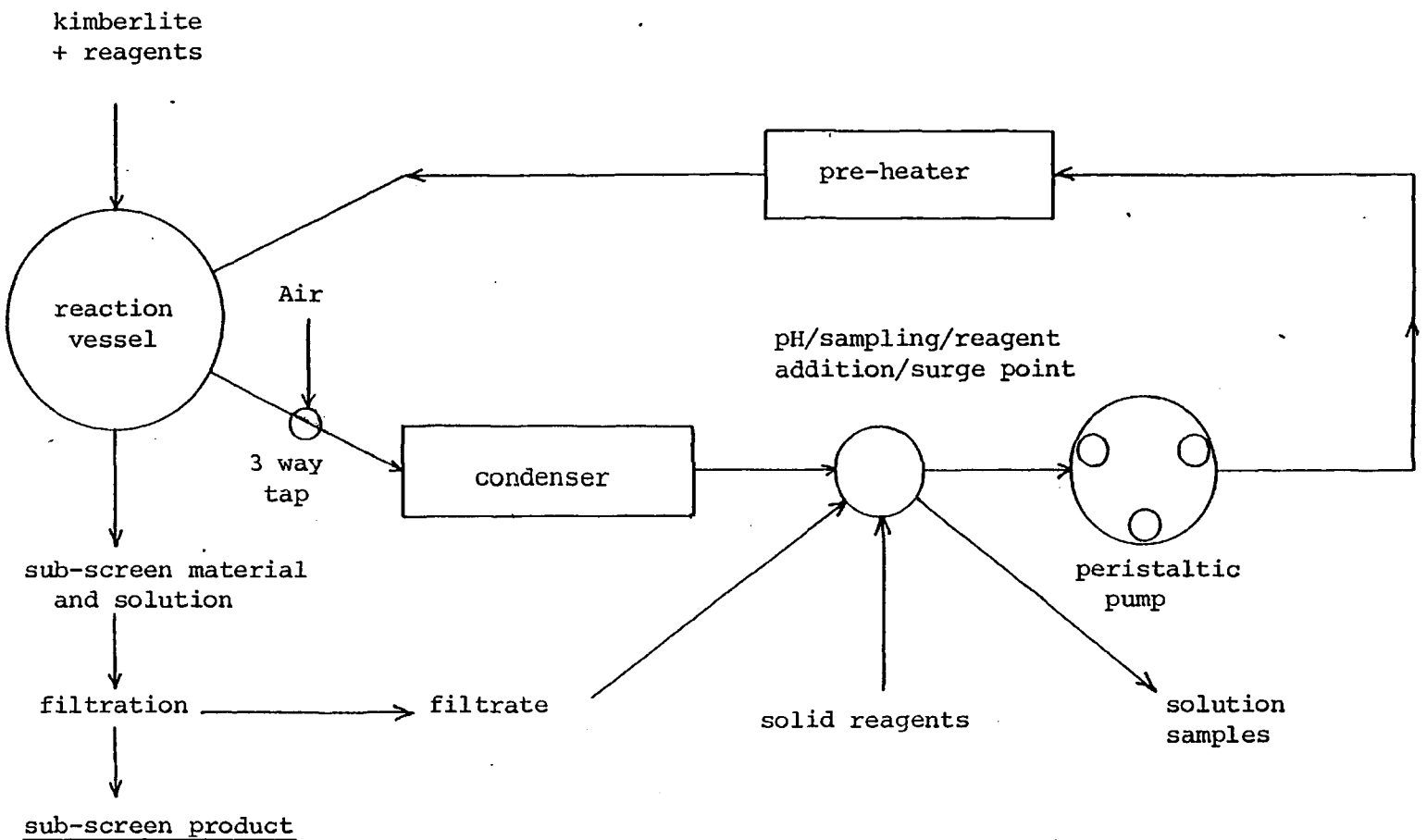


Figure 5.3.2 Diagram representing circulation of reaction solution.

Plates 5.1 and 5.2. The reaction vessel, which is shown together with the pre-heating tubes in Figure 5.3.1, was located in the central region of the experimental rig illustrated in Plate 5.1. Referring to Figure 5.3.1 : the reaction vessel consisted of two Pyrex tubes connected by a B45 Quickfit joint. The overall length as shown was 287 mm with an internal volume 320 ml. The lower half of the reaction vessel consisted of a male glass ground joint, cylindrical reaction chamber and a conical settling chamber, to which a 6 mm bore PTFE tap had been affixed to act as an 'undersize' drawpoint. The upper half of the vessel consisted of a female B45 glass ground joint, to which three reagent addition points and an outlet for a B24 Quickfit condenser were attached. The three reagent addition points consisted of B10 tubes fitted with Sovirel 15 mm screw caps. A thermometer was usually placed in one, a 10 ml burette in another with the third being used for other purposes such as stirring.

A PTFE 'cartridge' (Plate 5.2) consisting of two closely fitting (31 mm internal diameter) tubes 87 mm and 28 mm in length, holding the screen deck, was supported within the lower half of the reaction vessel on a glass ledge as shown in Figure 5.3.1. This 'cartridge' contained the kimberlite charge, which was supported on 75 µm or 600 µm mesh Monel alloy discs (Figure 5.3.1). This screen deck prevented large kimberlite particles from falling into the settling chamber, while at the same time facilitating passage of fines and reagent solutions.

The reaction vessel was fitted with a Gallenkamp HEF-480-070B heating wire, insulated by calcium silicate impregnated material and connected to a circulation system (Figure 5.3.2, Plate 5.1) as follows.

The exit tube immediately below the screen deck was connected via a three-way tap to a water cooled condenser. The tap allowed the

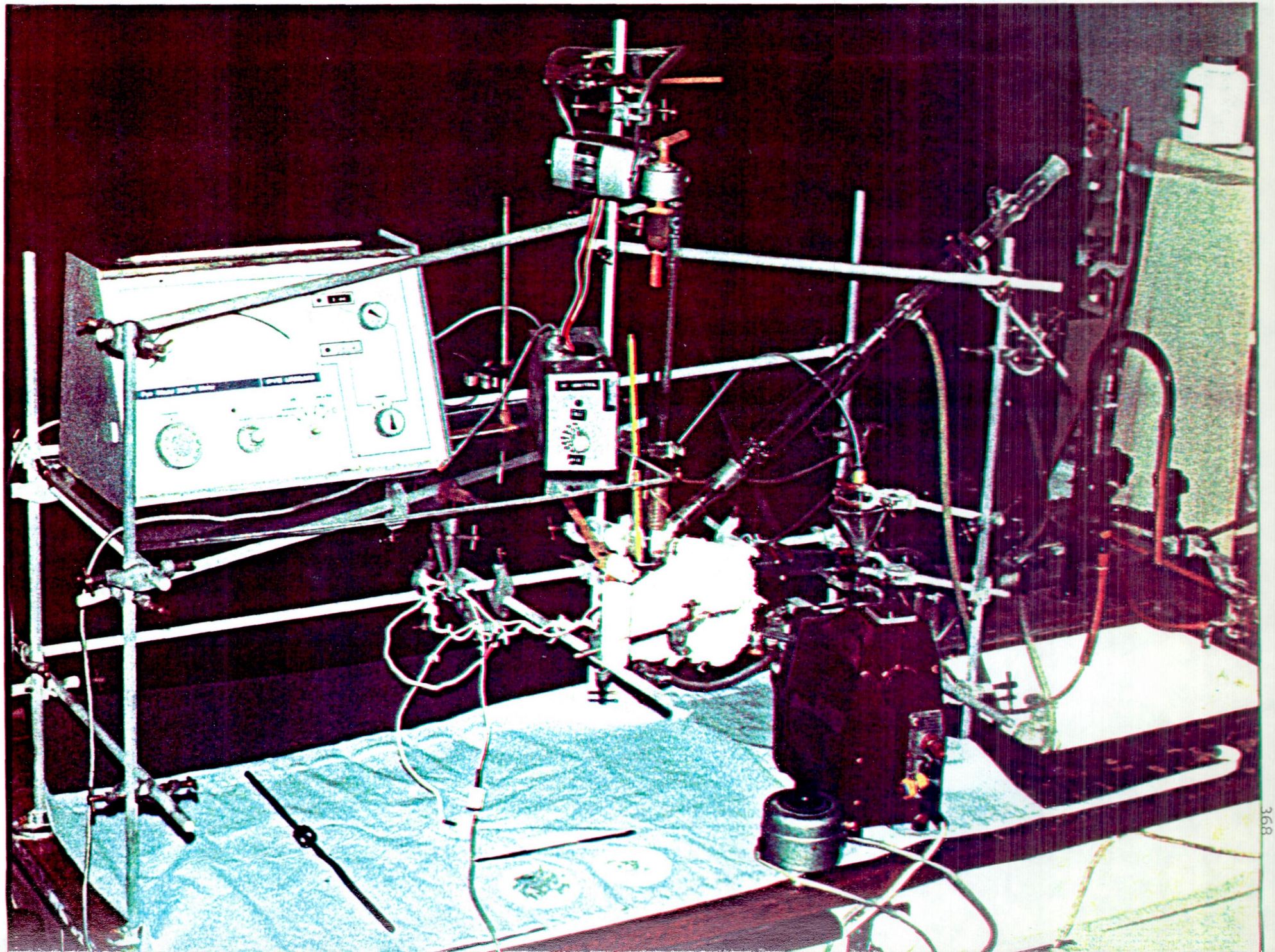


Plate 5.1

Semi-continuous alteration equipment

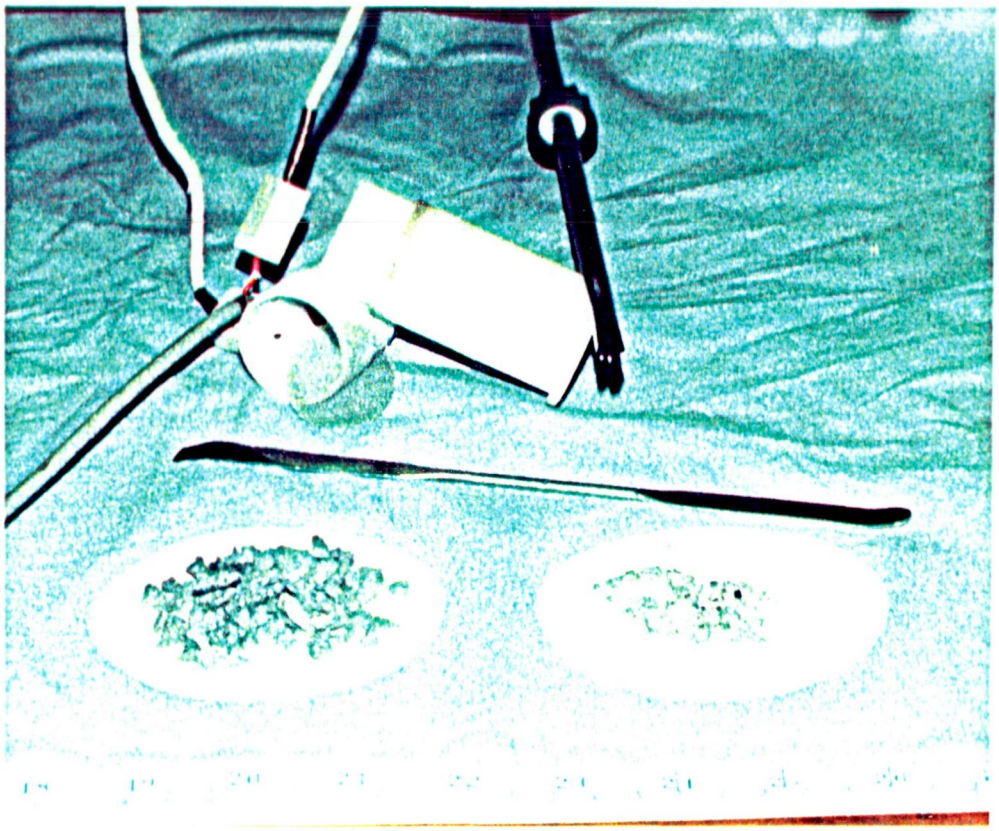


Plate 5.2 Stirrer, reaction cartridge and unaltered/altered kimberlite. Four 40 mm long grooves were made along the length of a 5 mm diameter glass rod to produce the stirrer. The cartridge consists of three sections, one being the screen deck which is secured between two interlinking PTFE tubes. The left hand side of the plate shows a 25 g kimberlite charge. The right hand side shows the residual ∿ 2 g altered +600 µm kimberlite after semi-continuous alteration using the most favourable conditions (see text : Figure 5.3.8).

condenser to be cleared of any blockages with the aid of an air stream. The condenser was designed to cool the reacting medium prior to pH measurement. It was connected in turn to a funnel-T-piece arrangement which served as an access for a Pye Unicam 401E7 pH electrode, a reagent addition and sampling point as well as a 'surge' reservoir. The T-piece was attached to a peristaltic pump which pumped the solution back to the upper half of the reaction vessel via a pre-heater. The pre-heater consisted of four glass loops (as shown in Figure 5.3.1) which were capable of reheating the solution to 100°C, during a residence time of 7-10 s.

The following procedure was normally adopted : a 25 g -1180+850 μm or -6.18+3.18 mm kimberlite sample was placed in the PTFE cartridge (which was fitted with either a 75 μm or 600 μm mesh disc respectively), and the apparatus assembled as shown in Plate 5.1. A volume of 90-100 ml of distilled water was added depending on the concentration of acid to be used in the test. A feed/reagent volume ratio of ∿ 1:4 was employed throughout, as in earlier work. A weighed charge of hydrated aluminium chloride was added to the water via the pH measuring point. A steady flow (of about 100 ml/min) was then established prior to heating. The heating current was slowly increased, using a small variac, until a temperature of 100°C was recorded in the reaction chamber. Known volumes of 11.5M Analar hydrochloric acid were added from a 10 ml burette.

When a -1180+850 μm feed was employed solids attrition was provided by the intense bubbling action of the solution. However, where the larger sized feed was employed a grooved stirrer facilitated attrition between the particles. Throughout a test, (where used) the stirrer speed and its depth of immersion in the kimberlite were adjusted as far as was possible, by eye, to maintain a steady deposition rate of -600 μm material.

The stirring action (where present), the temperature, circulation flow and pH were constantly monitored. Sub-screen material was regularly withdrawn and filtered, the filtrate being returned to the system via the pH measuring point. In this way, interaction between reagents and fine solids could be prevented. At 1.5-2.5 h intervals the solution was sampled and further quantities of acid and aluminium chloride added as appropriate (see later). Overall reaction times did not exceed 8 h. After the reaction, the apparatus was allowed to cool to ∿ 80°C and the solution was washed out and filtered. The 'cartridge' was withdrawn and the residual coarse kimberlite and the sub-sieve sized product separately washed, filtered, screened and weighed. The total reaction solution was analysed by AAS.

5.3.2 Results and discussion : -1180+850 µm feed

The experimental procedure was based on the results of the batch testwork at 100°C (Sections 3.3, 4.2 and 5.2). As alteration was induced by acid hydrolysis followed by/combined with aluminium ion exchange, a procedure involving the cyclical addition of reagents was employed. The full importance of such additions will become evident. Results were conveniently represented as plots of recorded pH against time. Figure 5.3.3, which related to the first test using a 25 g -1180+850 µm feed, is illustrative of the results obtained. The pH increased as the reaction proceeded, whereas the rate of deposition of the -75 µm product decreased. As the pH approached 3, the rate of acid consumption (and thus the rate of reaction) became almost negligible. Further additions of 11.5M Analar hydrochloric acid were consequently made as indicated by the volume values in the figure.

The nature of the alteration products was also studied. Noting that a significant drop in the rate of deposition of altered material

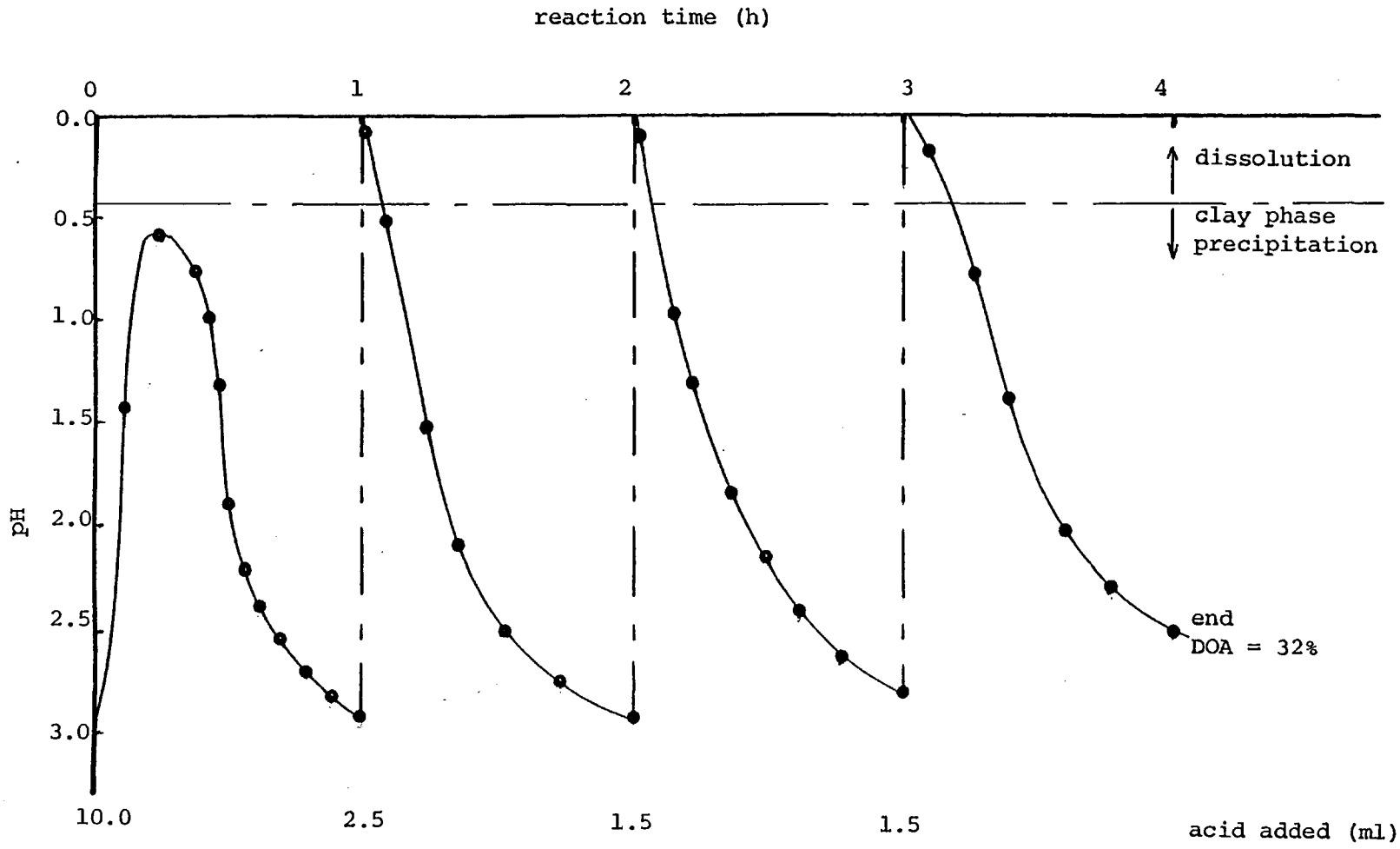


Figure 5.3.3 pH/time relation for semi-continuous alteration of a 25 g -1180+850 µm feed. 1.0 g $AlCl_3$ $6H_2O$ charge added at 0 h.

occurred at pH 2,separate -75 μm fractions were collected, in order to investigate any changes in product type. XRD analysis showed that as well as residual olivine and serpentine being deposited in the -75 μm product, 14 Å phases, chiefly vermiculites, formed in the pH regime 0.4-2, whereas comparatively amorphous ones were deposited at higher pHs. A high initial deposition rate was observed at the start of each reaction cycle and the solution had a marked green colouration (due to Fe^{2+} ions), the pH being 0-1. The deposition rate progressively decreased and the liberated ions in part reprecipitated as indicated by the solution becoming colourless at pH 2. The results of the preliminary testwork demonstrated that the most effective degradation took place within the pH range 0-2. The series of experiments that followed were designed accordingly.

Figure 5.3.4 shows the pH-time relationship for another semi-continuous alteration test which involved addition of acid when the reaction pH rose to 2.0, as well as an initial charge of 5 g hydrated aluminium chloride at the start of the reaction. However, although a DOA of 45% was obtained, little aluminium appeared to be utilised in clay mineral formation, as shown by AAS of the residual solution. Hence other tests were conducted to determine the optimum aluminium concentration for degradation. Despite various aluminium chloride charges being tested (in the range 0-15 g), using comparable quantities of acid, no significant change in the DOA or the aluminium used was observed. Furthermore, increasing the dosages of the acid such that the total volume increased from 21.9 ml (Figure 5.3.4) to 30 ml (not shown, though equivalent to Figure 5.3.4) did not affect the result either.

Figure 5.3.4 represents a typical result obtained for the alteration of kimberlite using 0-15 g hydrated aluminium chloride with 21-30 ml 11.5M hydrochloric acid. As shown, eight reaction 'cycles'

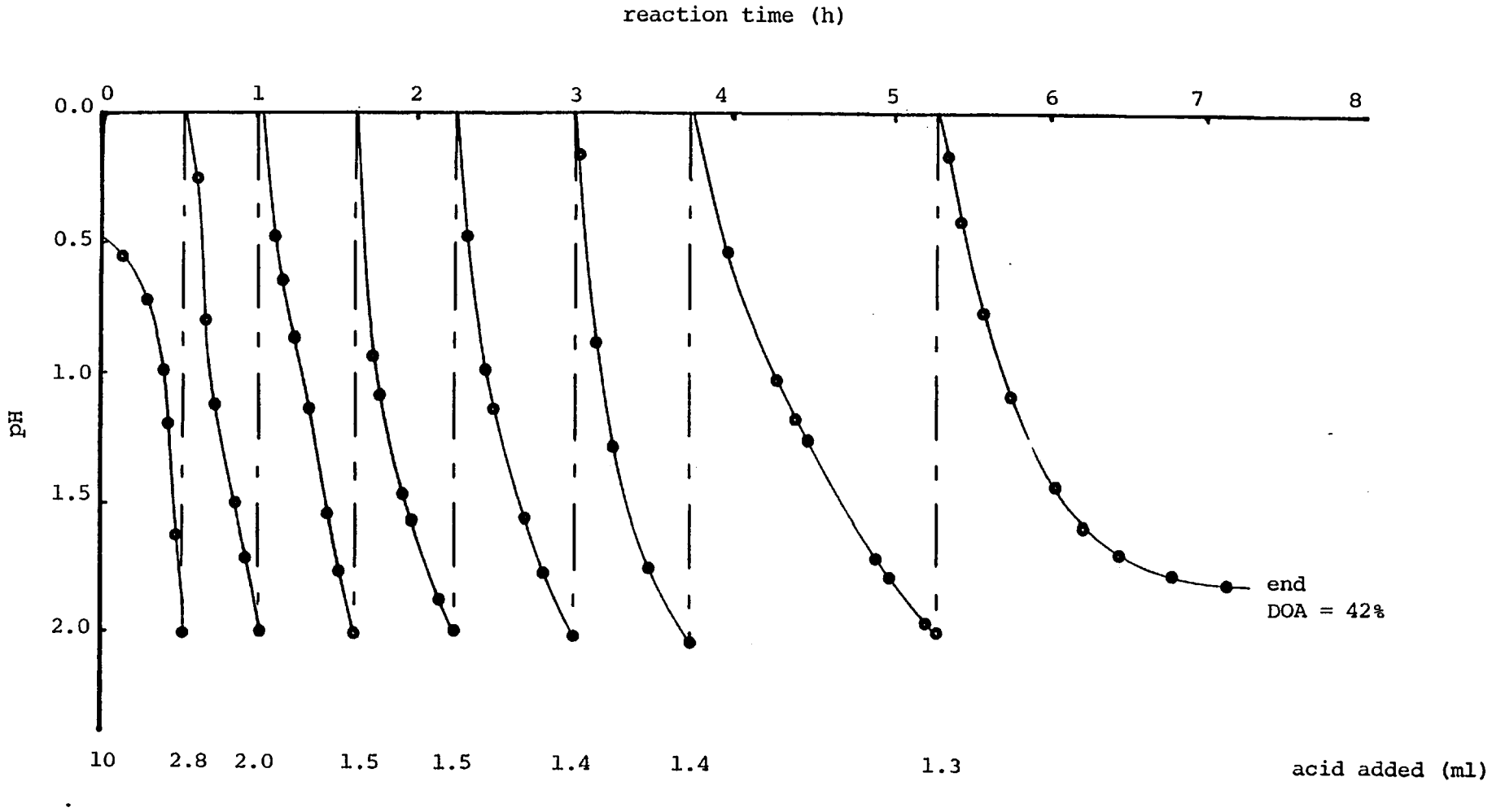


Figure 5.3.4 pH/time relation for semi-continuous alteration of a 25 g -1180+850 µm feed. 5.0 g $AlCl_3$ $6H_2O$ charge added at 0 h.

were applied, the rate of reaction (shown by the gradient of the pH curve) decreasing with time. The duration of each cycle was seen to increase from 0.5 h (cycle 1) to 1.75 h (cycle 8). Comparing the results with those from batch tests it could be seen that the DOAs, which varied from 40-45% after a 7 h reaction, were slightly larger than those obtained under comparable conditions in the previous testwork. This was attributable to the removal of fines from the site of reaction which was not possible in the apparatus employed earlier. Larger proportions of the liberated ions also appeared to remain in solution in the case of the semi-continuous alteration equipment compared to the batch apparatus :

apparatus	mean proportion of ion entering solution (%)			
	Mg	Fe	Ca	Al
semi-continuous	56	52	87	95
batch	25	20	75	70

It was evident that the reactions in the semi-continuous apparatus involved acid hydrolysis in the main, whereas aluminium interaction to form clay minerals (as noted in batch tests) was small in comparison. The drop in the rate of reaction appeared to reflect the build up of hydrolyzed product some of which was loosely held and broke off early in the reaction to join the -75 μm fraction. Such material included unaltered kimberlite which was presumably coated with softer (vermiculite) phases. Other hydrolyzed products were more tenaciously held, despite the attrition process, and in due course prevented reaction by increasing the diffusion path length to the unreacted core of kimberlite. Such a crust appears to have been silica rich, due to the paucity of this species concentration in solution compared with those of the other ions, Mg^{2+}, Fe^{2+} and Fe^{3+}, Ca^{2+} and Al^{3+}. This crust

consisted of a leached kimberlite, the interstices of which were filled with gelatinous siliceous products. Consequently, as indicated by AAS analyses, aluminium ions required longer times than those available in each cycle to participate in clay formation and was therefore inactive under the conditions used. Regardless of concentration, the hydrogen ions became inactive as the hydrolyzed product diffusion layer built up. This conclusion was verified by the fact that residual olivine and serpentine were found in both the +75 μm and -75 μm fractions after 7 h and that the solution was not saturated with respect to the major ion species.

5.3.3 Results and discussion : -6.18+3.18 mm feed

In this series of tests a 600 μm screen was used in the reaction chamber in preference to a 75 μm one; 600 μm being the smallest size of marketable gem quality diamonds (Section 1.2.2).

The result of applying similar alteration conditions (to those employed in Section 5.3.2) to this larger-sized feed was relatively little alteration. The addition of larger quantities of acid (47 ml of 11.5M Analar hydrochloric acid) as shown in Figure 5.3.5a produced a lower rate of reaction. This was indicated from the gradient of the pH-time plot. In the figure the pH only increased to 1 after 1 h, whereas pH 2 was readily achieved after half the time when the smaller (-1180+850 μm) feed was tested. Examining sections of the residual particles revealed that a concentric reacted layer surrounded a core of relatively fresh kimberlite (Figure 5.3.5b). Although scanning electron micro-photographs had shown that such smooth concentric layering of fresh and altered layers did not occur in the case of the -1180+850 μm particles, such a shrinking core model appeared to hold for the larger -6.18+3.18 mm feed. However, by rubbing partially reacted particles against one

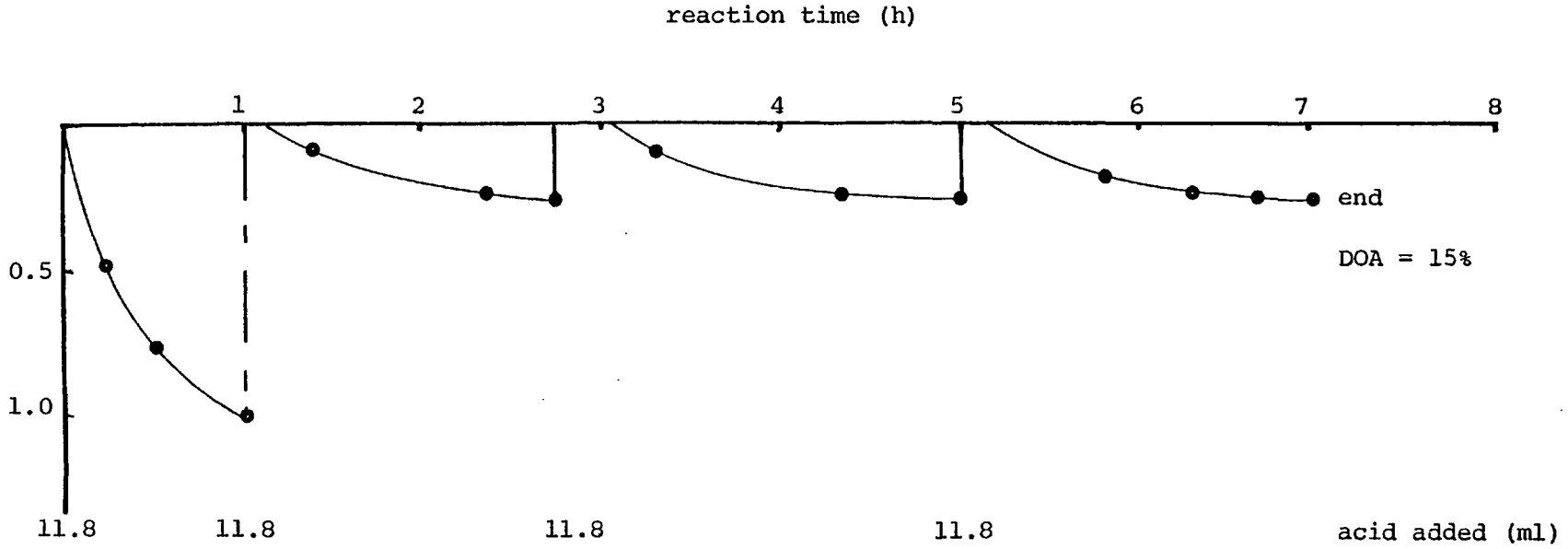


Figure 5.3.5a **pH/time relation for** semi-continuous alteration of a 25 g -6.18+3.18 mm feed. 5.0 g $AlCl_3$ $6H_2O$ charge added at 0 h.

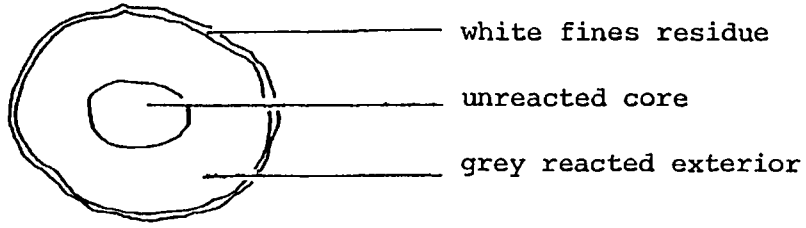


Figure 5.3.5b Cross-section of a reacted particle (x4.5).

another it could be seen that these reacted layers were friable and considerably less competent than the fresh kimberlite. Washing a bed of these particles under a powerful water jet, however, did not break up the particles. A grooved stirrer, as described in Section 5.3.1, was subsequently introduced to the system (Figure 5.3.1 and Plates 5.1 and 5.2).

By rotating the 5 mm diameter grooved glass rod in a packed bed of these particles in the PTFE cartridge it was seen that the reacted layer of the particles was abraided and removed. Abrasion took place not only between the stirrer and the kimberite, but also between the particles themselves. From this action it was evident that the dimensions of the reaction chamber and the mass of the kimberlite charge would have an important effect on the efficiency of the attrition.

The introduction of the grooved stirring action had a dramatic effect on the DOA, as shown in Figure 5.3.6. In the series of tests, the results of which are summarised in the figure, 0-6.4 g charges of hydrated aluminium chloride were added to the reaction solution with 11.8 ml of 11.5M Analar hydrochloric acid being added at the start of each cycle. This reagent addition procedure was preferred to those described in Figures 5.3.3 and 5.3.4 since extensive alteration through aluminium interaction had not been achieved. Consequently higher acid concentrations at the start of each cycle had to be employed to promote greater degradation (as inferred from the optimum conditions determined in Section 5.2). Indeed, an incomplete test using such reagent concentrations yielded a DOA of 60% for a -1180+850 μm feed.

As shown in Figure 5.3.6 only three additions of acid were required to reduce more than 93% of the rock to -600 μm (cf. a DOA of 45% for a similar total acid volume as noted in Section 5.3.2). The remaining +600 μm material had apparently reacted but had not passed

through the screen owing to the decreasing efficiency of the stirring action, as fewer particles became available for attrition. It was evident that a minimum mass (∿ 2 g) of rock had to be present to ensure attrition between the particles and the stirrer.

Figure 5.3.6 gives some indication of the influence of the matrix on on the nature of the reaction. At the start of the experiment the highest rate of reaction was recorded, the trend being comparable with the pH-time relations observed for the smaller sized feed. Again, a marked green colouration was noted with a comparatively high deposition rate ∿ 0.06 g/min. The majority of these particles deposited at this time were relatively coarse, with sizes ranging up to 600 μm. The size of product and rate of deposition decreased as the reaction progressed, as observed before. The colour of the solutions faded, as in earlier tests. The rate of reaction continued to decrease, despite the second addition of acid until the reaction time was about 2.3 h. The pH then increased rapidly from 0.7 to 1.5, in a reproducible manner. It would appear that a diffusion barrier to the alteration reactions was built up and then, given sufficient time, broke down probably through the attrition process resulting in essentially complete degradation of the kimberlite. At the end of the reaction time acid consumption had become very low.

Additional data concerning the reactions was provided from elemental mass balances and XRD, the results of which are shown in Table 5.3.1 and Figure 5.3.7 respectively. In the case of the former, three separate -600 μm products were obtained, one for each of the three reaction cycles. The solution was sampled at the end of each cycle, at 1.2, 3 and 4.5 hours, and are represented as C1, C2, C3 respectively in the table.

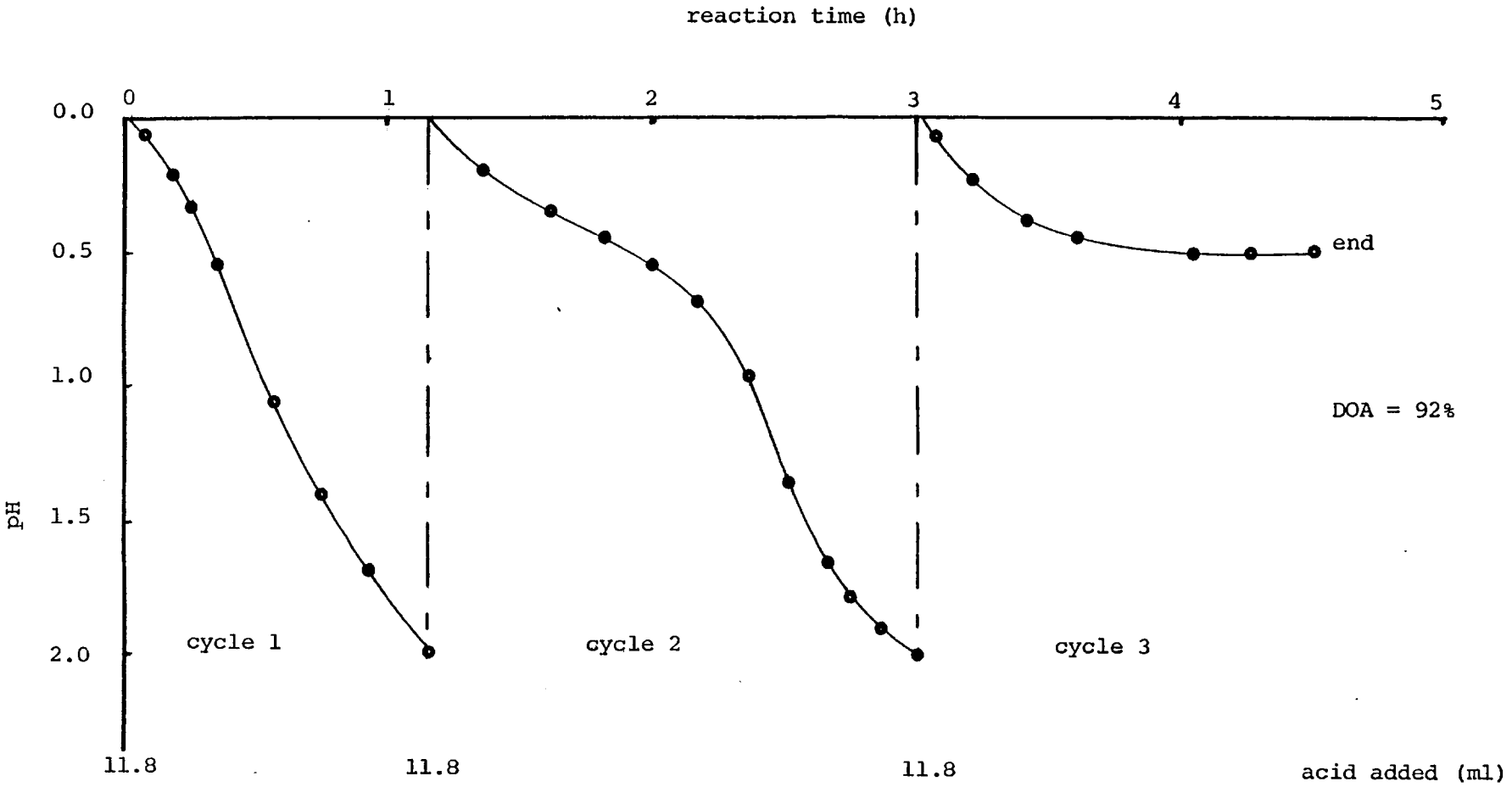


Figure 5.3.6 pH/time relation for semi-continuous alteration of a 25 g -6.18+3.18 mm feed. 0-6.3 g $AlCl_3$ $6H_2O$ added.

TABLE 5.3.1 ELEMENTAL MASS BALANCE DATA FOR SEMI-CONTINUOUS ALTERATION OF KIMBERLITE : -6.18+3.18 mm; THREE REACTION CYCLES

DISTRIBUTION (%)	Mg	Si	Fe	Ca	Al
phase					
+600	7.9	8.9	8.4	7.4	8.1
-600 (C1)	4.2	13.4	4.2	1.2	5.4
-600 (C2)	11.9	43.7	13.3	4.3	21.6
-600 (C3)	9.2	30.6	9.8	3.1	10.8
solution (C1)	18.4	1.1	16.8	32.1	10.8
solution (C2)	45.9	2.0	37.8	55.6	32.4
solution (C3)	66.7	3.4	64.4	84.0	54.0
ASSAY (%)					
+600	16.0	15.7	6.0	6.3	1.5
-600 (C1)	9.4	25.3	3.4	1.0	1.2
-600 (C2)	8.6	26.9	3.4	1.2	1.4
-600 (C3)	8.8	25.9	3.4	1.1	1.0
HEAD	16.1	15.8	6.0	6.3	1.5

As can be seen from Table 5.3.1, the residual +600 μm fraction had the same assay values (for the five elements) as the original head. This result would be expected for a reaction which was modelled as a shrinking core. With the exception of silicon, a large proportion of the constituent cations in the altered part of the kimberlite reported to the solution : namely 66.8% of the total magnesium, 64.4% of the iron, 84.0% of the calcium, 54.0% of the aluminium. As much as 87.7% of the silicon reported to a -600 μm phase. The highest contributions

to the distribution values in the sets of results for the -600 μm products and the solution generated were those deduced from cycle 2, the longest reaction cycle in the test. The only exception to this trend was calcium, where a higher value, 32.1%, was recorded for cycle 1. It would appear that whereas substantial penetration of the kimberlite by the reagents occurred during cycle 1, reactions taking place in cycle 2 had the most significant contribution regarding the general degradation of the kimberlite. The -600 μm products had mutually similar assay values, but different from the head sample, thus indicating their different composition, as demonstrated by XRD.

XRD analyses of the -600 μm products obtained from cycles 1, 2 and 3 are shown in Figure 5.3.7a,b. Figure 5.3.7a (cycle 1) shows that the principal minerals present were indeed olivine, mica and serpentine, but also phyllosilicate and amorphous phases, notably 14.7-15 Å clays. A similar mineralogical composition was observed for the -600 μm products from cycles 2 and 3 (summarised in Figure 5.3.7b) though the clay phase was not so readily apparent because of its lower degree of crystallinity and/or its lower concentration in the product. Figures 5.3.7a,b also showed that poorly crystalline 11 Å and amorphous phases were present. The latter was indicated by the broad envelope in the 2.49-5.15 Å (18-36° 2θ) region. This may be ascribed to simple oxides and hydroxyoxides of magnesium, iron and aluminium. The presence of an 11 Å phase would be expected from considerations of the reaction mechanism as described in Section 4.5.

Whereas systems employing hydrochloric acid only were successful in altering the kimberlite, the effect of the addition of extra aluminium was small; the alteration reactions being similar to those observed for hydrochloric acid (Sections 3.3.2 and 3.3.4).

Noting the results obtained for the kinetic experiments in

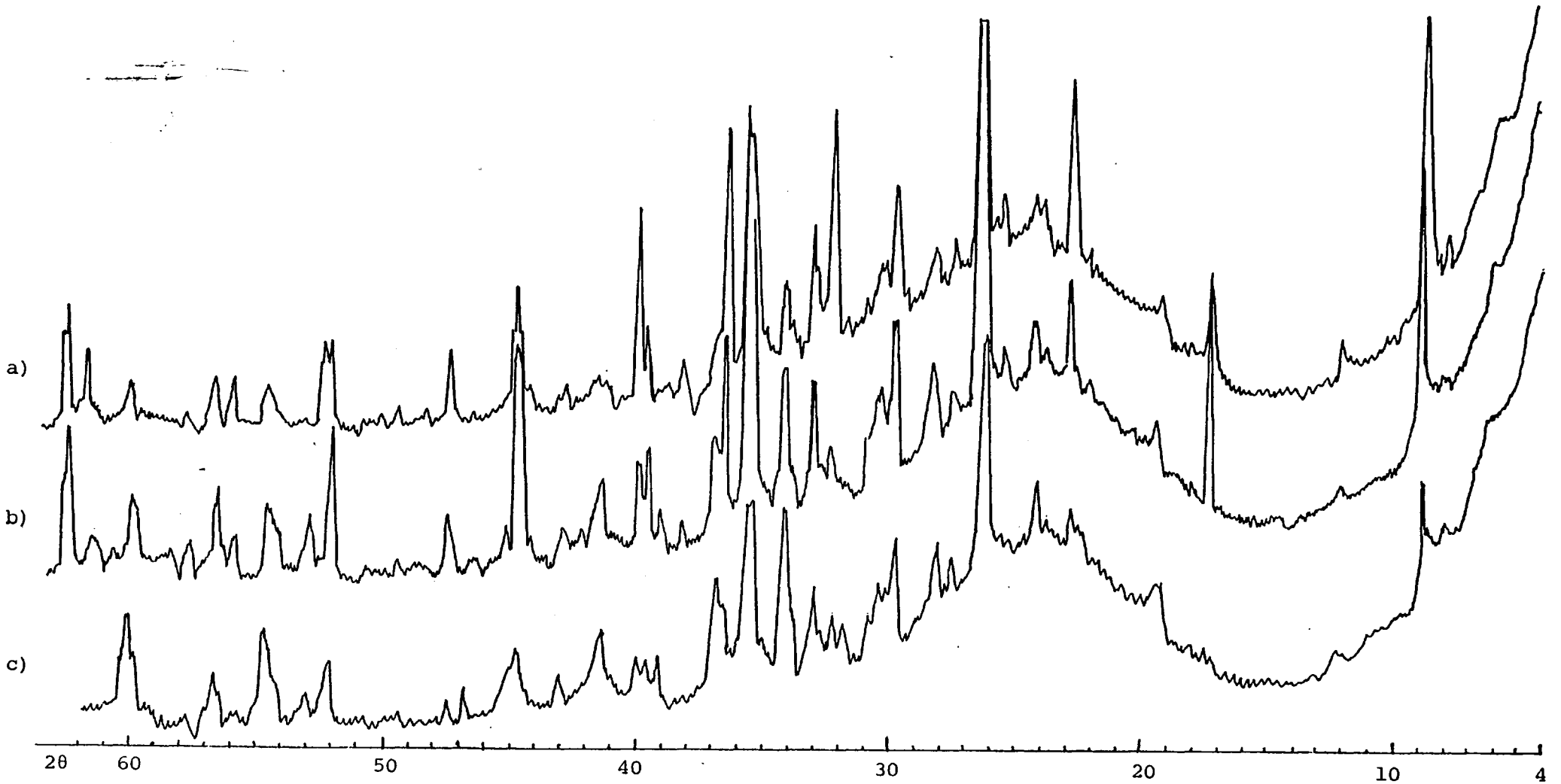


Figure 5.3.7 X-ray diffractograms for

a) -600 µm product obtained from cycle 1 for the semi-continuous alteration of kimberlite described in Figure 5.3.6.
b) -600 µm products obtained from cycles 2 and 3 for the same test
c) -600 µm products from cycles 1, 2 and 3 for the semi-continuous alteration of kimberlite described in Figure 5.3.8.

Section 4.2.3 it appeared that aluminium entered into the coarse phase after 1.5 h. By allowing the feed to react with the aluminium-charged solution for 1.5 h before any attrition took place by stirring, the addition of the cation was found to have a positive effect. The pH-time relationship for this test is shown in Figure 5.3.8.

As shown in the figure, the overall reaction time was 7.5 h (cf. 4.5 hours, Figure 5.3.6) but the stirring time required to reduce more than 90% of the feed to -600 μm was only 4.0 h. Furthermore, the rate of reaction after storing started was greater in cycle 2 than that recorded in Figure 5.3.6. During the experiment it was noticeable that the stirring action was facilitated by the inclusion of aluminium under these conditions. In previous tests the stirrer became jammed between the particles and care had to be exercised to prevent the glass rod from breaking. In this case however the competency of the rock appeared to be reduced even further.

XRD analysis of the residual -600 μm products obtained were as shown in Figure 5.3.7c. There was a substantial reduction in the proportion of serpentine present compared with the results obtained in Figure 5.3.7a,b and negligible olivine. Micas persisted, and there appeared to be a higher concentration of 11-15 Å clay mineral phases. Mass balance analysis showed that some 50% of the total aluminium reported to the solid phase, hence reacting to form clay phases, to an extent at least ten times that previously recorded. The proportion of magnesium and iron exsolving from solution also appeared to increase, to form 11-15 Å clay phases as opposed to simple hydroxyoxide compounds. The silicon distribution was similar to that described in Table 5.3.1. The residual calcium assay indicated that 92% of the rock had been penetrated by the reagents.

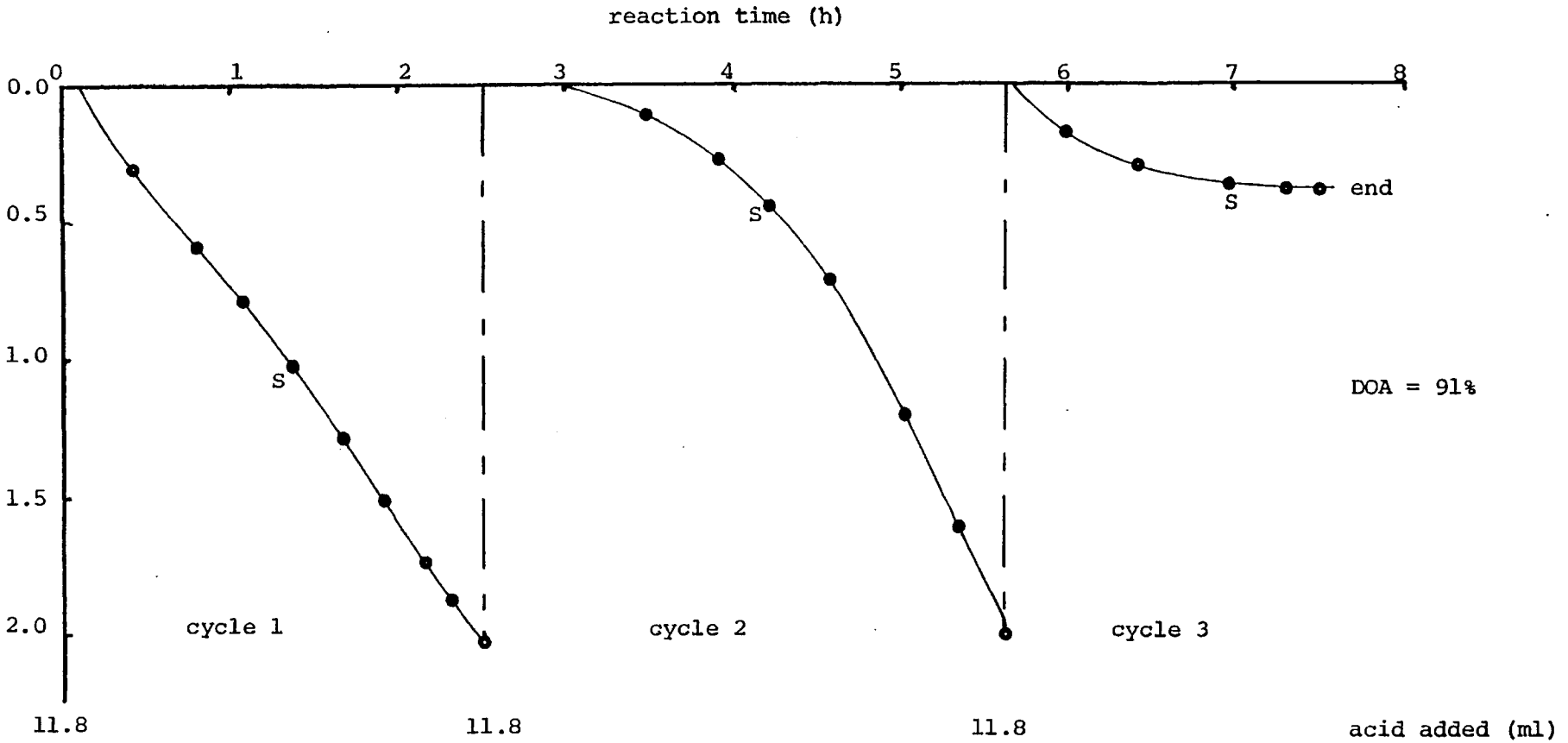


Figure 5.3.8 pH/time relation for semi-continuous alteration of kimberlite -6.18+3.18 mm feed. 2 g $AlCl_3$ $6H_2O$ added at 0 and 5.6 hours. Stirring started at S and stopped on further acid addition.

5.4 Discussion : Process Design

It is not the purpose here to present a complete process design and economic evaluation. Some consideration has, however, been given to the possibilities of the industrial application of kimberlite hydrothermal alteration which are linked, of course, to diamond liberation at the natural grain size, rather than to any production of a marketable clay product.

5.4.1 The semi-continuous alteration process : Optimised conditions

The reactions conducted using the semi-continuous alteration equipment were effective in rapidly reducing coarse sized particulate charges to a readily discardable solid product. Liberation of diamonds (which are chemically inert under the conditions used) at their natural grain size would result. A general comparison between the process and conventional diamond extraction procedures is given later. Features of the new process are considered immediately below.

The practice of the removal of final product from the site of reaction by attrition in a chemical alteration process has both advantages and disadvantages in terms of mineral processing. Sub-sieve sized product removed through the provision of a screen deck and settling chamber enhanced the rate of degradation in two respects. The first was to simply provide new kimberlite surface for continuing the reaction, thus minimising reagent diffusion as much as possible, and the second was to physically remove fine sized product from the reaction chamber to prevent unnecessary acid consumption.

Removal of hydrolyzed kimberlite immediately after acid attack prevented the development of phyllosilicates within the cavities formed in the kimberlite, by inhibiting inter-reaction between the aluminium ions with the hydrolysis products. Delaying the stirring action by 1.5 h after acid addition, however, to some extent facilitated

clay mineral formation within the kimberlite. The rock subsequently became less competent compared with that resulting from simple acid leaching procedures.

There is some reason in attempting to maximise the formation of phyllosilicates in the above manner (as opposed to the precipitation of cationic hydroxides) :

a) the greater degree of crystallinity of clay minerals facilitated their separation from the unreacted product,

b) there is some evidence that reaction with aluminium reduced the effective thickness of the diffusion layer, by forming products less tenaciously held to the kimberlite residue and

c) the formation of phyllosilicates facilitates removal of silica from the coarse particles as well as precipitation of cationic species causing the alteration process to proceed further according to the equilibrium :

$$\text{head minerals} \leftrightarrow \text{solution phase} \leftrightarrow \text{clay minerals} \qquad (5.4.1)$$

In the absence of other constraints aluminium should be considered as a useful reagent.

On the basis of the work carried out on the semi-continuous alteration apparatus the optimum conditions for the degradation of Wesselton kimberlite are as follows :

Acid : Cyclical additions of hydrochloric acid at

pH ≥ 2 to yield initial concentrations of

1.4M H^+

Aluminium : 'Steady state' concentration 0.08M Al^{3+}

Attrition : Started 1.5 h after initial contact between kimberlite and acid additions

Temperature : 100°C

Further alteration studies relating either to other kimberlites or scaling-up the present work might take these values as a starting point.

5.4.2 Process considerations

In addition to those processes described, important options for study would include reactions carried out under ambient conditions of temperature and pressure for long time periods. In this section a brief comparison is made between three possible options which are described in the Table 5.4.1 : a long term leach, L; a long term leach-alteration process, LTA; and a hydrothermal alteration process, HTA.

TABLE 5.4.1 PROCEDURES ADOPTED FOR LONG-TERM AND SHORT-TERM DEGRADATION PROCESSES

	Procedure		
	L	LTA	HTA
Mass of -6.18+3.18 mm feed (g)	10.0	10.0	25.0
Reagent volume (ml)	40	40	100
Initial acid concentration (M)	6.65	1.5	1.4
Initial aluminium concentration (M)	-	0.44	0.08
Temperature (°C)	25	25	100
Duration (h)	2880	2880	8

Whereas the acid leach test, L, consisted of one bulk addition of reagent at the start of the test, cyclical additions of the reagents were made in the case of test LTA on exhaustion of the hydrogen and aluminium ions supplied. Throughout the four-month time period for LTA, the solution was replaced once, with new reagent concentrations as listed above. The procedure noted for test HTA has been discussed before, and related to Figure 5.3.8.

The results of the tests are expressed in terms of the effects on a 25 g -6.18+3.18 mm feed in Table 5.4.2.

TABLE 5.4.2 COMPARISON OF TESTED ALTERATION PROCEDURES

	Procedure		
	L	LTA	HTA
DOA	60.0	39.1	92.0
Acid consumed (% SRTD)	105	57	71
Acid consumed (% SRAV)	N/A	166	205
Aluminium consumed (% SRAV)	N/A	30	5
% mass reporting at -600 µm	2	2	31
% penetration by reagents	88	100	100

Notes

a) SRTD represents "stoichiometric requirement for total dissolution". The number of hydrochloric acid moles required is 0.52 for a 25 g kimberlite charge.

b) SRAV represents "stoichiometric requirement for total alteration to vermiculite". Vermiculite was selected as it is the most common alteration product formed, as observed in the present study. For a 25 g kimberlite charge SRAV (hydrochloric acid) = 0.18 moles; SRAV (Aluminium chloride) = 0.17 moles.

Table 5.4.2 shows that room temperature leaching with high concentrations of hydrochloric acid resulted in 40% of the feed remaining oversize (+600 μm) after 4 months, but nevertheless consumed the full stoichiometric requirement of acid for total reaction. The residue appeared to consist of a hard residual siliceous skeletal structure in which diamonds would presumably remain entrapped. This residual hydrolyzed product inhibited rapid penetration of the kimberlite by the reagents as indicated by the residual calcium assay and the residual acid concentration being 1M H^+ after 4 months. This degradation procedure was clearly unattractive from the industrial point of view, because the basic criterion of diamond liberation was not achieved despite virtually complete leaching of the constituent cations in the kimberlite.

For test LTA, the DOA was lower than test L namely 39%. However, the acid consumption was also lower and it appeared that the reagents were more efficiently utilised. The extent of penetration was slightly greater, but despite large quantities of aluminium being consumed (0.053 mole for a 25 g feed) the amount of -600 μm alteration product was small (2% of the total mass). Noting this observation, and that the rock remained competent, this process too, proved to be unattractive for further development, despite the low % SRTD and % SRAV values for acid consumption (Table 5.4.2).

The reagents added in test HTA were the most efficiently used of the three tested procedures. The test satisfied the criterion of (almost) total degradation, and hence liberation of any entrained values. Slightly more acid was consumed than in test LTA but the DOA value was 2.3 times as large. Furthermore, one sixth of the aluminium was consumed and fifteen times more discardable waste was generated within a smaller time period. From the % SRTD and % SRAV values it

could be seen that the reactions were a combination of hydrolysis types and those relating to hydrolysis followed by clay formation. The higher temperature had an important effect in that it increased the mobilisation of silica from the site of reaction. (Increasing the temperature from 25 to 100°C raises the solubility of amorphous silica by approximately a factor of 4[269].) Although liberated silica later polymerizes to form solid products, where the localised ion concentrations are favourable, the importance of solubilization of silica at the site of reaction was illustrated by testwork conducted using sulphuric acid (Section 3.2); complete solubilization of the kimberlite being achieved on raising the temperature from 70 to 100°C under optimum conditions.

A schematic flowsheet for an extraction plant which would liberate and concentrate diamonds using the hydrothermal alteration process is given in the form of a block diagram in Figure 5.4.1. A preliminary conceptual flowsheet is given in Figure 5.4.2.

Five types of unit operation are involved : primary crushing, screening, hydrothermal alteration, water recovery and ion exchange. Although the majority of diamond liberation would be effected by kimberlite alteration the run-of-mine ore would have to be broken to a 'manageable' size. In the figure this size is taken to be 300 mm, which is three times the longest dimension of the largest diamond ever found (Cullinan : 3106 carats). The broken ore is then screened into various size fractions the smallest, the gemstone undersize (set at -600 μm), being discarded.

The kimberlite is screened into various fractions rather than being treated as a whole in order to prevent any crushing of small kimberlite particles by larger ones, as well as to induce breakage along natural planes of weakness - consequently the size of kimberlite

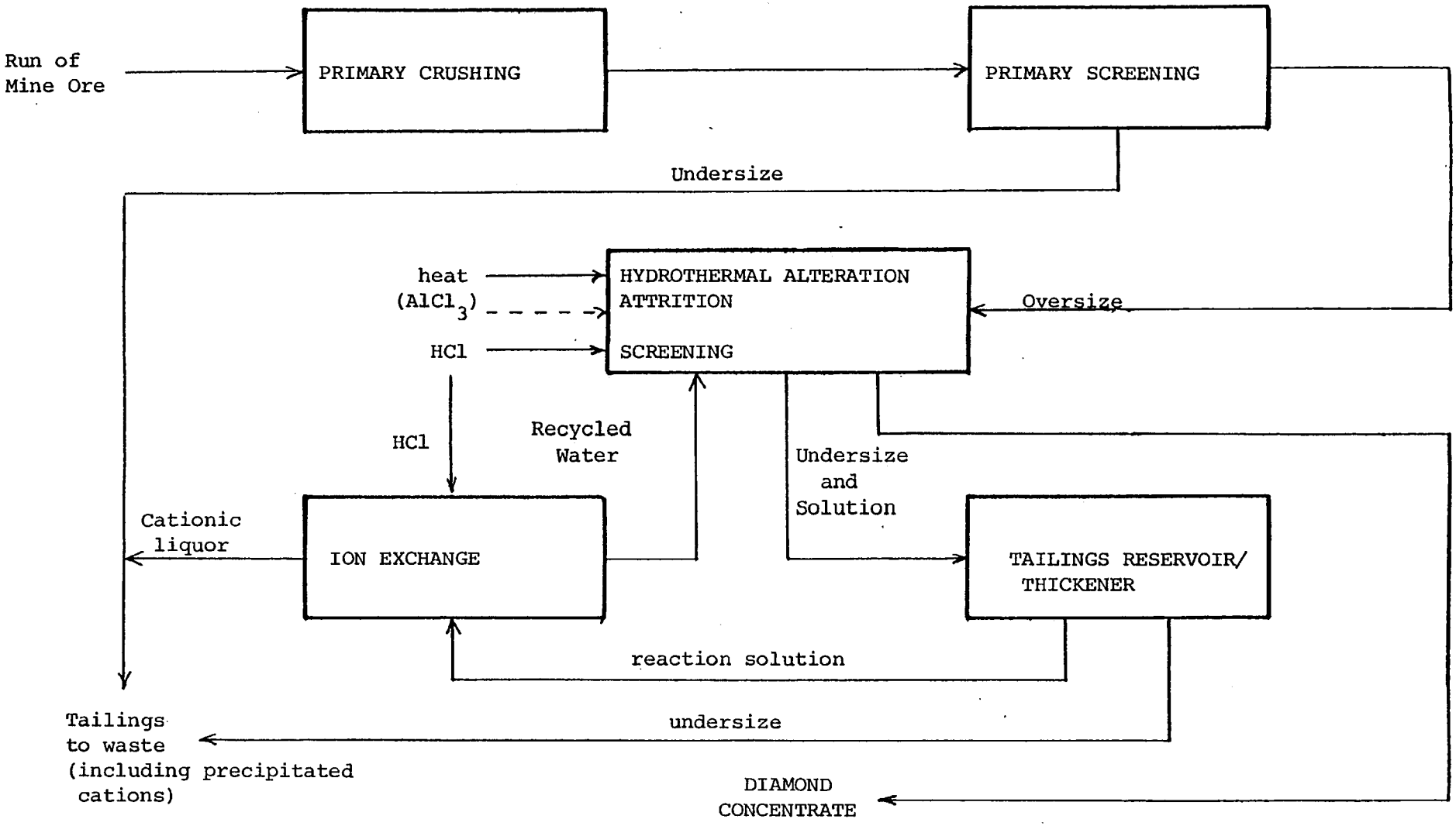


Figure 5.4.1 General flowsheet for diamond recovery by hydrothermal alteration of kimberlite.

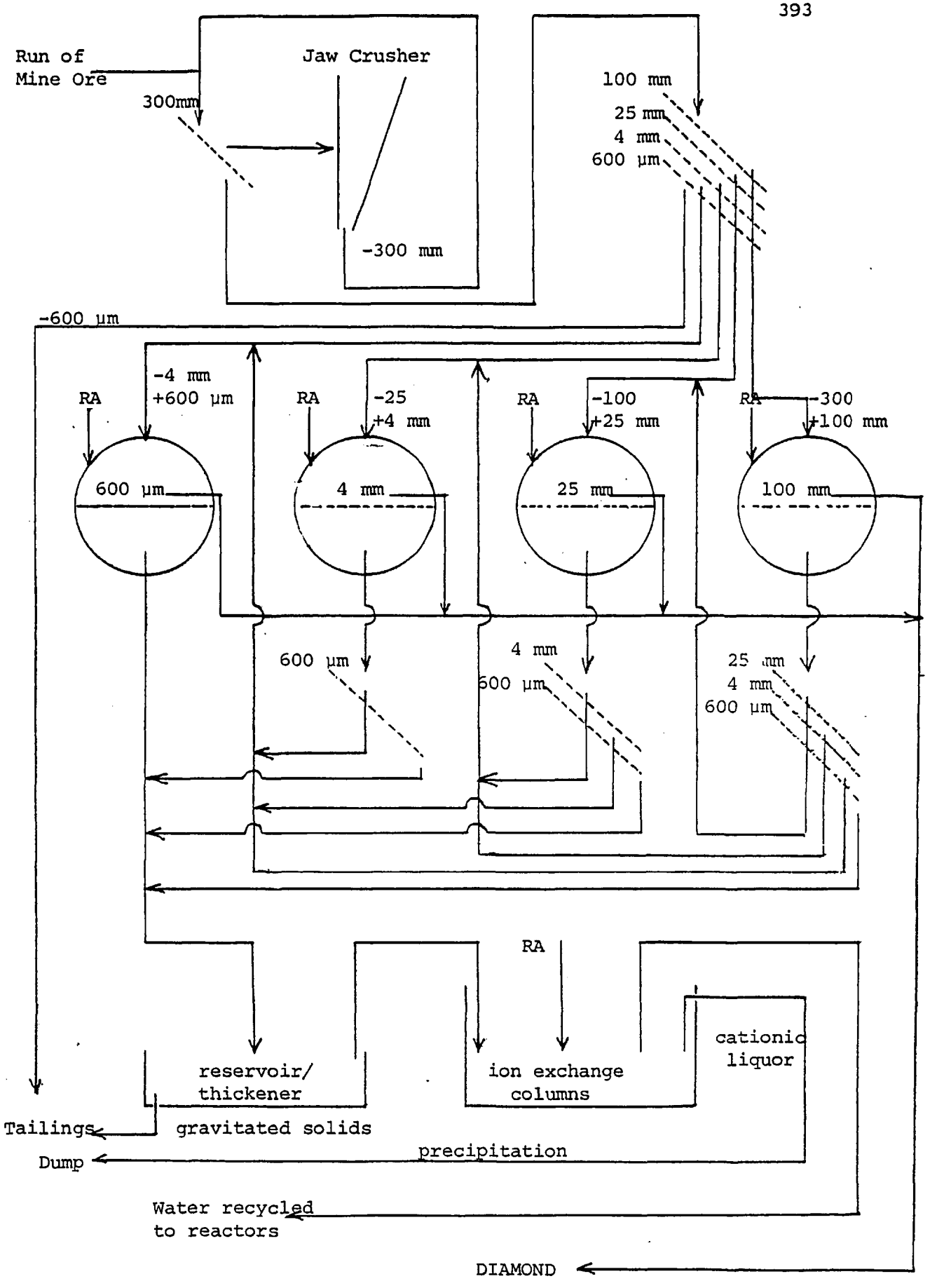


Figure 5.4.2 Conceptual flowsheet for diamond recovery by hydrothermal alteration of kimberlite.
(RA denotes reagent addition point)

would be progressively reduced. The separate fractions are then fed separatedly to reaction chambers in which the kimberlite is altered and degraded by acid hydrolysis. Residual top-sized product from each chamber becomes the concentrate which is then hand sorted for marketing. The reaction chamber undersize is then screened again and the fractions routed to the next reaction chamber (as shown in Figure 5.4.2).

The reaction chambers would have to be operated on a semi-continuous basis such that residual unreacted product (diamond concentrate) could be removed. Processed undersize (which in the conceptual flowsheet comprises the -100 mm +600 μm fractions) however would be continually removed and re-routed to further alteration chambers as noted above. The -600 μm solids, with the reaction solution, would be pumped to a tailings reservoir, dam or thickener where the solids would be allowed to separate, perhaps under the influence of a flocculant. The solids-free overflow containing high concentrations of various cations (namely Mg^{2+}, Ca^{2+}, Fe^{2+}, Fe^{3+}, Ni^{2+}) is directed to a series of ion-exchange columns where these ions would be reduced in concentration using cationic resins in the (H^{+}) form. This procedure would be necessary so as to prevent the reaction solution becoming saturated with respect to these ions. The water would then be recycled to the alteration chambers as indicated in the figures. To regenerate the resin, hydrochloric acid would be added and the separate solution, highly concentrated in metallic cations, directed to a separate part of the tailings dam where these ions may be re-precipitated, perhaps by the action of soda-lime. Any associated water consequently need play no further part in the process. The hydrochloric acid used to regenerate the resins would be liberated during the following contact with the tailings dam/thickener, overflow, and be used to form part

of that acid added at the start of each reaction cycle. (Supplementary acid dosages are added directly as shown in Figures 5.4.1 and 5.4.2.)

The process design would also allow for the inclusion of aluminium as a reagent. The aluminium chloride reagent would be added at the start of each cycle and the attrition processes delayed so as to ensure total interaction between the reacting kimberlite and the cation (cf. Figure 5.3.8). The concentration of aluminium in the reaction solution leaving the reaction chambers should be minimised to avoid loss during ion exchange.

In comparison with conventional flowsheets which relate to the extraction and concentration of diamonds from kimberlite, the hydrothermal alteration process outlined in Figures 5.4.1 and 5.4.2 appears to afford three important advantages. Firstly diamonds can be liberated at their natural grain size as the likelihood of a previous stone being crushed is minimised. Only attrition processes are involved, in which the resistance to abrasion of diamond is superior to the altering kimberlite. Secondly, the nature of diamond liberation by the new process would yield an increase in recovery compared with conventional plants. The recovery at Finsch is presently about 70%[61]. In conventional processing, ground stones may be lost in the fine solids stream (Section 1.2.2). Thirdly, the simplicity of the proposed flowhseet (cf. Figures 5.4.1 and 1.2.3) should produce savings in the capital cost of plant equipment. Operational costs are difficult to judge at present.

The use of hydrochloric acid as a bulk reagent and the employment of elevated temperatures represent large cost centres in the operation of a hydrothermal alteration plant and would need detailed consideration in a full economic evaluation. Although the acid requirements are less than those for complete dissolution they would

still be large i.e. ∿ 500 l/tonne of kimberlite at £0.06/l hydrochloric acid. The need to employ 1.4-1.5M hydrochloric acid concentrations also raises problems with regard to corrosion. In practice, the reaction chambers and attrition mechanisms would have to be fitted with replaceable chemically inert liners (e.g. specialised rubbers). However, corrosion would not be such a problem elsewhere in the plant.

The costs implied through the use of elevated temperatures can be set against those in conventional crushing and grinding circuits (which are only ∿ 2% efficient).

A third cost centre relates to the possible inclusion of aluminium as a reagent in the system.

These and other major cost centres would have to be considered as part of a more detailed process study.

In conclusion, although there are problems with respect to development of a chloride medium-hydrothermal alteration system, it would appear that the process offers an alternative method of diamond extraction. Further work is therefore recommended.

APPENDIX 1

CHEMICAL COMPOSITIONS AND MODE OF FORMATION FOR KIMBERLITE MINERALS AND THEIR ALTERATION PRODUCTS[30-177]

In the following table the mineral name, chemical composition and mode of formation are given in the first, second and third columns respectively. In the case of the latter, the nature of origin is abbreviated as follows :

cognate (cg)
alteration products - autometamorphic (am)
alteration induced by hydrothermal fluid (hf) or
supergene (sp) activity

This table is not meant to be a complete list but rather a collection of those minerals referred to directly in the thesis. A few minerals mentioned not normally present in kimberlites are included.

actinolite	$Ca_2(Mg\ Fe^{II})_5(Si_8O_{22})(OH,F)_2$	am
albite	$Na\ Al\ Si_3\ O_8$ (Ab)	cg
allophane	$Al_2\ SiO_5\ 5H_2O$	hf
almandine	$Fe_3\ Al_2\ Si_3\ O_{12}$	cg
amesite	$(Mg_4\ Al_2)(Si_2\ Al_2)\ O_{10}\ (OH)_8$	hf

analcite	$Na\ Al\ Si_2\ O_6\ H_2O$	hf
andradite	$Ca_3\ Fe_2\ Si_3\ O_{12}$	cg
andulusite	$Al_2\ SiO_5$	am,cg
anhydrite	$Ca\ SO_4$	hf,sp
anorthosite	$Ca\ Al_2\ Si_2\ O_8$ (An)	cg
antigorite	$(Mg,Fe,Ca,Al)_3\ Si_2\ O_5\ (OH)_4$	cg,am,hf
apatite	$Ca_5\ (PO_4)\ (F,Cl,OH)$	hf
apophyllite	$KF\ Ca_4\ (Si_8\ O_{20})\ 8H_2O$	hf
awaruite	$Fe\ Ni$	cg,hf
bayerite	$Al\ (OH)_3$	hf
beidellite	$(Ca,Na)_{.3}\ (Al,Mg,Fe)_2\ (Si,Al)_4\ O_{10}\ (OH)_2\ nH_2O$	hf
biotite	$K(Mg,Fe^{II})_{3-2}\ (Fe,^{III}Al)_{0-2}(Si\ AL)_4O_{10}\ (O,OH,F)_2$	cg
boehmite	$ALOOH$	hf
bowlingite	mixture - no formula available	hf,am
breunnerite	$Mg\ CO_3$	hf,sp
bronzite	$(Mg,Fe^{II})_2\ Si_2\ O_6$	cg
brucite	$Mg\ (OH)_2$	hf
calcite	$Ca\ CO_3$	cg,hf
chamosite	$(Fe^{II}_4\ Al_2)\ (Si_2Al_2)\ O_{10}\ (OH)_8$	hf,am
chalcopyrite	$Cu\ Fe\ S_2$	hf
chlorite	$(Mg,Al,Fe)_6\ (Si,Al)_4\ O_{10}\ (OH)_8$	am,hf
chromite	$(Mg,Fe)\ Cr_2O_4$	cg,hf
chrysotite	$(Mg,Fe,Ca,Al)_3\ Si_2\ O_5\ (OH)_4$	cg,am,hf
clinopyroxene	$(Mg,Fe,Ca,Al,Na,Li)\ Si_2\ O_6$	cg
corundum	$Al_2\ O_3$	cg,hf

cummingtonite	$(Mg,Fe^{II})_7\ (Si_8O_{22})\ (OH,F)_2$	am
diamond	C	cg
diaspore	AlOOH	hf
dickite	$Al_2\ Si_2\ O_5\ (OH)_4$	am,hf
diopside	$Ca\ Mg\ Si_2\ O_6$	cg
dolomite	$Ca\ Mg\ (CO_3)_2$	hf
eckermannite	$(Na,K)_2\ (Fe,Mg,Al)_5\ Si_8\ O_{22}\ (F,OH)_2$	am
enstatite	$Mg_2\ Si_2\ O_6$	cg
epsomite	$Mg\ SO_4\ 7H_2O$	sp,hf
fayalite	$Fe_2\ Si\ O_4$	cg
feldspar	$((K,Na)/(Na,Ca))\ (Al\ Si)_4O_8$	cg
forsterite	$Mg_2\ Si\ O_4$	cg
garnet	$(Mg,Mn,Fe^{II})_3\ (Ca,Al,Fe^{III}\ Cr)\ Si_3\ O_{12}$	cg
gedrite	$(Mg,Fe,Al)_7\ Al_2\ Si_6\ O_{22}\ (OH)_2$	am
gibbsite	$Al\ (OH)_3$	hf,sp
glaucophane	$Na_2\ (Mg,Fe,Al)_5\ Si_8O_{22}\ (OH)_2$	am
goethite	Fe OOH	hf
graphite	C	cg
grossular	$Ca_3\ Al_2\ Si_3\ O_{12}$	cg
gypsum	$Ca\ SO_4\ 2H_2O$	hf,sp
haematite	$Fe_2\ O_3$	
halloysite	$Al_2\ Si_2\ O_5\ (OH)_4\ 2H_2O$	hf
hectorite	$(Ca,Na)_3\ (Mg,Li)_3\ (Si,Al)_4\ O_{10}\ (OH)_2\ nH_2O$	am
hedenburgite	$Ca\ Fe^{II}\ Si_2\ O_6$	cg
hornblende	$Na\ Ca_2\ (Mg,Fe,Al)_5\ (Si\ Al)_8\ O_{22}\ (OH)_2$	am
hydrobiotite	$(K,H_3O^+)\ (Mg,Fe,Al)_3\ (Si,Al)_4\ O_{10}\ (OH)_2$	am

hypersthene	$(Mg,Fe^{II})_2\ Si_2\ O_6$	cg
iddingsite	mixture of chlorite minerals	am,hf
ilmenite	$Fe\ Ti\ O_3$	cg
illite	$K_5\ Al_2\ (Si\ Al)_4\ O_{10}\ (OH)_2$	am,hf
jadeite	$Na\ Al\ Si_2\ O_6$	cg
jarosite	$K\ Fe_3\ (SO_4)_2\ (OH)_6$	sp,hf
kaolinite	$Al_2\ Si_2\ O_5\ (OH)_4$	hf
kyanite	$Al_2\ Si_2\ O_5$	cg,am
lepidocrocite	$Fe\ OOH$	am,sp
lepidolite	$K_2\ (Li,Al)_{2-3}\ (Si,Al)_4\ O_{10}\ (OH,F)_2$	am,cg
leucite	$K\ Al\ Si_2\ O_6$	am
lizardite	$(Mg,Fe,Ca,Al)_3\ Si_2\ O_5\ (OH)_4$	cg,am,hf
magnesite	$Mg\ CO_3$	hf,sp
magnetite	$Fe_3\ O_4$	hf,am
melilite	$(Ca,Na,K)_2\ (Mg,Fe,Al,Si)_3\ O_7$	cg
microcline	$K\ Al\ Si_3\ O_8$	cg
millerite	$Ni\ S$	hf
monticellite	$Ca\ Mg\ SiO_4$	cg
montmorillonite	$(Ca,Na)_{.3}\ (Al,Mg)_2\ Si_4\ O_{10}\ (OH)_2\ nH_2O$	am
mullite	$Al_2\ SiO_5$	cg,am
muscovite	$K\ Al_2\ (Si_3\ Al\ O_{10})\ (OH,F)_2$	cg,am
nephaline	$Na\ Al\ Si\ O_4$	cg
nontronite	$(Ca,Na)_{.3}\ Fe_4\ (Si,Al)_4\ O_{10}\ (OH)_2\ nH_2O$	am

olivine	$(Ca,Mg,Fe)\ Si\ O_4$	cg
omphacite	$(Ca,Na)\ (Mg,Fe,Al)\ Si_2O_6$	cg
orthopyroxene	$(Mg,Fe)_2\ Si_2\ O_6$	cg
paragonite	$Na\ Al_2\ (Si_3\ Al\ O_{10})\ (OH)_2$	am,hf
pentlandite	$(Fe,Ni)_9\ S_8$	hf
phlogopite	$K\ (Mg,Fe)_3\ (Si_3\ Al\ O_{10})\ (OH,F)_2$	cg
picotite	$(Mg,Fe)\ (Al,Fe,Cr)_2\ O_4$	cg
plagioclase	$(Na,Ca)\ (Al,\ Si)_4\ O_8$	cg
pyrite	$Fe\ S_2$	hf,sp
pyrope	$Mg_3\ Al_2\ Si_3\ O_{12}$	cg
pyrophyllite	$Al_2\ Si_4\ O_{10}\ (OH)_2$	am,hf
pyrrhotite	$Fe\ S$	hf
quartz	$Si\ O_2$	hf
saponite	$(Ca,Na)_{.3}\ Mg_3\ (si,Al)_4\ O_{10}\ (OH)_2\ nH_2O$	am,hf
sepiolite	$(Na,Mg)_2\ (Si,Al)_3\ O_8\ 2H_2O$	am,hf
serpentine	$(Mg,Fe,Ca,Al)_3\ Si_2\ O_5\ (OH)_4$	cg,am,hf
sillimanite	$Al_2\ Si\ O_5$	cg,am
sodalite	$Na_8\ Al_6\ Si_6\ O_{24}\ Cl_2$	hf
spessartine	$Mn_3\ Al_2\ Si_3\ O_{12}$	cg
spinel	$Mg\ Al_2\ O_4$	cg
stevensite	$Mg_{2.9}\ (Mn,Fe)_{.04}\ Si_4\ O_{10}\ (OH)_2$	hf
talc	$Mg_3\ Si_4\ O_{10}\ (OH)_2$	am,hf
tremolite	$Ca_2\ Mg_5\ (Si_8\ O_{22})\ (OH,F)_2$	am
vermiculite	$(Mg,Ca)_{.3}\ (Mg,Fe,Al)_3\ (Si,Al)_4\ O_{10}\ (OH)_2\ 4H_2O$	am,hf
zeolite	$(Ca,Ma)_2\ Al_2\ Si_{3-4}\ O_{10-12}\ 2\text{-}7H_2O$	hf

APPENDIX 2

FORMULAE USED IN THE EVALUATION OF SAMPLING AND GRAIN COUNTING ERRORS

Barbery's Formula[181]

This is used to estimate the error involved in sampling a sized fraction :

$$\theta^2 = f_o \, p_o \, d_o^3 / Pm$$

where θ is the relative error; f_o, the shape factor; p_o, the relative density of the mineral in question; d_o^3, the meaned cubed size of the particles; P, the mass fraction of the total and m, the total mass.

Gy's formula[182,183]

This estimates the error in sampling a quantity for chemical assay :

$$\theta^2 = (P-S) \, f \, g \, l \, m \, d_{95}^3 / PS$$

where θ is the relative error; P, the population mass; S, the sample mass; f, the shape factor; g, the size factor; l, the liberation factor; m, the mineralogical factor and d_{95}, the 95% passing size.

Errors in grain counting

The error in estimating the proportion of the phase of interest (as based on the Binomial Theorem[238]) is given by

$$\theta_1^2 = 4(1-p)/p\ N_F\ \bar{x}$$

where θ_1 is the relative error; p, the proportion of the phase of interest; N_F, the number of fields of view; $\bar{x}$, the mean number of grains per field of view.

The error on $\bar{x}$ is given by

$$\theta_2 = 2s/(\bar{x}\ N_F^{\frac{1}{2}})$$

where s is the standard deviation of the population of $\bar{x}$.

Hence the total error is given by θ_T :

$$\theta_T = (\theta_1^2 + \theta_2^2)^{\frac{1}{2}}$$

APPENDIX 3

PROGRAM CSDF : ANALYSIS OF COULTER COUNTER DATA

The following printout lists the program written in FORTRAN to interpret the Coulter Counter data obtained, for the purposes of quantitative XRD analysis of olivine and serpentine. The program may be considered in four sections :

a) Data input

b) Calculation of cumulative per cent coarser/ finer for the data in accordance with the procedures described in the Operators' Handbook

c) Linear regressions using the Gaudin-Schumann and Rosin-Rammler size distribution functions; employing subroutines GRAPH, EVAL and DEDUCT

d) Output : consisting of parameters mentioned in (a), (b) and (c) above.

```
      PROGRAM CSDF (INPUT,OUTPUT,TAPE6=INPUT,TAPE7=OUTPUT)
      REAL N2(20)
      REAL C(20),B(20),V(20),D(20),N1(20),V1(20),X(20),
     *Y(20),T(20),E(20),J1(20),G(2,3)
      REAL W(20),W1(20)
      DIMENSION CPF(9)
      REAL K,P
      INTEGER TOTAL
      INTEGER DATANO
      DATANO=1
      READ(6,999) TOTAL
C     READ NO. OF DATA PER SAMPLE,CALIBRATION
C     AND BACKGROUND CONSTANTS
    1 READ (6,1001) N,K,P
      WRITE(7,1005)
C     PRINT TITLE OF ANALYZED SAMPLE
      IF(DATANO.EQ.1) WRITE(7,2000)
      IF(DATANO.EQ.2) WRITE(7,2001)
      IF(DATANO.EQ.3) WRITE(7,2002)
      IF(DATANO.EQ.4) WRITE(7,2003)
      IF(DATANO.EQ.5) WRITE(7,2004)
      IF(DATANO.EQ.6) WRITE(7,2005)
      IF(DATANO.EQ.7) WRITE(7,2006)
      IF(DATANO.EQ.8) WRITE(7,2007)
      DO 5 I=1,N
      Y(I)=0.0
C     READ RECORDED(C) AND BACKGROUND(B) COUNTS
C     AT THRESHOLD VALUES(V)
      READ (6,1001) C(I),B(I),V(I)

C     CALCULATE CUMULATIVE PER CENT, MASS AT SIZE D
      N1(I)=C(I)+((C(I)/1000.0)**2.0)*P-B(I)
      D(I)=K*(V(I)**(1.0/3.0))
    5 CONTINUE
      V(N+1)=V(N)/2.0
      DO 10 I=1,N
      IF(I.EQ.1) GOTO 6
      N2(I)=N1(I)-N1(I-1)
    6 CONTINUE
      N2(1)=N1(1)
      V1(I)=(V(I+1)+V(I))/2.0
      X(I)=N2(I)*V1(I)
      IF(I.EQ.1) GOTO 8
      Y(I)=Y(I-1)+X(I)
    8 CONTINUE
      Y(1)=X(1)
   10 CONTINUE
C     CALCULATE INTERCEPT AT D=0
      GRAD=(ALOG(Y(N))-ALOG(Y(N-1)))/(D(N)-D(N-1))
      Y(N+1)=EXP(ALOG(Y(N))-GRAD*D(N))
      DIFF=ALOG(Y(N+1))-ALOG(Y(N))
      Y(N+1)=EXP(ALOG(Y(N))+DIFF/3.0)
      N=N+1
      DO 15 I=1,N
      W(I)=Y(I)*100.0/Y(N)
      W1(I)=100.0-W(I)
   15 CONTINUE
      WRITE(7,1002)
      WRITE(7,1003)
      DO 20 I=1,N
C     PRINT RESULTS
      WRITE(7,1004) V(I),C(I),B(I),D(I),W(I),W1(I)
   20 CONTINUE
C     COMPUTE GAUDIN-SCHUMANN FUNCTION
      WRITE(7,1005)
      WRITE(7,1006)
      N=N-1
      N5=N
      DO 25 I=1,N
      E(I)=ALOG(D(I))
      IF(W1(I).GE.100.0) CALL DEDUCT(N5,E,V,I)
      IF(W1(I).LE.000.0) CALL DEDUCT(N5,E,V,I)
       IF(W1(I).LE.000.0) GOTO 25
       IF(W1(I).GE.100.0) GOTO 25
      V(I)=ALOG(W1(I)/100.0)
   25 CONTINUE
      CALL GRAPH(E,V,A,DZ,N5,N)
      WRITE(7,1007) DZ
      XO=EXP(-A/DZ)
      WRITE(7,1008) XO
      WRITE(7,1009)
      DO 30 I=1,8
      CPF(I)=100.0*((FLOAT(I)*10.0/XO)**DZ)
   30 CONTINUE
```

```
      WRITE(7,1010) CPF(1),CPF(2),CPF(3),CPF(4),CPF(5)
     *,CPF(6),CPF(7)
C     COMPUTE ROSIN-RAMMLER FUNCTION
      WRITE(7,1011)
      N5=N
      DO 35 I=1,N
      E(I)=ALOG(D(I))
      IF(W(I).GE.99.0) CALL DEDUCT(N5,E,V,I)
      IF(W(I).LE.00.0) CALL DEDUCT(N5,E,V,I)
      IF(W(I).GE.99.0) GOTO 35
      IF(W(I).LE.00.0) GOTO 35
      V(I)=ALOG(ALOG(100.0/W(I)))
   35 CONTINUE
      CALL GRAPH(E,V,A,OZ,N5,N)
      WRITE(7,1012) OZ
      XO=EXP(-A/OZ)
      WRITE(7,1013) XO
      WRITE(7,1009)
      DO 40  I=1,8
      CPF(I)=100.0*(1.0-EXP(-(FLOAT(I)*10.0/XO)**OZ))
   40 CONTINUE
      WRITE(7,1010) CPF(1),CPF(2),CPF(3),CPF(4),CPF(5)
     *,CPF(6),CPF(7)
      DATANO=DATANO+1
      IF(DATANO.GT.TOTAL) GOTO 50
      GOTO 1
   50 CONTINUE
  999 FORMAT (I2)

 1000 FORMAT(I2,2X,F7.5,2X,F5.2)
 1001 FORMAT(F7.1,2X,F6.2,2X,F9.3)
 1002 FORMAT (2X,23HCOULTER COUNTER RESULTS)
 1003 FORMAT(/5X,9HTHRESHOLD,8X,5HCOUNT,8X,10HBACKGROUND,
     *6X,8HSIZE(UM),3X,15HCUM.0/0.COARSER,15H CUM.0/0.FINER )
 1004 FORMAT(2X,6(3X,F7.1,5X))
 1005 FORMAT (//2X,27HSIZE DISTRIBUTION FUNCTIONS)
 1006 FORMAT (/2X,24HGAUDIN-SCHUMANN FUNCTION)
 1007 FORMAT (2X,21HDISTRIBUTION MODULUS=,F5.3)
 1008 FORMAT (2X,21HSIZE MODULUS       =,F5.1)
 1009 FORMAT (/2X,36HCUMULATIVE PERCENTAGE FREQUENCIES AT)
 1010 FORMAT(2X,2H10,2X,F5.1,4X,2H20,2X,F5.1,5X,2H30,2X,F5.1,5X
     *,2H40,F5.1,5X,2H50,2X,F5.1,5X,2H60,2X,F5.1,5X,2H70
     *,2X,F5.1)
 1011 FORMAT (/2X,22HROSIN-RAMMLER FUNCTION)
 1012 FORMAT (2X,23HUNIFORMITY COEFFICIENT=,F5.3)
 1013 FORMAT  (2X,23HABSOLUTE SIZE CONSTANT=,F5.1)
 1050 FORMAT(/2X,90("-")/)
 2000 FORMAT(2X,7H112I+75)
 2001 FORMAT(2X,7H112J+75)
 2002 FORMAT(2X, 7H112K+75)
 2003 FORMAT(2X,7H112L+75)
 2004 FORMAT(2X,7H112M+75)
 2005 FORMAT(2X,7H112N+75)
 2006 FORMAT(2X,7H112P+75)
 2007 FORMAT(2X,7H112Q+75)
      STOP
      END


      SUBROUTINE GRAPH (E,V,A,OZ,N5,N)
      DIMENSION T(20),E(20),V(20),G(2,3)
      S1=0.0
      S2=0.0
      S3=0.0
      S4=0.0
      S5=0.0
C     STUDENT T-TEST VALUES
      T(1)=318.310
      T(2)=22.327
      T(3)=10.215
      T(4)=7.173
      T(5)=5.893
      T(6)=5.208
      T(7)=4.785
      T(8)=4.501
      T(9)=4.297
      T(10)=4.144
      T(11)=4.025
      T(12)=3.930
      T(13)=3.852
      T(14)=3.787
```

```
      DO 100 I=1,N
      S1=S1+E(I)
      S2=S2+V(I)
      S3=S3+E(I)**2.0
      S4=S4+E(I)*V(I)
      S5=S5+V(I)**2.0
  100 CONTINUE
      G(1,1)=N5
      G(1,2)=S1
      G(1,3)=S2
      G(2,1)=S1
      G(2,2)=S3
      G(2,3)=S4
      DO 150 I=1,2
      DO 150 J=1,2
      IF(I.NE.J) CALL EVAL (G,I,J)
  150 CONTINUE
C     2X2 MATRIX INVERSION FOR LINEAR REGRESSION
      A=G(1,3)/G(1,1)
      DZ=G(2,3)/G(2,2)
      R=(S4-S1*S2/FLOAT(N5))/SQRT(ABS((S3-S1**2.0/FLOAT(N5)
     *))*(S5-((S2**2.0)/FLOAT(N5))))
      TS=R*SQRT(FLOAT(N5-2))/SQRT(1.0-R**2.0)
      WRITE(7,1014) R


      IF (TS.LE.T(N5-2)) GOTO  160
      WRITE(7,1015)
 1014 FORMAT (2X,24HCORRELATION COEFFICIENT=,F7.5)
 1015 FORMAT (2X,30HSIGNIFICANTLY DIFFERENT FROM 0)
  160 CONTINUE
      RETURN
      END



      SUBROUTINE EVAL(G,I,J)
      DIMENSION G(2,3)
      F=G(I,I)/G(J,I)
      DO 200 K1=1,3
      G(J,K1)=G(J,K1)*F-G(I,K1)
  200 CONTINUE
      RETURN
      END


      SUBROUTINE DEDUCT(N5,E,V,I)
      DIMENSION E(20),V(20)
      N5=N5-1
      E(I)=0.0
      V(I)=0.0
      RETURN
      END
```

112I+75
COULTER COUNTER RESULTS

THRESHOLD	COUNT	BACKGROUND	SIZE(UM)	CUM.0/0.COARSER	CUM.0/0.FINER
5120.0	0	0	85.9	0	100.0
2560.0	.8	0	66.2	3.2	96.8
1280.0	2.3	0	54.1	6.2	93.8
640.0	10.0	.5	42.9	13.4	86.6
320.0	43.0	2.0	34.1	29.2	70.8
160.0	86.3	2.5	27.1	40.0	60.0
80.0	175.0	11.0	21.5	50.1	49.9
40.0	370.5	15.5	17.0	62.2	37.8
20.0	647.3	28.0	13.5	70.7	29.3
10.0	1078.5	35.0	10.7	77.5	22.5
5.0	1813.3	53.0	8.5	83.4	16.6
2.5	2977.0	73.0	6.8	88.4	11.6
1.3	4480.0	88.5	5.4	91.7	8.3
.6	7427.0	118.0	4.3	95.3	4.7
.3	I	I	I	100.0	.0

SIZE DISTRIBUTION FUNCTIONS

GAUDIN-SCHUMANN FUNCTION
CORRELATION COEFFICIENT= .97834
SIGNIFICANTLY DIFFERENT FROM 0
DISTRIBUTION MODULUS=1.072
SIZE MODULUS = 49.9

CUMULATIVE PERCENTAGE FREQUENCIES AT
10 17.8 20 37.5 30 58.0 40 78.9 50 100.3 60 121.9 70 143.8

ROSIN-RAMMLER FUNCTION
CORRELATION COEFFICIENT= .99821
SIGNIFICANTLY DIFFERENT FROM 0
UNIFORMITY COEFFICIENT=1.499
ABSOLUTE SIZE CONSTANT= 28.1

CUMULATIVE PERCENTAGE FREQUENCIES AT
10 19.2 20 45.2 30 66.8 40 81.7 50 90.7 60 95.6 70 98.0

APPENDIX 4

DERIVATION OF FINAL EQUATIONS FOR XRD QUANTITATIVE ANALYSIS

Olivine

Size calibration : this prescribed an S-shaped plot as seen in Figure 2.3.6. The values for each part of the relation between the absolute size constant and relative peak intensity $X_{s,ol}$ are as below.

ASC	$X_{s,ol}$	ASC	$X_{s,ol}$
<21	0.90	43	0.47
range :	1.06-	45	0.44
21-33	0.0078 ASC	47	0.41
33	0.79	49	0.39
35	0.72	51	0.38
37	0.64	53	0.37
39	0.55	>53	0.37
41	0.52		

These values were obtained for an olivine concentration in the sample mass of 15% (9% for the prepared 1 g mixture).

Concentration calibration : using some standard ground to yield an overall ASC = 42 μm, the relative peak intensity for a certain concentration, c, of olivine, ol, was given by

$$X_{c,ol} = -0.095 + 0.035 \% ol \qquad \text{(eqn. 2.3.7)}$$

Theoretical peak intensity : $X_{th,ol}$ is obtained by combining the above; and referencing the size effect to the peak intensity observed at the concentration used in equation 2.3.7

$$X_{th,ol} = X_{c,ol} \cdot X_{s,ol} / X_{s,(c = 15\%)}$$

where $X_{s,(c = 15\%)}$ is the peak intensity obtained for the standard used in the concentration calibration, ASC = 42 μm. This value was 0.48.

Error calibration : mixtures of the standards of known composition yielded an experimental peak intensity for olivine $X_{app,ol}$. This was related to the theoretical peak intensity :

$$X_{th,ol} = 0.135 + 0.474\, X_{app,ol} + 0.731\, X^2_{app,ol} \qquad \text{(eqn. 2.3.9)}$$

Final form : from above :

$$2.325(X_{c,ol} \cdot X_{s,ol}) = 0.135 + 0.474\, X_{app,ol} + 0.731\, X^2_{app,ol}$$

hence,

$$(-0.095 + 0.035[ol]) = 0.0581 + 0.2038\, X_{app,ol} + 0.3143\, X^2_{app,ol}$$

$$X_{s,ol}$$

$$\text{s.t.} \quad \%ol = ((1.66 + 5.81\ X_{app,ol} + 8.96\ X^2_{app,ol})/X_{s,ol}) + 2.73 \qquad \text{(eqn. 2.3.11)}$$

Serpentine

Adopting a similar procedure, allowing for the presence of olivine :

Size calibration : for (adjusted) serpentine concentrations = 37.5%

$$X_{s,sp} = 1.454 - 0.0231\ (ASC) \qquad \text{(eqn. 2.3.6)}$$

Concentration calibration : as the serpentine contained some olivine, peak intensities were first read for the latter. The olivine concentration was deduced using equation 2.3.7 after allowing for the effect of size. For example, in the case of a mounted mixture the sample weight of which contained 50% ground serpentine standard (ASC = 39 μm) the proportion of entrained olivine was deduced as follows :

The peak intensity of forsterite (100) line was 0.392. Hence, as the ASC of the standard used in the concentration calibration (Figure 2.3.8) was 42 μm) the peak intensity used to deduce to olivine concentration was 0.392. 0.48/0.55 where 0.48 and 0.55 are the values of $X_{s,ol}$ at 42 μm and 39 μm respectively in Figure 2.3.6.

From equation 2.3.7 the concentration of olivine in the sample was 12.5%, which in the overall serpentine standard is equivalent to 25.0%.

By readjusting the previous concentration values for the serpentine as present in the mounts used for concentration calibration it was found that

$$X_{c,sp} = 0.010 + 0.016 \% sp$$

where $X_{c,sp}$ is the peak intensity observed for serpentine at an ASC of 39 μm.

Theoretical peak intensity $X_{th,sp}$

As for olivine,

$$X_{th,sp} = X_{c,sp}.X_{s,sp} / X_{s,(c = 37.5\%)}$$

Error Calibration Equating the experimental with the theoretically derived values

$$X_{th,sp} = -0.022 + 0.815 X_{app,sp} \qquad \text{(eqn.2.3.10)}$$

Final Form : From above

$$1.694 X_{c,sp} X_{s,sp} = -0.022 + 0.815 X_{app,sp}$$

$$0.016 \% sp = (-0.022 + 0.815 X_{app,sp})/ (2.455 - 0.039 ASC) - 0.010$$

$$\% sp = (-1.41 + 52.21 X_{app,sp})/ (2.455 - 0.039 ASC) - 0.655 \qquad \text{(eqn.2.3.12)}$$

APPENDIX 5

PROGRAM CECPM : QUANTITATIVE CLAY PHASE ANALYSIS

The following printout lists the program used to deduce the phase proportions in the solid products generated in a series of kinetic experiments (Chapter 4). The program may be considered in nine sections.

a) Setting of elemental concentration and program loop control variables
b) Data input : selected system, d spacing of 14-14.5 Å peak, elemental and water assay data
c) Selection of end-member chlorites (where relevant)
d) Setting of test EM matrix for chosen system using Subroutine KF1X1 or KF1X2
e) Solution of simultaneous equations using Subroutine F04ATF
f) Testing of data for physical reality : water mass balance
g) Storage of satisfactory solutions via Subroutine CONEVAL
h) Testing of loop control variables and continuation of test permutations

i) Output : 10 example solutions in full (phase concentrations, elemental and water assays) and a table which lists the meaned phase concentrations, standard deviations, meaned elemental and water compositions and structural formulae in terms of Si_{no}, Al_{no}, Fe_{no}, Mg_{no} for a $(Al,Si)_4\ O_{10}$ clay structural unit.

Maximum and minimum elemental assays

These values, as published for various clay minerals were used in Program CECPM.

	Element Assay (%)			
Mineral	Si	Al	Fe	Mg
chlorite	15.8, 10.5	14.7, 5.8	33.9, 0.0	21.3, 0.7
kandite	21.7, 19.8	20.9, 3.3	7.21,0.0	15.0, 0.0
montmorillonite	30.8, 21.9	13.0, 8.1	7.5, 0.0	4.5, 0.0
saponite*	25.2, 18.5	7.7, 2.1	6.3, 0.0	1.5, 0.0
vermiculite	17.0, 15.4	9.5, 5.7	8.3, 2.7	16.4, 11.6

* Although saponite was not included in the program, as this mineral was not produced in sufficiently significant quantities in the kinetic experiments, elemental assay data is presented here in consideration of those products noted in the phase diagrams.

```
      PROGRAM CECPM(INPUT,OUTPUT,TAPE6=INPUT,TAPE7=OUTPUT)
      REAL K(4,4),M(8,6),W(4),ALSI(5),WTR(4)
      REAL T(4),AA(4,4),WKS1(30),WKS2(10),S(4),ACC(4,4)
      REAL FECHL,SICHL,SISME,ALSME,NWTRINC,NWATER,KAOCON
      INTEGER COUNTCH,FEVERM,MGVERM,ALVERM,FESME,MGSME,ALCHL
C     M MATRIX READS
C     CHLORITE...M(X,1)   VERMICULITE...M(X,2)
C     SERPENTINE/KAOLINITE...M(X,3)   SMECTITE...M(X,5)
C     AMORPHOUS AL-HYDROXIDE...M(X,4)
      M(3,2)=9.46
      M(4,2)=5.65
      M(5,2)=8.28
      M(6,2)=2.68
      M(7,2)=16.43
      M(8,2)=11.56
      M(1,3)=19.78
      M(3,3)=3.15
      M(5,3)=7.21
      M(7,3)=15.00
      M(2,3)=21.76
      M(4,3)=20.91
      M(6,3)=0.0
      M(8,3)=0.0
      M(3,4)=51.0
      M(4,4)=1.0
      M(1,5)=28.67
      M(2,5)=23.51
      M(5,5)=4.8
      M(6,5)=0.1
      M(7,5)=4.50
      M(8,5)=0.50
      DO 4 I=1,4
    4 WTR(I)=0.0
      DO 5 I=1,5
    5 ALSI(I)=0.0
C     GENERAL LOOP VARIABLES
      ITOT=1
      IDSPAC=0
      DSPACN=1
      IDETECT=0
      JDETECT=0
      N=0
      PRNTSUM=0
C     PHASE ELEMENTAL ASSAY CONTROL VARIABLES FOR
C     9A SILICATE,CHLORITE,KAOLINITE/HALLOYSITE(KFIX2)
      COUNTCH=0
      RALFE=0.0
      RFE=0.0
      RMOLWT=0.0
      YI=0.0
      NWTRINC=1.48
      TETINCR=0.136
      TETMAX=1.0
      GIBBOEM=0.0
      RKHMAX=2.0
      RKHINCR=2.0
      ALOOHMX=30.0
      ALOOHIC=2.0
      MAXHYDR=20
      HYDMAX=44.98
C     STORES FOR ACCEPTED SOLUTIONS
      TCONCH=0.0
      TCONVR=0.0
      TCONIL=0.0
      TCONSM=0.0
      TCALOH=0.0
      TCCH2=0.0
      TCVR2=0.0
      TCIL2=0.0
      TCSM2=0.0
      TCALOH2=0.0
      DO 30 I=1,4
      DO 30 J=1,4
      ACC(I,J)=0.0
   30 CONTINUE
C     VARIABLES SET FOR F04ATF
      IA=4
      IAA=4
      IFAIL=0
      NDIM=4
C     SYSTEMS FIXED ACCORDING TO IDENT,IDENT1
```

```
C       1,0    CHL/VERM/KAND/9A ALSILICATE
C       1,1    CHL/VERM/KAND/AL-OH
C       1,2    CHL/VERM/KAND/9A ALSILICATE/AL-OH
C       3,X    AS ABOVE SM REPLACING CHL
C       2,0    KAND/MG-CAR8-SERP/9A ALSILICATE/AL-FE-OH
C       4,0    CHL/VERM/KAND/SM
C       4,2    CHL/VERM/KAND/SM/AL-OH
C       ENTER SYSTEM CODE,ASSAY DATA(SI,AL,FE,MG),WATER CONTENT,ERROR
        READ(6,1001) IDENT,IDENT1,(T(I),I=1,4),TGAH2O,ERROR
        TINTER=T(2)
        IF(IDENT1.EQ.2) ALHYDR=((T(2)-T(1))/0.4498)*0.6
        IF(IDENT1.EQ.2) ALOOHMX=2.0*ALHYDR
        IF(IDENT1.EQ.2) ALOOHIC=ALOOHMX-ALHYDR
        IF((IDENT.NE.3).AND.(IDENT1.EQ.2)) ALOOHIC=ALOOHIC/4.0
        IF((IDENT.EQ.3).AND.(IDENT1.EQ.2)) ALOOHIC=ALOOHIC/2.0
        WRITE(7,1250)
        WRITE(7,1251)
        WRITE(7,1252)
        WRITE(7,1625)
        WRITE(7,1253)(T(I),I=1,4)
        WRITE(7,1625)
        WRITE(7,1254) TGAH2O
        WRITE(7,1625)
        IF((IDENT.EQ.2).OR.(IDENT.EQ.3)) GOTO 20
        READ(6,1002)DSPAC,DSPAC1
        DSPACDF=DSPAC1-DSPAC
        DSPAC2=DSPAC
   20   CONTINUE
        IF((IDENT.EQ.2).OR.(IDENT.EQ.3)) GOTO 16
C       FIXATION OF SILICON CONCENTRATION LIMITS IN
C       CHLORITE FROM D SPACING (XRD)
C       DSPAC/AL4 REF.F.H.GILLERY AM.MIN.44(1959)PP150-151
        AL4=125.4661-8.721*DSPAC
        SI4=8.0-AL4
        SICHL=2.658813469*SI4-1.894798023
        IF((SICHL.GT.10.0).AND.(SICHL.LE.11.0)) COUNTCH=1
        IF(COUNTCH.NE.1) GOTO 10
        M(7,1)=2.0
        M(8,1)=0.0
        M(3,1)=11.6
        M(4,1)=11.0
   10   CONTINUE
        IF((SICHL.GT.11.0).AND.(SICHL.LE.12.4)) COUNTCH=2
        IF(COUNTCH.NE.2) GOTO 11
        M(7,1)=12.2
        M(8,1)=0.0
        M(3,1)=11.2
        M(4,1)=10.0
   11   CONTINUE
        IF((SICHL.GT.12.4).AND.(SICHL.LE.12.5)) COUNTCH=3
        IF(COUNTCH.NE.3) GOTO 12
        M(7,1)=6.0
        M(8,1)=0.0
        M(3,1)=10.3
        M(4,1)=9.2
   12   CONTINUE
        IF((SICHL.GT.12.5).AND.(SICHL.LE.13.6)) COUNTCH=5
        IF(COUNTCH.NE.5) GOTO 13
        M(7,1)=20.0
        M(8,1)=14.8
        M(3,1)=14.8
        M(4,1)=11.8
   13   CONTINUE
        IF((SICHL.GT.13.6).AND.(SICHL.LE.14.0)) COUNTCH=6
        IF(COUNTCH.NE.6) GOTO 14
        M(7,1)=16.0
        M(8,1)=14.0
        M(4,1)=10.0
        M(3,1)=10.8
   14   CONTINUE
        IF((SICHL.GT.14.0).AND.(SICHL.LE.15.2)) COUNTCH=7
        IF(COUNTCH.NE.7) GOTO 15
        M(7,1)=21.8
        M(8,1)=14.0
        M(3,1)=10.8
        M(4,1)=7.7
   15   CONTINUE
        IF(SICHL.GT.15.2) COUNTCH=8
        IF(COUNTCH.NE.8 ) GOTO 16
        M(7,1)=21.0
        M(8,1)=20.0
        M(3,1)=7.35
        M(4,1)=6.6
C       START OF LOOP PROCEDURES FOR INSERTION OF ESTIMATED CHEMICAL
C       ASSAY OF PHASES PRESENT,AND ESTIMATION OF MINERAL CONCENTRATION
```

```
   16 CONTINUE
      GIBBOEM=0.0
   19 CONTINUE
      ALCHL=0
   21 CONTINUE
      MGSME=0
   22 CONTINUE
      FESME=0
   23 CONTINUE
      ISISME=0
   24 CONTINUE
      NOKAND=0
   25 CONTINUE
      MGVERM=0
   26 CONTINUE
      FEVERM=0
      NWATER=1.5
   27 CONTINUE
      ALVERM=0
      TETRAAL=0.0
   28 CONTINUE
      MGCHL=0
      HYDROKH=0.0
   29 CONTINUE
      ALOOH=0.0
      IF(IDENT1.EQ.2) ALOOH=ALHYDR
   18 CONTINUE
      TETAL=0.0
   31 CONTINUE
      HYDRO=0.0
      IF(IDENT1.EQ.1) HYDRO=34.0
   32 CONTINUE
      IDETECT=IDETECT*JDETECT
      IF(IDENT1.NE.0) GOTO17
      IF(IDETECT.EQ.0) GOTO 17
      ALSI(1)=ALSI(1)+RALFE
      ALSI(2)=ALSI(2)+RFE
      ALSI(3)=ALSI(3)+RMOLWT
      ALSI(4)=ALSI(4)+TETAL
      ALSI(5)=ALSI(5)+YI
   17 CONTINUE
      IF(IDENT1.EQ.2) T(2)=TINTER-0.4498*ALOOH
C     SET UP EM MATRIX FOR MINERAL SYSTEM
      IF(IDENT.NE.2)CALL KFIX1(K,M,MGCHL,HYDRO,ALVERM,FEVERM,
     *MGVERM,SICHL,ALCHL,NOKAND,IDETECT,W,IDENT1,T,TETAL,
     *IDENT,ISISME,FESME,MGSME,RALFE,RFE,YI,RMOLWT)
      IF(IDENT.EQ.2) CALL KFIX2(K,HYDRO,HYDROKH,
     *NWATER,TETRAAL,T,W,GIBBOEM,RALFE,RFE,YI,RMOLWT)
      TOTAL=0.0
      TOTH2O=0.0
C     INVERT 4X4 MATRIX (REF.NAGFILE I.C.C.C.)
      CALL F04ATF(K,IA,T,NDIM,S,AA,IAA,WKS1,WKS2,IFAIL)
      IF(IFAIL.EQ.0)GOTO 35
      WRITE(7,2000) IFAIL
      GOTO 71
   35 CONTINUE
      DO 38 I=1,4
      TOTH2O=TOTH2O+(S(I)*W(I))
   38 TOTAL=TOTAL+S(I)
C     TEST RESULTS(NON-NEGATIVITY,SUMMATION,WATER BALANCE)
      IF(S(1).LT.0.0) GOTO 71
      IF(S(2).LT.0.0) GOTO 71
      IF(S(3).LT.0.0) GOTO 71
      IF(S(4).LT.0.0) GOTO 71
      IF(TGAH2O.LE.0.1) GOTO 36
      TOTH2O=TOTH2O+(ALOOH*0.15)
      IF((TOTH2O.GT.(TGAH2O*(1.0+ERROR/100.0))).OR.(TOTH2O.LT.(TGAH2O*
     *(1.0-(ERROR/100.0))))GOTO 71
   36 CONTINUE
      TOTAL=TOTAL+ALOOH/100.0
      IF(.(TOTAL.LE.1.1).AND.(TOTAL.GE.0.9))GOTO 39
      GOTO 71
   39 CONTINUE
C     ACCUMULATE ACCEPTABLE SOLUTIONS
      CALL CONEVAL(S,TCONCH,TCONVR,TCONIL,TCONSM,
     *TCCH2,TCVR2,TCIL2,TCSM2,WTR,W,ALOOH)
      IF(IDENT1.EQ.2) TCALOH=TCALOH+ALOOH
      IF(IDENT1.EQ.2) TCALOH2=TCALOH2+ALOOH**2.0
      IDETECT=1
      JDETECT=1
      N=N+1
      DO 37 IS=1,4
      DO 37 JS=1,4
      ACC(IS,JS)=ACC(IS,JS)+K(IS,JS)
   37 CONTINUE
```

```
      IF(PRNTSUM.GT.10) GOTO 73
C     PRINT FIRST 10 SOLUTIONS AND ASSOCIATED CHEMICAL ASSAYS
      AU=IDENT
      IF(IDENT.EQ.4) IDENT=1
      IF(IDENT.EQ.1)CALL K1PRNT(COUNTCH,S)
      IF(IDENT.EQ.2)WRITE(7,1100)(S(I),I=1,4)
      IF(IDENT.EQ.3)WRITE(7,1150)(S(I),I=1,4)
      IDENT=AU
      WRITE (7,1290)
      WRITE(7,1291)(K(1,I),I=1,4),W(1),(S(1)*W(1))
      WRITE(7,1292)(K(2,I),I=1,4),W(2),(S(2)*W(2))
      WRITE(7,1293)(K(3,I),I=1,4),W(3),(S(3)*W(3))
      WRITE(7,1294)(K(4,I),I=1,4),W(4),(S(4)*W(4))
      WRITE(7,1295)
      PRNTSUM=PRNTSUM+1
      IF(PRNTSUM.GT.10) WRITE(7,1296)
      GOTO 73
   71 CONTINUE
      JDETECT=0
   73 CONTINUE
C     LOOP ROUTINE CONTROL.SYSTEMS 1 AND 4
      IF(IDENT.EQ.4) GOTO 50
      IF(IDENT.NE.1) GOTO 75
      IF(IDENT1.EQ.1) GOTO 74
      IF(HYDRO.LT.MAXHYDR) GOTO32
      TETAL=TETAL+TETINCR
      IF(TETAL.LT.TETMAX) GOTO 31
   50 CONTINUE
      IF(IDENT1.EQ.0) GOTO 76
      ALOOH=ALOOH+ALOOHIC
      IF(ALOOH.LT.ALOOHMX) GOTO 18
      GOTO 76
   74 CONTINUE
      IF(HYDRO.LT.HYDMAX) GOTO 32
   76 CONTINUE
      IF((COUNTCH.EQ.9).AND.(TETAL.GE.TETMAX)) GOTO 40
      IF((IDENT1.EQ.1).AND.(COUNTCH.EQ.9))  GOTO 40
      IF((IDENT.EQ.4).AND.(COUNTCH.EQ.9)) GOTO 40
      I=1
      IF(COUNTCH.EQ.8)COUNTCH=9
      IF(COUNTCH.EQ.9)M((I+6),1)=10.0
      IF(COUNTCH.EQ.9)M((I+7),1)=8.0
      IF(COUNTCH.EQ.9)M((I+2),1)=6.2
      IF(COUNTCH.EQ.9)M((I+3),1)=5.0
      IF((COUNTCH.EQ.4).OR.(COUNTCH.EQ.9)) GOTO 31
   40 CONTINUE
      MGCHL=MGCHL+1
      IF(MGCHL.LE.ITOT) GOTO 29
      IF(MGCHL.GT.ITOT)ALVERM=ALVERM+1
      IF(ALVERM.LE.ITOT) GOTO 28
      IF(ALVERM.GT.ITOT) FEVERM=FEVERM+1
      IF(FEVERM.LE.ITOT) GOTO 27
      IF(FEVERM.GT.ITOT) MGVERM=MGVERM+1
      IF(MGVERM.LE.ITOT) GOTO 26
      IF(MGVERM.GT.ITOT) NOKAND=NOKAND+1
      IF(NOKAND.LE.ITOT) GOTO 25
      IF(IDENT.NE.4) GOTO 55
      ISISME=ISISME+1
      IF(ISISME.LE.ITOT) GOTO 24
      FESME=FESME+1
      IF(FESME.LE.ITOT) GOTO 23
      MGSME=MGSME+1
      IF(MGSME.LE.ITOT) GOTO 22
   55 CONTINUE
      IF(NOKAND.GT.ITOT) ALCHL=ALCHL+1
      IF(ALCHL.LE.ITOT) GOTO 21
      DSPAC=(DSPACDF*IDSPAC/DSPACN)+DSPAC2
      IDSPAC=IDSPAC+1
      IF(IDSPAC.LE.DSPACN) GOTO 20
      GOTO 72
   75 CONTINUE
C     LOOP ROUTINE CONTROL.SYSTEM 2
      IF(IDENT.NE.2) GOTO 77
      HYDRO=HYDRO+1.0
      IF(HYDRO.LE.1.5) GOTO 32
      HYDROKH=HYDROKH+RKHINCR
      IF(HYDROKH.LE.RKHMAX) GOTO 29
      TETRAAL=TETRAAL+TETINCR
      IF(TETRAAL.LE.TETMAX) GOTO 28
      NWATER=NWATER+NWTRINC
      IF(NWATER.LE.MAXHYDR) GOTO 27
      GIBBOEM=GIBBOEM+1.0
      IF(GIBBOEM.LE.1.5) GOTO 19
      GOTO 72
   77 CONTINUE
```

```
C       LOOP ROUTINE CONTROL.SYSTEM 3
        IF(IDENT.NE.3) GOTO 72
        IF(IDENT1.EQ.1) GOTO 78
        IF(HYDRO.LT.MAXHYDR) GOTO 32
        TETAL=TETAL+TETINCR
        IF(TETAL.LT.TETMAX) GOTO 31
        IF(IDENT1.EQ.0) GOTO 79
        ALOOH=ALOOH+ALOOHIC
        IF(ALOOH.LT.ALOOHMX) GOTO 18
        GOTO 79
   78   CONTINUE
        IF(HYDRO.LT.HYDMAX) GOTO 32
   79   CONTINUE
        ALVERM=ALVERM+1
        IF(ALVERM.LE.ITOT) GOTO 28
        IF(ALVERM.GT.ITOT) FEVERM=FEVERM+1
        IF(FEVERM.LE.ITOT) GOTO 27
        IF(FEVERM.GT.ITOT) MGVERM=MGVERM+1
        IF(MGVERM.LE.ITOT) GOTO 26
        IF(MGVERM.GT.ITOT) NOKAND=NOKAND+1
        IF(NOKAND.LE.ITOT) GOTO 25
        ISISME=ISISME+1
        IF(ISISME.LE.ITOT) GOTO 24
        FESME=FESME+1
        IF(FESME.LE.ITOT) GOTO 23
        MGSME=MGSME+1
        IF(MGSME.LE.ITOT) GOTO 22
   72   CONTINUE
C       END OF PERMUTATION TRIALS
        IF(N.EQ.0)WRITE(7,1300)
        IF(N.EQ.0)GOTO 100
        DO 61 I=1,4
        DO 62 J=1,4
        ACC(I,J)=ACC(I,J)/N
        K(I,J)=10.0
   62   CONTINUE
        WTR(I)=WTR(I)/N
   61   CONTINUE
        DO 63 I=1,5
        ALSI(I)=ALSI(I)/N
   63   CONTINUE
C       CALCULATE MEANED PHASE CONCENTRATIONS AND
C       STANDARD DEVIATION OF DISTRIBUTED VALUES
        CONCH=TCONCH/N
        CONVR=TCONVR/N
        CONIL=TCONIL/N
        CONSM=TCONSM/N
        IF(IDENT1.EQ.2) CONALOH=TCALOH/N
        IF(N.EQ.1) GOTO 65
        SDCH=SQRT((TCCH2-(N*(CONCH**2.0)))/(N-1))
        SDVR=SQRT((TCVR2-(N*(CONVR**2.0)))/(N-1))
        SDIL=SQRT((TCIL2-(N*(CONIL**2.0)))/(N-1))
        SDSM=SQRT((TCSM2-(N*(CONSM**2.0)))/(N-1))
        IF(IDENT1.EQ.2) SDALOH=SQRT((TCALOH2-(N*(CONALOH**2.0)))/(N-1))
   65   CONTINUE
        IF(N.EQ.1)SDCH=0.0
        IF(N.EQ.1) SDIL=0.0
        IF(N.EQ.1) SDVR=0.0
        IF(N.EQ.1) SDSM=0.0
        IF(IDENT.NE.2) GOTO 64
C       CALCULATE SI,AL,FE,MG NUMBERS IN STRUCTURAL FORMULAE
        K(1,1)=4.0
        K(2,1)=4.0
        K(3,1)=0.0
        K(4,1)=0.0
C       9A SILICATE STRUCTURAL FORMULA
        K(1,3)=4.0-2.0*ALSI(4)
        K(2,3)=2.0*(ALSI(4)+ALSI(5)*ALSI(1))
        K(3,3)=2.0*(ALSI(2)*ALSI(5))
        K(4,3)=2.0*(ALSI(5)*(1.0-ALSI(1)-ALSI(2)))
   64   CONTINUE
        J=1
        A=ACC(1,J)
        B=ACC(2,J)
        C=ACC(3,J)
        D=ACC(4,J)
        IF(IDENT.NE.1) GOTO 80
C       CHLORITE STRUCTURAL FORMULA
        K(1,1)=1.53+0.112*A+0.0132*B-0.0151*C-0.0148*D
       *+0.0023*(A**2.0)-0.0021*(B**2.0)+0.0002*(C**2.0)
       *-0.0007*(D**2.0)
        K(2,1)=2.56-0.261*A+0.255*B-0.0066*C-0.031*D
       *+0.0079*(A**2.0)-0.0034*(B**2.0)+0.0002*(D**2.0)
        K(3,1)=0.388+0.051*A-0.0641*B+0.103*C-0.0269*D
       *-0.0028*(A**2.0)+0.0025*(B**2.0)+0.0004*(C**2.0)
```

```
     *+0.0009*(D**2.0)
      K(4,1)=2.77-0.274*A+0.0297*B-0.0221*C+0.276*D
     *+0.0076*(A**2.0)-0.004*(B**2.0)+0.0002*(C**2.0)
     *-0.0027*(D**2.0)
      IF(AU.EQ.4) GOTO 83
   80 CONTINUE
      IF(IDENT1.EQ.1) GOTO 66
C     9A SILICATE STRUCTURAL FORMULA
      K(1,4)=4.0-2.0*ALSI(4)
      K(2,4)=2.0*(ALSI(4)+ALSI(5)*ALSI(1))
      K(3,4)=2.0*(ALSI(2)*ALSI(5))
      K(4,4)=2.0*(ALSI(5)*(1.0-ALSI(1)-ALSI(2)))
   66 CONTINUE
      IF((IDENT.EQ.1).OR.(IDENT.EQ.2)) GOTO 83
C     SMECTITE STRUCTURAL FORMULA
      K(1,1)=3.58+0.0917*A-0.139*B-0.0653*C-0.0954*D
     *-0.002*(A**2.0)+0.0047*A*B-0.0024*(B**2.0)
     *+0.0038*(C**2.0)+0.0055*(D**2.0)
      K(2,1)=1.63-0.0235*A+0.0756*B+0.0163*C-0.0154*D
     *-0.0004*(A**2.0)+0.0016*(B**2.0)-0.0066*(C**2.0)
     *-0.0042*(D**2.0)
      K(3,1)=1.36-0.109*A+0.0326*B+0.0751*C-0.0108*D
     *+0.002*(A**2.0)-0.0018*(B**2.0)-0.0005*(C**2.0)
     *+0.0009*(D**2.0)
      K(4,1)=-0.722+0.0752*A-0.0097*B+0.0027*C+0.137*D
     *-0.0016*(A**2.0)-0.0015*(C**2.0)+0.0033*(D**2.0)
      IF(IDENT.EQ.3) GOTO 83
      K(1,4)=K(1,1)
      K(2,4)=K(2,1)
      K(3,4)=K(3,1)
      K(4,4)=K(4,1)
      AU=IDENT
      IDENT=1
      GOTO 64
   83 CONTINUE
      IF(IDENT.EQ.2) GOTO 85
      J=2
      A=ACC(1,J)
      B=ACC(2,J)
      C=ACC(3,J)
      D=ACC(4,J)
C     VERMICULITE STRUCTURAL FORMULA
      K(1,2)=2.97+0.0717*A-0.0778*B-0.0366*C-0.0414*D
      K(2,2)=1.56-0.0541*A+0.139*B-0.0199*C-0.0202*D
      K(3,2)=0.513-0.0143*A-0.0153*B+0.0797*C-0.0096*D
      K(4,2)=3.27-0.0696*A-0.121*B-0.0596*C+0.106*D
      J=3
      A=ACC(1,J)
      B=ACC(2,J)
      C=ACC(3,J)
      D=ACC(4,J)
C     KANDITE STRUCTURAL FORMULA
      K(1,3)=-3.01+0.474*A-0.0369*B-0.0096*C-0.032*D
     *-0.0093*(A**2.0)-0.0003*(B**2.0)+0.0052*(C**2.0)
     *+0.0001*(D**2.0)
      K(2,3)=-0.73+0.0842*A+0.145*B+0.0315*C-0.0266*D
     *-0.0025*(A**2.0)-0.0021*(B**2.0)-0.0269*(C**2.0)
     *+0.0011*(D**2.0)
      K(3,3)=-2.910+0.23*A+0.0432*B+0.0468*C+0.005*D
     *-0.0053*(A**2.0)-0.0011*(B**2.0)-0.0048*(C**2.0)
     *+0.0005*(D**2.0)
      K(4,3)=-4.53+0.569*A-0.149*B+0.0177*C+0.0429*D
     *-0.0134*(A**2.0)+0.0037*(B**2.0)-0.0057*(C**2.0)
     *+0.0006*(D**2.0)
   85 CONTINUE
      WRITE(7,1625)
      WRITE(7,1500)
      WRITE(7,1501)
      WRITE(7,1503)
      WRITE(7,1501)
      WRITE(7,1500)
      WRITE(7,1502)
      WRITE(7,1504)
      WRITE(7,1502)
      WRITE(7,1510)
      WRITE(7,1502)
      IF(IDENT.EQ.4) IDENT=1
      IF(IDENT.EQ.1) WRITE(7,1505) (100.0*CONCH), (100.0*SDCH),
     *(ACC(I,1),I=1,4),(K(I,1),I=1,4),WTR(1)
      IF(IDENT.EQ.2) WRITE(7,1506) (100.0*CONCH), (100.0*SDCH),
     *(ACC(I,1),I=1,4),(K(I,1),I=1,4),WTR(1)
      IF(IDENT.EQ.3) WRITE(7,1507) (100.0*CONCH), (100.0*SDCH),
     *(ACC(I,1),I=1,4),(K(I,1),I=1,4),WTR(1)
      WRITE(7,1502)
      IF(IDENT.EQ.1) WRITE(7,1515) (100.0*CONVR),(100.0*SDVR),
```

```
     *(ACC(I,2),I=1,4),(K(I,2),I=1,4),WTR(2)
      IF(IDENT.EQ.2) WRITE(7,1516) (100.0*CONVR),(100.0*SDVR),
     *(ACC(I,2),I=1,4),(K(I,2),I=1,4),WTR(2)
      IF(IDENT.EQ.3) WRITE(7,1515) (100.0*CONVR),(100.0*SDVR),
     *(ACC(I,2),I=1,4),(K(I,2),I=1,4),WTR(2)
      WRITE(7,1502)
      IF(IDENT.EQ.1) WRITE(7,1525)(100.0*CONIL),(100.0*SDIL),
     *(ACC(I,3),I=1,4),(K(I,3),I=1,4),WTR(3)
      IF(IDENT.EQ.2) WRITE(7,1526)(100.0*CONIL),(100.0*SDIL),
     *(ACC(I,3),I=1,4),(K(I,3),I=1,4),WTR(3)
      IF(IDENT.EQ.3) WRITE(7,1525)(100.0*CONIL),(100.0*SDIL),
     *(ACC(I,3),I=1,4),(K(I,3),I=1,4),WTR(3)
      IF(IDENT.EQ.2) GOTO 90
      KAOCON=(ACC(1,3)-M(1,3))*CONIL/(M(2,3)-M(1,3))
      SERPCON =CONIL-KAOCON
   90 CONTINUE
      IDENT=AU
      WRITE(7,1502)
      IF((IDENT1.EQ.1).OR.(IDENT.EQ.2)) WRITE(7,1535)(100.0*CONSM)
     *,(100.0*SDSM),(ACC(I,4),I=1,4),(K(I,4),I=1,4),WTR(4)
      IF(IDENT.EQ.4) WRITE(7,1507) (100.0*CONSM)
     *,(100.0*SDSM),(ACC(I,4),I=1,4),(K(I,4),I=1,4),WTR(4)
      IF((IDENT.EQ.1).AND.(IDENT1.NE.1)) WRITE(7,1526) (100.0*CONSM)
     *,(100.0*SDSM),(ACC(I,4),I=1,4),(K(I,4),I=1,4),WTR(4)
      WRITE(7,1502)
      IF(IDENT1.EQ.2) WRITE(7,1536) CONALOH,SDALOH
      WRITE(7,1502)
      WRITE(7,1500)
      WRITE(7,1540)
      IF(IDENT.NE.2) WRITE(7,1545)(100.0*SERPCON),(100.0*KAOCON)
      WRITE(7,1650) ERROR
  100 CONTINUE
 1001 FORMAT(I1,2X,I1,6F8.3)
 1002 FORMAT(2F8.3)
 1250 FORMAT(///50X,27HCOMPUTED SOLUTIONS FOR CLAY)
 1251 FORMAT(50X,27HMINERAL CONCENTRATIONS FROM)
 1252 FORMAT(47X,35HAA ANALYSES OF -75 RESIDUAL PRODUCT)
 1253 FORMAT(1/X,6HSI 0/0,F8.3,8X,10X,6HAL 0/0,F8.3,8X,10X,
     *6HFE 0/0,F8.3,8X,10X,6HMG 0/0,F8.3,8X)
 1254 FORMAT(50X,17H 0/0 WT.LOSS TGA.,F11.3)
 1290 FORMAT (2X,21HCHEMICAL COMPOSITIONS,
     *63X,29HSTRUCTURAL WATER DISTRIBUTION)
 1291 FORMAT(2X,6HSI 0/0,9X,F6.3,2X,6HSI 0/0,7X,F6.3,2X,
     *6HSI 0/0,3X,F6.3,2X,6HSI 0/0,6X,F6.3,
     *5X,17HMINERAL 1 H20 0/0,F7.3,1X,12HDISTRIBUTION,F7.3)
 1292 FORMAT(2X,6HAL 0/0,9X,F6.3,2X,6HAL 0/0,7X,F6.3,2X,
     *6HAL 0/0,3X,F6.3,2X,6HAL 0/0,6X,F6.3,
     *5X,17HMINERAL 2 H20 0/0,F7.3,1X,12HDISTRIBUTION,F7.3)
 1293 FORMAT(2X,6HFE 0/0,9X,F6.3,2X,6HFE 0/0,7X,F6.3,2X,
     *6HFE 0/0,3X,F6.3,2X,6HFE 0/0,6X,F6.3,
     *5X,17HMINERAL 3 H20 0/0,F7.3,1X,12HDISTRIBUTION,F7.3)
 1294 FORMAT(2X,6HMG 0/0,9X,F6.3,2X,6HMG 0/0,7X,F6.3,2X,
     *6HMG 0/0,3X,F6.3,2X,6HMG 0/0,6X,F6.3,
     *5X,17HMINERAL 4 H20 0/0,F7.3,1X,12HDISTRIBUTION,F7.3)
 1295 FORMAT (2X,130("-"))
 1296 FORMAT (2X,26HEXCESS READOUT.NOT PRINTED)
 1100 FORMAT(2X,10HAL-KANDITE,F11.3,2X,13HMG-FE-KANDITE,
     *F6.3,2X,12HPYROPHYLLITE,F3.2,2X,12HME-HYDROXIDE,F6.3)
 1150 FORMAT (2X,7HKANDITE,F14.3,2X,11HVERMICULITE,F8.3,2X,
     *8HSMECTITE,F7.3,2X,12HAL-HYDROXIDE,F6.3)
 1300 FORMAT(2X,22HNO SOLUTIONS AVAILABLE)
 1500 FORMAT(132("*"))
 1501 FORMAT(16X,1H*,9X,1H*,8X,1H*,27X,1H*,27X,1H*,9X,1H*)
 1502 FORMAT(16X,1H*,9X,1H*,8X,1H*,6X,1H+,6X,1H+,6X,1H+,6X,1H*,6X,
     *1H+,6X,1H+,6X,1H+,6X,1H*,9X,1H*)
 1503 FORMAT(5X,7HMINERAL,4X,1H*,10H MASS0/0 *,9H ST.DEV *,
     *28H ELEMENTAL COMPOSITION 0/0 *,28H     ELEMENTAL FORMULA     *,
     *10H H20 0/0 *)
 1504 FORMAT(35X,1H*,2(6H  SI  ,1H+,6H  AL  ,1H+,6H  FE  ,1H+
     *,6H  MG  ,1H*),9X,1H*)
 1505 FORMAT(4X,13HCHLORITE    *,
     *2X,F6.2,1X,1H*,1X,F6.2,1X,1H*,3(1X,F4.1,1X,1H+),1X,F4.1,1X,
     *1H*,3(1X,F4.2,1X,1H+),1X,F4.2,1X,1H*,F7.2,3H  *)
 1506 FORMAT(17H 7-10A KANDITE  *,
     *2X,F6.2,1X,1H*,1X,F6.2,1X,1H*,3(1X,F4.1,1X,1H+),1X,F4.1,1X,
     *1H*,3(1X,F4.2,1X,1H+),1X,F4.2,1X,1H*,F7.2,3H  *)
 1507 FORMAT(17H   SMECTITE     *,
     *2X,F6.2,1X,1H*,1X,F6.2,1X,1H*,3(1X,F4.1,1X,1H+),1X,F4.1,1X,
     *1H*,3(1X,F4.2,1X,1H+),1X,F4.2,1X,1H*,F7.2,3H  *)
 1510 FORMAT(35X,57("*"))
 1515 FORMAT(17H  VERMICULITE   *,
     *2X,F6.2,1X,1H*,1X,F6.2,1X,1H*,3(1X,F4.1,1X,1H+),1X,F4.1,1X,
     *1H*,3(1X,F4.2,1X,1H+),1X,F4.2,1X,1H*,F7.2,3H  *)
 1516 FORMAT(17H ME-C03/SI205   *,
     *2X,F6.2,1X,1H*,1X,F6.2,1X,1H*,3(1X,F4.1,1X,1H+),1X,F4.1,1X,
```

```
     *1H*,3(1X,F4.2,1X,1H+),1X,F4.2,1X,1H*,F7.2,3H   *)
 1525 FORMAT(4X,13HKANDITE        *,
     *2X,F6.2,1X,1H*,1X,F6.2,1X,1H*,3(1X,F4.1,1X,1H+),1X,F4.1,1X,
     *1H*,3(1X,F4.2,1X,1H+),1X,F4.2,1X,1H*,F7.2,3H   *)
 1526 FORMAT(17H 9A ALSILICATE    *,
     *2X,F6.2,1X,1H*,1X,F6.2,1X,1H*,3(1X,F4.1,1X,1H+),1X,F4.1,1X,
     *1H*,3(1X,F4.2,1X,1H+),1X,F4.2,1X,1H*,F7.2,3H   *)
 1535 FORMAT(17H ME-HYDROXIDE     *,
     *2X,F6.2,1X,1H*,1X,F6.2,1X,1H*,3(1X,F4.1,1X,1H+),1X,F4.1,1X,
     *1H*,3(1X,F4.2,1X,1H+),1X,F4.2,1X,1H*,F7.2,3H   *)
 1536 FORMAT(17H ALOOH.BOEHMITE *,2X,F6.2,1X,1H*,1X,F6.2,1X,1H*,3(6X,1H
     *+),6X,1H*,3(6X,1H+),6X,1H*,9X,1H*)
 1540 FORMAT(///15HADDITIONAL DATA)
 1545 FORMAT(/14HSERPENTINE 0/0,F5.1,13HKAOLINITE 0/0,F5.1)
 1625 FORMAT(1H )
 1650 FORMAT(//2X,21HH2O BALANCE ERROR IS ,F4.1,4H 0/0)
 2000 FORMAT (24HERROR IN F04ATF IFAIL = ,I2)
      STOP
      END

      SUBROUTINE CONEVAL (S,TCONCH,TCONVR,TCONIL,TCONSM,
     *TCCH2,TCVR2,TCIL2,TCSM2,WTR,W,ALOOH)
      REAL S(4),WTR(4),W(4)
      TOTAL=0.0
      DO 10 I=1,4
      WTR(I)=WTR(I)+W(I)
   10 TOTAL=TOTAL+S(I)
      TOTAL=TOTAL+ALOOH/100.0
      DO 20 I=1,4
      S(I)=S(I)/TOTAL
   20 CONTINUE
      TCONCH=TCONCH+S(1)
      TCONVR=TCONVR+S(2)
      TCONIL=TCONIL+S(3)
      TCONSM=TCONSM+S(4)
      TCCH2=TCCH2+S(1)**2.0
      TCVR2=TCVR2+S(2)**2.0
      TCIL2=TCIL2+S(3)**2.0
      TCSM2=TCSM2+S(4)**2.0
      RETURN
      END


      SUBROUTINE KFIX1(K,M,MGCHL,HYDRO,ALVERM,FEVERM,
     *MGVERM,SICHL,ALCHL,NOKAND,IDETECT,W,IDENT1,I,TETAL,
     *IDENT,ISISME,FESME,MGSME,RALFE,RFE,YI,RMOLWT)
C     FIXATION OF CHLORITE-VERMICULITE-KANDITE
CC    (SERPENTINE-KAOLINITE)-SMECTITE(MONTMORILLONITE)-
C     9A SILICATE-AL-OH SYSTEM
      INTEGER FEVERM,MGVERM,ALVERM,FESME,ALCHL
      REAL K(4,4),M(8,6),W(4),T(4)
      RALFE=T(2)/(T(2)+T(3)+T(4))
      RFE=T(3)/(T(2)+T(3)+T(4))
      YI=(3.0+TETAL)/(3.0*(RALFE+RFE)+(1.0-RFE-RALFE)*2.0)
      RMOLWT=26.98*(YI*RALFE+TETAL)+(55.85*YI*RFE)+24.312*(YI*(1.0-RFE
     *-RALFE))+28.086*(2.0-TETAL)+97.0+HYDRO*18.0
      ITOT=1
      I=1
      IF(IDENT.EQ.4) GOTO 10
      IF(IDENT.NE.1) GOTO 11
   10 CONTINUE
      K(1,1)=SICHL
      K(2,1)=(M((I+2),1)-M((I+3),1))*ALCHL/ITOT+M((I+3),1)
      K(4,1)=(M((I+6),1)-M((I+7),1))*MGCHL/ITOT+M((I+7),1)
      K(3,1)=K(4,1)*(-1.571796478)+34.3801641
      W(1)=11.75
   11 CONTINUE
      IF(IDENT.NE.3) GOTO 12
      K(1,1)=((M(1,5)-M(2,5))*ISISME/ITOT)+M(2,5)
      K(2,1)=10.11
      IF(K(1,1).GT.26.0) K(2,1)=11.61
      K(3,1)=((M(5,5)-M(6,5))*FESME/ITOT)+M(6,5)
      K(4,1)=((M(7,5)-M(8,5))*MGSME/ITOT)+M(8,5)
      W(1)=19.12
   12 CONTINUE
      K(1,2)=16.29
      K(2,2)=((M(3,2)-M(4,2))*ALVERM/ITOT)+M(4,2)
      K(3,2)=((M(5,2)-M(6,2))*FEVERM/ITOT)+M(6,2)
      K(4,2)=((M(7,2)-M(8,2))*MGVERM/ITOT)+M(8,2)
      K(1,3)=((M(1,3)-M(2,3))*NOKAND/ITOT)+M(2,3)
```

```
      K(2,3)=((M(3,3)-M(4,3))*NOKAND/ITOT)+M(4,3)
      K(3,3)=((M(5,3)-M(6,3))*NOKAND/ITOT)+M(6,3)
      K(4,3)=((M(7,3)-M(8,3))*NOKAND/ITOT)+M(8,3)
      W(2)=20.1
      W(3)=13.58
      IF(NOKAND.EQ.0)W(3)=14.1
      IF(IDENT.NE.4) GOTO 14
      K(1,4)=((M(1,5)-M(2,5))*ISISME/ITOT)+M(2,5)
      K(2,4)=10.11
      IF(K(1,4).GT.26.0) K(2,4)=16.
      IF(K(1,4).GT.26.0) K(2,4)=11.61
      K(3,4)=((M(5,5)-M(6,5))*FESME/ITOT)+M(6,5)
      K(4,4)=((M(7,5)-M(8,5))*MGSME/ITOT)+M(8,5)
      W(4)=19.12
      GOTO 20
   14 CONTINUE
        IF(IDENT1 .EQ.1) GOTO15
      K(1,4)=(2.0-TETAL)*2808.6/RMOLWT
      K(2,4)=2698.0*(TETAL+YI*RALFE)/RMOLWT
      K(3,4)=5585.0*RFE*YI/RMOLWT
      K(4,4)=2431.2*YI*(1.0-RFE-RALFE)/RMOLWT
      W(4)=1800.0*(HYDRO+0.5)/RMOLWT
      GOTO 20
   15 CONTINUE
      K(1,4)=0.0
      K(2,4)=HYDRO*T(2)/(T(2)+T(3))
      K(3,4)=62.85*T(3)/(T(2)+T(3))
        K(4,4)=0.0
      W(4)=((94.9357-1.8883*HYDRO)*T(2)+10.01*T(3))/(T(2)+T(3))
   20 CONTINUE
      IF(IDETECT.EQ.1) HYDRO=HYDRO+1.0
      IF(IDETECT.EQ.0) HYDRO=HYDRO+1.6
      RETURN
      END



      SUBROUTINE KFIX2(K,HYDRO,HYDROKH,
     *NWATER,TETRAAL,T,W,GIBBOEM,RALFE,RFE,YI,RMOLWT)
C       FIXATION OF AL-MG-FE-KANDITE(S)-AL-SI-HYDROXIDE
C       ME-HYDROXIDE-MG CARBONATE(NO.6-484) SYSTEM
      REAL K(4,4),T(4),W(4),NWATER
      RALFE=T(2)/(T(2)+T(3)+T(4))
      RFE=T(3)/(T(2)+T(3)+T(4))
      DIV=(258.132+HYDROKH*18.0)/100.0
      YI=(3.0+TETRAAL)/(3.0*(RFE+RALFE)+(1.0-RFE-RALFE)*2.0)
      RMOLWT=26.98*(YI*RALFE+TETRAAL)+55.85*YI*RFE+24.312*(YI*(1.0-RFE
     *-RALFE))+28.086*(2.0-TETRAAL)+97.0+NWATER*18.0
      K(1,1)=56.172/DIV
      K(2,1)=53.96/DIV
      K(3,1)=0.0
      K(4,1)=0.0
      K(1,2)=19.78*HYDRO
      K(2,2)=3.15*HYDRO
      K(3,2)=7.21*HYDRO
      K(4,2)=26.00-11.0*HYDRO
      K(1,3)=(2.0-TETRAAL)*2808.6/RMOLWT
      K(2,3)=2698.0*(TETRAAL+YI*RALFE)/RMOLWT
      K(3,3)=5585.0*RFE*YI/RMOLWT
      K(4,3)=2431.2*YI*(1.0-RFE-RALFE)/RMOLWT
      K(1,4)=0.0
      K(4,4)=0.0
      K(2,4)=((10.39*GIBBOEM)+34.6)*T(2)/(T(2)+T(3))
      K(3,4)=62.85*T(3)/(T(2)+T(3))
      W(1)=(2.0+HYDROKH)*18.0/DIV
      W(2)=36.0-23.0*HYDRO
      W(3)=1800.0*(NWATER+0.5)/RMOLWT
      W(4)=((34.62-19.62*GIBBOEM)*T(2)+10.01*T(3))/
     *(T(2)+T(3))
      RETURN
      END
```

```
      SUBROUTINE K1PRNT(COUNTCH,S)
      REAL S(4)
      INTEGER COUNTCH
      IF(COUNTCH.EQ.1)WRITE(7,1280)(S(I),I=1,4)
      IF(COUNTCH.EQ.2)WRITE(7,1281)(S(I),I=1,4)
      IF(COUNTCH.EQ.3)WRITE(7,1282)(S(I),I=1,4)
      IF(COUNTCH.EQ.4)WRITE(7,1283)(S(I),I=1,4)
      IF(COUNTCH.EQ.5)WRITE(7,1284)(S(I),I=1,4)
      IF(COUNTCH.EQ.6)WRITE(7,1285)(S(I),I=1,4)
      IF(COUNTCH.EQ.7)WRITE(7,1286)(S(I),I=1,4)
      IF(COUNTCH.EQ.8)WRITE(7,1287)(S(I),I=1,4)
      IF(COUNTCH.EQ.9)WRITE(7,1288)(S(I),I=1,4)
1280  FORMAT(2X,8HDAPHNITE,F13.3,2X,
     *11HVERMICULITE,F9.3,2X,7HKANDITE,F8.3,2X
     *12HSM/9A/ME-OH ,F6.3)
1281  FORMAT (2X,12HRIPIDOLITE I,F9.3,2X,
     *11HVERMICULITE,F8.3,2X,7HKANDITE,F8.3,2X
     *12HSM/9A/ME-OH ,F6.3)
1282  FORMAT (2X,11HBRUNSVIGITE,F10.3,2X,
     *11HVERMICULITE,F8.3,2X,7HKANDITE,F8.3,2X
     *12HSM/9A/ME-OH ,F6.3)
1283  FORMAT (2X,13HRIPIDOLITE II,F8.3,2X,
     *11HVERMICULITE,F8.3,2X,7HKANDITE,F8.3,2X
     *12HSM/9A/ME-OH ,F6.3)
1284  FORMAT (2X,11HSHERIDANITE,F10.3,2X,
     *11HVERMICULITE,F8.3,2X,7HKANDITE,F8.3,2X
     *12HSM/9A/ME-OH ,F6.3)
1285  FORMAT (2X,9HRODINGITE,F12.3,2X,
     *11HVERMICULITE,F8.3,2X,7HKANDITE,F8.3,2X
     *12HSM/9A/ME-OH ,F6.3)
1286  FORMAT (2X,11HCLINOCHLORE,F10.3,2X,
     *11HVERMICULITE,F8.3,2X,7HKANDITE,F8.3,2X
     *12HSM/9A/ME-OH ,F6.3)
1287  FORMAT (2X,9HPENNINITE,F12.3,2X,
     *11HVERMICULITE,F8.3,2X,7HKANDITE,F8.3,2X
     *12HSM/9A/ME-OH ,F6.3)
1288  FORMAT (2X,10HDIABANTITE,F11.3,2X,
     *11HVERMICULITE,F8.3,2X,7HKANDITE,F8.3,2X
     *12HSM/9A/ME-OH ,F6.3)
      RETURN
      END
```

COMPUTED SOLUTIONS FOR CLAY
MINERAL CONCENTRATIONS FROM
AA ANALYSES OF -75 RESIDUAL PRODUCT

SI 0/0 16.120 AL 0/0 7.420 FE 0/0 4.230 MG 0/0 9.710

0/0 WT.LOSS TGA. 16.860

SHERIDANITE	.193	VERMICULITE	.585	KANDITE	.081	SM/9A/ME-OH	.141		
CHEMICAL COMPOSITIONS								STRUCTURAL WATER DISTRIBUTION	
SI 0/0	12.729	SI 0/0	16.290	SI 0/0	21.760	SI 0/0	25.640	MINERAL 1 H2O 0/0 11.750 DISTRIBUTION	2.273
AL 0/0	11.800	AL 0/0	5.650	AL 0/0	20.910	AL 0/0	5.042	MINERAL 2 H2O 0/0 20.100 DISTRIBUTION	11.749
FE 0/0	11.118	FE 0/0	2.680	FE 0/0	0	FE 0/0	5.950	MINERAL 3 H2O 0/0 14.100 DISTRIBUTION	1.143
MG 0/0	14.800	MG 0/0	11.560	MG 0/0	0	MG 0/0	5.946	MINERAL 4 H2O 0/0 17.254 DISTRIBUTION	2.431
SHERIDANITE	.172	VERMICULITE	.591	KANDITE	.068	SM/9A/ME-OH	.168		
CHEMICAL COMPOSITIONS								STRUCTURAL WATER DISTRIBUTION	
SI 0/0	12.729	SI 0/0	16.290	SI 0/0	21.760	SI 0/0	23.731	MINERAL 1 H2O 0/0 11.750 DISTRIBUTION	2.026
AL 0/0	11.800	AL 0/0	5.650	AL 0/0	20.910	AL 0/0	6.897	MINERAL 2 H2O 0/0 20.100 DISTRIBUTION	11.878
FE 0/0	11.118	FE 0/0	2.680	FE 0/0	0	FE 0/0	6.177	MINERAL 3 H2O 0/0 14.100 DISTRIBUTION	.964
MG 0/0	14.800	MG 0/0	11.560	MG 0/0	0	MG 0/0	6.172	MINERAL 4 H2O 0/0 17.134 DISTRIBUTION	2.883
SHERIDANITE	.142	VERMICULITE	.600	KANDITE	.050	SM/9A/ME-OH	.208		
CHEMICAL COMPOSITIONS								STRUCTURAL WATER DISTRIBUTION	
SI 0/0	12.729	SI 0/0	16.290	SI 0/0	21.760	SI 0/0	21.847	MINERAL 1 H2O 0/0 11.750 DISTRIBUTION	1.667
AL 0/0	11.800	AL 0/0	5.650	AL 0/0	20.910	AL 0/0	8.727	MINERAL 2 H2O 0/0 20.100 DISTRIBUTION	12.066
FE 0/0	11.118	FE 0/0	2.680	FE 0/0	0	FE 0/0	6.400	MINERAL 3 H2O 0/0 14.100 DISTRIBUTION	.703
MG 0/0	14.800	MG 0/0	11.560	MG 0/0	0	MG 0/0	6.395	MINERAL 4 H2O 0/0 17.016 DISTRIBUTION	3.539
SHERIDANITE	.093	VERMICULITE	.615	KANDITE	.020	SM/9A/ME-OH	.271		
CHEMICAL COMPOSITIONS								STRUCTURAL WATER DISTRIBUTION	
SI 0/0	12.729	SI 0/0	16.290	SI 0/0	21.760	SI 0/0	13.990	MINERAL 1 H2O 0/0 11.750 DISTRIBUTION	1.095
AL 0/0	11.800	AL 0/0	5.650	AL 0/0	20.910	AL 0/0	11.531	MINERAL 2 H2O 0/0 20.100 DISTRIBUTION	12.364
FE 0/0	11.118	FE 0/0	2.680	FE 0/0	0	FE 0/0	6.620	MINERAL 3 H2O 0/0 14.100 DISTRIBUTION	.288
MG 0/0	14.800	MG 0/0	11.560	MG 0/0	0	MG 0/0	6.616	MINERAL 4 H2O 0/0 16.900 DISTRIBUTION	4.584
SHERIDANITE	.020	VERMICULITE	.596	KANDITE	.054	SM/9A/ME-OH	.330		
CHEMICAL COMPOSITIONS								STRUCTURAL WATER DISTRIBUTION	
SI 0/0	12.729	SI 0/0	16.290	SI 0/0	19.760	SI 0/0	18.158	MINERAL 1 H2O 0/0 11.750 DISTRIBUTION	.238
AL 0/0	11.800	AL 0/0	5.650	AL 0/0	3.150	AL 0/0	12.311	MINERAL 2 H2O 0/0 20.100 DISTRIBUTION	11.979
FE 0/0	11.118	FE 0/0	2.680	FE 0/0	7.210	FE 0/0	6.838	MINERAL 3 H2O 0/0 13.580 DISTRIBUTION	.735
MG 0/0	14.800	MG 0/0	11.560	MG 0/0	15.000	MG 0/0	6.833	MINERAL 4 H2O 0/0 16.785 DISTRIBUTION	5.533
SHERIDANITE	.018	VERMICULITE	.552	KANDITE	.080	SM/9A/ME-OH	.350		
CHEMICAL COMPOSITIONS								STRUCTURAL WATER DISTRIBUTION	
SI 0/0	12.729	SI 0/0	16.290	SI 0/0	19.760	SI 0/0	18.158	MINERAL 1 H2O 0/0 11.750 DISTRIBUTION	.217
AL 0/0	11.800	AL 0/0	5.650	AL 0/0	3.150	AL 0/0	12.311	MINERAL 2 H2O 0/0 20.100 DISTRIBUTION	11.088
FE 0/0	2.944	FE 0/0	2.680	FE 0/0	7.210	FE 0/0	6.838	MINERAL 3 H2O 0/0 13.580 DISTRIBUTION	1.082
MG 0/0	20.000	MG 0/0	11.560	MG 0/0	15.000	MG 0/0	6.833	MINERAL 4 H2O 0/0 16.785 DISTRIBUTION	5.878
SHERIDANITE	.180	VERMICULITE	.596	KANDITE	.057	SM/9A/ME-OH	.167		
CHEMICAL COMPOSITIONS								STRUCTURAL WATER DISTRIBUTION	
SI 0/0	12.729	SI 0/0	16.290	SI 0/0	21.760	SI 0/0	25.640	MINERAL 1 H2O 0/0 11.750 DISTRIBUTION	2.120
AL 0/0	14.800	AL 0/0	5.650	AL 0/0	20.910	AL 0/0	5.042	MINERAL 2 H2O 0/0 20.100 DISTRIBUTION	11.978
FE 0/0	11.118	FE 0/0	2.680	FE 0/0	0	FE 0/0	5.950	MINERAL 3 H2O 0/0 14.100 DISTRIBUTION	.798
MG 0/0	14.800	MG 0/0	11.560	MG 0/0	0	MG 0/0	5.946	MINERAL 4 H2O 0/0 17.254 DISTRIBUTION	2.882
SHERIDANITE	.150	VERMICULITE	.602	KANDITE	.045	SM/9A/ME-OH	.195		
CHEMICAL COMPOSITIONS								STRUCTURAL WATER DISTRIBUTION	
SI 0/0	12.729	SI 0/0	16.290	SI 0/0	21.760	SI 0/0	23.731	MINERAL 1 H2O 0/0 11.750 DISTRIBUTION	1.853
AL 0/0	14.800	AL 0/0	5.650	AL 0/0	20.910	AL 0/0	6.897	MINERAL 2 H2O 0/0 20.100 DISTRIBUTION	12.099
FE 0/0	11.118	FE 0/0	2.680	FE 0/0	0	FE 0/0	6.177	MINERAL 3 H2O 0/0 14.100 DISTRIBUTION	.634
MG 0/0	14.800	MG 0/0	11.560	MG 0/0	0	MG 0/0	6.172	MINERAL 4 H2O 0/0 17.134 DISTRIBUTION	3.349
SHERIDANITE	.125	VERMICULITE	.610	KANDITE	.029	SM/9A/ME-OH	.235		
CHEMICAL COMPOSITIONS								STRUCTURAL WATER DISTRIBUTION	
SI 0/0	12.729	SI 0/0	16.290	SI 0/0	21.760	SI 0/0	21.847	MINERAL 1 H2O 0/0 11.750 DISTRIBUTION	1.481
AL 0/0	14.800	AL 0/0	5.650	AL 0/0	20.910	AL 0/0	8.727	MINERAL 2 H2O 0/0 20.100 DISTRIBUTION	12.267
FE 0/0	11.118	FE 0/0	2.680	FE 0/0	0	FE 0/0	6.400	MINERAL 3 H2O 0/0 14.100 DISTRIBUTION	.405
MG 0/0	14.800	MG 0/0	11.560	MG 0/0	0	MG 0/0	6.395	MINERAL 4 H2O 0/0 17.016 DISTRIBUTION	3.997
SHERIDANITE	.018	VERMICULITE	.592	KANDITE	.061	SM/9A/ME-OH	.329		
CHEMICAL COMPOSITIONS								STRUCTURAL WATER DISTRIBUTION	
SI 0/0	12.729	SI 0/0	16.290	SI 0/0	19.760	SI 0/0	18.158	MINERAL 1 H2O 0/0 11.750 DISTRIBUTION	.209
AL 0/0	14.800	AL 0/0	5.650	AL 0/0	3.150	AL 0/0	12.311	MINERAL 2 H2O 0/0 20.100 DISTRIBUTION	11.898
FE 0/0	11.118	FE 0/0	2.680	FE 0/0	7.210	FE 0/0	6.838	MINERAL 3 H2O 0/0 13.580 DISTRIBUTION	.833
MG 0/0	14.800	MG 0/0	11.560	MG 0/0	15.000	MG 0/0	6.833	MINERAL 4 H2O 0/0 16.785 DISTRIBUTION	5.522

EXCESS READOUT.NOT PRINTED

MINERAL	MASS0/0	ST.DEV	ELEMENTAL COMPOSITION 0/0				ELEMENTAL FORMULA				H20 0/0
			SI	AL	FE	MG	SI	AL	FE	MG	
CHLORITE	10.14	6.82	12.7	13.3	9.8	15.7	2.60	2.81	1.02	3.67	11.75
VERMICULITE	59.28	2.13	16.3	5.7	2.7	11.6	3.12	1.18	.30	2.52	20.10
KANDITE	5.28	2.43	21.1	15.0	2.4	5.0	2.08	1.45	.11	.35	13.93
9A ALSILICATE	25.29	7.50	21.3	9.3	6.5	6.5	3.37	1.54	.52	1.18	16.98

ADDITIONAL DATA

H20 BALANCE ERROR IS 5.0 0/0

APPENDIX 6

OVERALL MASS BALANCES : DETAIL OF THE PROCEDURES EMPLOYED

The procedures outlined in Section 4.5.4 are described in detail here in terms of an example. The selected example related to the alteration of kimberlite under the following conditions : 10 g -1180+850 μm feed reacted with 40 ml 0.441M Al^{3+}, 0.31M H^{+} (as the chloride) for 100°C, 4 h. Table A6.1 outlines the experimental data used in the mass balance calculation obtained from the olivine, serpentine assays of the +75 μm fraction, and elemental assay of both solid fractions. From the known elemental assays of the olivine and serpentine (Section 2.4.3) the residual elemental assay in the altered rim of the +75 μm fraction was calculated. This was assumed to consist of minerals similar to those reporting to the -75 μm fraction as inferred from the SEM photomicrographs (Plates 3.12-3.19). The clay phase concentration in both solid phases was computed accordingly using Program CECPM.

TABLE A6.1 DATA USED IN ELEMENTAL-MINERAL MASS BALANCE CALCULATION FOR THE EXAMPLE REACTION 82KINF

Fraction	Mass (g)	Assay (%) Mg	Si	Fe	Al
total +75 μm	8.19	16.1	18.6	6.8	2.5
+75 μm (-head minerals)	2.99	8.6	17.7	5.7	3.9
-75 μm	0.23	16.5	16.6	6.9	6.8

	Mass (g)	Structural Formulae
$chlorite_{+75}$	0.165	$Al_{1.37}Mg_{3.98}Fe_{.77}(Al_{1.43}Si_{2.57})O_{10}(OH)_8$
$vermiculite_{+75}$	0.777	$Ca_{.28}Al_{.18}Mg_{2.74}Fe_{.28}(Al_{.96}Si_{3.04})O_{10}(OH)_2\ 4.4H_2O$
$kandite_{+75}$	0.273	$Ca_{.28}Al_{.71}Mg_{1.35}Fe_{.29}Si_2O_5(OH)_4$
9-11 Å $phase_{+75}$	1.725	$Al_{.5}Mg_{1.12}Fe_{.75}Si_4O_{10}(OH)_2\ 13.5H_2O$
$chlorite_{-75}$	0.045	$Al_{1.28}Mg_{4.57}Fe_{.30}(Al_{1.49}Si_{2.51})O_{10}(OH)_8$
$vermiculite_{-75}$	0.108	$Ca_{.28}Mg_{2.70}Fe_{.39}(Fe_{.21}Al_{.97}Si_{2.51})O_{10}(OH)_2\ 4.5H_2O$
$kandite_{-75}$	0.056	$Ca_{.28}Al_{.34}Mg_{1.8}Fe_{.39}Si_2O_5(OH)_4$
9-11 Å $phase_{-75}$	0.015	$Al_{.64}Mg_{1.56}Fe_{.67}(Al_{.98}Si_{3.02})\ O_{10}(OH)_2\ 15.3\ H_2O$

Notes

a) Mass of residual olivine = 2.6 g

Mass of residual serpentine = 2.6 g

By adding the respective stages of the alteration mechanism given in Sections 4.5.2 and 4.5.3 sixteen equilibria could be deduced for the alteration of olivine and serpentine to form directly each of

the eight phyllosilicate minerals listed in Table A6.1. Example equilibria are given below :

olivine → chlorite$_{+75}$

$$4Ca_{.07}Mg_{1.62}Fe_{.21}Ni_{.1}Al_{.01}SiO_4 + 2.76Al^{3+} + 7.72\ H_2O$$
$$\leftrightarrow Al_{1.37}Mg_{3.98}Fe_{.77}(Al_{1.43}Si_{2.57})\ O_{10}(OH)_8 + 0.28Ca^{2+} +$$
$$2.50Mg^{2+} + 0.07Fe^{2+} + 0.40Ni^{2+} + 1.72H^{+} + 1.43Si(OH)_4 \qquad (A6.1)$$

serpentine → vermiculite$_{+75}$

$$2Ca_{.28}Mg_{1.8}Fe_{.39}Al_{.34}Si_2O_5(OH)_4 + 0.46Al^{3+} + 2.4H^{+} + 2.2H_2O$$
$$\leftrightarrow Ca_{.28}Al_{.18}Mg_{2.74}Fe_{.28}(Al_{.96}Si_{3.04})\ O_{10}(OH)_2\ 4.4H_2O$$
$$+ 0.28Ca^{2+} + 0.86Mg^{2+} + 0.5Fe^{3+} + Si(OH)_4 \qquad (A6.2)$$

olivine → kandite$_{-75}$

$$2Ca_{.07}Mg_{1.62}Fe_{.21}Ni_{.1}Al_{.01}SiO_4 + 0.38Al^{3+} + 0.14Ca^{2+} + 2H^{+} + H_2O$$
$$\leftrightarrow Ca_{.28}Al_{.34}Mg_{1.8}Fe_{.39}Si_2O_5(OH)_4 + 1.44Mg^{2+} + 0.03Fe^{2+} + 0.2Ni^{2+}$$
$$(A6.3)$$

serpentine → 9-11 Å phase$_{-75}$

$$2Ca_{.28}Mg_{1.8}Fe_{.39}Al_{.34}Si_2O_5(OH)_4 + 0.94Al^{3+} + 2.0H^{+} + 13.3H_2O$$
$$\leftrightarrow Al_{.64}Mg_{1.56}Fe_{.67}(Al_{.98}Si_{3.02})O_{10}(OH)_2\ 15.3H_2O + 0.56Ca^{2+} +$$
$$2.04Mg^{2+} + 0.11Fe^{3+} + Si(OH)_4 \qquad (A6.4)$$

The proportions of olivine and serpentine reacting to produce each of the eight types of phyllosilicate mineral were unknown. In the calculations x_a referred to the number of moles of a phyllosilicate phase as produced from olivine alteration; y_a the number of moles of the same phase formed from serpentine alteration. From the sixteen equilibria

obtained, Table A6.1 was obtained which summarised the moles produced/required of magnesium, silicon, iron and aluminium for the possible alterations of olivine and serpentine per mole of phyllosilicate mineral. (Hence in the following table, x_a and y_a assumed values of unity.)

TABLE A6.2 MOLE PRODUCED/REQUIRED OF MAGNESIUM, SILICON, IRON AND ALUMINIUM FOR THE ALTERATION OF OLIVINE AND SERPENTINE

	Mg	Si	Fe	Al
x_{chl+75} [1]	2.50	1.43	0.07	-2.76
$x_{verm+75}$	3.74	1.00	0.56	-1.10
$x_{kand+75}$	1.89	0	0.14	-0.69
$x_{9Å+75}$	5.36	0	0.09	-0.46
x_{chl-75}	1.91	1.49	0.54	-2.73
$x_{verm-75}$	3.78	1.28	0.14	-0.93
$x_{kand-75}$ [3]	1.44	0	0.03	-0.38
$x_{9Å-75}$	4.92	1.00	0.17	-1.58
y_{chl+75}	-0.38	1.43	0	-2.12
$y_{verm+75}$ [2]	0.86	1.00	0.50	-0.46
$y_{kand+75}$	0.45	0	0.11	-0.37
$y_{9Å+75}$	2.48	0	0.03	0.18
y_{chl-75}	-0.97	1.49	0.48	-2.09
$y_{verm-75}$	0.90	1.28	0.08	-0.29
$y_{kand-75}$	0	0	0	0
$y_{9Å-75}$ [4]	2.04	1.0	0.11	-0.94

Notes

a) chl, verm, kand, 9Å refer to chlorite, vermiculite, kandite and the 9-11 Å phase respectively.

b) 1, 2, 3, 4 refer to equations A6.1-4 respectively.

c) A positive value represents production of the element from the alteration reaction, a negative value, a reaction requirement.

Noting the structural formulae for each mineral the total moles produced were calculated using the data presented in Table A6.1. Hence :

$$
\begin{aligned}
x_{chl+75} + y_{chl+75} &= 0.000283 \\
x_{verm+75} + y_{verm+75} &= 0.001612 \\
x_{kand+75} + y_{kand+75} &= 0.00096 \\
x_{9\text{Å}+75} + y_{9\text{Å}+75} &= 0.000282 \\
x_{chl-75} + y_{chl-75} &= 0.000079 \\
x_{verm-75} + y_{verm-75} &= 0.000219 \\
x_{kand-75} + y_{kand-75} &= 0.000193 \\
x_{9\text{Å}-75} + y_{9\text{Å}-75} &= 0.000022
\end{aligned}
\qquad \text{(A6.5)}
$$

The equations formulating the theoretical number of moles of magnesium, silicon, iron and aluminium entering the solution could now be written. The total number of moles of magnesium in solution, T_{Mg}, was as follows, from Table A6.2 :

$$
\begin{aligned}
T_{Mg} = {} & 2.50x_{chl+75} + 3.74x_{verm+75} + 1.89x_{kand+75} + \\
& 5.36x_{9\text{Å}+75} + \ldots - 0.97y_{chl-75} + 0.90y_{verm-75} + \\
& 2.04y_{9\text{Å}-75}
\end{aligned}
\qquad \text{(A6.6)}
$$

rearranging

$$= 2.88(x_{chl+75} + x_{verm+75} + x_{9Å+75} + x_{chl-75} + x_{verm-75} + x_{9Å-75}) + 1.44(x_{kand+75} + x_{kand-75}) - 0.38(x_{chl+75} + y_{chl+75}) + 0.86(x_{verm+75} + y_{verm+75}) + 0.45(x_{kand+75} + y_{kand+75}) + 2.48(x_{9Å+75} + y_{9Å+75}) - 0.97(x_{chl-75} + y_{chl-75}) + 0.9(x_{verm-75} + y_{verm-75}) + 2.04(x_{9Å-75} + y_{9Å-75}) \quad \text{(A6.7)}$$

From the olivine head assay and the residual mass of olivine in the +75 μm fraction, the number of moles of totally reacted olivine were evaluated. From the form of equations A6.1-4, it was evident that the following equality held :

$$4(x_{chl+75} + x_{chl-75} + x_{verm+75} + x_{verm-75} + x_{9Å+75} + x_{9Å-75}) + 2(x_{kand+75} + x_{kand-75}) = \text{No. of reacted olivine moles} = 0.00566 \quad \text{(A6.8)}$$

Multiplying equation A6.8 by (2.88/4) and accordingly substituting the right hand side value deduced, as well as the equalities in equation A6.5 in equation A6.7, enabled the total number of magnesium moles entering the solution to be evaluated, i.e.

$$\text{No. of magnesium moles entering solution} = \frac{2.88}{4} \cdot 0.005566 + 0.008896 = 0.0129 \text{ mole}$$

The experimentally found value was 0.0102 mole.

Repeating this procedure for silicon, iron and aluminium produced the results given in Section 4.5.4.

REFERENCES

1. Bruton, E., Diamonds (London : NAG Press, 1974), 56.

2. Properties of Diamond, De Beers Industrial Diamond Division.

3. Linari-Linholm, A.A., Occurrence, mining and recovery of diamonds, De Beers Consolidated Mines Ltd (London : Kenian, 1973), pp.30.

4. Wagner, P.A., The diamond fields of Southern Africa (Cape : Gothic, 1914), 200-205.

5. Borley, G.D., Deformation textures in nodules from kimberlites. The physics and chemistry of minerals and rocks, Strens R.G.J. ed. (London : Wiley, 1975), 93-105.

6. Woolsey, T.S., McCallum, M.E. and Schumann, S.A., Modelling of a diatreme emplacement by fluidisation. The physics and chemistry of the earth, Ahrens, L.H., Dawson, J.B., Duncan, A.R., Erlank, A.J. eds., (Oxford : Pergamon, 1975), 9, 29-42.

7. McCallum, M.E., An emplacement model to explain contrasting mineral assemblages in adjacent kimberlite pipes, J. Geol., 84, 1976, 673-684.

8. Harris, P.G. and Middlemost, E.A.K., The evolution of kimberlites. Lithos, 3, 1970, 77-78.

9. Nixon, P.H., Van Knorring, O. and Rooke, J.M., Kimberlites and associated inclusions of Basutoland : a mineralogical and geochemical study. Am.Min., 48, 1963, 1090-1133.

10. Meyer, H.O.A., Kimberlites of the continental United States : a review. J. Geol., 84, 1976, 377-403.

11. Dawson, J.B., Recent researches on kimberlite and diamond geology. Econ. Geol., 63, 1968, 504-511.

12. Mining Mag. 138, 1978, 485.

13. Reid, A.M. and Manor, J.S., Pyrope in kimberlite, Am.Min. 55, 1970, 1374-1379.

14. Devlin, S.W., The treatment of gravels for the recovery of diamonds at CDM, Proc. South African Inst. Min. Metall., 60, 1960, 430-452.

15. Linari-Linholm, A.A., Electrostatic separation of diamonds from gravel, Proc. South African Inst. Min. Metall., 64, 1963, 299-305.

16. Adamson, R.J., Presidential address : Some account of diamond mining practices in Southern Africa, Proc. South African Inst. Min. Metall., 59, 1959, 23-55.

17. Shanks, R.I., Treatment plant and diamond recovery at the Premier mine, Proc. South African Inst. Min. Metall., 61, 1960, 90-109.

18. Nesbitt, A.C. and Wearind, R.G., Study of the efficiency of dense media separators used in diamond dressing, Int.Min.Proc. Cong. (London : Inst. Min. Metall, 1960), No.26, 533-562.

19. Smit, D.B., Orsmond, N. and Delange-Strydon, J.E., Diamond recovery plant state alluvial diggings, Alexander Bay, Proc. South African Inst. Min. Metall., 60, 1960, 453-465.

20. Napier-Munn, T.J., Private communication.

21. Adamson, R.J. and Hodgson, M.F., The retreatment plant at Premier diamond mine, Proc. South African Inst. Min. Metall., 64, 1963, 45-67.

22. Chaston, I.R.M. and Napier-Munn, T.J., Design and operation of dense medium cyclone plants for recovery of diamonds in Africa, Proc. South African Inst. Min. Metall., 75, 1974, 120-130.

23. Loftus, W.K.B., Simpson, H.S. and King, M.J., Recovery plant practice at De Beers Consolidated Mines Ltd., Kimberley, with particular reference to improvements made for the sorting of final concentrates, Proc. South African Inst. Min. Metall., 70, 1970, 317-329.

24. Cleasby, J.V., Wright, M.J. and Davies, M.T.G., Mining practice in the Kimberley Division of De Beers Consolidated Mines Ltd., Proc. South African Inst. Min. Metall., 76, 1975, 248.

25. Napier-Munn, T.J., Diamond recovery in the 21st centry, DRL De Beers Consolidated Mines Ltd., unpublished.

26. Flowsheet of Premier mine. De Beers Consolidated Mines Ltd.

27. Van der Schyff, P., Planetary mill, Proc. South African Inst. Min. Metall., 67, 1967, 317-318.

28. Andres, V.Ts., private communication.

29. Le Roux, N.W., Wkaerley, D.S. and Dacey, P.W., private communication.

30. Whitten D.G.A. and Brooks, J.R.V., The Penguin dictionary of geology (London : Penguin, 1972).

31. Dawson, J.B., Advances in kimberlite geology, Earth Sci. Rev., 7, 1971, 187-214.

32. Clement, C.R., The emplacement of some diatreme facies kimberlites, The physics and chemistry of the earth, Ahrens, L.H., Dawson, J.B., Duncan A.R., Erlank, A.J., eds (Oxford : Pergamon, 1975), 9, 51-59.

33. Stephens, W.E. and Dawson, J.B., Statistical comparison between pyroxenes from kimberlites and their associated xenoliths, J. Geol., 85, 1977, 433-449.

34. Clarke, D.B. and Mitchell, R.H., Mineralogy and Petrology of the kimberlite from Somerset Island, North West Territories,

Canada, The physics and chemistry of the earth, Ahrens, L.H., Dawson, J.B., Duncan, A.R., Erlank, A.J., eds (Oxford : Pergamon, 1975), 9, 123-137.

35. Dawson, J.B., Basutoland kimberlites, Geol. Soc. Am. Bull., 73, 1962, 545-560.

36. Ferguson, J., Martin, H., Nicolayson, L.O. and Danchin, R.V., Gross Brukkaros a kimberlite-carbonatite volcano, The physics and chemistry of the earth, Ahrens, L.H., Dawson, J.B., Duncan, A.R., Erlank, A.J., eds. (Oxford : Pergamon, 1975), 9, 219-234.

37. Meyer, H.O.A., Kimberlite from Norris Lake Eastern Tennessee, mineralogy and petrology, J. Geol., 83, 1975, 518-526.

38. Beyth, M., Grunhagen, H. and Zilberfarb, A., An ultramafic rock in the pre-cambrian of eastern Sinai, Geol.Mag., 115, 1978, 373-378.

39. Smith, J.V., Brennesholtz, B. and Dawson, J.B., Chemistry of micas from kimberlites and xenoliths I : micaceous kimberlites. Geochim. Cosmochim. Acta, 42, 1978, 959-971.

40. Wilshire, H.G. and Shervais, J.W., Al augite and Cr diopside ultramafic xenoliths, The physics and chemistry of the earth, Ahrens, L.H., Dawson, J.B., Duncan, A.R., Erlank, A.J., eds. (Oxford : Pergamon, 1975), 9, 257-272.

41. Suwa, K., Ysa, Y. and Kishida, N., Petrology of periodotite nodules from Ndanywo Olncharo Samburu District, Central Kenya, The physics and chemistry of the earth, Ahrens, L.H., Dawson, J.B., Duncan, A.R., Erlank, A.J., eds (Oxford : Pergamon, 1975), 9, 273-286.

42. Smith, J.V. and Dawson, J.B., Chemistry of Ti poor spinels, ilmenites and rutiles from peridotite and eclogite xenoliths, Ibid, 309-322.

43. Lloyd, F.E. and Bailey, D.K., Light element metasomatism of the continental mantle : the evidence and the consequences, Ibid, 389-416.

44. Carswell, D.A., Primary and secondary phlogopites and clino-pyroxenes in garnet lherzolite xenoliths, Ibid, 417-429.

45. Boyd, F.R. and Nixon, P.H., Origins of the ultramafic nodules from some kimberlites of Northern Lesotho and the Monastery Mine, South Africa, Ibid, 431-454.

46. O'Hara, M.J., Saunders, M.J. and Mercy, E.L.P., Garnet-peridotite primary ultrabasic magma and eclogite; interpretation of upper mantle processes in kimberlite, Ibid, 571-604.

47. Boullier, A.M. and Nicolas, A., Classification of textures and fabrics of peridotite xenoliths from South African kimberlites, Ibid, 467-475.

48. Harte, B., Cox, K.G. and Gurney, J.J., Petrography and geological history of upper mantle xenoliths from the Matsoku kimberlite pipe, Ibid, 477-523.

49. Reid, A.M., Donaldson, C.M., Brown, R.W., Ridley, W.I. and Dawson, J.B., Mineral chemistry of peridotite xenoliths from the Lashire Volcano, Tanzania, Ibid, 525-543.

50. Lappin, M.A. and Dawson, J.B., Two Roberts Victor cumulate eclogites and their re-equilibration, Ibid, 351-365.

51. McCallum, M.E., Eggler, D.H. and Burns, L.K., Kimberlitic diatremes in Northern Colorado and Southern Wyoming, Ibid, 149-161.

52. Watson, K.D. and Morton, D.M., Eclogite inclusions in kimberlite pipes at Garnet Ridge, North Eastern Arizona, Am. Min., 53, 1968,

53. Berg, G.W., Secondary alteration in eclogites from kimberlite pipes, Am.Mineral., 53, 1968, 1336-1347.

54. Kushiro, I. and Aoki, K.I., Origin of some eclogite inclusions in kimberlite, Ibid, 1347-1367.

55. Rickwood, P.C. and Mathias, M., Diamondiferous eclogite xenoliths in kimberlite, Lithos, 3, 1970, 223-235.

56. Borley, G.D. and Suddaby, P., Stressed pyroxenite nodules from the Jagersfontein kimberlite, Mineral. Mag., 40, 1975, 6-12.

57. Rodgers, K.A., Brothers, R.N. and Searle, E.J., Ultramafic nodules and their host rocks from Auckland, New Zealand, Geol. Mag., 112, 1975, 163-174.

58. Robinson, M.R., Diamond deposits : their geology, exploration and evaluation, MSc thesis, Imperial College, 1976.

59. Wyllie, P.J., Petrography and Petrology, Ultramafic and Related Rocks, Wyllie, P.J. ed. (New York : Wiley, 1967), p.1-17.

60. Bloomer, A.G. and Nixon, P.H., The geology of Letseng-la-terae kimberlite pipes, Lesotho kimberlites, Nixon, P.H. ed. (Cape and Transvaal Printers, 1973), 20-36.

61. Hodgson, M., unpublished data.

62. Clement, R., private communication.

63. Deer, W.A., Howie, R.A. and Zussman, J., Rock forming minerals, (London : Longmans, 1965), 1, 1-29.

64. Coleman, R.G., Petrologic and geophysical nature of serpentinites, Geol.Soc.Am.Bull., 82, 1971, 897-918.

65. Wicks, F.J. and Whittaker, E.J.W., Serpentine textures and serpentinization, Can.Mineral., 15, 1977, 459-488.

66. Butler, J.R., The geochemistry and mineralogy of rock weathering (2), The Nordmarka area, Oslo, Geochim. Cosmichim. Acta, 6, 1954, 268-281.

67. Hostetler, P.B., Coleman, R.G., Mumpton, F.A. and Evans, B.W., Brucite in alpine serpentinites, Am. Mineral., 51, 1966, 75-98.

68. Thayer, T.P., Serpentinization considered as a constant volume metasomatic process, Am. Mineral., 51, 1966, 685-710.

69. Thayer, T.P., Serpentinization considered as a constant volume metasomatic process, Am. Mineral., 52, 1967, 549-553.

70. Page, N.J., Serpentinization considered as a constant volume metasomatic process, Ibid, 545-549.

71. Barnes, I. and O'Neill, J.R., The relationship between fluids in some fresh alpine-type ultramafics and possible modern serpentinization, Western United States, Geol. Soc. Am. Bull., 80, 1969, 1947-1960.

72. Deer, W.A., Howie, R.A. and Zussman, J., Rock forming minerals, (London : Longmans, 1965), 3, 164-246.

73. Campbell, I.H., Direct evidence of present day serpentinization in the Jimberlana intrusion, Western Australia, Geol. Mag., 112, 1975, 77-80.

74. Page, N.J., Serpentinization at Burro Mountain, California, Contr. Min. Petrol. 14, 1967, 321-342.

75. Causse, C. and Brousse, R., Une "chlorite gonflante" parmi les produits de degradation des olivines. Le problème de l'iddingsitisation, 91 Congrès des Sociétés (Rennes, 1966) Tome II.

76. Edwards, A.B., The formation of iddingsite, Am. Min., 23, 1938, 277-281.

77. Payne, J.H. and Man, K.T., A study of the chemical alteration of basalt in the Kiluaea region of Hawaii, J. Geol., 54, 1946, 345-358.

78. Ming Shan Sun, The nature of iddingsite in some basaltic rocks of New Mexico., Am. Mineral., 42, 1957, 525-533.

79. Prider, R.T. and Cole, W.F., The alteration products of olivine and bucite in the leucite lamphroites from the West Kimberley area, Western Australia, Am. Mineral., 27, 1942, 373-384.

80. Wilshire, H.G., Alteration of olivine and orthopyroxene in basic lavas and shallow intrusions, Am. Mineral., 43, 1958, 120-147.

81. Wilshire, H.G. and Hobbs, B.E., Structure sedimentary inclusions and hydrothermal alteration of a latite intrusion, J. Geol., 70, 1962, 328-345.

82. Gastauche, M.C., Fripiat, J.J. and De Kimpe, C., La genèse des mineraux argileaux de la famille du kaolin. 1, aspect colloidal, Genèse et synthèse des argiles (Paris : CNRS, 1962) 57-65.

83. McIver, J.R. and Ferguson, J., Kimberlite, melilitic, trachytic and carbonatitic eruptives at Saltpetre Kop, Sutherland, South Africa, 2nd Int. Kimb. Conf. (Abstr) (Santa Fe : 1977).

84. Bowen, N.L. and Tuttle, O.F., The system MgO-SiO_2-H_2O, Geol. Soc. Am. Bull., 60, 1949, 439-460.

85. Yoder, H.S., The MgO-Al_2O_3-SiO_2-H_2O system and the related metamorphic facies, Am. J. Sci., 250, 1952, 569-627.

86. Kitahara, S. and Kennedy, G.C., The calculated equilibrium curves for some reactions in the system MgO-SiO_2-H_2O at pressures up to 30 kilobars, Am. J. Sci., 265, 1967, 211-217.

87. Kitahara, S., Takenouchi, S. and Kennedy, G.C., Phase relations in the system MgO-SiO_2-H_2O at high temperatures and pressures, Am. J. Sci., 264, 1966, 223-233.

88. Johannes, W., Experimental investigation of the reaction forsterite + H_2O → serpentine + brucite, Contr. Mineral. Petrol., 19, 1968, 309-315.

89. Moody, J.B., An experimental study on the serpentinization of iron bearing olivines, Can. Mineral., 14, 1975, 462-478.

90. Hazen, R.M., Effects of temperature and pressure on the crystal structure of ferromegnesian olivine, Am. Min., 62, 1977, 286-295.

91. Korytkova, E.N., Kosulina, G.I. and Makarova, T.A., Experimental serpentinization of olivine, Int. Geol. Rev., 14, 1972, 1074-1078.

92. Tantar Borash, Z.J., Petrochemistry of ultramafics of the Belozersk iron ore deposit, Geochem. Int., 3, 1964, 431.

93. Butler, J.R., The geochemistry and mineralogy of rock weathering (1) the Lizard area Cornwall, Geochem. Cosmochim. Acta, 4, 1953, 157-178.

94. Lemon, G.G., Serpentinites in the North East Ox Mountains, Eire, Geol. Mag., 103, 1966, 124-137.

95. Bricker, O.P., Nesbitt, H.W. and Gunter, W.D., The stability of talc, Am. Min., 58, 1973, 64-72.

96. Milashev, M.A., Paragenesis of secondary minerals in kimberlite, Geochem., 6, 1963, 572-580.

97. Naldrett, A.J., Talc-carbonate alteration of some serpentinized ultramafic rocks south of Timmins, Ontario, J. Petrol., 7, 1966, 489-499.

98. Cauffman, L.B. Jr and Bayliss, P., Clay mineralogy and depositional enviroment of Melville Island, NWT, Canada, Clay mineral. conf. (abstr.) No.21, 1973, 51.

99. Wildman, W.E., Whittig, L.D. and Jackson, M.L., Serpentine stability in relation to formation of iron rich montmorillonite in some Californian soils, Am. Mineral., 56, 1971, 587-602.

100. Keller, W.D., Origin of high alumina clays, 12th nat. conf. clays, clay minerals (London : Pergamon, 1963), 129-151.

101. Nagy, B. and Bates, T.F., Stability of chrysotile asbestos, Am. Min., 38, 1953, 1055-1058.

102. Wildman, W.E., Jackson, M.L. and Whittig, L.D., Serpentinite rock dissolution as a function of carbon dioxide pressure in aqueous solution, Am. Mineral., 53, 1968, 1252-1263.

103. Seyfried, W.E. and Bischoff J.L., Low temperature basalt alteration by seawater : an experimental study at 70°C and 150°C, Geochim. Cosmochim. Acta, 43, 1979, 1937-1947.

104. Ellis, A.J. and Mahon, W.A.J., Natural hydrothermal systems and experimental hot water/rock interactions, Geochim. Cosmochim. Acta, 28, 1964, 1323-1357.

105. Deer, W.A., Howie, R.A. and Zussman, J., Rock forming minerals, (London : Longmans, 1965) 2.

106. Ferguson, J., Danchin, R.V. and Nixon, P.H., Fenitization associated with kimberlite magmas, in Lesotho kimberlites (Lesotho National Development Corporation, 1973), 207-213. Nixon, P.H. ed. (Cape and Transvaal Printers, 1973) 207-213.

107. Gittins, J., Allen, C.R. and Cooper, A.F., Phlogopitization of pyroxenite : its bearing on the composition of carbonatite magmas, Geol. Mag., 112, 1975, 503-507.

108. Currie, K.L. and Ferguson, J., A study of fenitization in mafic rocks with special reference to the Callander Bay Complex, Can. J. Earth Sci., 9, 1972, 1254.

109. Barshad, I., Vermiculite and its relation to biotite as revealed by base exchange reactions, X-ray analyses, differential thermal curves and water content, Am. Mineral., 33, 1948, 655-678.

110. Roy, R. and Romo, L.A., Weathering studies, 1. New data on vermiculite, J. Geol., 65, 1957, 603-610.

111. Kelly, W.C. and Zumberge, J.H., Weathering of a quartz diorite at Marble Point, McMurdo Sound, Antarctica, J. Geol., 69, 1961, 433-446.

112. Smith-Aitken, W.W., An occurrence of phlogopite and its transformation to vermiculite by weathering, Min. Mag. 35, 1965, 157-164.

113. Wilson, M.J., The weathering of biotite in some Aberdeenshire soils, Ibid, 1080-1092.

114. Stoch, L. and Sikora, W., Transformations of micas in the process of kaolinization of granites and gneisses, Clays Clay Mineral 24, 1976, 156-162.

115. Barshad, I., The effect of the interlayer cations on the expansion of the mica type of crystal lattice, Am. Mineral., 35, 1950, 225-238.

116. Newman, A.C.D. and Brown, G., Chemical changes during the alteration of micas, Clay Mineral., 14, 1966, 297-310.

117. Hoda, S.N. and Hood, W.C., Laboratory alteration of trioctahedral micas, Clays Clay Mineral., 20, 1972, 343-358.

118. Robert, M., The experimental transformation of mica toward smectite; relative importance of total charge and tetrahedral substitution, Clays Clay Mineral., 21, 1973, 167-174.

119. Kittrick, J.A., Mica derived vermiculites as unstable intermediates, Clays Clay Mineral., 2k, 1973, 479-488.

120. Vicente, M.A., Razzaghe, M. and Robert, M., Formation of aluminium hydroxy vermiculite (intergrade) and smectite from mica under acidic conditions, Clay Mineral., 12, 1977, 101-112.

121. St Serstevens, A., Rouxhet, P.G. and Herbillon, A.J., Alteration of mica surfaces by water and solutions, Clay Mineral., 13, 1978, 401-410.

122. Garrels, R.M., Mineral equilibria at low temperature and pressure, (New York : Harper and Brothers, 1960), 203.

123. Dimanche, F. and Bartholone, P., The alteration of ilmenite in sediments, Mineral. Sci. Eng., 8, 1976, 187-202.

124. Iler, R.K., The colloid chemistry of silica and silicates, (Ithaca : Cornell University Press, 1955), 324 p.

125. Loughran, F.C., Chemical weathering of silicate minerals, (New York : Elsevier, 1969), 154 p.

126. Weyl, W.A., A new approach to surface chemistry and to heterogenous catalysts, Mineral. Ind. Exp. Bull., 57, 1951, 46-48.

127. Roy, R. and Osborn, E.F., The system Al_2O_3-SiO_2-H_2O, Am. Mineral., 39, 1954, 853-885.

128. Crawley, M.S. and Roy, R., A possible case of Al-Si ordering, Geochim. Cosmochim. Acta, 18, 1960, 94-100.

129. Sand, L.B., Roy, R. and Osborn, E.F., Stability relations of some minerals in the Na_2O-Al_2O_3-SiO_2-H_2O system, Econ. Geol., 52, 1957, 169-179.

130. Carr, R.M. and Fyfe, W.S., Synthesis fields of some aluminium silicates, Geochim. Cosmochim. Acta, 21, 1960, 99-109.

131. Carr, R.M., Synthesis fields of some aluminium silicates. Further studies, Geochim. Cosmochim. Acta, 27, 1963, 133-135.

132. Rodrique, L., Poncelet, G. and Herbillon, A., Importance of the silica subtraction process during the hydrothermal kaolinitization of amorphous silico-aluminas, Proc. 7th Clay Conf. Serratosa, J.M. ed. (Madrid : Association Internationale pour l'Etude des Argiles, 1973), 187-198.

133. De Kimpe, C.R., Hydrothermal aging of synthetic alumino-silicate gels, Clay Minerals, 7, 1967, 203-214.

134. De Kimpe, C.R. and Fripiat, J.J., Kaolinite crystallization from H-exchanged zeolites, Am. Mineral., 53, 1968, 216-232.

135. Eberl, D. and Hower, J., Kaolinite synthesis : the role of the Si-Al and (alkali)/(H^+) ratio in hydrothermal systems, Clays Clay Minerals, 23, 1975, 301-309.

136. Eberl, D., Synthesis of pyrophyllite polytypes and mixed layers, Am. Mineral., 64, 1979, 1091-1096.

137. Brindley, G.W. and De Kimpe, C.R., Attempted low temperature synthesis of kaolin minerals, Nature, 190, 1961, 254.

138. De Kimpe, C.R., Gastauche, M.C. and Brindley, G.W., Ionic coordination in aluminosilicilic gels in relation to clay mineral formation, Am. Mineral., 46, 1961, 1370-1381.

139. De Kimpe, C.R., Gastauche, M.C. and Brindley, G.W., Low temperature syntheses of kaolin minerals, Am. Mineral., 49, 1964, 1-15.

140. Kittrick, J.A., Free energy of formation of kaolinite from solubility measurements, Am. Mineral., 51, 1966, 1457-1466.

141. Reesman, A.L. and Keller, W.D., Aqueous solubility studies of high alumina and clay minerals, Am. Mineral., 53, 1968, 929-942.

142. Gardner, L.R., A chemical model for the origin of gibbsite from kaolinite, Am. Mineral, 55, 1970, 1380-1389.

143. Kittrick, J.A., Precipitation of kaolinite at 25°C and 1 atm. Clays, Clay Minerals , 18, 1970, 261-267.

144. Linares, J. and Huertas, F., Kaolinite synthesis at room temperature, Nature, 171, 1971, 896-897.

145. McHardy, W.J. and Thomson, A.P., Conditions for the formation of bayerite and gibbsite, Mineral. Mag., 38, 1971, 358-368.

146. Hem, J.D. and Lind, C.J., Kaolinite synthesis at 25°C, Science, 184, 1974, 1171-1174.

147. Siffert, B. and Wey, R., Contribution à la connaissance de la synthèse des kaolins, Proc. Int. Clay. Conf., Sarratosa, J.M. ed. (Madrid : Division de Ciencias, CSIC, 1972), 159-185.

148. La Iglesia, A. and Martin Vivaldi, J.L., Synthesis of kaolinite by homogeneous precipitation at room temperature. 1 : Use of anionic resins in the (OH) form, Clay Minerals, 10, 1975, 399-405.

149. Schnitzer, M. and Skinner, S.I.M., Organometallic interaction in soils. 1 : Reactions between a number of metal ions and the organic matter of a Podzol Bh horizon, Soil Sci., 109, 1963, 86-98.

150. La Iglesia, Fernandez A. and Martin Vivalid, J.L., A contribution to the synthesis of kaolinite, Proc. Int. Clay. Conf., Serratosa, J.M. ed. (Madrid : Division de Ciencias CSIC, 1972) 173-185.

151. La Iglesia, Fernandez A., Martin Vivalid, J.L. and Lopez Aguayo, F., Kaolinite crystallization at room temperature by homogeneous precitipation. III : Hydrolysis of feldspars, Clays, Clay Minerals., 24, 1976, 36-42.

152. La Iglesia, Fernandez A. and Van Ooosterwyck-Gastauche, M.C., Kaolinite synthesis I. Crystallization conditions at low temperatures and calculation of thermodynamic equilibria. Application to laboratory and field observations, Clays Clay Minerals, 26, 1978, 397-408.

153. Van Oosterwyck-Gastauche, M.C. and La Iglesia, Fernandez A., Kaolinite synthesis II : A review and discussion of the factors influencing the rate process, Clays Clay Minerals, 26, 1978, 409-417.

154. Grim, R.E., Clay Mineralogy (London : McGraw Hill, 1953), 384 p.

155. White, J., Transformation of illite into montmorillonite, Proc. Soil Soc. Am., 15, 1951, 129-133.

156. Caillère, S., Hénin, S. and Esquevin, J., Transformation experimentale de chlorite en montmorillonte, Clay Mineral Bull., 2, 1952, 166-170.

157. Earley, J.W., Brindley, G.W., McVeagh, W.J. and Van der Heuvel, R.C., A regular interstratified montmorillonite-chlorite, Am. Mineral., 41, 1956, 258-267.

158. April, R.H., Regularly interstratified chlorite/vermiculite in contact metamorphosed red beds, Newark Group, Connecticut Valley, Clays Clay Minerals, 28, 1980, 1-11.

159. Carstea, D.D., Harward, M.E. and Knox, E.G., Formation and stability of hydroxy-mg interlayers in phyllosilicates, Clays Clay Minerals, 18, 1970, 213-222.

160. Ross, G.J. and Kodama, H., Experimental transformation of a chlorite into a vermiculite, Clays Clay Minerals, 22, 1974, 205-211.

161. Heller-Kallai, L. and Rozenson, I., Dehydroxylation of dioctahedral phyllosilicates, Clays Clay Minerals, 28, 1980, 355-368.

162. Roy, D.M., Roy, R. and Osborn, E.F., The system $MgO-Al_2O_3-H_2O$ and influence of carbonate and nitrate ions on the phase equilibria, Am. J. Sci., 251, 1953, 337-361.

163. Roy, D.M. and Roy, R., Synthesis and stability of minerals in the system $MgO-Al_2O_3-SiO_2-H_2O$, Am. Min., 40, 1955, 147-178.

164. Nelson, B.W. and Roy, R., Synthesis of the chlorites and their structural and chemical composition, 43, 1958, 707-725.

165. Brindley, G.W. and Gillery, F.H., X-ray identification of chlorite species, Am. Min., 41, 1956, 169-186.

166. Gillery, F.H., The X-ray study of synthetic Mg-Al serpentines and chlorites, Am. Mineral, 44, 1959, 143-152.

167. Granquist, W.T. and Pollack, S.S., Clay mineral synthesis II : A randomly interstratified aluminian montmorillonoid, Am. Mineral., 52, 1967, 212-226.

168. Iiyama, J.T. and Roy, R., Controlled synthesis of heteropolytypic (mixed layer) clay minerals, Proc. 10th Nat. Conf. Clays Clay Minerals, Swindford, A. ed (Austin : Clays and Clay Minerals, 1961) 4-22.

169. Velde, B., Phase equilibria in the system $MgO-Al_2O_3-SiO_2-H_2O$: chlorites and associated minerals, Mineral. Mag., 39, 1973, 297-312.

170. Hénin, S., Synthesis of clay minerals at low temperatures, Proc. 4th Nat. Conf. Clays Clay Minerals, Swineford, A. ed. (Washington : National Academy of Sciences, 1955) 54-60.

171. Wey, R. and Siffert, B., Réactions de la silice monomoléculaire en solution avec les ions Al^{3+} et Mg^{2+}, Genèse et synthèse des argiles (Paris : CNRS, 1962), 11-19.

172. Caillère, S. and Hénin, M.S., Vues d'ensemble sur le problème de la synthèse des minéraux phylliteaux à basse température, Genèse et synthèse des argiles (Paris : CNRS, 1962), 31-41.

173. De Kimpe, C.R., Gastauche, M.C. and Brindley, G.W., Low temperature syntheses of kaolin minerals, Am. Mineral., 49, 1964, 1-16.

174. Wollast, R., Mackenzie, F.T. and Bricker, O.P., Experimental precipitation and genesis of sepiolite at earth-surface conditions, Am. Mineral., 53, 1968, 1645-1662.

175. Harder, H., The role of magnesium in the formation of smectite minerals, Chem. Geol., 12, 1972, 31-39.

176. Harder, H., Illite mineral synthesis at surface temperatures, Chem. Geol., 14, 1974, 241-253.

177. Harder, H., Synthesis of iron layer silicate minerals under natural conditions, Clays Clay Minerals, 26, 1978, 65-72.

178. Cochran, W., Sampling techniques (London : Wiley, 1963), 51.

179. Levin, J., Mixing and sampling procedures used at the NIM, South Africa, Proc. symp. (London : Inst.Min.Metall., 1973), 210.

180. Jones, M.P. and Beavan, C.H.J., Sampling of non-gaussian mineralogical distribution, Trans. Instn. Min. Metall., (Sect.B : Applied Earth Sciences), 80, 1971, B316-318.

181. Barbery, G., The derivation of a formula to estimate the mass of sample for size analysis, Trans. Instn. Min. Metall., (Sect.C : Mineral Process Extr. Metall.), 81, 1972, 49.

182. Gy, P.H., The sampling of broken ores. Sampling in the mineral and metallurgical processing industries, Proc. symp. (London : Inst.Min.Metall., 1973), 16.

183. Gy, P.H., Sampling nomogram (Paris, Minerais et Métaux)

184. Jones, M.P. and Fleming, M.G., Identification of mineral grains (London : Elsevier, 1965), 102p.

185. Hawthorne, J.B., Carrington, A.J., Clement C.R. and Skinner, E.M.W., Geology of the Dokolwayo kimberlite and associated palaeo-alluvial diamond deposits, Proc. 2nd Int. Kimb. Conf. (Abstr.) 1979, 57-70.

186. Mitchell, R.H., Mineralogy of the Turraq kimberlite, Somerset Island, NW Territories, Canada, Ibid, 161-171.

187. Akella Jagannadham Rao, R.S., MaCallister, R.H., Boyd, F.R. and Myer, H.O.A., Diamondiferous kimberlite of the Wajrakharur, Southern India, Ibid, 172-177.

188. Smith, C.B., McCallum, M.E., Coopersmith, H.G. and Eggler, D.H., Petrochemistry and structure of kimberlites in the Front Range and Laramie Range, Colorado-Wyoming, Ibid, 178-190.

189. Zussman, J. (ed.) Physical methods in determinative mineralogy, (London : Academic Press, 1967), 514p.

190. Kitagawa, Y., An aspect of the water in clay minerals : an application of nuclear magnetic resonance spectrometry to clay mineralogy, Am. Mineral., 57, 1972, 751-764.

191. Shillam, D., personal communication.

192. Fritz, J.S. and Schenk, G.H., Quantitative analytical chemistry, (London : Allyn and Bacon Inc., 1979), 660p.

193. MacKenzie, R.C. and Mitchell, B.D., Differential thermal analysis. A review, Analyst, 87, 1962, 420-434.

194. Farmer, V.C., The infra-red spectra of minerals (London : Mineralogical Society, 1974), 333-359.

195. Brindley, G.W. and Brown, G., The X-ray identification and crystal structure of clay minerals (London : Mineralogical Society, 1961), 544p.

196. Moore, W.J., Physical chemistry, (London : Longmans, 1974), 850.

197. Greene-Kelly, R., Identification of montmorilloids in clays, J. Soil, Sci., 4, 1953, 233-236.

198. Gibbs, R.J., Quantitative X-ray diffraction analysis using clay mineral standards extracted from the samples to be analysed, Clay Minerals, 7, 1967, 79-91.

199. Carroll, D., Clay minerals : a guide to their X-ray identification, Geol. Soc. Am. (Special Paper No.126), 1970, 1-41.

200. Thorez, J., Phyllosilicates and clay minerals : a laboratory handbook for their X-ray diffraction analysis (Dison, Belgium : Editions G. Lelotte, 1975), 582p.

201. Gordon, R.L. and Nagelschmidt, G., Application of X-ray diffraction to quantitative analysis of rocks, Acta Cryst., 7, 1954, 626.

202. Mitchell, W.A., A method of quantitative mineralogical analysis by X-ray powder diffraction, Mineral. Mag., 32, 1960, 492-499.

203. Norrish, K. and Taylor, R.M., Quantitative analysis by X-ray diffraction, Clay Minerals Bull., 5, 1962, 98-109.

204. Marel, an der, H.R., Quantitative analysis of clay minerals and the admixtures, Contrib. Mineral Petrol., 12, 1966, 96-132.

205. Cody, R.D. and Thompson, G.L., Quantitative X-ray powder diffraction analyses of clays using an orientating internal standard and pressed disks of bulk shale samples, Clays Clay Minerals, 11, 1976, 224-231.

206. Brindley, G.W. and Kurtossy, S.S., Quantitative determination of kaolinite by X-ray diffraction, Am. Mineral., 46, 1961, 1205-1215.

207. Niskanen, E., Reduction of orientation effects in the quantitative X-ray diffraction analysis of kaolin minerals, Am. Mineral., 49, 1964, 705-714.

208. Gibbs, R.J., Error due to segregation in quantitative clay mineral X-ray diffraction mounting techniques, Am. Mineral, 50, 1965, 741-751.

209. Gordon, R.L. and Harris, G.W., Effect of particle size on the quantitative determination of quartz by X-ray diffraction, Nature, 175, 1955, 1135.

210. Schultz, L.G., Note : mineralogical-particle size variations in orientated clay aggregates, J. Sed. Petrol., 25, 1955, 124-125.

211. Bearson, R.E., Ray, C. and Treweek, H.B., Plant practice in non-metallic mineral flotation, Froth flotation 50th anniversary volume, (New York : AIME, 1962), 435.

212. Cyanamid, Mining chemicals handbook (1980).

213. Beavan, C.H.J. and Napier-Munn, T.J., Separation of mica flakes by aspect ratio, (London : RSM, 1978).

214. Ayres, P., Personal communication.

215. Orr, C., Particulate technology (New York : MacMillan Co., 1966), 562p.

216. DRL, unpublished data (Johannesburg, 1979).

217. Van Olphen, H. and Fripiat, J.J. (eds.), Data handbook for clay materials and other non-metallic minerals, (London : Pergamon, 1980).

218. Gruver, R.M., The precision method of thermal analysis, J. Am. Ceram. Soc., 31, 1948, 323-328.

219. Smykatz-Kloss, W., Differential thermal analysis (New York : Springer-Verlag, 1974), 1-25.

220. Cuthbert, F.L. and Rowland, R.A., Differential thermal analysis of some carbonate minerals, Am. Mineral, 32, 1947, 111-116.

221. Grim, R.E., Differential thermal curves of prepared mixtures of clay minerals, Am. Mineral., 32, 1947, 493-501.

222. Carthew, A.R., The quantitative estimation of kaolinite by differential thermal analysis, Am. Mineral., 40, 1955, 107.

223. Marel can der H.W., Quantitative differential thermal analysis of clays and other minerals, Am. Mineral., 41, 1956, 232-244.

224. Cole, W.F. and Rowland, N.M., An abnormal effect in the differential thermal analysis of clay minerals, Am. Mineral., 46, 1961, 304-312.

225. Wendlandt, W. Wm., Thermal methods of analysis (London : Wiley 1974), 134-193.

226. Blazek, A., Thermal analysis (London : Van Nostrand-Reinhold, 1972), 286 p.

227. Duyckaerts, G., The infra-red analysis of solid solutions, Analyst, 84, 1959, 201-214.

228. Farmer, V.C. and Russel, J.D., The infra-red spectra of layer silicates, Spect. Acta, 20, 1964, 1149-1173.

229. Duke, D.A. and Stephens, J.D., Infra-red investigation of olivine group minerals, Am. Mineral., 49, 1964, 1388-1406.

230. Farmer, V.C., Infra-red spectroscopy in clay mineral studies, Clay Mineral., 7, 1968, 373-386.

231. Kuentzel, L.E., Calcium carbonate as an internal standard for quantitative infra-red analysis, Anal. Chem., 27, 1955, 301.

232. Stubican, V. and Roy, R., Infra-red spectra of layer structure silicates, J. Am. Ceram. Soc., 44, 1961, 625-627.

233. Stubican, V. and Roy, R., Isomorphous substitution and infra-red spectra of the layer lattice silicates, Am. Mineral., 46, 1961, 32-51.

234. Perkin-Elmer, Analytical methods for atomic absorption spectrophotometry, 1971

235. Garrett, H.E. and Walker, A.J., The spectrophotometric determination of silicilic acid in dilute solution, Analyst , 89, 1964, 642-650.

236. Kato, K., Spectrophotometric determination of dissolved silica based on α-molybdosilicilic acid formation, Anal. Chimica Acta, 82, 1976, 401-408.

237. Pearson, M.J., Quantitative clay mineralogical analyses from the bulk chemistry of sedimentary rocks, Clays Clay Minerals, 26, 1978, 423-433.

238. Chatfield, C., Statistics for technology, (London : Chapman and Hall, 1970), 358p.

239. Wiegel, R.L., A quantitative approach to mineral liberation, 7th Int. Mineral. Process. Cong., Arbiter, N. ed. (London : Gordon and Breach,), 3-8.

240. King, R.P., A quantitative model for mineral liberation, J. South African Instn. Min. Metall., 76, 1975, 170-172.

241. Marshall, W.L. and Warakomski, J.M., Amorphous silica solubilities - II. Effect of aqueous salt solutions at 25°C, Geochim. Cosmochim. Acta. 44, 1980, 915-924.

242. Marshall, W.L., Amorphous silica solubilities - III. Activity coefficient relations and predictions of solubility behaviour in salt solutions 0-350°C, Ibid, 925-931.

243. Garrels, R.M. and Christ, C.L., Solutions, minerals and equilibria, (London/Tokyo : Harper and Row/John Weatherhill, 1965), pp.437.

244. Weaver, R.M., Jackson, M.L. and Syers, J.K., Clay mineral stability as related to activities of aluminium, silicon and magnesium in matrix solution of montmorillonite-containing soils, Clay, Clay minerals, 24, 1976, 246-252.

245. Cohen, H.E., Dudeney, A.W.L. and Shaw R., Preparation of active clay minerals by grinding of igneous rocks under hydrothermal conditions at 350-450°C, 13th Int. Mineral Proc. Cong. (Warsaw, 1979) 3, 23-46.

246. Anderson, J.C., Hum, D.M., Neal, B.G. and Whitelaw, J.H., Data and formulae for engineering students (London : Pergamon, 1967) 54p.

247. Helgeson, H.C., Evaluation of irreversible reactions in geochemical processes involving minerals and aqueous solution - I : Thermodynamic relations, Geochim. Cosmochim. Acta, 32, 1968, 853-877.

248. Helgeson, H.C., Garrels, R.M. and Mackenzie, F.T., Evaluation of irreversible reactions in geochemical processes involving minerals and aqueous solutions - II : Applications, Geochim. Cosmochim. Acta, 33, 1969, 455-481.

249. Giggenbach, W.F., Geothermal mineral equilibria, Geochim. Cosmochim. Acta, 45, 1981, 393-410.

250. Tardy, Y. and Garrels, R.M., A method of estimating the Gibbs energies of formation of layer silicates, Geochim. Cosmochim. Acta, 38, 1974, 1101-1116.

251. Barner, H.E. and Scheuerman, R.V., Handbook of thermochemical data for compounds and aqueous species, (New York : Wiley Interscience, 1978), 29-73.

252. Rimstadt, J.D. and Barnes, H.L., The kinetics of silica-water reactions, Geochim. Cosmochim. Acta, 44, 1980, 1683-1699.

253. Weaver, C.E., The distribution and identification of mixed layer clays in sedimentary rocks, Am. Mineral, 41, 1956, 203-221.

254. Bradley, W.F. and Weaver, C.E., A regularly interstratified chlorite-vermiculite clay mineral, Am. Mineral, 41, 1956, 497-504.

255. Farmer, V.C., Fraser, A.R. and Tait, J.M., Characterisation of the chemical structures of natural and synthetic aluminosilicate gels and sols by infra-red spectroscopy, Geochim. Cosmochim. Acta, 43, 1979, 1417-1420.

256. Bauer, J.F. and Sclar, C.B., The "10 Å phase" in the system $MgO-SiO_2-H_2O$, Am Mineral, 66, 1981, 576-585.

257. Siever, R., Woodford, N., Dissolution kinetics and the weathering of mafic minerals, Geochim. Cosmochim. Acta, 43, 1979, 717-724.

258. Crerar, D.A., Axtmann, E.V. and Extmann, R.C., Growth and ripening of silica polymers in aqueous solutions, Geochim. Cosmochim. Acta, 45, 1981, 1259-1266.

259. Okamoto, Go, Okura, T. and Goto, K., Properties of silica in water, Geochim. Cosmochim. Acta, 12, 1957, 123-132.

260. De Jong, B.H.W.S. and Brown, G.E.Jr, Polymerization of silicate and aluminate tetrahedra in glasses, melts and aqueous solutions I. Electronic structure of $H_6Si_2O_7$, H_6AlSiO_7, $H_6Al_2O_7^{2-}$, Geochim. Cosmochim. Acta, 44, 1980, 491-511.

261. Brindley, G.W. and Kao Chih Chun, Formation, composition and properties of hydroxy-Al and hydroxy-Mg montmorillonite, Clays, Clay Minerals, 28, 1980, 435-443.

262. Dibble, W.E. and Tiller, W.A., Non-equilibrium water/rock interactions - I. Model for interface-controlled reactions, Geochim. Cosmochim. Acta, 45, 1981, 79-92.

263. Bircumshaw, L.L., Riddiford, A.C., Transport control in heterogeneous reactions, Quart. Reviews, 6, 1952, 157-185.

264. Kesler, S.B. and Shergold, H.L., Behaviour of oxidized zinc minerals in sodium cyanide solutions, Trans. Instn Min. Metall. (Sect.C : Mineral Process Extr. Metall.) 87, 1978, C50-59.

265. Helgeson, H.C., Kinetics of mass transfer among silicates and aqueous solutions, Geochim. Cosmochim. Acta, 35, 1971, 421-469.

266. Luce, R.W., Bartlett, R.W. and Parks, G.A., Dissolution kinetics of magnesium silicates, Geochim. Cosmochim. Acta, 36, 1972, 35-50.

267. Paces, T., Steady-state kinetics and equilibrium between ground water and granitic rock, Geochim. Cosmochim. Acta, 37, 1973, 2641-2663.

268. Holdren, G.R. Jr and Berner, R.A., Mechanism of feldspar weathering - I. Experimental studies, Geochim. Cosmochim. Acta, 43, 1979, 1161-1171.

269. Fournier, R.O. and Rowe, J.J., The solubility of amorphous silica in water at high temperature and high pressures, Am.Mineral. 62, 1977, 1052-1056.